A Fundamental Study of Electrocatalysts for Acid Mediated Electrochemical-Photoelectrochemical Water Splitting and Hydrogen Fuel Cell

by

Shrinath Dattatray Ghadge
Bachelor of Chemical Engineering (B. Chem),
Institute of Chemical Technology (ICT), Mumbai, India (2015)

Submitted to the Graduate Faculty of the
Swanson School of Engineering in partial fulfillment
of the requirements for the degree of
Doctor of Philosophy

University of Pittsburgh

2021

UNIVERSITY OF PITTSBURGH

SWANSON SCHOOL OF ENGINEERING

This dissertation was presented

by

Shrinath Dattatray Ghadge

It was defended on

March 1, 2021

and approved by

Dr. Robert Enick, Ph.D., Assistant Chair for Research & Covestro Professor, Department of Chemical & Petroleum Engineering

Dr. James McKone, Ph.D., Assistant Professor, Department of Chemical & Petroleum Engineering

Dr. Susheng Tan, Ph.D., Associate Professor, Department of Electrical and Computer Engineering & Petersen Institute of Nanoscience and Engineering

Dr. Moni Datta, Ph.D., Assistant Professor, Department of Bioengineering

Dr. Oleg Velikokhatnyi, Ph.D., Assistant Professor, Department of Bioengineering

Dissertation Director: Dr. Prashant N. Kumta, Ph.D., Edward R. Weidlein Chair Professor, Department of Bioengineering, Department of Chemical and Petroleum Engineering, Department of Mechanical Engineering and Materials Science

A Fundamental Study of Electrocatalysts for Acid Mediated Electrochemical-Photoelectrochemical Water Splitting and Hydrogen Fuel Cell

Shrinath Dattatray Ghadge, Ph.D.

University of Pittsburgh, 2021

Rapid depletion of fossil fuels juxtaposed with deleterious effects of greenhouse gas emissions on global warming have provided a tremendous impetus to develop alternative environmentally-friendly energy sources. Therefore, the development of highly efficient technology for clean energy production is the foremost research priority worldwide. However, the large-scale commercialization of innovative technologies such as proton exchange membrane water electrolyzers (PEMWE) and fuel cell (PEMFC) is majorly thwarted by lack of high performance electrocatalysts for catalyzing the energy-intensive electrochemical oxygen and hydrogen evolution reaction (OER-HER) of PEMWE and oxygen reduction and hydrogen oxidation reaction (ORR-HOR) of PEMFC. Therefore, identification, development, and engineering of novel reduced platinum group metal (PGM) containing as well as PGM-free electrocatalysts (ECs) for oxygen and hydrogen electrocatalysis as well as the development of photoanodes are of paramount importance in fostering commercialization of PEMWE, PEMFC as well as solar-energy driven photoelectrochemical (PEC) water-splitting devices. Accordingly, the present work focuses on the synthesis and fundamental study of OER, ORR, HER, HOR ECs, and photoanodes for PEC water splitting.

Accordingly, employing thermodynamics and kinetics based density functional theory (DFT), the as-synthesized reduced PGM based (Mn,Ir)O_2:F thin films/nanorods and (Sn,Ir)O_2:F nanotubes (NTs) and PGM-free (Mn, Nb)O_2:F NTs and $Cu_{1.5}Mn_{1.5}O_4$ including $Cu_{1.5}Mn_{1.5}O_4$:F display

remarkably higher electrochemical performance than benchmark IrO_2 and many PGM/PGM-free ECs for OER in PEMWE. Furthermore, as-synthesized PGM-free Co and S containing Ni_2P [$(Ni_{0.95}Co_{0.05})_2P$:S] system exhibits excellent HER performance comparable to benchmark Pt/C for PEMWE.

Similarly, for PEMFC, a PGM-free spinel $Cu_{1.5}Mn_{1.5}O_4$, $Cu_{1.5}Mn_{1.5}O_4$:F and ultra-low PGM based Pt doped titanium silicide [$(Ti_{1-x}Pt_x)_5Si_3$] ECs are engineered for ORR and HOR, respectively. These studies provide fundamental insight into influence of ordered-disordered structures and rearrangement of oxidation state of active species and their combined synergistic effects on the electrochemical performance (ORR) for PEMFC. In the PEC water splitting area, in order to enhance the optoelectronic properties and PEC performance, as-developed $(W_{0.98}Mo_{0.02})O_3$-$(Sn_{0.95}Nb_{0.05})O_2$:N bilayer photoanode reveals an excellent performance with promising solar-to-hydrogen efficiency (STH) for PEC water splitting. This dissertation provides a detailed account of the fundamental study conducted into the materials identification, synthesis, development, and physicochemical- electrochemical characterizations ably supported by DFT studies.

Table of Contents

List of Tables

List of Figures

Acknowledgements

I would like to thank my Ph.D. supervisor Dr. Prashant N. Kumta for his mentorship and giving me an opportunity to be a part of his research group. I’m grateful for his support and guidance that motivated me throughout this project. I would also like to thank the members of my dissertation committee – Dr. Robert Enick, Dr. James McKone, Dr. Susheng Tan, Dr. Moni Datta, and Dr. Oleg Velikokhatnyi for their critical feedback, valuable suggestions, and encouragement during the course of my doctoral program.

I would take this opportunity to express my gratitude to the faculty and administrative staff of Department Chemical Engineering as well as technicians at the Nanoscale Fabrication and Characterization Facility (NFCF) for their continuous assistance and guidance during my academic and Ph.D. journey. I would also like to acknowledge the different funding agencies – National Science Foundation (NSF), U.S. Department of Energy (DOE), and Center for Complex Engineered Multifunctional Materials (CCEMM) for sponsoring the present research.

Finally, I would like to express my immense gratitude towards my family and friends, especially my parents – Prof. Dattatray and Ms. Pratibha Ghadge, sister – Ms. Tejashri Ghadge, and grandparents – Mr. Sampatrao and Ms. Gangubai Ghadge for being there, their unconditional love, and providing me a spiritual and emotional support throughout my Ph.D. journey.

Sincerely,

Shrinath Ghadge.

1.0 Introduction

"Water will one day be employed as a fuel, that hydrogen and oxygen that constitute it, used singly or together, will furnish an inexhaustible source of heat and light, of an intensity of which coal is not capable. Someday the coal rooms of steamers and the tenders of locomotives will, instead of coal, be stored with these two condensed gases, which will burn in the furnaces with enormous caloric power. I believe, that when the deposits of coal are exhausted, we shall heat and warm ourselves with water. Water will be the coal of the future."

Jules Verne (The Mysterious Island, 1984), French Novelist and Poet

The ever-increasing global population, rapid depletion of fossil fuels, and upsurge of carbon footprint causing perilous impacts on the global climate are the prime incentives for the pursuit of renewable, nontoxic, and non-carbonaceous clean energy sources. At present fossil fuels play dominant role in offering the major portion of energy to meet the ever-increasing global energy demand [~12,000 Million Tonne of oil equivalent (Mtoe) in 2019] [1, 2]. However, the excessive consumption of fossil fuels has triggered harmful effects on the environment due to the increased level of greenhouse gas pollutants in the atmosphere. In the year 2019, the conventional and dominant carbon-based energy sources such as coal, oil, and natural gas constituted ~ 85% of the total global energy consumption whereas renewable energy sources such as solar and wind represent only ~ 5% of the energy consumption. Such massive energy consumption from fossil fuels is accountable for increasing carbon dioxide (CO_2) emissions and thus, global warming. For example, in the last two decades, ~75% of the global CO_2 emissions are attributed to the exploitation of coal, oil, and natural gas. **Figure 1-1** displays territorial CO_2 emissions ($MtCO_2$)

with a global $MtCO_2$ of ~ 36,441 in 2019 (http://www.globalcarbonatlas.org). The larger circle represents higher CO_2 emissions. As can be seen from the country-wise distribution of global CO_2 emissions, China, United States, India, and Russia are the major CO_2 emitters with ~ 10175, 5285, 2616, and 1678 Mt of CO_2 emissions, respectively in 2019.

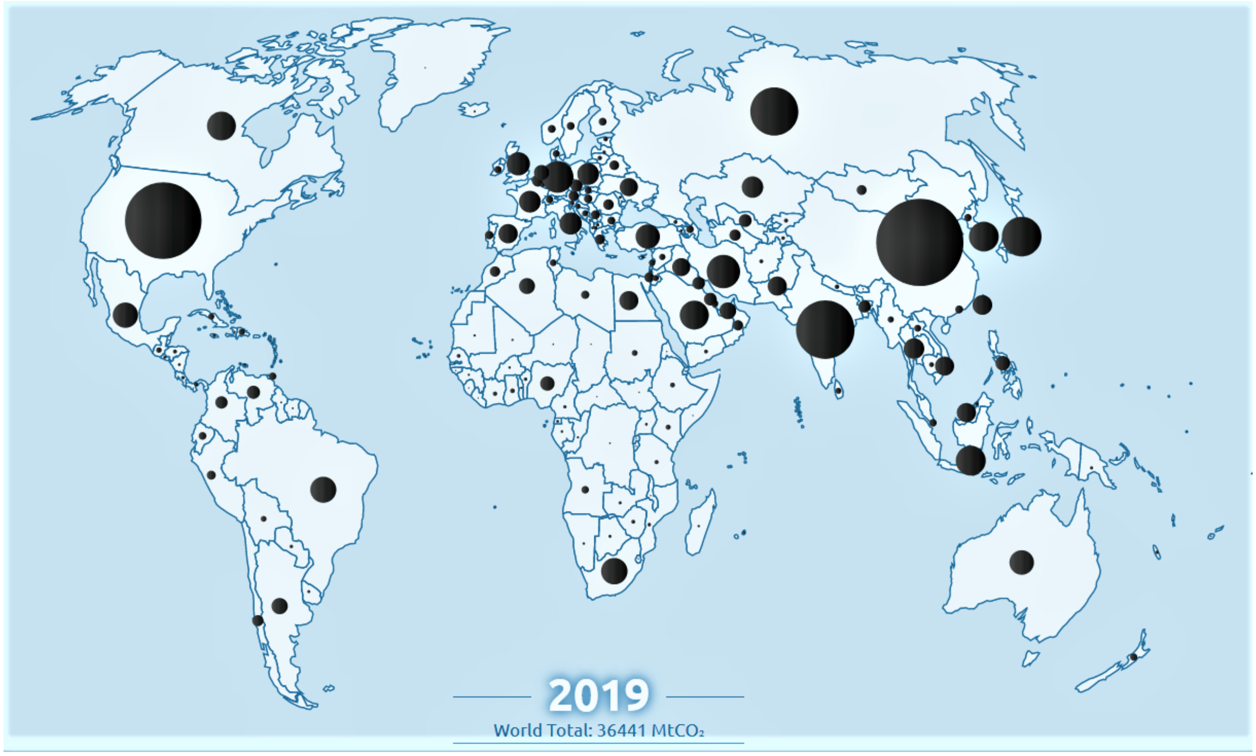

Figure 1-1 Global CO_2 emission in 2019

(http://www.globalcarbonatlas.org)

In order to fulfill the colossal global energy demand which is expected to be ~ 20,000 Mtoe by 2050[3] and to simultaneously reduce our reliance on the carbon-based conventional energy sources and thus, to effectively lower the greenhouse gas (GHG) emissions, identification of an alternate novel, clean, sustainable, and renewable energy systems; capable of meeting the future global energy demand is the need of an hour. Accordingly, in such circumstances, carbon-free renewable energy sources (solar and wind) are rapidly penetrating the energy market. Amongst the various types of renewable energy sources (solar, wind, hydro, tidal, geothermal, biomass, etc.), solar energy is one the most promising energy sources. The sun delivers massive solar energy of ~ 173,000 terawatts (TW, 10^{12}) per year to the earth’s surface, out of which ~ 30 % is reflected by the clouds and earth's surface, and thus, retaining ~ 120, 000 TW power on the surface of the earth [4]. Comparing the global power consumption of ~17.92 TW in 2018 to the enormous ~ 120, 000 TW solar energy, sun unequivocally shows the great promise for a dominant energy source. In addition, it is estimated that the wind has the potential to deliver ~ 25 to 70 TW, which makes wind energy another promising candidate. Therefore, owing to such beneficial attributes of solar and wind energy, it is anticipated that renewable energy sources will fulfill ~16 % of the global energy demand in coming decades.

Nonetheless, the sporadic nature (i.e., variability) in terms of the output power of these renewable energy sources due to the weather fluctuation suggests the unpredictability and unreliability of solar and wind energy approaches. In order to address these issues, there is a critical need for the energy conversation and storage with minimized losses and easy accessibility. Amongst various energy storage technologies including electrical, mechanical, chemical, and thermal, the electrochemistry driven ‘Hydrogen fuel cell’- is a chemical energy conversion technology has garnered increased interest in the last decade.

1.1 The Critical Need for an Energy Revolution

Hydrogen (H_2), a non-carbonaceous high-efficiency fuel, possessing higher energy density than petroleum-based energy sources has generated significant attention in recent years (**Table 1-1**), demonstrating a promise to substitute the finite fossil fuels, particularly in the transportation and electricity storage sectors (**Figure 1-2**)[5]. Although hydrogen is the most abundant element in the universe, it unfortunately does not exist in a pure state in the nature. There are various approaches for the large scale (~ 96%) hydrogen production such as steam reforming of natural gas, partial oxidation of hydrocarbons, coal gasification whereas currently only ~ 4% hydrogen is produced from the water electrolysis[5].

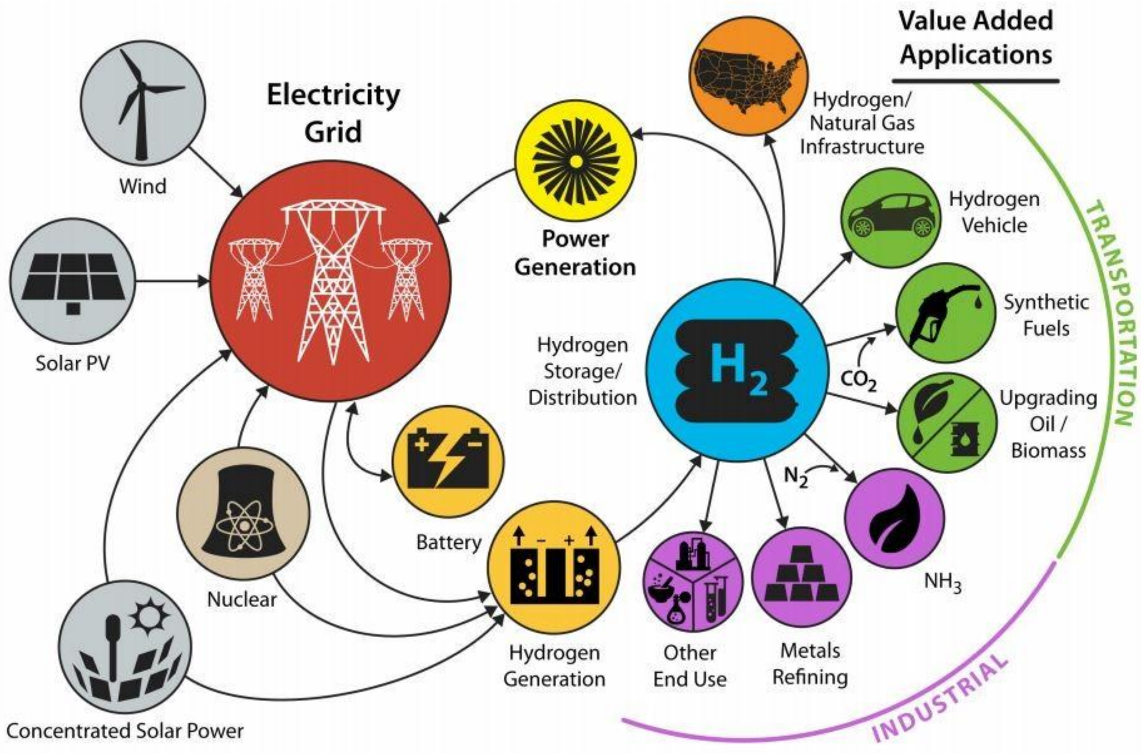

Figure 1-2 Overview of the hydrogen economy

Reprinted with permission from ref. [6] Copyright © 2019, Elsevier

The various hydrogen production processes are summarized below:

- Steam reforming of natural gas:

$$CH_4 + H_2O \rightarrow CO + 3H_2$$

$$CO + H_2O \rightarrow CO_2 + H_2$$

- Partial oxidation of hydrocarbons:

$$C_nH_m + 0.5n\ O_2 \rightarrow nCO + 0.5mH_2$$

- Coal gasification:

$3C\ (coal) + O_2 + H_2O \rightarrow 3CO + H_2$

- Water electrolysis:

$H_2O \rightarrow 2H_2 + 0.5O_2$

Although, natural gas steam reforming, hydrocarbon oxidation, and coal gasification are the predominant hydrogen production approaches; producing ~ 70 million tons of H_2 per year, these conventional approaches suffer from various disadvantages such as a requirement of high operating temperature (700^{o}C-1000^{o}C), production undesired greenhouse pollutants (CO, CO_2), low purity of hydrogen, a requirement of hydrogen purifications - resulting in additional manufacturing costs. The hydrogen produced from these approaches is typically identified as grey, brown, or blue hydrogen (**Figure 1-3**) (https://knowledge.energyinst.org/collections/hydrogen). Typically, pressure-swing adsorption, cryogenic distillation, and membrane technologies are utilized for the hydrogen purification. However, these methods are energy-intensive and do not produce ultra-high purity (~99.99%) hydrogen. Due to the high energy requirements and need for hydrogen separation from product mixtures, these technologies require high capital investments, ultimately making these conventional hydrogen production approaches unsustainable and less efficient. Currently, the global hydrogen production of ~ 70 million tons per year results in CO_2 emissions of ~ 830 million tons per year. In addition, these conventional methods do not relieve our reliance on the finite and rapidly diminishing fossil fuels or reduce their pollutants, and thus, ultimately, not contributing to the formation of a carbon-balanced or ‘green energy’ matrix. Therefore, it is highly crucial to engineering a technology for the production of efficient hydrogen, preferably utilizing a clean source (i.e., low carbon footprint) at a low operating temperature without producing any GHG emissions and generating any toxic/corrosive byproducts.

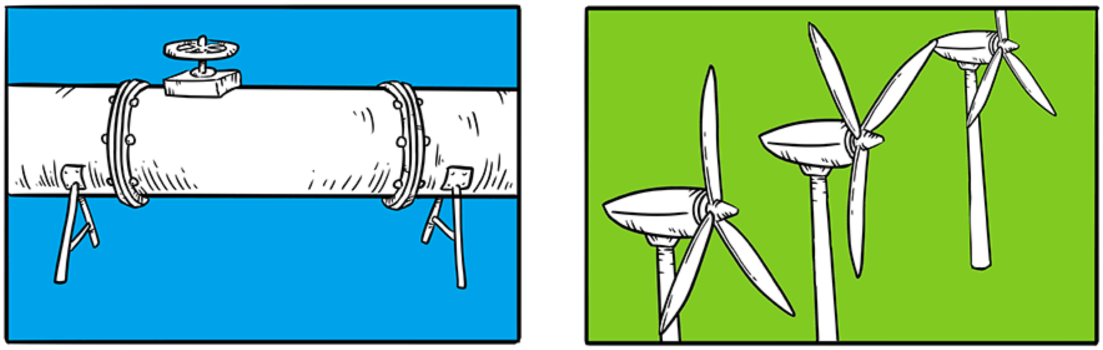

Blue hydrogen

Made from natural gas, CO_2 emissions captured and stored

Green hydrogen

Made from renewable electricity, no CO_2 emitted

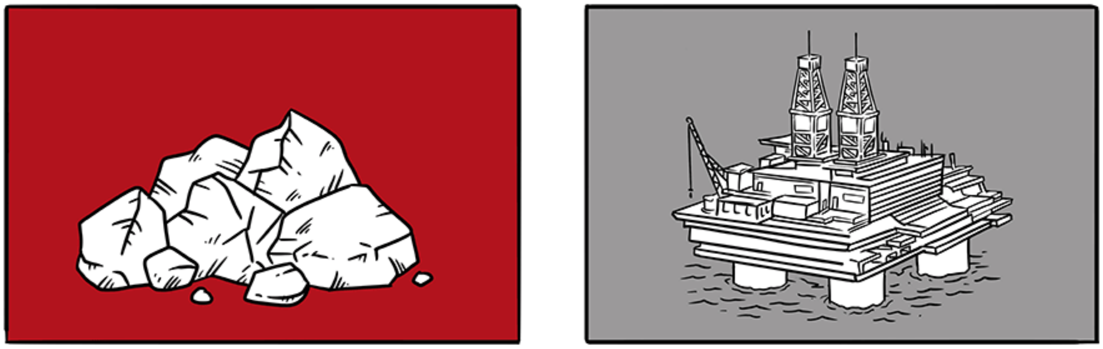

Brown hydrogen

Made from coal, CO_2 emitted into the atmosphere

Grey hydrogen

Made from natural gas, CO_2 emitted into the atmosphere

Figure 1-3 Different types of hydrogen

Table 1-1 Energy content of different fuel sources

Fuel Source	**Energy Content (MJ/kg)**
Hydrogen	143
Methane	55.6
Natural gas	54.4
LPG Propane	49.6
LPG Butane	49.1
Automotive Gasoline (Petrol)	46.4
Automotive Diesel	45.6
Gasohol	43.54
Jet Fuel	43
Ammonia	22.5
Ethanol	29.6
Methanol	19.7
Coke	27
Coal	21
Dry Wood	16.2

1.2 Water Electrolysis

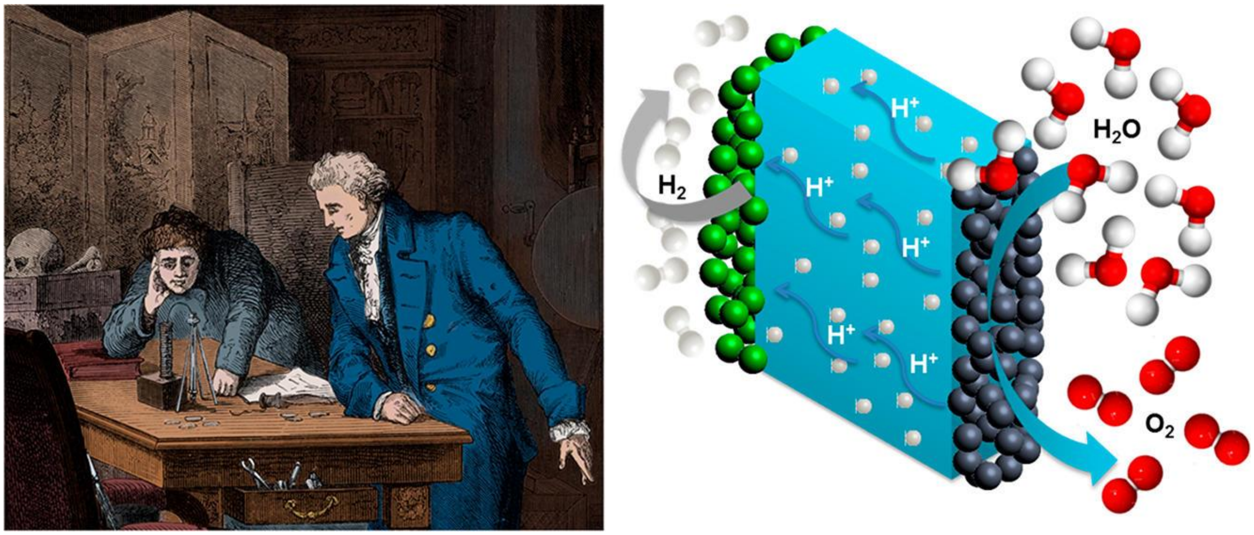

Figure 1-4 William Nicholson and Anthony Carlisle observing water electrolysis (London, May 1800). They took a small tube, mounted vertically, filled with water then sealed, into which at either end was inserted a platinum wire connected to one of the two terminals of a voltaic pile. As the tips of the wires were gradually advanced toward each other they observed that a stream of bubbles was produced from each tip, one found to be of oxygen, the other hydrogen. Figure supplied by Science Source. On the right, a scheme of a water electrolyzer where on the anodic electrode (gray spheres) water is oxidized to oxygen and on the cathodic electrode (green spheres) hydrogen evolution takes place.

Reprinted with permission from Ref. [7](Copyright © 2018, American Chemical Society)

One the most promising approaches for clean or green hydrogen production is the electricity induced water electrolysis/splitting. The water electrolysis technology can be categorized into Alkaline Electrolysis Cell (AEC), Proton Exchange Membrane Electrolysis cell (PEMEC), and Solid Oxide Electrolysis Cell (SOEC) [8-12]. The electrolysis technology is less efficient than a direct chemical path but it offers virtually no pollution and toxic byproducts with zero carbon footprint if the electric current is generated using renewable energy such as wind, solar, geothermal, and hydropower[9, 11, 13-20]. **Figure 1-5** shows the schematics of AEC, PEMEC, and SOEC systems.

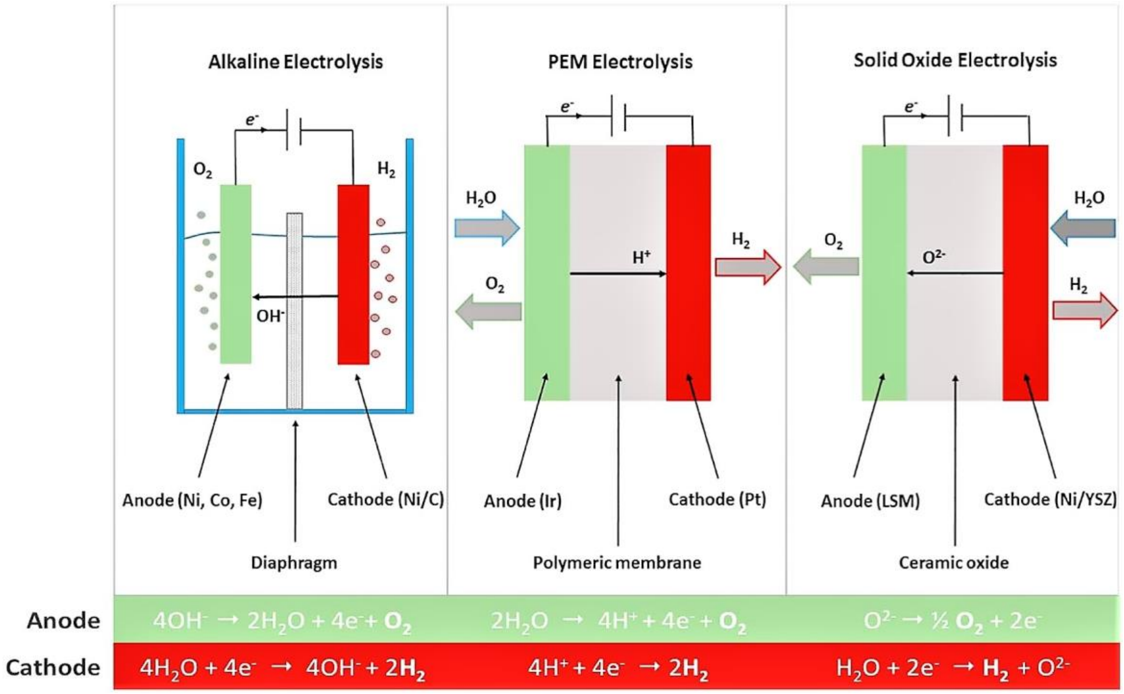

Figure 1-5 Schematics of Alkaline, PEM, and Solid oxide electrolyzer systems

Reprinted with permission from Ref.[21] (Copyright © 2017, Elsevier)

1.2.1 Alkaline Electrolysis

Among three major types of electrolysis technologies, alkaline water electrolysis is the most mature, market available, and well-understood technology which has been commercially available for decades (since 1920) and has shown economic competitiveness in comparison to the conventional hydrogen production approaches such as coal gasification and steam reforming. In alkaline electrolysis cell (AEC), an aqueous alkaline solution (KOH or NaOH) is used as the electrolyte. The AEC comprises two electrodes separated by a gas-tight diaphragm, which is immersed in a high concentration (25-30 wt.%) aqueous KOH electrolyte, selectively allowing the hydroxyl ions to permeate through it, while limiting the mixing of the evolved gases (O_2 and H_2). The AEC is typically operated at low temperatures i.e., ranging from 60°C and 80°C. The half-reactions involved at the anode (oxidation, oxygen evolution reaction, OER) and cathode (reduction, hydrogen evolution reaction, HER) compartments of AEC are -

Anode (OER): $2OH^-_{(aq)} \rightarrow H_2O_{(l)} + 2e^- + 0.5O_{2\,(g)}$

Cathode (HER): $2H_2O_{(l)} + 2e^- \rightarrow 2OH^-_{(aq)} + H_{2\,(g)}$

Overall Reaction: $H_2O_{(l)} \rightarrow H_{2\,(g)} + 0.5O_{2\,(g)}$

In general, state-of-the-art Pt/C as well as non-precious or platinum group metal (PGM)-free electrocatalysts (ECs) such as Ni, Ni-Co, Ni-Mo alloys are utilized for the anodic and cathodic reaction of AEC. As tabulated in **Table 1-2**, although AEC is a mature, commercially available, and well-known technology for its long lifetime and relatively low capital cost, the major drawbacks include: lower current density, high ohmic losses, low operating pressure, low hydrogen purity, corrosive electrolyte, higher hydrogen crossover, etc. In addition, one of the major problems with AEC are that it takes ~30-60 min to restart the system following its shutdown and thus, requiring continuous operation which increases the maintenance costs. The current research in AEC arena has been focused on increasing current density via high performance ECs and optimization of AEC, especially with respect to efficiency and total investment [15, 22, 23].

1.2.2 PEM Electrolysis

Polymer Electrolyte Membrane or Proton Exchange Membrane-based Electrolysis Cell (PEMEC) system is based on the solid polymer electrolyte (SPE) concept - wherein a solid sulfonated polystyrene membrane (Nafion) is used as an electrolyte. In order to overcome the drawbacks of the AEC system, the PEMEC technology was first introduced by General Electric (GE) in the 1960s. In comparison to AEC, PEMEC is a relatively novel technology, with the first commercial PEM electrolyzer available for purchase in 1978. As PEMEC employs the immobilized SPE membrane, the system is highly compact with a strong/resistant structure, allowing the high pressure (~200 bar) operation of PEMEC. In such a case, hydrogen can be directly delivered at high pressure to end-user, thus less energy is required for further compression and hydrogen storage. The Nafion membrane exhibits very high protonic conductivity and low crossover rates and thus, PEMEC offers various advantages such as higher current density, low ohmic losses, higher flexibility, faster start-up time, and better coupling with dynamic and intermittent systems. Moreover, PEMEC offers ultra-high purity hydrogen (99.99%), requiring practically no need for further gas purification and thus, circumventing gas purification/separation costs. The OER and HER reactions of PEMEC are given below -

Anode (OER): $2H_2O_{(l)} \rightarrow O_{2\,(g)} + 4H^+_{(aq)} + 4e^-$

Cathode (HER): $4H^+ + 4e^- \rightarrow 2H_{2\,(g)}$

Overall Reaction: $2H_2O_{(l)} \rightarrow 2H_{2\,(g)} + O_{2\,(g)}$

Nonetheless, owing to the highly corrosive acidic environment (pH ~ 0.2) and high working potential (up to 2 V), the anode components, not only electrocatalysts but also current collector and separator plates, require robust and corrosion-resistant materials that can withstand the harsh operating condition of OER. The PEMEC typically involves use of PGM containing, expensive, and environmentally scarce (0.001-0.0003 ppm in earth's crust) ECs such as IrO_2, RuO_2, Pt which exhibit sufficient electrocatalytic activity and durability for the PEM water splitting. The requirement of such expensive ECs and fluorinated membrane materials, high system complexity due to high pressure operation and water purity requirements, and shorter lifetime as compared to AEC are the major bottlenecks in the successful and wide-scale commercialization of PEMEC. Therefore, the current research efforts in this area are targeted at reducing electrocatalyst and system capital costs via less expensive, earth-abundant, reduced PGM as well as PGM-free highly active and robust electrocatalyst materials, lowering the system complexity to enable system scale-up and engineering more sophisticated stack manufacturing processes [24].

1.2.3 Solid Oxide Electrolysis

Solid Oxide Electrolysis Cell (SOEC) (also known as high temperature electrolysis) is the recently developed (1980) electrolysis technology which is still in the laboratory stage. SOEC involves the use of thermally and chemically stable solid ion-conducting ceramics such as Y_2O_3 doped ZrO_2 as the electrolyte, which is highly conductive for oxygen ions (charge carrier) at high temperatures ($1000^{o}C$). The OER and HER reactions of SOEC are given below-

Anode (OER): $2O^{2-}{}_{(g)} \rightarrow O_{2\,(g)} + 4e^-$

Cathode (HER): $2H_2O_{(g)} + 4e^- \rightarrow 2H_{2\,(g)} + 2O^{2-}{}_{(g)}$

Overall Reaction: $2H_2O_{(g)} \rightarrow 2H_{2\,(g)} + O_{2\,(g)}$

Since SOEC is operated at a significantly higher temperatures than AEC and PEMEC, the equilibrium cell voltage of SOEC is relatively lower (0.7-1.5 V). Accordingly, due to less electricity requirement for water splitting operation, SOECs exhibit higher electrical efficiencies

(~90%). However, due to the high operating temperatures, SOECs suffer from the fast material degradation and lower long-term stability. In addition, such high-temperature operation results in the production of hydrogen along with steam, and thus, demanding additional processing for the hydrogen separation; thereby further increasing the processing costs. Also, SOEC systems are unstable against fluctuating and intermittent power sources which limits the coupling of SOEC with renewable energy sources. Accordingly, current research in SOEC focuses on the development of thermally and chemically robust and cost-efficient materials as well as design and production of large size (multi-MW) systems. **Table 1-2** summarizes the key characteristics of these three electrolysis technologies [24].

Table 1-2 Comparison of different water electrolysis technologies

Electrolysis Technology	**PEM Electrolysis**	**Alkaline Electrolysis**	**Solid Oxide Electrolysis**
Typical Electrolyte	H_2SO_4, Polymer membrane (e.g., Nafion)	Alkaline solution (KOH)	Yttria stabilized Zirconia (Y_2O_3/ZrO_2)
Charge carrier	H_3O^+/H^+	OH^-	O_2^-
Anode	RuO_2, IrO_2	Ni, Ni-Co alloys	LSM/YSZ
Cathode	Pt, Pt-Pd	Ni, Ni-Mo alloys	Ni/YSZ
Cell voltage (V)	1.8-2.2	1.8-2.4	0.7-1.5
Current density (Acm^{-2})	0.6-2	0.2-0.7	0.3-2
Cell area (m^2)	<0.3	<4	<0.01
Operating temperature (ºC)	50-80	60-80	650-1000

Table 1-2 (continued)

Operating pressure (bar)	<200	<30	<25
Energy consumption ($kWhkg^{-1}$ H_2)	47–73	57–73	-
Production rate ($m^3_{H2}h^{-1}$)	<40	<760	<40
System response	Milliseconds	Seconds	Seconds
Cold-start time (min.)	<20	<60	<60
Stack lifetime (h)	20,000-60,000	60,000-90,000	10,000
State of development	Commercial	Commercial	Laboratory
System efficiency (%)	45-80	50-60	85-90
Gas purity (%)	99.99	99.5	99
Capital cost ($\$\ kW_{el}^{-1}$) (electrical power consumption)	2300-2900	1200-1400	2500
Advantages	Higher current density, efficiency, pressure, gas purity	Relative low cost, vast materials available, available for large plant sizes	High efficiency, working Pressure, non-noble, electrocatalysts, integration of waste heat possible
Disadvantages	Expensive, fast degradation, limited choices of stable electrocatalysts	Limited current density, low gas purity, high ohmic losses, low operational pressure	Poor durability, expensive, laboratory stage, bulky system design

1.3 Fuel Cells

In addition to the water electrolyzers, fuel cells (FCs) have been attracting significant interest in clean and efficient energy applications for the past several decades. A FC is a galvanic cell that efficiently converts chemical energy (H_2 and O_2 gases) to electrical energy and useful heat. Fundamentally, FC works on a reverse principle of water electrolyzer cell (EC) [$2H_2O \rightleftharpoons O_2 + 2H_2$]. In water EC, the oxygen evolution reaction (OER) takes place at the anode and the hydrogen evolution reaction (HER) takes at the cathode. Inversely in a FC, the hydrogen oxidation reaction (HOR) takes occurs at the anode and the oxygen reduction reaction (ORR) occurs at the cathode (**Figure 1-6**).

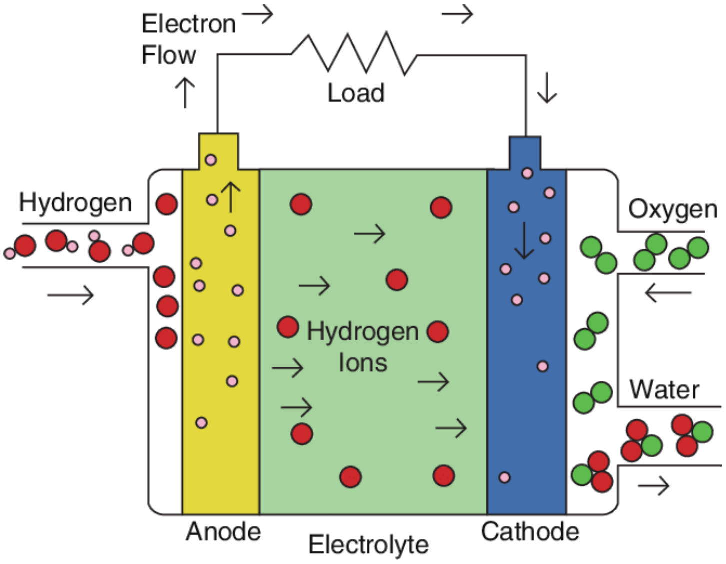

Figure 1-6 Schematic of a PEM fuel cell

Adapted from www.greencarcongress.com

Figure 1-6 depicts the schematic of a hydrogen fuel cell (PEMFC) which consists of two electrodes (anode and cathode) separated by an electrolyte (proton exchange membrane). At anode (Pt/C), the input gas (H_2) gets oxidized (HOR) into protons and electrons. The produced electrons follow through an external circuit to the cathode, whereas the protons get conducted through the electrolyte. This flow of electrons through the external circuit is the produced electricity that can be used to do work. At cathode (Pt/C), the protons, electrons, and reactant O_2 combine (ORR) to produce H_2O as a product.

Anode (HOR): $H_2 \rightarrow 2H^+ + 2e^-$, $E^\circ = 0.0$ V

Cathode (ORR): $O_2 + 4H^+ + 4e^- \rightarrow 2H_2O$, $E^\circ = 1.23$ V

Overall: $2H_2 + O_2 \rightarrow 2H_2O$

The power produced by FC depends on various factors such as the type of FC, size, electrocatalyst materials, operating temperature, and the pressure at which gases are supplied. Typically, a single FC generates approximately 1 volt or less, which is indeed not a significant amount. Thus, in order to increase the amount of electricity, generally, individual FCs are combined in a series to form the FC stack. Such interesting feature of 'scalability' makes FCs ideal for a wide variety of applications, such as laptop/computers (50-100 Watts), homes (1-5kW), vehicles (50-125 kW), and central power generation (1-200 MW or more)[25].

Owing to their higher efficiency (~2 to 3-fold higher than traditional combustion technologies) and pollution-free energy production approach, the hydrogen-powered FCs have gained immense attention for the various energy applications.

In general, FCs are classified primarily based on the electrolyte used. Accordingly, there are six different types of FCs, depending on the electrolyte type. These are: solid oxide fuel cell (SOFC), molten carbonate fuel cell (MCFC), phosphoric acid fuel cell (PAFC), direct methanol fuel cell (DMFC), polymer electrolyte membrane fuel cell (PEMFC), and alkaline fuel cells (AFC), which exhibit different chemical reactions occurring at the anode and cathode of FC. **Figure 1-7** depicts the different types of FCs and Error! Reference source not found. summarizes their key characteristics[21].

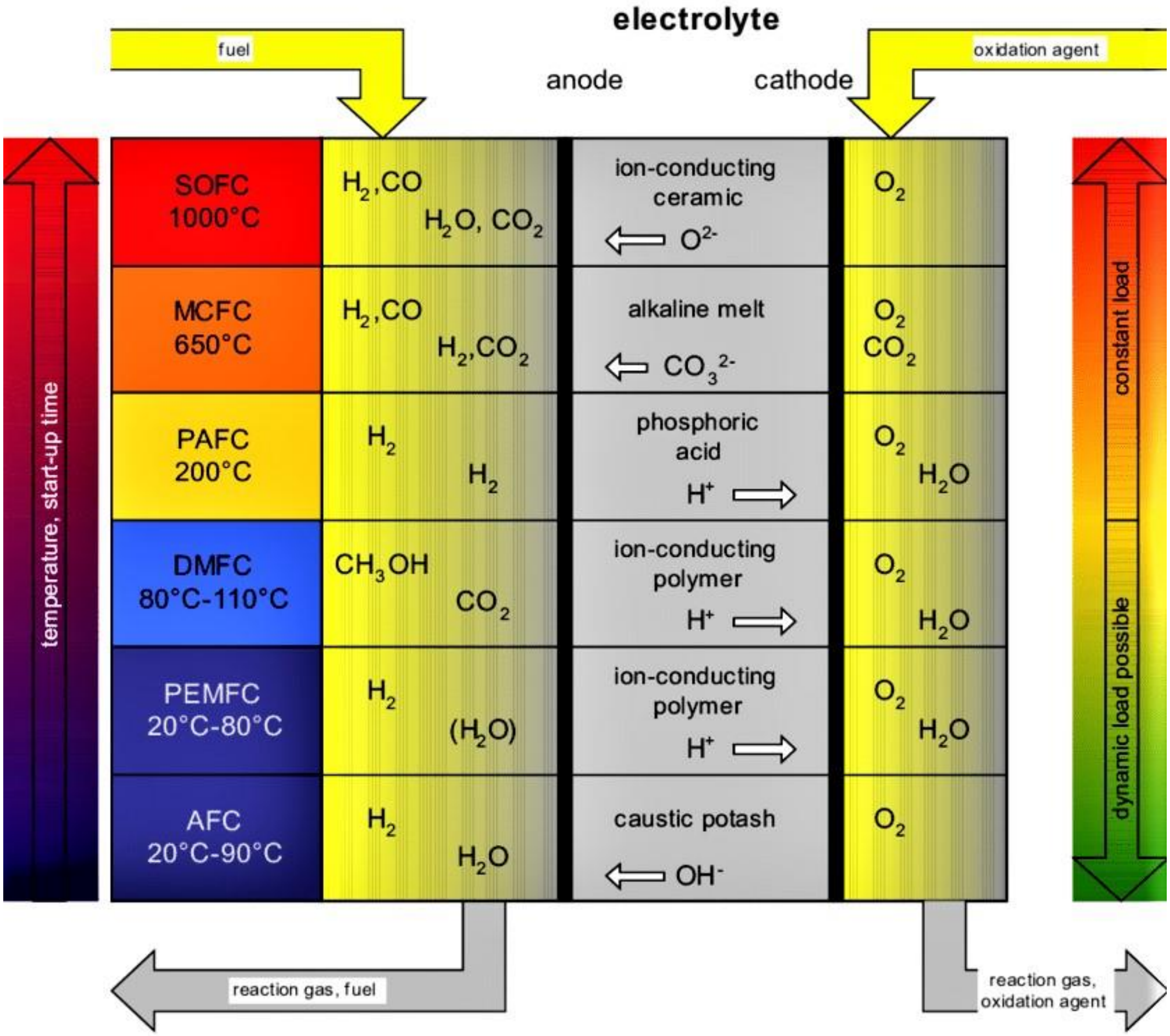

Figure 1-7 Different types of fuel cells

Reprinted with permission from Ref.[21] (Copyright © 2017, Elsevier)

Table 1-3 Different types of fuel cells

Generation	**1st**		**2nd**	**3rd**		
FC type	**AFC**	**PAFC**	**MCFC**	**PEMFC**	**DMFC**	**SOFC**
Electrolyte	OH^{-1} (In water)	H^+ (In water)	CO_3^{-2} (Molten)	H^+ (In polymer)	H^+ (In polymer)	O_2- (In oxide)
Fuel	H_2	H_2	H_2	H_2	CH_3OH	H_2, CH_4
Oxidant	Air	Air	Air+CO_2	Air	Air	Air
Efficiency (%)	>40	>40	45-60	50-60	40-50	50-60
System output	10–100	50kW-1MW	<1 MW	<250kW		5kW-3MW
Cathode	Pt	Pt	NiO	Pt	Pt	$La_ySr_xMnO_3$
Anode	Pt	Pt	Ni-Cr/Al	Pt	Pt-Ru	Ni/YSZ
Op. temperature (ºC)	50-200	220	650	50-100	50-100	600-900
Applications	Military, space	Distributed generation	Electric utility	Backup/portable power, vehicles	Backup/portable power	Auxiliary, electric utility

1.4 Photoelectrochemical Water Electrolysis (PECWE)

Among various hydrogen production approaches, the solar energy driven water splitting, also known as photoelectrochemical (PEC) water splitting is regarded as one of the most promising and advanced technologies based on the grounds of its potential for producing hydrogen by utilizing solar energy in an environmentally friendly manner without producing any greenhouse gas emissions.

The schematic of the PEC water splitting using H-type cell is illustrated in **Figure 1-8**.

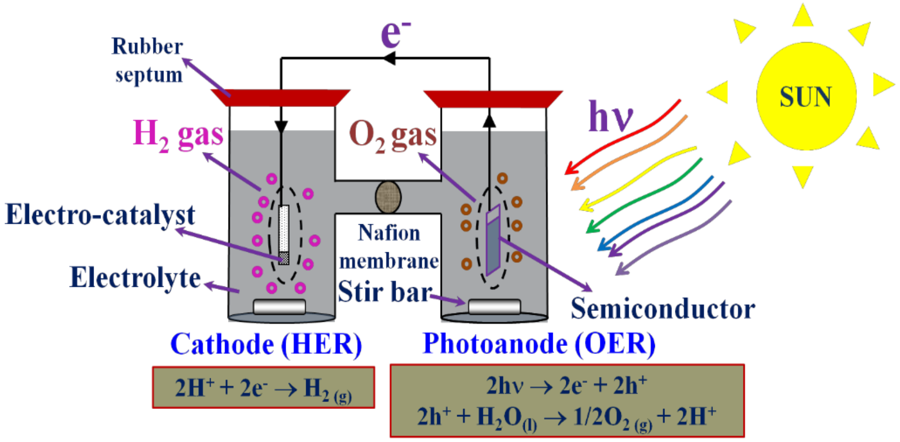

Figure 1-8 Schematic diagram of PEC water splitting in H-type cell

As depicted in **Figure 1-8**, the PEC cell consists of the photoanode and cathode, separated by Nafion membrane. The steps involved PEC water splitting are listed below:

1. Absorption of solar energy by photoanode, which results in the excitation of the electrons from the valence band to the conduction band leaving behind holes in valence band of semiconductor material.
2. Separation of the photogenerated electron-hole (e^--h^+) pairs at the semiconductor-electrolyte interface.
3. Migration of the photogenerated electrons to the cathode.
4. Hydrogen evolution reaction (HER) at the cathode and oxygen evolution reaction (OER) at the photoanode.

In order to design the efficient photoelectrocatalysts, several factors should be taken into considerations:

- Appropriate band structure such that the reduction (0 V *vs* NHE) and oxidation potential of water (1.23 V *vs* NHE) lie within the band gap of the semiconductor

- Suitable band gap with superior light absorption in the visible region (1.23 eV < Eg < 3 eV)
- Superior separation, transport, and collection of the photogenerated carriers ($e^- - h^+$ pairs)
- High solar-to-hydrogen efficiency (SHE) [SHE of 10% is the target set up by the US Department of Energy (DOE) for H_2 production from PEC water splitting]
- Superior long term photoelectrochemical stability (> 24 h) in the electrolyte solution under illumination.

2.0 Theory and Background

2.1 Water Electrolysis

2.1.1 The Overall Reactions in Water Splitting

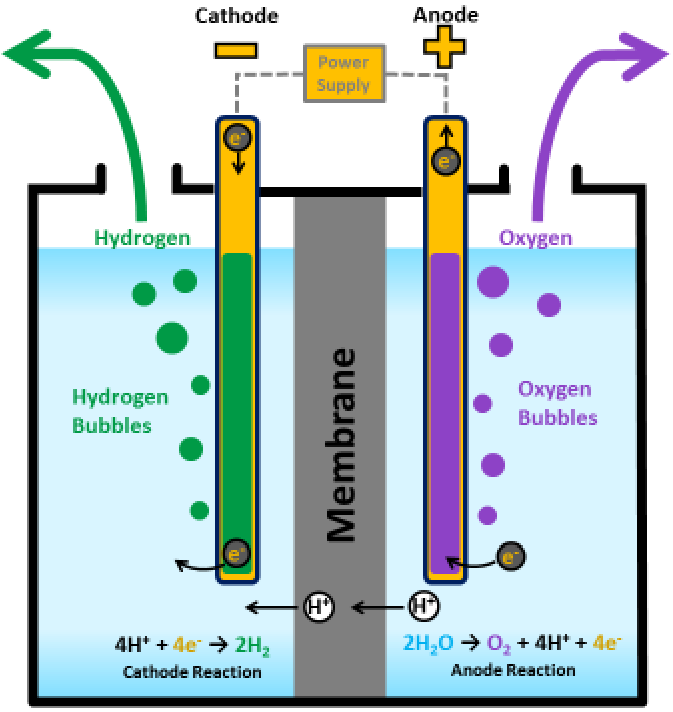

Figure 2-1 Schematic diagram of PEM water electrolyzer

Adapted from https://www.energy.gov/eere/fuelcells/hydrogen-production-electrolysis

Figure 2-1 shows the typical configuration of PEM electrolyzer with anodic oxygen evolution reaction (OER) and cathodic hydrogen evolution reaction (HER). Under the working mode, ultra-pure water is fed to its anode side which gets split into oxygen and protons on the electrocatalyst surface. Then the as-formed solvated protons migrate through the PEM to the cathode side, where they react with the electrons provided by the external DC power and are reduced to molecular hydrogen. The reactions involved in the PEM electrolyzer are given below:

Anode (oxidation): $2H_2O_{(l)} \rightarrow O_{2\,(g)} + 4H^+_{(aq)} + 4e^-$, $E^o_{ox} = 1.23V$ (OER)

Cathode (reduction): $4H^+ + 4e^- \rightarrow 2H_{2\,(g)}$, $E^o_{red} = 0V$ (HER)

Overall Reaction: $2H_2O_{(l)} \rightarrow 2H_{2\,(g)} + O_{2\,(g)}$, $E^o_{cell} = 1.23V$

According to the Nernst equation under standard conditions (25 °C, 1 atm), the thermodynamic voltage of the PEM electrolyzer is estimated to be 1.23 V with respect to the reversible hydrogen electrode (RHE), regardless of the type of electrolyte used. In practice, for the water splitting process, owing to the high activation energy, ohmic losses, and sluggish OER kinetics, a greater applied potential (higher than 1.23 V) is required. The difference between additional applied potential and thermodynamic potential (1.23 V) is termed as an overpotential (η). The practical voltage of electrolysis can be expressed as $V = \eta_a + |\eta_c| + iR$, where iR designates the ohmic potential drop owing to the resistance of the ionic electrolyte. η_a and η_c represent the overpotential applied on the anode and the cathode, respectively, to activate the OER and HER, respectively. This overpotential is significantly affected by various factors based on the practical conditions, such as resistance and activation energy of electrode materials, electrolyte diffusion rate, and bubble evolution and desorption, etc. Therefore, on the basis of various theoretical as well as experimental studies, in order to understand the underlying reaction mechanisms, to reduce the energy loss, accelerate the reaction kinetics, and finally promote the total cell efficiency, the rational design of highly efficient, active, and durable OER and HER electrocatalysts is the current focus of the electrolysis research community.

2.1.2 Oxygen Evolution Reaction (OER)

2.1.2.1 OER Mechanism

OER is one of the most researched electrochemical processes. Although copious research efforts have been dedicated for the study of OER electrocatalysis, its reaction mechanism is still not widely understood and very difficult to interpret, which is attributed to the following reasons[26]:

1. High energy reaction intermediates and complex pathways of high activation energy making the reaction very sensitive to the electrode surface properties.
2. At the potential ranges required, the electrode surface can go through dramatic changes.
3. As the electrodes change, the kinetics may also be time dependent.

Accordingly, as shown below, there are many proposed reaction mechanisms for the OER.

Table 2-1 Reaction mechanisms for the OER

Mechanism No 1: Bockris path (Electrochemical oxide path)	Mechanism No 2: Bockris path (Oxide path)
(a) $S* + H_2O \rightarrow S\text{-}OH + H^+ + e^-$ (b) $S\text{-}OH \rightarrow S\text{-}O + H+ + e^-$ (c) $2S\text{-}O \rightarrow 2S + O_2$ (S* is surface active site)	(a) $S + H_2O \rightarrow S\text{-}OH + H^+ + e^-$ (b) $2S\text{-}OH \rightarrow S\text{-}O + S + H_2O$ (c) $2S\text{-}O \rightarrow 2S + O_2$
Mechanism No 3: Krasil' shchikov path	**Mechanism No 4: DFT predicted peroxide path**
(a) $S + H_2O \rightarrow S\text{-}OH + H^+ + e^-$ (b) $S\text{-}OH \rightarrow S\text{-}O^- + H^+$ (c) $S\text{-}O\text{-} \rightarrow S\text{-}O + e^-$ (d) $2S\text{-}O \rightarrow 2S + O_2$	(a) $H_2O + S \rightarrow S\text{-}OH + H^+ + e^-$ (b) $S\text{-}OH \rightarrow S\text{-}O + H^+ + e^-$ (c) $S\text{-}O + H_2O \rightarrow S\text{-}OOH + H^+ +e^-$ (d) $S\text{-}OOH \rightarrow S + O_2 + H^+ + e^-$

Depending on a specific electrocatalyst, the catalysis mechanism is not limited to one single mechanism model, but it can be a combination of several of the above-proposed mechanism paths.

2.1.2.2 OER electrocatalysts

As mentioned above, although thermodynamically only 1.23 V is required to split the water, due to the sluggish kinetics of OER, some extra energy (i.e., the overpotential) is required in order to have the reaction proceed at a reasonable rate. It is well-known that in chemical processes, catalysts are chosen in order to expedite the reaction kinetics as well as to improve other important aspects of the reaction process. Similarly, in electrochemistry, such catalysts, known as electrocatalysts (ECs) are utilized to decrease the overpotentials, charge transfer resistance, and accordingly, enhance the reaction kinetics. A good ECs should possess high surface area, high electrical conduction, excellent electrocatalytic property, long-term mechanical and chemical stability, good wetting characteristic i.e., minimized gas bubble problem, good selectivity, earth-abundance, low cost, and health safety[26]. In addition, the electrocatalytic performance typically depends on various factors such as surface electronic structure, chemical nature and oxidation state of the catalyst, morphology (dispersion, crystal size, crystallinity, lattice distortion etc.), non-stoichiometry (ionic defects, electronic defects, solid-state redox, etc.), band structure of the oxide, bond strength of metal(M)–oxygen(O), number of d-electrons, and synergetic effects (mixed and doped oxides)[26].

In order to investigate the OER activity of the different ECs, the energy states of two subsequent intermediates ($\Delta G^{O}_{HOO*} - \Delta G^{O}_{HO*}$) as a descriptor is typically used. **Figure 2-2** depicts the volcano plot (which follows the Sabatier principle), showing the activity of O_2 generation on the first-row transition metal oxide surfaces against the transition enthalpy of the oxides in either acidic or basic conditions. According to the Sabatier principle, in the case of surfaces that bind oxygen too weakly, intermediates cannot easily react, and the potential is limited by the oxidation of HO*.

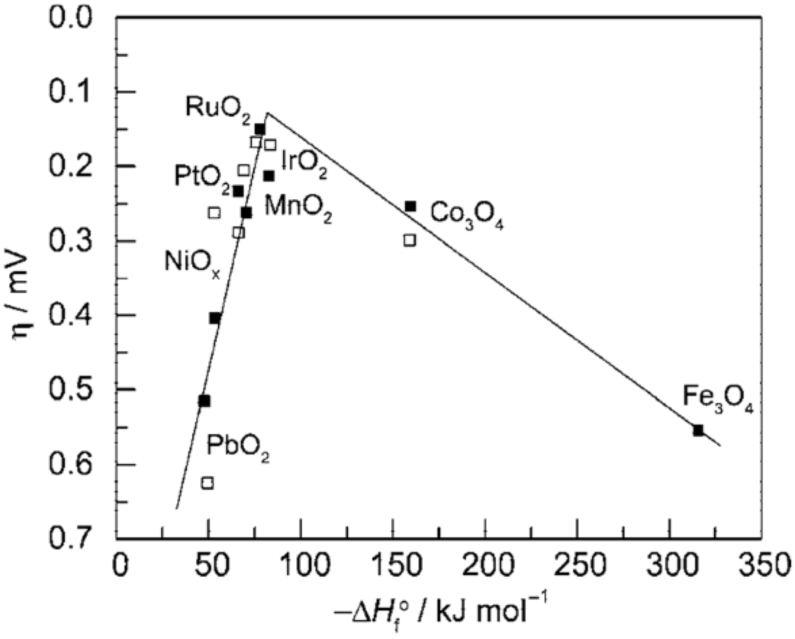

Figure 2-2 Volcano plot showing activity for O_2 production on metal oxide surfaces versus the enthalpy of transition of the oxide in acidic (■) and basic (□) solutions. Overpotential measured relative to 0.1 mA cm^{-2} current density

Reprinted with permission from ref. [27] (Copyright 2016, Royal Society of Chemistry)

On the other hand, in the opposite case of strong oxygen bonding, the intermediate states and the adsorbed products are quite stable, and the potential is limited by the formation of HOO* species. It can be seen that noble metal oxides such as RuO_2, PtO_2, and IrO_2 are located at the top of the volcano plot, suggesting their excellent OER electrocatalytic activity.

2.1.2.3 Design of high performance OER electrocatalysts

Materials that exhibit high corrosion resistance and endurance to OER operating conditions of high potential (~ 1.8 to 2 V) and harsh acidic conditions (pH ~ 0.2-0.5), typically demonstrate low electrochemical OER activity. It is, however, well-known that platinum group metal (PGM) or noble metal-based electrocatalysts (such as RuO_2, IrO_2) are considered the state-of-the-art electrocatalysts owing to their excellent OER electrocatalytic activity (1-5 A cm^{-2}), lower overpotential (~200 mV), and good durability (>24h) for producing sustained oxygen and hydrogen under stringent acidic conditions of PEMWE[28]. Unfortunately, PGM systems are environmentally scarce (~ 0.001-0.0003 ppm in earth's crust)[29], expensive (e.g. $\$210/g_{IrO2}$) and also possess high toxicity (higher than 2×10^{-5} ppm in the atmosphere is considered as hazardous[30]), limiting their extensive employment in the PEM water electrolyzers.[31] Therefore, significant research efforts are directed towards identification and development of earth-abundant cost-efficient, and reduced PGM containing as well as PGM-free electrocatalyst systems.

In recent years, continuous efforts have been devoted to the discovery of cost-effective materials for the promising anode candidates for PEM water electrolysis. In this quest, various inexpensive non-noble metal oxides possessing excellent corrosion resistance in strong acidic electrolytes have been explored over the years. These materials include tantalum oxide (Ta_2O_5)[32], nickel oxide (NiO)[33, 34], niobium oxide (Nb_2O_5)[35, 36], tin oxide (SnO_2)[37], titanium oxide (TiO_2)[38], silicon oxide (SiO_2)[39, 40], cobalt(II,III) oxide (Co_3O_4)[41], molybdenum oxide (Mo_xO_y)[42], cerium(IV) oxide (CeO_2)[43] etc. which exhibit good stability in the harsh acidic environment. Though, these low-cost non-noble metal oxides provide advantage due to their high durability (>24h) in acidic media, using such metal oxides in their pure or mixed form for OER in PEM water electrolysis is certainly not a plausible approach as these metal oxides exhibit insignificant electrocatalytic activity (5-10 μAcm^{-2}) towards OER.[44] In addition to this limitation, the above mentioned non-noble metal-based oxides are electrochemically inert and possess extremely poor electronic conductivity (~0.001-0.005 S cm^{-1}) which inhibits the mobility of induced charge across electrocatalyst surface thus, afflicting the reaction kinetics[45].

Thus, the current research is directed at identifying, developing, and synthesizing highly efficient electrocatalyst which can offer following desired characteristics.

Desired requirements for electrocatalyst materials:

In order to enable efficient large-scale electrolysis, abundant, stable and active electrocatalyst materials need to be developed. On the fundamental level, the main requirements for a good OER electrocatalyst are[45]:

(a) Low intrinsic overpotential (~200-400 mV) for the desired reaction.

(b) Ultra-low (~20-30 atm %) /zero noble (e.g., Ir/Ru/Pt) metal content.

(c) High active surface (~50-500 m^2g^{-1}) which facilitates both good accessibility to the reactants and sufficiently rapid removal of products.

(d) High electrical conductivity (~5-10 S cm^{-1}) (providing pathways for electrons).

(e) Sufficient electrochemical and mechanical stability (> 24h, compatibility with the electrolyte).

2.1.3 Hydrogen Evolution Reaction (HER)

2.1.3.1 HER Mechanism

Based on the acidic or basic nature of the electrolyte, HER occurs on either Volmer-Heyrovsky or Volmer-Tafel mechanism. The specific reaction pathways are described below:

(1) Volmer steps: A reaction species adopts an electron at an active site to form an adsorbed hydrogen.

(2) Heyrovsky steps: A reaction species (a proton or molecular water) and an electron are adopted by adsorbed hydrogen to form a hydrogen molecule and then desorb from electrode surface.

(3) Tafel step: Two adsorbed hydrogen atoms are coupled to produce a hydrogen molecule and then desorb from the surface.

Table 2-2 HER Mechanism

Reaction step	**Reaction**	**Electrolyte**
Volmer	$H^+ + e^- \rightarrow H_{ad}$ $H_2O + e^- \rightarrow H_{ad} + OH$	Acid Base
Tafel	$2H_{ad} \rightarrow H_2$	Acid/Base
Heyrovsky	$H_{ad}+H^++e^- \rightarrow H_2$ $H_{ad}+H_2O+e^- \rightarrow OH^-+H_2$	Acid Base

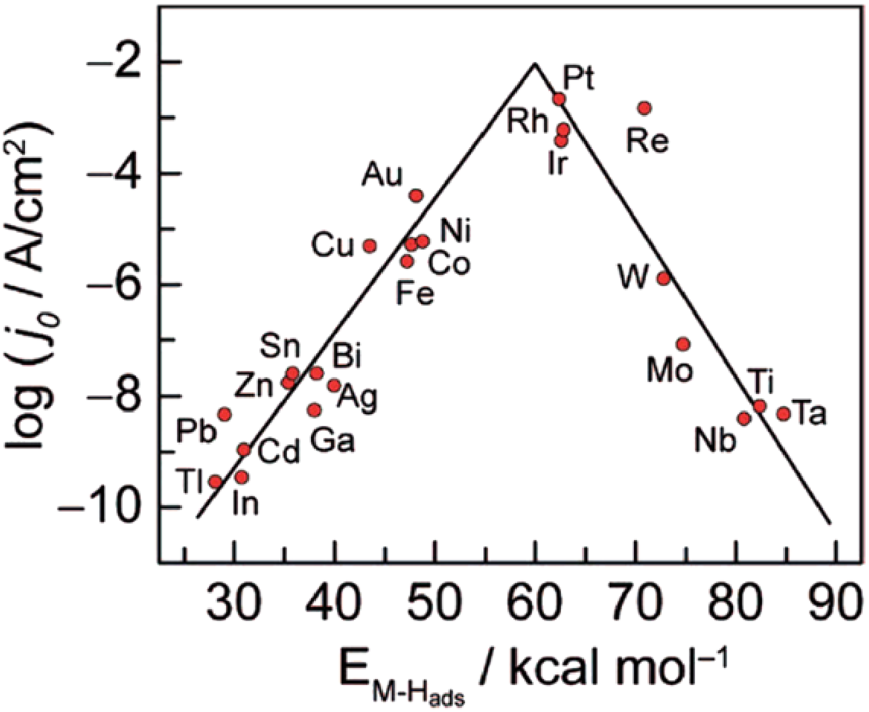

Figure 2-3 Volcano curve for the HER on metal electrodes in acidic media. The log of the exchange current density j_0 is plotted versus the M–H bond energy for each metal surface

Reprinted with permission from ref. [27](Copyright 2016, Royal Society of Chemistry)

It is well known that HER electrocatalytic activity depends on the electronic structure of electrocatalyst materials. Similar to the OER volcano plot, the HER volcano curve permits a quick comparison of the HER activities of different metals. **Figure 2-3** displays the logarithm of the exchange current densities (log j_0) on different metals vs. the metal–hydrogen (M–H) bond strength for the acidic HER. It can be seen that materials located at top of volcano plot i.e., PGM based Pt, Ir, Ru, and Au exhibit excellent activity towards acidic HER.

2.1.3.2 HER electrocatalysts

In recent years, numerous transition-metal (e.g., Fe, Cu, Ni, Co) phosphides (TMPs), sulfides, carbides, selenides, nitrides, etc. have been explored for the more advantageous proton exchange membrane (PEM) based acidic hydrogen evolution. [46-48] Amongst these systems, TMPs, owing to their excellent hydrodesulfurization (HDS) characteristics which rely on reversible binding of hydrogen on the catalyst surface, similar to HER, are highly promising and widely studied HER electrocatalyst systems.[49] Therefore, various TMPs such as copper phosphides, nickel phosphide, iron phosphides, molybdenum phosphides, tungsten phosphides, etc. have been studied as an active HER electrocatalysts.[50, 51] Among these TMP systems, Ni_2P has been reported to be a highly promising HER electrocatalyst owing to the presence of (i) a weak "ligand effect" due to Ni-P bonds, expediting the dissociation of molecular H_2, (ii) the "ensemble effect" of P which decreases the number of active sites on the surface preventing the poisonous effects due to high coverage, and (iii) presence of P sites providing an adequate bonding strength to the evolved H_2 molecule.[49, 52] Nevertheless, despite demonstrating noticeable HER performance, pristine Ni_2P suffers from a larger overpotential (>150 mV) and thus, lower HER performance in the stringent acidic electrolytes in comparison to the characteristic HER performance of benchmark, state-of-the-art Pt/C electrocatalyst. Therefore, on basis of theoretical studies, an appropriate dopant for such TMPs can be identified which can enhance the HER kinetics and activity.

2.2 Fuel Cell

2.2.1 Oxygen Reduction Reaction (ORR) and Hydrogen Oxidation Reaction (HOR)

The cathodic ORR reaction of PEMFC is the reverse reaction of OER of PEMEC. A simplified schematic of a common PEMFC is shown in **Figure 1-6**. The cathodic ORR and anodic HOR are shown below:

Anode: $H_2 \rightarrow 2H^+ + 2e^-$, $E^\circ = 0.0$ V

Cathode: $O_2 + 4H^+ + 4e^- \rightarrow 2H_2O$, $E^\circ = 1.23$ V

Overall: $2H_2 + O_2 \rightarrow 2H_2O$

The electrochemical efficiency of a fuel cell can be calculated as a simple ratio of the cell operating voltage, E_{cell} and the thermodynamic voltage ($E_{rev} = 1.23$ V)

$$E_{cell} = E_{rev} - \Delta E_{ohmic} - \eta_{ORR} - \eta_{HOR} - \eta_{tx}$$

Herein ΔE_{ohmic} is the voltage loss in the cell due to ohmic resistance, including both the electronic contact resistance between fuel cell components and proton conduction resistance in the membrane, η_{ORR} and η_{HOR} are the potential difference between the thermodynamic ORR (1.23 V) and HOR (0 V) potential and the experimentally observed potential, respectively. η_{tx} is the mass transfer loss, caused by the poor oxygen-transport through the diffusion medium and the catalyst layer. In comparison to the anodic HOR, cathodic ORR the most challenging, kinetically sluggish, and energy-intensive reaction.

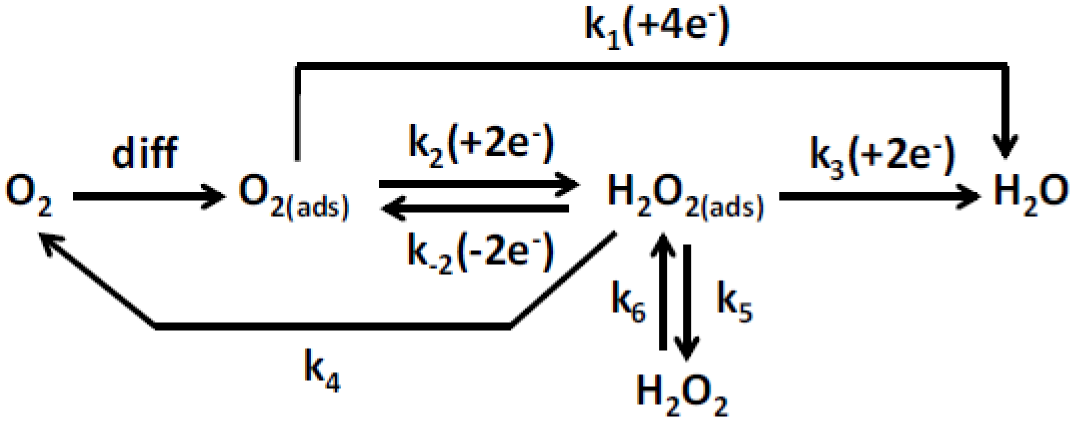

Figure 2-4 Reaction mechanisms of ORR

Reprinted from ref. [53]

There are two possible pathways for the ORR: a partial two-electron reduction to hydrogen peroxide (H_2O_2) or a full four-electron reduction to water (H_2O) (**Figure 2-4**). As peroxide is detrimental to the polymer electrolyte (Nafion) which reduces the energy conversion efficiency, it is desirable to avoid or minimize the peroxide formation during ORR. For ORR as well as HOR, the platinum nanoparticles supported on carbon black (Pt/C) is considered as state-of-the-art electrocatalyst which offers ideal oxygen and hydrogen adsorption energy. However, the high cost and environmental scarcity of Pt are the major bottlenecks for its large-scale application and thus, successful commercialization of PEMFCs. Therefore, current research in the PEMFC area is focused on the exploration of non-platinum (NPM) as well as platinum group metal-free (PGM-free) earth-abundant ECs, exhibiting superior electrochemical activity, stability, electrical conductivity, and good charge transfer kinetics for the ORR.

2.3 Photoelectrochemical Water Electrolysis (PECWE)

2.3.1 Solar Water Splitting

Every year the sun delivers massive amount of solar energy of ~ 173 ,000 TW to the surface of the earth, out of which ~ 30 % is reflected by the clouds and earth's surface, and thus, retaining ~ 120 ,000 TW power on the surface of the earth.[4] Solar energy is a de-concentrated and a seemingly limitless and environmentally clean natural source of energy, and thus, has been considered as an attractive approach for alleviating the global energy crisis. The photocatalytic or photoelectrochemical (PEC) water splitting is a promising approach for clean hydrogen production which combines two promising systems i.e., (I) solar cell which produces electricity and (II) water electrolysis which is driven by electricity produced from solar cell [50]. As the water splitting is an endothermic reaction, it demands external energy [$\Delta G^o = 237.13$ kJ mol^{-1} or 1.23 eV/(electron in H_2O)] to split the water into hydrogen and oxygen molecules [54, 55]. Since the discovery of PEC water splitting via low cost semiconductor material i.e. titania (TiO_2) by Fujishima and Honda in 1972, significant attention has been given to the engineering of novel high-performance semiconductor photoelectrocatalysts to expediate the overall performance of PEC cells[54, 56].

PEC water splitting involves generation of H_2 and O_2 gases in separate compartments of H-type cell **(Figure 2-5**) and thus, avoids the formation of explosive gaseous mixture. The separate production of H_2 and O_2 gases avoids their back-reaction, which eliminates any gas separation assembly. The following reactions occur at photoelectrodes:

Photoanode (OER)

$2h\nu \rightarrow 2e^- + 2h^+$

$2h^+ + H_2O_{(l)} \rightarrow 1/2O_{2\,(g)} + 2H^+$

Cathode (HER)

$2H^+ + 2e^- \rightarrow H_2$ (g)

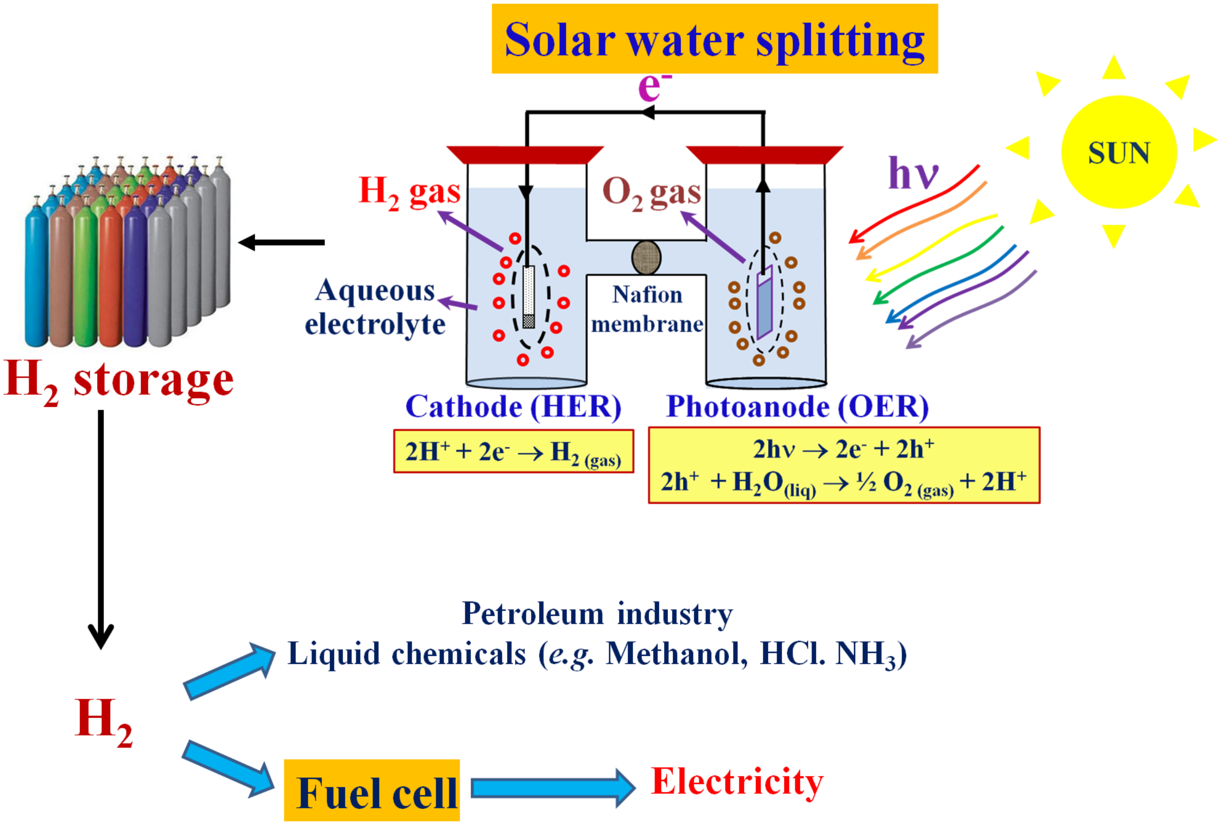

Figure 2-5 Hydrogen production via solar water splitting

2.3.2 Desired Properties of Photoanode

2.3.2.1 Band Gap

The solar spectrum consists of abundant visible light (~ 45%) with small amount of incoming solar energy lying in UV region (~ 3%) [54, 55]. Henceforth, it is important for photoanode to display superior visible light absorbing properties. Considering the range of the visible light wavelength range (390-700 nm) and also, the required water splitting voltage of >1.23 V, the desired photoanode must exhibit band gap in the range of ~1.6 eV- 3 eV [54, 55]. Accordingly, the U.S. Department of Energy [57] has set the target band gap of 2 eV for usable semiconductor band gap in PEC water splitting [58].

2.3.2.2 Band Structure

In order to achieve HER and OER at cathode and photoanode, respectively, it is imperative to match the band gap of semiconductor material with potential of its conduction and valence bands.

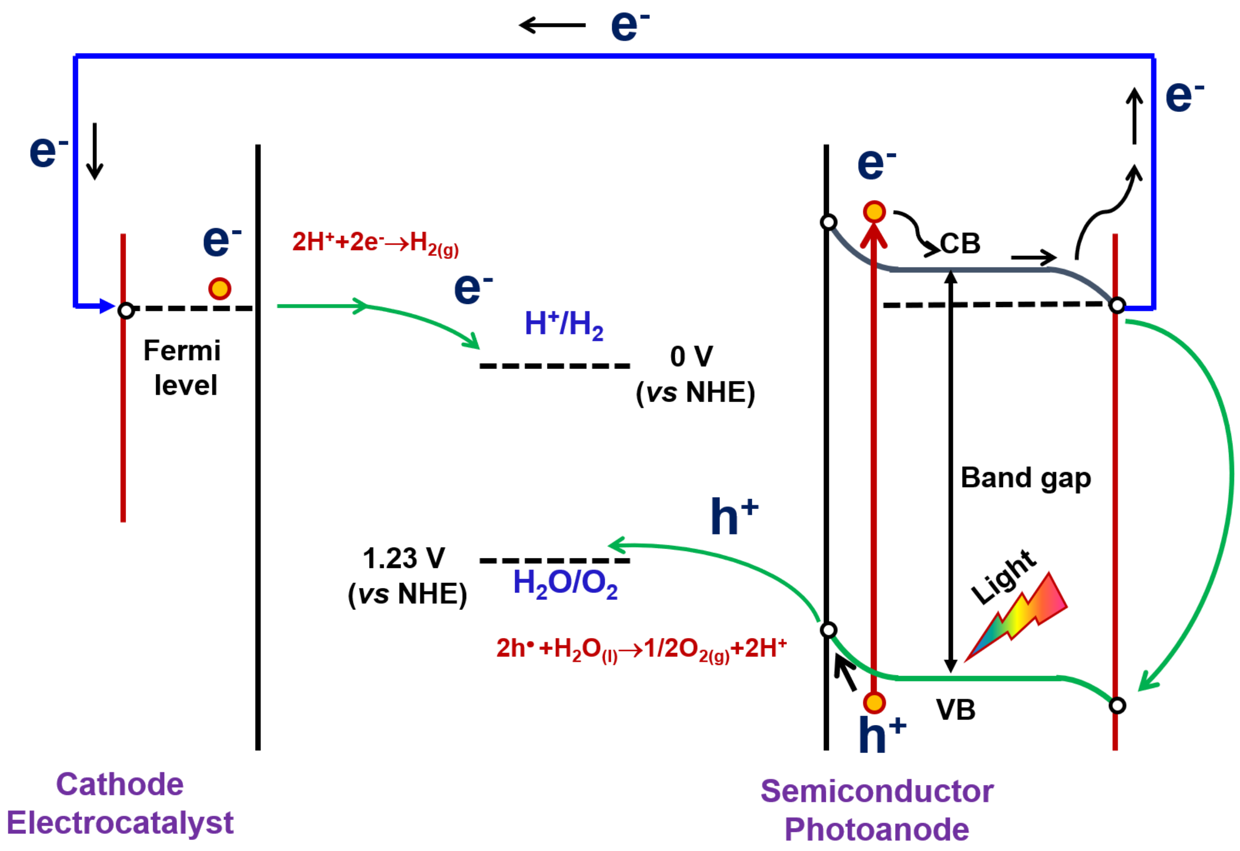

Figure 2-6 Energy band diagram for semiconductor material (photoanode) and cathode electrocatalyst

As shown in **Figure 2-6** when the photoanode is illuminated by light, the electrons are excited from the valence band to the conduction band leaving behind holes in the valence band. The photogenerated electrons in the conduction band of photoanode flow to the cathode, where they react with H^+ ions (present in the electrolyte solution) to generate H_2 gas. Holes present in the valence band of the photoanode oxidize water to generate O_2 gas by the OER. The driving force for the flow of photogenerated electrons depends on the difference between the conduction band edge of semiconductor electrode and the redox potential of HER (0 V *vs* NHE) [54, 55]. If the conduction band edge of the photoelectrode is more negative than the standard HER potential, then no external potential is needed to flow electrons from photoanode to cathode [54, 55, 59].

Similarly, if the valence band of semiconductor material is more positive than standard redox potential of oxidation of water (1.23 V *vs* NHE), then the generated holes can easily migrate to the surface of the semiconductor material and oxidize water without the need of any additional potential [54, 55, 59]. Thus, for the efficient PEC the semiconductor material should possess an appropriate band structure such that the reduction and oxidation potential of water lie within its band gap [54, 55].

2.3.2.3 Electrical Conductivity

For efficient PEC water splitting, the semiconductor materials should possess high electrical conductivity which can offer facile charge transport in the semiconductor material. As electrical conductivity is directly proportional to the product of number of carriers or carrier density and electron mobility of the semiconductor material, electrical conductivity can offer high carrier density and electron mobility for achieving superior PEC water splitting [60-62]. In addition, the high electron mobility is expected to offer fast movement of the photogenerated electrons from the semiconductor material to the current collector and then to the cathode, and thus, minimizing the recombination of electrons and holes [54, 55, 63, 64].

2.3.2.4 Recombination of the Photogenerated Carriers

During PEC water splitting, the photogenerated carriers, i.e., electrons and holes, recombine very rapidly (~10 ns) emitting light or generating phonons, due to which very few carriers are available for the reaction at both the electrodes leading to poor efficiency [65-68]. The recombination of the photogenerated carriers is known as a deactivation process and includes recombination from both, the surface and the bulk[54, 55]. The defect sites in the semiconductor material act as sites for trapping and recombination of the photogenerated carriers. Hence, the photoelectrocatalyst materials should exhibit high crystallinity or possess very low density of defects to achieve minimum recombination of photogenerated carriers.

2.3.2.5 Photoelectrochemical Stability

For efficient PEC water splitting, the photoelectrodes should exhibit excellent long term photoelectrochemical stability for continuous H_2 production. Typically, the photogenerated holes are mainly responsible for the photo-corrosion (oxidation) of the semiconductor material [54, 55]. Thus, photoanode should possess good corrosion resistance, and chemical and mechanical stability. Accordingly, various transition metal oxides (TiO_2, SnO_2, Nb_2O_5, etc.) are a good candidate for photoanode systems.

3.0 Research Objectives and Specific Aims

The focus of the present thesis is to identify, synthesis, and development highly efficient, earth-abundant, and cost-efficient electrocatalyst materials for the PEM electrolyzer, PEM fuel cell, and PEC water splitting. Accordingly, the objectives of the current Ph.D. thesis are outlined below encompassing the following specific aims as discussed below:

__Specific Aim 1A:__ **To identify and engineer reduced PGM containing and PGM-free multi-metal oxide (MMO) based electrocatalyst materials of different architectures for oxygen evolution reaction (OER) in proton exchange membrane-based water electrolysis (PEMWE)**

This aim was executed and accomplished in the following manner:

(a) Synthesis of high performance architectures of ultra-low noble metal (Ir) containing fluorine (F) doped solid solution electrocatalyst systems such as (i) 2D thin film of $(Mn_{1-x}Ir_x)O_2$:10F, (ii) 1D vertically aligned nanotubes (VANTs) of $(Sn_{1-x}Ir_x)O_2$:10F, and (iii) 1D $(Mn_{1-x}Ir_x)O_2$:10F nanorods on Ti substrate (current collector). The results of these studies are already published.[45, 69, 70]

(b) Synthesis of active and durable multi-metal-based earth abundant PGM-free ECs such as 1D $(Mn_{1-x}Nb_x)O_2$:10F and $Cu_{1.5}Mn_{1.5}O_4$:10F for acidic OER.

(c) Phase analysis and microstructural characterization of the above ECs by utilizing X-ray diffraction (XRD), scanning/transmission electron microscopy (SEM/TEM), energy dispersive X-ray spectroscopy (EDX), X-ray photoelectron spectroscopy (XPS), contact angle etc.

(d) Electrochemical analysis of the as-synthesized ECs by performing electrochemical impedance spectroscopy (EIS), linear scan voltammetry (LSV), Tafel analysis, and chronoamperometry

(CA) test, electrochemically active surface area (ECSA) analysis, evaluation of the EC performance in full cell PEM electrolyzer, etc.

<u>Specific Aim 1B:</u> To identify and develop high performance electrocatalysts for oxygen reduction reaction (ORR) in proton exchange membrane fuel cells (PEMFCs)

This aim was executed and accomplished in the following manner:

(a) Influence of defects and order-disorder on the ORR performance of spinel $Cu_{1.5}Mn_{1.5}O_4$ and $Cu_{1.5}Mn_{1.5}O_4$:F for PEMFC

(b) Phase analysis and microstructural characterizations via X-ray diffraction (XRD), scanning/transmission electron microscopy (SEM), energy dispersive X-ray spectroscopy (EDX), X-ray photoelectron spectroscopy (XPS), etc.

(c) Electrochemical characterizations via linear scan voltammetry (LSV), electrochemical impedance spectroscopy (EIS), Tafel analysis, and chronoamperometry (CA) stability tests, rotating ring disk electrode (RRDE) including full cell membrane analysis, etc.

<u>Specific Aim 2A:</u> To develop multi-metal containing phosphosulphide based electrocatalyst materials for hydrogen evolution reaction (HER) in proton exchange membrane-based water electrolysis (PEMWE)

This aim was executed and accomplished in the following manner:

(a) Synthesis of PGM-free electrochemically active and robust electrocatalysts of cobalt doped nickel phosphosulfide solid solutions $[(Ni_{1-x}Co_x)_2P:S]$ for hydrogen evolution.

(b) Phase analysis and microstructural characterizations via X-ray diffraction (XRD), scanning/transmission electron microscopy (SEM), energy dispersive X-ray spectroscopy (EDX), X-ray photoelectron spectroscopy (XPS), contact angle measurements, etc.

(c) Electrochemical characterization of Co and S containing Ni_2P electrocatalysts by utilizing electrochemical impedance spectroscopy (EIS), linear scan voltammetry (LSV) and chronoamperometry (CA) stability tests, etc.

<u>Specific Aim 2B:</u> To identify and develop high performance electrocatalysts for hydrogen oxidation reaction (HOR) in proton exchange membrane fuel cells (PEMFCs)

This aim was executed and accomplished in the following manner:

(a) In order to develop high performance ECs for HOR possessing low over-potential, excellent reaction kinetics as well as long term durability in acidic media for PEMFCs, exploiting theoretical first principles calculations for identifying transition metal silicides (Ti_5Si_3) and Pt doped silicide materials ($Ti_{5-x}Pt_xSi_3$), the corresponding systems identified by theory has been accordingly synthesized and investigated for HOR.

(b) Phase analysis and microstructural characterizations by utilizing X-ray diffraction (XRD), scanning/transmission electron microscopy (SEM/TEM), energy dispersive X-ray spectroscopy (EDX), X-ray photoelectron spectroscopy (XPS), etc.

(c) Electrochemical characterizations by employing electrochemical impedance spectroscopy (EIS), rotating ring disk electrode (RRDE) kinetic analysis, and chronoamperometry (CA) stability tests, including full cell membrane analysis, etc.

Specific Aim 3: **Synthesis of bilayer structured 1-D multi-metal oxide semiconductor nanostructures to enhance the fundamental optoelectronic properties (by modification of electronic structure) for photo-anode applications in photo-electrochemical (PEC) water splitting via systematic bandgap engineering (achieved by incorporation of suitable dopants)**

This aim was executed and accomplished in the following manner:

(a) Identifying suitable dopant (Mo) to enhance the PEC performance of bilayer WO_3:$(Sn,Nb)O_2$:N photoanode in PEC water splitting.

(b) Phase analysis and microstructural characterizations via utilizing X-ray diffraction (XRD), scanning/transmission electron microscopy (SEM/TEM), energy dispersive X-ray spectroscopy (EDX), X-ray photoelectron spectroscopy (XPS), etc.

(c) Study of the photoelectrochemical properties by utilizing UV-vis absorption spectroscopy, Tauc analysis, Mott-Schottky analysis, linear scan voltammetry (LSV), electrochemical impedance spectroscopy (EIS), and chronoamperometry (CA) stability tests, Hall-effect measurements for charge carrier density, etc.

4.0 Specific Aim 1A - To Identify and Engineer Reduced PGM Containing and PGM-Free Multi-Metal Oxide (MMO) Based Electrocatalyst Materials of Different Architectures for Oxygen Evolution Reaction (OER) in Proton Exchange Membrane-Based Water Electrolysis (PEMWE)

The Specific Aim 1A comprises of five different chapters related to reduced PGM and PGM-free electrocatalysts for OER, each of which have been published in peer reviewed archived journals. In chapter 4, 5 and 6, the electrocatalyst studies of reduced PGM (Ir) containing solid solution electrocatalysts are investigated. Chapter 7 and 8 include electrocatalyst studies of PGM-free OER electrocatalysts for acidic water electrolysis.

Details of each of these five different electrocatalysts taken from the published manuscripts are outlined below.

- Chapter 4: Fluorine substituted $(Mn,Ir)O_2$: F thin-film electrocatalysts for OER

Excerpts reprinted with permission from Ghadge, Shrinath Dattatray, et al. "Fluorine substituted $(Mn,Ir)O_2$: F high performance solid solution oxygen evolution reaction electrocatalysts for PEM water electrolysis." RSC advances 7.28 (2017): 17311-17324. This article is licensed under a Creative Commons Attribution 3.0 Unported Licence. Material from this article can be used in other publications provided that the correct acknowledgement is given with the reproduced material.

4.1 Abstract

Identification and development of high performance with reduced overpotential (i.e., reduced operating electricity cost) oxygen evolution reaction (OER) electrocatalyst for proton exchange membrane (PEM) based water electrolysis with ultra-low noble metal content (i.e., reduced materials cost) is of significant interest for economic hydrogen production thus increasing the commercialization potential of PEM water electrolysis. Accordingly, the novel electrocatalyst should exhibit low overpotential, excellent electrochemical activity and durability superior to state-of-the-art noble metals based electrocatalysts (e.g., Pt, IrO_2, RuO_2). Herein, for the very first time to the best of our knowledge, exploiting first-principles theoretical calculations of the total energies and electronic structures, we have identified reduced noble metal content fluorine doped solid solution of MnO_2 and IrO_2, denoted as $(Mn_{1-x}Ir_x)O_2$:F (x = 0.2, 0.3, 0.4), OER electrocatalyst system exhibiting lower overpotential and higher current density than state of the art IrO_2 and other previously reported systems for PEM water electrolysis. The doped solid solution displays excellent electrochemical performance with a lowest reported onset potential to date of ~1.35 V (*vs* RHE), ~80mV lower than that of IrO_2 (~1.43 V *vs* RHE) and ~15 fold (x=0.3 and 0.4) higher electrochemical activity compared to pure IrO_2. In addition, the system displays excellent long term electrochemical durability, similar to that of IrO_2 in harsh acidic OER operating conditions. Our study therefore demonstrates remarkable, ~60-80% reduction in noble metal content along with lower overpotential and excellent electrochemical performance clearly demonstrating the potential of $(Mn_{1-x}Ir_x)O_2$:F system as OER electrocatalysts for PEM water electrolysis.

4.2 Introduction

The inherent unceasing global energy demand, accelerating diminution of fossil fuels and the continuing upsurge of carbon footprint causing potentially perilous damage to the global climate are the primary thrusts for the pursuit of renewable and non-carbonaceous clean energy sources.[8, 71-73] In this milieu, hydrogen has garnered immense attention for transportation and stationary application on the grounds of its high energy density and low carbon footprint.[74-78] However, efficient and economic production of hydrogen from non-carbonaceous clean source along with cost-effective storage and distribution are major challenges that need to be addressed before hydrogen can be commercially developed as an energy carrier for transportation at industrial scales.[79, 80] In this direction, hydrogen production from water splitting, via water electrolysis is considered as a promising approach due to its non-toxic and non-carbonaceous nature.[81, 82] In specific, water electrolysis operation in acidic media, known as proton exchange membrane (PEM) water electrolysis, is considered to be more advantageous than that in neutral and basic media due to higher efficiency, superior production rates, more compact design and increased product purity for operation in acidic media.[83-85] Oxygen evolution reaction (OER) for efficient hydrogen production is the major driver for water electrolysis under PEM conditions.

The slow reaction kinetics as well as the concomitant high reaction overpotential (i.e. high operating electricity cost) of OER electrocatalyst (~200mV overpotential for IrO_2) and the high materials cost due to need of expensive and precious noble metals OER electrocatalysts (Pt, IrO_2, RuO_2) has thwarted the progress and commercialization of PEM based water electrolysis.[86-89] Therefore, the OER reaction (E^o=1.23 V *vs* NHE), which occurs at the anode of PEM water electrolysis cells, is an important, challenging and energy intensive process.[81, 90-92] Hence, the identification and development of high performance, faster reaction kinetics, highly active and low overpotential OER electrocatalyst with ultra-low noble metal content will considerably aid in achieving high efficiency and also help reduce the materials and electricity costs of PEM based water electrolysis cells.[33, 93, 94]

In the pursuit of identifying low noble metal content electrocatalysts as a replacement of currently used expensive pure IrO_2 or RuO_2 electrocatalysts, one of the widely adopted approaches is mixing of robust and cheap transition metal oxides (e.g. SnO_2, Ta_2O_5, Nb_2O_5, TiO_2) with IrO_2 and/or RuO_2 (e.g. IrO_2–SnO_2, RuO_2–SnO_2, IrO_2–Ta_2O_5, IrO_2–SnO_2–Nb_2O_5, etc.) maintaining the electronic conductivity and catalytic activity similar to IrO_2 and/or RuO_2 and improving the durability of IrO_2 and/or RuO_2.[81, 92, 95, 96] However, in this approach, with increase in the content of non-noble metal oxides above 50wt. %, there is deterioration in catalytic activity due to a decrease in the electrochemical active surface area and electronic conductivity.[81, 92, 95] We [97, 98] have recently identified several F doped binary and ternary solid solution oxides [$(M,M',Ir)O_2$:F; M,M′=Sn, Nb] with significant reduction in IrO_2 (~70-80 mol.% reduction) content albeit exhibiting similar electrochemical performance to pure IrO_2 electrocatalyst, thus offering significant reduction in materials cost of the PEM water splitting process. However, all these developed [$(M,M',Ir)O_2$:F; M,M′=Sn, Nb] electrocatalysts show similar electrochemical performance (i.e. overpotential and activity) to that of pure IrO_2.[97, 98] In addition to lowering the materials cost, a novel electrocatalyst offering lower operating electricity cost with significantly improved electrochemical performance (lower overpotential and faster kinetics) with respect to IrO_2 needs to be identified in order to commercialize PEM water electrolysis technology. The focus of the current work is thus not only on the identification and development of novel electrocatalyst with reduced noble metal content but more importantly, identifying reduced noble metal containing systems that exhibit faster reaction kinetics, low overpotential, superior electrochemical performance than that of pure IrO_2 utilizing the prudent two pronged theoretical and experimental approach.

In this work, for the very first time to the best of our knowledge, exploiting first-principles theoretical calculations of the total energies and electronic structures, we have identified fluorine doped solid solution of MnO_2 and IrO_2, denoted as $(Mn_{1-x}Ir_x)O_2$:F electrocatalyst system exhibiting lower overpotential and higher current density than state of the art IrO_2 and also superior electrochemical performance as compared to other solid solution based OER electrocatalyst systems in PEM water electrolysis.[94, 97-100] These results will portend significant reduction in noble metal content in electrocatalyst aiding in achieving significantly reduced material's cost as well as operating electricity cost. In addition, in the current study, a thorough investigation of total energies, electronic structure and density of electronic states of the as-synthesized electrocatalysts, employing the density functional theory has been implemented. The present study also determines the free energy (ΔG) values of $(Mn,Ir)O_2$ electrocatalyst system which successfully shows the significant decrease in the onset potential of $(Mn,Ir)O_2$ electrocatalyst system.

In the present study, Fluoride (F) is chosen as a dopant for the $(Mn_{1-x}Ir_x)O_2$ solid solution due to its pivotal role in improving the electrochemical activity of $[(M,M',Ir)O_2$:F; $M,M'=Sn, Nb]$ for OER in acidic media as already demonstrated by us previously following experiments and first principles calculations.[97, 98] The results of the theoretical studies are experimentally verified by synthesizing thin film architectures of $(Mn_{1-x}Ir_x)O_2$ ($x=0, 0.3, 1$) and $(Mn_{1-x}Ir_x)O_2$:10F ($x=0.2, 0.3, 0.4$) electrocatalysts on Ti foil (substrate). Thus, for the very first time, we document the theoretical studies, synthesis, physical characteristics, and electrochemical performance of nanostructured

$(Mn_{1-x}Ir_x)O_2$ (x=0, 0.3, 1) and $(Mn_{1-x}Ir_x)O_2$:10 F (x=0.2, 0.3, 0.4) thin film electrocatalysts for OER in PEM water electrolysis.

4.3 Computational Methodology

The overall electro-catalytic activity and the overpotential of $(Mn,Ir)O_2$:F OER electrocatalyst is expected to depend on the electronic structure and thermodynamics of the four elementary OER.

$$2H_2O \xrightarrow{\text{I}} HO^* + H_2O + H^+ + e^- \xrightarrow{\text{II}} O^* + H_2O + 2H^+ + 2e^- \xrightarrow{\text{III}} HOO^* + 3H^+ + 3e^- \xrightarrow{\text{IV}} O_2 + 4H^+ + 4e^- \quad (4\text{-}1)$$

wherein * represents an active site on the metal oxide surface[101].

To study the influence of compositions on the electronic structure as well as the activity of the electrocatalyst, theoretical analysis has been performed. The computational component of the current study is to understand the electronic structure of $(Mn,Ir)O_2$:F oxides with the following chemical compositions: $(Mn_{1-x}Ir_x)O_2$, with x=0.17, 0.33, 0.5 and $(Mn_{0.83}Ir_{0.17})O_{1.33}F_{0.67}$, corresponding approximately to 10 wt% of F. Also, for comparison purposes pure IrO_2 oxide has been considered as a standard electrocatalyst for PEM based water electrolysis. In order to determine the electric potentials at which a certain specific reaction would occur, the free energies (ΔG) of all the four anodic intermediate reactions (I-IV) have been considered. Therefore, a methodical analysis of all the calculated free energies may explain the rate determining step of the oxygen evolution reaction. This systematic analysis is essential for the knowledge of electro-catalytic activity of the specific material used as an electrocatalyst in water electrolysis reaction. For comparison purposes two different materials have been chosen for calculation of the OER elementary steps: pure IrO_2 and IrO_2 doped with small amount of Mn as a substituent of Ir at the corresponding Ir-type lattice sites. For calculations of the total energies and electronic structure of the above-mentioned oxides bulk and (110) surface rutile structure with a tetragonal unit cell and space group $P4_2/mnm$ have been utilized. The rutile structure of IrO_2 and $(Mn,Ir)O_2$:F have been experimentally confirmed from XRD analysis which will be presented in the experimental results section to follow.

For bulk calculations [1x1x3] supercell containing three elementary unit cells stacked in c direction has been chosen as the basis for construction of different Ir, Mn, and F concentrations of the oxide solid solution. Such a supercell contains 6 transition metal atoms and 12 atoms of oxygen/fluorine. Thus, for convenience of calculations the basic composition has been chosen i.e. several different atomic ratios of Mn/Ir, such as 5/1 corresponds to $(Mn_{0.83}Ir_{0.17})O_2$ formula unit, while 2/4 and 3/3 correspond to $(Mn_{0.67}Ir_{0.33})O_2$ and $(Mn_{0.5}Ir_{0.5})O_2$ formula units, respectively. For simulation of 10 wt.% of fluorine, 4 atoms of oxygen were randomly replaced with corresponding number of fluorine atoms generating the following formula unit: $(Mn_{0.83}Ir_{0.17})O_{1.33}F_{0.67}$. Such composition has been chosen for smaller representative super-cells for all the calculation of bulk and surface electronic structures employed in the present study. For calculation of the (110) surface electronic properties of the materials, a two-dimensional slab repeated in [1,-1, 0] direction with 24 atom unit cell containing four oxygen layers with three oxygen-metal mixed layers in between them. A vacuum distance ~ 12 Å between adjacent images of the slab was selected. Following the previous studies[101, 102], for the calculation of the free energies of all the elementary reactions i.e. (I) - (IV) for IrO_2 with and without Mn atoms located at the surface, the rutile type (110) preferred surface which is covered with oxygen has been selected. The 2x2 surface unit cell for a symmetric 7-layer slab of ~10.3 Å thickness which is separated between its image's perpendicular to the surface direction by vacuum space of ~20 Å has been taken which will prevent the interaction between the slab and its adjacent images. On the coordinated unsaturated sites of both sides of the chosen slab, all intermediate species involved in the OER i.e., O*, OH*, and OOH* have been attached. Three middle layers of the slab were fixed with the lattice parameter corresponding to the bulk IrO_2. Apart from these three middle layers, all other layers of the slab together with the intermediate species were fully relaxed and therefore, all the mathematical data obtained from such model should be divided by two.

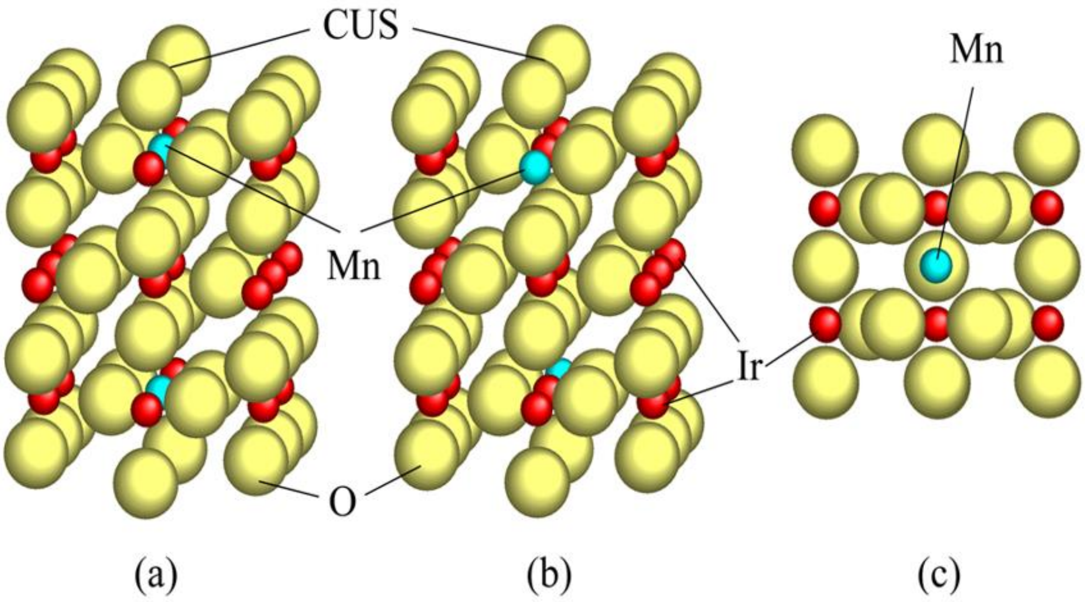

Figure 4-1 Angle and top view of the elementary unit cell of the (110) rutile surface slab used in the present study: red – Ir, blue – Mn, yellow – oxygen (a) represents Mn at the center of the unit cell, (b) represents Mn at the side, (c) top view of the unit cell with Mn at the center. A coordinatively unsaturated site (CUS) is indicated by black lines

A unit cell chosen for the calculations in the present study has been shown in **Figure 4-1** Two different atomic positions of Mn as a replacement of Ir in the unit cell have been considered to investigate the difference between the electronic structures of pure and doped IrO_2 compounds as well as to assess the role of Mn on lowering of the overpotential of the $(Mn,Ir)O_2$. The first Mn-atomic distribution consists of one Mn-atom located in place of Ir just below the coordinatively unsaturated site (CUS) with an oxygen vacancy shown on **Figure 4-1(a)**. The second distribution is characterized by introduction of Mn-atom at the lower part of the unit cell while the CUS locates above the Ir atom [**Figure 4-1 (b)**]. In order to calculate the free energies of all the four elementary reaction steps discussed above, such two different unit cells which have been covered by adsorbed oxygen monolayers in conjunction with intermediate species at the surface have been used.

For calculating the total energies, electronic structure and density of electronic states of the studied materials, the density functional theory implemented in Vienna Ab-initio Simulation Package (VASP) was used within the projector-augmented wave (PAW) method[103-105] and the spin-polarized generalized gradient approximation (GGA) for the exchange-correlation energy functional in a form described by Perdew and Wang.[106] This computational package analyses the electronic structure and via Hellmann-Feynman theorem, the inter-atomic forces are determined from first-principles. The standard PAW potentials were utilized for the elemental components and the Ir, Mn, O and F potentials thus contained nine, seven, six and seven valence electrons, respectively. In the present theoretical analysis, to maintain the high precision for total energy calculations for all the electrocatalyst compositions, the plane wave cutoff energy of 520 eV has been chosen. By employing the double relaxation procedure, the internal positions as well as the lattice parameters of atoms have been completely optimized. Moreover, the minima of the total energies with respect to the lattice parameters and internal ionic positions have been determined. Also, by minimizing the Hellman–Feynman forces via a conjugate gradient method, the geometry optimization was achieved. This will cause the net forces applied on every ion in the lattice close to zero. The total electronic energies were converged within 10-5 eV/un.cell which result into the residual force components on each atom to be lower than 0.01 eV/Å/atom. This allows the accurate determination of the internal structural parameters. Herein, the Monkhorst-Pack scheme has been used to sample the Brillouin Zone (BZ) and create the k-point grid for the solids and the different isolated atoms used in the current study. The selection of an appropriate number of k-points in the irreducible part of the BZ was made on the grounds of the convergence of the total energy to 0.1 meV/atom.

It is noteworthy to mention that, for Mn-Ir-O-F compositions, the corresponding atomic distributions are uncertain and thus, different spatial configurations can be used for exemplification of the atomic distributions. This uncertainty has been eliminated by assembling the various atomic configurations for each selected composition and the configurations which correspond to the minimum total energy, have been selected for conducting further numerical analysis of these specific compositions of the binary oxides.

4.4 Experimental Methodology

4.4.1 Synthesis of $(Mn_{1-x}Ir_x)O_2$ (x=0, 0.3, 1) and $(Mn_{1-x}Ir_x)O_2$:10 wt.% F (x=0.2, 0.3, 0.4)

Iridium tetrachloride ($IrCl_4$, 99.5%, Alfa Aesar), manganese chloride ($MnCl_2$, 99.5%, Aldrich) and ammonium fluoride (NH_4F, 98%, Alfa Aesar) were used as the sources for Ir, Mn and F respectively. Stock solutions of $IrCl_4$, $MnCl_2$ and NH_4F of the desired compositions were prepared in deionized (D.I.) water (18 MΩ cm, MilliQ Academic, Millipore). These stock solutions were mixed together according to the desired composition of the electrocatalyst material and then spin coated onto titanium foils (Alfa Aesar) of ~1 cm^2 area (0.5 cm × 2 cm) (used as a substrate). The spin coating (Speciality coating Systems Inc., Model P6712) was performed employing a rotating speed of 500 rpm for 10 sec with suitable amount of the precursors selected to achieve a desired total loading of ~0.3mg cm^{-2} of $(Mn_{1-x}Ir_x)O_2$ and $(Mn_{1-x}Ir_x)O_2$:10 F oxide electrocatalyst. The precursors spin coated on Ti foil were then thermally treated at 400 ^oC for 4 h in air to initiate decomposition and adequate reaction of the precursors to form $(Mn_{1-x}Ir_x)O_2$ and $(Mn_{1-x}Ir_x)O_2$:10F solid solutions on the Ti foil to achieve a total electrocatalyst loading of ~0.3mg.cm^{-2}. It should be noted that the same chemical approach was used to generate IrO_2 thin films on the Ti foil serving as the control for comparing the electrochemical activity of the Mn substituted IrO_2 solid solutions and F-doped Mn substituted IrO_2 solid solutions.

4.4.2 Electrocatalyst Materials Characterization

4.4.2.1 Structural Characterization

XRD has been performed using the Philips XPERT PRO system employing CuK_α radiation source (λ = 0.15406 nm) at an operating current and voltage of 40 mA and 45 kV, respectively. The least square refinement techniques have been utilized to determine the molar volume and lattice parameters of the electrocatalyst materials of different compositions.[76, 107] Scanning electron microscopy (SEM) has been conducted to investigate the microstructure of electrocatalysts. Quantitative elemental analysis and elemental x-ray mapping of elements have been performed by utilizing the energy dispersive x-ray spectroscopy (EDX) analyzer attached with the SEM machine. Philips XL-30FEG equipped with an EDX detector system comprising of an ultrathin beryllium window and Si(Li) detector operating at 20 kV was used for obtaining information on the microstructure as well as conducting elemental and x-ray mapping analysis of the electrocatalyst. X-ray photoelectron spectroscopy (XPS) was used to investigate the oxidation states of Mn and Ir in $(Mn_{1-x}Ir_x)O_2$ and $(Mn_{1-x}Ir_x)O_2$:10F electrocatalysts. XPS analysis was carried out using the ESCALAB 250 Xi system (Thermo Scientific) equipped with a monochromated Al Kα X-ray source. The standard analysis spot of 400×400 μm^2 was defined by the micro-focused X-ray source. The system is operated at a room temperature in an ultra-high vacuum chamber with a base pressure less than 5×10^{-10} mbar. The binding energy (BE) scale of the analyzer was calibrated to produce <50 meV deviations of the three standard peaks from their standard values. The aliphatic C1s peak was observed at 284.6 eV. High-resolution elemental XPS data in C2p, S2p, Mg2p, and Zn2p regions were acquired with the analyzer pass energy set to 20 eV (corresponding to energy resolution of 0.36 eV) and the step size set to 0.1 eV. The Avantage software package (Thermo Fisher Scientific) was used to fit the elemental spectra based on the calibrated analyzer transmission functions, Scofield sensitivity factors, and effective attenuation lengths for photoelectrons from the standard TPP-2M formalism.

4.4.2.2 Electrochemical characterization

Electrochemical characterization of $(Mn_{1-x}Ir_x)O_2$ and $(Mn_{1-x}Ir_x)O_2$:10F electrocatalysts was performed in a three electrode configuration at 40°C (maintained using a Fisher Scientific 910 Isotemp refrigerator circulator) on a VersaSTAT 3 (Princeton Applied Research) electrochemical workstation. 1N sulfuric acid (H_2SO_4) was used as the electrolyte solution and also, as a proton source for OER. Prior to electrochemical testing, oxygen from the electrolyte solution was expelled by purging the electrolyte solution with ultra-high pure (UHP) argon gas (Matheson) for ~15 min.[108, 109] The thin film electrodes of the various electrocatalyst materials were used as the working electrode, Pt wire (Alfa Aesar, 0.25 mm thick, 99.95%) was used as the counter electrode and mercury/mercurous sulfate (Hg/Hg_2SO_4) electrode (XR-200, Hach) having a potential of +0.65 V with respect to normal hydrogen electrode (NHE) was used as the reference electrode. All the potential values reported in this study are determined with respect to reversible hydrogen electrode (RHE), calculated from the formula[75, 110]:

$$E_{RHE} = E_{Hg/Hg2SO4} + E^{o}_{Hg/Hg2SO4} + 0.059pH.$$

where, E_{RHE} is the potential versus RHE. $E_{Hg/Hg2SO4}$ is the potential measured against the Hg/Hg_2SO_4 reference electrode. $E^o_{Hg/Hg2SO4}$ is the standard electrode potential of Hg/Hg_2SO_4 reference electrode (+0.65 V *vs* NHE).

The EIS was conducted to determine the solution resistance (R_s), the electrode resistance (R_e), the ohmic resistance (R_Ω) ($R_\Omega=R_s+R_e$) and the charge transfer resistance (R_{ct}) of the synthesized electrocatalyst materials.[76, 111] The ohmic resistance (R_Ω) obtained from the EIS was further utilized for iR_Ω ($iR_s + iR_e$) correction[76, 111] in the polarization curves of the electrocatalysts. The EIS was performed in the frequency range of 100 mHz-100 kHz (Amplitude = 10 mV) using the electrochemical work station (Versa STAT 3, Princeton Applied Research) in 1N H_2SO_4 electrolyte solution at 40°C, at the constant applied potential of ~1.45 V (*vs* RHE, iR_Ω corrected) using a total loading of 0.3 $mg.cm^{-2}$ for $(Mn_{1-x}Ir_x)O_2$ (x=0.3 and 1) and $(Mn_{1-x}Ir_x)O_2$:10F (x=0.2, 0.3, 0.4). Impedance data for OER has been modeled by using the ZView software from Scribner Associates employing the $R_s(R_eQ_1)(R_{ct}Q_{dl})$ equivalent circuit model. In the present circuit model (similar to that of used in earlier reports[94, 97]) R_s is in series with the parallel combination of the R_e and Q_1 and further in series with the parallel combination of the R_{ct} and Q_{dl}. The components of this model are given as below: [76, 111]

R_s = Solution resistance faced at high frequency due to charge transfer in the electrolyte solution

R_e = Electrode resistance for electron transfer from the electrode to current collector (Ti foil)

R_{ct} = Charge transfer resistance (i.e., polarization resistance)

Q_1 = Constant phase element

Q_{dl} = Contribution from both double layer capacitance and pseudo capacitance

The electrochemical activity of the electrocatalysts for OER was determined by conducting linear scan polarization in 1N H_2SO_4 electrolyte solution employing a scan rate of 10 $mVsec^{-1}$ at 40^oC. Polarization curves of different electrocatalysts were iR_Ω corrected (R_Ω, the ohmic resistance was determined from electrochemical impedance spectroscopy analysis). The current density at ~1.45 V (*vs* RHE, which is the typical potential used for assessing the electrochemical activity of the electrocatalyst for OER[112]) in iR_Ω corrected polarization curves was used for comparison of the electrochemical performance of the different electrocatalyst materials. The Tafel plot after iR_Ω correction given by the $\eta = a + b \log i$ (plot of overpotential η *vs* log current, log i) was used to determine the Tafel slope (b), which was further used to study the reaction kinetics for all the synthesized electrocatalysts.

The electrochemical stability of $(Mn_{1-x}Ir_x)O_2$:10F electrocatalyst for long term operation was studied by conducting chronoamperometry (CA) test (current *vs* time), wherein, the electrode was maintained for 24 h in the electrolyte solution of 1N H_2SO_4 at 40^oC under a constant potential of ~1.45 V (*vs* RHE, iR_Ω corrected). For comparison, the CA test was also conducted for the in-house synthesized IrO_2 electrocatalyst used as the control.

4.5 Results and Discussion

4.5.1 Computational Study to Predict the High Electrochemical Activity of $(Mn_{1-X}Ir_x)O_2$ and $(Mn_{1-X}Ir_x)O_2$:10F

In the present study, we have continued to adopt the concept proposed by J.K. Nørskov and his group[113, 114] and accordingly, we have used it for qualitative evaluation of the electrochemical activity of $(Mn,Ir)O_2$ and $(Mn,Ir)O_2$:10F. The concept shows the existence of a simple descriptor for determining the surface catalytic activity of the two electrocatalyst systems. This descriptor has been defined as a gravity center of the transition metal d-band ε_d usually located in the vicinity of the Fermi level. An optimal position of the d-band center thus, provides an optimal interaction between the catalytic surface and various species participating in the catalytic reactions predominantly occurring on the surface leading to the expected maximum catalytic activity. Thus, such an interaction should be considered optimal allowing the reactants and products to both adsorb at the surface and desorb most efficiently. Hence, an adjustment of the d-band center position with respect to the Fermi level may likely play a critical role in designing the novel highly active and electrochemically stable electrocatalysts discussed herein. As mentioned earlier in the present study, the electronic structure of the stable surfaces for all electrocatalysts have been calculated and the positions of the corresponding d-band centers have been obtained as a first moment of $n_d(E)$: $\varepsilon_d = \int n_d(E)EdE / \int n_d(E)dE$, where $n_d(E)$ is the projected d-band density of states of the corresponding materials.

Figure 4-2 (a) thus accordingly shows the projected d-band densities of states together with the corresponding centers of these zones marked with vertical arrows on the graphs for pure IrO_2, Ir substituted MnO_2, $(Mn_{0.83}Ir_{0.17})O_2$, as well as F doped Mn substituted MnO_2,

$(Mn_{0.83}Ir_{0.17})O_{1.33}F_{0.67}$. Since, IrO_2 is a recognized OER electrocatalyst, the d-band positions for IrO_2, marked with a dashed vertical line throughout the whole graph, could serve as a reference point or a benchmark attesting to the optimal catalytic activity for the designed electrocatalysts. Our calculations have showed that IrO_2 is characterized by the d-band centers located at ~ (-1.33 eV). The closer the corresponding d-band center of the solid solution electrocatalyst studied herein to IrO_2 d-band center position, it can be considered as the likely indication of the substituted solid solution exhibiting electrochemical activity matching that of IrO_2 and thus an indicator of expected improvement of overall catalytic activity of the electrocatalyst. Such an approach can thus help in understanding the effect of fluorine on the electro-catalytic activity of $(Mn,Ir)O_2$:F.

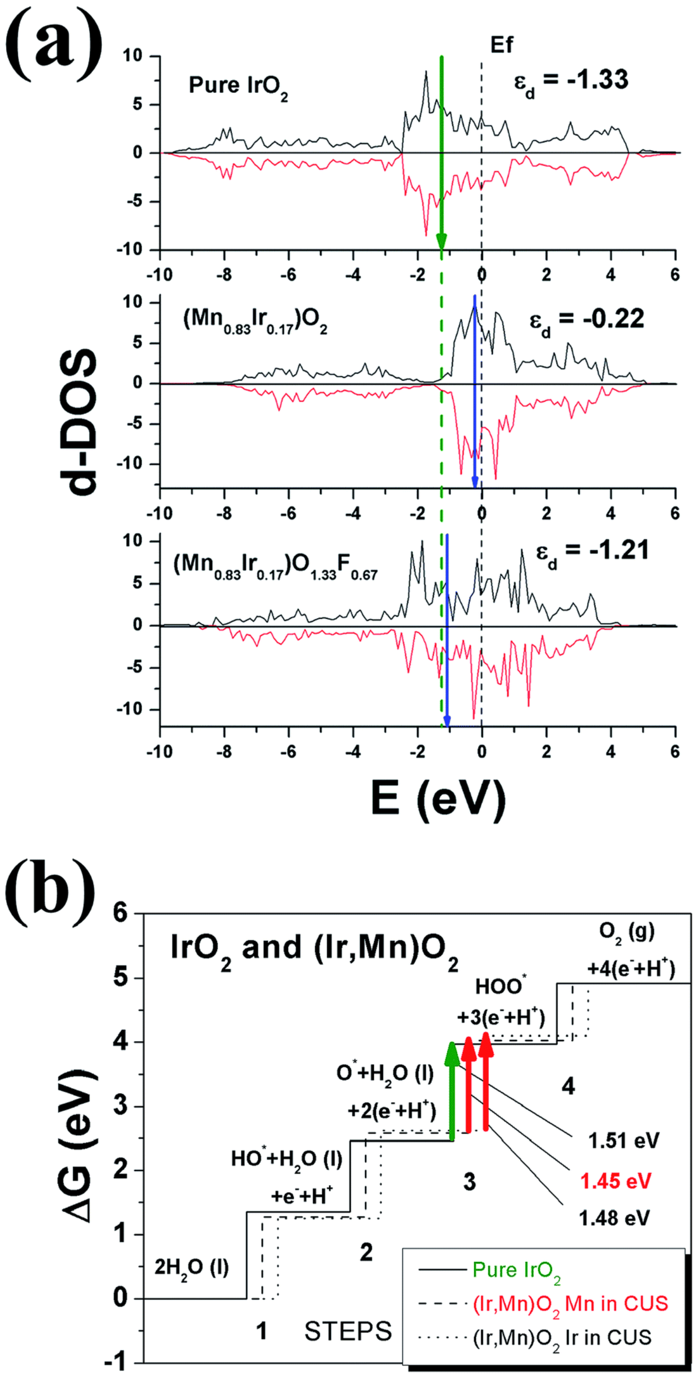

Figure 4-2 (a) Projected d-band density of electronic states calculated for pure IrO_2, $(Mn_{0.83}Ir_{0.17})O_2$, and $(Mn_{0.83}Ir_{0.17})O_{1.33}F_{0.67}$. Fermi level is set to zero, a vertical dashed line represents d-band centers for pure IrO_2, while arrows denote corresponding d-band centers for $(Mn_{0.83}Ir_{0.17})O_2$, and $(Mn_{0.83}Ir_{0.17})O_{1.33}F_{0.67}$. (b) Free energies of the intermediate reactions for pure IrO_2 and $(Mn_{0.83}Ir_{0.17})O_2$ with two different Mn-configurations

It can be seen from **Figure 4-2 (a)** that the projected density of d-electronic states for $(Mn_{0.83}Ir_{0.17})O_2$ can be presented as a sum of Mn3d and Ir5d electrons characterized by the d-band center position located at -0.22 eV vs the Fermi level. However, an introduction of F into $(Mn_{0.83}Ir_{0.17})O_2$ changes the overall electronic structure in such a way that formation of the hybridized F2p-Mn3d and F2p-Ir5d electronic states shifts the d-band center downward to -1.21 eV very close to that of IrO_2 (-1.33 eV). Of course, it should be noted that this approach is very qualitative and does not provide exact chemical compositions demonstrating the optimal catalytic activity of the material. Nevertheless, it provides a basic understanding of the effect of F doping on the electro-catalytic activity of $(Mn_{0.83}Ir_{0.17})O_2$:F. An identical effect of F on the electronic structure has also been seen earlier and reported by us in the study of $(Sn,Ir)O_2$:F electrocatalysts.[97] Similar to $(Mn_{0.83}Ir_{0.17})O_2$:F, formation of F2p-Ir5d hybridized electronic states shift the d-band center of $(Ir,Sn)O_2$:F down toward the optimal position, and thus, improved the overall catalytic activity of $(Ir,Sn)O_2$:F with substantial reduction of ~70-80% in the noble metal content.[97] The theoretical calculations were also validated experimentally and reported by us in the corresponding reports[97]. Although the d-band center concept can provide a qualitative explanation of the basic origins of high catalytic activity of $(Mn,Ir)O_2$:F, it does not provide insights to elucidate effect of Mn introduction into the IrO_2 lattice on the overpotential of the $(Ir,Mn)O_2$ solid solution oxide. To study this effect, it is imperative to consider all the four elementary steps involved in the oxygen evolution reaction discussed in **Figure 4-2 (b)** and also outlined in the earlier section. **Figure 4-2 (b)** demonstrates the free energies of all the four elementary steps of OER calculated for pure IrO_2 and the two different Ir-Mn atomic configurations discussed above and illustrated in **Figure 4-1**. Also, some of the data used for plotting these graphs are collected in the Table 4-2Table 4-1. One can see that the most energetically challenging step for all the three materials is step 3, resulting in the formation of the hydroperoxide HOO* from the second water molecule. This step determines the major overpotential that is required to be overcome to meet the four steps outlined in **Figure 4-2 (b)**, leading to the evolution of oxygen. For pure IrO_2 the overpotential is 1.51 -1.23 = 0.28 V, while for $(Ir,Mn)O_2$ it is 0.22 V and 0.25 V for the two different positions of Mn in the unit cell, thus indicating that the presence of Mn is critical to lower the overpotential for the electrolysis reaction in comparison with pure IrO_2. Such a decrease in the energy difference for the third elementary step in the case of Mn-doped IrO_2 is due to the stronger interaction between the adsorbed oxygen O^* and the surface resulting in a decrease in the total energy of the system in comparison with pure IrO_2; making it more feasible for the species to adsorb at the surface and thus, resulting in a reduction of the overpotential of the overall OER for $(Mn,Ir,)O_2$ oxide. From **Table 4-1**, it can also be seen that the ΔG values for all the intermediates in the case of both the Mn-configurations of $(Mn,Ir)O_2$ are consistently lower than those for pure IrO_2 indicating a stronger binding of the intermediates to the Mn-containing surface. Such an enhancement in adsorption is indirectly confirmed by the d-band calculations discussed above, when the introduction of Mn shifts the resulted d-band center upward towards the Fermi level, thus making the effective interactions between the intermediate species and the catalytic surface stronger in comparison to pure IrO_2. The more close the d-band center to the Fermi level of the material, the larger is the overlap between the d-orbitals of the surface and oxygen s,p-orbitals in O^*, HO^*, and HOO^* intermediate species leading to a stronger overall interaction between the surface and the adsorbed species. These results clearly demonstrate that the coordinatively unsaturated sites (CUS) on the oxidized surface could serve as the main active sites for water oxidation regardless of the local distribution of the Mn-ions with the difference in the over-potential of 0.03V for different surface configurations [**Figure 4-2 (b)**].

Table 4-1 Computational data obtained from the present study. (ΔZPE - TΔS data taken from previously published study[101])

Configuration	E_{tot} slab (eV) for pure IrO_2	ΔZPE - TΔS (eV)	ΔG (eV)		
			Pure IrO_2	Mn at the center	Mn at the side
Vac+$2H_2O$	-259.47	-	0	0	0
HO*+H_2O+1/$2H_2$	-279.21	0.35	1.36	1.16	1.17
O*+H_2O+H_2	-270.31	0.05	2.46	2.31	2.28
HOO*+3/$2H_2$	-289.85	0.40	3.97	3.75	3.66
Vac+O_2+$2H_2$	-259.47	-	4.92	4.92	4.92
ΔG of Step 3 (eV) (Over-potential in V)			1.51 (0.28)	1.45 (0.22)	1.48 (0.25)

As demonstrated in various previous studies, introduction of F into the different solid solutions of IrO_2 with SnO_2 and/or NbO_2 oxides did not result in decreasing the overpotential for OER.[97, 98] The onset potential remained the same for all the materials ~1.43V (the corresponding overpotential was ~0.20V), while the kinetic properties (e.g. exchange current density) strongly depended on the F-content of the material.[97, 98] In light of this, computational investigation of the effect of F on the overpotential of $(Mn,Ir)O_2$ oxide was therefore deemed redundant and hence, has not been conducted in the current study. Thus, the present theoretical study has demonstrated different effects of introduction of Mn and F into the IrO_2 lattice: an introduction of Mn makes interactions between the surface and intermediate species more strong thus decreasing the overpotential and increasing the propensity for the overall OER, while F-doping modifies the electronic structure of the material in a such way, that the d-band center moves towards the ideal position corresponding to the optimal electro-catalytic activity. Also, fluorine introduces more free electrons into the system resulting in improving the overall electronic conductivity of $(Mn,Ir)O_2:F$ and, in turn, the overall catalytic activity. These theoretical findings correlate very well with experimental observations discussed in the present study.

4.5.2 Experimental Characterization of $(Mn_{1-x}Ir_x)O$ (x=0, 0.3, 1) Electrocatalyst

4.5.2.1 Structural Characterization of $(Mn_{1-x}Ir_x)O_2$ (x=0, 0.3, 1)

The XRD patterns of pure IrO_2 (x = 1) and pure MnO_2 (x = 0) electrocatalyst produced by the thermal decomposition of $IrCl_4$ and $MnCl_2$ solutions (deposited on Ti foil) respectively at 400°C for 4 h in air are shown in **Figure 4-3 (a)**. Both IrO_2 and MnO_2 exhibit tetragonal structure similar to earlier reports.[93, 115, 116] The calculated lattice parameters of pure IrO_2 are $a = b = 4.63 \pm 0.06$ Å and $c = 3.06 \pm 0.04$ Å, with molar volume of 19.75 cm^3mol^{-1} which is consistent with the reported literature values.[97, 117] Similarly, the calculated lattice parameters of MnO_2 are $a = b = 9.88 \pm 0.07$ Å and $c = 2.82 \pm 0.02$ Å with molar volume of ~20.72 cm^3mol^{-1} is similar to the earlier reported results.[118-120] On the other hand, the XRD patterns of $(Mn_{0.7}Ir_{0.3})O_2$ electrocatalyst, shown in **Figure 4-3 (a)**, represent tetragonal structure with a lattice parameter of $a = b = 4.64 \pm 0.04$ Å and $c = 3.07 \pm 0.03$ Å, with a molar volume of ~19.77 cm^3mol^{-1}. The XRD patterns of $(Mn_{0.7}Ir_{0.3})O_2$ electrocatalyst show no other peaks of Ir or Mn based compounds thus confirming the formation of homogeneous single phase solid solution of $(Mn_{1-x}Ir_x)O_2$ (x = 0.3).

Table 4-2 The lattice parameters and molar volume of MnO_2, IrO_2, $(Mn_{1-x}Ir_x)O_2$ (x=0.3) and $(Mn_{1-x}Ir_x)O_2$:10F (x = 0.2, 0.3, 0.4)

Composition	**Lattice parameter (Å)**		**Molar volume (cm^3 mol^{-1})**
	a = b	**c**	
MnO_2	9.88 ± 0.07	2.82 ± 0.02	20.72
$(Mn_{0.7}Ir_{0.3})O_2$	4.64 ± 0.04	3.07 ± 0.03	19.77
$(Mn_{0.8}Ir_{0.2})O_2$:10F	4.63 ± 0.06	3.06 ± 0.04	19.75
$(Mn_{0.7}Ir_{0.3})O_2$:10F	4.64 ± 0.06	3.08 ± 0.04	19.96
$(Mn_{0.6}Ir_{0.4})O_2$:10F	4.65 ± 0.06	3.06 ± 0.04	19.92
IrO_2	4.63 ± 0.06	3.06 ± 0.04	19.75

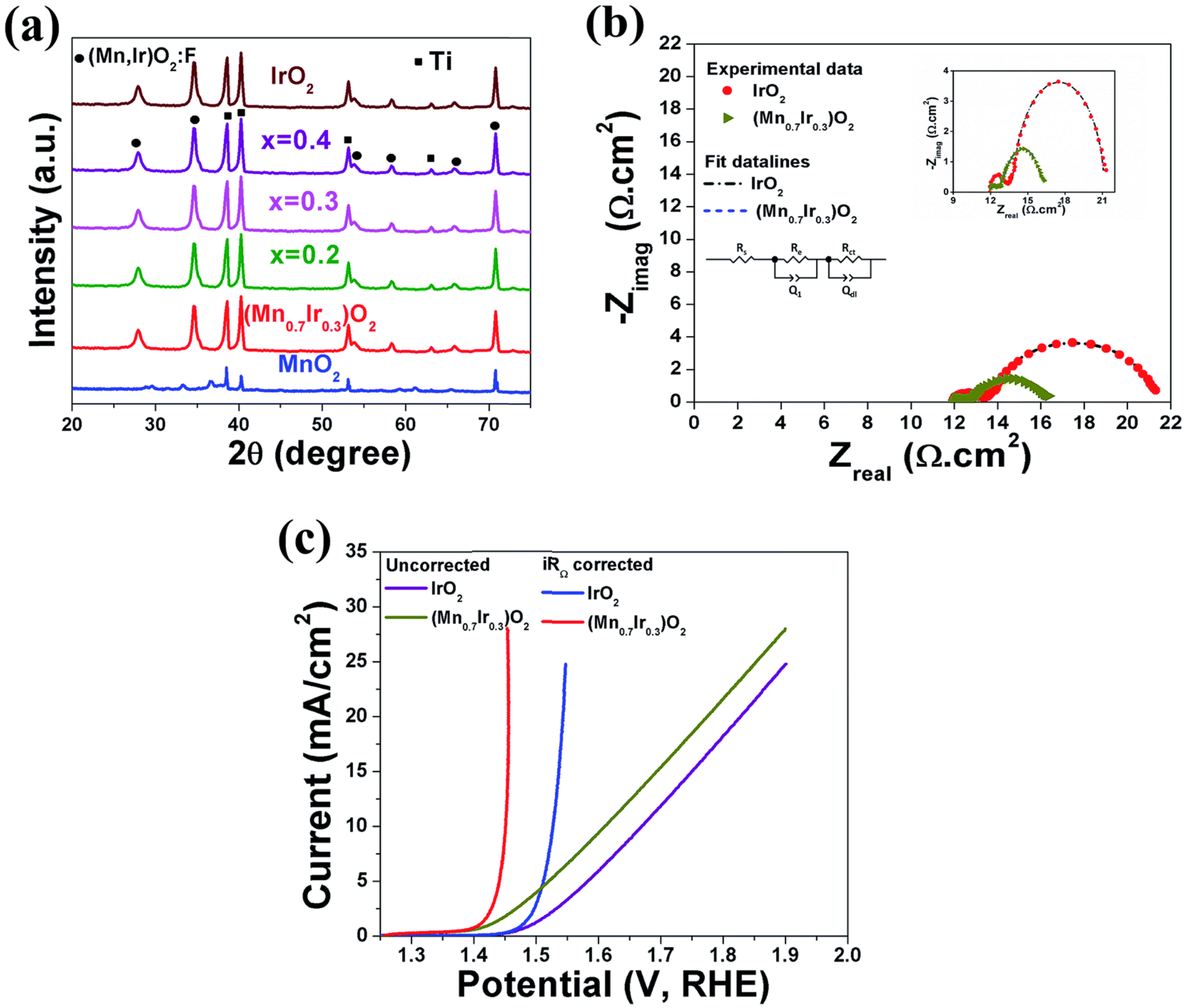

Figure 4-3 (a) The XRD patterns of $(Mn_{1-x}Ir_x)O_2$ (x = 0.3) and $(Mn_{1-x}Ir_x)O_2$:10F (x = 0.2, 0.3 and 0.4), electrocatalysts coated on Ti foil, (b) EIS spectra of $(Mn_{0.7}Ir_{0.3})O_2$ and pure IrO_2 (total loading of 0.3 mg.cm^{-2}) performed at ~1.45 V (*vs* RHE, iR_Ω corrected) in 1N H_2SO_4 at 40°C in the frequency range of 100 mHz to 100 kHz (inset: EIS equivalent circuit and magnified view of EIS), (c) The polarization curve of pure IrO_2 and $(Mn_{0.7}Ir_{0.3})O_2$ electrocatalyst using total loading of 0.3 mg.cm^{-2} obtained in 1N H_2SO_4 solution at 40^{0}C with scan rate of 10 mVsec^{-1} before and after iR_Ω correction

4.5.2.2 Electrochemical Characterization of $(Mn_{1-x}Ir_x)O_2$ (x = 0.3, 1)

The EIS of $(Mn_{0.7}Ir_{0.3})O_2$ along with pure IrO_2 (x=1), measured at ~1.45V (iR_Ω corrected) and performed in the electrolyte solution of 1N H_2SO_4 at 40°C, is shown in **Figure 4-3 (b),** to determine solution resistance (R_s), electrode resistance (R_e) and charge transfer resistance (R_{ct}). As discussed in the experimental section, equivalence circuit model $R_s(R_eQ_1)(R_{ct}Q_{dl})$ has been used in which R_s is in series with the parallel combination of the R_e and Q_1 and further in series with the parallel combination of the R_{ct} and Q_{dl} . It is interesting to note that the charge transfer resistance (R_{ct}), determined from the diameter of the semi-circle in the low frequency region of the EIS plot, of $(Mn_{0.7}Ir_{0.3})O_2$ (R_{ct} ~3.6 Ω cm^2) is lower than pure IrO_2 (R_{ct} ~8.5Ω cm^2 comparable with our earlier report).[121] This result clearly suggests that the activation polarization of $(Mn_{0.7}Ir_{0.3})O_2$ is much lower than pure IrO_2 for OER, and as a result, $(Mn_{0.7}Ir_{0.3})O_2$ is expected to have better reaction kinetics and electrochemical activity than pure IrO_2.[78, 116]

Table 4-3 Results of electrochemical characterization for OER of IrO_2, $(Mn_{1-x}Ir_x)O_2$ (x = 0.3) and $(Mn_{1-x}Ir_x)O_2$:10F (x= 0.2, 0.3, 0.4) electrocatalysts, obtained in 1N H_2SO_4 electrolyte solution at 40°C

Composition	Onset potential (V *vs* RHE)	Current density at ~1.45 V (*vs* RHE) (mA. cm^{-2})	R_s (Ω.cm^2)	R_e (Ω.cm^2)	R_Ω(Ω.cm^2)	R_{ct} (Ω.cm^2)	Tafel slope (mV dec^{-1})
$(Mn_{0.7}Ir_{0.3})O_2$	~1.35	~9.09	~11.73	~1.85	~13.58	~3.6	~67
$(Mn_{0.8}Ir_{0.2})O_2$:10F	~1.35	~5.45	~11.72	~2.4	~14.12	~4	~68
$(Mn_{0.7}Ir_{0.3})O_2$:10F	~1.35	~10.65	~11.68	~1.78	~13.46	~2.6	~65
$(Mn_{0.6}Ir_{0.4})O_2$:10F	~1.35	~11.03	~11.71	~1.7	~13.41	~2.1	~62
IrO_2	~1.43	~0.75	~11.73	~2.5	~14.23	~8.5	~71

In order to analyze the electrochemical activity of $(Mn_{0.7}Ir_{0.3})O_2$ electrocatalyst, linear scan polarization has also been performed in the electrolyte solution of 1N H_2SO_4 at 40^{o}C with the scan rate of 10 mVsec^{-1}. The electrolyte solution resistance (R_s), electrode resistance (R_e) and bubble resistance (R_{bub}) are mainly responsible for the linear nature of polarization curve and non-linearity in the Tafel plot[122, 123]. Thus, to study the inherent electrochemical activity of the electrocatalysts, ohmic resistance (R_Ω) correction ($iR_\Omega = iR_s+iR_e$)[75, 76, 111, 124] has been performed in the polarization curves as well as in Tafel plots of $(Mn_{0.7}Ir_{0.3})O_2$ and IrO_2. **Figure 4-3 (c)** shows the uncorrected and iR_Ω corrected polarization curves of pure IrO_2 and $(Mn_{0.7}Ir_{0.3})O_2$ electrocatalyst. The electrochemical activity of pure MnO_2 has not been performed due to the inherent instability of MnO_2 in the acidic electrolyte solution.[125-127] The onset potential of OER for $(Mn_{0.7}Ir_{0.3})O_2$ is ~1.35 V (*vs* RHE) with ~120mV overpotential (w.r.t. the standard potential for OER i.e. 1.23 V *vs* RHE) which is much lower than that of IrO_2 which shows an onset potential of ~1.43 V (*vs* RHE) with ~200mV overpotential similar to earlier reports.[97, 102, 128] The significant decrease in the overpotential, lowest reported to date, measured for $(Mn_{0.7}Ir_{0.3})O_2$ electrocatalyst is in good agreement with the results of the theoretical calculation discussed in the earlier section. The current density obtained at ~1.45 V for $(Mn_{0.7}Ir_{0.3})O_2$ (total loading=0.3 mg.cm^{-2}) is ~9.09 mA.cm^{-2} which is ~12 fold higher than that of IrO_2 (0.75 mA.cm^{-2} at 1.45V with an identical loading=0.3 mg.cm^{-2}). The excellent electrochemical performance (i.e. low over-potential and higher current density) of $(Mn_{0.7}Ir_{0.3})O_2$ is due to the improved reaction kinetics for OER of $(Mn_{0.7}Ir_{0.3})O_2$ than that of IrO_2 as predicted by the theoretical calculations

In order to further improve the reaction kinetics of $(Mn,Ir)O_2$ electrocatalyst, 10wt.% F has been introduced as a dopant in the $(Mn,Ir)O_2$ electrocatalyst as proposed from the theoretical studies discussed earlier. In addition, a higher (x=0.4) and lower (x=0.2) IrO_2 content solid solution electrocatalysts [$(Mn_{1-x}Ir_x)O_2$:10F (x=0.2, 0.3, 0.4)] has also been explored to identify the nominal composition with an excellent electrochemical activity towards OER in PEM based water electrolysis.

4.5.3 Characterization of $(Mn_{1-x}Ir_x)O_2$:10F (x=0.2, 0.3, 0.4) Electrocatalyst

4.5.3.1 Structural Characterization of $(Mn_{1-x}Ir_x)O_2$:10F Electrocatalysts

The XRD patterns of $(Mn_{1-x}Ir_x)O_2$:10F (x =0.2, 0.3, 0.4) electrocatalysts of different compositions, shown in **Figure 4-3 (a)**, reveal the tetragonal structure similar to that of pure IrO_2 and $(Mn_{0.7}Ir_{0.3})O_2$ without any other peaks of Mn or Ir based compounds, suggesting the formation of complete homogeneous single phase solid solution without any undesired phase separation for the F doped compositions containing varying amounts of Mn. The calculated lattice parameters and molar volume of $(Mn_{1-x}Ir_x)O_2$:10F (x = 0.2, 0.3, 0.4) are quite similar to that of pure $(Mn_{0.7}Ir_{0.3})O_2$ as shown in **Table 4-2**. The effective crystallite size of $(Mn_{1-x}Ir_x)O_2$:10F (x = 0.2, 0.3, 0.4), calculated using the Scherrer formula from the integral breadth of the Lorentzian contribution determined from peak profile analysis using the single line approximation method after eliminating the instrumental broadening and lattice strain contribution[129] is ~5 to 7 nm, indicating the nanocrystalline nature of the solid solution electrocatalyst materials of different compositions.

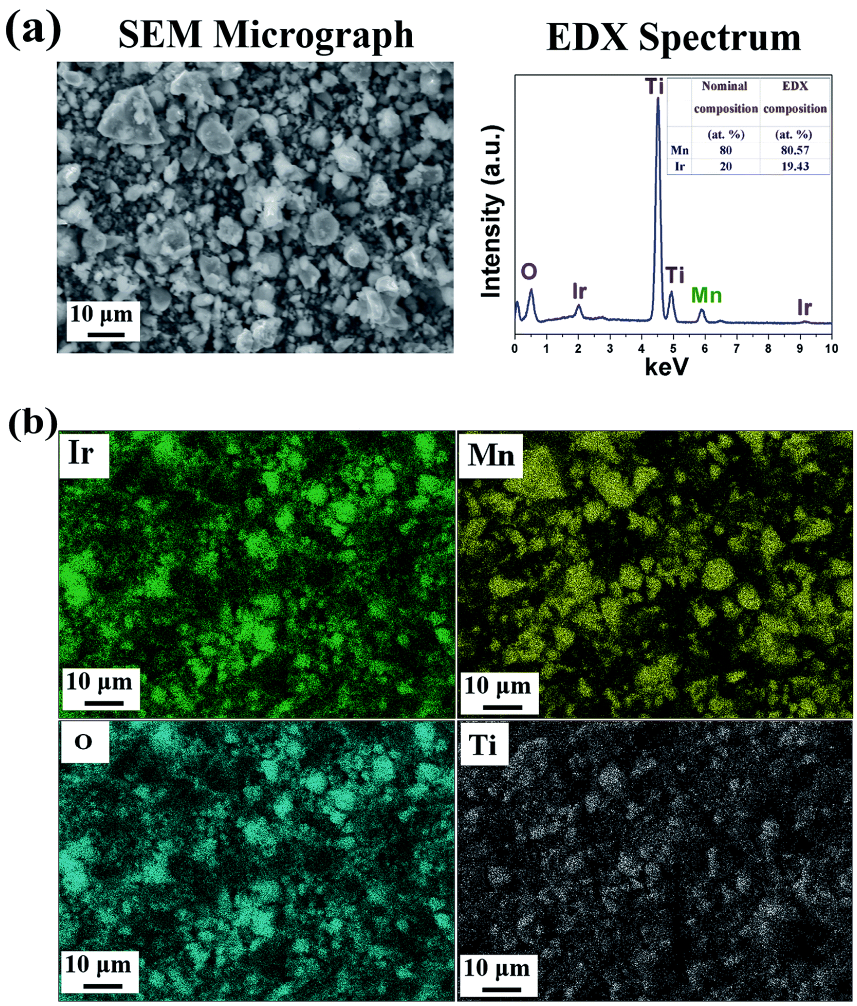

	Nominal composition	EDX composition
	(at. %)	(at. %)
Mn	80	80.57
Ir	20	19.43

Figure 4-4 (a) The SEM micrograph and EDX spectrum, (b) Elemental x-ray mapping of ($Mn_{0.8}Ir_{0.2}$)O_2:10F

The SEM micrograph combined with the EDX pattern of the representative composition, ($Mn_{1-x}Ir_x$)O_2:10F (x=0.2) shows the presence of Ir, Mn and O [**Figure 4-4 (a)**]. The quantitative elemental composition analysis of ($Mn_{1-x}Ir_x$)O_2:10F (x=0.2) obtained from EDX shows the measured elemental composition of Ir and Mn close to the nominal composition. The elemental x-ray maps of Ir, Mn and O for ($Mn_{1-x}Ir_x$)O_2:10F (x = 0.2) [**Figure 4-4 (b)**] show the homogeneous distribution of elements within the particles indicating absence of any segregation at any specific site.

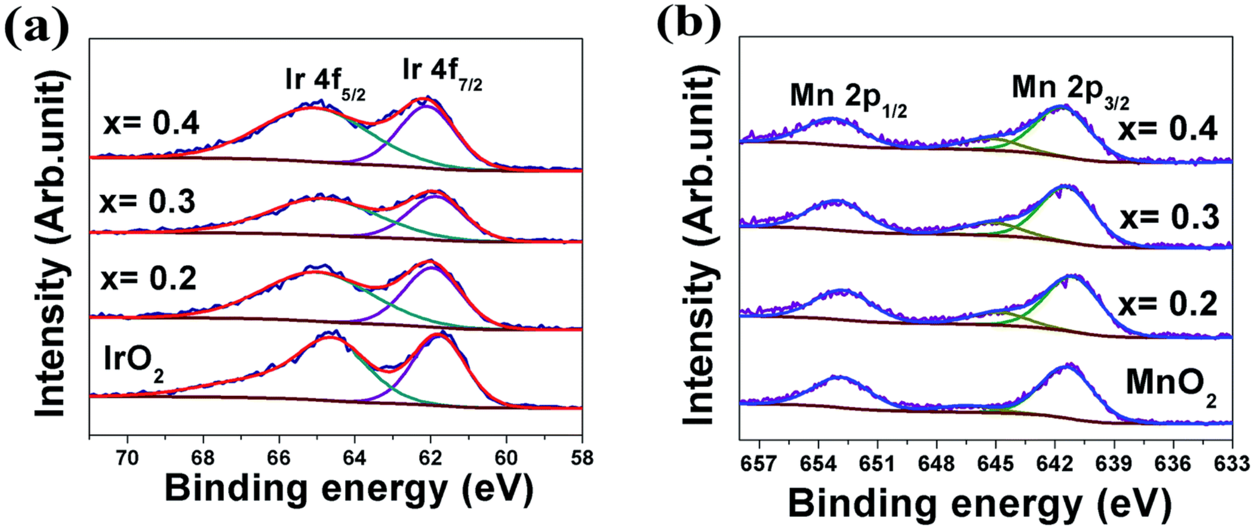

Figure 4-5 The XPS and corresponding deconvoluted spectra of (a) Ir 4f$_{7/2}$ and 4f$_{5/2}$ doublet, (b) Mn 2P$_{1/2}$ and Mn 2P$_{3/2}$ doublet of pure IrO$_2$ and pure MnO$_2$ and (Mn$_{1-x}$Ir$_x$)O$_2$:10F (x = 0.2, 0.3 and 0.4) electrocatalysts

XPS analysis has been performed on (Mn$_{1-x}$Ir$_x$)O$_2$:10F electrocatalysts with different Mn content to study the valence states of Ir and Mn. The XPS analysis has been plotted in the **Figure 4-5** for Ir and Mn, respectively. The deconvoluted XPS spectrum of Ir in pure IrO$_2$ shows the presence of Ir 4f doublet centered at binding energy of ~61.7 eV and ~ 64.6 eV (similar to earlier report[130]) which corresponds to Ir 4f$_{7/2}$ and Ir 4f$_{5/2}$ respectively, consistent with that of pure IrO$_2$.[116] **Figure 4-5** shows the XPS spectra of Mn 2p doublet for MnO$_2$ centered at ~641.6 eV and ~653.8 eV (similar to earlier report[131-133]) for Mn 2p$_{3/2}$ and Mn 2p$_{1/2}$, respectively, which corresponds to that of pure MnO_2.[131, 134] The deconvoluted XPS spectra of $(Mn_{1-x}Ir_x)O_2$:10F (for x= 0.2, 0.3,0.4) exhibit an additional peak centered near ~ 645.5 eV, similar to the previous studies, which may be a shake-up peak and can be referred as a satellite peak. [131, 132] However, the positive shift in Ir 4f doublet and Mn 2p doublet positions of $(Mn_{1-x}Ir_x)O_2$:10F after incorporation of F in the solid solution lattice as well as with increase in Ir content suggests modification of the electronic structure of $(Mn_{1-x}Ir_x)O_2$:10F for the different compositions upon formation of solid solution and due to the presence of fluorine in the solid solution lattice leading to stronger binding due to the higher electronegativity of fluorine.[97,135] The presence of F in $(Mn_{1-x}Ir_x)O_2$:10F of different compositions could not be unequivocally ascertained by the XPS analysis similar to our earlier publications on Sn substituted IrO_2[97, 98], probably due to the low concentration of F actually retained within the lattice. Nevertheless, F incorporation has indeed beneficial effect on the electrochemical activity (as witnessed in the polarization curve, discussed later) of $(Mn,Ir)O_2$:F solid solution most likely due to the improved electronic conductivity.[97]

4.5.3.2 Electrochemical Characterization of $(Mn_{1-x}Ir_x)O_2$:10F Electrocatalysts

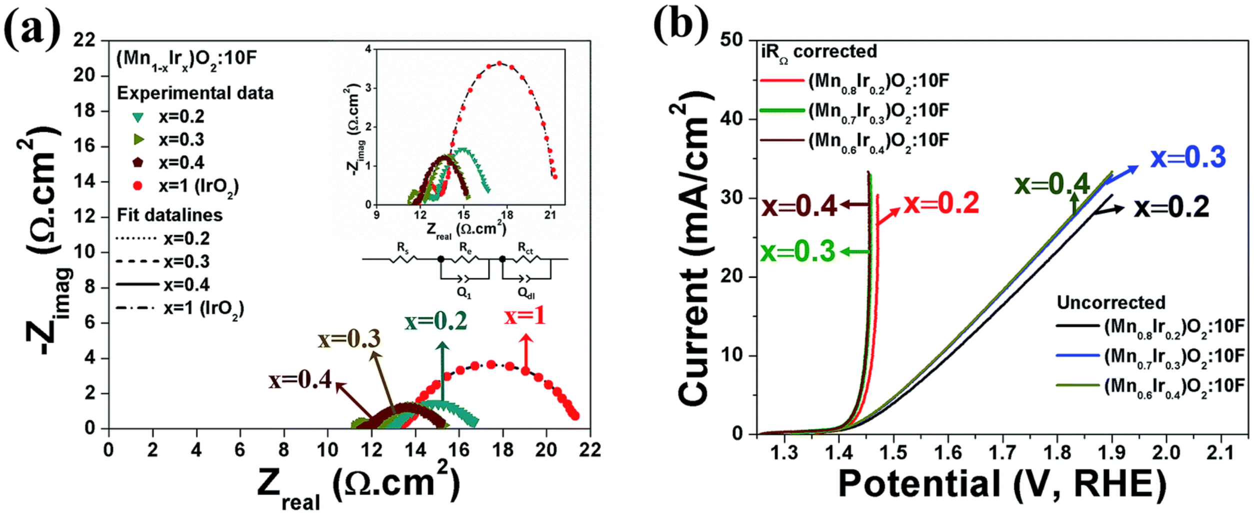

Figure 4-6 (a) EIS spectra of $(Mn_{1-x}Ir_x)O_2$:10F for (x = 0.2, 0.3 and 0.4) and pure IrO_2 (total loading of 0.3 mg.cm^{-2}) performed at ~1.45 V (*vs* RHE, iR_Ω corrected) in 1N H_2SO_4 at 40°C in the frequency range of 100 mHz to 100 kHz (inset: EIS equivalent circuit and magnified view of EIS), (b) The polarization curve of $(Mn_{1-x}Ir_x)O_2$:10F for (x = 0.2, 0.3 and 0.4) (total loading of 0.3 mg.cm^{-2}) obtained in 1N H_2SO_4 solution at 40^0C with scan rate of 10 mVsec^{-1} before and after iR_Ω correction

The electrochemical performance of $(Mn_{1-x}Ir_x)O_2$:10F (x = 0.2, 0.3, 0.4) has been studied by conducting EIS to determine R_s, R_e and R_{ct} using $R_s(R_eQ_1)(R_{ct}Q_{dl})$ as the equivalent circuit model, as discussed in the experimental section [**Figure 4-6(a)**]. It is noteworthy that the R_{ct}, determined from the diameter of the semi-circle in the low frequency region of the EIS plot, of $(Mn_{0.7}Ir_{0.3})O_2$:10F (R_{ct}~2.6 Ω cm^2) and $(Mn_{0.6}Ir_{0.4})O_2$:10F (R_{ct}~ 2.1 Ω cm^2) is lower than $(Mn_{0.7}Ir_{0.3})O_2$ (R_{ct}~ 3.6 Ω cm^2) and pure IrO_2 (~8.5 Ω cm^2) which clearly suggests that F doping has a significant influence on the kinetics of the water splitting reaction as also predicted by the theoretical analysis. These results thus indicate that the activation polarization of $(Mn_{1-x}Ir_x)O_2$:10F for x=0.3 and x=0.4 is significantly lower than $(Mn_{0.7}Ir_{0.3})O_2$ and pure IrO_2 for OER. On the other hand, the R_{ct} of $(Mn_{0.8}Ir_{0.2})O_2$:10F (R_{ct}~ 4 Ω cm^2) which is comparable with $(Mn_{0.7}Ir_{0.3})O_2$ (R_{ct}~ 3.6 Ω cm^2), and much lower than pure IrO_2. In addition, it has been noticed that the R_e decreases with increase in Ir content for $(Mn_{1-x}Ir_x)O_2$:10F and x=0.4 shows the lowest R_e of ~1.7 Ω.cm^2. The decrease in R_e with increase in Ir content for $(Mn_{1-x}Ir_x)O_2$:10F can be due to an improved electronic conductivity of $(Mn_{1-x}Ir_x)O_2$:10F with increase in Ir content. Furthermore, the ohmic resistance, ($R_\Omega = R_s + R_e$) as shown in **Table 4-3** also decreases with increase in Ir content.

Based on the above results, it is anticipated that $(Mn_{1-x}Ir_x)O_2$:10F (x=0.3 and 0.4) will show enhanced reaction kinetics as well as electrochemical activity than $(Mn_{0.7}Ir_{0.3})O_2$ and pure IrO_2. The uncorrected and iR_Ω corrected linear scan polarization curves of $(Mn_{1-x}Ir_x)O_2$:10F (x = 0.2, 0.3, 0.4) obtained in the electrolyte solution of 1N H_2SO_4 at 40°C with the scan rate of 10 $mVsec^{-1}$are shown in **Figure 4-6 (b)**. The onset potential of OER for $(Mn_{1-x}Ir_x)O_2$:10F (x = 0.2, 0.3, 0.4) is ~1.35V (*vs* RHE) which is comparable to $(Mn_{0.7}Ir_{0.3})O_2$ with ~120mV overpotential and lower than IrO_2 which shows ~200mV overpotential. The current density obtained at ~1.45 V (*vs* RHE) for $(Mn_{0.7}Ir_{0.3})O_2$:10F, $(Mn_{0.6}Ir_{0.4})O_2$:10F is ~10.65 $mA.cm^{-2}$ and ~11.03 $mA.cm^{-2}$ respectively, which is ~14 and ~15 fold higher than that of IrO_2 (0.75 $mA.cm^{-2}$ at 1.45V), respectively. Although the current density obtained at ~1.45 V for $(Mn_{0.8}Ir_{0.2})O_2$:10F electrocatalyst (i.e. ~5.54 $mA.cm^{-2}$) is lower than that of $(Mn_{0.7}Ir_{0.3})O_2$:10F, $(Mn_{0.6}Ir_{0.4})O_2$:10F and $(Mn_{0.7}Ir_{0.3})O_2$, $(Mn_{0.8}Ir_{0.2})O_2$:10F shows a significantly higher current density (~7 fold) than that of pure IrO_2 observed at ~1.45 V with a hallmark 80% reduction in noble metal content and even ~11 fold higher current density than $(Mn_{0.87}Ir_{0.13})O_2$ solid solution system reported in a recent publication.[100] The Tafel slope of $(Mn_{1-x}Ir_x)O_2$:10F (x=0.2, 0.3, 0.4) is ~68±0.0001 $mVdec^{-1}$, ~65±0.0001 $mVdec^{-1}$ and ~62±0.0001 $mVdec^{-}1$, respectively **(Figure 4-7)**.Thus, Tafel slope of $(Mn_{1-x}Ir_x)O_2$:10F decreases with increase in Ir content with the lowest obtained for $(Mn_{0.6}Ir_{0.4})O_2$:10F indicating increase in the reaction kinetics and higher electrochemical activity with the largest value obtained for $(Mn_{0.6}Ir_{0.4})O_2$:10F. In addition, the Tafel slope of $(Mn_{1-x}Ir_x)O_2$:10F does reflect the desired two electron pathway for OER in accordance with published reports[82].

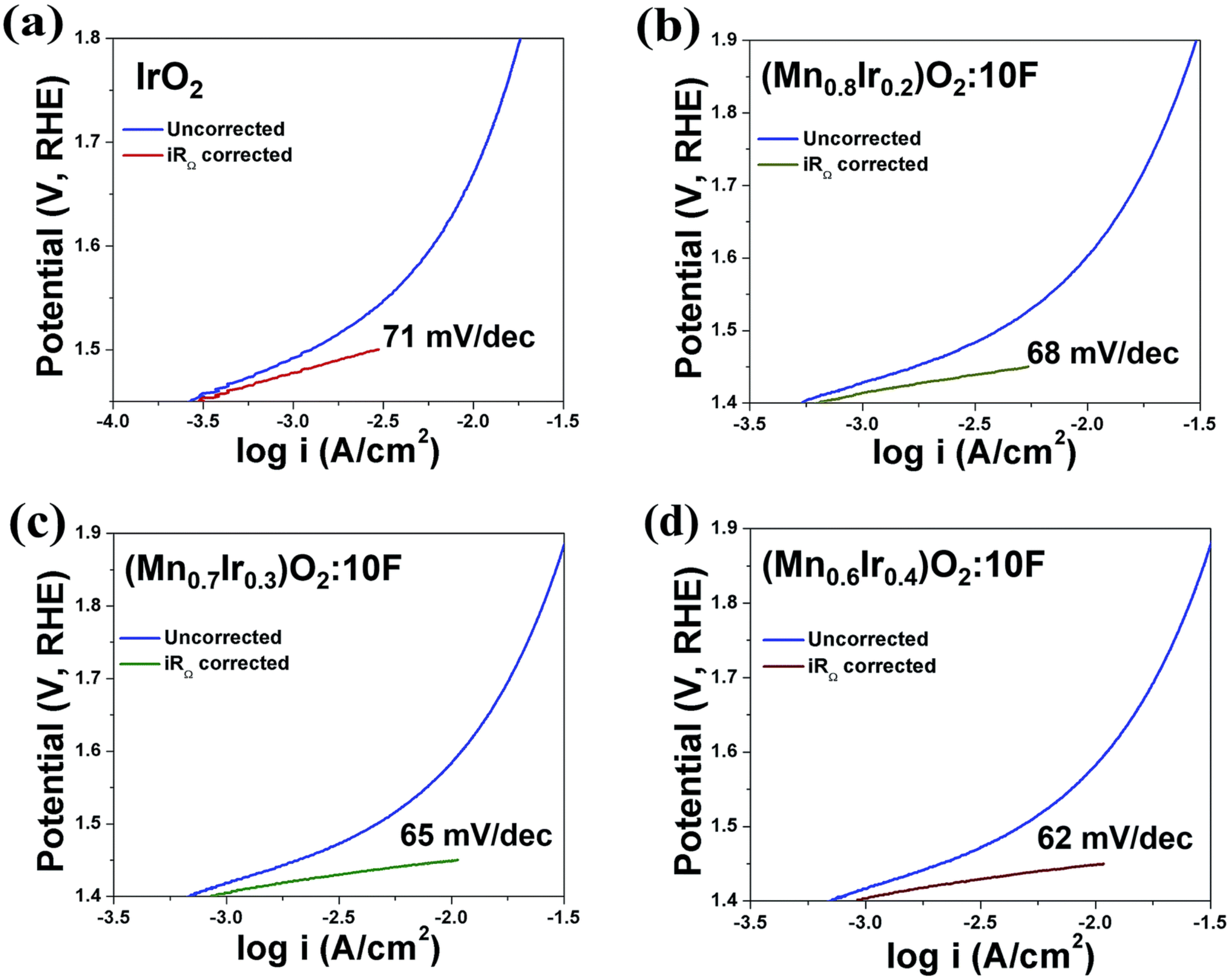

Figure 4-7 The Tafel plot of (a) IrO_2 (b) $(Mn_{0.8}Ir_{0.2})O_2$:10F (c) $(Mn_{0.7}Ir_{0.3})O_2$:10F and (d) $(Mn_{0.6}Ir_{0.4})O_2$:10F, before and after iR_{Ω} correction

It is extremely important for electrocatalyst to exhibit excellent long term electrochemical durability in harsh acidic operating conditions of OER, which will aid in efficient continuous long-term operation in PEM water electrolysis cells. Therefore, to assess the electrochemical stability/durability of $(Mn_{1-x}Ir_x)O_2$:10F electrocatalyst, chronoamperometry (CA) test has been performed at the constant applied potential of ~1.45 V [iR_{Ω} corrected, i.e., ~ 1.55 V in the uncorrected polarization curve) in 1N H_2SO_4 at 40°C. The CA curve obtained for the higher Mn content electrocatalyst $(Mn_{0.8}Ir_{0.2})O_2$:10F, shown in **Figure 4-8,** displays minimal loss in current density, indicating the superior long term electrochemical stability, similar to that of in-house synthesized IrO_2. The initial decrease in current density seen in CA curves of both in-house synthesized IrO_2 and $(Mn_{1-x}Ir_x)O_2$:10F (x = 0.2) can possibly be due to dissolution of irregular electrocatalyst coating and/or diffusion controlled reaction, similar to earlier reports.[97, 136] Thus, excellent long term electrochemical stability of $(Mn_{1-x}Ir_x)O_2$:10F (x = 0.2) can possibly be due to good alloying of IrO_2 and MnO_2 and beneficial modification in the electronic structure upon formation of F-doped solid solution, resulting in unique active phase exhibiting superior electrochemical stability.

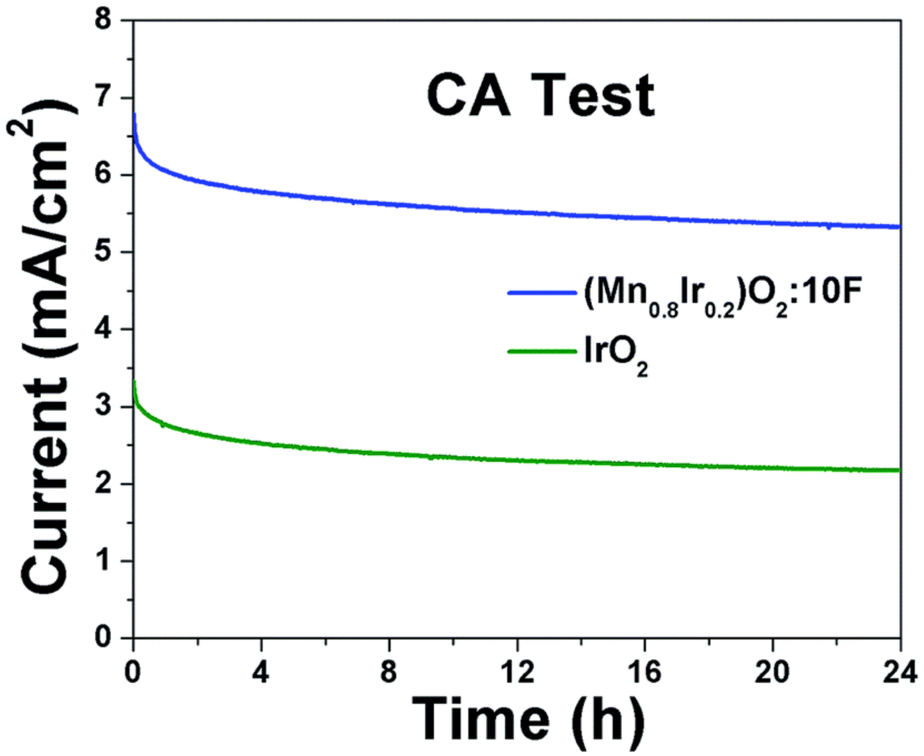

Figure 4-8 The variation of current density *vs* time in the chronoamperometry test of $(Mn_{1-x}Ir_x)O_2$:10F for (x = 0.2) and pure IrO_2 performed in 1N H_2SO_4 solution under a constant potential of ~1.45 V (*vs* RHE, iR_Ω corrected) at 40^0C for 24 h

The above results clearly suggest that the incorporation of IrO_2 in the framework of MnO_2 along with incorporation of F in the lattice offers a unique opportunity to tailor the electronic, physical, chemical and electro-catalytic properties of $(Mn,Ir)O_2$:10F. The formation of a single phase solid solution $(Mn,Ir)O_2$:10F offers modified electro-catalytic properties due to a change in the d-band center energy leading to change in adsorption strength of the corresponding adsorbed species on the electrocatalyst surface. Additionally, significant decrease in overpotential and improvement in electrochemical performance contributes to efficient OER electro-catalytic activity for PEM water electrolysis. The present study also demonstrates remarkable, ~60-80% reduction in the noble metal content along with substantial reduction in over-potential for the $(Mn_{1-x}Ir_x)O_2$:F solid solution systems indicative of the excellent electrochemical performance. The study thus clearly demonstrates the potential of $(Mn_{1-x}Ir_x)O_2$:F system as an efficient OER electrocatalysts for PEM water electrolysis. However, it should be noted that the true potential of the electrocatalyst can only be realized when tested in a full PEM based water electrolyzer. Although electrolyzer evaluation of these electrocatalysts is beyond the scope of the current study, it can be mentioned that the present electrocatalyst system displays superior electrochemical response compared to F-doped IrO_2 when evaluated in a half-cell configuration. Our evaluation of F-doped IrO_2 in a full PEM electrolyzer was also reported in a previous publication.[137] It is therefore likely, that if the current system were tested in a full PEM based electrolyzer system, the electrocatalyst would also potentially exhibit superior electrochemical response. These studies will nevertheless, be planned in the near future and reported in subsequent publications.

4.6 Conclusions

The present study successfully demonstrates nanostructured solid solution of 10 wt. % F doped IrO_2 and MnO_2 solid solutions denoted as $(Mn_{1-x}Ir_x)O_2$:10F (x = 0.2, 0.3, 0.4) with thin film architecture coated on Ti foil as potential anode electrocatalysts for OER in PEM based water electrolysis. The corresponding solid solutions $(Mn_{1-x}Ir_x)O_2$:10F (x = 0.2, 0.3, 0.4) with unique electronic/molecular structure showed excellent electrochemical activity with the lowest reported to date, onset potential of ~1.35 V (*vs* RHE) with ~120mV overpotential (w.r.t 1.23 V *vs* RHE, which is the standard potential for OER), lower than that of IrO_2 (~1.43 V *vs* RHE, i.e. ~200mV overpotential). In addition, remarkable ~ 7, ~14 and ~15 fold higher electrochemical activity was obtained for $(Mn_{1-x}Ir_x)O_2$:10F (x = 0.2, 0.3, 0.4) than that of pure IrO_2, respectively. Additionally, $(Mn_{0.8}Ir_{0.2}O_2$:10F displayed excellent long term stability in acidic media, similar to that of IrO_2. Hence, $(Mn_{1-x}Ir_x)O_2$:10F (x = 0.2, 0.3, 0.4) indeed shows excellent promise for replacing state of the art OER electrocatalyst (IrO_2) based on the excellent electrochemical performance demonstrated in this study. Moreover, this study portends significant reduction in noble metal content for OER electrocatalyst and thus, can likely lead to electrocatalysts development with significant reduction in capital costs of water electrolysis cells for economic and efficient hydrogen production from acid-based PEM water electrolysis.

5.0 Specific Aim 1A - To Identify and Engineer Reduced PGM Containing and PGM-Free Multi-Metal Oxide (MMO) Based Electrocatalyst Materials of Different Architectures for Oxygen Evolution Reaction (OER) in Proton Exchange Membrane-Based Water Electrolysis (PEMWE)

This aim describes the second reduced PGM containing OER electrocatalyst that was studied.

- Chapter 5: Fluorine substituted $(Sn,Ir)O_2$: F electrocatalysts for OER

Excerpts reprinted with permission from Ghadge, Shrinath Dattatray, et al. "First report of vertically aligned $(Sn,Ir)O_2$: F solid solution nanotubes: highly efficient and robust oxygen evolution electrocatalysts for proton exchange membrane-based water electrolysis." Journal of Power Sources 392 (2018): 139-149. Copyright © 2018, Journal of Power Sources.

5.1 Abstract

One dimensional (1D) vertically aligned nanotubes (VANTs) of $(Sn_{0.8}Ir_{0.2})O_2$:10F are synthesized for the first time by a sacrificial template assisted approach. The aim is to enhance the electrocatalytic activity of F doped $(Sn,Ir)O_2$ solid solution electrocatalyst for oxygen evolution reaction (OER) in proton exchange membrane (PEM) based water electrolysis by generating $(Sn_{0.8}Ir_{0.2})O_2$:10F nanotubes (NTs). The 1D vertical channels and the high electrochemical active surface area (ECSA ~38.46 m^2g^{-1}) provide facile electron transport. This results in low surface charge transfer resistance (4.2 Ω cm^2), low Tafel slope (58.8 mV dec^{-1}) and excellent

electrochemical OER performance with ~ 2.3 and ~ 2.6 fold higher electrocatalytic activity than 2D thin films of $(Sn_{0.8}Ir_{0.2})O_2$:10F and benchmark IrO_2 electrocatalysts, respectively. Furthermore, $(Sn_{0.8}Ir_{0.2})O_2$:10F NTs exhibit excellent mass activity (21.67 A g^{-1}), specific activity (0.0056 $mAcm^{-2}$) and TOF (0.016 s^{-1}), which is ~ 2–2.6 fold higher than thin film electrocatalysts at an overpotential of 270 mV, with a total mass loading of 0.3 mg cm^{-2}. In addition, $(Sn_{0.8}Ir_{0.2})O_2$:10F NTs demonstrate remarkable electrochemical durability - comparable to thin films of $(Sn_{0.8}Ir_{0.2})O_2$:10F and pure IrO_2, operated under identical testing conditions in PEM water electrolysis. These results indicate promise of $(Sn_{0.8}Ir_{0.2})O_2$:10F NTs as OER electrocatalysts for efficient and sustainable hydrogen production.

5.2 Introduction

The identification, synthesis, and development of high-performance oxygen evolution reaction (OER) electrocatalysts for proton exchange membrane (PEM) based water electrolysis with reduced noble-metal (e.g., IrO_2, RuO_2 and Pt/C) content or with non-noble metal electrocatalysts is a major challenge facing the PEM fuel cell area. Added to this is the challenge of the system exhibiting excellent electrocatalytic activity and faster reaction kinetics along with the prolonged stability during electrolysis operation together representing the foremost challenge facing researchers in the OER electrocatalyst research area [70, 74, 84, 97]. In an attempt to make major strides, the present authors have exploited the theoretical first principles electronic structure calculations and have identified several highly active OER electrocatalysts with substantial reduction in the noble metal content of IrO_2/RuO_2 (i.e. ~ 70-80 mol. %)[70, 97, 98, 136]. Accordingly, the solid solution of electrochemically non-active parent oxides with significantly lower noble metal (up to ~80 mole % Ir) content such as fluorine (F) doped binary and ternary solid solution oxides, synthesized in 2D thin films architectures have displayed comparable electrocatalytic activity and stability to that of pure IrO_2 [97, 98]. The thin film approach for electrocatalyst synthesis is well known and beneficial due to several reasons. In contrast to powder electrocatalysts, the film composition can be precisely controlled by the metal ions added to the precursor solutions, which is not easily accessible by conventional high temperature based pathways[138]. In addition, the film electrocatalysts extensively lack the porous structure which results in facile mass transport of the evolving gases[138]. Also, as thin film electrocatalysts are the directly fabricated/grown on the substrate or current collector, it eliminates requirement of any conductive additives or expensive binders, which are predominantly required in the powder based electrocatalysts[139, 140].

Based on the work conducted to date, for further enhancing the electrocatalytic activity of these reduced noble metal containing 2D thin film solid solution electrocatalysts, we have embarked on the challenge to tailor the material length scales into one-dimensional (1D) nanoscale motifs. Accordingly, 1D vertically aligned nanotubular (VANT) architectures of electrochemically active systems have been generated in an attempt to improve the reaction kinetics and correspondingly, the nanotubular structures exhibit superior electrocatalytic activity towards the water splitting reaction [44, 74, 141, 142].

In recent years, 1D nanostructures with nanotube (NT) as well as nanowire (NW) based morphologies have been widely studied for the application of electrocatalysts such as Pt NTs [139], nitrogen-containing carbon nanotubes (NCNTs)[143], Pt-Ru/Co NWs [144], Co_4N NWs [140], Pt–Ni–TiO_2 NTs [145] etc. in the water splitting and direct methanol fuel cell (DMFC) research area. Assembling the nanoparticles of electrocatalyst into tubular nanostructures offers various added benefits such as high active surface area, high aspect ratios (length-to-width ratio), dense catalytic sites - which expedite the catalytic activity for surface electrochemical reactions [74, 139, 146]. For example, Pt nanostructures with 1D nanotubular architectures have demonstrated ~ 1.4 times higher electrochemical active surface area than Pt black; leading to significantly improved catalytic activity (4.4 fold) towards oxygen reduction reaction[139, 147]. In addition, 1D vertically oriented nanostructures offer sufficient porosity between the adjacent 1D nanostructures which facilitates mass as well as charge transport including superior electrocatalyst-electrolyte contact due to the easy accessibility of electrolyte molecules into the deep portion of the electrode/catalyst surface, which ultimately bolsters the electrocatalytic performance [74, 130, 141, 146, 148]. Besides, due to the presence of vertical channels, the 1D vertically aligned motifs expedite the facile charge transport between the catalyst surface and the current collector path by directing effects in the catalyst electrodes which decreases the surface charge transfer resistance (R_{ct}) and thus, enhancing the electronic conductivity i.e. reaction kinetics on the electrocatalyst surface[139, 140]. Moreover, the1D nanostructures also offer the unique prospect of developing the electrocatalyst nanostructures directly grown on the current collectors - without any requirement of conductive additives or binders [139, 140].

It has been reported that the electrocatalysts with similar composition yet different morphologies significantly influence the electrocatalytic activity due to an alternation in the charge transport properties, electrochemically active surface area and diffusion of reactants and products during the reaction process [149, 150]. Therefore, in the present study, we have explored the ‘nanotube (NT) structured-1D morphology for the solid solution $(Sn_{1-x}Ir_x)O_2$:10F (x= 0.2) electrocatalyst’; comprising earth abundant tin oxide (SnO_2), fluorine (F) and ultra-low noble metal (Iridium, Ir) content, for the very first time to the best of our knowledge. Accordingly, we have studied and compared the electrochemical performance for OER of the solid solution metal oxide based electrocatalysts of different architectures (nanostructured 2D thin film and 1D nanotubes) and correlated their materials length scale parameters to the electrocatalytic properties. We have already studied the system as an optimum 2D thin film composition [$(Sn_{0.8}Ir_{0.2})O_2$:10F] for OER in PEM based water electrolysis in our prior published report[97]. Thus, herein, a versatile sacrificial template-assisted approach has been employed to fabricate $(Sn_{0.8}Ir_{0.2})O_2$:10F VANTs on titanium (Ti) substrate. In order to generate 1D nanomaterials, various methods such as physical vapor deposition[151], thermal decomposition[152], and vapor-liquid-solid deposition[153, 154] etc. have been reported. Among such techniques, the template-assisted or template-directed approach is simplistic, cost-effective and well known for the reliable fabrication of uniformly arranged one-dimension architectures, offering efficient control over size and shape of the various nano-structured materials [155-157]. Accordingly, in the present study, 1D $(Sn_{0.8}Ir_{0.2})O_2$:10F VANTs are synthesized via ZnO nanowires as a sacrificial template-assisted approach. The as-synthesized 1D $(Sn_{0.8}Ir_{0.2})O_2$:10F VANTs exhibit superior electrocatalytic activity toward OER with lower surface charge transfer resistance (R_{ct}), lower Tafel slope, higher electrochemical active surface area (ECSA), higher specific activity and turnover frequency (TOF) than the corresponding 2D thin film architectures of $(Sn_{0.8}Ir_{0.2})O_2$:10F and state-of-the art IrO_2 electrocatalysts. This research outlines the synthesis of the vertically aligned nanotubes, structural and detailed electrochemical characterization of the $(Sn_{0.8}Ir_{0.2})O_2$:10F nanotubular electrocatalyst.

5.3 Experimental Methodology

5.3.1 Synthesis of Electrocatalysts

5.3.1.1 Vertically Aligned Nanotubes (VANTs) of $(Sn_{1-x}Ir_x)O_2$:10 wt.% F (x=0.2)

Synthesis of ZnO based nanowires (NWs) as sacrificial template

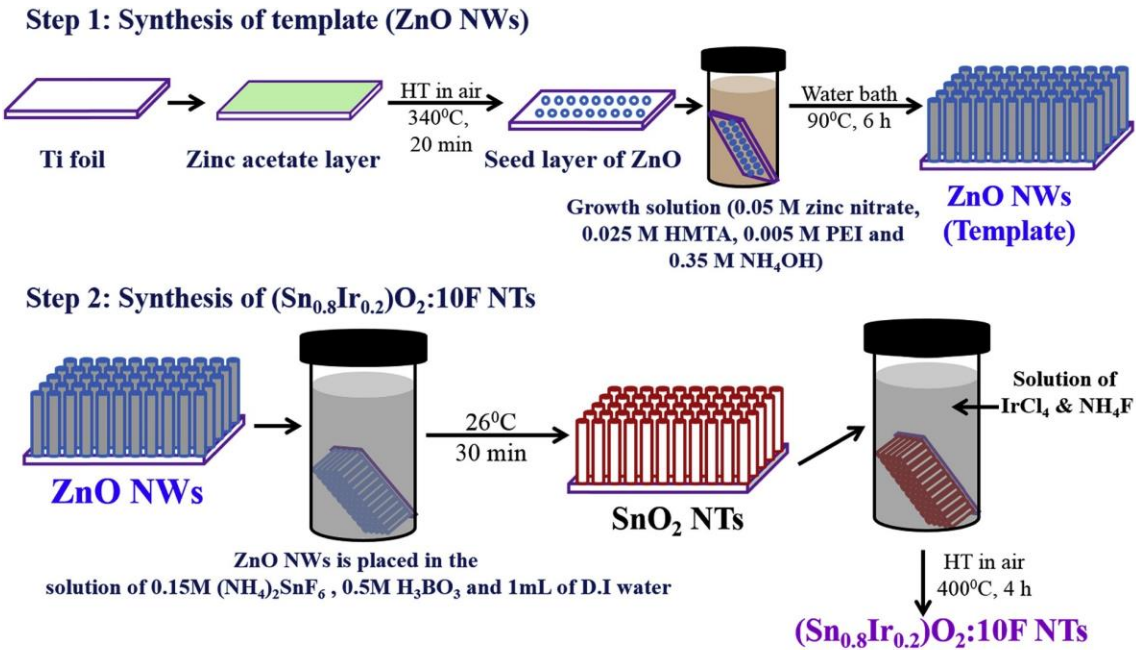

Figure 5-1 Schematic illustration of the synthesis process of $(Sn_{0.8}Ir_{0.2})O_2$:10F NTs using the template assisted approach

Synthesis of $(Sn_{1-x}Ir_x)O_2$:10F VANTs has been achieved using ZnO NWs as a sacrificial template. ZnO NWs were grown on titanium (Ti) foil (substrate) by the hydrothermal method [74, [148, 158-160]. Prior to growing the NWs, the Ti foil (0.5cm×2cm, Aldrich) was thoroughly cleaned by ultra-sonication in a mixture of acetone, ethanol, and deionized water (18 MΩ.cm, MilliQ Academic, Millipore). 5.5 mM of zinc acetate solution in ethanol (anhydrous, 200 proof, 99.5+%, Aldrich) was then spin-coated on the cleaned Ti substrate using Specialty coating Systems Inc., Model P6712 at 500 rpm for 40 sec and then heated (for drying) at 125^{o}C. The Ti foil containing the zinc acetate layer was then subjected to heat treatment in air at 340^{o}C for 20 min, which resulted in the seed layer of ZnO on Ti foil. In order to grow the ZnO NW template from the ZnO seed layer, the Ti foil containing ZnO seed layer was placed in a sealed container - enclosing the growth solution of zinc nitrate hexahydrate (0.05 M, Alfa Aesar), hexamethylenetetramine (HMTA, 0.025 M, Alfa Aesar), polyethylenimine (5.0 mM, end-capped, molecular weight 800 gmol^{-1} LS, Aldrich) and ammonium hydroxide (0.35 M). Next, this sealed container was placed in a water bath, preheated to 90^{o}C for 6 h. The formed nanowires were then carefully washed with ethanol and D.I. water followed by drying at 50^{o}C for 6 h.

Synthesis of SnO_2 VANTs

Vertically aligned SnO_2 nanotubes on Ti substrate were synthesized by placing the ZnO NWs grown Ti substrate in an aqueous solution consisting of 3 ml of 0.15 M ammonium hexafluorostannate (AHFS) [$(NH_4)_2SnF_6$, Aldrich], 1 mL of 0.5 M boric acid (H_3BO_3, Aldrich) and 1 mL of D.I. water at 26^{o}C for 30 min. In this process, the ZnO NWs template (formed on Ti substrate) was replaced by SnO_2 nanotubes; retaining the pre-formed vertically aligned morphology of ZnO which has been further confirmed by the experimental techniques discussed in the results section. After 30 min, the resultant SnO_2 VANTs were washed with D.I. water followed by drying at 50^{o}C for 6 h.

Synthesis of $(Sn_{1-x}Ir_x)O_2$:10F VANTs (x=0.2)

The IrO_2 and F containing SnO_2 solid solution [$(Sn_{1-x}Ir_x)O_2$:10F] was generated by infiltrating Ir and F containing precursors into the SnO_2 VANTs. For infiltration of Ir and F into SnO_2 VANTs, the Ti substrate on which SnO_2 VANTs were formed, was placed in a solution of iridium tetrachloride ($IrCl_4$, 99.5%, Alfa Aesar) and ammonium fluoride (NH_4F, 98%, Alfa Aesar), prepared in DI water corresponding to the desired composition [i.e. $(Sn_{0.8}Ir_{0.2})O_2$:10 wt.% F]. The Ti substrate containing SnO_2 NTs infiltrated with $IrCl_4$ and NH_4F solution was then subjected to heat treatment at 400^oC for 4h to form $(Sn_{1-x}Ir_x)O_2$:10F VANTs on Ti foil. Schematic illustration of the synthesis process for generating $(Sn_{1-x}Ir_x)O_2$:10F NTs (x= 0.2) with electrocatalyst loading of ~0.3 $mg.cm^{-2}$ on Ti substrate has been depicted in **Figure 5-1**.

5.3.1.2 Thin Films of $(Sn_{1-x}Ir_x)O_2$:10 wt.% F (x=0.2) and IrO_2

The electrochemical performance of the synthesized 1D $(Sn_{0.8}Ir_{0.2})O_2$:10F VANTs were compared to 2D thin film architectures. Hence, thin films of $(Sn_{0.8}Ir_{0.2})O_2$:10F and pure IrO_2 were synthesized on Ti foil following the protocol described in detail in an earlier study reported by us [97]. In brief, Iridium tetrachloride ($IrCl_4$, 99.5%, Alfa Aesar), tin (II) chloride dihydrate [$SnCl_2.2H_2O$, 98%, Alfa Aesar] and ammonium fluoride (NH_4F, 98%, Alfa Aesar) were used as the sources for Ir, Sn and F, respectively. $IrCl_4$ and $SnCl_2.2H_2O$ stock solutions with the desired composition are prepared in an absolute ethanol. NH_4F stock solution was made by dissolving NH_4F in an ethanol–DI water mixture with a volume ratio of 5: 1. The above stock solutions are then mixed together according to the desired composition of the electrocatalyst material [$(Sn_{1-x}Ir_x)O_2$:10 wt.% F, x= 0.2] and then spin coated (Speciality coating Systems Inc. Model P6712) onto pretreated (sandblasted and then etched in boiling HCl for 30 min) substrate-titanium foil (Alfa Aesar) having area of ~ 1 cm^2 (0.5 cm × 2 cm). The spin coating was performed with a rotating speed of 500 rpm for 10 s. The suitable amount of the precursors was selected to achieve a desired electrocatalyst loading of ~0.3 mg cm^{-2}. The precursors deposited Ti substrate was dried in air at 60^{o}C for 2 h. The dried substrate was then subjected to the thermal treatment in air at 400^{o}C for 4 h, which resulted into the formation of $(Sn_{0.8}Ir_{0.2})O_2$:10F thin film on the Ti foil. Similar approach was employed to synthesize pure IrO_2 thin film on the Ti substrate.

5.3.2 Electrocatalyst Materials Characterization

5.3.2.1 Structural Characterization

The crystalline structure of the resulting materials was characterized using x-ray diffraction (XRD) analysis which has been performed to both qualitatively and quantitatively analyze the as-prepared electrocatalysts. XRD is performed using the Philips XPERT PRO system employing CuK_{α} radiation source (λ = 0.15406 nm) at an operating current and voltage of 40 mA and 45 kV, respectively. The least square refinement techniques have been utilized to determine the molar volume of the electrocatalyst.

The microstructure of $(Sn_{0.8}Ir_{0.2})O_2$:10F NTs has been studied by performing scanning electron microscopy (SEM). Energy dispersive x-ray spectroscopy (EDX) analyzer (attached with the SEM machine) has been used for conducting quantitative elemental analysis. Philips XL-30FEG equipped with an EDX detector system comprising of an ultrathin beryllium window and Si(Li) detector, operating at 20 kV was used for the corresponding evaluation of the microstructure as well as conducting elemental and x-ray mapping analysis of the electrocatalyst. Transmission electron microscopy (TEM) (JEOL JEM-2100F system operating at 200 kV) was performed to analyze the structure of the as-prepared nanotubes. Energy Dispersive Spectroscopy (EDS) as well as line scan analysis was conducted for the elemental analysis and investigation of the solid solution formation of as-prepared $(Sn_{0.8}Ir_{0.2})O_2$:10F NTs. The quantitative elemental analysis was also carried out by utilizing inductively coupled plasma optical emission spectroscopy (ICP-OES, iCAP 6500 duo Thermo Fisher).

To investigate the oxidation states of Sn and Ir in the as-synthesized electrocatalysts, X-ray photoelectron spectroscopy (XPS) was performed. ESCALAB 250 Xi system (Thermo Scientific) equipped with a monochromatic Al Kα X-ray source was utilized to perform XPS analysis. The standard analysis spot of 400×400 μm^2 was defined by the micro-focused X-ray source. The mentioned XPS system is operated at room temperature in an ultra-high vacuum chamber with the base pressure less than 5×10^{-10} mbar. The calibration of the binding energy (BE) scale was done to generate <50 meV deviations of the three standard peaks from their standard values. The Aliphatic C1s peak was observed at 284.6 eV. High-resolution elemental XPS data in C2p, S2p, Mg2p, and Zn2p regions were acquired with the analyzer pass energy set to 20 eV (corresponding to energy resolution of 0.36 eV) and the step size was set to 0.1 eV. Fitting of the elemental spectra based on calibrated analyzer transmission functions, Scofield sensitivity factors and effective attenuation lengths for photoelectrons from the standard TPP-2M formalism was conducted using the Avantage software package (Thermo Fisher Scientific).

5.3.2.2 Electrochemical Characterization

Electrochemical characterization of the as-prepared electrocatalysts (total electrocatalyst loading ~ 0.3 $mg.cm^{-2}$) was carried out in a three-electrode configuration at 40°C (maintained using a Fisher Scientific 910 Isotemp refrigerator circulator) on a VersaSTAT 3 (Princeton Applied Research) electrochemical workstation. 1N sulfuric acid (H_2SO_4) was used as the electrolyte solution and also as a proton source for oxygen evolution reaction (OER). Oxygen gas from the electrolyte solution was expelled by purging the electrolyte solution with ultra-high pure (UHP) argon gas (Matheson) for ~15 min [108]. The as-prepared electrocatalysts were used as a working electrode (anode), Pt wire (Alfa Aesar, 0.25 mm thick, 99.95%) was used as the counter electrode (cathode) and mercury/mercurous sulfate (Hg/Hg_2SO_4) electrode (XR-200, Hach) having a potential of +0.65 V with respect to reversible hydrogen electrode (RHE) was used as the reference electrode. All the potential values reported in the present study are determined with respect to RHE and calculated from the formula:[70, 78, 110] $E_{RHE} = E_{Hg/Hg2SO4} + E^0_{Hg/Hg2SO4} + 0.059pH$, where E_{RHE} is the potential versus RHE. $E_{Hg/Hg2SO4}$ is the potential measured against the Hg/Hg_2SO_4 reference electrode and $E^o_{Hg/Hg2SO4}$ is the standard electrode potential of Hg/Hg_2SO_4 reference electrode (+0.65 V *vs* RHE).

Electrochemical impedance spectroscopy (EIS)

To determine the solution resistance (R_s), electrode resistance (R_e), ohmic resistance (R_Ω) ($R_\Omega=R_s+R_e$) and the surface charge transfer resistance (R_{ct}) of as-prepared electrocatalysts, EIS has been performed. The polarization curves of the synthesized electrocatalysts have been iR_Ω ($iR_\Omega= iR_s + iR_e$) corrected utilizing the ohmic resistance (R_Ω) obtained from EIS analysis. The EIS was performed in the frequency range of 100 mHz-100 kHz (Amplitude = 10 mV) using the electrochemical workstation (Versa STAT 3, Princeton Applied Research) in 1N H_2SO_4 electrolyte solution at 40°C, at ~1.5 V (*vs* RHE). ZView software from Scribner Associates employing the $R_s(R_eQ_1)(R_{ct}Q_{dl})$ equivalent circuit was used to model the impedance data for OER. In this model R_s is in series with the parallel combination of the R_e and Q_1 and further in series with the parallel combination of the R_{ct} and Q_{dl}. The components of this model are: [78, 97]

R_s = Resistance faced at high frequency due to surface charge transfer in electrolyte solution,

R_e = Resistance for electron transfer from the electrode to current collector (Ti foil),

R_{ct} = Surface charge transfer resistance (i.e., polarization resistance) for electrocatalyst-electrolyte interface,

Q_1 = Constant phase element, and

Q_{dl} = Contribution from both the double layer capacitance and pseudo capacitance.

Linear scan polarization

The electrochemical performance of the as-prepared electrocatalysts (for OER) was studied by conducting linear scan polarization in 1N H_2SO_4 electrolyte solution with a scan rate of 10 mVs^{-1} at 40°C. Polarization curves of electrocatalysts were iR_Ω corrected, as described above in the EIS section. The current density at ~1.5 V (*vs* RHE, which is the typical potential used for measuring the electrochemical activity of the electrocatalyst for OER[94]) in iR_Ω corrected polarization curves was used for comparing the electrochemical performance of the different electrocatalysts. In order to study and compare the reaction kinetics of the as-synthesized electrocatalysts, Tafel plots are developed after iR_Ω correction using the equation:

$$\eta = a + b \log i \qquad (5\text{-}1)$$

[i.e., plot of overpotential (η) *vs* log current (log i)][70, 137]. In this equation, ‘a’ and ‘b’ represent the exchange current density and Tafel slope, respectively. Further, the cyclic voltammetry (CV) curves were recorded to assess the electrochemical active surface area (ECSA) of the as-prepared electrocatalysts with various scan rates in the potential range from 0.1 to 1.2 V (*vs* RHE). The differences in current density ($j_{anode} - j_{cathode}$) at 0.7 V (*vs* RHE) are plotted against the scan rate ($mV\ s^{-1}$) and fitted to a linear regression [161, 162] to obtain the corresponding C_{dl} and ECSA values. In addition, the intrinsic OER activity of as-prepared electrodes was investigated by calculating specific activity, mass activity, turnover frequency (TOF) and normalization of current densities by ECSA (m^2g^{-1}) and electrocatalyst mass loading.

Electrochemical stability test

Chronoamperometry (CA) test (current *vs* time) was performed to study the electrochemical stability of as-synthesized electrocatalysts for the long-term operation. In the CA test, the working electrode was maintained for 24 h in 100 ml electrolyte solution of 1N H_2SO_4 at 40^oC under a constant voltage of ~1.5 V (*vs* RHE). In order to determine the amount of Ir and Sn leached out from the working electrode, electrolyte solutions (10 ml) collected after 24 h of CA test were subjected to elemental analysis in an inductively coupled plasma optical emission spectroscopy (ICP-OES, iCAP 6500 duo Thermo Fisher). This analysis is beneficial to understand the robustness and corrosion resistance of the as-prepared electrocatalysts towards long term OER in PEM water electrolysis. In addition, the post stability characterizations (XRD and XPS) were carried out to investigate the structural robustness of $(Sn_{0.8}Ir_{0.2})O_2$:10F NTs during OER.

5.4 Results and Discussion

5.4.1 Experimental Characterization of Electrocatalysts

5.4.1.1 Structural Characterization of Electrocatalysts

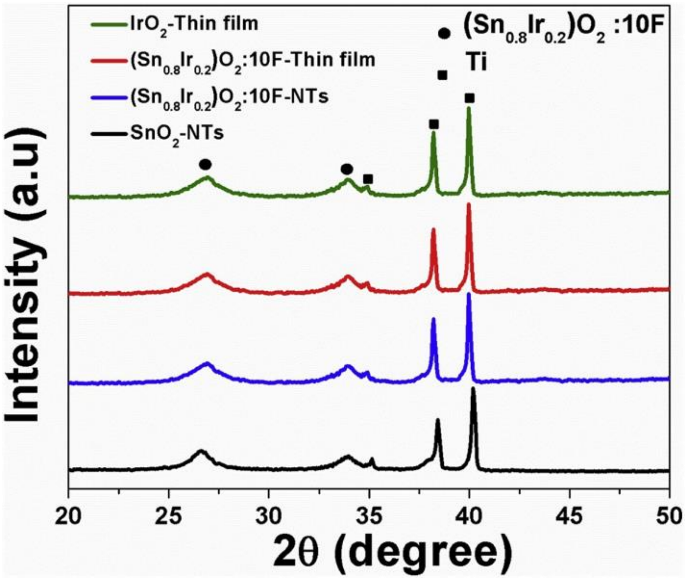

Figure 5-2 The XRD patterns of nanostructured 2D thin films of pure IrO_2 and $(Sn_{0.8}Ir_{0.2})O_2$:10F; and nanotubes (NTs) of pure SnO_2 and $(Sn_{0.8}Ir_{0.2})O_2$:10F electrocatalysts fabricated on Ti foil

The XRD pattern of SnO_2 NTs (**Figure 5-2**) shows the rutile type tetragonal structure and the patterns match with the reported patterns confirming the formation of SnO_2[35, 97]. Similarly, the XRD pattern of $(Sn_{0.8}Ir_{0.2})O_2$:10F NTs reveals the rutile type tetragonal structure similar to that of pure SnO_2 NTs, which suggests the formation of a single phase homogeneous solid solution of SnO_2 and IrO_2 [i.e. (Sn,Ir)O_2:F] without any other peaks of Sn or Ir based compounds or any undesired phase separation [35, 97]. The XRD patterns of 2D thin films of pure IrO_2 and $(Sn_{0.8}Ir_{0.2})O_2$:10F generated on Ti foil also show the similar XRD patterns as reported earlier, suggesting the successful formation of fully crystalline IrO_2 and solid solution of SnO_2 and IrO_2 [i.e. (Sn,Ir)O_2:F], respectively[97]. Furthermore, the molar volume of $(Sn_{0.8}Ir_{0.2})O_2$:10F NTs, calculated using the least square refinement technique is ~ 21.18 cm^3mol^{-1} which is comparable to that of 2D thin film of $(Sn_{0.8}Ir_{0.2})O_2$:10F as reported in the previous study [97]. In the various OER electrocatalysts studies it has been observed and reported that the electro-catalytic activity of IrO_2 starts decreasing from annealing temperatures of 400°C to 600°C while the more stable electrodes were formed at T ≥ 400°C[163-165]. Furthermore, according to study conducted by Geiger et al.[164] it has been concluded that the electrodes synthesized at 400°C-500°C are identified as the most promising for the acidic OER on the basic of their intrinsic activity and catalytic dissolution rate. Therefore, in the present study, based on these studies as well as previous acidic OER studies by our group[35, 97, 128, 136], we have selected the optimum annealing temperature of 400 °C to synthesize the fully crystalline electrocatalysts, possessing excellent catalytic activity as well as stability for acidic OER.

The morphology of SnO_2 NTs [**Figure 5-3(a)**] and $(Sn_{0.8}Ir_{0.2})O_2$:10F NTs [**Figure 5-3 (b)**] has been studied by performing the SEM analysis. Accordingly, the SEM image of SnO_2 NTs shows the highly dense, well-spaced and vertically aligned nanotubes, suggesting formation of nanotubular morphology. Similarly, the top and cross-sectional views of $(Sn_{0.8}Ir_{0.2})O_2$:10F NTs also show highly dense, well-spaced and vertically aligned nanotubes (VANTs), suggesting the retention of the nanotubular morphology of SnO_2 upon the solid solution formation of F incorporated SnO_2 and IrO_2 [$(Sn,Ir)O_2$:F], (similar to that of pure SnO_2). The SEM image of $(Sn_{0.8}Ir_{0.2})O_2$:10F NTs clearly shows the formation of vertically aligned nanotubes having diameter and length of ~220 nm and ~10μm, respectively, without the presence of any other morphologies. Herein, based on the SEM images and the geometrical data approximate specific surface area (SSA) of $(Sn_{0.8}Ir_{0.2})O_2$:10F nanotubes has been calculated. The approximate SSA of $(Sn_{0.8}Ir_{0.2})O_2$:10F NTs was obtained as 7.33 m^2g^{-1}. The presence of Sn and Ir in $(Sn_{0.8}Ir_{0.2})O_2$:10F NTs has been further verified by conducting EDX analysis. Correspondingly, EDX analysis showed that the measured elemental composition of Sn (80.61%) and Ir (19.39%) was very close to the chosen nominal composition of Sn (~80 at. %) and Ir (~ 20 at. %). In addition, inductively coupled plasma optical emission spectroscopy (ICP-OES) analysis showed the atomic % of Sn and Ir as 81.55 and 18.45 respectively. These atomic % obtained from the ICP-OES are almost consistent with the values obtained from the EDX. Thus, the ICP and EDX analysis provided strong corroboration of the nominal composition [i.e. Sn (80 at.%) and Ir (20 at.%)]. Furthermore, the TEM image obtained on a representative $(Sn_{0.8}Ir_{0.2})O_2$:10F NT [**Figure 5-3 (c)**] shows the nanotubular geometry of $(Sn_{0.8}Ir_{0.2})O_2$:10F with a diameter of ~220 nm and a wall thickness of ~40 nm, respectively. [**Figure 5-3 (d)**] shows the EDS elemental mapping images of Sn, Ir and O for a $(Sn_{0.8}Ir_{0.2})O_2$:10F NT, suggesting that the Sn and Ir elements are well and uniformly distributed in the as-synthesized NT. There is also no segregation of any elements at any specific region. In addition, it is quite clear from the line scan analysis [**Figure 5-3 (e)]** that there is a homogenous dispersion of Sn and Ir in the as-synthesized $(Sn_{0.8}Ir_{0.2})O_2$:10F NT. This EDS and line scan analysis further reveals the formation of a single phase homogeneous solid solution of SnO_2 and IrO_2 [i.e. $(Sn,Ir)O_2$:F], denying the possibility of IrO_2 coverage the SnO_2 bulk phase.

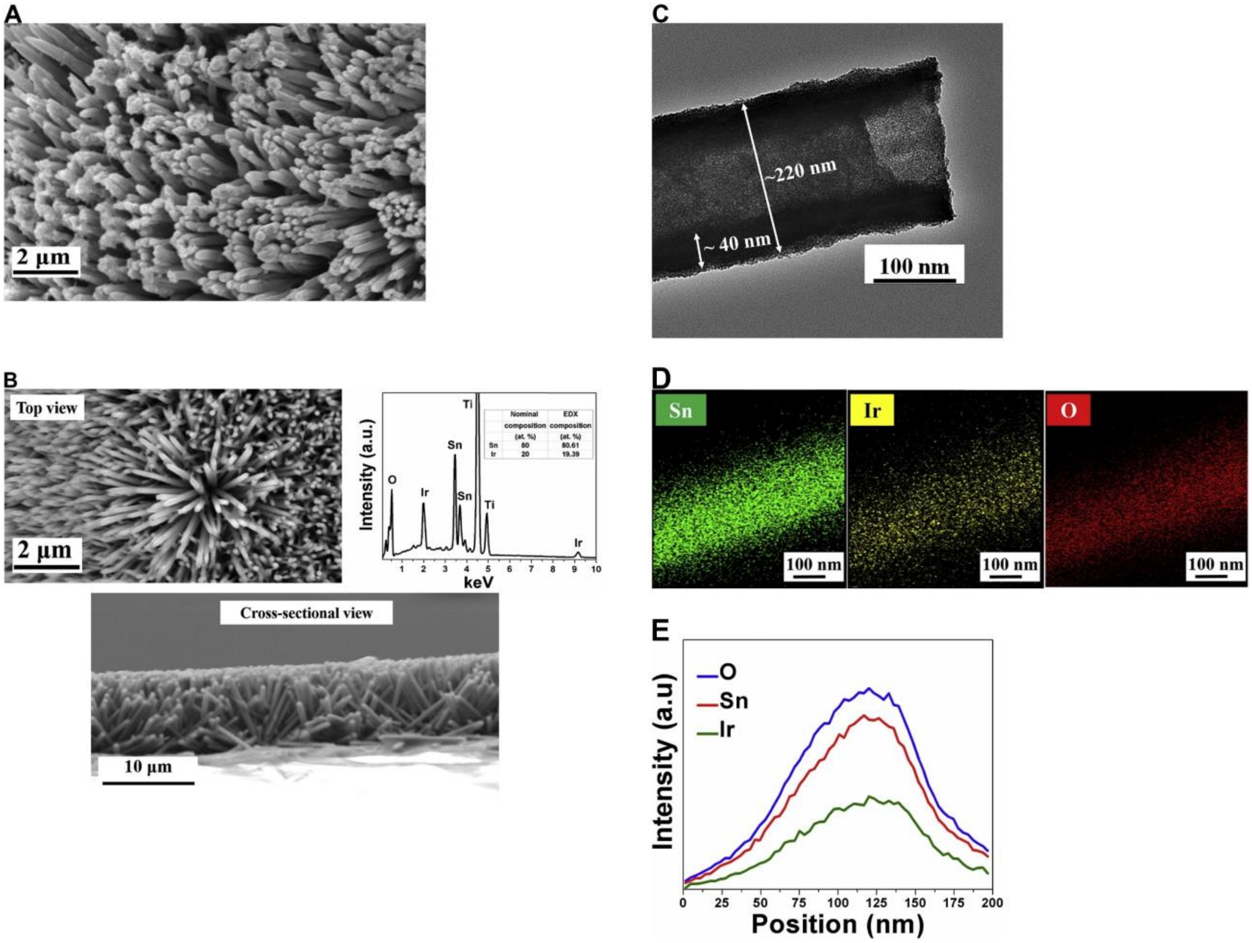

	Nominal composition (at. %)	EDX composition (at. %)
Sn	80	80.61
Ir	20	19.39

Figure 5-3 (a) The SEM micrograph showing top view of SnO_2 NTs, (b) The SEM micrograph showing top view, cross-sectional view and EDX spectrum of $(Sn_{0.8}Ir_{0.2})O_2$:10F NTs, (c) The bright field TEM image of $(Sn_{0.8}Ir_{0.2})O_2$:10F NT, (d) EDS elemental mapping of Sn, Ir and O of the $(Sn_{0.8}Ir_{0.2})O_2$:10F NT, and (e) line scan analysis across a $(Sn_{0.8}Ir_{0.2})O_2$:10F NT

XPS analysis has been conducted to identify the valence states of Ir and Sn in $(Sn_{0.8}Ir_{0.2})O_2$:10F NTs, SnO_2 NTs, and thin films of $(Sn_{0.8}Ir_{0.2})O_2$:10F and IrO_2 (**Figure 5-4**). The XPS spectrum of Ir of $(Sn_{0.8}Ir_{0.2})O_2$:10F NTs and thin films of $(Sn_{0.8}Ir_{0.2})O_2$:10F and IrO_2 show the presence of Ir $4f_{5/2}$ and Ir $4f_{7/2}$ doublet. The XPS spectra of Ir of IrO_2 shows the presence of Ir

4f$_{5/2}$ and Ir 4f$_{7/2}$ doublet with binding energy values of ~64.58 eV and ~ 61.68 eV, respectively[70] . As compared to pure IrO$_2$, in the case of (Sn$_{0.8}$Ir$_{0.2}$)O$_2$:10F thin film and NTs, the positive shift of ~ 0.7 to 0.9 eV towards higher binding energy in the Ir 4f$_{5/2}$ and Ir 4f$_{7/2}$ doublet

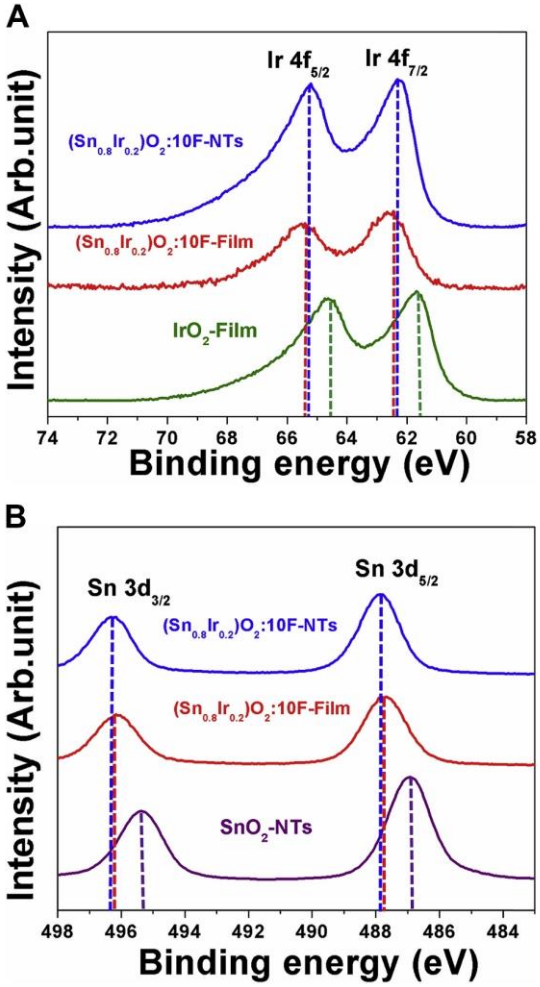

Figure 5-4 The XPS spectra of (a) Ir 4f$_{7/2}$ and 4f$_{5/2}$ doublet and (b) Sn 3d$_{5/2}$ and Sn 5d$_{3/2}$ doublet of as-synthesized electrocatalyst

positions were observed, which is consistent with the previously reported results for F doped solid solution electrocatalysts[70, 94, 97]. This positive shift suggests the likely binding of the fluorine in the $(Sn_{0.8}Ir_{0.2})O_2$:10F NTs and film electrocatalyst, which contributes to the modification of the electronic structure of $(Sn_{0.8}Ir_{0.2})O_2$:10F as a result of the solid solution formation and incorporation of F[70, 97]. The pure SnO_2 exhibits the binding energy values of ~ 495.37 eV and ~486.95 eV for Sn $3d_{3/2}$ and Sn $3d_{5/2}$, respectively[166, 167], whereas $(Sn_{0.8}Ir_{0.2})O_2$:10F film and NTs demonstrated the positive shift of ~ 0.7 eV towards higher binding energy values, similar to as reported in earlier studies [94, 97]. The presence of F in the as-synthesized $(Sn_{0.8}Ir_{0.2})O_2$:10F NTs and film could not be unequivocally determined in XPS, EDX, and elemental mappings which is consistent with the earlier publications on Sn/Mn/Nb substituted IrO_2 electrocatalysts[70, 94, 97, 98]. However, the observed positive shifts in the binding energy values w.r.t. pure SnO_2 and IrO_2 can be an indicator of the of F incorporation into the lattice of solid solution oxide. This implies the modification of the electronic structure due to the formation of solid solution electrocatalyst as well as due to the existence of fluorine in the solid solution lattice which results in the superior binding attributed to the higher electronegativity of fluorine[70, 97, 102].

5.4.1.2 Electrochemical Characterization of Electrocatalysts

Figure 5-5 (a) shows the electrochemical impedance spectroscopy (EIS) of $(Sn_{0.8}Ir_{0.2})O_2$:10F NTs along with the synthesized 2D thin films of identical composition of $(Sn_{0.8}Ir_{0.2})O_2$:10F and pure IrO_2 electrocatalysts used as the benchmark electrocatalyst measured at ~1.5V (*vs* RHE) in the electrolyte solution of 1N H_2SO_4 at 40°C (inset: EIS equivalent circuit and magnified views of EIS). As discussed in the experimental section, the $R_s(R_eQ_1)(R_{ct}Q_{dl})$ equivalent circuit model in which R_s is in series with the parallel combination of the R_e and Q_1 and further in series with the parallel combination of the R_{ct} and Q_{dl} was utilized to determine the R_e, R_s and R_{ct}, which are correspondingly tabulated in **Table 5-1**. The surface charge transfer resistance (R_{ct}), determined from the diameter of the semi-circle in the low frequency region of the EIS plot of $(Sn_{0.8}Ir_{0.2})O_2$:10F NTs (R_{ct} ~4.2 Ω cm^2) is significantly lower than $(Sn_{0.8}Ir_{0.2})O_2$:10F thin film (R_{ct} ~6.7 Ω cm^2) as well as the thin film of pure IrO_2 (R_{ct} ~8 Ω cm^2), suggesting the lower activation polarization and higher electronic conductivity of $(Sn_{0.8}Ir_{0.2})O_2$:10F NTs as compared to 2D thin film of $(Sn_{0.8}Ir_{0.2})O_2$:10F and thin film of pure IrO_2 electrocatalysts [97]. In addition, $(Sn_{0.8}Ir_{0.2})O_2$:10F NTs exhibit lower R_e (~0.8 Ω cm^2) as compared to thin films of $(Sn_{0.8}Ir_{0.2})O_2$:10F and thin film of pure IrO_2 . The decrease in R_{ct} and R_e for the characteristic nanotubular structure of $(Sn_{0.8}Ir_{0.2})O_2$:10F is an indicator of the improved electronic conductivity afforded by the nanotubular architecture as is known for nanotubes of other systems including Pt electrocatalysts as mentioned earlier. These results furnish the highly efficient pathway for facile charge (electron) transport on the entire $(Sn_{0.8}Ir_{0.2})O_2$:10F nanotubular electrode as well as between the electrocatalyst surface and the current collector (Ti substrate) due to the 1D vertical channels in $(Sn_{0.8}Ir_{0.2})O_2$:10F tendered by the nanotubular architecture[44, 141, 146]. Therefore, these experimental results collectively suggest that due to reduction in the material's dimension (i.e. from 2D to 1D), $(Sn_{0.8}Ir_{0.2})O_2$:10F NTs expedite the OER kinetics contributing to enhanced electrochemical activity as compared to the 2D thin films of $(Sn_{0.8}Ir_{0.2})O_2$:10F and pure IrO_2.

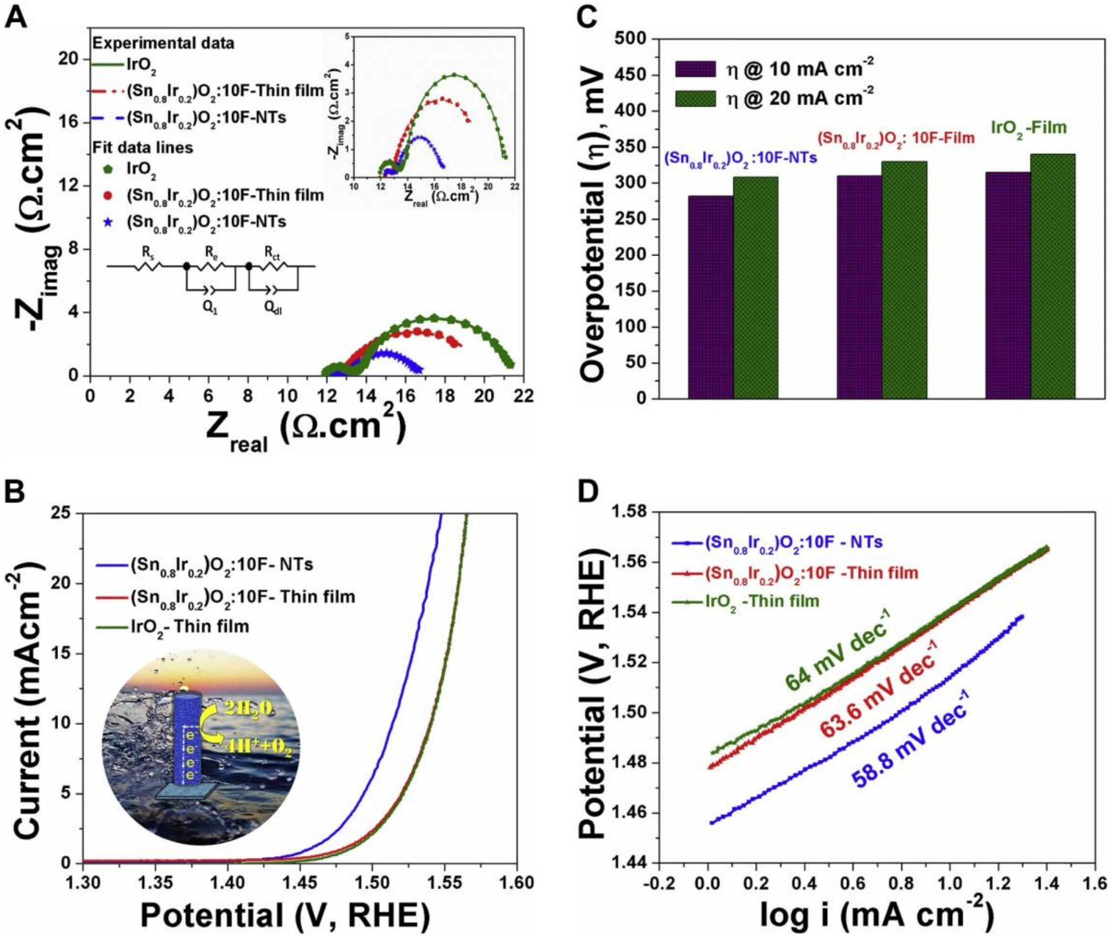

Figure 5-5 (a) EIS plot of thin film of pure IrO_2, $(Sn_{0.8}Ir_{0.2})O_2$:10F and $(Sn_{0.8}Ir_{0.2})O_2$:10F NTs electrocatalysts, performed at ~1.5 V (*vs* RHE) (inset: EIS equivalent circuit and magnified view of EIS), (b) The polarization curves of $(Sn_{0.8}Ir_{0.2})O_2$:10F NTs and thin film of $(Sn_{0.8}Ir_{0.2})O_2$:10F and pure IrO_2 thin film performed in 1N H_2SO_4 solution at 40°C, (c) Overpotential (η, mV) required to achieve current density of 10 and 20 $mAcm^{-2}$ and (d) Tafel plots for as-synthesized electrocatalyst

Table 5-1 Results of electrochemical characterization for OER of nanostructured thin films of IrO_2 and $(Sn_{0.8}Ir_{0.2})O_2$:10F and $(Sn_{0.8}Ir_{0.2})O_2$:10F NTs, performed in 1N H_2SO_4 electrolyte solution at 40°C

Electrocatalyst Composition	**Onset potential V (*vs* RHE)**	**Current density at ~1.5 V (mA cm^{-2})**	**R_s (Ω cm^2)**	**R_s (Ω cm^2)**	**R_s (Ω cm^2)**	**Tafel slope (mV dec^{-1})**	**Mass activity (Ag^{-1})**	**ECSA (m^2g^{-1})**	**TOF at ~ 1.5 V (s^{-1})**
IrO_2 –Thin film	1.43	~2.5	12	1.1	8	64	8.33	29.17	0.0048
$(Sn_{0.8}Ir_{0.2})O_2$:10F –Thin film	1.43	~2.8	12.1	1	6.7	63.6	9.33	30.89	0.0068
$(Sn_{0.8}Ir_{0.2})O_2$:10F -NTs	1.43	~6.5	12.1	0.8	4.2	58.8	21.67	38.46	0.016

Further electrochemical characterization has been carried out by performing the linear scan polarization of as-prepared electrodes in the electrolyte solution of 1N H_2SO_4 at 40°C, employing a scan rate of 10 mVs^{-1}. **Figure 5-5 (b)** shows the linear scan polarization curves of as-prepared electrocatalyst for OER. The onset potential of OER for $(Sn_{0.8}Ir_{0.2})O_2$:10F NTs is ~1.43V (*vs* RHE, w.r.t. the equilibrium OER potential, 1.23V *vs* RHE) which is consistent with the nanostructured thin films of $(Sn_{0.8}Ir_{0.2})O_2$:10F and pure IrO_2 [97]. The current density obtained at ~1.5V *vs* RHE (typical potential considered to evaluate electrocatalytic performance of the electrocatalysts) for $(Sn_{0.8}Ir_{0.2})O_2$:10F NTs is ~ 6.5 mA cm^{-2}, which is ~2.3 and ~ 2.6 fold higher than that of thin films of $(Sn_{0.8}Ir_{0.2})O_2$:10F (~ 2.8 mA cm^{-2}) and pure IrO_2 (~ 2.5 mA cm^{-2}), respectively. However, as expected, pure SnO_2 NTs exhibited extremely poor OER electrocatalytic activity (~ 50 μAcm^{-2} at ~1.5V *vs* RHE) (**Appendix A Figure 1**). This insignificant OER activity is indeed attributed to the considerably higher charge transfer resistance of SnO_2 NTs ($R_{ct} > 2000\ \Omega\ cm^2$), which indicates its poor electronic conductivity (i.e. semiconductor nature)[168].

Furthermore, it can be seen in **Figure 5-5 (c)**, that $(Sn_{0.8}Ir_{0.2})O_2$:10F NTs approach the current density of 10 mA cm^{-2} and 20 mA cm^{-2} with a lesser overpotential (η) of ~ 285 and 308 mV, respectively (w.r.t. the equilibrium OER potential, 1.23 V *vs* RHE). On the other hand, thin films of $(Sn_{0.8}Ir_{0.2})O_2$:10F and IrO_2 require a relatively higher overpotential of ~ 310 mV and 315 mV, respectively to deliver the current density of 10 mA cm^{-2} . Further, as shown in **Table 5-1** $(Sn_{0.8}Ir_{0.2})O_2$:10F NTs exhibited a mass activity of 21.67 A g^{-1}, specific activity of ~ 0.01486 mA cm^{-2}, and TOF of 0.016 s^{-1} at ~1.5V *vs* RHE (i.e. η = 0.27 V). It is noteworthy that the OER mass activity, specific activity as well as TOF value of $(Sn_{0.8}Ir_{0.2})O_2$:10F NTs is about 2−2.6 fold higher than that of thin films motifs of $(Sn_{0.8}Ir_{0.2})O_2$:10F and pure IrO_2 at the potential of ~1.5V *vs* RHE. Thus, these results clearly indicate the intrinsically higher electrocatalytic activity of $(Sn_{0.8}Ir_{0.2})O_2$:10F NTs towards water oxidation reaction (OER) as compared to the $(Sn_{0.8}Ir_{0.2})O_2$:10F and IrO_2 thin films electrocatalysts. This superior electro-catalytic activity of $(Sn_{0.8}Ir_{0.2})O_2$:10F NTs can be ascribed to the enhancement in the OER kinetics[78] i.e. lower R_{ct} (i.e. facile charge transport along the 1D vertical channels of NTs) than the as-prepared thin film based electrocatalysts. Further, the lower Tafel slope of $(Sn_{0.8}Ir_{0.2})O_2$:10F NTs (58.8 mV dec^{-1}) [**Figure 5-5 (d)**] as compared to the thin films of $(Sn_{0.8}Ir_{0.2})O_2$:10F (63.6 mV dec^{-1}) and IrO_2 (64 mV dec^{-1}), suggests favorable OER kinetics i.e. likely faster electron transport and enhanced electrical conductivity/electrocatalytic activity owing to the nanotubular structure; translating to the superior OER kinetics for $(Sn_{0.8}Ir_{0.2})O_2$:10F NTs as compared to the as-synthesized thin film electrocatalyst architectures. The Tafel slope obtained for thin films of $(Sn_{0.8}Ir_{0.2})O_2$:10F and IrO_2 are relatively similar to each other, indicating similar OER kinetics.

Furthermore, to shed light on the superior electrocatalytic activity of $(Sn_{0.8}Ir_{0.2})O_2$:10F NTs and compare it with the thin films of $(Sn_{0.8}Ir_{0.2})O_2$:10F and state-of-the art IrO_2, the electrochemical active surface area (ECSA) was evaluated. The ECSA was measured from the double-layer capacitance (C_{dl}) and the linear slope of the current density ($j_{anode} - j_{cathode}$) *vs* scan rate (which is equivalent to twice the double layer capacitance, C_{dl}) was used to characterize the ECSA (**Figure 5-6**), following previous reports in the literature [161, 162, 169-171]. It is noteworthy to mention that the obtained slope for $(Sn_{0.8}Ir_{0.2})O_2$:10F NTs (~150 mF cm^{-2}) is considerably higher than the $(Sn_{0.8}Ir_{0.2})O_2$:10F thin film (120.5 mF cm^{-2}), and IrO_2 thin film (113.8 mF cm^{-2}), which clearly suggests the higher C_{dl}, and thereby higher ECSA for $(Sn_{0.8}Ir_{0.2})O_2$:10F NTs and comparable ECSA (electrocatalytic activity) for thin films of $(Sn_{0.8}Ir_{0.2})O_2$:10F and IrO_2. This higher ECSA presumably results from the relatively higher surface-to-volume ratio of the highly ordered nanotubes and thus, is another reflection of the superior electrochemical performance compared to the as-prepared thin film based electrocatalysts [140, 162, 169, 170, 172]. The ECSA (m^2g^{-1}) of the $(Sn_{0.8}Ir_{0.2})O_2$:10F NTs was calculated as ~ 38.46 m^2g^{-1}, higher than that of $(Sn_{0.8}Ir_{0.2})O_2$:10F thin film (~30.89 m^2g^{-1}) and IrO_2 thin film (~29.17 m^2g^{-1}), respectively, which further accentuates and confirms the superior presence of effective active sites[147] on the $(Sn_{0.8}Ir_{0.2})O_2$:10F NTs.

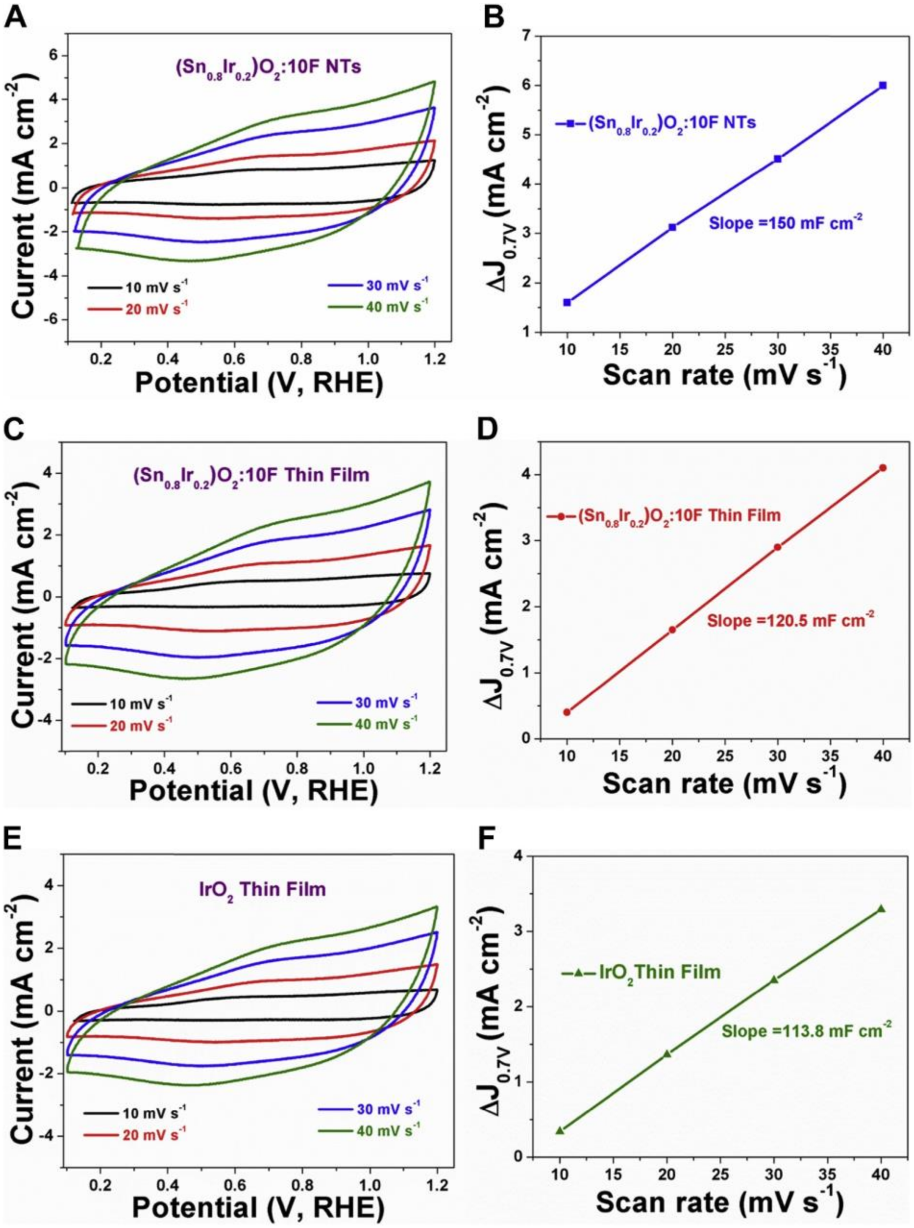

Figure 5-6 CV curves and differences in current density (janode − jcathode) at 0.7 V (vs RHE) plotted against scan rate and fitted to a linear regression for (a-b) $(Sn_{0.8}Ir_{0.2})O_2$:10F NTs, (c-d) $(Sn_{0.8}Ir_{0.2})O_2$:10F Thin film, and (e-f) IrO_2 thin film

Herein, the calculated ECSA values (m^2g^{-1}) are not very high in comparison to the surface area obtained by BET for F doped SnO_2 (173 m^2g^{-1})[173] and Ir substituted nanopowder (100-200 m^2g^{-1})[137, 163, 174, 175] based oxide materials reported in the literature. In this regard, recent study conducted by Jung et al.[176], sheds light on such discrepancy in the area values (m^2 g^{-1}) obtained by the ECSA and BET gas adsorption for the crystalline metal oxide OER catalysts having similar crystal structure. According to this study, to investigate the intrinsic/specific activities of the electrocatalysts, a recommended practice is to report both ECSA and BET surface area values and normalization of activity data by the areas obtained by BET and ECSA. However, it should be noted that, as electrocatalysts synthesized in the present study are directly grown/fabricated on the current collector (Ti) with the thin film structure, it is unfeasible to measure the BET surface area (m^2g^{-1}) and compare it with ECSA value (m^2g^{-1}) of the as-prepared electrocatalyst materials. Therefore, to gain precise insights into the intrinsic OER activity of as-prepared electrocatalysts, the current densities have been normalized by utilizing calculated ECSA (m^2g^{-1}) and mass loading of the electrocatalysts (0.3 $mgcm^{-2}$), and the respective OER performance was evaluated. It can be seen that, (**Figure 5-7**) the ECSA normalized current density and mass activity for $(Sn_{0.8}Ir_{0.2})O_2$:10F NTs is significantly higher than the $(Sn_{0.8}Ir_{0.2})O_2$:10F and IrO_2 thin films, which reflects the higher intrinsic OER activity of NTs, which can be attributed to the higher accessible surface area as well as the intrinsic activity of each accessible site[163, 173]. It should be also noted that in the present study, the specific capacitance (C*) of single crystal IrO_2 (100) ~ 650 μFcm^{-2} [171, 177] is used to evaluate ECSA of pure IrO_2 thin film as well as ECSA of $(Sn_{0.8}Ir_{0.2})O_2$:10F NTs and $(Sn_{0.8}Ir_{0.2})O_2$:10F thin film, which is on the basis of the isoelectronic characteristic of pure IrO_2 and $(Sn_{0.8}Ir_{0.2})O_2$:10F[97]. Thus, it should be noted that it is possible that if actual specific capacitance (C*) of single crystal/monolayer are determined and selected for $(Sn_{0.8}Ir_{0.2})O_2$:10F

NTs and $(Sn_{0.8}Ir_{0.2})O_2$:10F thin film, the actual ECSA values will be more representative. Therefore, as evidenced from the higher- electrochemical active surface area, specific activity, TOF and lower charge transfer resistance and Tafel slope, $(Sn_{0.8}Ir_{0.2})O_2$:10F NTs exhibit superior electrocatalytic activity towards OER as compared to the film architectures of the $(Sn_{0.8}Ir_{0.2})O_2$:10F and IrO_2 electrocatalysts.

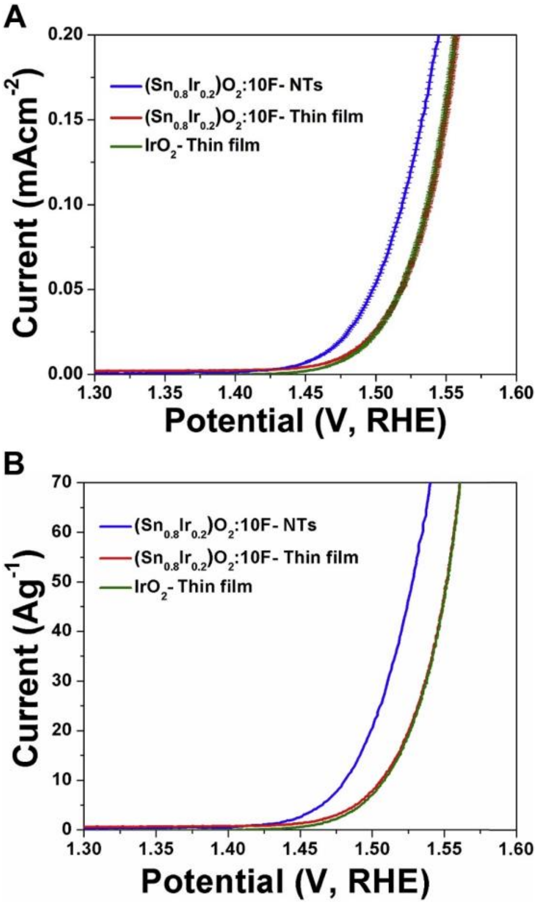

Figure 5-7 The Current density curves of $(Sn_{0.8}Ir_{0.2})O_2$:10F NTs and thin film of $(Sn_{0.8}Ir_{0.2})O_2$:10F and IrO_2, normalized by (a) respective ECSA ($m^2\,g^{-1}$) and (b) electrocatalyst mass loading

Long term electrochemical stability is an imperative criterion for the high performance OER electrocatalysts in terms of their commercial applications. Herein, the electrochemical stability of $(Sn_{0.8}Ir_{0.2})O_2$:10F NTs, $(Sn_{0.8}Ir_{0.2})O_2$:10F thin film and IrO_2 thin film electrocatalysts was studied by performing the chronoamperometry (CA) test for OER at the constant potential of ~1.5 V (*vs* RHE) in 1N H_2SO_4 at 40°C for 24 h. As shown in **Figure 5-8**, $(Sn_{0.8}Ir_{0.2})O_2$:10F NTs exhibit higher current owing to the exceptional electrochemical activity discussed above. However, more importantly what is clearly apparent is the excellent long term electrochemical stability, similar to $(Sn_{0.8}Ir_{0.2})O_2$:10F thin film as well as pure IrO_2 thin film with a minimal loss in current density[97]. It is noteworthy to mention that the F doped $(Sn,Ir)O_2$ solid solution electrocatalyst with different morphologies (NTs and thin film) and similar composition [$(Sn_{0.8}Ir_{0.2})O_2$:10F] exhibits comparable electrochemical stability under identical operating conditions. This can be attributed to the unique electronic structure obtained upon F containing solid solution formation of $(Sn,Ir)O_2$:F[97, 178]. As reported earlier by the present authors[98], more negative cohesive energy (E_{coh}) is obtained upon solid solution formation due to the stronger bond dissociation energy for Sn-O bonds (-528 kJ mol^{-1}) than Ir-O bonds (-414 kJ mol^{-1})[179]. Further, the E_{coh} of the F doped $(Sn,Ir)O_2$ solid solution electrocatalyst becomes equal to that of pure IrO_2 approximately at ~8-10 wt.% of F as shown earlier[98]. Thus, these previous theoretical studies have demonstrated that introduction of F modifies the overall electronic structure of the system in such a manner that the electrochemical performance of the doped surface becomes similar to the surface of the pure IrO_2, suggesting the beneficial role of F in the as-synthesized electrocatalysts. This is indeed observed experimentally and the observed stability, wherein $(Sn_{0.8}Ir_{0.2})O_2$:10F exhibits excellent electrochemical stability in both nanotubular and thin film morphologies, identical to that of pure IrO_2.

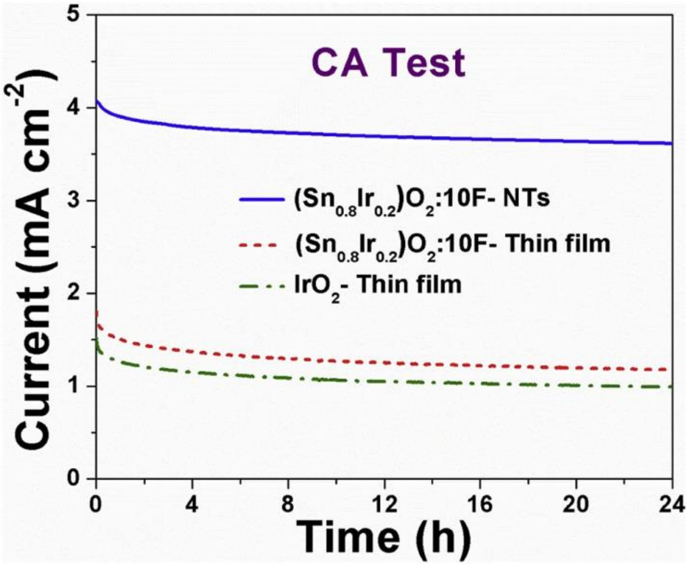

Figure 5-8 The chronoamperometry (CA) test of $(Sn_{0.8}Ir_{0.2})O_2$:10F NTs and thin films of $(Sn_{0.8}Ir_{0.2})O_2$:10F and pure IrO_2 electrocatalysts conducted in 1N H_2SO_4 solution under a constant potential of ~1.5 V (*vs* RHE) at 40ºC for 24 h

In addition, the approach of using F as a doping agent to enhance the stability of the oxide electrocatalysts is seen to be positive as reportedly confirmed by various studies[33, 178, 180]. The stabilizing effect of F on the transition metal oxide-based supports such as tin (Sn) has also been thoroughly investigated by various groups. For example, Geiger et al.[178] conducted the investigation of the potential dependent dissolution rates of various catalyst supports such as fluorine doped tin oxide (FTO), indium tin oxide (ITO) and antimony doped tin oxide (ATO) in the broad potential window ranging from −0.6 to 3.2 V RHE in 0.1 M H_2SO_4 electrolyte. Their study concludes that FTO exhibits best electrochemical stability with no sign for any measurable catalysts' dissolution in the potential limits of −0.34 V RHE < E < 2.7 V RHE, making FTO as an appropriate candidate for electrocatalyst supports for acidic OER. Besides, in the theoretical study by Binninger et al.[181], it has been reported that oxygen anion-free salts containing anion species with a very high oxidation potential such as fluorides, chlorides, or sulfates are promising candidates for thermodynamically stable OER. Thus, our obtained results are indeed in good agreement with these reported studies, wherein the incorporation of F in the high Sn: Ir ratio (80:20) containing solid solution electrocatalysts exhibit superior activity as well as excellent electrochemical stability for acidic OER.

Furthermore, the inductively coupled plasma - optical emission spectroscopy (ICP-OES) analysis conducted on the 1 N H_2SO_4 electrolyte solution after the 24 h CA test shows very low (~0 ppm) dissolution of Ir and Sn for the as-prepared $(Sn_{0.8}Ir_{0.2})O_2$:10F NTs and thin films of $(Sn_{0.8}Ir_{0.2})O_2$:10F and IrO_2 electrocatalysts[97]. Therefore, in addition to the superior electrocatalytic activity of $(Sn_{0.8}Ir_{0.2})O_2$:10F NTs, the ICP-OES results suggest the excellent robustness of $(Sn_{0.8}Ir_{0.2})O_2$:10F NTs towards OER in PEM water electrolysis. Further, to investigate the possible structural changes occurring during the OER durability test, XRD and XPS analysis for the $(Sn_{0.8}Ir_{0.2})O_2$:10F NTs was carried out after performing the 24 h OER chronoamperometry test. As shown in **Appendix A Figure 2**, the XRD pattern of the $(Sn_{0.8}Ir_{0.2})O_2$:10F NTs did not feature any major change in the rutile type tetragonal structure, suggesting structural properties are considerably unaffected during the OER process[182]. Further, in the XPS spectra recorded after 24 h chronoamperometry test (**Appendix A Figure 3**), the stable $(Sn_{0.8}Ir_{0.2})O_2$:10F NTs contained Ir and Sn. The Sn 3d signal of $(Sn_{0.8}Ir_{0.2})O_2$:10F NTs post stability exhibited appearance of Sn $3d_{3/2}$ and Sn $3d_{5/2}$ with similar binding energies values as those in the as-synthesized fresh electrode. However, in the case of XPS spectra of Ir corresponding to $(Sn_{0.8}Ir_{0.2})O_2$:10F NTs following post stability tests, it is interesting to note that Ir $4f_{5/2}$ and Ir $4f_{7/2}$ doublet positions exhibited slight negative shift of ~ 0.25 eV (i.e. towards lower binding energy) as compared to the corresponding doublet positions of the as-synthesized fresh $(Sn_{0.8}Ir_{0.2})O_2$:10F NTs. This negative shift in the XPS suggests the formation of sub-stoichiometric IrO_2 i.e. partial conversion of IrO_2 to hydrated sub-stoichiometric IrO_x species[182, 183]. Similar behavior in the XPS analysis for the Ir signal was observed in the recent study by Siracusano et al.[182]. Such negative shift in binding energy values can be attributed to beneficial surface modification occurring during the high rate of oxygen evolution reaction. In addition, the role of hydrated structures arising from such surface modification is well known to stimulate the OER kinetics [33, 182, 184, 185]. Thus, the as-performed post stability characterization results suggest the excellent robustness and beneficial surface modification of $(Sn_{0.8}Ir_{0.2})O_2$:10F NTs towards prolonged OER in the PEM based water splitting process.

Consequently, the above electrochemical results demonstrate that the rational fabrication of earth abundant SnO_2 , F and ultra-low noble metal (Ir) containing solid solution electrocatalyst with the nanotubular functionalities indeed enhances the electrocatalytic activity and offers a unique opportunity to tailor the electronic, physical and electrocatalytic properties of $(Sn,Ir)O_2$:10F. Strikingly, it turns out that our $(Sn_{0.8}Ir_{0.2})O_2$:10F electrocatalyst - directly grown on the current collector represents a novel highly active electrode configuration for OER. This is owing to the facile pathway for electron transport aided by the likely improved electronic conductivity i.e., low surface charge transfer resistance (R_{ct}) and presence of 1D vertical channels contributing the high electrochemical active surface area (ECSA) and thus, attainment of excellent electrochemical performance towards OER in PEM water electrolysis.

5.5 Conclusions

In summary, the present study demonstrates the suitability of 1D vertically aligned nanotubes (VANTs) of $(Sn_{0.8}Ir_{0.2})O_2$:10F as a potential electrocatalyst system for oxygen evolution reaction (OER) in PEM based water electrolysis. The VANTs of $(Sn_{0.8}Ir_{0.2})O_2$:10F fabricated on Ti substrate exhibit excellent electrochemical performance with significant ~2.3 and ~ 2.6 times higher electrocatalytic activity than that of the 2D thin film architectures of identical composition of $(Sn_{0.8}Ir_{0.2})O_2$:10F and state-of-the-art IrO_2 electrocatalysts, respectively. In addition, $(Sn_{0.8}Ir_{0.2})O_2$:10F NTs displayed lower surface charge transfer resistance, lower Tafel slope, higher electrochemical active surface area, higher mass and specific activity and higher TOF than the as-synthesized benchmark IrO_2 and $(Sn_{0.8}Ir_{0.2})O_2$:10F thin film based electrocatalysts. Moreover, the as-prepared $(Sn_{0.8}Ir_{0.2})O_2$:10F NTs demonstrate excellent electrochemical stability in the harsh acidic media - identical to that of IrO_2 and $(Sn_{0.8}Ir_{0.2})O_2$:10F thin film electrocatalyst, operated for OER under similar conditions. Thus, the present study contributes the major enhancement in the electrocatalytic performance of $(Sn_{0.8}Ir_{0.2})O_2$:10F composition contrasted with nanostructured 2D thin film by fabricating 1D vertically aligned nanotubular architectures with substantial reduction in Ir content (~ 80 mol.%). The superior performance will ultimately likely result in reduction in overall capital cost of water splitting process. Therefore, the as-prepared $(Sn_{0.8}Ir_{0.2})O_2$:10F NTs are indeed promising as OER electrocatalysts for generation of highly efficient and sustainable hydrogen via PEM based water electrolysis.

6.0 Specific Aim 1A - To Identify and Engineer Reduced PGM Containing and PGM-Free Multi-Metal Oxide (MMO) Based Electrocatalyst Materials of Different Architectures for Oxygen Evolution Reaction (OER) in Proton Exchange Membrane-Based Water Electrolysis (PEMWE)

This aim describes the results of the third reduced PGM containing OER electrocatalyst.

- Chapter 6: Nanorods of Fluorine substituted (Mn,Ir)O_2: F electrocatalysts for OER

Excerpts reprinted with permission from Ghadge, Shrinath Dattatray, et al. "Experimental and theoretical validation of high efficiency and robust electrocatalytic response of one-dimensional (1D) (Mn,Ir)O_2: 10F nanorods for the oxygen evolution reaction in PEM-based water electrolysis." ACS Catalysis 9.3 (2019): 2134-2157. Copyright © 2019, American Chemical Society.

6.1 Abstract

Development of highly efficient, earth-abundant and cost effective electrocatalysts for kinetically sluggish and energy intensive anodic oxygen evolution reaction (OER) is crucial for realizing the largescale commercialization of proton exchange membrane-based water electrolysis (PEMWE). Herein, we report the results of one-dimensional (1D) nanorods (NRs) of ultra-low noble metal (Iridium, Ir) containing and 10 wt. % fluorine (F) doped $(Mn_{0.8}Ir_{0.2})O_2$:10F as an efficient anode electrocatalyst, synthesized via a simple hydrothermal and wet chemical approach for acidic OER. The as-synthesized $(Mn_{0.8}Ir_{0.2})O_2$:10F NRs demonstrate promising electrocatalytic performance for OER with significantly lower overpotential (η) and higher current density than

state-of-the art IrO_2 and many other noble/reduced noble metal containing electrocatalysts. Owing to the presence of 1D channels of nanorod architecture and unique electronic structure obtained upon formation of F containing solid solution, the $(Mn_{0.8}Ir_{0.2})O_2$:10F NRs exhibit low charge transfer resistance (~2.5 Ω.cm^2), low Tafel slope (~38 mV dec^{-1}), low water contact angle (~18^o), high electrochemical active surface area (ECSA ~704.76 m^{2}g^{-1}), high roughness factor (~2114) and notable OER performance with ~6 , ~2.1 and ~ 2.2 fold higher electrocatalytic activity than IrO_2, $(Mn_{0.8}Ir_{0.2})O_2$ NRs and 2D thin film of $(Mn_{0.8}Ir_{0.2})O_2$: 10F, respectively. The significantly higher ECSA and BET specific activity, mass activity (40 Ag^{-1}) and TOF (0.01s^{-1}) at overpotential (η) of 220 mV suggest the intrinsically higher catalytic activity of $(Mn_{0.8}Ir_{0.2})O_2$:10F NRs than other as-synthesized electrocatalysts. In addition, $(Mn_{0.8}Ir_{0.2})O_2$:10F NRs function as robust electrocatalysts by delivering current density of 10 mAcm^{-2} at η of ~ 200 mV and displaying long term durability, devoid of any degradation of the catalytic activity, suggesting the structural robustness for displaying prolonged OER activity. Herein, based on the synergistic effects of tailoring of 2D materials length scales into 1D nanorod framework and corresponding formation of F substituted unique solid solution structure (as validated by density functional theory), $(Mn_{0.8}Ir_{0.2})O_2$:10F NRs offer a promise for efficient OER in PEMWE.

6.2 Introduction

The alarming concerns related to rapid depletion of conventional fossil fuels and the associated deleterious warning effects of global warming has provided tremendous impetus to develop alternative clean, environmental friendly and sustainable energy sources which can alleviate the global reliance on rapidly depleting fossil fuels (natural gas, coal, oil)[70, 186, 187]. With these constant incessant concerns, hydrogen (H_2) gas having completely non-carbonaceous nature, higher energy density (~120 MJ/kg) than petroleum based energy sources (~45 MJ/kg) and environmental friendliness offers an ecologically ideal energy vector to counter the growing energy demand. The burgeoning positive influence of hydrogen fuel has thus, garnered immense attention as the foremost energy carrier over the last decade[50, 188-190]. Along these lines, generation of clean and sustainable hydrogen fuel via advantageous acidic electrolysis i.e. proton exchange membrane (PEM) based water electrolysis is hitherto considered as one of the most efficient and reliable technologies among all other conventional hydrogen production approaches[22, 70]. Although PEM water electrolysis is a promising approach for large scale generation of ultra-high purity (UHP) hydrogen, commercial development of this technology has been largely constrained due to energy intensive, technologically challenging and sluggish anodic oxygen evolution reaction, OER ($2H_2O \rightarrow O_2 + 4H^+ + 4e^-$) which requires an electrochemical overpotential of ~ 1.8 to 2 V; significantly higher than the standard thermodynamic water splitting OER value of ~1.23 V[22, 81, 191]. To address this bottleneck, platinum group metal (PGM) based electrocatalysts such as Pt, RuO_2 and IrO_2 are considered as pioneering electrocatalysts which facilitate sustained oxygen evolution under highly acidic condition and exhibit excellent electrocatalytic OER performance towards PEM based water electrolysis[50, 192]. However, the very high cost (e.g. \$210/g_{IrO2}) and environmentally scarcity (~ 0.001-0.0003 ppm in earth's crust)[29] of these benchmark precious metal group (PGM) electrocatalysts has seriously restricted their applications for the large-scale PEM water electrolyzer[22, 84]. Therefore, the identification, synthesis and development of novel reduced noble metal containing electrocatalysts, unveiling remarkable electro-catalytic activity with low overpotential and excellent long term electrochemical stability - superior to state-of-the art OER electrocatalyst (IrO_2) in acidic operating conditions of OER, will universally assist in the reduction of capital cost of PEM water electrolyzer cells[193]. The consequent scientific advances will help trigger commercialization enabling clean and regenerated energy production by making water splitting reaction more energy efficient[70, 94, 97].

In view of the above considerations to realize the much desired progress, our previous research efforts over the past decade in the PEM water electrolysis and OER electrode development arena have encompassed the unique strategies of solid solution formation utilizing ultra-low noble metal (Ir/Ru) content with earth abundant and low-cost catalyst supports (Sn, Nb, Mn) combined with anionic doping (F) to improve the IrO_2/RuO_2 electrode performance (activity as well as stability)[35, 70, 94, 97, 98, 102, 137]. In one of our previous reports[70], utilizing this solid solution formation strategy, we have exploited the first-principles theoretical calculations of total energies and electronic structures and have accordingly established the major paradigm for enhancing the electrocatalytic activity of IrO_2 by generating solid solution OER electrocatalyst of $(Mn_{1-x}Ir_x)O_2$:10F (x = 0.2, 0.3, 0.4). These novel compositions comprise earth abundant - manganese oxide (MnO_2) combined with anionic dopant-fluorine (F) serving as the primary electronic conductivity stimulant juxtaposed with ultra-low noble metal content of Ir. Arising from the unique electronic/molecular structure and beneficial solid solution formation, the as-synthesized $(Mn_{1-x}Ir_x)O_2$:10F electrocatalyst system fabricated in the 2D thin film architecture, demonstrated remarkable electrocatalytic performance with a significantly lower onset potential of ~ 1.35 V (vs. RHE) i.e. ~ 80 mV lower than that of IrO_2 (~1.43 V) in acid mediated water electrolysis[70]. In addition, $(Mn_{1-x}Ir_x)O_2$:10F electrocatalyst with substantial reduction (~ 80 at.%) in the noble metal content [$(Mn_{0.8}Ir_{0.2})O_2$:10F], exhibited excellent OER activity (~ 7 fold higher than IrO_2 film) as well as excellent durability as compared to IrO_2 film electrocatalyst [70].

This previous work serving as a guide and by exploiting the attributes of nanostructure engineering to further enhance the electrocatalytic performance of 2D thin film solid solution electrocatalysts, we have embarked on a pathway to design highly active, highly robust, and scalable electrocatalysts system by tailoring the material length scales into one-dimensional (1D) nanoscale architectures. Among the various electrocatalyst development strategies, the design and fabrication of nanostructured one-dimensional (1D) electrocatalysts architectures such as nanowires (NWs), nanorods (NRs) and nanotubes (NTs) etc. has been gathering significant attention[139, 146, 194-196] and a plethora of research funding have been invested to fabricate various 1D electrocatalysts such as CoP NRs[197], Ni_3S_2 NRs[198], Pt NTs[139], nitrogen-containing carbon nanotubes (NCNTs)[143, 199], TiO_2 NRs[200-202], Pt–Ni–TiO_2 NTs[144, 145, 203], Pt-Ru/Co NWs[144, 145], Co_4N NWs[140], Ir-Ni and Ir-Co NWs[204] etc. with tunable morphology and phase resulting in distinct performances in electrolytic/photo-electrochemical water splitting as well as in the direct methanol fuel cell (DMFC) research area [144, 205].

It is well known that, in general, 1D nanostructures offer various benefits either by favorably exposing the vicinal i.e. high-index facets (or active sites for reaction) and/or electrically linking these active sites for facile electron or charge transport within the 1D channels of nanomaterials[146]. In addition, the 1D materials possess high active specific surface areas, large aspect ratio (L/D), high active-site densities and high roughness factors which can substantially increase the efficiency and performance of electrocatalyst material [144]. Furthermore, due to the presence of 1D channels and lattice planes with fewer crystal boundaries, 1D nanomaterials encounter fast charge transport pathways with reduced scattering offering lower charge transfer resistance (R_{ct}) and high electronic conductivity[144]. Besides, it is reported that, the presence of sufficient porosity and open space between the adjacent 1D channels is significantly beneficial for enabling rapid release of oxygen bubbles as well as offering excellent electrocatalyst to electrolyte contact due to ease of accessibility of the electrolyte molecules into the deep portion of the electrode/catalyst surface [130, 146]. This evidently expedites the reaction kinetics offering faster mass as well as charge transport. In addition to these various benefits to enhance the catalytic activity, 1D nanostructures are also well known in terms of their excellent electrocatalytic stability [144]. Based on these previous studies, the asymmetric structure of 1D architecture is regarded as a beneficial factor for displaying the superior catalytic stability while alleviating the dissolution and suppression of the physical ripening processes which commonly occurs in nano- particular or film based catalyst materials [144, 206-208].

Thus, as a culmination of all of these excellent attributes, 1D morphologies are primarily regarded as an essential building block for the development of high performance electrocatalysts. For example, in our recently reported study, we have successfully demonstrated the suitability of 1D vertically aligned nanotubes (VANTs) of ultra-low noble metal containing and F substituted $(Sn_{0.8}Ir_{0.2})O_2$:10F as an efficient electrocatalyst system for OER in the PEM based water electrolysis system[187]. The as-synthesized 1D NTs unveiled the excellent electrochemical performance with significant ~ 2.3 fold higher electrocatalytic activity, lower charge transfer resistance and higher electrochemically active surface area (ECSA) than that of the 2D thin film architecture of identical composition of the $(Sn_{0.8}Ir_{0.2})O_2$:10F [97, 187]. Thus, following the same vein of electrocatalyst development displaying significant enhancement in the electrocatalytic performance of our previously reported $(Mn_{1-x}Ir_x)O_2$:10 F system[70], herein, we report for the first time, the synthesis of 1D nanorods of $(Mn_{1-x}Ir_x)O_2$: 10F (x= 0.2) and also correspondingly demonstrating the system as a highly efficient and robust OER electrocatalyst morphology for PEM water electrolysis. The OER performance of the as-synthesized $(Mn_{0.8}Ir_{0.2})O_2$:10F NRs has been compared with the state-of-the art IrO_2 and our previously reported 2D thin film architecture of $(Mn_{0.8}Ir_{0.2})O_2$:10F[70]. In order to fabricate the 1D nanomaterials, various techniques such as physical vapor deposition[151], thermal decomposition[152], and vapor-liquid-solid deposition[154] etc. have been reported. Among the various techniques, hydrothermal or autoclave-based approach is comparatively simple, time efficient, inexpensive, and easily scalable for the reliable fabrication of various 1D architectures, offering facile control over size and shape of the various nano-structured materials. Therefore, herein, 1D solid solution NRs of $(Mn_{0.8}Ir_{0.2})O_2$:10F have been synthesized using a two-step method wherein in the first step, MnO_2 NRs are synthesized via a simple and inexpensive hydrothermal approach. The second step involves the wet chemical approach of incorporating Ir and F into the MnO_2 framework, followed by calcination to form the solid solution of $(Mn,Ir)O_2$:F.

In the current study, as anticipated, the as-synthesized pure 1D $(Mn_{0.8}Ir_{0.2})O_2$:10F NRs exhibited remarkable electrocatalytic performance for OER in acidic media by attaining the benchmark current density of 10 mA cm^{-2} at a low over-potential (η) of 200 mV, superior to the state-of-the-art IrO_2, $(Mn_{0.8}Ir_{0.2})O_2$:10F 2D thin film and many other reported noble/reduced noble metal containing electrocatalysts for acidic OER including Ir doped cryptomelane-type manganese oxide $[K_{1.65}(Mn_{0.78}Ir_{0.22})_8O_{16}]$ based electrocatalyst system (η ~ 340 mV) as recently reported by Sun et al.[209] Furthermore, $(Mn_{0.8}Ir_{0.2})O_2$:10F NRs demonstrated significantly lower charge transfer resistance (2.5 Ω cm^2), lower Tafel slope (38 mV dec^{-1}) and particularly, higher ECSA as well as BET specific activity combined with high turnover frequency (TOF) of ~0.01s^{-1} at η of 220 mV. In addition, the OER stability test conducted using $(Mn_{0.8}Ir_{0.2})O_2$:10F NRs demonstrated no significant decay in the current density, suggesting its excellent structural and morphological robustness as witnessed from the post-stability characterization of the electrocatalytic activity. It is therefore, worth mentioning that the superior electrocatalytic performance of the as-synthesized $(Mn_{0.8}Ir_{0.2})O_2$:10F NRs is well supported by our density function theory (DFT) computational calculations which further illustrate that F substituted $(Mn_{0.8}Ir_{0.2})O_2$:10F NRs possess lower over-potential and superior catalytic activity contrasted with that of the corresponding 2D film, leading to the excellent electrocatalytic activity with significant reduction (~ 80 at. %) in the noble metal content. Thus, all of these results taken in total and discussed in detail in the following sections indicate the promise of $(Mn_{0.8}Ir_{0.2})O_2$:10F NRs as an attractive OER electrocatalyst for efficient and sustainable hydrogen production using the PEM based water splitting approach.

6.3 Experimental Methodology

6.3.1 Materials

Manganese (II) sulfate monohydrate ($MnSO_4.H_2O$, ≥ 99%, Sigma Aldrich), Potassium permanganate ($KMnO_4$, ≥99.0%, Fisher scientific), Iridium tetrachloride ($IrCl_4$, 99.5%, Alfa Aesar) and ammonium fluoride (NH_4F, 98%, Alfa Aesar) were used as precursors for electrocatalysts synthesis. Nafion 117 (5 wt. % solution in lower aliphatic alcohols, Sigma Aldrich) was used as binder. Deionized (DI) water (18 MΩ.cm, MilliQ Academic, Millipore) was used throughout the experiments. All the chemical reagents were used as received without any further purification.

6.3.2 Preparation of Electrocatalyst Materials

6.3.2.1 Synthesis of MnO_2 Nanorods (NRs)

A hydrothermal (autoclave) approach was utilized for the synthesis of MnO_2 NRs.[210] In a typical synthesis of MnO_2 NRs, $MnSO_4.H_2O$ (0.2 g) and $KMnO_4$ (0.5 g) were dissolved in a 100 ml D.I. water under continuous stirring for 30 min at a room temperature to form a homogeneous solution. This solution was then transferred into a Teflon-lined stainless-steel autoclave (120 ml capacity) and the autoclave was subjected to heat treatment at 160 °C for 12h (Ramp rate = $10^{o}Cmin^{-1}$). After the reaction involving generation of the corresponding MnO_2 [$2KMnO_4+3MnSO_4+2H_2O \rightarrow 5\alpha\text{-}MnO_2+K_2SO_4+2H_2SO_4$] was complete, the autoclave was naturally cooled to room temperature. The obtained brownish solid product was thoroughly washed with D.I. water several times (9500 rpm, 3 min), followed by drying overnight in an air at $60^{o}C$ for further characterizations.

6.3.2.2 Synthesis of $(Mn_{0.8}Ir_{0.2})O_2$ and $(Mn_{0.8}Ir_{0.2})O_2$:10F NRs

For the preparation of $(Mn_{0.8}Ir_{0.2})O_2$ and 10 wt. % F doped $(Mn_{0.8}Ir_{0.2})O_2$ [$(Mn_{0.8}Ir_{0.2})O_2$:10F], stoichiometric amount of $IrCl_4$ was added in the DI water along with the stoichiometric amount of the as-prepared MnO_2. Similarly, for the synthesis of $(Mn_{0.8}Ir_{0.2})O_2$:10F, stoichiometric amount of $IrCl_4$ and NH_4F were mixed in the DI water along with the appropriate amount of the as-prepared MnO_2. These solutions were stirred vigorously for 1 h and transferred into the alumina crucibles and then, dried in an in an electric oven at 60˚C for ~ 3 hours. The crucibles containing the dried oxide precursors were then subjected to heat-treatment in air at 400˚C (Ramp rate = $10^{o}C\ min^{-1}$) for 4 hours in order to form the corresponding $(Mn_{0.8}Ir_{0.2})O_2$ and $(Mn_{0.8}Ir_{0.2})O_2$:10F solid solution electrocatalyst, respectively. The obtained electrocatalyst products were washed with D.I. water several times and the dried overnight in air at 60°C for further characterizations. In addition, in order to investigate the influence of F on the as-synthesized MnO_2, the F doped MnO_2 (MnO_2:10F) has also been synthesized by employing the above-described approach. Herein, it is noteworthy to mention that the major objective of the present study is to demonstrate the superior electrochemical performance of 1D $(Mn_{0.8}Ir_{0.2})O_2$ NRs to that of our previously reported[70] 2D thin film of $(Mn_{0.8}Ir_{0.2})O_2$ under identical synthesis (atomic ratio, calcination temperature and time, mass loading etc.) as well as OER operating conditions. Therefore, in the current work, in order to execute unbiased comparison between 1D NRs and 2D thin film, we have fabricated $(Mn_{0.8}Ir_{0.2})O_2$ NRs at the calcination temperature of 400°C. Furthermore, it is well known that α-MnO_2 initiates its transformation from α-MnO_2 to α-Mn_2O_3 phase beyond the calcination temperature of 500°C (typically 600-800°c) [209, 211]. Thus, in order to prevent any undesired phase transformation during the calcination process, we have performed the electrocatalyst synthesis and calcination of $(Mn_,Ir)O_2$ at 400°C. It should be noted that similar calcination temperature (400°C) has been utilized for the thin film fabrication of Ir-Mn oxide based electrocatalysts in literature[212], wherein optimum electrocatalytic performance has been achieved at 400°C. The schematic illustration of the synthesis process for generating MnO_2 and $(Mn_{0.8}Ir_{0.2})O_2$:10F NRs has been depicted in the **Figure 6-1 (a)**.

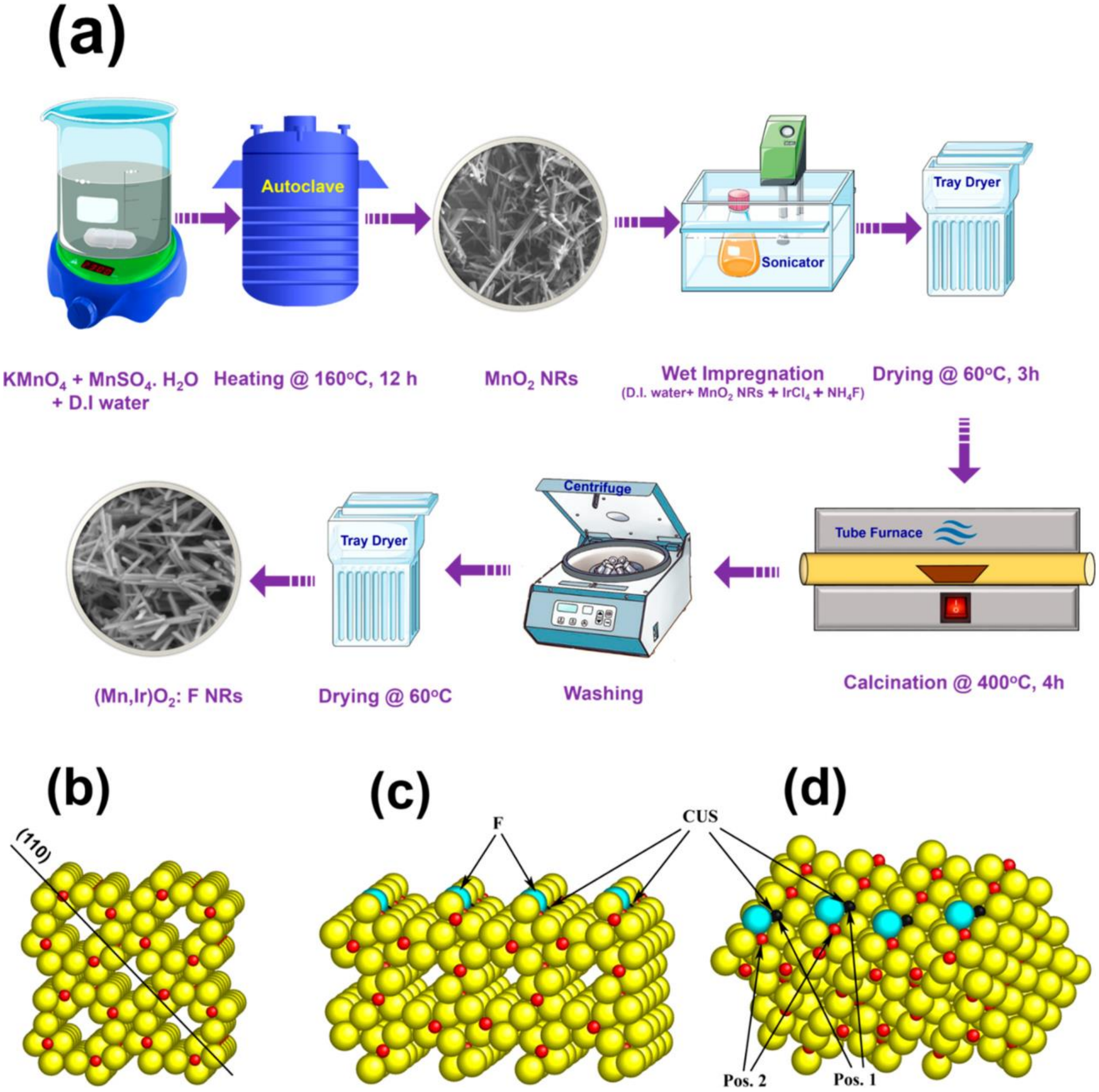

Figure 6-1 (a) Schematic illustration for the synthesis process of $(Mn_{0.8}Ir_{0.2})O_2$:10F NRs, (b) general view of α-MnO_2 crystal structure with coordinatively unsaturated sites (CUS) at (110) crystallographic surfaces, (c) and (d) demonstrate (110) surface at different angles. Pos.1 and Pos.2 represent two possible positions of Ir atom considered in the present study

6.3.2.3 Synthesis of IrO_2 Nanoparticles

For the synthesis of IrO_2 nanoparticles, a well-known modified Adams fusion method was utilized[137]. In specific, $IrCl_4$ and $NaNO_3$ were separately dissolved in the D.I. water. The solution containing the dissolved $IrCl_4$ was then mixed with excess $NaNO_3$ solution. Next, the resulting solution mixture was thoroughly stirred for ~ 2 h to make it completely homogenous. The water from this uniform mixture was then evaporated using a heating furnace operated at 60^{o}C, followed by heat treatment in air at 500^{o}C for 1h (Ramp rate = 10^{o}C/min). The thermally treated solid mixture was naturally cooled down to room temperature and then crushed into fine powder using an agate mortar and pestle. This powder was then vigorously washed using D.I. water, and the resulting product (IrO_2) was then dried in an oven at 60^{o}C for further characterizations. Herein, for the synthesis of IrO_2, the calcination temperature of 500^{o}C was selected on the basic of various critical viewpoints elucidated in the literature. For example , in the study conducted by Geiger et al.[164] , it has been observed and reported that the catalytic activity (for acidic OER) of IrO_2 starts declining from calcination temperature of 400^{o}C to 600^{o}C and more stable electrodes are formed at $T \geq 400^{o}$C. In addition, based on the intrinsic activity and dissolution of IrO_2 based electrocatalysts, Geiger et al.[164] concluded that the IrO_2 electrodes synthesized at ~500^{o}C are identified as most promising for acidic OER. Added to this, Siracusano et al.[182] reports that, mild annealing process (~500^{o}C) for IrO_2 is critical to avoid excessive growth of the catalyst particles while favoring the proper crystallization in the bulk. Thus, in agreement with these viewpoints, in order to attain optimum electrocatalytic performance (activity and stability) as well as to form crystalline IrO_2, we have employed the calcination temperature of ~500°C for synthesizing IrO_2. It is noteworthy to mention that, in addition to IrO_2, fluorinated IrO_2 (IrO_2:10F) was also synthesized (using earlier reported approach[137]) for assessment of the electrochemical results.

6.3.3 Electrocatalyst Materials Characterization

6.3.3.1 Physicochemical Characterizations

X-ray diffraction (XRD) analysis was carried out to acquire qualitative phase information of the as-synthesized electrocatalyst powders. XRD has been performed by using Philips XPERT PRO system, with CuK$_\alpha$ (λ = 0.15406 nm) radiation at an operating voltage and current of 45 kV and 40 mA, respectively. XRD peak profiles have been analyzed using pseudo-Voigt function to determine Lorentzian and Gaussian contribution of the peaks[97]. The least square refinement techniques have been utilized to evaluate the molar volume and lattice parameters of as-synthesized electrocatalysts. The textural properties (specific surface area, BJH pore size distribution) of the electrocatalyst powders were derived from the nitrogen adsorption-desorption analysis and Brunauer-Emmett-Teller (BET) technique was used to analyze the surface area. The as-synthesized electrocatalyst powders were first vacuum degassed and then analyzed using a Micromeritics ASAP 2020 instrument. The BET surface area values were obtained using Multipoint BET technique. The electronic conductivity values of the as-synthesized electrocatalyst samples were investigated by utilizing Jandel Micro position Probe apparatus. The morphology and microstructure of the electrocatalyst powders has been investigated by performing scanning electron microscopy (SEM). Energy dispersive x-ray spectroscopy (EDX) analyzer (attached with the SEM instrument) was used for the quantitative elemental analysis and to study the distribution of elements by elemental x-ray mapping technique. The elemental and x-ray mapping analysis of as-prepared electrocatalyst was carried out using Philips XL-30FEG system, operated at a voltage of 20 kV. The size and microstructure of electrocatalyst materials was studied by using JEOL JEM-2100F transmission electron microscope (TEM) and high-resolution transmission electron microscopy (HRTEM). In addition to EDX analysis, the atomic ratio of Mn and Ir was investigated by using inductively coupled plasma optical emission spectroscopy (ICP-OES, iCAP 6500 duo Thermo Fisher). The electrocatalyst sample was digested with aqua regia at 60 °C for 2 h and diluted with deionized water before analysis.

The X-ray photoelectron spectroscopy (XPS) was performed to study the element binding and valence states of the electrocatalysts. The XPS analysis was conducted using ESCALAB 250 Xi system (Thermo Scientific) equipped with a monochromated Al Kα X-ray source. The analysis spot of $400 \times 400\ \mu m^2$ was well-defined by the micro-focused X-ray source. The XPS system was functioned in an ultra-high vacuum chamber with the base pressure less than 5×10^{-10} mBar and at a room temperature. The binding energy (BE) scale of the analyzer was calibrated to produce <50 meV deviations of the three standard peaks from their standard values. The aliphatic C1s peak was observed at 284.6 eV. High-resolution elemental XPS data was acquired with the analyzer pass energy set to 20 eV (corresponding to energy resolution of 0.36 eV) and the step size set to 0.1 eV [187]. The fitting of the elemental spectra based on calibrated analyzer transmission functions and Scofield sensitivity factors. The effective attenuation lengths for photoelectrons from the standard TPP-2M formalism was achieved using the Avantage software package (Thermo Fisher Scientific). During the fitting of the XPS spectra, the fitting parameters such as L/G mix, tail mix, tail height and tail exponent were fixed at 30%, 100%, 0% and 0%, respectively. All the XPS spectra in the present study were fitted symmetrically with Gaussian-Lorentzian functions without introducing any constraints. The wetting characteristics of as-synthesized electrocatalysts were investigated by using AST products VCA 2000 video contact angle goniometer. In static water contact angle measurement, water droplet (10 μl) was vertically dropped onto the electrode surface and contact angle was detected by sensitive drop method by drawing tangent to the edge of the droplet and intersecting it with the measurement baseline.

6.3.4 Electrochemical Characterization

The electrochemical characterization of as-prepared electrodes has been carried out in a three-electrode configuration using a VersaSTAT 3 (Princeton Applied Research) electrochemical workstation. 1 N sulfuric acid (H_2SO_4) was used as the electrolyte solution and also, as a proton source for oxygen evolution reaction (OER), maintained at a constant temperature of 40°C using a Fisher Scientific 910 Isotemp refrigerator circulator during electrochemical characterization. The oxygen from the electrolyte solution was expelled by purging the electrolyte solution with ultra-high pure (UHP) argon gas (Matheson) for ~10 min prior to electro-chemical testing. In order to prepare the working electrodes (WE), the electrocatalyst inks of different compositions were produced by using 85 wt.% electrocatalyst powder and 15 wt.% Nafion 117 (5 wt.% solution in lower aliphatic alcohols, Aldrich). The resulting electrocatalyst inks were subjected to sonication for 1 h. After sonication, the catalyst inks were homogenized using Tissuemiser (Fisher Scientific) for ~ 3 min and then uniformly spread on the titanium (Ti) foils (Alfa Aesar) followed by drying under ambient conditions. The digital images of electrocatalyst ink coated electrodes are depicted in **Appendix B Figure 1**. Pt wire (Alfa Aesar, 0.25 mm thick, 99.95%) has been used as the counter electrode (CE) and mercury/mercurous sulfate (Hg/Hg_2SO_4) electrode (XR-200, Hach) having a potential of +0.65 V with respect to reversible hydrogen electrode (RHE) was used as the reference electrode (RE). The electrochemical performance of as-synthesized electrocatalysts for OER (total electrocatalyst loading =0.3 mg cm^{-2}) has been compared with in-house synthesized IrO_2 electrocatalyst (total loading =0.3 mg cm^{-2}) under identical operating conditions. The potential values reported in this study have been determined and reported with respect to reversible hydrogen electrode (RHE) and calculated from the formula as below:

$$E_{RHE} = E_{Hg/Hg2SO4} + E^{o}_{Hg/Hg2SO4} + 0.059\times pH$$

where E_{RHE} is the potential versus RHE and $E_{Hg/Hg2SO4}$ is the potential measured against the Hg/Hg_2SO_4 reference electrode. $E^{0}_{Hg/Hg2SO4}$ is the standard electrode potential of Hg/Hg_2SO_4 reference electrode (+0.65 V *vs* RHE).

Electrochemical impedance spectroscopy (EIS)

In order to determine the ohmic resistance (R_{Ω}) and the charge transfer resistance (R_{ct}) of the as-synthesized electrocatalysts, the electrochemical impedance spectroscopy (EIS) has been carried out. The EIS was conducted using the electrochemical workstation (Versa STAT 3, Princeton Applied Research) in 1 N H_2SO_4 electrolyte solution maintained at $40^{0}C$ and at ~1.5 V (which is the typical potential used for assessing the electrochemical activity of the electrocatalysts for OER). EIS has been operated in the frequency range of 100 mHz-100 kHz (Amplitude = 10 mV). The ZView software from Scribner Associates employing the equivalent circuit model given as $R_s(R_eQ_1)(R_{ct}Q_{dl})$ in which R_s (solution resistance) is in series with the parallel combination of the R_e (electrode resistance) and Q_1 (constant phase element) and further in series with the parallel combination of the R_{ct} (surface charge transfer) and Q_{dl} (contribution from double layer capacitance and pseudo capacitance). The ohmic resistance ($R_{\Omega} = R_{s} + R_e$) obtained from the EIS was further used for iR_{Ω} correction in the polarization curves of as-prepared electrocatalysts. It should be noted that the $R_s(R_eQ_1)(R_{ct}Q_{dl})$ equivalent circuit model was utilized for the impedance characterization of as-synthesized $(Mn_{0.8}Ir_{0.2})O_2$ and $(Mn_{0.8}Ir_{0.2})O_2$:10F NRs, whereas following the previous report[137] of powder IrO_2 electrocatalyst, $R_s(R_{ct}Q_{dl})$ model in which R_s (solution/ohmic resistance) is in series with the parallel combination of R_{ct} and Q_{dl} was suitably used for EIS fits for as-synthesized IrO_2 and MnO_2.

The electro-catalytic activity of as-synthesized electrocatalysts for OER was analyzed by conducting LSV measurements in 1 N H_2SO_4 electrolyte solution with a scan rate of 10 $mVsec^{-1}$ at 40^0C. The experimentally obtained polarization curves of electrocatalysts having different compositions were iR_Ω corrected (R_Ω - the ohmic resistance was determined from EIS analysis). The onset potential is defined as the potential where the initiation of current inflection is observed on the polarization curve. To compare the electro-catalytic activity of as-prepared electrocatalysts, the current density at particular potential of ~1.45 V (which is typical potential selected for comparison of activity) in iR_Ω corrected polarization curves was used. In order to investigate the intrinsic catalytic activity, the obtained current density values are normalized to the BET as well as electrochemical active surface area (ECSA) values. It should be noted that the current density values referred to geometric surface area (1 cm^2), BET surface area and ECSA are denoted as $mAcm^{-2}_{geo,}$ $mAcm^{-2}_{BET}$ and $mAcm^{-2}_{ECSA,}$ respectively. To study qualitative mechanistic insights of as-synthesized electrocatalysts, Tafel plots are developed after iR_Ω correction using the equation (5-1). Further, the electrochemical active surface area (ECSA) of the as-prepared electrocatalysts was examined by recording the cyclic voltammetry (CV) curves with various scan rates (10, 30, 50 and 70 mVs^{-1}) in the potential range from 0.1 to 1.2 V (*vs* RHE). The C_{dl} ($mFcm^{-2}$) values were obtained from the slope i.e., from plot of differences in current density ($j_{anode} - j_{cathode}$) at 0.7 V (*vs* RHE) *vs.* scan rate. In addition, the intrinsic OER activity of as-prepared electrodes was evaluated by calculating specific activity, mass activity, turnover frequency (TOF) and normalization of current densities by ECSA and BET surface area (m^2g^{-1}).

In order to evaluate the electro-catalytic stability of as-synthesized electrocatalysts for long term operation, chronoamperometry (CA) test (current *vs* time) has been carried out wherein, the electrode was maintained for 24 h in the electrolyte solution of 1 N H_2SO_4 at 40^0C

under a constant voltage of ~1.45 V. Further, to investigate the amount of Ir and/or Mn leached out from the working electrode during OER operation, the electrolyte solutions collected after 24 h of CA test were subjected to elemental analysis in an inductively coupled plasma optical emission spectroscopy (ICP-OES, iCAP 6500 duo Thermo Fisher). In addition, ICP-OES analysis has been conducted on the post stability electrode to investigate the Mn:Ir ratio. Furthermore, in order to assess the structural stability and robustness of as-prepared electrodes, post stability characterizations such as phase (XRD), morphology (SEM) and electronic/ surface oxidation states (XPS) analysis were conducted on the electrodes tested for 24 h of chronoamperometry test.

It should also be noted that all the experiments reported in the present study were repeated and analyzed with at least three repeats and the data is reported as the average of three independently generated as-prepared electrocatalyst samples.

6.4 Computational Methodology

The overall electrocatalytic activity and the overpotential of $(Mn,Ir)O_2$:F OER electrocatalyst is anticipated to depend on the electronic and crystal structure of the catalyst material as well as the thermodynamics of the four elementary steps of the oxygen evolution reaction as shown in equation (4-1), wherein * represents an active site on the metal oxide surface[101]. As it will be described in the experimental results section of the present study, the as-synthesized $(Mn,Ir)O_2$:F NRs exhibit tetragonal crystal analogous to the α-MnO_2 structure with tetragonal symmetry and the space group I4/m (no. 87).[205] The crystal structure of α-MnO_2 shown in **Figure 6-1 (b-d)** will be utilized to study the influence of compositions on the electronic structure as well as the onset potential and structural stability in the computational component of the current study. Herein, the following compositions with α-MnO_2 structure have been considered in the computational study: pure MnO_2, $(Mn_{0.75}Ir_{0.25})O_2$, and F-doped $(Mn_{0.75}Ir_{0.25})O_{2-x}F_x$ with x=0.25, 0.625 and 1.0. Such F-doped formula units correspond approximately to 4, 10, and 15 wt% of F. Such compositions have been chosen based on the elementary unit cell of α-MnO_2 structure comprising of 8 atoms of Mn and 16 atoms of O.

The free energies (ΔG) of all the four anodic intermediate reactions (I-IV) were utilized to calculate the electric potentials at which a certain specific reaction. Consequently, a systematic analysis of all the calculated free energies may assist in identifying the rate determining steps (RDS) as well as the corresponding over-potential of the oxygen evolution reaction taking place at the electrochemically active surface. This computational analysis is critical to assess the catalytic activity of the specific material used as an electrocatalyst in OER process. For the comparison purposes, three different materials have been chosen for calculation of the OER elementary steps: (a) pure MnO_2, (b) MnO_2 doped with small amount of Ir as a substituent of Mn at the corresponding Mn-type lattice sites, and (c) $(Mn,Ir)O_2$ doped with F as a substituent of O. For calculations of the total energies, electronic structure, and free energies of the four elementary steps qualitatively characterizing the electro-catalytic activity of the above-mentioned oxides, bulk and (110) surface α-MnO_2 structure have been utilized.

For bulk calculations a tetragonal 24-atom unit cell with α-MnO_2 crystal structure has been selected as the basis for construction of different Ir, Mn, and F concentrations of the solid solution oxides. Such a unit cell contains 8 transition metal atoms and 16 atoms of oxygen/fluorine. Thus, for the convenience of theoretical calculations, the basic compositions without introduction of fluorine have been chosen as following: pure MnO_2 with 8 Mn and 16 O atoms as well as Ir-doped oxide $(Ir_{0.25}Mn_{0.75})O_2$ with 2 Ir, 6 Mn, and 16 O atoms. For simulation of various dopant of fluorine

2, 5 and 8 atoms of oxygen were randomly replaced with corresponding number of fluorine atoms generating the following formula units: $(Mn_{0.75}Ir_{0.25})O_{1.75}F_{0.25}$, $(Mn_{0.75}Ir_{0.25})O_{1.375}F_{0.625}$, and $(Mn_{0.75}Ir_{0.25})O_{1.0}F_{1.0}$ which approximately corresponded to 4, 10, and 15 wt% of F content, respectively. Such compositions have been chosen for all calculation of the bulk and surface electronic structures employed in the present study. For calculation of the (110) surface electronic properties of the materials, a two-dimensional slab of ~6.7 Å of thickness repeated in [1,-1, 0] direction with 24 atom unit cell and a vacuum distance ~ 13 Å between adjacent images was selected. In order to calculate the free energies of all the elementary reactions i.e. (I) - (IV) for pure and doped α-MnO_2, the coordinatively unsaturated sites (CUS) located at the (110) surface have been considered as an active sites following previous computational studies on similar systems.[70, 101, 102, 114] All the intermediate species involved in the OER i.e. O*, OH*, and OOH* have been attached to the top surface layer. Three bottom layers of the slab were fixed with the lattice parameter corresponding to the bulk α-MnO_2. Apart from these three bottom layers, all other layers of the slab together with the intermediate species were fully relaxed which resulted into the residual force components on each atom to be lower than 0.01 eV/Å/atom.

A crystal structure chosen for the calculations in the present study has been shown in **Figure 6-1 (b)**. Two different atomic positions of Ir as a replacement of Mn at the (110) surface have been considered and marked as Pos.1 and Pos.2 to investigate the difference between the electronic structures of pure and Ir-doped MnO_2 compounds as well as to assess the effects of Mn and Ir on the overpotential of the $(Mn,Ir)O_2$. The first Ir-atomic distribution consists of one Ir-atom located in place of Mn just below the CUS. The second distribution is characterized by putting Ir-atom at the neighbor position denoted as Pos.2, while the CUS locates above the Mn atom. Also, to mimic F-doping in the electrocatalyst material, one oxygen atom has been replaced for F atom at the oxygen site adjacent to the CUS at the top layer**.** To measure the free energies of all the 4 elementary reaction steps as discussed above, such atomic distributions at the (110) surface covered by adsorbed oxygen monolayers in combination with intermediate species have been used. For calculating the total energies, electronic structure and density of electronic states (DOS) of the studied materials, the density functional theory (DFT) executed in Vienna Ab-initio Simulation Package (VASP) was utilized within the projector-augmented wave (PAW) method[104] and the spin-polarized generalized gradient approximation (GGA) for the exchange-correlation energy functional in a form described by PBE (Perdew-Burke-Ernzerhof Perdew).[213, 214] This computational package examines the electronic structure and via Hellmann-Feynman theorem and the inter-atomic forces are determined from the first-principles. The standard PAW potentials were employed for the elemental components and the iridium, manganese, oxygen and fluorine potentials thus contained nine, seven, six and seven valence electrons, respectively. Furthermore, to maintain the high accuracy for total energy calculations for all the electrocatalyst compositions, the plane wave cutoff energy of 520 eV has been selected. By utilizing the double relaxation procedure, the internal positions as well as the lattice parameters of atoms have been entirely optimized[70].

Furthermore, in the present study the minima of the total energies with respect to the lattice parameters and internal ionic positions have been evaluated. Also, by minimizing the Hellman–Feynman forces via a conjugate gradient method, the geometry optimization was attained which will cause the net forces applied on every ion in the lattice close to zero. The total electronic energies were converged within 10-5 eV/un.cell which result into the residual force components on each atom to be lower than 0.01 eV/Å/atom. This permits the accurate determination of the internal structural parameters. Herein, the Monkhorst-Pack scheme has been employed to sample the Brillouin Zone (BZ) and create the k-point grid for the solids and the different isolated atoms used in the current study. The choice of an appropriate number of k-points in the irreducible part of the BZ was made on the basis of the convergence of the total energy to 0.1 meV/atom. It is significant to remark that, for Mn-Ir-O-F compositions, the corresponding atomic distributions are uncertain and thus, different spatial configurations can be used for exemplification of the atomic distributions. This uncertainty has been disregarded by assembling the various atomic configurations for each selected composition and the configurations which correspond to the minimum total energy, have been chosen for executing the additional numerical analysis of these specific compositions of the binary oxides electrocatalysts.

6.5 Results and Discussions

6.5.1 Physical Characterization of Electrocatalysts

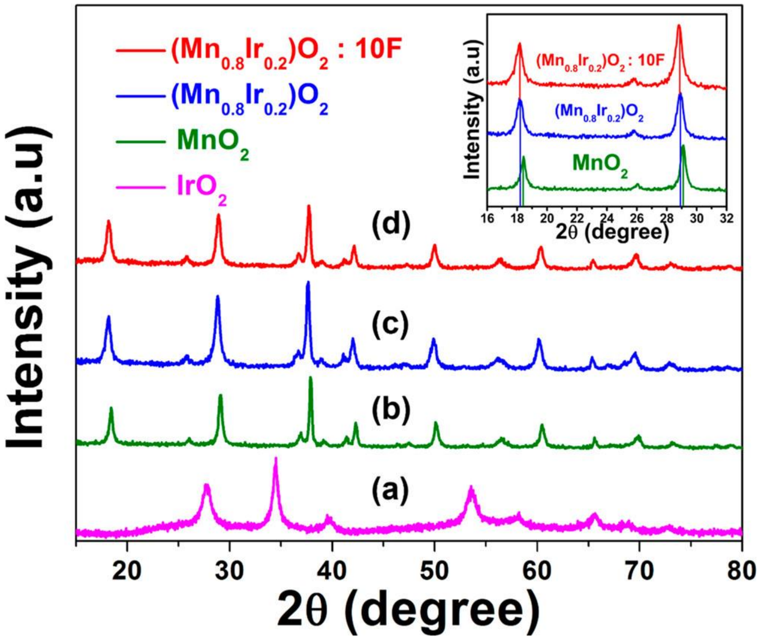

Figure 6-2 Powder XRD patterns of the as-synthesized (a) IrO_2, (b) MnO_2, (c) $(Mn_{0.8}Ir_{0.2})O_2$ and (d) $(Mn_{0.8}Ir_{0.2})O_2$:10F electrocatalysts (inset: Magnified view of XRD patterns)

To characterize the crystal phase and phase purity of as-synthesized electrocatalysts, the powder X-ray diffraction (XRD) patterns of MnO_2, $(Mn_{0.8}Ir_{0.2})O_2$, $(Mn_{0.8}Ir_{0.2})O_2$:10F and IrO_2 are studied and compared in Figure 6-2. The as-synthesized IrO_2 reveals the rutile type tetragonal structure (JCPDS 15-870) with lattice constants of a = 4.49 Å, c =3.15 Å and unit cell and molar volume of ~ 63.78 Å^3 and 19.20 cm^{3}mol^{-1} respectively (Table 6-1), similar to earlier reports.[137, 215] **Figure 6-2 (b)** shows the diffraction patterns of the hydrothermally synthesized MnO_2. All the diffraction peaks can be readily indexed to the pure tetragonal phase of α-MnO_2 [space group: I4/m (no. 87), JCPDS 44-0141] with lattice constants a = 9.784 Å, c = 2.852 Å and unit cell volume of 273Å^3 (**Table 6-1**), which is in a good agreement with the computationally calculated lattice parameters (

Appendix B Table 1) as well as earlier studies[205, 210], indicating formation of highly pure and crystalline α-MnO_2. The XRD patterns of $(Mn_{0.8}Ir_{0.2})O_2$ and $(Mn_{0.8}Ir_{0.2})O_2$:10F are depicted in **Figure 6-2 (c)** and **Figure 6-2 (d),** respectively. The XRD pattern reflections of $(Mn_{0.8}Ir_{0.2})O_2$ and $(Mn_{0.8}Ir_{0.2})O_2$:10F corresponds to that of the tetragonal structured α-MnO_2. The Ir and/or F doped MnO_2 did not demonstrate presence of any secondary phase of Mn or Ir or F based compounds, which can be attributed to the incorporation of dopants into the MnO_2 lattice. Herein, it is noteworthy to mention that the magnified XRD patterns of our as-synthesized $(Mn,Ir)O_2$ samples did not feature any characteristic amorphous hump at 2θ peak positions of ~ 22° which is typically observed in the XRD pattern of amorphous IrO_2, which further evidences the incorporation of Ir into the crystalline MnO_2 lattice [216, 217]. This result has been substantiated by the change in the lattice parameters and molar volumes of the Ir and F incorporated MnO_2 samples.

Electrocatalyst composition	**Lattice parameters (Å)**		**Unit cell volume (Å3)**
	a = b	**c**	
α-MnO2	9.784	2.867	274.44
Mn0.75Ir0.25O2	9.826	2.906	280.57
Mn0.75Ir0.25O1.37F0.625	9.849	2.963	287.41

Table 6-1 The lattice parameters, volume and BET surface area of as-synthesized electrocatalysts

Electrocatalyst composition	Lattice parameter (Å)		Volume		BET Surface area (m^2g^{-1})
	a = b	c	Unit cell ($Å^3$)	Molar (cm^3mol^{-1})	
MnO_2	9.784	2.852	273.012	20.55	3.72
$(Mn_{0.8}Ir_{0.2})O_2$	9.831	2.881	278.44	20.96	3.70
$(Mn_{0.8}Ir_{0.2})O_2$:10F	9.835	2.879	278.47	20.96	3.55
IrO_2	4.49	3.15	63.78	19.20	189

As shown in the inset of **Figure 6-2**, close inspection of XRD patterns of $(Mn_{0.8}Ir_{0.2})O_2$ and $(Mn_{0.8}Ir_{0.2})O_2$:10F indicated that the XRD peaks of these synthesized solid solution electrocatalysts are slightly shifted towards lower angle by 2θ value of ~ 0.3 degree. This negative shift in 2θ positions clearly suggests the lattice expansion[218] of $(Mn_{0.8}Ir_{0.2})O_2$ and $(Mn_{0.8}Ir_{0.2})O_2$:10F, which is primarily instigated by the incorporation of Ir into the MnO_2 crystalline framework. This lattice expansion can be attributed to the difference in ionic radii between the host element (Mn^{+4} = 0.54 Å)[219] and the dopant solute ion (Ir^{+4} = 0.62 Å)[220]. Furthermore, the increased lattice parameters and unit cell volume of $(Mn_{0.8}Ir_{0.2})O_2$ (278.44 $Å^3$) and $(Mn_{0.8}Ir_{0.2})O_2$:10F (278.47 $Å^3$) evidently suggests the successful incorporation of dopant ions (Ir^{+4}) into the host MnO_2 framework. It is noteworthy to mention that as-synthesized $(Mn_{0.8}Ir_{0.2})O_2$ and $(Mn_{0.8}Ir_{0.2})O_2$:10F exhibited comparable lattice parameters and molar volume, suggesting that F doping in the O^{2-} sites has no significant effect on the molar volume of $(Mn_{0.8}Ir_{0.2})O_2$: 10F. This can be ascribed to the comparable ionic radius of O^{2-} (1.25 Å) and F^- (1.20 Å) [97]. This result conforms well with various F substituted solid solution oxide electrocatalysts as reported in earlier studies [70, 97, 98]. Furthermore, as-synthesized IrO_2:10F [**Appendix B Figure 2 (a)]** and MnO_2:10F [**Appendix B Figure 2 (b)]**, exhibited XRD reflections similar to their respective parent electrocatalyst structures. These results suggest that fluorinated IrO_2 and MnO_2 demonstrate formation of solution devoid of any undesirable phase separation and/or mixed phase formation due to F incorporation. Herein, it is noteworthy to mention that, as elucidated in the electrocatalyst synthesis section, α-MnO_2 initiates its transformation from α-MnO_2 to α-Mn_2O_3 phase beyond the calcination temperature of 500°C (typically 600-800°c) [209, 211]. Thus, as can be seen from the XRD pattern of α-MnO_2 calcined at 400°C [**Appendix B Figure 2 (c)]** any possibilities of structure degradation in the α-MnO_2 based electrocatalysts synthesized at 400°C are clearly ruled out.

Furthermore, the Brunauer–Emmett–Teller (BET) based specific surface area (SSA) of as-synthesized MnO_2, $(Mn_{0.8}Ir_{0.2})O_2$, $(Mn_{0.8}Ir_{0.2})O_2$:10F and IrO_2 derived from the N_2 adsorption-desorption analysis is tabulated in **Table 6-1** and depicted in **Figure 6-3**. According to international union of pure and applied chemistry (IUPAC) classification, the N_2-sorption isotherms of these materials exhibit a type IV shape with H3 hysteresis loop, similar to the previous reports of MnO_2 nanorods, indicating that the as-synthesized materials possess slit-shape mesoporous structure (as also witnessed from the Barrett-Joyner-Halenda (BJH) pore size distribution results shown in **Appendix B Figure 3**. Such mesoporous nature is indeed beneficial for facile electrolyte penetration by offering efficient transport pathways to the interior voids of the electrocatalyst surface[221, 222]. The measured BET surface areas of the pure MnO_2 and $(Mn_{0.8}Ir_{0.2})O_2$ were ~ 3.72 m^2g^{-1} and ~ 3.70 m^2g^{-1}, respectively. These comparable BET surface area values suggest that the Ir incorporation has negligible effect on the BET surface area of MnO_2. However, $(Mn_{0.8}Ir_{0.2})O_2$:10F exhibited slightly lower BET surface area (~ 3.55 m^2g^{-1}) than that of MnO_2 and $(Mn_{0.8}Ir_{0.2})O_2$. Such decrease in surface area of fluorinated $(Mn_{0.8}Ir_{0.2})O_2$ can be attributed to the exothermic phenomenon of NH_4F (i.e. fluorine precursor) burning during the calcination of $(Mn_{0.8}Ir_{0.2})O_2$:10F NRs, which may lead to increase in the size of $(Mn_{0.8}Ir_{0.2})O_2$:10F NRs, causing reduction in the BET surface area. Similar behavior regarding the decrease in BET surface area with incorporation of F has been observed in the various reported studies[137]. The as-synthesized IrO_2 exhibited significantly higher BET surface area of ~189 m^2g^{-1}, comparable to the earlier report [137].

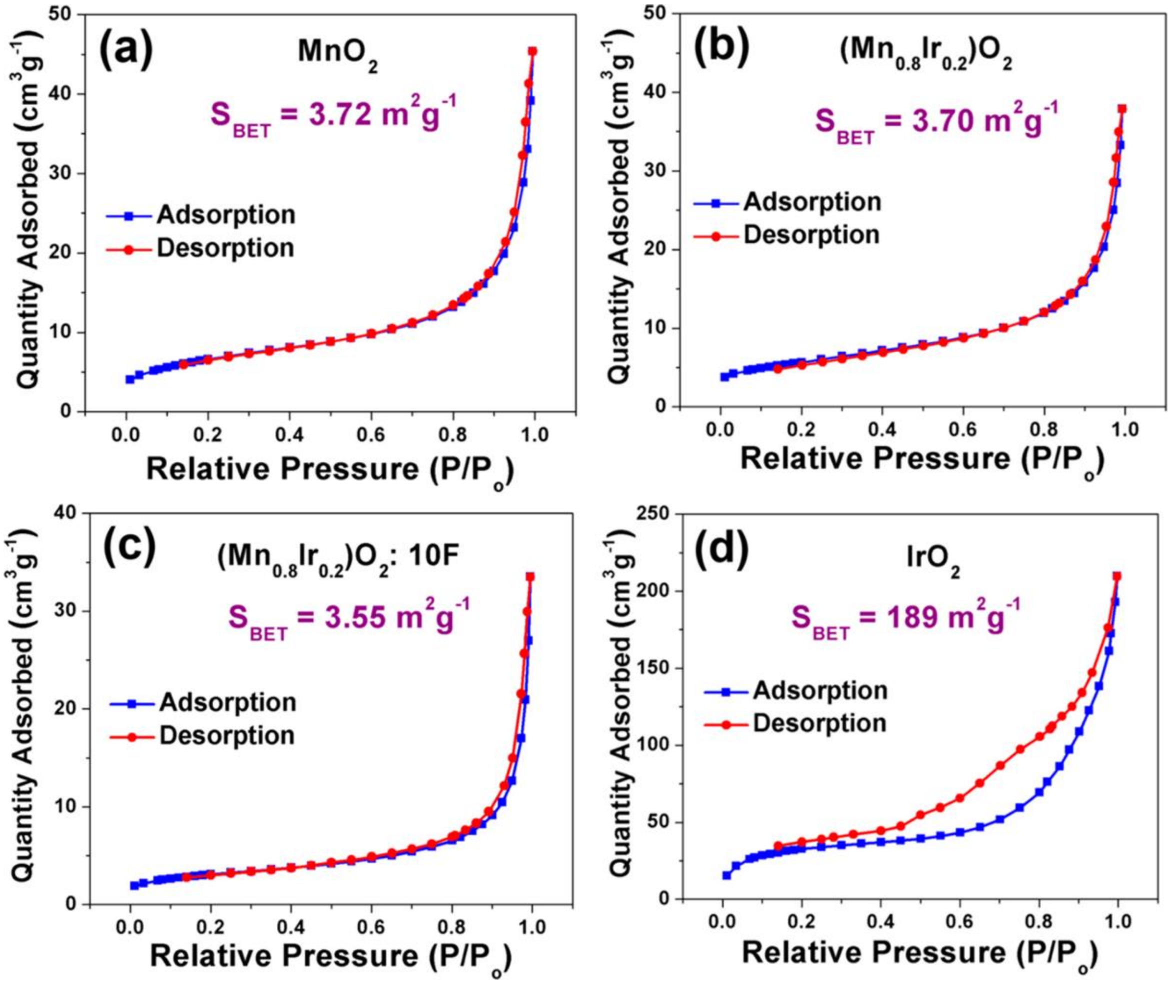

Figure 6-3 N_2 adsorption–desorption isotherms of the as-synthesized (a) MnO_2, (b) $(Mn_{0.8}Ir_{0.2})O_2$ and (c) $(Mn_{0.8}Ir_{0.2})O_2$:10F and (d) IrO_2

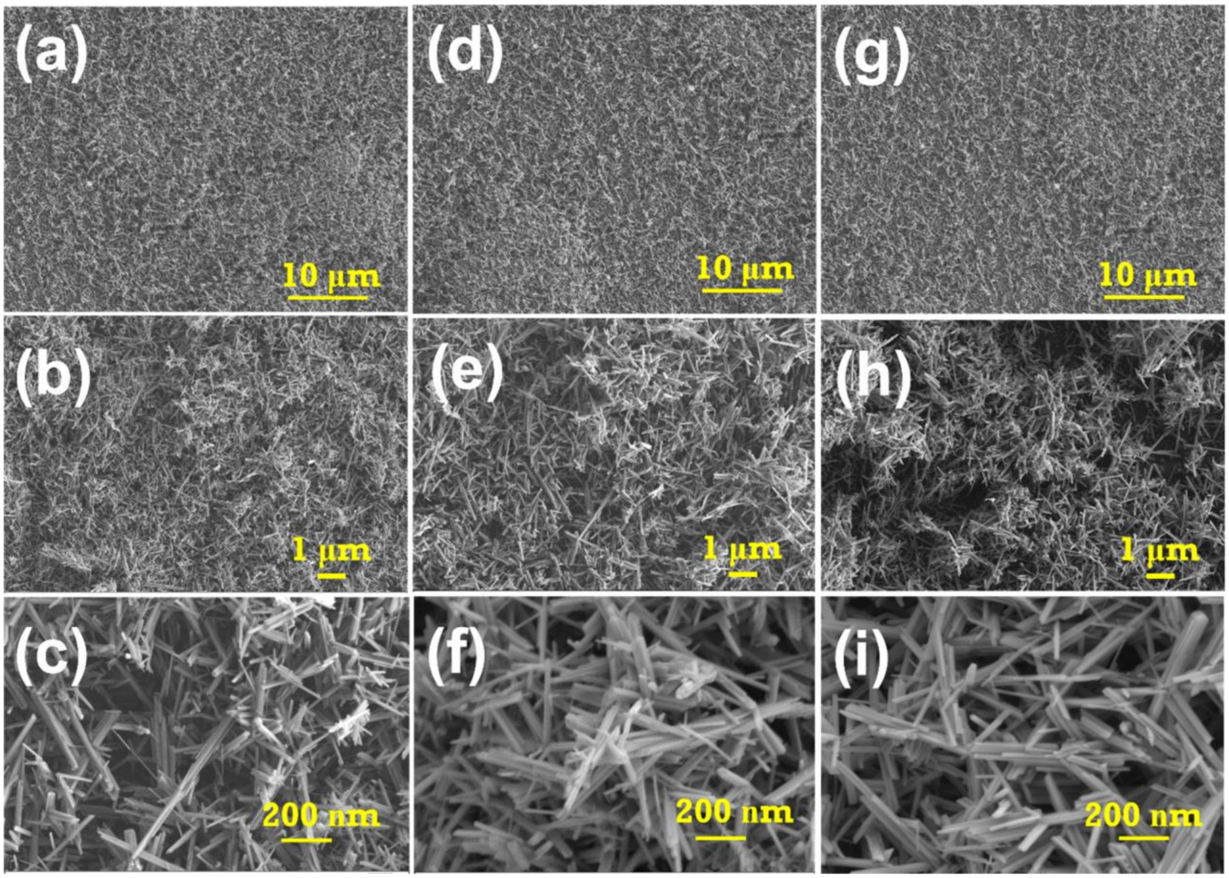

Figure 6-4 (a) SEM micrographs of the as-synthesized (a-c) MnO_2, (d-f) $(Mn_{0.8}Ir_{0.2})O_2$, and (g-i) $(Mn_{0.8}Ir_{0.2})O_2$:10F NRs

Figure 6-4 depicts the scanning electron microscope (SEM) images of as-synthesized α-MnO_2, $(Mn_{0.8}Ir_{0.2})O_2$, $(Mn_{0.8}Ir_{0.2})O_2$:10F electrocatalyst powders. As shown in **Figure 6-4 a-c**, the as-synthesized MnO_2 possesses highly dense, well-spaced and randomly aligned uniform one-dimensional (1D) rod shape morphology. The 1D MnO_2 rods exhibited diameter of ~ 40-50 nm and length ranging from ~0.5 to 3µm throughout the catalyst material, clearly indicating the attainment of high aspect ratios (L/D) for as-synthesized nanorods (NRs). Further, as can be seen from SEM micrograph of $(Mn_{0.8}Ir_{0.2})O_2$ and $(Mn_{0.8}Ir_{0.2})O_2$:10F demonstrate similar nanorod motifs with nanoscale diameter (~ 40-50 nm) and diverse lengths. In addition, $(Mn_{0.8}Ir_{0.2})O_2$ and $(Mn_{0.8}Ir_{0.2})O_2$:10F electrocatalysts show the similar well-spaced nanorods structure which is beneficial for the rapid release of oxygen bubbles during the OER process.[187] These SEM results evidently suggest that the nanorod architecture of pure MnO_2 is well preserved after incorporation of Ir and F and forming the homogeneous solid solution with MnO_2 during the calcination process. Furthermore, the energy dispersed X-ray spectroscopy (EDX) elemental mapping images of $(Mn_{0.8}Ir_{0.2})O_2$:10F confirm the homogeneous distribution of elements within as-synthesized nanorods, suggesting the formation of a highly pure solid solution, without any undesired impurity from the precursors as well as segregation of the species at any specific region. In addition, the quantitative elemental analysis derived from the EDX spectrum of $(Mn_{0.8}Ir_{0.2})O_2$:10F indicated the atomic ratio of Mn and Ir as 80.24 : 19.76, which is in a good agreement with the ICP-OES results as well as the selected nominal composition (Mn:Ir = 80:20). In addition, the EDX elemental mapping images and EDX spectrum of IrO_2 also demonstrate the uniform dispersion of elements within the as-synthesized catalyst particles.

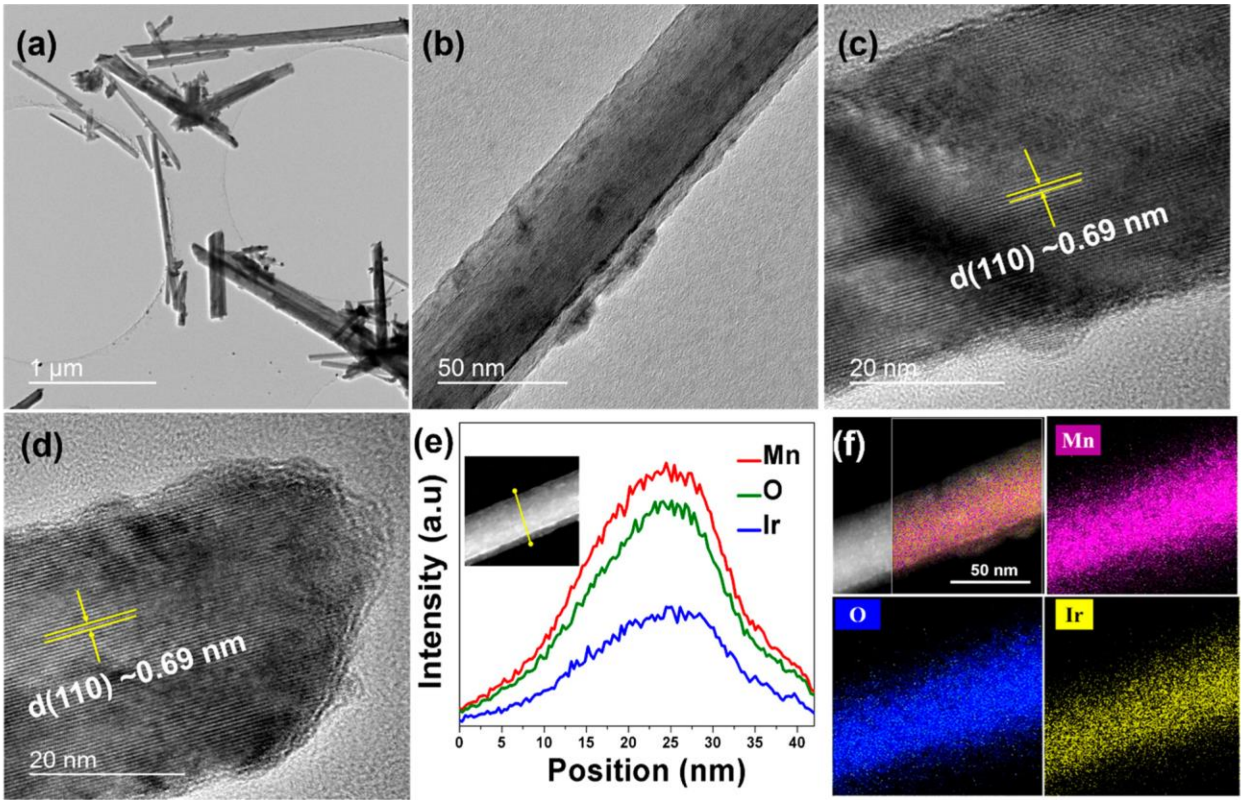

Figure 6-5 (a-b) TEM images of as-synthesized $(Mn_{0.8}Ir_{0.2})O_2$:10F NRs, (c-d) HRTEM images of a representative $(Mn_{0.8}Ir_{0.2})O_2$:10F NR, highlighting lattice fringe of ~ 0.69 nm that corresponds to the (110) plane, (e) line scan analysis across a representative $(Mn_{0.8}Ir_{0.2})O_2$:10F NR and (f) EDX elemental mapping of Mn, O and Ir of the $(Mn_{0.8}Ir_{0.2})O_2$:10F NR

The morphology of the $(Mn_{0.8}Ir_{0.2})O_2$:10F NRs was further examined by transmission electron microscopy (TEM). As can be seen from **Figure 6-5 a-b (**$(Mn_{0.8}Ir_{0.2})O_2$:10F electrocatalyst dispersed on the TEM grid demonstrated the typical rod shape morphology with a diameter of ~ 40 nm. The high-resolution transition electron microscopy (HRTEM) images of $(Mn_{0.8}Ir_{0.2})O_2$:10F NR, show the distinguishable and well-resolved uniform lattice fringe space of ~0.6954 nm, corresponding to the (110) crystallographic planes of $(Mn_{0.8}Ir_{0.2})O_2$:10F. In addition, from the

HRTEM image of MnO_2, the lattice fringe space corresponding to the (110) crystallographic plane of α-MnO_2 was obtained as ~0.6890 nm, which is indeed in good agreement with that of the XRD results. The larger lattice fringe of $(Mn_{0.8}Ir_{0.2})O_2$:10F (~0.6954 nm) as compared to that of α-MnO_2 (~0.6890 nm)[205] evidently shows the lattice expansion due to Ir incorporation into the MnO_2 crystalline lattice. As already discussed in XRD results, this lattice expansion can be attributed to the difference in ionic radii between the host element (Mn^{+4} = 0.54 Å)[219] and the dopant solute ion (Ir^{+4} = 0.62 Å) [220]. Furthermore, the line scan analysis on the $(Mn_{0.8}Ir_{0.2})O_2$:10F NR, was undertaken to confirm the homogenous dispersion of Mn and Ir within the as-synthesized $(Mn_{0.8}Ir_{0.2})O_2$:10F NR. In addition, **Figure 6-5 (f)** illustrates the EDX elemental mapping images of Mn, Ir and O for the $(Mn_{0.8}Ir_{0.2})O_2$:10F NR, suggesting the uniform spatial distribution of these elements over the examined surface of $(Mn_{0.8}Ir_{0.2})O_2$:10F NR; lacking any segregation of elements at any specific site. Thus, in addition to XRD results, together these EDX and line scan analysis results justified the formation of a single phase homogeneous solid solution of MnO_2 and IrO_2 [i.e. $(Mn,Ir)O_2$:F]. Moreover, the EDX elemental analysis conducted on the $(Mn_{0.8}Ir_{0.2})O_2$:10F NR is in a good agreement with the particular nominal composition of Mn and Ir.

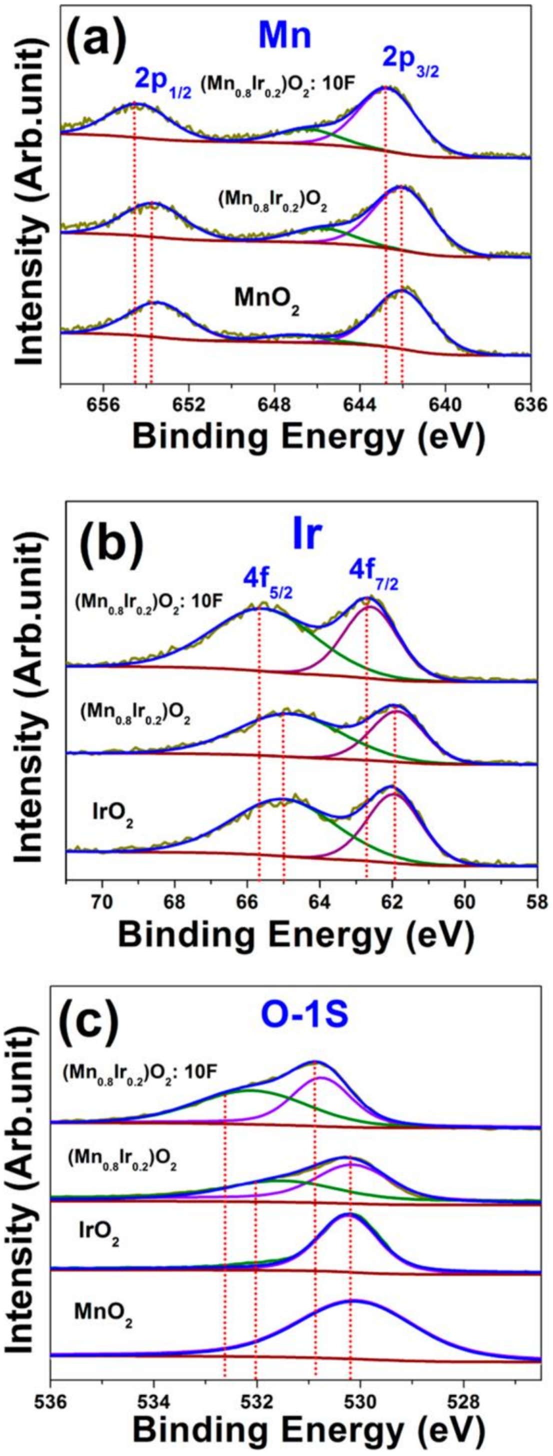

Figure 6-6 XPS spectra of (a) Mn 2p, (b) Ir 4f and (c) O1s for the as-synthesized electrocatalysts

The chemical valence states of Mn, Ir and O in the as-synthesized MnO_2, $(Mn_{0.8}Ir_{0.2})O_2$, $(Mn_{0.8}Ir_{0.2})O_2$:10F electrocatalysts were investigated by employing the X-ray photoelectron spectroscopy (XPS). **Figure 6-6** displays the XPS spectra of Mn, Ir and O for MnO_2, $(Mn_{0.8}Ir_{0.2})O_2$, $(Mn_{0.8}Ir_{0.2})O_2$:10F NRs, respectively. The XPS spectrum of Mn 2p (Figure 6a) of the as-prepared α-MnO_2 reveals the two peaks located at binding energy values of ~642 eV and ~ 653.8 eV which are attributed to the Mn $2p_{3/2}$ and Mn $2p_{1/2}$ doublet, respectively, with a spin-energy separation of 11.8 eV (similar to earlier reports).[70, 223] As can be seen from the Figure 6a, in the XPS spectrum of Mn 2p, an additional peak was observed at ~646 eV, similar to previous XPS reports of Mn which can be considered as a shake-up or satellite peak.[131, 224] The XPS spectrum of $(Mn_{0.8}Ir_{0.2})O_2$ exhibited the presence of Mn $2p_{3/2}$ and Mn $2p_{1/2}$ doublet with the binding energy values comparable to that of pure MnO_2. However, it is interesting to note that the peak positions of Mn $2p_{3/2}$ and Mn $2p_{1/2}$ doublet of $(Mn_{0.8}Ir_{0.2})O_2$:10F exhibited significant positive shift of ~ 0.7 to 0.9 eV towards higher binding energy as compared to that of pure MnO_2 and $(Mn_{0.8}Ir_{0.2})O_2$, which is consistent with the previously reported XPS results of F doped solid solution electrocatalysts systems .[35, 70, 97] This positive shift in binding energy indicates the beneficial binding of F in the $(Mn_{0.8}Ir_{0.2})O_2$:10F NRs, which is attributable to the modification of the electronic structure (details are in the Computational results section 3.3) of $(Mn_{0.8}Ir_{0.2})O_2$:10F as a result of the solid solution formation and incorporation of F, leading to stronger binding due to the higher electronegativity of F[70]. Furthermore, the Mn:Ir ratio in the XPS analysis of of $(Mn_{0.8}Ir_{0.2})O_2$:10F was obtained as 80.17: 19.83 which is in a good agreement with the nominal composition as well as EDX results, suggesting the presence of Mn and Ir in a nominal composition ratio (80:20) on the surface as well as in the bulk of the as-synthesized $(Mn_{0.8}Ir_{0.2})O_2$:10F NRs and thus, negates the possibility of only surface modification of MnO_2 NRs or Ir richness at the surface of MnO_2 NRs due to Ir incorporation. It should be noted that, following the comprehensive XPS studies by Schlogl and Morgan group in the literature[184, 225, 226], the XPS plot details of binding energies (eV), full width at half maximum (FWHM) and spin-energy separation (ΔS) are provided in Appendix B Table 3Table S3.

Figure 6-6 (b) shows the high-resolution XPS spectra of Ir for IrO_2, $(Mn_{0.8}Ir_{0.2})O_2$, $(Mn_{0.8}Ir_{0.2})O_2$:10F electrocatalysts, respectively. XPS spectrum of Ir in IrO_2 and $(Mn_{0.8}Ir_{0.2})O_2$ displays the presence of Ir $4f_{7/2}$ and Ir $4f_{5/2}$ doublet corresponding to the binding energy of ~61.8 eV and 64.9 eV, respectively [70, 227]. In the case of $(Mn_{0.8}Ir_{0.2})O_2$:10F, similar behavior of positive shift (~0.8 eV) in binding energy values for the Ir 4f doublet positions was witnessed, which can be again ascribed to the modification of the electronic structure of $(Mn_{0.8}Ir_{0.2})O_2$:10F upon F substituted solid solution formation. It is also noteworthy to mention that in the present XPS study, the Ir $4f_{7/2}$: Ir $4f_{5/2}$ intensity ratios (for symmetrical peak shapes) were obtained in the range of ~ 1.22:1 to ~1.26:1 which is in rational agreement with the theoretical value of 1.33:1[225]. Furthermore, the spin orbit splitting of Ir 4f $_{5/2}$ and Ir 4f $_{7/2}$ was obtained as ~ 3.1, which is again in very good agreement with the (symmetrical or asymmetrical) peak separation constraint of 3 eV, as witnessed in the various published XPS reports[225, 228]. In addition, the fitting of the Ir 4f components with the unusual asymmetric core-electron line shapes in the metallic oxide-IrO_2 is well-documented in the literature. However, in the literature, there are also Ir-oxide based electrocatalyst systems such as pure IrO_x[229] as well as doped-IrO_x (IrNi@IrO_x)[230] wherein the less asymmetric or lack of asymmetric nature has been evidently witnessed, similar to the presently observed Ir 4f results. According to Strasser and co-workers[230], the pronounced symmetric nature in these components can be attributed to the formation of surface hydroxide or potentially numerous defects during electrocatalysts synthesis.

Next, as shown in **Figure 6-6 (c)**, a dominant peak for O 1s at the binding energy of ~ 530.1 eV was observed for MnO_2 and IrO_2, which corresponded to the metal-oxygen bond.[227] Similarly, the deconvoluted O1s spectra of $(Mn_{0.8}Ir_{0.2})O_2$ and $(Mn_{0.8}Ir_{0.2})O_2$:10F also exhibited a dominant peak at ~ 530.1 eV and ~ 530.8 eV, respectively. Herein, as can be seen from deconvoluted O1s spectra of $(Mn_{0.8}Ir_{0.2})O_2$ and $(Mn_{0.8}Ir_{0.2})O_2$:10F, a shoulder peak centered at ~ 531.8 eV to 532.3 eV, respectively was detected. As reported in various studies, this shoulder peak at the higher binding energy is attributed to the high binding energy component (HBEC) developed due to an oxygen deficiencies or vacancies within the solid solution framework[231-233]. Herein, a similar positive shift in binding energy value for O 1s was observed for F containing $(Mn_{0.8}Ir_{0.2})O_{2,}$ clearly indicating the beneficial effect of the F substitution. However, the presence of F could not be unequivocally determined by XPS and EDX analysis which is similar to the various F doped solid solution electrocatalyst systems reported in previous studies[35, 70, 97]. Nonetheless, as elucidated in above XPS discussions, the positive shifts in the binding energy values for Mn 2p, Ir 4f and O1S, indicates the attainment of stronger binding due to the higher electro-negativity of fluorine incorporated into the solid solution electrocatalyst lattice. This result is in a good agreement with the various XPS studies on the F doped SnO_2, MnO_2, Nb_2O_5, RuO_2, IrO_2 etc. as a solid solution electrocatalysts[70, 94, 98]. In light of this XPS discussion of F, various researchers (Shaltout et al.[234], Amanullah et al.[235], Datta et al.[97]) have postulated that low concentration of F (or fluorine content is lower than the detection limit of XPS [234, 235]) in the as-synthesized material can be attributed to show the absence of F 1s peak. Similar experimental observations and difficulties for detecting fluorine either by XPS techniques or Auger electron spectroscopy (AES) have been mentioned by other researchers[234, 236]. Nonetheless, in the study conducted by Sun et al.[237], the presence of F 1s XPS spectrum has been detected at the higher (18 wt.%) F content in the carbon black. In any event, the presence of F in the as-synthesized $(Mn_{0.8}Ir_{0.2})O_2$:10F NRs has been detected by solid state NMR spectroscopy (see **Appendix B Figure 5**).

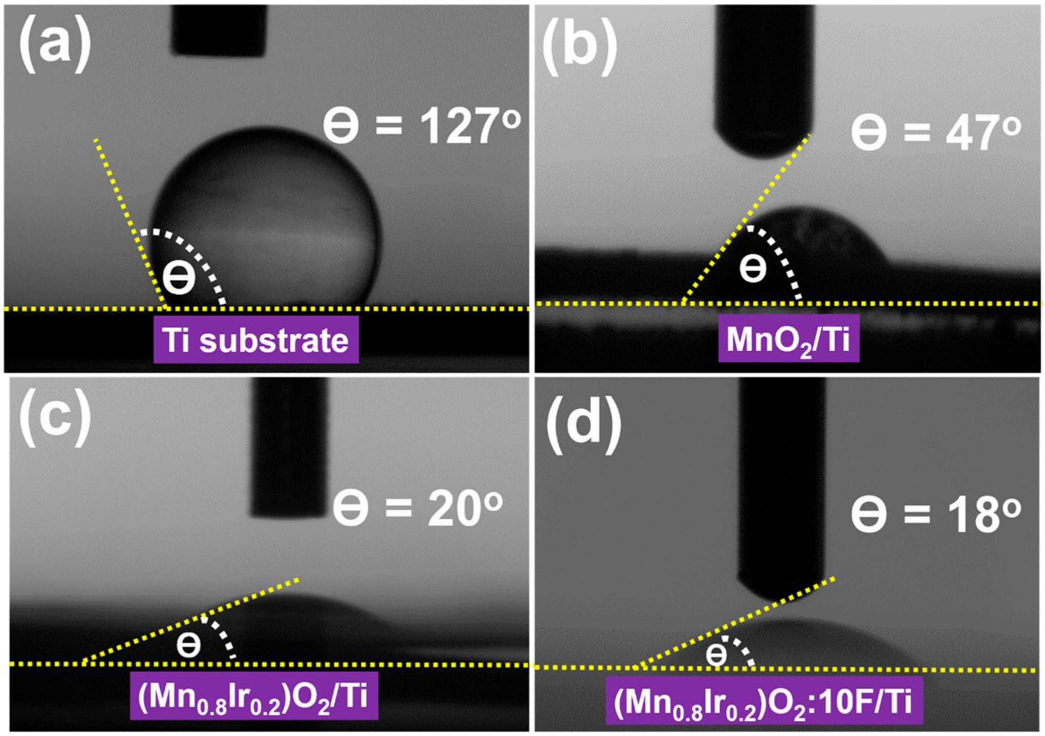

Figure 6-7 Contact angle images of (a) bare Ti substrate, (b) MnO_2, (c) $(Mn_{0.8}Ir_{0.2})O_2$ and (d) $(Mn_{0.8}Ir_{0.2})O_2$:10F NRs obtained from the droplet experiments

Further, the static contact angle method by using a water droplet (10 μL) was employed to investigate the wetting characteristics of the as-synthesized electrocatalyst nanorods deposited on the Ti substrate (current collector) and shown in Figure 6-7. In the absence of any electrocatalyst coating, the bare Ti foil exhibited an average water contact angle of ~ 127±1.07° (which is in a good agreement with the water contact angle measurements reported for Ti/Titania foils[238]) suggesting the highly hydrophobic nature for the aqueous electrolyte. In contrast, MnO_2 NRs coated on the Ti foil (MnO_2/Ti) exhibited good hydrophilic nature with significantly lower average water contact angle of ~ 47 ± 0.67^o; reflecting close agreement with the previously reported values[239]. This hydrophilic behavior can be attributed to various factors such as hydroxyl (OH^-) group interaction of Mn atoms with the constitutional water within the as-synthesized MnO_2 powder[239-241]. Also, the meso-porous nature of the as-synthesized MnO_2 is indeed beneficial for the electrode-electrolyte interaction which certainly improves the wettability of the electrode surface. In addition, the hydrophilic domain containing $-SO_3^-$ group in Nafion (used as a binder to prepare the catalyst ink) is also well known for its efficient water adsorption properties and can be another possible contributor to enhancing the wetting characteristics of the surface of the MnO_2 electrode[242-244]. The contact angle value of MnO_2 ($\sim47^o$) was noticeably influenced when the $(Mn_{0.8}Ir_{0.2})O_2$ and $(Mn_{0.8}Ir_{0.2})O_2$: 10F electrocatalysts were coated on the Ti foil. Interestingly, $(Mn_{0.8}Ir_{0.2})O_2$ and $(Mn_{0.8}Ir_{0.2})O_2$: 10F coating on Ti foil exhibited the significantly reduced average contact angle of ~ 20 ± 0.82^o and 18 ± 0.54^o, respectively, indicating their excellent hydrophilic nature. These decreased contact angle values evidently suggest that the nanorods of $(Mn_{0.8}Ir_{0.2})O_2$ and $(Mn_{0.8}Ir_{0.2})O_2$: 10F solid solution electrocatalysts possess higher roughness than that of bare Ti substrate and MnO_2 NRs, which predominantly offers a favorable structure for facile intercalation of aqueous electrolyte on the electrode surface[245]. The improved wettability of $(Mn_{0.8}Ir_{0.2})O_2$ and $(Mn_{0.8}Ir_{0.2})O_2$: 10F electrode would ensure the fast electrolyte penetration and accelerate oxygen release thus, offering enhancement in the OER kinetics.

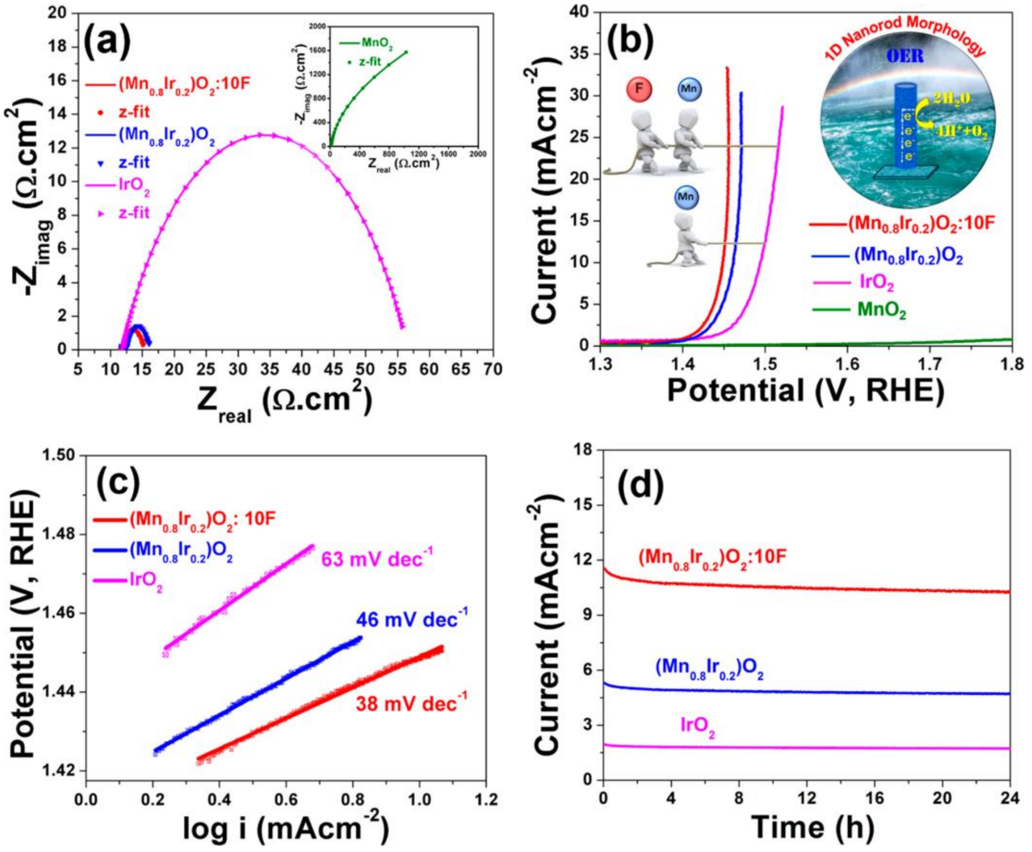

Figure 6-8 Comparison of electrochemical performances of the as-synthesized MnO_2, $(Mn_{0.8}Ir_{0.2})O_2$, $(Mn_{0.8}Ir_{0.2})O_2$:10F NRs and the standard IrO_2 measured in a 1 N H_2SO_4 electrolyte at 40 °C (a) EIS plots performed at ~1.45 V (*vs* RHE), (b) OER polarization (mAcm$^{-2}{}_{geo}$ vs. potential) curves with a scan rate of 10 mV s^{-1}, (c) Tafel plots of as-synthesized IrO_2, $(Mn_{0.8}Ir_{0.2})O_2$ and $(Mn_{0.8}Ir_{0.2})O_2$:10F NRs and (d) Chronoamperometry (CA) tests conducted in 1N H_2SO_4 solution under a constant potential of ~1.45 V (*vs* RHE) at 40ºC for 24 h

6.5.2 Electrochemical Characterization of Electrocatalysts

The electrochemical impedance spectroscopy (EIS) analysis was carried for the as-synthesized MnO_2, $(Mn_{0.8}Ir_{0.2})O_2$, $(Mn_{0.8}Ir_{0.2})O_2$:10F and IrO_2 electrocatalysts to investigate the charge transportation feasibility on the as-prepared electrode surface. **Figure 6-8 (a)** shows the EIS plots of $(Mn_{0.8}Ir_{0.2})O_2$, $(Mn_{0.8}Ir_{0.2})O_2$:10F and IrO_2 (inset: EIS of MnO_2), obtained at ~1.45V (*vs* RHE) in the electrolyte solution of 1N H_2SO_4 at 40°C. Herein, as discussed in the experimental section, the semicircles in the Nyquist are plots of $(Mn_{0.8}Ir_{0.2})O_2$ and $(Mn_{0.8}Ir_{0.2})O_2$:10F are fitted with the $R_s(R_eQ_1)(R_{ct}Q_{dl})$ as an equivalent circuit model. The surface charge transfer resistance (R_{ct}), obtained from the diameter of the semi-circle in the low frequency region of the EIS [using $R_s(R_{ct}Q_{dl})$ circuit model] plot of IrO_2 was obtained as ~41Ω cm^2 while the solution resistance (R_s) was obtained as ~ 12 Ω cm^2, comparable to the earlier report[137]. On the other hand, as-expected, MnO_2 NRs exhibited considerably higher R_{ct} (>2200 Ω cm^2), which clearly reflects the poor electronic conductivity and unfavorable electron transfer of MnO_2 NRs during the electrochemical catalytic processes[246].

It is very interesting to note that $(Mn_{0.8}Ir_{0.2})O_2$ exhibits an R_e of ~1.3 Ω cm^2 and R_{ct} of ~ 3.8 Ω cm^2 - significantly lower than that of as-synthesized pure IrO_2 as well as MnO_2 **(Table 6-2)**. This result suggests the attainment of lower activation polarization and higher electronic conductivity after introduction of minimal Ir content (20 at. %) into the parent MnO_2 framework. Similar results regarding reduction in the R_{ct} values of MnO_2 upon minimum Ir incorporation have been witnessed in the study conducted by Ye et al.[212] Additionally, as anticipated, the R_{ct} of $(Mn_{0.8}Ir_{0.2})O_2$ NRs was significantly further reduced after incorporation of 10 wt. % F [$(Mn_{0.8}Ir_{0.2})O_2$:10F NRs, R_{ct}~ 2.5 Ω cm^2, R_e ~0.7 Ω cm^2). Such considerable reduction in R_{ct} upon F doping evidently suggests the enhancement in the electronic conductivity and thus, $(Mn_{0.8}Ir_{0.2})O_2$

:10F is expected to have superior OER kinetics and electrochemical activity as compared to pure IrO_2, MnO_2 NRs as well as $(Mn_{0.8}Ir_{0.2})O_2$ NRs.

Table 6-2 Results of electrochemical characterization for OER of as-synthesized electrocatalysts, performed in 1N H_2SO_4 electrolyte solution at 40°C

Electrocatalyst Composition	**Onset potential V (*vs* RHE)**	**Charge transfer resistance (R_{ct}, Ω.cm^2)**	**Current density at ~1.45 V (mAcm$^{-2}_{geo}$)**	**Overpotential (η in mV) at 10 mAcm^{-2}**	**Tafel slope (mV dec^{-1})**	**Mass activity at ~1.45 V (Ag^{-1})**	**ECSA (m^{2}g^{-1})**	**TOF at ~ 1.45 V (s^{-1})**
$(Mn_{0.8}Ir_{0.2})O_2$ NRs	~1.35	~3.8	~5.5	~240	46	~18.34	~419.04	~0.0054
$(Mn_{0.8}Ir_{0.2})O_2$:10F NRs	~1.35	~2.5	~12	~200	38	~40	~704.76	~0.010
IrO_2	~1.43	~41	~2	~280	63	~6.67	~214.28	~0.0038
MnO_2 NRs	~1.8	~2300	~0	--	300	--	--	--

These results are in an excellent agreement with the results of the theoretical studies discussed in the later section. Interestingly, it is also noteworthy that the R_{ct} of as-synthesized 1D $(Mn_{0.8}Ir_{0.2})O_2$:10F NRs is ~ 1.6 fold lower than that of our previously reported $(Mn_{0.8}Ir_{0.2})O_2$:10F 2D thin film electrocatalyst (R_{ct}~ 4 Ω cm^2)[70]. This reduction in R_{ct} value is indeed contributed by the improved electronic charge transport i.e. highly efficient facile charge (electron) transport pathways created on the entire $(Mn_{0.8}Ir_{0.2})O_2$:10F 1D nanorod electrode by virtue of the nanorod morphology as well as between the electrocatalyst surface and the current collector (Ti substrate). Therefore, these experimental results collectively suggest that due to tailoring the material's dimension (i.e. from 2D to 1D), the OER kinetics of $(Mn_{0.8}Ir_{0.2})O_2$:10F electrocatalyst system was remarkably enhanced. Additionally, it is noteworthy to mention that the beneficial influence of F incorporation on reducing R_{ct} values has also been demonstrated in the EIS results of fluorinated IrO_2 and MnO_2, wherein IrO_2:10F (~37 Ω cm^2) and MnO_2:10F (~2100 Ω cm^2) exhibited lower R_{ct} than that of pristine IrO_2 and MnO_2, respectively.

We next investigated the electrocatalytic OER activity of MnO_2, $(Mn_{0.8}Ir_{0.2})O_2$ and $(Mn_{0.8}Ir_{0.2})O_2$:10F electrocatalysts supported on Ti substrate in 1N H_2SO_4 at 40^oC, and compared the performance with IrO_2. **Figure 6-8 (b)** depicts the iR_Ω corrected linear sweep voltammetry (LSV) curves for the as-prepared electrodes. The polarization curve of $(Mn_{0.8}Ir_{0.2})O_2$ NRs and $(Mn_{0.8}Ir_{0.2})O_2$:10F NRs show the onset potential of ~1.35 V w.r.t. RHE (reversible hydrogen electrode), which is similar to that of the $(Mn_{0.8}Ir_{0.2})O_2$ 2D thin film system as reported earlier[70]. This onset potential is considerably lower (~ 80 mV) than that of IrO_2 (~1.43 V, vs. RHE), similar to earlier reports[97, 137]. On the other hand, MnO_2 NRs demonstrated extremely poor OER electrocatalytic activity with no sharp increase in current density . Furthermore, to compare the apparent OER activity of these electrodes, current density was measured at ~1.45 V *vs* RHE (typical potential considered to evaluate electrocatalytic performance of the electrocatalysts). As can be seen from **Figure 6-8 (b)**, $(Mn_{0.8}Ir_{0.2})O_2$:10F NRs exhibit excellent geometric current density of ~ 12 mA cm^{-2}_{geo}, which is ~600%, ~218% , ~ 220% and ~923% higher than that of the in-house synthesized IrO_2 (~2 mA cm^{-2}_{geo}), $(Mn_{0.8}Ir_{0.2})O_2$ NRs (~5.5 mA cm^{-2}_{geo}), and previously reported 2D thin film architecture of $(Mn_{0.8}Ir_{0.2})O_2$:10F (~5.45 mA cm^{-2}_{geo})[70] and recently reported

$K_{1.65}(Mn_{0.78}Ir_{0.22})_8O_{16}$ (~1.3 mA cm^{-2}_{geo}), respectively[209]. This remarkable increase in the current density of $(Mn_{0.8}Ir_{0.2})O_2$:10F NRs is indeed credited to the enhanced charge transfer (i.e. lower R_{ct}) and formation of unique electronic structure of F incorporated $(Mn_{0.8}Ir_{0.2})O_2$:10F NRs, as investigated by our theoretical calculations. However, as expected, MnO_2 NRs exhibited negligible OER activity (~ 0 $mAcm^{-2}_{geo}$) in acid assisted water electrolysis[125, 127]. This insignificant OER activity is emerged from significantly higher charge transfer resistance of MnO_2 NRs, indicating its poor electronic conductivity/kinetics towards acidic OER. In addition, it can be seen from **Table 6-2** that, $(Mn_{0.8}Ir_{0.2})O_2$:10F NRs delivered the benchmark current density of 10 mA cm^{-2} and 20 mA cm^{-2} at an overpotential of ~ 200 mV and ~238 mV (w.r.t. the equilibrium OER potential, 1.23 V *vs* RHE), respectively, clearly outperforming the IrO_2, $(Mn_{0.8}Ir_{0.2})O_2$ NRs, and thin film of $(Mn_{0.8}Ir_{0.2})O_2$:10F[70] which required overpotential of ~ 280 mV, ~ 240 mV and 245 mV to reach the current density of 10 mA cm^{-2}. Furthermore, in accordance with the EIS results, F incorporated IrO_2:10F [**Appendix B Figure 6 (d)**] and MnO_2:10F [**Appendix B Figure 6 (e)**] displayed higher OER catalytic activity which evidently suggests the beneficial impact of F on the current density. Herein, it is worth mentioning that our as-prepared 1D $(Mn_{0.8}Ir_{0.2})O_2$:10F NRs demonstrated substantially lower over-potential (~200 mV) as compared to various other reported electrocatalysts for acidic OER including the recently reported Ir doped cryptomelane-type manganese oxide $[K_{1.65}(Mn_{0.78}Ir_{0.22})_8O_{16}]$[209] (~340 mV), illustrating the superior electrocatalytic performance of $(Mn_{0.8}Ir_{0.2})O_2$:10F NRs towards water splitting. Thus, the improved OER activity of $(Mn,Ir)O_2$ system evidently stems from synergistic effect of IrO_2 and α/β-MnO_2. The obtained results are indeed in a good agreement with the earlier work on Ir-Mn oxide film system for acidic OER, wherein mixed IrO_2(x) + MnO_2(1-x) revealed electrocatalytic performance superior to the pristine rutile IrO_2 and β-MnO_2.[212] Furthermore, it is noteworthy to point out that our previously reported 2D thin film of $(Mn_{0.8}Ir_{0.2})O_2$:10F was directly fabricated on the Ti substrate (i.e. without utilizing Nafion binder), whereas in the current work, Nafion 117 (5 wt.% solution in lower aliphatic alcohols) binder was used for the preparation of electrocatalyst inks. Therefore, the contribution of Nafion in the electrochemical activity needs to be verified and discussed. Accordingly, we prepared Nafion containing electrodes (mass loading ~0.3 $mgcm^{-2}$) and the electrochemical characterizations (impedance and polarization) were performed under similar OER conditions as that of other as-synthesized electrocatalyst materials studied in the current work. It can be clearly seen from **Appendix B Figure 6 (f-g)** that Nafion coated working electrode possess negligible catalytic activity for acidic OER, which is ably complemented by its very high charge transfer resistance (>5000 Ω cm^2), evidently suggesting its negligible OER performance. Thus, these results markedly indicate the insignificant contribution of Nafion towards reduction in the R_{ct} of 1D $(Mn_{0.8}Ir_{0.2})O_2$:10F as well as in the OER electrochemical activity.

Herein, although 1D $(Mn_{0.8}Ir_{0.2})O_2$:10F NRs demonstrate electrocatalytic activity superior to other as-synthesized electrocatalysts, evaluation of the intrinsic OER activity of these catalyst materials is very essential to draw conclusions about the increased OER activity of $(Mn_{0.8}Ir_{0.2})O_2$:10F NRs as perceived from the polarization curves. Therefore, normalization of the current density by the BET surface area, calculation of the electrochemical active surface area (ECSA) and mass loading as well as calculations of the turnover frequency (TOF) have been carried out. The calculated corresponding mass activity, BET normalized current density ($mAcm^{-2}{}_{BET}$), ECSA normalized current density ($mAcm^{-2}{}_{ECSA}$) and TOF of $(Mn_{0.8}Ir_{0.2})O_2$:10F NRs was found to be ~ 40 Ag^{-1}, 1.126 $mAcm^{-2}{}_{BET}$, 5.6 $\mu Fcm^{-2}{}_{ECSA}$and 0.01 s^{-1}, respectively at an overpotential of 220 mV. All these values are expressively higher than that of IrO_2, $(Mn_{0.8}Ir_{0.2})O_2$ NRs and previously reported $(Mn_{0.8}Ir_{0.2})O_2$:10F thin film electrocatalyst, evidently revealing superior intrinsic OER electrocatalytic activity of $(Mn_{0.8}Ir_{0.2})O_2$:10F NRs. This excellent activity of $(Mn_{0.8}Ir_{0.2})O_2$:10F NRs is a characteristic indicator of the enhancement in the OER kinetics i.e. lower R_{ct} (i.e. efficient electron transport along the 1D NRs) as well as the beneficial electronic structure modification achieved upon F substituted solid solution formation which has been expertly supported by our DFT calculations. Next, the lower Tafel slope of $(Mn_{0.8}Ir_{0.2})O_2$:10F NRs (~38 mV dec^{-1}) as compared to that of $(Mn_{0.8}Ir_{0.2})O_2$(~46 $mVdec^{-1}$), IrO_2(~63 $mVdec^{-1}$)[165, 247, 248] and recently reported[209] $K_{1.65}(Mn_{0.78}Ir_{0.22})_8O_{16}$ (~76 mV dec^{-1}) suggests the favorable OER kinetics with faster electron transport and enhanced electrical conductivity/electrocatalytic activity. The significantly higher Tafel slope for MnO_2 (~300 mV dec^{-1}) indicates its inferior OER kinetics towards water splitting.

In addition to the excellent electrocatalytic activity, long term electrochemical stability is indeed an important criterion for the high performance OER electrocatalysts. Thus, to investigate the endurance of the as-synthesized electrocatalysts for OER in 1 N H_2SO_4 electrolyte media, chronoamperometry (CA) tests at the constant potential of 1.45 V (*vs.* RHE) in 1N H_2SO_4 at 40^oC for 24 h were carried out. As depicted in **Figure 6-8 (d),** the as-synthesized $(Mn_{0.8}Ir_{0.2})O_2$:10F electrocatalyst demonstrated excellent long-lasting durability over 24 h, comparable to that of $(Mn_{0.8}Ir_{0.2})O_2$ NRs, IrO_2 and thin film of $(Mn_{0.8}Ir_{0.2})O_2$:10F. Furthermore, to bolster these results of excellent electrochemical stability, we conducted elemental analyses using inductively coupled plasma - optical emission spectroscopy (ICP-OES) to determine the amount of Mn and/or Ir that might have leached out from the electrode surface into the electrolyte solution. The ICP-OES analysis revealed negligible dissolution of Mn and Ir from the as-prepared $(Mn_{0.8}Ir_{0.2})O_2$:10F, $(Mn_{0.8}Ir_{0.2})O_2$ and IrO_2 electrocatalysts suggesting the remarkable structural stability of these as-synthesized electrocatalysts. In addition, the ICP-OES analysis performed on the post stability electrodes showed the Mn:Ir ratio as 80.32:19.68 and 79.91:20.09 for $(Mn_{0.8}Ir_{0.2})O_2$:10F and $(Mn_{0.8}Ir_{0.2})O_2$, respectively, which is for are in a good agreement with the post stability EDX result. On the other hand, MnO_2 displayed extremely poor electrochemical OER stability with rapid drop in current density, similar to the earlier studies of MnO_2 as an OER electrocatalyst[125, 246]. Thus, it is interesting to note that the incorporation of reduced amounts of IrO_2 into the framework structure of MnO_2 along with incorporation of F significantly improved not only the OER kinetics but also enhanced the electrochemical stability of pure MnO_2 NRs, as clearly evidenced from the chronoamperometry results. The stabilizing effect of F on the transition metal oxide (TMO) based supports has been comprehensively investigated by various groups. For example, Geiger et al.[164], investigated the influence of various dopants (fluorine, indium, antimony) incorporated in transition metal oxides such as SnO_2. Based on the potential dependent dissolution rates of these oxides, Geiger et al. concluded that fluorine doped tin oxide (FTO) shows best OER stability in 0.1 M H_2SO_4 electrolyte with a stability window of FTO ranging from -0.34 V RHE $< E <$ 2.7 V RHE with no indication for any measurable dissolution for compositions between these limits, making fluorine a promising dopant for acidic OER among indium tin oxide (ITO) and antimony doped tin oxide (ATO) based supports. In addition, in the theoretical study conducted by Binninger et al.[181], it has been reported that oxygen anion-free salts containing anion species with a very high oxidation potential such as fluorides, chlorides, or sulfates are promising candidates for truly thermodynamically stable OER catalysts. Therefore, in the present study, F doping not only enhances the electronic conductivity of MnO_2 but is also beneficial for stabilizing the as-synthesized electrocatalysts for acidic OER.

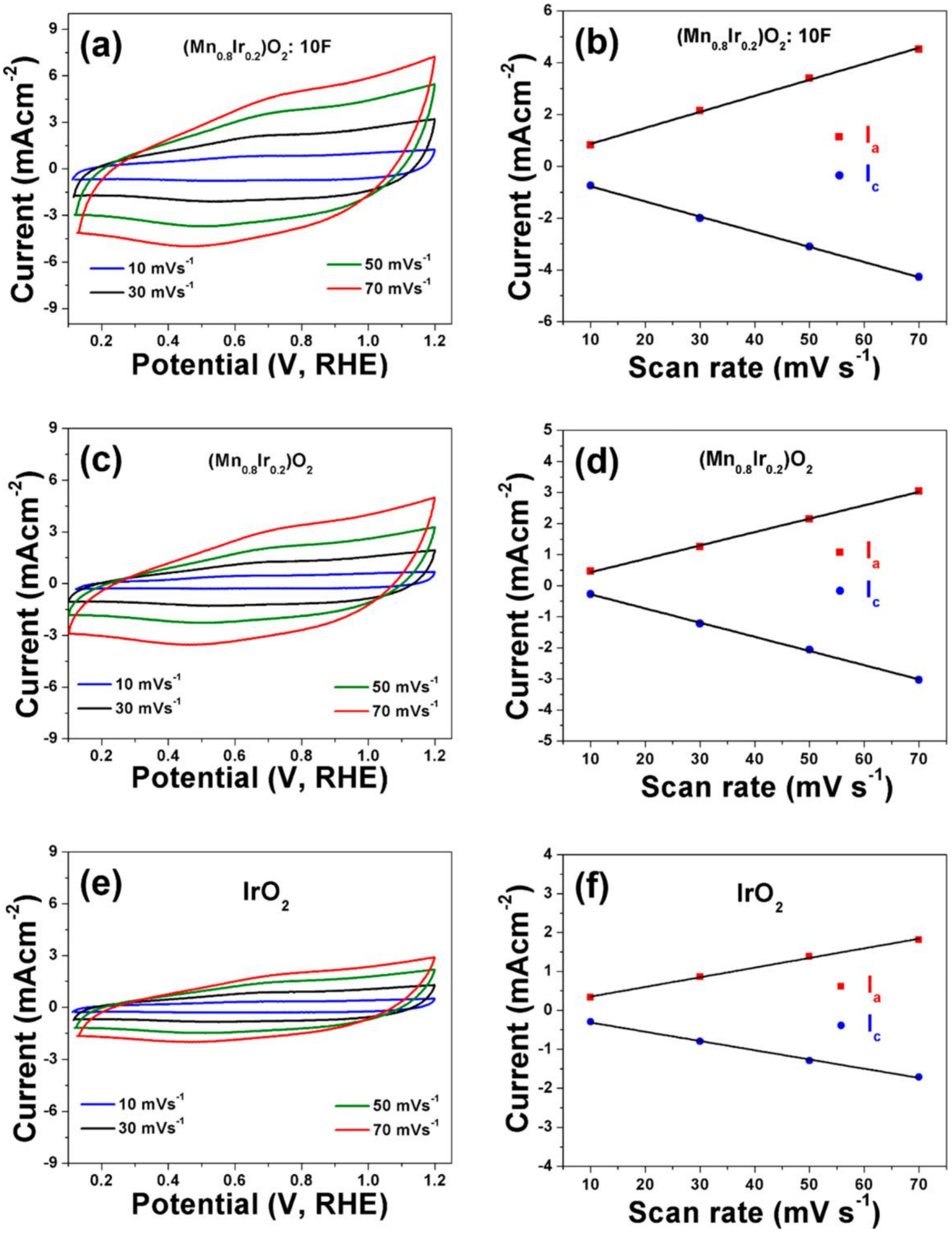

Figure 6-9 Cyclic voltammograms and the capacitive currents at 0.70 V *vs.* RHE with a scan rate of 10, 30, 50, and 70 mVs $^{-1}$ in 1N H_2SO_4 solution for as-synthesized (a-b) $(Mn_{0.8}Ir_{0.2})O_2$:10F NRs, (c-d) and $(Mn_{0.8}Ir_{0.2})O_2$ NRs and (e-f) IrO_2 electrocatalysts

Furthermore, we evaluated the electrochemically active surface area (ECSA) to gain deeper insights into OER electrocatalytic activity. Herein, in order to determine the ECSA of $(Mn_{0.8}Ir_{0.2})O_2$ NRs, $(Mn_{0.8}Ir_{0.2})O_2$:10F NRs and IrO_2 electrocatalysts, the electrical double-layer capacitance (EDLC) measurements were carried out in 1 N H_2SO_4 electrolyte at 40°C. **Figure 6-9 a, c and e** show the cyclic voltammogram (CV) curves recorded at various scan rates (10, 30, 50, and 70 mVs^{-1}). It can be clearly seen in **Figure 6-9 (b)** that, $(Mn_{0.8}Ir_{0.2})O_2$:10F NRs exhibited relatively higher anodic (j_a) and cathodic (j_c) current densities than those of $(Mn_{0.8}Ir_{0.2})O_2$ and IrO_2. Next, the double-layer capacitance (C_{dl}) was determined from the linear slope of the current density ($j_a - j_c$) *vs* scan rate (which is equivalent to twice the double layer capacitance, C_{dl}), following previous studies for ECSA calculations[161, 162]. The considerably higher C_{dl} (~74 mF cm^{-2}) of $(Mn_{0.8}Ir_{0.2})O_2$:10F NRs indicates that it possesses a higher catalytically active surface than $(Mn_{0.8}Ir_{0.2})O_2$ (~44 mF cm^{-2}) and IrO_2 (~22.5 mF cm^{-2}). Furthermore, the ECSA (m^2g^{-1}) of the as-synthesized electrocatalysts was obtained by dividing double capacitance (C_{dl}) by the specific capacitance (C^*) of electrocatalyst, similar to the previous reports of ECSA determination[249-251]. A general specific capacitance (C^*) of metal electrodes in acidic solutions is taken as 35 μF cm^{-2}.[91, 249, 252] Based on this specific capacitance (C^* ~35 μFcm^{-2}) value, ECSA of $(Mn_{0.8}Ir_{0.2})O_2$:10F NRs was obtained as ~704.76 $m^2\,g^{-1}$ which is remarkably higher than that of $(Mn_{0.8}Ir_{0.2})O_2$ NRs(~419.04 m^2g^{-1}), IrO_2 (~214.28 m^2g^{-1}) and Ir doped cryptomelane-type manganese oxide (~55 m^2g^{-1}) as reported in the recent study[209]. As elucidated in the introduction, owing to the large aspect ratio (L/D) and high density of active-sites, the 1D nanomaterials commonly exhibit superior electrochemically active surface area. For example, in the study conducted by Wang et al., 1D Pd/Pt NWs array demonstrated extremely high electrochemical active area of ~6791 $m^2\,g^{-1}$, which is ~ 51 fold higher than that of thin film architecture of Pt (~133 m^2 g^{-1}).[172] Such excellent electrochemically active surface area materials can show markedly improved electrocatalytic activity, offering efficient catalyst utilization for the electrochemical processes. [253] Furthermore, the higher roughness factor (RF) for $(Mn_{0.8}Ir_{0.2})O_2$:10F NRs (~2114.28) than that of $(Mn_{0.8}Ir_{0.2})O_2$ NRs (~1257.14) and IrO_2 (~642.85) clearly indicates the enhancement of the real electrochemical surface area in comparison with the geometric area of the electrode. Moreover, the above results are in an excellent agreement with the contact angle analysis wherein, $(Mn_{0.8}Ir_{0.2})O_2$:10F NRs (~2114.28) exhibited relatively lower water contact angle i.e. higher roughness factor. In addition, in the present study, ECSA has also been evaluated by utilizing the specific capacitance (C^*) of single crystal IrO_2 (~650 μFcm^{-2}) [187, 251]. Values obtained using the C^* for single crystal IrO_2 though lower nevertheless, still indicate that the F doped compositions of $(Mn_{0.8}Ir_{0.2})O_2$:10F reflect higher ECSA values compared to the un-doped $(Mn_{0.8}Ir_{0.2})O_2$ and IrO_2 in agreement with the arguments presented above.

It is noteworthy to mention that, although $(Mn_{0.8}Ir_{0.2})O_2$: 10F NRs exhibited lower BET specific area (~ 3.55 m^2g^{-1}) than that of $(Mn_{0.8}Ir_{0.2})O_2$ and IrO_2. The ECSA measurements revealed that, 1D $(Mn_{0.8}Ir_{0.2})O_2$:10F NRs possess intrinsically higher electrocatalytically ‘active’ surface area (~704.76 m^2g^{-1}), enabling more active sites to be exposed to the electrolyte, which in principle contributed to the enhanced OER kinetics. Such general discrepancy in area obtained by BET and ECSA is well elucidated in the recent study conducted by Jung et al.[91] According to this study, BET is an empirical technical to determine ‘total’ surface area which can over or under-estimate the catalytically ‘active’ surface area. Thus, it is recommended to normalize the current density by BET as well as ECSA which can essentially provide a conservative estimate of specific activity of the electrocatalysts. Thus, the obtained current densities from LSV curves were normalized to the

BET as well as ECSA area values. The 1D $(Mn_{0.8}Ir_{0.2})O_2$:10F NRs still demonstrated higher BET and ECSA specific activity as compared to that of $(Mn_{0.8}Ir_{0.2})O_2$ and IrO_2. This clearly accentuates the intrinsically superior OER electrocatalytic activity of 1D $(Mn_{0.8}Ir_{0.2})O_2$:10F NRs, proffered by the lower charge transfer resistance (i.e. lower activation polarization) and unique F containing solid solution formation as discussed in details in DFT results.

Finally, in order to investigate the structural stability and mechanical integrity of the high performance $(Mn_{0.8}Ir_{0.2})O_2$:10F NRs electrocatalyst after its rigorous OER stability test in harsh acidic medium, post stability characterizations (XRD, SEM, XPS) were carried out. As shown in **Appendix B Figure 8,** post-XRD patterns collected of $(Mn_{0.8}Ir_{0.2})O_2$:10F did not feature any major changes in the XRD peak positions, suggesting that the $(Mn_{0.8}Ir_{0.2})O_2$:10F structure is well maintained, retaining its original tetragonal phase with no undesired crystal phase transformations. In addition, the electrocatalysts following post-stability chronoamperometry tests were subjected to SEM analyses. Accordingly, SEM images **[Appendix B Figure 9 (a-b)**] and EDX spectrum [**Appendix B Figure 9 (c)**] collected on $(Mn_{0.8}Ir_{0.2})O_2$:10F/Ti revealed the existence of similar 1D nanorod architectures indicating no significant change or deterioration of the morphology of the electrocatalyst as well as change in the elemental composition. These results thus not only indicate the robust nature of the electrocatalysts but also suggest the firm adhesion/binding of $(Mn_{0.8}Ir_{0.2})O_2$:10F NRs on the current collector substrate. Furthermore, post-XPS characterizations (Appendix B Figure 10**)** revealed the stable state of the $(Mn_{0.8}Ir_{0.2})O_2$:10F electrode indicating the presence of Mn, Ir and O. Furthermore, the XPS spectrum of Mn indicated a negative shift in the XPS peak positions after 24 h durability test when compared with the pristine $(Mn_{0.8}Ir_{0.2})O_2$:10F NRs. Such lower binding energy shifts in the case of Mn2p indicates the electronic environment change during OER (suggesting manganese (III) oxyhydroxide of (MnOOH) formation)[254-256].

Such beneficial surface modification (i.e. formation of meta-stable OER active Mn^{+3} ions[254, 256]) during prolonged exposure to OER is commonly observed in various electrocatalyst materials, which play a critical role in stimulating the OER kinetics as well as shielding both dissolution and disproportionation of MnO_2 under the harsh acidic OER conditions[255, 256]. Interestingly, in the XPS spectrum of Ir [**Appendix B Figure 10 (b)**] of $(Mn_{0.8}Ir_{0.2})O_2$:10F NRs following the stability tests, Ir $4f_{5/2}$ and Ir $4f_{7/2}$ doublet positions also exhibited negative shift of ~ 0.25 eV as compared to freshly prepared $(Mn_{0.8}Ir_{0.2})O_2$:10F. Such negative shifts in the doublet positions of Ir containing electrocatalyst were similarly detected in the earlier studies conducted by Siracusano et. al.[182] and Ghadge et. al.[187] which indicates the formation of sub-stoichiometric IrO_x i.e. partial conversion of IrO_2 to the hydrated sub-stoichiometric IrO_x species during prolonged exposure to the OER conditions. For example, as elucidated by Huang et al.[257], in the XPS spectrum of post stability $(Mn_{0.8}Ir_{0.2})O_2$:10F, in additional to the peak at ~62 eV (Ir^{+4}), another peaks at ~ 62.9 eV and 67 eV were observed which corresponds to that of Ir^{+3} and Ir^{+6}, respectively[257]. According to various literature reports[182, 257], the shifts in the binding energy as well as formation of different oxidation states Ir^{n+} can be attributed to the lattice oxidized ions O^{2-} or hydroxide or bound water/ adsorbed H_2O or O_2. Such surface modification developing during the intense rate of oxygen evolution is considered to be beneficial, resulting in enhancement in the OER kinetics.[182] In the comprehensive XPS study conducted by Siracusano et al.[182], the formation of hydrated sub-stoichiometric species and the positive influence of weakly bonded surface hydroxyls in Ir-based electrocatalysts on the OER catalytic activity has been exclusively elucidated. In addition, from various studies it has been identified that the surface OH groups play a crucial role as reactive surface intermediates on active sites of the oxygen evolution process. Thus, in accordance with above discussions, as witnessed in our post stability XPS characterizations, the modified electronic environments of Ir and Mn evidently suggests the acceleration of OER kinetics.

In line with the above discussion, XPS spectrum of O shows in addition to peak at ~530.8 eV, two more peaks. The peak at ~533 eV can be referred to the low binding energy component (LBEC) which is attributed to the enhanced hydroxide formation[257] during OER, similar to the earlier reported studies[182, 226, 258]. In the recent Co-doped IrCu OER electrocatalyst work by Kwon et al.[259], such increase in the peak intensity (at binding energy of ~533 eV) is ascribed to the evolution of IrO_x species as well as surface Ir-OH species. As mentioned above as well as in a good agreement with various reported studies[259-261], the formation $Ir(O)_x(OH)_y$ phase is regarded as an active phase for OER. Thus, these postmortem XPS characterizations suggest the beneficial surface modification of Ir, Mn during the OER process. The peak observed at higher binding energy value of ~ 536 eV corresponds to the Nafion[262], which is used as a binder during the preparation of electrocatalyst ink (discussed in the experimental section). Herein it is important to underline that, as the primary objective of the present work is to demonstrate the promising attributes of 1D architectures and although, our preliminary XPS results indicate the beneficial surface amendment and change in the electronic environment of as-synthesized $(Mn_{0.8}Ir_{0.2})O_2$:10F system during extended OER, the in-depth post stability structural analysis (computational as well as experimental) is highly desirable for the advance understanding of the structural parameters and surface modifications during OER process that can contribute to the high OER activity and electrochemical durability. Such fundamental electrochemical benchmarking studies will be the object of our successive work in the Ir based OER electrocatalyst systems for the acid mediated water electrolysis.

6.5.3 Computational Study Results

6.5.3.1 Computational Study of the Electrochemically Active α-MnO_2 based ECs

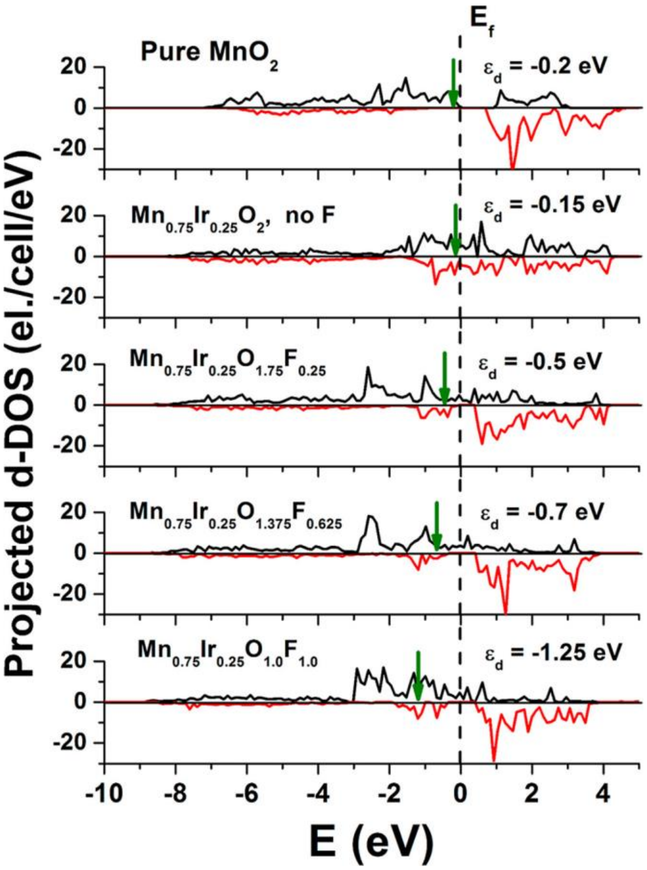

Figure 6-10 Projected d-band density of the electronic states calculated for pure α-MnO_2, $(Mn_{0.75}Ir_{0.25})O_2$, and F-doped $(Mn_{0.75}Ir_{0.25})O_2$ with 4, 10 and 15 wt% of F. Fermi level is set to zero. The arrows denote the corresponding d-band centers

The main origins of enhanced electro-catalytic activity of fluorine doped $Mn_{0.75}Ir_{0.25}O_2$ could be understood from the electronic structure point of view as well as from the thermodynamic consideration of all the four elementary steps of the OER occurring at the active surface. Similar to our previous publications[70, 97, 137], we have continued to adopt the concept proposed by J.K. Nørskov and his group[113, 114] and accordingly, we have used it for qualitative evaluation of the electrochemical activity of $Mn_{0.75}Ir_{0.25}O_2$ and $Mn_{0.75}Ir_{0.25}O_2$:F.As mentioned earlier in the computational methodology, the electronic structure of the stable surfaces for all electrocatalysts have been calculated and the positions of the corresponding d-band centers have been obtained as a first moment of $n_d(E)$: $\varepsilon_d = \int n_d(E)EdE / \int n_d(E)dE$, where $n_d(E)$ is the projected d-band density of states of the corresponding materials. **Figure 6-10** thus accordingly depicts the projected d-band densities of states together with the corresponding centers of these zones marked with vertical arrows on the graphs calculated for (110) surface for pure α-MnO_2, Ir substituted α-MnO_2, $(Mn_{0.75}Ir_{0.25})O_2$, as well as F doped Ir substituted α-MnO_2, $(Mn_{0.75}Ir_{0.25})O_{1.75}F_{0.25}$, $(Mn_{0.75}Ir_{0.25})O_{1.375}F_{0.625}$, and $(Mn_{0.75}Ir_{0.25})O_{1.0}F_{1.0}$. Since, IrO_2 is a benchmark OER electrocatalyst, the d-band positions for IrO_2, marked with a dashed vertical line throughout the whole graph, could serve as a reference point, showing the optimal electrocatalytic activity for the as-synthesized electrocatalysts.[70] In our previous studies[70, 97, 137] we have showed that IrO_2 is characterized by the d-band centers located at ~ -1.33 eV marked with a solid vertical line at the graph. The closer the corresponding d-band center position of the solid solution electrocatalyst studied herein to -1.33 eV, the higher the catalytic activity of the substituted solid solution will be expected to be achieved, so that the d-band center position can serve as an indicator of expected improvement of overall catalytic activity of the electrocatalyst. Such an approach can thus help in understanding the effect of fluorine on the electro-catalytic activity of α-$(Mn,Ir)O_2$:F.

Table 6-3 Computational data obtained from the present study (ΔZPE - TΔS data taken from previously published study[41])

Configuration	ΔZPE - TΔS (eV)	ΔG (eV)					
		Pure α-MnO₂	**α-(Mn,Ir)O₂ Ir at Pos.1**	**α-(Mn,Ir)O₂ Ir at Pos.2**	**α-(Mn,Ir)O₂:F Ir at Pos.2**	**Rutile (Mn,Ir)O₂ Ir at Pos.1**	**Rutile (Mn,Ir)O₂ Ir at Pos.2**
Vac+2H_2O	-	0	0	0	0	0	0
HO*+H_2O+1/2H_2	0.35	1.33	1.28	1.30	1.25	1.25	1.28
O*+H_2O+H_2	0.05	2.58	2.52	2.55	2.60	2.62	2.58
HOO*+3/2H_2	0.40	3.99	3.98	3.98	4.02	4.10	4.03
Vac+O_2+2H_2	-	4.92	4.92	4.92	4.92	4.92	4.92
ΔG of Step 3 (eV) (Over-potential in V)		1.41 (0.18)	1.46 (0.23)	1.43 (0.20)	1.42 (0.19)	1.48 (0.25)	1.45 (0.22)

It can be seen from **Figure 6-10** that MnO_2 is a poor electronic conductor with a band gap of ~0.9 eV. Similar computations made by Tripkovic et. al.[263] indicated the corresponding value of 1.0 eV. The electronic conductivity of the as-synthesized MnO_2 at room temperature (σ_{300K}**)** was obtained as ~0.0032 $S.cm^{-1}$ (resistivity, ρ_{300K} ~312.5 Ω.cm), which is in a good accordance with various literature reports[264, 265]. Thus, it can be inferred that such MnO_2 possessing substandard electronic conductivity would not be an efficient electrocatalyst for water splitting, which is indeed validated by the present impedance and polarization results**.** Also, the corresponding d-band center of the material locates at -0.2 eV which is far away from the optimal position -1.33 eV featured by IrO_2, the benchmark electrocatalyst used for the OER in PEM based electrolyzers. However, introduction of 20 at. % Ir into the α-MnO_2 lattice leads to lattice expansion and also, improvement in the electronic conductivity. The improved electronic conductivity of Ir containing α-MnO_2 [$(Mn_{0.8}Ir_{0.2})O_2$] has been evidenced from the impedance as well as electrical conductivity measurements (σ_{300K} = 0.11 S.cm^{-1}). However, this modification of the electronic structure alone does not help improve the d-band center position. It still locates the Fermi level in the vicinity of -0.15eV of the energetic scale. Although an improvement in the electronic conductivity would lead to increase in the electrocatalytic activity of $(Mn, Ir)O_2$ compared to that of pure MnO_2, it still has probability to further improve due to the sub-optimal position of the d-band center. Such improvement could be achieved with the introduction of fluorine into the $(Mn,Ir)O_2$ lattice. **Figure 6-10** clearly demonstrates the calculated projected density of d-electronic states for $(Mn,Ir)O_2$ with different F-contents. One can see that the addition of F from ~ 4wt% up to ~15wt% moves the d-band center from -0.5 eV to -1.25eV which allows one to expect a significant improvement in the electrocatalytic activity. This shift in the d-band center takes place due to formation of the hybridized F2p-Mn3d and F2p-Ir5d electronic states well below the Fermi level. An identical effect of F on the electronic structure has also been seen earlier and reported by us in the study of $(Sn,Ir)O_2$:F electrocatalysts.[97] Similar to $(Mn,Ir)O_2$:F, the formation of F2p-Ir5d hybridized electronic states shift the d-band center of $(Ir,Sn)O_2$:F down toward the optimal position, and thus, improves the overall electronic conductivity and catalytic activity of $(Ir,Sn)O_2$:F with substantial reduction of ~70-80% in the noble metal content.[97] These theoretical finding have been well supported in the corresponding reports[97] as well as in the experimental results of the present work wherein F containing $(Mn_{0.8}Ir_{0.2})O_2$:10F exhibited improved electronic conductivity (σ_{300K}) of ~5.88 S cm^{-1}.

Due to simplicity, the d-band center concept can provide only a qualitative explanation of the basic origins of high catalytic activity of (Mn,Ir)O_2:F. In order to investigate the effects of Ir and F introduction into the α-MnO_2 lattice on the overpotential of the (Mn,Ir)O_2:F solid solution oxide, there is a need to consider all the four elementary steps involved in the oxygen evolution reaction as outlined in the computational methodology section. **Figure 6-11 (a)** demonstrates the free energies of all the four elementary steps of OER calculated for the pure α-MnO_2 and three different atomic configurations with introduced Ir and F atoms discussed above and illustrated in **Figure 6-1 b-d**. Also, some of the data used for plotting these graphs have been collected in **Table 6-3**.

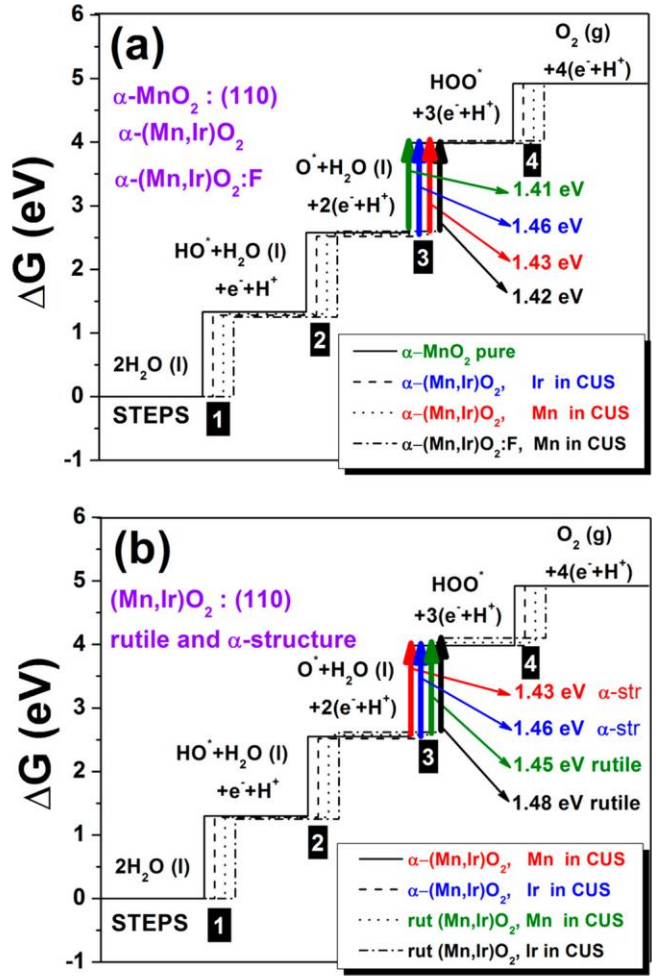

Figure 6-11 Free energies of the intermediate reactions for (a) pure and Ir-doped α-MnO_2 with the same CUS at (110) surfaces and (b) Ir-doped α-MnO_2 and Ir-doped rutile MnO_2 with the same CUS at (110) surfaces

It can be seen that the most energetically challenging step for all the four systems is step 3, which results in the formation of the hydroperoxide HOO* from the second water molecule. This step determines the major overpotential required to overcome in order to meet the four steps of OER outlined in **Figure 6-11 a-b**. For pure α-MnO_2 the OER overpotential is 1.41-1.23 = 0.18 V , while for (Mn,Ir)O_2 it is 0.20 V and 0.23 V for the two different positions of Mn in the unit cell.

Thus, these results indicate that the presence of Ir in MnO_2 increases the overpotential for the OER in comparison with the pure MnO_2. Such increase in the energy difference for the third elementary step in the case of Ir-doped MnO_2 is attributable to the weaker interaction between the adsorbed oxygen (O^*) and the surface resulting in an increase in the total energy of the system in comparison with pure MnO_2; making it less feasible for the species to adsorb at the surface and thus, resulting in an increase of the overpotential of the overall OER for $(Mn,Ir)O_2$ electrocatalyst system. Furthermore, it can be seen from **Figure 6-11 (a)** that additional introduction of F into $(Mn,Ir)O_2$ oxide system leads to a slight reduction of the overpotential from 0.20 V to 0.19 V, evidently suggesting the reduced reaction barrier and improved electrocatalytic activity as compared to that of un-doped $(Mn,Ir)O_2$ oxide. From these results one can conclude that among all the materials considered in the present study (i.e., pure MnO_2 and MnO_2 doped with Ir and F), pure MnO_2 is expected to have the lowest overpotential for the OER reaction. This result indicates that MnO_2 electrocatalyst itself has a good ability to oxidize water very efficiently provided it attains good electronic conductivity together with the excellent electrochemical stability in the harsh acidic OER conditions of PEM water electrolysis. Both these properties related to catalytic activity as well as stability are fairly mediocre in the α-MnO_2 (owing to its semiconducting nature and poor OER stability in the acidic environment), which together suggest that there is a strong need to improve the electronic conductivity and stability by introduction of some appropriate elements into MnO_2 framework. In this direction, the approach of incorporating active/foreign elements in the earth abundant and cheap materials has been widely employed to fabricate the high performance electrocatalyst systems. Such elements which should not necessarily be noble metals (Ir,Ru, Pt) could modify the electronic structure and the overall structural stability in the positive manner, allowing one to synthesize the highly efficient and completely noble metal free electrocatalyst systems for acid assisted oxygen evolution reaction. Along these lines, it is worth mentioning that various researchers have already embarked on the journey to explore various acid stable-element doped MnO_2 electrocatalyst systems for acidic OER [for example, recent work on $Mn_{0.8}Ti_{0.2}O_2$ electrocatalyst system reported by Frydendal et al.[266], $(Mn–Co–Ta–Sb)O_x$ system reported by Shinde et al.[267], $Ni_xMn_{1-x}Sb_{1.6–1.8}O_y$ electrocatalyst by Moreno-Hernandez[268], and $CoMnO_x$ work by Nocera and co-workers[269, 270] etc.]

Furthermore, another aspect of the present study is to compare the catalytic activity of 1D α-$(Mn,Ir)O_2$ NRs with a 2D thin film $(Mn,Ir)O_2$ system having rutile crystal structure as reported by us recently[70]. **Figure 6-11 (b)** depicts the free energies of all the four intermediate steps of the OER reaction for both rutile and the α-structures of $(Mn,Ir)O_2$. Graphs for the two Ir-Mn configurations with rutile structure are taken from the earlier report[70] while another two graphs reflect the calculated free energies for α-structure and reproduced from **Figure 6-11 (a)** for the α-($Mn,Ir)O_2$ system. It can be seen that for atomic configuration at (110), the rate determining step (steps 3) for α-structure demonstrate consistently lower values than the corresponding steps 3 for the (110) rutile structure. The lowest step 3 is 1.43 eV for the α-structure with Mn atom under the CUS. The corresponding value for step 3 at the rutile surface is 1.45 eV with the similar atomic configuration. The difference in the overpotential for the same CUS but with different local distribution of the Mn and Ir-ions is ~ 0.02 to 0.03 eV for both rutile and α-MnO_2 crystal structures. Thus, these results clearly demonstrate that not only the 1D nanorod morphology benefits in improving the catalytic activity, but also the crystal structure itself plays a major role in enhancing the catalytic activity (since our calculations did not involve any considerations of the different morphologies of nano-structured surfaces.) Accordingly, the present theoretical results correspondingly attest to the excellent electrocatalytic performance of the as-synthesized α-

$(Mn,Ir)O_2$ NRs for OER in PEM water electrolysis. In addition, the current theoretical work also provides an excellent boulevard to engineer the high performance nonprecious OER electrocatalysts for efficient hydrogen production via PEM based water electrolysis.

6.6 Conclusions

In summary, we have demonstrated a facile hydrothermal and wet chemical approach for the synthesis of 1D $(Mn_{0.8}Ir_{0.2})O_2$:10F nanorods (NRs) as an efficient electrocatalyst for acidic OER. The as-synthesized $(Mn_{0.8}Ir_{0.2})O_2$:10F NRs possessing unique electronic/molecular structure exhibit notable electrochemical activity with the lower onset potential of ~ 1.35 V (vs. RHE) than that of IrO_2 (~1.43 V vs. RHE). In addition, owing to the presence of 1D channels of nanorod architecture and unique electronic structure obtained upon formation of fluorine (F) containing solid solutions, $(Mn_{0.8}Ir_{0.2})O_2$:10F NRs exhibit low charge transfer resistance (~2.5 $\Omega.cm^2$), low Tafel slope (~38 mV dec^{-1}), high electrochemically active surface area (ECSA ~704.76 m^2g^{-1}) and notable OER performance with ~6, ~2.1 and ~ 2.2 fold higher electrocatalytic activity than IrO_2, $(Mn_{0.8}Ir_{0.2})O_2$ NRs and 2D thin film of $(Mn_{0.8}Ir_{0.2})O_2$: 10F, respectively. Additionally, considerably higher ECSA and BET specific activity, mass activity (40 Ag^{-1}) and TOF (0.01s^{-1}) at overpotential of ~ 220 mV clearly suggests the intrinsically higher electro-catalytic activity of $(Mn_{0.8}Ir_{0.2})O_2$:10F NRs as compared to other as-synthesized electrocatalysts. Moreover, in a 24 h OER durability study, no major deviation in current density was witnessed for our as-synthesized $(Mn_{0.8}Ir_{0.2})O_2$:10F NRs, suggesting its structural robustness, chemical and electrochemical integrity for displaying sustained and prolonged OER response under harsh acidic conditions which is also competently reinforced by the post stability characterization analyses. Furthermore, our extensive DFT calculations suggest that the solid solution of α-MnO_2 based crystal structure [$(Mn_{0.8}Ir_{0.2})O_2$:10F] demonstrates higher catalytic activity than that of rutile MnO_2 based crystal structure with the similar chemical compositions and ionic distributions. Also, the results reported herein further demonstrate the inherent capability of MnO_2 to promote the OER reaction if it could be made displaying high electronic conductivity combined with the required chemical stability for OER in the acidic media. Indeed, following the pathway discussed, doping with some non-noble materials could meet these requirements transforming the electronic structure, and thus opening new pathways for synthesizing novel families of platinum group metal (PGM)-free electrocatalysts for PEM water electrolysis. Correspondingly, the present work demonstrates the fidelity of 1D $(Mn,Ir)O_2$:10F nanorod electrocatalyst system for the efficient hydrogen generational and water splitting via PEM based water electrolysis.

7.0 Specific Aim 1A - To Identify and Engineer Reduced PGM Containing and PGM-Free Multi-Metal Oxide (MMO) Based Electrocatalyst Materials of Different Architectures for Oxygen Evolution Reaction (OER) in Proton Exchange Membrane-Based Water Electrolysis (PEMWE)

This aim describes the fourth OER electrocatalyst focused on the PGM-free system.

- Chapter 7: Fluorine substituted $(Mn,Nb)O_2$: F nanorod electrocatalysts for OER

Excerpts reprinted with permission from Ghadge, Shrinath Dattatray, et al. "Computational and Experimental Study of Fluorine Doped $(Mn_{1-x}Nb_x)O_2$ Nanorod Electrocatalysts for Acid-Mediated Oxygen Evolution Reaction." ACS Applied Energy Materials 3.1 (2019): 541-557.

7.1 Abstract

Identification, development, and engineering of high performance, earth-abundant, and cost- effective precious group metal (PGM)-free electrocatalysts for catalyzing oxygen evolution reaction (OER) in acidic electrolytes are vital for the commercialization of proton exchange membrane-based water electrolysis (PEMWE) technology. Utilizing the density functional theory (DFT) calculations to rationalize the thermodynamics and kinetics of adsorption of OER, juxtaposed with cohesive energy and electronic structure, we report the generation of 10 wt. % fluorine (F) doped $(Mn_{1-x}Nb_x)O_2$:10F nanorods (NRs) as active and durable PGM-free solid solution electrocatalysts for acid-mediated OER. The DFT calculations reveal an optimal solid

solution composition of $(Mn_{0.8}Nb_{0.2})O_2$:10F containing Nb and F in α-MnO_2 structure, exhibiting the optimized surface electronic structure (ΔG for OER rate determining step ~ 1.72 eV) and cohesive energy (E_{coh} ~ -16.30 eV/formula unit) for OER, contributing to its higher catalytic performance in comparison to α-MnO_2. Consequently, $(Mn_{1-x}Nb_x)O_2$:10F compositions with well-defined one dimensional (1D) nanorod architectures are synthesized with the optimal composition of $(Mn_{0.8}Nb_{0.2})O_2$:10F demonstrating improved electrocatalytic performance for acidic OER in good agreement with the DFT calculations. The superior electrochemical performance of $(Mn_{0.8}Nb_{0.2})O_2$:10F NRs includes significantly lower charge transfer resistance (~11.8 Ω cm^2), lower Tafel slope (~371.17 mV dec^{-1}), lower overpotential to deliver current density of 10 mA cm^{-2}_{geo} (~0.68 V), higher mass activity (~29 A g^{-1}), large electrochemically active surface area (ECSA ~26 m^2 g^{-1}), and turnover frequency (TOF ~ 0.0065 s^{-1}) with higher BET and ECSA normalized activity (~0.5 mA cm^{-2}_{BET} and 0.11 mA cm^{-2}_{ECSA}) contrasted with $(Mn_{1-x}Nb_x)O_2$:10F (x= 0, 0.1 and 0.3) compositions, at an overpotential of 0.67 mV. Further, $(Mn_{0.8}Nb_{0.2})O_2$:10F NRs exhibit good electrochemical stability in acidic OER regimes, with no substantial catalytic activity degradation validating its structural robustness for prolonged OER and making it a promising PGM-free OER electrocatalyst for acid mediated PEMWE.

7.2 Introduction

The ever-increasing worldwide energy demand combined with the accelerated depletion of fossil fuels and the growing alarming environmental concerns have led to the exploration of hydrogen (H_2) as an alternative clean, sustainable, and environmentally benign potential energy source. Hydrogen garnered much attention over the past two decades mainly due to its higher specific energy density (~120 MJ/kg) than conventional petroleum-based fuels (~45 MJ/kg) and its non-carbonaceous nature making it an ideal substitute for the finite fossil fuels, particularly in the transportation and electricity storage sectors[50, 271]. Amongst the various hydrogen production approaches, electrochemical water splitting is most promising and reliable for efficient and clean hydrogen generation although restricted in energy efficiency. This is mainly due to the kinetically sluggish and energy uphill anodic oxygen evolution reaction (OER) demanding a significantly higher overpotential than the standard OER potential of ~1.23 V for practical operation[50]. Much research has therefore been targeted towards developing highly active and stable electrocatalysts for lowering the OER overpotential; thereby directly translating into electricity cost reduction with simultaneous efforts targeted at identifying cheaper alternatives to the ideal precious group metal (PGM) based electrocatalysts. This search has led to exploration of various transition-metal (e.g. Fe, Cu, Ni, Mn, Co) oxides, phosphides, borides, carbides, selenides, nitrides, sulfides, and many other multi-metal based non-precious transition metal compounds, predominantly for alkaline and neutral medium water electrolysis[47]. Unfortunately, despite major advances, hydrogen production via alkaline/neutral water electrolysis is severely circumscribed by its relatively lower production rate and substandard hydrogen purity. In contrast, acid mediated proton exchange membrane or polymer electrolyte membrane-based water electrolysis (PEMWE) is much more appealing.

The PEMWE approach offers numerous distinct advantages over water electrolysis technologies in alkaline as well as neutral electrolyte media. These include superior adaptability to fluctuating energy inputs, high efficiency at high current density, production of ultra-pure and electrochemically pressurized H_2 due to a low gas crossover rate and compact system design, faster start-up and low ohmic losses due to high conductivity of protons (>1.5 fold higher than that of hydroxide ions)[272], and low carbon footprint combined with good suitability for renewable energy storage. However, the major bottleneck to PEMWE is the universal inferior chemical stability of various OER active earth-abundant electrocatalysts, susceptible to anodic dissolution or corrosion in the harsh acidic media driven OER conditions. Materials that traditionally exhibit significant corrosion resistance and high endurance to OER conditions are compromised by electrochemical OER inactivity in PEMWE conditions. It is well-known that PGM or noble metal based electrocatalysts (such as RuO_2, IrO_2) are the paragon electrocatalysts owing to their excellent OER electrocatalytic activity, lower overpotential, and durability for producing sustained oxygen under stringent acidic conditions of PEMWE. Unfortunately, PGM systems are characterized by natural environmental scarcity (~ 0.001-0.0003 ppm in earth's crust)[29] adding to their prohibitive cost (e.g. \$210/g_{IrO2}) and high toxicity limiting their extensive employment in the PEM water electrolyzers[31]. Therefore, significant research efforts are directed towards the identification and development of earth- abundant cost-efficient, reduced PGM containing including PGM-free electrocatalyst systems. An integral goal of this intense research is to demonstrate good electrochemical performance in corrosive acidic regime for the current electrochemical, photo-electrochemical water splitting field and other emerging fuel-producing technologies of electrochemical CO_2 reduction (for production of organic feedstocks of CO, CH_4, CH_3OH etc.), and N_2 reduction (for production of NH_3)[273].

This intense activity conducted over the years has focused at reducing the PGM content. A common approach is alloying IrO_2 and/or RuO_2 with earth-abundant and cheap transition metal oxides such as $(Ru,Sn)O_2$[136], $(Ir,Sn)O_2$[187], $(Ir,Ta)O_2$[95], $(Ir,Ti)O_2$[227], $(Ir,Cu)O_2$[274], $(Ir,Ni)O_2$[174], $(Ir,W)O_2$[275], $(Ir,Co)_2$[276], $(Ir, Mn)O_2$[70], $(Ru/Ir, Nb)O_2$[277], $(Ir, Si)O_2$[40], etc. The strategy of mixing earth-abundant metals with substantially lower contents of IrO_2 and RuO_2 will reduce the overall cost of electrocatalyst while effectively optimizing the surface electronic structure of IrO_x and

RuO_x. The solid solution systems thus offer enhancement in electrocatalytic performance of the solid solution/alloyed electrocatalysts matching PGM systems thus positively impacting the PEMWE technology. In the context of PGM-free based OER catalysts, manganese oxide (MnO_x) system has garnered special attention. This is primarily owing to its variable crystallographic phases (α, β, γ, δ, λ), feasibility to construct different (1D, 2D, 3D) architectures and morphologies, sufficient abundance in the earth's crust, environmental friendliness, low toxicity, low cost, and more importantly, promising electrocatalytic activity[246]. In addition, in photosystem II (PS II) system, the core of the catalytic center - $CaMn_4O_5$ cluster efficiently catalyzes water oxidation at low overpotential stimulating significant interest in MnO_x based water oxidation catalysts (WOCs).[278] Although promising, the low activity and poor stability of MnO_2 in highly acidic PEMWE conditions have restricted its utilization as an efficient OER electrocatalyst[279].

Nocera et al.[270] as well as Stephens et al.[266] report that at low pH of ~1 , MnO_2 can oxidize water within its bulk thermodynamic stability range. In order to shield the dissolution of MnO_2 in acidic electrolytes, however, it is imperative to stabilize the MnO_2 surface by incorporating non-precious metal acid stable cations (Ti, Nb, Ta, Sn etc.) into the MnO_2 to generate effective electrocatalytic activity for acidic OER. This notion led to intense research directed at identifying MnO_x based active and durable electrocatalysts systems for acidic OER. In the recent computational and experimental study[45], we demonstrated the improved electrochemical activity and stability of $(Mn_{0.8}Ir_{0.2})O_2$:10F nanorods for acidic OER by incorporating 20 atom % iridium (Ir) and 10 wt. % fluorine (F) into MnO_2. In addition, Shinde et al. [267] and Zhou et al.[280] reported on the fidelity of acid stable dopants (Ta, Sb) stabilizing MnO_x for acid mediated OER in their work on $(Mn–Co–Ta–Sb)O_x$ and $(Mn_{1-x}Sb_x)O_2$ electrocatalyst systems. Furthermore, Moreno-Hernandez et al. [268] reported crystalline nickel manganese antimonate ($Ni_xMn_{1-x}Sb_{1.6–1.8}O_y$) as an active and robust electrocatalyst for acidic OER. We also recently showed the stabilization and improved OER activity of F and Cu containing spinel $Cu_{1.5}Mn_{1.5}O_4$:10F electrocatalyst for PEMWE[281]. Additionally, Frydendal et al.[266] reported that Ti-doped MnO_2 i.e. $(Mn_{0.8}Ti_{0.2})O_2$ exhibited significant improvement in electrochemical stability of MnO_2 for acidic OER. Inspired by these studies, we have attempted to stabilize MnO_2 without comprising OER catalytic activity. Accordingly exploiting density functional theory (DFT) based calculations of the total energies and electronic structures, for the very first time, we have identified and synthesized 0-30 atom % niobium (Nb) and 10 wt.% fluorine (F) containing MnO_2, denoted as $(Mn_{1-x}Nb_x)O_2$:10F solid solution electrocatalyst systems for acidic OER.

The rationale for selection of Nb is its greater natural abundance, chemical stability as well as excellent corrosion resistance under stringent acidic conditions[282] rendering Nb a promising dopant for acidic OER systems[283]. We have also described the efficacy of minute additions of Nb in IrO_2 [$(Ir_{0.75}Nb_{0.25})O_2$ and $(Ir_{0.4}Sn_{0.3}Nb_{0.3})O_2$] demonstrating its chemical stability and substantial improvement in the electrochemical stability thus validating the viability of the strategy to introduce Nb into the IrO_2 lattice as a reasonable and promising approach for reducing the costs of OER electrocatalysts for PEMWE[35, 282]. Additionally, Hu et al. reported on Nb-doped $IrO_2/Nb_{0.05}Ti_{0.95}O_2$ system, demonstrating superior OER electrochemical stability to pristine IrO_2[284]. Similarly, Santana et al. reported that systematically substituting Nb_2O_5 for CeO_2 [$(Ru_{0.3}Ti_{0.6}Ce_{0.07})O_2(Nb_2O_5)_{0.03}$] offered significant improvement in electrochemical stability for OER[43, 283]. Puthiyapura et al. also showed that Nb containing RuO_2 ($Ru_{0.8}Nb_{0.2}O_2$) offered substantial enhancement in the electrochemical stability of RuO_2 for acidic OER[277]. In earlier DFT studies conducted by us, we have demonstrated and attributed the superior OER electrocatalytic stability of Nb containing solid solution systems to the more negative cohesive energy values in comparison to un-doped/pristine metal oxides (IrO_2, SnO_2)[35, 282]. Further, according to various literature reports incorporating high valence ion species (such as Nb^{+5}, Bi^{+5}) into metal oxides (MnO_2) results in the enhanced chare transfer kinetics i.e. reduced charge transfer resistance (R_{ct}) and thus, improved electrochemical activity [285].

In line with the above, in addition to Nb, in the present study, we have investigated the introduction of another earth-abundant dopant (fluorine, F) in $(Mn\text{-}Nb)O_2$ system. Owing to its ability to modify the electronic structure as well as enhance the electronic conductivity of the parent electrocatalyst system, high oxidation potential containing anionic F is well known to expedite the electrochemical performance[102]. In our previously published reports[70, 187] employing DFT calculations, we have successfully demonstrated that the introduction of optimal F content (~10 wt.%) into metal oxides of MnO_2, IrO_2, SnO_2, Nb_2O_5, $Cu_{1.5}Mn_{1.5}O_4$ etc. optimizes the surface electronic structure for oxygen evolution. Hence, F is promising for enhancing electronic conductivity, lowering charge transfer resistance and improve electrochemical stability contributing to enhanced acidic OER electrocatalytic response of solid solution electrocatalysts[178]. Consequently, based on the above encouraging insights and our prior DFT calculations, we report the solid solution of one-dimensional (1D) nanorod (NR) structured $(Mn_{1-x}Nb_x)O_2$:10F as an active and robust OER electrocatalyst for acidic water electrolysis. 1D-nanostructured architectures are widely documented and utilized in the water splitting research area for their numerous exciting benefits such as high electrochemically active specific surface area (ECSA), large aspect ratio (L/D), and better active site densities, which can significantly improve electrocatalytic activity[144]. Additionally, 1D electrocatalyst architectures offer lower charge transfer resistance (R_{ct}) and thus better electronic conductivity, which can be attributed to the existence of 1D channels and lattice planes with less crystal boundaries[45]. Furthermore, 1D architectures are well known for demonstrating higher catalytic stability in comparison to nano-particular or film based catalyst materials which often experience physical ripening processes and higher catalytic dissolution[207].

Therefore, in light of these promising attributes of 1D nanostructure, we have synthesized 1D NRs of MnO_2 as the parent framework structure utilizing a simple and scalable hydrothermal approach. Accordingly, as anticipated by our DFT simulations, Nb and F doped MnO_2 NRs [denoted as $(Mn_{1-x}Nb_x)O_2$:10F] exhibit OER catalytic activity and electrochemical durability superior to pure MnO_2. The theoretical as well as experimental study results indicate the promise of as-synthesized $(Mn_{1-x}Nb_x)O_2$:10F (for x =0.2) NRs as an OER electrocatalyst in acid mediated water splitting.

7.3 Computational Methodology

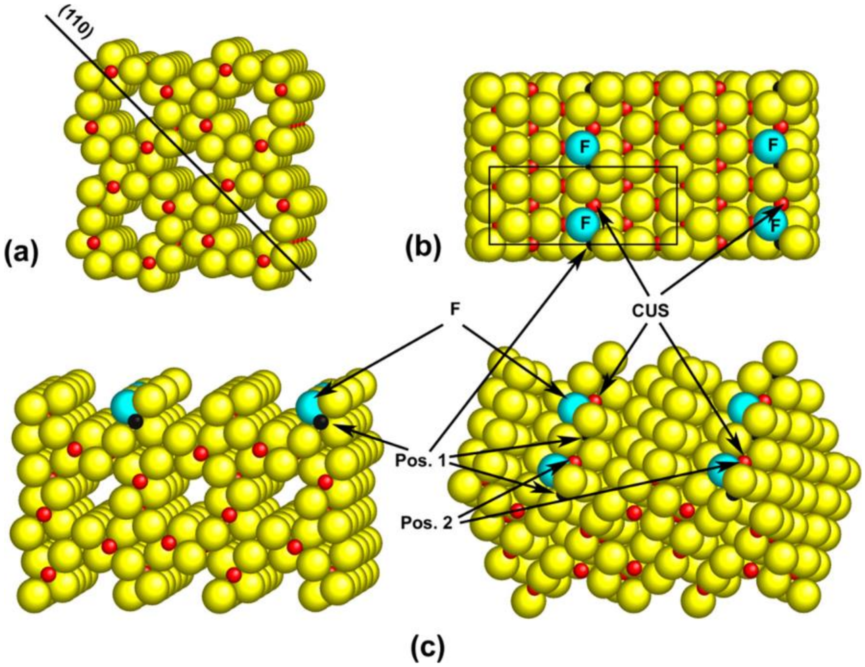

Figure 7-1 (a) General view of α-MnO_2 crystal structure. Small spheres represent Mn, large ones - oxygen atoms, (b) a top view of the oxidized (110) surface with coordinatively unsaturated sites (CUS) and F ions replacing some oxygen ions. Rectangle denotes the unit cell used for (110) surface slab modeling, and (c) (110) surface at different angles. Pos.1 and Pos.2 represent two possible positions of the Nb atom considered in the present study

In order to engineer the better electrocatalyst materials, it is imperative to understand the mechanistic pathways, electronic and crystal structure, and the reaction barriers related to the acidic OER pathway. As shown in (4-1), * represents an active site on the metal oxide surface[286].

The crystal structure of α-MnO_2, shown in **Figure 7-1 (a)** will be used to investigate the effect of composition of the solid solution on the electronic structure, overpotential, and the structural stability as part of the computational aspect conducted to supplement the experimental work in the present study. Correspondingly, the following electrocatalyst compositions having α-MnO_2 structure have been utilized for the *ab-initio* computational study: pure α-MnO_2, $(Mn_{0.875}Nb_{0.125})O_2$, $(Mn_{0.75}Nb_{0.25})O_2$, $(Mn_{0.625}Nb_{0.375})O_2$, and F-doped $(Mn_{0.75}Nb_{0.25})O_{1.375}F_{0.625}$. The F-doped formula unit considered here corresponds to incorporation of approximately 10 wt.% of F in the oxide lattice. These compositions have been selected based on the elementary unit cell of α-MnO_2 structure containing 8 atoms of Mn and 16 atoms of O[70]. The electric potentials at which a specific reactions take place are calculated by evaluating the free energies (ΔG) of all the four anodic intermediate reactions given in above equation. Consequently, a methodical investigation of all the calculated ΔG values could help in identifying the rate determining step (RDS) and the associated overpotential of the OER for the oxygen evolution reaction occurring at the electrochemically active surface. This computational investigation is indeed useful to assess the electrocatalytic activity of the potential electrocatalyst in the OER pathway. For comparisons, three different electrocatalysts have been selected for calculation of the OER elementary steps: (a) Pure MnO_2, (b) MnO_2 with a small content of Nb introduced as a replacement for Mn at the associated Mn-type lattice sites, and (c) $(Mn, Nb)O_2$ doped with F as a substituent for O. Herein, the above stated oxides, bulk and (110) surface α-MnO_2 structure are utilized to study the electronic structure and free energies of the four elementary OER steps, which qualitatively describe the electrocatalytic activity. In order to compute the bulk calculations, a tetragonal 24-atom unit cell with α-MnO_2 crystal configuration has been employed for construction of various Mn, Nb, and F concentrations in the solid solution materials, which includes 8 transition metal

(TM) atoms and 16 atoms of oxygen/fluorine. Herein, for the ease of DFT calculations, the following basic oxide compositions without the incorporation of fluorine have been selected: pure MnO_2 with 8 Mn and 16 O atoms as well as 3 Nb-containing oxides: $(Mn_{1-x}Nb_x)O_2$ with x=0.125, 0.25, 0.375 corresponding to 1, 2, and 3 atoms of Nb introduced in the unit cell, respectively.

For simulating fluorine doping, 5 atoms of oxygen were arbitrarily substituted with 5 fluorine atoms producing the formula unit of $(Mn_{0.75}Nb_{0.25})O_{1.375}F_{0.625}$-approximately corresponding to 10 wt.% of F content. These compositions have been selected for calculation of the bulk electronic structure utilized in this study. Similar to the previous study, the electronic properties of (110) surface of the materials have been studied by using a two-dimensional (2D) slab of ~7 Å of thickness which is repeated in [1,-1, 0] direction, containing 48 atom unit cell and a vacuum distance of ~ 13 Å between adjoining images[45]. To compute the free energies of all the elementary reactions, the co-ordinatively unsaturated sites (CUS) located at the (110) surface are employed as an active sites[102, 286]. All the transition metal sites are oxidized and covered by oxygen layer except CUS. The OER intermediate species (O*, OH*, and OOH*) were affixed to the top surface layer whereas three bottom layers of the slab were fixed with the lattice parameter associated to the bulk α-MnO_2[45].

In order to examine the electronic structures of pristine and Nb-doped MnO_2 compounds as well as to evaluate the influence of Mn and Nb on the overpotential of the $(Mn,Nb)O_2$, two different atomic positions of Nb as a replacement of Mn at the (110) surface are taken into account and marked as Pos.1 and Pos.2. The first Nb-containing atomic distribution is characterized by placing a Nb-atom at the position adjacent to CUS and is denoted as Pos.1, while the CUS itself locates above the Mn atom. The second distribution consists of a Nb-atom located in place of Mn just below the CUS and is denoted as Pos.2 shown in **Figure 7-1b and c**. Also, in order to introduce the F-doping in the electrocatalyst framework, one oxygen atom has been substituted for F atom at the oxygen site adjacent to the CUS at the top layer**.** The atomic distributions at the (110) surface enclosed by adsorbed oxygen monolayers along with the OER intermediate species are utilized to evaluate the free energies of all the four elementary reactions.

7.4 Experimental Methodology

7.4.1 Materials

Manganese (II) sulfate monohydrate ($MnSO_4.H_2O$, ≥ 99%, Sigma Aldrich), Potassium permanganate ($KMnO_4$, ≥ 99.0%, Fisher scientific), Niobium (V) chloride ($NbCl_5$, 99.95%, Alfa Aesar), and ammonium fluoride (NH_4F, 98%, Alfa Aesar) were utilized as precursors for synthesizing the electrocatalysts. Nafion 117 (5 wt. % solution in lower aliphatic alcohols, Sigma Aldrich) was utilized as the binder to prepare the electrocatalyst ink. Deionized (DI) water (18 MΩ cm, MilliQ Academic, Millipore) was used for the synthesis experiments.

7.4.2 Synthesis of α-MnO_2 Nanorods (NRs)

Nanorods of α-MnO_2 were synthesized by utilizing a hydrothermal approach[45]. Accordingly, $MnSO_4.H_2O$ (0.2 g) and $KMnO_4$ (0.5 g) were dissolved in a 100 mL D.I. water with a constant stirring for ~30 min at a room temperature to generate a homogeneous solution. The above solution was then transferred into a 120 ml Teflon-lined stainless-steel autoclave. The autoclave was heated at 160 °C for 12h with a ramp rate of 10°C min^{-1}. The autoclave was cooled to room temperature after reaction time of 12h. The generated solid product was then vigorously washed with D.I. water and absolute ethanol repeatedly (9500 rpm, 3 min), followed by drying in air at 60^{o}C before subjecting the product to further characterization.

7.4.3 Synthesis of $(Mn_{1-x}Nb_x)O_2$ and $(Mn_{1-x}Nb_x)O_2$: 10F (x =0, 0.1, 0.2 and 0.3)

Solid solutions of $(Mn_{1-x}Nb_x)O_2$ and $(Mn_{1-x}Nb_x)O_2$: 10F electrocatalyst samples with varying composition were then subsequently synthesized utilizing stoichiometric amounts of $NbCl_5$ and mixture of $NbCl_5$ + NH_4F, respectively in D.I. water along with stoichiometric amounts of the as-prepared MnO_2 NRs. The as-prepared solutions were sonicated for 1 h and transferred into alumina crucibles for drying in an electric oven at 60˚C for ~ 3 hours. The dried electrocatalyst samples were then calcined in air at 400˚C using a ramp rate of 10^{o}C min^{-1} for 4 hours. The thermally treated samples were thoroughly washed with D.I. water and ethanol followed by drying at 60^{o}C before subjecting to further characterizations. A schematic illustration of the steps used for synthesizing α-MnO_2 and $(Mn_{1-x}Nb_x)O_2$:10F NRs is depicted in **Figure 7-2**.

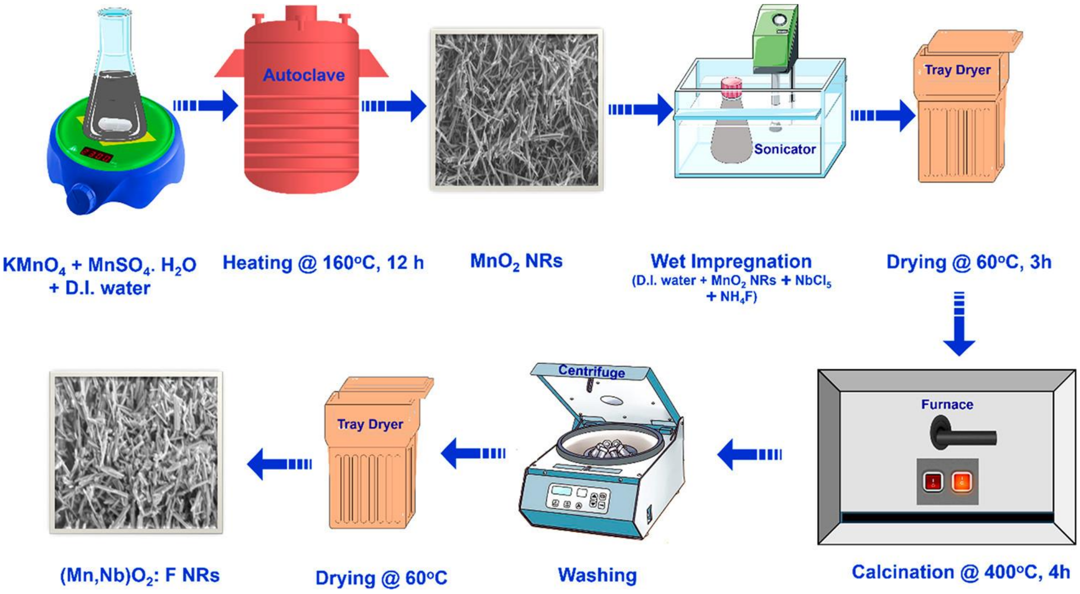

Figure 7-2 Schematic illustration of the synthesis process of $(Mn_{0.8}Nb_{0.2})O_2$:10F NRs

7.5 Results and Discussions

7.5.1 Results of the Computational Study

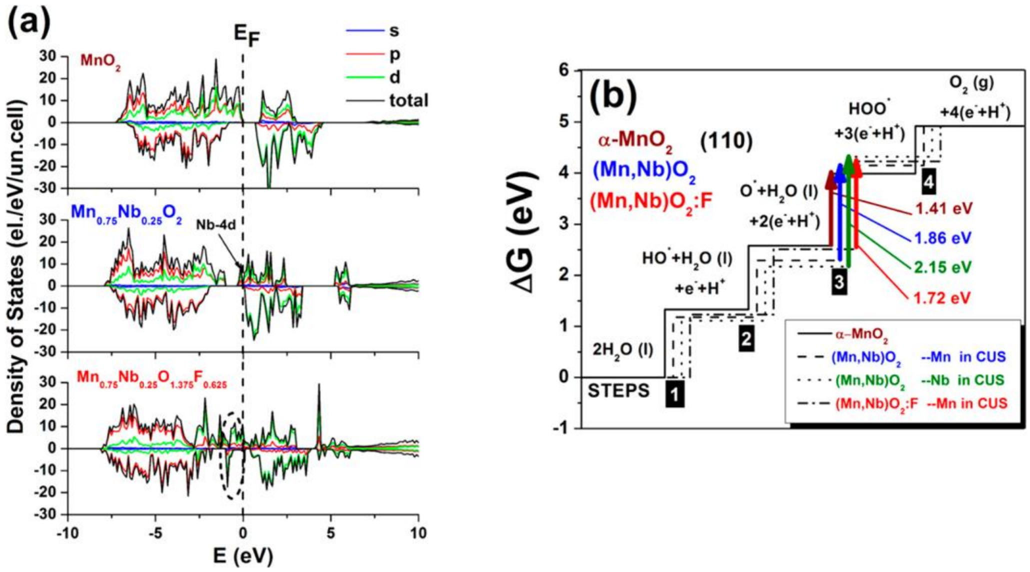

Figure 7-3 (a) Total and projected density of electronic states calculated for pure α-MnO_2, $(Mn_{0.75}Nb_{0.25})O_2$, and F-doped $(Mn_{0.75}Nb_{0.25})O_2$. Fermi level is set to zero, (b) free energies of the intermediate reactions for pure and doped α-MnO_2 with the same CUS at (110) surface

The electrocatalytic performance of virtually all electrocatalysts depends on its electronic structure, electronic conductivity, and the electrochemical stability of the electrocatalytically active surface of the material. Also, as the structural and electrochemical stability of the electrocatalyst is anticipated to qualitatively depend on the cohesive energy of the system, the influence of the electrocatalyst compositions on the electronic-catalytic properties and on the structural durability of the material cab be comprehended from the theoretical investigations in general, and also from the electronic structure, in particular. Accordingly, **Figure 7-3 (a)** displays the calculated total and projected density of electronic states (DOS) for all the materials considered in the present study. From **Figure 7-3 (a)**, it is clear that pure α-MnO_2 is a semiconductor with a band gap of ~0.9 eV which is in an good agreement with the computations reported by Tripkovic et al.[263]. It can be accordingly inferred that α-MnO_2 exhibiting poor electronic conductivity would not be an efficient electrocatalyst for water splitting and has been indeed validated by various OER studies reported.[278] However, introduction of Nb into the MnO_2 lattice changes the electronic structure shifting the Fermi level toward the conduction zone rendering the Nb-doped MnO_2 oxide electronically conductive. In fact, the beneficial influence of incorporating ionic species of high valence states (such as Nb^{+5}, Bi^{+5}) on improving the electronic conductivity of α-MnO_2 is well documented in various studies reported[285, 287].

An appearance of the Nb-4d electronic states within the band gap [as indicated by the black arrow in **Figure 7-3 (a)**] makes this material semi-metallic with a band gap of zero. Incorporation of F ion by suitable doping results in additional F-2p electronic states added into the vicinity of the Fermi level [denoted by the dashed circle in the bottom plot in **Figure 7-3 (a)**] contributing to further enhancing the conductivity and thus rendering the F-doped oxide ($Mn_{0.75}Nb_{0.25}O_{1.375}F_{0.625}$), a metallic conductor favorably impacting the overall electrocatalytic activity. Moreover, the introduction of F^- on the O^{2-} sites brings additional charge carriers into the system thus, further increasing the electronic conductivity. Furthermore, the simultaneous effect of Nb and F introduction on the lattice parameters is shown in **Table 7-1**.

Table 7-1 Computationally Calculated Lattice Parameters and Cohesive Energies (E_{coh}) for the Electrocatalyst Compositions Considered in the Present Computational Study

Electrocatalyst composition	Lattice parameters (Å)		Unit cell volume (Å^3)	Cohesive energy E_{coh} (eV/form.unit)
	a =b	c		
α-MnO_2	9.786	2.866	274.46	-15.61
$(Mn_{0.875}Nb_{0.125})O_2$	9.864	2.905	282.65	-16.29
$(Mn_{0.75}Nb_{0.25})O_2$	10.011	2.954	296.05	-16.97
$(Mn_{0.625}Nb_{0.375})O_2$	10.060	3.017	305.33	-17.65
$(Mn_{0.75}Nb_{0.25})O_{1.375}F_{0.625}$	10.110	3.00	306.63	-16.30

Table 7-1 also shows that the computationally calculated lattice parameters agree well with the experimental measurements tabulated in **Appendix C Table 1** thus, validating the conclusions of the present theoretical study. Another critical aspect characterizing the electrocatalytic activity, is the consideration of the four OER elementary steps as outlined in the computational methodology section. **Figure 7-3(b)** displays the effects of Nb and F doped α-MnO_2 on the overpotential of the $(Mn,Nb)O_2$:F. The free energies of the OER elementary steps are computed for α-MnO_2 and the three different configurations with the incorporation of Nb and F atoms as

discussed in the computational methodology illustrated in **Figure 7-1**. Moreover, some of the data used for generating these graphs are tabulated in **Table 7-2**.

Table 7-2 Computational data obtained from the present DFT study. Calculated Etot for H_2O and H_2 molecules are -14.28 eV and -6.82 eV, respectively

	E_{tot}^{slab} (eV)				**ΔZPE - TΔS (eV)**	**ΔG (eV)**			
Configurations	**Pure α-MnO_2**	**Nb @ Pos 1 no F**	**Nb @ Pos 2 no F**	**Nb @ Pos 1 with F**		**Pure α-MnO_2**	**α-$(Mn,Nb)O_2$ Nb at Pos.1 (Mn in CUS)**	**α-$(Mn,Nb)O_2$ Nb at Pos.2 (Nb in CUS)**	**α-$(Mn,Nb)O_2$:F Nb at Pos.1 (Mn in CUS)**
Vac+$2H_2O$	-365.82	-369.23	-368.75	-367.18	-	0	0	0	0
HO^*+H_2O+$1/2H_2$	-375.71	-379.27	-378.86	-377.17	0.35	1.33	1.18	1.11	1.23
O^*+H_2O+H_2	-370.75	-374.45	-373.99	-372.18	0.05	2.58	2.29	2.17	2.51
HOO^*+$3/2H_2$	-380.56	-383.81	-383.16	-381.68	0.40	3.99	4.15	4.32	4.23
Vac+O_2+$2H_2$	-365.82	-369.23	-368.75	-367.18	-	4.92	4.92	4.92	4.92
ΔG of Step 3 (eV) (Overpotential in V)						1.41 (0.18)	1.86 (0.63)	2.15 (0.92)	1.72 (0.49)

As is known, the most energetically crucial step for all the four systems is step III, which is the step contributing to hydroperoxide (HOO*) formation. This step controls the major OER overpotential required for water oxidation and is thus, appropriately considered as the rate-determining step (RDS). The OER overpotential for pure α-MnO_2 is 0.18 V (1.41-1.23). However, for $(Mn,Nb)O_2$ the overpotential is obtained as 0.63 V (1.86-1.23) and 0.92 V (2.15-1.23) for the two different positions of Mn considered in the unit cell. These results therefore suggest that the existence of Nb in MnO_2 increases the overpotential for OER as compared to the pure MnO_2 which can be ascribed to the weaker interaction between the surface and adsorbed oxygen (O^*). Such weaker interaction results in an increase in the total energy of the system in comparison to pure MnO_2[45]. This weaker interaction between O^* and the surface offers lower feasibility for the species to adsorb at the surface which results in the raise in an overpotential of the overall OER for the $(Mn,Nb)O_2$ electrocatalyst system. This result is indeed understandable since NbO_x is catalytically inactive for OER, and correspondingly, a replacement of Mn for Nb in the CUS or in its vicinity increases the overpotential, lowering the expected catalytic activity. It is nevertheless, noteworthy to see from **Figure 7-3 (b)** that an introduction of F into the $(Mn,Nb)O_2$ crystal lattice leads to a noticeable reduction in the overpotential up to 1.72-1.23 = 0.49 V, evincing and suggesting the reduced reaction barrier and thus, the expected improved electrocatalytic activity for OER[45] in comparison to that of the non-fluorinated $(Mn,Nb)O_2$. Furthermore, in the case of F-incorporation, due to the lower negative charge of F-ion (-1) as compared to O-ion (-2), charge conservation dictates that Nb-ion will be adjusting its own positive charge owing to its ability to assume different oxidation states making it less positive, which decreases the electrostatic interaction between the surface and adsorbed O^* in step 3 of OER pathway. This makes the surface less stable (with higher total energy) resulting in reduction in the overpotential and improvement in the overall electrocatalytic activity. As a result, the F-doped $(Mn_{0.75}Nb_{0.25})O_2$ shows a decrease in the reaction barrier (1.72 eV) and enhanced activity in comparison to that of $(Mn_{0.75}Nb_{0.25})O_2$ (1.86 eV). Such beneficial role of F incorporation and its detailed mechanism have been computationally studied and reported by our group wherein F-doped IrO_2 exhibited reduced reaction barrier and higher OER activity in comparison to that of pure IrO_2[102].

Based on these above results, it is concluded that among all the materials investigated in the present study (i.e., MnO_2 and Nb and F doped MnO_2), pure α-MnO_2 is anticipated to demonstrate the lowest overpotential for the OER. This result thus signifies that MnO_2 inherently possesses electrocatalytic characteristics indicative of its preferred catalytic ability to oxidize water very efficiently provided it were to possess good electronic conductivity accompanied by the desired electrochemical durability in acidic OER conditions. This hypothesis is indeed well supported by various MnO_2 based electrocatalyst studies reported in the literature[266, 267, 280]. The properties related to both the electrocatalytic activity as well as electrochemical stability are however, mediocre for α-MnO_2. Thus, it is imperative that its electronic conductivity and durability be improved by incorporating some appropriate acid stable dopant elements into the MnO_2 framework. Consequently, introduction of a small amount of Nb and F into the oxide lattice, as shown in the present study, certainly plays a vital role in increasing its activity and electrochemical stability.

The calculated cohesive energies serve as qualitative descriptors for the structural and electrochemical stability of the studied materials and are correspondingly collected and listed in **Table 7-1.** It can be seen that Nb-introduction into the α-MnO_2 lattice indeed increases the cohesive energy (making it more negative) of the solid solution electrocatalyst, which improves the overall electrochemical stability owing to the stronger Nb-O bonds (726 $kJmol^{-1}$) than that of the parent Mn-O (362 $kJmol^{-1}$)[179]. However, introduction of F into the substituted binary $(Mn,Nb)O_2$ oxide slightly decreases the cohesive energy, although maintaining it higher than that of pure MnO_2. This observation is indeed in rational agreement with our prior OER published report on fluorinated $(Sn,Nb,Ir)O_2$ system[98] wherein such reduction in the cohesive energy (absolute value) was ascribed to the weaker metal (M)-F^{-1} bonds compared to the corresponding

$M\text{-}O^{2-}$ lattice bonds. Thus, based on the present computational work, it is anticipated that the overall OER electrocatalytic performance of α-MnO_2 can be improved by adopting a doping strategy in which the introduction of Nb into the α-MnO_2 framework structure likely improves the electrochemical stability/conductivity. However, it may induce a reduction in the electrocatalytic activity via increase in the overpotential of the $(Mn,Nb)O_2$. Nevertheless, the incorporation of F on the oxygen sites could offset this reduction in the electrocatalytic activity. Correspondingly, the obtained theoretical results illustrate that the introduction of 10 wt. % F into $(Mn,Nb)O_2$ system can tune the electronic structure in a beneficial fashion offering enhancement in the electronic conductivity as well as causing a reduction in the overpotential for the rate determining step of OER.

In order to validate the results of these theoretical studies with the added objective of obtaining a clear understanding of the computational insights into the Nb and F incorporated systems, the corresponding oxides of 10 wt. % F-doped $(Mn_{1-x}Nb_x)O_2$:10F (x= 0-30 atom %) have been synthesized in the present study. At the same time, a systematic characterization of the physical and electrochemical characteristics is conducted. Accordingly, 10 wt. % F-doped $(Mn_{1-x}Nb_x)O_2$:10F (x= 0-30 atom %) nanorods (NRs) are synthesized and studied for their electrochemical response as acidic OER electrocatalysts.

7.5.2 Results of experimental study

7.5.2.1 Physical Characterization of Electrocatalysts

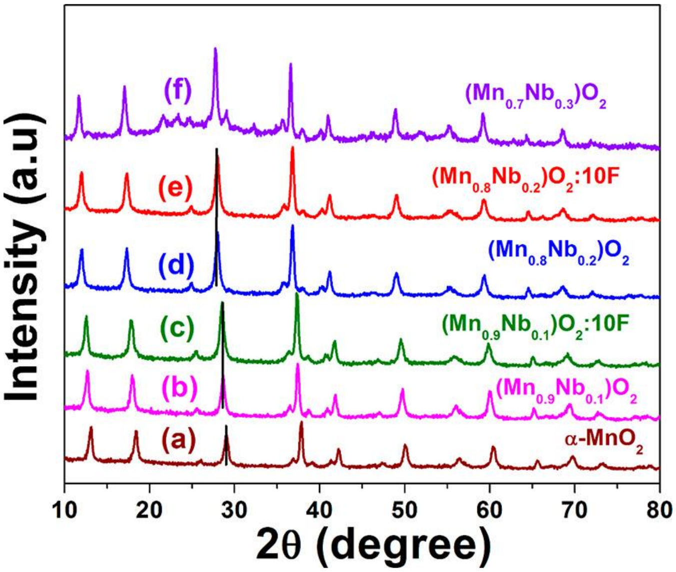

Figure 7-4 Powder XRD patterns of the as-synthesized electrocatalysts materials, (a) α-MnO_2, (b) $(Mn_{0.9}Nb_{0.1})O_2$, (c) $(Mn_{0.9}Nb_{0.1})O_2$:10F, (d) $(Mn_{0.8}Nb_{0.2})O_2$, (e) $(Mn_{0.8}Nb_{0.2})O_2$:10F, and (f) $(Mn_{0.7}Nb_{0.3})O_2$

The crystal structure and phase purity of the as-synthesized electrocatalysts with different compositions are examined via X-ray diffraction (XRD) analysis in the 2θ range of 10-80°. **Figure 7-4(a)** shows the powder XRD spectrum of α-MnO_2. The diffraction peaks of MnO_2 correspond to the tetragonal phase of α-MnO_2 [space group: I4/m (no. 87), JCPDS 44-0141] with the lattice constants a = 9.79 Å, c = 2.85 Å and unit cell volume of 273.15 Å^3 (**Appendix C Table 1**), which are in good agreement with the reported earlier studies[45]. This result indicates the formation of pure and crystalline α-MnO_2. Further, as can be viewed from **Figure 7-4 b, c, d, and e**, all the XRD pattern reflections of Nb as well as F doped $(Mn_{1-x}Nb_x)O_2$:10F (for x =0.1 and 0.2) electrocatalysts exhibit diffraction patterns analogous to the tetragonal structured pristine α-MnO_2. This indicates that the incorporation of substituents (Nb and F) into the α-MnO_2 framework does not cause any secondary phases of Mn or Nb or F based compounds, suggesting the formation of single-phase solid solution electrocatalysts. It is also noteworthy to mention that the careful inspection of XRD patterns of $(Mn_{1-x}Nb_x)O_2$:10F nevertheless revealed that XRD peaks of these solid solution electrocatalysts are slightly shifted towards the lower 2θ angle. Such negative shift in 2θ positions after Nb doping evidently suggests the lattice expansion of the electrocatalyst materials. Similar lattice expansion has been observed in various prior reported studies of Nb doped metal oxides.[288] This lattice expansion can be attributed to the incorporation of Nb^{+5}, which has higher ionic radius (~0.64 Å)[35] than the host element (Mn^{+4} = 0.54 Å)[219]. The increased lattice parameters and unit cell volumes of the doped electrocatalysts compositions are also tabulated in **Appendix C Table 1.**

It is important to note that F doped/un-doped electrocatalyst materials exhibit comparable lattice parameters and molar volume. These results suggest that the incorporation of F on O^{2-} sites has insignificant effect on the molar volume of $(Mn_{1-x}Nb_x)O_2$: 10F which can be ascribed to the comparable ionic radius of O^{2-} (1.25 Å) and F^- (1.20 Å).[97] This observation is also consistent with various F incorporated solid solution oxide electrocatalysts, as discussed in earlier reports[70, 97, 98]. Furthermore, the addition of higher Nb content (30 atom %) in the MnO_2 lattice results in the appearance of various additional peaks in the XRD pattern of $(Mn_{0.7}Nb_{0.3})O_2$. These additional peaks at 2θ of ~ 22.9, 24.42, 29.96, 54.19 etc. corresponding to the niobium oxide (Nb_xO_y) phases suggest that phase separation from the solid solution lattice occurs at ~30 atom % Nb addition into the α-MnO_2 lattice. Similar phase separation response in the XRD patterns related to the appearance of Nb oxide based secondary phases due to addition of higher Nb content in metal oxides (e.g. TiO_2, RuO_2) has been reported in earlier studies[277, 289]. Accordingly, the characteristics of these XRD patterns demonstrate that incorporation of Nb into the α-MnO_2 lattice up to ~ 20 atom % does not cause any changes to the crystal structure of α-MnO_2. This implies the retention of homogeneous solid solution (also confirmed by the EDX elemental mappings, discussed later) further suggesting that the optimum limit for Nb incorporation into the as-synthesized α-MnO_2 is ~20 atom %. Furthermore, it is observed from **Appendix C Figure 1** that the lattice parameters (a, c) and unit cell volume, respectively, demonstrate the quasi-linear relationship with increasing Nb content indicating the good agreement of Nb incorporation into the crystal lattice of MnO_2 with the well-known Vegard's law and consequently, suggesting the formation of substitutional solid solution (i.e. substitution of Mn by Nb atoms and substitution of O by F atoms) for the as-synthesized electrocatalysts, which is in accordance with the theoretical considerations[290].

The Brunauer-Emmett-Teller (BET) adsorption-desorption analysis has also been conducted to investigate the specific surface area (SSA) ($m^2\ g^{-1}$) of the as-synthesized materials. The BET specific surface area of α-MnO_2 powder is calculated to be ~ 3.70 $m^2\ g^{-1}$. Such low BET surface area values are commonly observed in various literature reports of 1D nanomaterials which are ascribed to the pronounced aggregation issues known in 1D nanomaterials. The as-synthesized $(Mn_{0.9}Nb_{0.1})O_2$, $(Mn_{0.9}Nb_{0.1})O_2$:10F, $(Mn_{0.8}Nb_{0.2})O_2$, $(Mn_{0.8}Nb_{0.2})O_2$:10F, and $(Mn_{0.7}Nb_{0.3})O_2$ materials also exhibit a BET surface area of ~4.32, 4.1, 6.0, 5.66, and 9.47 $m^2\ g^{-1}$ respectively. A slight increase in SSA with increase in Nb content in the α-MnO_2 framework is seen which is in good agreement with the various Nb doped materials (MnO_2, TiO_2, ZnO etc.) showing that incorporation of Nb contributes to increase in the specific surface area[289]. In addition, it can be seen that fluorination of the $(Mn_{1-x}Nb_x)O_2$ samples contributes to a slight decrease in the BET surface area values in comparison to that of the un-doped $(Mn_{1-x}Nb_x)O_2$. As elucidated in earlier reports, such small reduction in the BET surface area of fluorinated materials is accredited to the exothermic reaction accompanying the decomposition of the fluorine containing precursor (NH_4F), which may cause agglomeration of the catalyst particles during calcination of the F containing electrocatalysts[137].

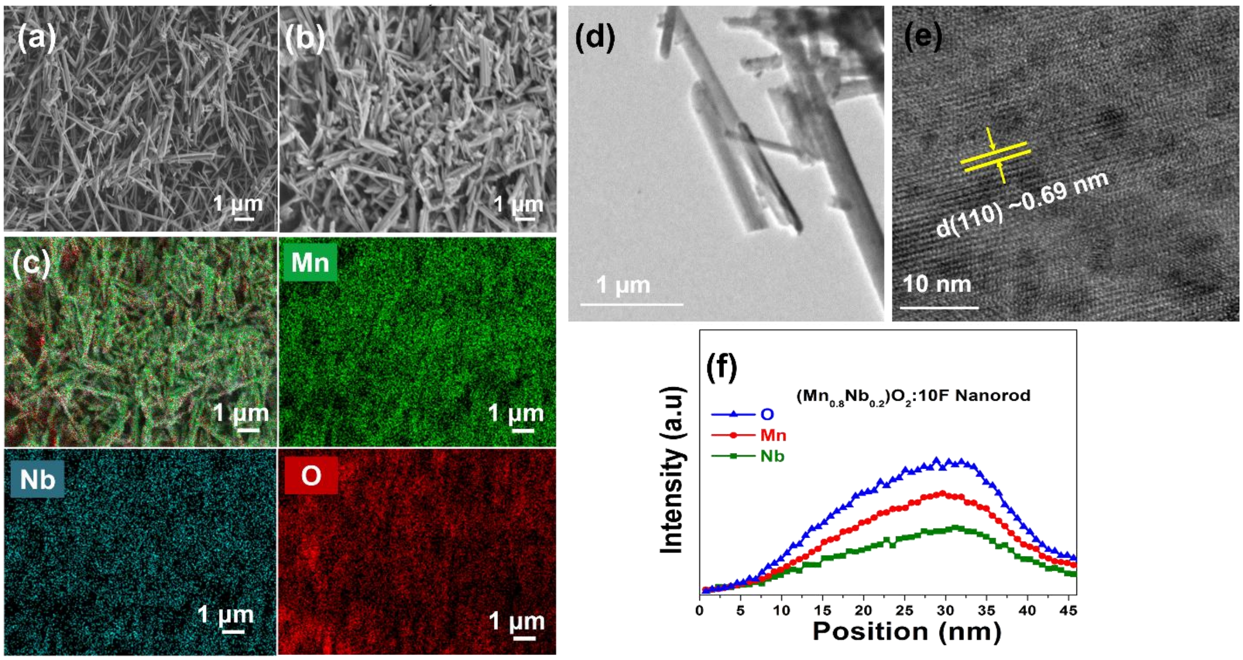

Figure 7-5 (a) SEM micrographs of the as-synthesized (a) α-MnO_2 NRs and (b) $(Mn_{0.8}Nb_{0.2})O_2$:10F NRs, (c) Elemental X-ray mapping of $(Mn_{0.8}Nb_{0.2})O_2$:10F NRs. (d) TEM image of as-synthesized $(Mn_{0.8}Nb_{0.2})O_2$:10F NRs, (e) HRTEM image of a representative $(Mn_{0.8}Nb_{0.2})O_2$:10F NR, highlighting lattice fringe of the 0.69 nm that corresponds to the (110) plane, and (f) Line scan analysis across a representative $(Mn_{0.8}Nb_{0.2})O_2$:10F NR

Scanning electron microscopy (SEM) images of the as-synthesized α-MnO_2 and $(Mn_{1-x}Ir_x)O_2$:10F (for x= 0.2, selected as a representative composition) are depicted in **Figure 7-5 a** and **b**, respectively. The SEM images of α-MnO_2 reveal the uniform one-dimensional (1D) rod shaped morphology with a diameter of ~ 40-50 nm and length ranging from ~0.5 to 3μm. As shown in **Figure 7-5 (b)**, the as-synthesized $(Mn_{0.8}Nb_{0.2})O_2$:10F NRs exhibits similar nanorod morphology with diameter and length comparable to that of MnO_2. These SEM images clearly suggest that the 1D nanorod architecture of the as-synthesized α-MnO_2 is well preserved after the simultaneous incorporation of Nb and F resulting in the formation of a homogeneous solid solution with MnO_2 during the synthesis process[45]. In addition, the energy dispersive X-ray spectroscopy (EDX) based elemental mapping images of $(Mn_{0.8}Nb_{0.2})O_2$:10F reveal the uniform and homogeneous distribution of the individual elements within the as-synthesized nanorods indicating absence of any undesired segregation of any of the elemental species at any specific region. Furthermore, the atomic ratio of Mn and Nb obtained from the quantitative elemental analysis is ~ 80.18: 19.82, in good agreement with the selected nominal composition (Mn:Nb = 80:20) as well as the results of ICP-OES (~ 80.13:19.87) and XPS analyses, discussed later. It is also noteworthy to mention that addition of higher Nb content into MnO_2 $[(Mn_{0.7}Nb_{0.3})O_2]$ displays dual morphologies of 1D nanorods as well as standalone (Nb) rich oxide particles (**Appendix C Figure 3**), indicating destruction of the desired 1D architecture. Accordingly, incorporation of 30-atom % Nb into the MnO_2 NRs demonstrate the destruction of solid solution which is in accordance with the secondary phase observed in the XRD analysis results. Transmission electron microscopy (TEM) is additionally performed to further investigate the morphology of the as-synthesized $(Mn_{0.8}Nb_{0.2})O_2$:10F NRs. As shown in **Figure 7-5(d)**, $(Mn_{0.8}Nb_{0.2})O_2$:10F electrocatalyst demonstrates the nanorod shaped morphology with a diameter of ~ 45 nm. The high-resolution transmission electron microscopy (HRTEM) image of $(Mn_{0.8}Nb_{0.2})O_2$:10F NR [**Figure 7-5(e)**] shows the well-resolved uniform lattice fringe spacing of ~0.69 nm, corresponding to the (110) crystallographic planes of $(Mn_{0.8}Nb_{0.2})O_2$:10F. In addition, the line scan analysis [**Figure 7-5(f)**] conducted across the width of the $(Mn_{0.8}Nb_{0.2})O_2$:10F NR reveals the uniform distribution of elements (Mn, Nb, O) in the as-synthesized nanorods. Herein, based on the geometrical data of $(Mn_{0.8}Nb_{0.2})O_2$ NRs, an approximate specific surface area (SSA) of $(Mn_{0.8}Nb_{0.2})O_2$ NRs is calculated. The approximate SSA of $(Mn_{0.8}Nb_{0.2})O_2$ NRs is obtained as ~20.65 m^2g^{-1}, which is on the same order of magnitude as that of measured by the BET surface area (~ 6 m^2g^{-1}).

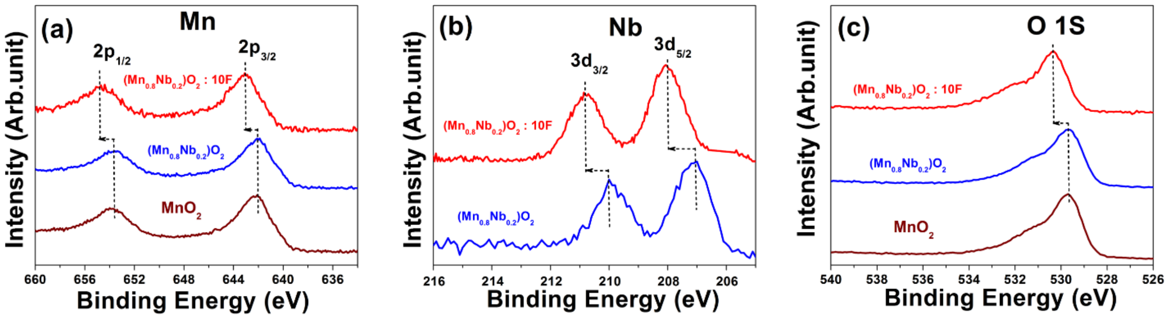

Figure 7-6 XPS spectra of (a) Mn 2p, (b) Nb 3d and (c) O1s for α -MnO_2, $(Mn_{0.8}Nb_{0.2})O_2$, and $(Mn_{0.8}Nb_{0.2})O_2$:10F NR electrocatalyst

X-ray photoelectron spectroscopy (XPS) analysis is conducted to investigate the electronic modulations and chemical valence states of the Mn, Nb and O in the as-synthesized electrocatalysts (**Figure 7-6**). The XPS spectra of Mn corresponding to α-MnO_2, $(Mn_{0.8}Nb_{0.2})O_2$, and $(Mn_{0.8}Nb_{0.2})O_2$:10F indicate the presence of Mn $2p_{3/2}$ and Mn $2p_{1/2}$ doublet. The Mn $2p_{3/2}$ and Mn

$2p_{1/2}$ peaks for pure MnO_2 and $(Mn_{0.8}Nb_{0.2})O_2$ reflect the binding energy of ~ 642 eV and ~ 653.8 eV, respectively, with a spin-energy separation of ~11.8 eV (comparable to previous reports).[70] However, it is interesting to note that the Mn $2p_{3/2}$ and Mn $2p_{1/2}$ doublet of the fluorinated $(Mn_{0.8}Nb_{0.2})O_2$:10F oxide reveal a positive shift of ~ 1 eV towards the higher binding energy values in comparison to that of the pristine α-MnO_2 and $(Mn_{0.8}Nb_{0.2})O_2$ **(Appendix C Table 2)**. Similar positive shifts in binding energy of F doped solid solution electrocatalysts systems are observed in various previously reported electrocatalysts studies[35, 70, 97]. These results thus clearly suggest the favorable binding of F in the solid solution $(Mn_{0.8}Nb_{0.2})O_2$:10F NRs reflecting the incorporation of F into the oxide lattice. The incorporation of F indeed modifies the electronic structure (details are in the computational results) of $(Mn_{0.8}Nb_{0.2})O_2$:10F as a result of the solid solution formation and stronger binding of F to Mn due to the higher electronegativity of F[70].

Another notable observation evident from **Figure 7-6(b)** is that the Nb 3d spectrum of $(Mn_{0.8}Nb_{0.2})O_2$ exhibits two peaks at 207 and 210 eV, representing the Nb $3d_{5/2}$ and Nb $3d_{3/2}$ electron spin states respectively, with a spin-orbit splitting of 3 eV which corresponds to that of XPS results of Nb_2O_5[284]. The incorporation of F results in a positive shift (~0.8 eV) in the binding energy values in comparison to that $(Mn_{0.8}Nb_{0.2})O_2$, in accordance with the XPS results of Mn as well as earlier reports[35, 70, 97]. Furthermore, based on the XPS analysis, the ratio of Mn:Nb in the electrocatalyst surface is found to be ~81:19, in good agreement with the nominal composition, suggesting the presence of Mn and Nb on the surface as well as in the bulk (**Appendix C Figure** 2) of the as-synthesized NRs. The O 1s spectra of pure MnO_2 and $(Mn_{0.8}Nb_{0.2})O_2$ demonstrate the dominant peak at ~ 529.8 eV, characteristic of metallic oxides. This result is in good agreement with O 1s electron binding energy for reported MnO_2 as well NbO_x[98]. In the case of $(Mn_{0.8}Nb_{0.2})O_2$:10F, a similar positive shift in the binding energy of O1s core level is observed with respect to that of $(Mn_{0.8}Nb_{0.2})O_2$. The above results are thus a clear reflection of the changes observed due to the incorporation of F into the oxide lattice serving as an indirect indicator of F incorporation into the oxide lattice. It is also worth mentioning as reported in previous reports that unequivocal identification of F in the $(Mn_{1-x}Nb_x)O_2$:10F cannot be directly determined by XPS and EDX analysis in agreement with the various F doped solid solution electrocatalyst systems reported[35, 70, 97, 98]. As elucidated in the above XPS discussions, the noticeable positive shifts in the binding energy values for Mn 2p, Nb 3d, and O1s are a clear reflection of the presence of fluorine in the as-synthesized $(Mn_{1-x}Nb_x)O_2$:10F due to the stronger binding arising from the higher electro-negativity of fluorine incorporated into the solid solution electrocatalyst lattice. However, the absence of F 1s XPS peak has been discussed by multiple researchers (Amanullah et al.[235], Datta et al.[97]) who have alluded this to the low concentration of F (or fluorine content below the detection limit of XPS [235]). Similar indirect observations confirming presence of fluorine either by XPS techniques or Auger electron spectroscopy (AES) are reported by other researchers[236].

7.5.2.2 Electrochemical Characterization of Electrocatalysts

In order to investigate the electrochemical reaction kinetics and the charge transfer resistance (R_{ct}) at the electrocatalyst/electrolyte interface, electrochemical impedance spectroscopy (EIS) analysis has been carried out at ~1.9 V (*vs* RHE) in the electrolyte solution of 1N H_2SO_4 at 40°C. As described in the electrochemical characterization section, based on the use of $R_s(R_{ct}Q_{dl})$ as the equivalent circuit model and from the diameter of the characteristic semi-circular arcs in the low frequency region of the EIS plots, the surface charge transfer resistance (R_{ct}) for the as-synthesized electrocatalysts was determined and tabulated in **Table 7-3**.

Table 7-3 Results of Electrochemical Characterization for OER of the as-synthesized Electrocatalysts.

Electrocatalyst Composition	**Charge transfer resistance R_{ct} (Ω cm^2)**	**Current density at ~1.9 V *vs* RHE (mA cm$^{-2}_{geo}$)**	**Overpotential η (mV) at 10 mA cm$^{-2}_{geo}$**	**Tafel slope (mV dec^{-1})**	**Mass activity at 1.9 V *vs* RHE (A g^{-1})**	**ECSA (m^2 g^{-1})**	**TOF at ~ 1.9 V *vs* RHE (S^{-1})**
MnO_2	38.2	2.2	900	480.86	7.33	9.23	0.0017
$(Mn_{0.9}Nb_{0.1})O_2$	33.3	3.2	870	478.12	10.66	12.57	0.0025
$(Mn_{0.9}Nb_{0.1})O_2$:10F	22.5	4	820	470.29	13.33	15.46	0.0029
$(Mn_{0.8}Nb_{0.2})O_2$	17.7	5.95	770	385.36	19.83	20.76	0.0049
$(Mn_{0.8}Nb_{0.2})O_2$:10F	11.8	8.7	680	371.17	29	26.28	0.0065
$(Mn_{0.7}Nb_{0.3})O_2$	44.3	1.8	--	483.45	6	7.52	0.0015

As shown in **Figure 7-7 (a)**, the as-synthesized MnO_2 NRs exhibit R_{ct} of ~ 38.2 Ω cm^2. The addition of 10 atom % Nb into MnO_2 exhibits a semicircle in the EIS plot with a smaller diameter, i.e. smaller R_{ct} (33.3 Ω cm^2) in comparison to that of pristine MnO_2, suggesting the improved electronic conductivity (due to substitution of Nb^{5+} at Mn^{4+} sites, providing free electrons[291], as also supported by the DFT results) of $(Mn_{0.9}Nb_{0.1})O_2$. For example, the recent study of Nb-doped MnO_2/reduced graphene oxide as an anode material for lithium-ion batteries has demonstrated ~1.35 fold reduction in the R_{ct}.[285] In another report, Nb doped perovskite $Ba_{0.5}Sr_{0.5}Co_{0.8}Fe_{0.2}O_{3-\delta}$ has revealed higher OER catalytic activity (~ 6 fold higher, at an overpotential of 0.35 V) than that of pure $Ba_{0.5}Sr_{0.5}Co_{0.8}Fe_{0.2}O_{3-\delta}$[292, 293]. The validation of such experimental results and conduction mechanism of Nb-doped α-MnO_2 has also been exclusively elucidated in the recent computational work conducted by Tripkovic et al.[263].

The R_{ct} value of $(Mn_{0.9}Nb_{0.1})O_2$ is further significantly decreased to ~22.5 Ω cm^2 for the fluorinated $(Mn_{0.9}Nb_{0.1})O_2$:10F electrocatalyst, which evidently corroborates further enhancement of electronic conductivity (as detailed in the present theoretical studies). As is further evident from **Figure 7-7 (a),** the addition of 20 atom % Nb into the MnO_2 systems results in further reduction in the R_{ct} values i.e. $(Mn_{0.8}Nb_{0.2})O_2$ and $(Mn_{0.8}Nb_{0.2})O_2$:10F systems exhibit an R_{ct} of ~17.7 Ω cm^2 and ~11.8 Ω cm^2, respectively.

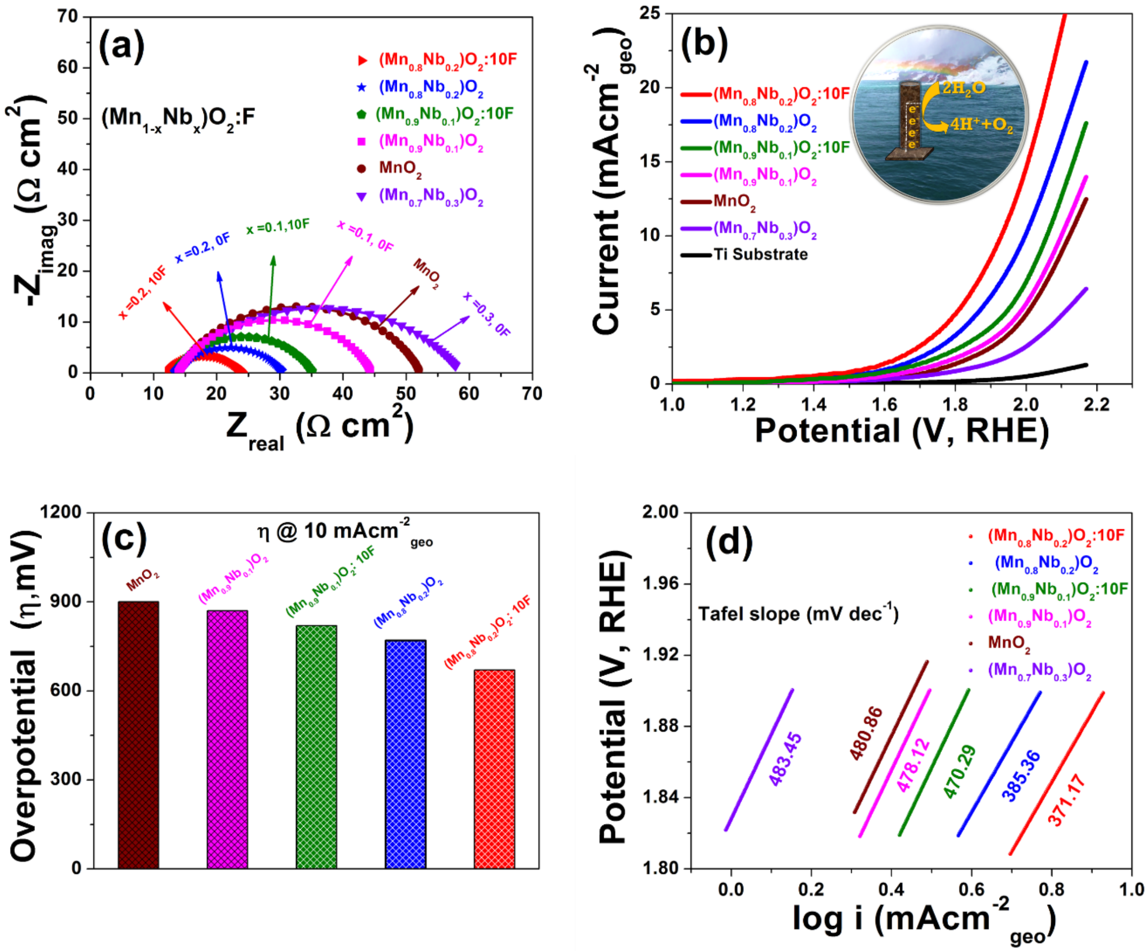

Figure 7-7 Comparison of the electrochemical performances of the as-synthesized electrocatalysts measured in a 1 N H_2SO_4 electrolyte at 40 °C (a) EIS plots performed at ~1.9 V (*vs* RHE), (b) OER polarization curves with a scan rate of 10 mV s^{-1}, (c) overpotential required to attain current density of 10 mA cm^{-2}_{geo}, and (d) Tafel plots

This suggests the further improvements in the charge transfer kinetics. However, incorporation of higher Nb content, i.e. $(Mn_{0.7}Nb_{0.3})O_2$ results in substantial increase in the diameter of the semicircle reflecting a higher R_{ct} of ~ 44.3 Ω cm^2. This increase in the charge transfer resistance is clearly a reflection of the deterioration of the electronic conductivity of $(Mn_{0.7}Nb_{0.3})O_2$ due to phase separation. As discussed in the XRD results, phase separation and destruction of the solid solution with presence of undesired secondary phases of NbO_x at 30 atom % Nb containing the MnO_2 primarily contributes to the reduction in the charge transfer kinetics and thus, electronic conductivity of $(Mn_{0.7}Nb_{0.3})O_2$. Similar trends regarding the electronic conductivity are detailed in previously reported studies on Nb-doped TiO_2, wherein the electrocatalytic conductivity is known to decrease once phase separation is initiated upon the addition of higher Nb contents[291, 294]. In this context, Yue et al.[294] reports that the higher Nb doping levels in the TiO_2 results in a decrease in the ionization efficiency along with reduction in the electron mobility (i.e. trapping of electrons at Ti^{4+}). Thus, in the case of $(Mn_{0.7}Nb_{0.3})O_2$, similar electron trapping mechanism (at Mn^{4+} sites) could occur, attributing to the reduction in the charge transfer kinetics and thus, suggesting a decline in the electrocatalytic activity. In addition, in the study conducted by Puthiyapura et al., it has been report that the standalone presence of dopant particles (such as Nb, Ta etc.) in the active catalyst material may restrict the electron conduction paths, resulting in reduction in the electrocatalytic conductivity (i.e. increase in the charge transfer resistance) of the electrocatalyst material[277]. Also, it is observed that such issue of conductivity reduction is generally more severe if two or more components do not form a complete solid solution resulting in mixed phases[277]. Therefore, the as-performed EIS results collectively suggest that 20 atom % Nb containing the MnO_2 systems i.e. $(Mn_{0.8}Nb_{0.2})O_2$ and $(Mn_{0.8}Nb_{0.2})O_2$:10F possess optimum charge transfer kinetics contributing to faster electron transfer, lower activation polarization, and correspondingly better OER kinetics than the other as-synthesized electrocatalyst counterparts.

The OER electrocatalytic activity of the as-synthesized electrocatalysts supported on Ti substrate is investigated by conducting linear sweep voltammetry (LSV) at a scan rate of 10 mV s^{-1} in 1N H_2SO_4 at 40°C. As indicated in **Figure 7-7 (b)** , the bare Ti substrate exhibits negligible catalytic activity, similar to the earlier report for acidic OER.[273] The polarization curve of α-MnO_2 NRs shows the current density of ~2.2 mA cm^{-2}_{geo} measured at ~1.9 V *vs* RHE which is in good agreement with the prior OER studies on MnO_2 in acidic media[266, 278]. As shown in **Figure 7-7 (a),** the 10 atom % Nb doped MnO_2 electrocatalyst composition [$(Mn_{0.9}Nb_{0.1})O_2$] exhibits improved electrochemical activity in comparison to that of un-doped MnO_2. As evidenced from the EIS results, the 10 atom % Nb doped MnO_2 [$(Mn_{0.9}Nb_{0.1})O_2$] shows the lower R_{ct} than that of pristine MnO_2 and thus, offering a higher current density of ~3.2 mA cm^{-2}_{geo} than that of MnO_2 at ~1.9 V (**Table 7-3**) . In agreement with the EIS results as well as the DFT study results, F incorporated $(Mn_{0.9}Nb_{0.1})O_2$:10F electrocatalyst display a higher current density(~4 mA cm^{-2}_{geo} at ~1.9 V) in comparison to the non-fluorine containing $(Mn_{0.9}Nb_{0.1})O_2$, suggesting the enhanced conductivity (i.e. lower R_{ct}), owing to the improved electronic structure of F doped $(Mn_{0.9}Nb_{0.1})O_2$:10F NRs. Furthermore, introduction of 20 atom % Nb into α-MnO_2 NRs demonstrate the better catalytic activity with the current density of ~5.95 mA cm^{-2}_{geo} and ~8.7 mA cm^{-2}_{geo} at ~1.9 V for the $(Mn_{0.8}Nb_{0.2})O_2$ and $(Mn_{0.8}Nb_{0.2})O_2$:10F systems, respectively. This improved electrocatalytic activity revealed by the F-doped oxide containing 20 atom % Nb is credited to the reduced charge transfer resistance as well as beneficial influence of introduction of F in the solid solution electrocatalysts as described in detail in the theoretical study. It is also noteworthy to mention that further addition of Nb (30 atom %) drastically lowered the catalytic activity, exhibiting significantly lower current density of ~1.8 mA cm^{-2}_{geo} at ~1.9 V. Such decline in the catalytic activity of $(Mn_{0.7}Nb_{0.3})O_2$ is indeed attributed to the destruction of the solid solution and consequent phase separation (as witnessed from the XRD results), leading to considerably higher charge transfer resistance (~44.3 Ω cm^2). Therefore, herein, the electrocatalyst composition with 20 atom % Nb content [$(Mn_{0.8}Nb_{0.2})O_2$:10F] is considered optimal for achieving the good acidic

OER electrochemical response. Furthermore, it is evident from **Figure 7-7(c)** that $(Mn_{0.8}Nb_{0.2})O_2$:10F NRs deliver the benchmark current density of 10 mA cm^{-2}_{geo} at an overpotential of ~ 680 mV (w.r.t. the equilibrium OER potential, 1.23 V *vs* RHE). This result clearly indicates that the NRs of composition, $(Mn_{0.8}Nb_{0.2})O_2$:10F outperforms the other compositions of $(Mn_{0.9}Nb_{0.1})O_2$, $(Mn_{0.9}Nb_{0.1})O_2$:10F, $(Mn_{0.8}Nb_{0.2})O_2$, and MnO_2 NRs which demand a higher overpotential of ~ 870 mV, ~820 mV, ~ 770 mV, and ~900 mV, respectively, to attain the current density of 10 mA cm^{-2}_{geo}.

Figure 7-7(d) shows the fitted Tafel plots for the as-synthesized electrocatalysts. The lower Tafel slope of $(Mn_{0.8}Nb_{0.2})O_2$:10F NRs (~371.17 $mVdec^{-1}$) in comparison to that of the other compositions is indicative of the relatively favorable OER kinetics of this particular optimal composition suggesting the faster electron transport and consequently, enhanced electrocatalytic activity. Furthermore, in order to assess the intrinsic catalytic activity of the as-synthesized materials, various parameters such as mass activity, turnover frequency (TOF), and BET normalized current density (mA cm^{-2}_{BET}) are calculated. Accordingly, as shown in **Figure 7-8(a)**, $(Mn_{0.8}Nb_{0.2})O_2$:10F NRs exhibit a TOF of ~ 0.0065 s^{-1} which is considerably higher than that of $(Mn_{0.9}Nb_{0.1})O_2$ (0.0025 s^{-1}), $(Mn_{0.9}Nb_{0.1})O_2$:10F (0.0029 s^{-1}), $(Mn_{0.8}Nb_{0.2})O_2$ (0.0049 s^{-1}), $(Mn_{0.7}Nb_{0.3})O_2$ (0.0015 s^{-1}), and MnO_2 NRs (0.0017 s^{-1}). Such relatively higher TOF values as well as mass activity (~29 A g^{-1}) clearly reflect the higher intrinsic OER electrocatalytic activity of NRs of $(Mn_{0.8}Nb_{0.2})O_2$:10F solid solution composition. Furthermore, the higher BET surface area normalized current density of $(Mn_{0.8}Nb_{0.2})O_2$:10F NRs (~ 0.51 mA cm^{-2}_{BET}) in comparison to other compositions further accentuates its higher intrinsic catalytic activity (**Appendix C Table 3**). This higher activity is indeed a characteristic indicator of the enhanced OER kinetics of the NRs of this particular composition of $(Mn_{0.8}Nb_{0.2})O_2$:10F i.e. lower R_{ct} (i.e. facile electron transport along the 1D NRs) as well as advantageous electronic structure amendment attained upon simultaneous incorporation of Nb and F into the solid solution.

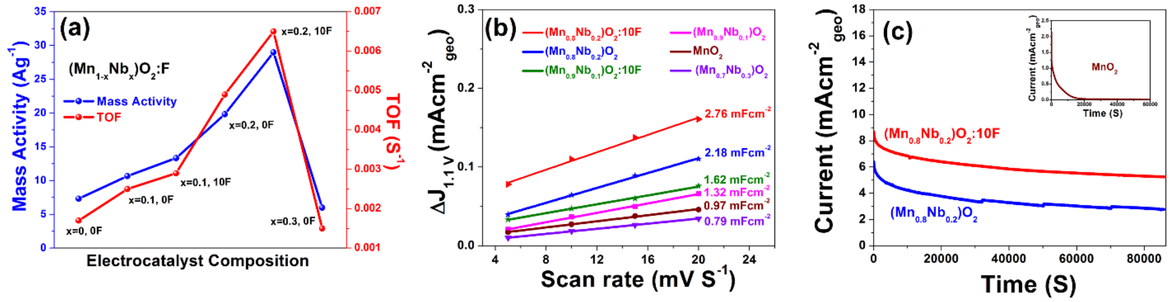

Figure 7-8 (a) Mass activity (A g^{-1}) and turnover frequency (S^{-1}) obtained at 1.9 V (vs RHE), (b) capacitive current ($\Delta J = J_a - J_c$) vs different scan rates of the as-prepared electrodes of the NRs and the corresponding double- layer capacitance (C_{dl}), and (c) chronoamperometric response of NRs of α-MnO_2, $(Mn_{0.8}Nb_{0.2})O_2$ and $(Mn_{0.8}Nb_{0.2})O_2$:10F at 1.9 V (vs RHE)

Furthermore, in order to obtain deeper insights into the OER electrocatalytic activity, the characteristic electrochemically active surface area (ECSA) of the as-synthesized materials is evaluated. Cyclic voltammetry (CV) curve of the electrodes collected in the non-faradic region with different scan rates. Correlation between the different scan rates and the currents values (obtained from difference between the anodic and cathodic currents at 1.1V) of different electrocatalyst composition are shown in **Figure 7-8(b)**. It can be seen from **Figure 7-8(b)** that, $(Mn_{0.8}Nb_{0.2})O_2$:10F NRs demonstrate a higher slope and thus, a higher double layer capacitance (C_{dl} = Slope/2 = 2.76 mF cm^{-2}) in comparison to that of $(Mn_{0.9}Nb_{0.1})O_2$ (1.32 mF cm^{-2}),

$(Mn_{0.9}Nb_{0.1})O_2$:10F (1.62 mF cm^{-2}), $(Mn_{0.8}Nb_{0.2})O_2$ (2.18 mF cm^{-2}), MnO_2 (0.97 mF cm^{-2}), and $(Mn_{0.7}Nb_{0.3})O_2$ (0.79 mF cm^{-2}). Accordingly, a higher ECSA of $(Mn_{0.8}Nb_{0.2})O_2$:10F NRs (26.28 m^2 g^{-1}) is clearly a reflective of the improved intrinsic catalytic activity of the $(Mn_{0.8}Nb_{0.2})O_2$:10F solid solution composition and thereby, enhanced OER activity.

Durability of the as-synthesized MnO_2 and $(Mn_{1-x}Nb_x)O_2$:F (x=0.2) NRs is investigated by conducting the time-dependent current density (I-t) i.e. chronoamperometry (CA) tests, performed at the constant potential of 1.9 V (*vs.* RHE) in 1N H_2SO_4 at 40°C. As shown in the inset of **Figure 7-8(c)**, the CA curve for α-MnO_2 NRs demonstrates a lower electrochemical stability under acidic OER test conditions, which is in good agreement with the earlier reports wherein MnO_2 exhibited rapid decay in the electrocatalytic stability[125, 278]. In contrast, as anticipated from the theoretical predictions and DFT results (discussed earlier in the section on Computational studies), the Nb and F containing $(Mn_{0.8}Nb_{0.2})O_2$ and $(Mn_{0.8}Nb_{0.2})O_2$:10F NRs demonstrate higher electrochemical stability, indicating a lower current attenuation in comparison to that of α-MnO_2NRs. These chronoamperometry test results thus suggest that the interactions between the dopants (Nb as well as F) and the active component (MnO_2) can effectively prevent degradation of the system contributing to the overall electrochemical stability of the electrocatalyst during the electrolysis process. These stability results are indeed substantiated by the computational studies herein, in which Nb and F containing MnO_2 demonstrate higher cohesive energy (absolute value) [$(Mn_{0.75}Nb_{0.25})O_2$: -16.97 eV/form. unit and $(Mn_{0.75}Nb_{0.25})O_{1.375}F_{0.625}$: -16.30 eV/form. unit] than that of pristine MnO_2 (-15.61 eV/form. unit), signifying the enhanced stability of $(Mn_{0.8}Nb_{0.2})O_2$ and $(Mn_{0.8}Nb_{0.2})O_2$:10F electrocatalyst systems. As discussed earlier in the computational results, the improved stability and cohesive energy can be attributed to the stronger bond dissociation energy for Nb-O bonds (726.5 kJ mol^{-1}) in comparison to that of Mn-O (362 kJ mol^{-1})[179]. Also, it is noteworthy to highlight that a similar cohesive energy based mechanism can be correlated to the various Mn-oxide based acid stable OER electrocatalyst systems such as Mn-Ti-O[266], Mn-Sb-O[280], Mn-Co-O[269], and Mn-Ir-O[45] wherein Ti-O (665.5 kJ mol^{-1}), Sb-O (434 kJ mol^{-1}), Co-O (397.4 kJ mol^{-1}), and Ir-O (414 kJ mol^{-1}) bonds demonstrate higher bond energies[179] compared to the pure Mn-O (362 kJ mol^{-1}) bonds present in MnO_2.

Additionally, the beneficial effect of F on the electrocatalytic stability of the electrocatalysts has been widely investigated in the literature. For example, in the study conducted by Geiger et al.[178], they demonstrate that fluorine doped tin oxide (FTO) shows the best OER stability in acidic electrolyte in comparison to antimony and indium doped tin oxide and thus, they suggest F as a promising anionic dopant for acidic OER. In another theoretical study performed by Binninger et al.[181], they report that the oxygen anion-free salts containing anionic species with a very high oxidation potential such as fluorides, chlorides, or sulfates are potential OER electrocatalyst candidates for demonstrating truly thermodynamically stable OER electrocatalytic activity. Furthermore, ICP-OES analysis conducted on the electrolyte solutions collected after the stability test **(Appendix C Table 5)** illustrate the lower dissolution of Mn and Nb for the $(Mn_{0.8}Nb_{0.2})O_2$ and $(Mn_{0.8}Nb_{0.2})O_2$:10F NRs, which further suggests the beneficial anchoring/stabilizing effect of simultaneous incorporation of Nb and F into the MnO_2 NRs.

Further studies into the structural stability of $(Mn_{0.8}Nb_{0.2})O_2$:10F NRs are conducted by characterizing the solid solution electrocatalyst subsequent to the durability tests. The XRD patterns of $(Mn_{0.8}Nb_{0.2})O_2$:10F NRs before and after the stability test are depicted in **Appendix C Figure 5.** As seen in **Appendix C Figure 5**, the XRD patterns of the solid solution, $(Mn_{0.8}Nb_{0.2})O_2$:10F post-stability analysis did not demonstrate any significant change in the XRD peak positions, suggesting that the crystalline phase of $(Mn_{0.8}Nb_{0.2})O_2$:10F is well maintained and there is no presence of any crystallographic phase transformations occurring during OER. Additionally, it is important to note that, as shown in inset of **Figure 7-8(c)**, MnO_2 exhibited poor acidic OER stability and higher electrocatalytic dissolution, in good agreement with the previous reports. Thus, as can be seen from the SEM images of post-stability MnO_2/Ti electrode (**Appendix C Figure 6)** following exposure to OER conditions, the MnO_2/Ti electrode did not show any significant and noticeable amount of MnO_2 nanorods present on the Ti substrate, suggesting its high dissolution in acidic OER. On the other hand, the SEM images of stable $(Mn_{0.8}Nb_{0.2})O_2$:10F/Ti electrode following OER stability tests (post-stability) **(**Appendix C Figure 7) reveal the existence of 1D nanorod architecture, similar to the pristine $(Mn_{0.8}Nb_{0.2})O_2$:10F NRs, before undergoing the OER stability tests (pre-stability) indicating no substantial change or deterioration of the morphology and composition (Mn:Nb ~ 80.02: 19.98) of this electrocatalyst following the electrochemical stability test. In addition, the TEM and HRTEM images of $(Mn_{0.8}Nb_{0.2})O_2$:10F/Ti electrode following the OER stability (post-stability) clearly show the retention of 1D nanorod architecture and no deterioration in the nanorods motifs, indicating the robust nature of the $(Mn_{0.8}Nb_{0.2})O_2$:10F NRs.

Furthermore, in order to gain deeper insights into any surface induced chemical changes occurring in the solid solution electrode, $(Mn_{0.8}Nb_{0.2})O_2$:10F during the acidic OER conditions, XPS studies have been again (**Appendix C Figure 8**) conducted the post stability tests. The XPS results indeed reveal the presence of Mn, Nb, and O with some noteworthy changes in the binding energy values. The XPS spectrum of Mn (after OER) demonstrates a negative shift (lower binding energy) in the XPS peak positions when compared to that of the XPS spectrum of Mn (before stability test). Such lower binding energy shifts in the case of Mn2p indicate the changes in the electronic structural environment occurring during the OER conditions and further suggests the formation of manganese (III) oxyhydroxide (MnOOH) similar to published reports.[254] Such advantageous surface modification (i.e. formation of meta-stable OER active Mn^{+3} ions) and surface electron reorganization during the OER process is reported to greatly stimulate the OER kinetics during acidic OER[255]. Similar XPS behavior regarding XPS spectrum of Nb (after OER) are observed, wherein the $(Mn_{0.8}Nb_{0.2})O_2$:10F electrode post stability analysis show the negative shifts in the binding energies for the Nb $3d_{5/2}$ and Nb $3d_{3/2}$. These shifts once again suggest the formation of protonated niobium hydroxide, which is well-known to form at a high potential and in a highly acidic environment.[295] Furthermore, as shown in the XPS spectrum of O 1s collected on the $(Mn_{0.8}Nb_{0.2})O_2$:10F NRs post stability test, in addition to the peak at ~530.8 eV, two more peaks are detected. The dominant peak at ~532.8 eV is attributed to the hydroxide formation during OER i.e. adsorption of OH^- on the electrocatalyst surface, similar to the previous OER studies and thus, substantiating the observations of surface hydroxide formation in Mn and Nb XPS spectra[232]. Another peak observed at the higher binding energy value of ~ 535 eV corresponds to the Nafion 117[296], which is utilized as a binder during the preparation of the electrocatalyst ink. In addition, as can be seen from **Appendix C Figure 9,** the $(Mn_{0.8}Nb_{0.2})O_2$:10F electrocatalyst prior to being exposed to OER conditions (pre-OER) exhibits the magnitude of spin energy separation (ΔS) of ~ 4.60 eV, which is in good agreement with the spin energy separation of MnO_2[297]. Interestingly, for $(Mn_{0.8}Nb_{0.2})O_2$:10F, following exposure to OER conditions (post-OER) the higher ΔS value of ~5.54 eV is observed, clearly indicating the formation of MnOOH (Mn^{3+}) species, similar to the previous studies[297]. Therefore, the observed change in the ΔS values for the electrocatalyst evidently before and after the OER stability tests suggests the beneficial electronic modulations occurring on the $(Mn_{0.8}Nb_{0.2})O_2$:10F electrode during OER, which is responsible for the observed good electrochemical stability and activity enabling facile acidic OER kinetics.

Furthermore, the post stability polarization and impedance results (**Appendix C Figure 10**) of $(Mn_{0.8}Nb_{0.2})O_2$:10F electrode demonstrated a slight decrease in the current density and increase in the charge transfer resistance in comparison to the electrode tested prior to the stability test. Specifically, in order to attain the current density of 10 mA cm^{-2}_{geo}, post stability $(Mn_{0.8}Nb_{0.2})O_2$:10F electrode required an overpotential of ~755 mV which is ~ 75 mV (or ~11%) higher than the $(Mn_{0.8}Nb_{0.2})O_2$:10F electrode tested prior to the stability test. In addition, the post stability $(Mn_{0.8}Nb_{0.2})O_2$:10F electrode exhibited ~ 31% and ~22% increase in the R_{ct} and Tafel slope (**Appendix C Table 6**), respectively in comparison with freshly prepared electrode, suggesting the slight decline in the electrocatalytic activity.

It should be noted that such electrocatalytic activity degradation, especially for PGM-free electrocatalysts is quite commonly observed and are typically higher than the state-of-the art OER electrocatalysts for PEM water electrolyzer, necessitating the use of higher than normal loadings seen in PGM based electrocatalysts[298]. The inexpensive nature of the earth abundant electrocatalyst composition could certainly alleviate the costs associated with the large loadings. This does not preclude the extensive research efforts that are currently ongoing both in our laboratory and elsewhere focused on understanding the catalyst degradation mechanisms by monitoring physicochemical changes occurring during OER. According to Strasser and co-workers[298], common mechanisms such as passivation, agglomeration, catalyst consumption (dissolution), blocking by oxygen bubbles, alteration in surface electronic environments (i.e. presence of intermediate species) etc. are generally accountable for change in the electrochemical activity-stability of electrocatalysts[299]. Based on the experimental approaches and DFT-based calculations, Strasser and co-workers[298] suggest that various strategies to mitigate the electrocatalyst degradation can be utilized which include introduction of 10-20 atomic % iridium (Ir) as has been evidently demonstrated by our previous reports[45, 70, 94]. Similarly, acid stable alternative support/backing electrodes such as $SnTa_2O_6$, $Sn_2Ta_2O_7$, and $Sn_2Nb_2O_7$ can be explored.[300] Also, altering the synthesis parameters such as temperature, atmosphere, precursors, use of chemical additives, binders, as well as other PGM-free dopants that are more stable under acidic conditions, etc. can be investigated to mitigate electrocatalytic degradation. Accordingly, the above points will be taken into consideration for the design of active and durable electrocatalyst materials in the near future. In summary, a new PGM-free system based on α-MnO_2 has been outlined and the results indeed demonstrate the viability of this PGM-free system involving modification of the α-MnO_2 structure and in particular, the use of NR morphologies serving to indeed validate the OER kinetics of Nb and F incorporated oxide solid solution composition, $(Mn_{0.8}Nb_{0.2})O_2$:10F in agreement with the theoretical DFT predictions.

7.6 Conclusions

In summary, the DFT calculations in tandem with the corresponding experimental validation suggest that the introduction of Nb and F into the solid solution of α-MnO_2 nanorods (NRs), in particular, $(Mn_{0.8}Nb_{0.2})O_2$:10F NRs demonstrate the higher electrocatalytic performance compared to the parent α-MnO_2 system. The favorable electronic structure as well as reduced charge transfer resistance of the as-generated solid solution electrocatalyst with optimum composition of $(Mn_{0.8}Nb_{0.2})O_2$:10F NRs contributes to significant improvement in the electrochemical activity and stability in comparison to pristine MnO_2 NRs. Specifically, $(Mn_{0.8}Nb_{0.2})O_2$:10F NRs exhibits a low Tafel slope (~371.17 mV dec^{-1}) and lower overpotential (~0.68 V) for OER to achieve the benchmark current density of 10 mA cm$^{-2}_{geo}$. Moreover, the solid solution composition of $(Mn_{0.8}Nb_{0.2})O_2$:10F generated in the nanorod (NR) morphology exhibits a higher mass activity (~29 A g^{-1}), larger electrochemically active surface area (ECSA ~26.28 m^2 g^{-1}), and higher turnover frequency (TOF~0.0065 s^{-1}) than other as-synthesized electrocatalyst counterparts. Additionally, the $(Mn_{0.8}Nb_{0.2})O_2$:10F NR composition exhibits a higher BET and ECSA normalized activity (0.51 mA cm^{-2}_{BET} and 0.11 mA cm^{-2}_{ECSA}) in comparison to that of $(Mn_{1-x}Nb_x)O_2$:10F (x= 0, 0.1, 0.3) compositions, at 1.9 V (*vs* RHE) which indeed demonstrate the higher intrinsic activity of $(Mn_{0.8}Nb_{0.2})O_2$:10F. The solid solution NRs of composition $(Mn_{0.8}Nb_{0.2})O_2$:10F also exhibit good electrochemical stability towards acidic OER, validating the cohesive energy results determined by the theoretical studied conducted herein. Based on the currently performed DFT results, the present study exhibits the intrinsic capability of MnO_2 to stimulate the OER reaction if it could be transformed to display high electronic conductivity combined with the required chemical stability under the conditions conducive for acidic OER. In the present work, in order to exploit the intrinsic OER activity of MnO_2, chemical stability as well as electronic conductivity enhancement is achieved via simultaneous incorporation of Nb and F into the α-MnO_2 framework. Consequently, the present work demonstrates the reliability of 1D $(Mn,Nb)O_2$:10F nanorod based electrocatalyst for acidic OER.

8.0 Specific Aim 1A - To Identify and Engineer Reduced PGM Containing and PGM-Free Multi-Metal Oxide (MMO) Based Electrocatalyst Materials of Different Architectures for Oxygen Evolution Reaction (OER) in Proton Exchange Membrane-Based Water Electrolysis (PEMWE)

This aim describes the fifth OER electrocatalyst focused on the PGM-free system.

- Chapter 8: $Cu_{1.5}Mn_{1.5}O_4$ and fluorine substituted $Cu_{1.5}Mn_{1.5}O_4$:F electrocatalysts for OER

Excerpts reprinted with permission from Ghadge, Shrinath Dattatray, et al. "Influence of Defects on Activity-Stability of $Cu_{1.5}Mn_{1.5}O_4$ for Acid-Mediated Oxygen Evolution Reaction." Journal of the Electrochemical Society 167.14 (2020): 144511. Copyright © 2020, Journal of the Electrochemical Society.

8.1 Abstract

The spinel oxide, $Cu_{1.5}Mn_{1.5}O_4$ (CMO) is a promising precious group metal free electrocatalyst (EC) known for acid mediated oxygen evolution reaction (OER). By employing density functional theory (DFT) based Bader analysis for active sites identification, the effective electronic charges of constituent ions in the ordered-disordered crystal structures were calculated. Accordingly, for DFT result validation, structurally disordered $Cu_{1.5}Mn_{1.5}O_4$ ECs were experimentally synthesized by heat treatment to 200^{o}C (CMO-200). The disorder – order transitions of CMO related change in surface atomic arrangement and alteration in the Mn^{3+}/ Mn^{4+} and Cu^{2+}/ Cu^{1+} states are modulated via corresponding heat treatment (200-800^{o}C) of CMO,

revealing significant influence on OER electrocatalytic activity and durability. The measured higher electrocatalytic activity of disordered CMO-200 contrasted with ordered CMO is attributed to higher Mn^{3+}/ Mn^{4+} and Cu^{2+}/ Cu^{1+} states, signifying the beneficial role of Mn^{3+} and Cu^{2+} for facilitating OER. The ordered CMO structures containing lower Mn^{3+}/ Mn^{4+} and Cu^{2+}/ Cu^{1+} ratios albeit reveal higher electrochemical stability than disordered CMO. The present studies, thus, provides fundamental insights into the influence of ordered-disordered structures and rearrangement of oxidation state of active species and their combined synergistic effects on the electrochemical performance for engineering high performance ECs for acidic OER.

8.2 Introduction

The rapidly growing global population and the simultaneous upsurge in the worldwide energy requirements; together with alarming environmental adverse effects due to the pollutants from combustion of conventional energy resources such as coal, petroleum, and natural gas have aspired researchers to develop clean, sustainable, and environmentally benign potential energy sources[186]. Hydrogen has been widely acknowledged as a promising and potential energy carrier owing to its clean, non-carbonaceous nature, and higher energy density (~120 MJ/kg) combined with the low atomic mass than that of petroleum-based fossil fuels (~45 MJ/kg)[50, 271]. Amongst the myriad conventional hydrogen production approaches employed, electricity-driven water electrolysis is one of the most promising and reliable pathways for efficient hydrogen generation. However, oxygen evolution reaction (OER), an important half reaction in the electrochemical water splitting is very energy intensive exhibiting sluggish reaction kinetics contrasted with corresponding hydrogen evolution reaction (HER)[70, 187]. The sluggish reaction kinetics of OER is consequently, a major efficiency limiting factor, demanding significantly higher over-potential (~500-800 mV) with respect to the thermodynamic equilibrium OER potential of ~ 1.23 V for water splitting[45].

Copious electrocatalysts have been intensely studied to overcome the reaction kinetics limitations. Consequently, platinum-group metals (abbreviated as the PGMs) or noble metal-based electrocatalysts such as IrO_2, RuO_2, Pt, etc. have been developed and considered as the state-of-the-art OER electrocatalysts, exhibiting high electrochemical activity and stability towards the advantageous acid mediated proton exchange membrane (PEM) based water splitting process[70, 187, 301]. Nonetheless, environmental scarcity and consequently the prohibitive cost of these materials are critical bottlenecks for the successful and large scale commercialization of PEM based water electrolyzers. [81] Therefore, considerable efforts have been directed to identify, synthesize, and develop earth abundant, cost-efficient, and PGM-free electrocatalysts materials, demonstrating compatible/superior electrochemical performance to the contemporary and expensive PGM metals based electrocatalysts to facilitate OER and is an integral research motive of current researchers in the electrocatalysis field[98, 189, 302].

Motivated by this challenge, to identify high-performance PGM-free electrocatalysts, researchers have dedicated significant efforts towards the exploration of various electrocatalyst systems which include various transition-metal (e.g. Fe, Cu, Ni, Mn, Co) oxides, phosphides, carbides, selenides, nitrides, sulfides and many other multi-metal based transition metal compounds[46, 47, 303]. Similarly, amongst the various heterogeneous electrocatalyst systems, binary mixed-valence oxides with unique $A_xB_{3-x}O_4$ structural formula representation constitutes an important class of versatile materials for OER electrocatalysis[304]. For example, numerous recent reports on various spinel oxides such as $TiCo_2O_4$, Co_3O_4, MFe_2O_4 (M = Cu, Co, Ni), $NiMn_2O_4$,

$Co_xNi_{1-x}Fe_2O_4$[304-308] have evidently demonstrated their fidelity for acidic/alkaline water oxidation. The copper manganite ($Cu_xMn_{3-x}O_4$) belonging to such a spinel system also tenders distinguished features such as good electrical conductivity, good electrocatalytic properties, better endurance towards mechanical, chemical, and electrochemical wear, and earth abundance[309-311]. Owing to its unique electronic - molecular structure and eminent feature of flexible valence states ($Cu^{1+/2+}$ and $Mn^{3+/4+}$), $Cu_xMn_{3-x}O_4$ spinel compositions have shown their feasibility and promise towards various reactions/applications, and thus have attracted significant interest for scientific and technological research. Some of the applications include oxygen evolution/reduction, water-gas shift reactions, selective catalytic reduction of NO_x, catalytic steam reforming of methanol, preferential CO oxidation, oxidative methanol reforming, selective oxidation of toluene to benzoic acid, absorbers in solar thermal collectors, or as adsorbents for air analysis, etc.[309, 312-314].

In our own previous research on identification of earth-abundant elements based spinel electrocatalyst system[281], we have studied the specific Cu–Mn spinel oxide composition, ($Cu_{1.5}Mn_{1.5}O_4$) with fluorine doping as an effective active electrocatalyst for the acidic water oxidation reaction generated by a simple wet chemical approach followed by mild heat treatment to obtain the single phase of the oxide spinel composition. The significant catalytic activity of $Cu_{1.5}Mn_{1.5}O_4$:F system was accredited to the optimized surface d-band structure for OER, contributing better electronic conductivity and electrocatalytic activity for acidic OER. The significance of Cu–Mn–O spinel system correspondingly resulted in much research efforts focused at understanding the phase equilibria, crystal structure, and interaction between Cu and Mn with different atomic ratios to design an archetype system for catalyzing the water oxidation reaction[310, 311]. In addition, it has been reported that the electrocatalytic performance is expected to vary depending on the various aspects such as the ionic distribution, thermal treatment temperature, and crystallinity, etc.[315].

Accordingly, currently various researchers are dealing with the investigation of active sites and ionic distributions in the search for PGM-free electrocatalysts for acidic OER. For example, in order to probe the active sites for acidic OER, in a recent study conducted by Liu and co-workers,[307] they synthesized Ag-doped spinel Co_3O_4 at different temperatures (400°C, 500°C, and 600°C), to modulate Co^{2+}/Co^{3+} ratios. Based on the XPS analysis, Liu and co-workers concluded that Ag-doped Co_3O_4 (400°C) containing higher Co^{2+}/Co^{3+} ratio demonstrated higher electrochemical performance for acidic OER in comparison to that of Ag-doped Co_3O_4 (500 and 600°C). Similarly, Zhu et al.[316] as well as Wang et al.[317] have investigated the OER electrocatalytic activity via variation of Co^{2+}/Co^{3+} ratios and they concluded that Co^{2+} sites served as an active site for water oxidation, and higher Co^{2+}/Co^{3+} ratios evidently resulted in higher OER performance. Similarly, Suntivich et al. proposed that the OER activity of spinel or perovskite oxides is at a maximum when the number of electrons in the e_g orbital are close to unity (e_g^1), for example, Co^{3+} ($t^5_{2g}\ e^1_g$), Ni^{3+} ($t^6_{2g}\ e^1_g$), and Mn^{3+} ($t^3_{2g}\ e^1_g$)[8, 318].

In the present study, therefore in order to theoretically investigate the ionic charges of Cu, Mn, and O of spinel $Cu_{1.5}Mn_{1.5}O_4$ and study their influence on the electrocatalytic performance, the Bader charge analysis of the charges distributed within an elementary unit cell has been conducted for the fully ordered and disordered structures using the density functional theory computational approach implemented in Vienna *Ab-initio* Simulation Package (VASP).[103-105] Based on the Bader charge analysis, the effective electronic charges of constituent ions (Mn^{3+}/ Mn^{4+} and Cu^{1+}/ Cu^{2+}) in the ordered and disordered states of the transition metals in the $Cu_{1.5}Mn_{1.5}O_4$ crystal structures have been calculated. Accordingly, based on the obtained theoretical results, in order to validate the effect of temperature modulated order-disorder crystal structure on the distribution of Cu^{1+}/Cu^{2+} and Mn^{3+}/Mn^{4+} and correlate their synergistic impact on the OER performance, the $Cu_{1.5}Mn_{1.5}O_4$ electrocatalysts are synthesized at various temperatures.

Typically, in order to synthesize Cu–Mn spinel oxides, various approaches such as co-precipitation, high-temperature ceramic method, wet impregnation method followed by thermal decomposition, sol-gel, synthesis under supercritical water conditions, redox-precipitation, soft reactive grinding, reverse micro-emulsion, and high temperature combustion methods, etc. are widely utilized. [312] However, high energy mechanical milling (HEMM or ball milling) combined with heat treatments at adequate temperature is one of the most efficient, facile, scalable, cost efficient, and reliable approaches synthesizing spinel oxide materials of different degree of order-disorder and atomic arrangements. Consequently, in the present study, the disordered Cu–Mn spinel oxide electrocatalyst compositions are synthesized via simple mechanical milling followed by thermal treatments at low temperatures (~200^{o}C) to create the disordered structure and higher temperature treatments to stabilize the more ordered structures at increasing temperatures (400-800^{o}C). Thermal energy provided by the systematic heat treatment is a critical parameter to modulate the active sites (Cu^{1+}/Cu^{2+} and Mn^{3+}/Mn^{4+}) and enable the transition from disordered to ordered structure of the $Cu_{1.5}Mn_{1.5}O_4$ electrocatalysts.

Furthermore, in order to target the fabrication of highly pure Cu–Mn spinel oxide, devoid of any undesired standalone phases of Cu_xO_y and/or Mn_xO_y, exploitation of different Cu/(Cu+Mn) ratios (0.44 to 0.5) was executed. Correspondingly, the Cu/(Cu+Mn) ratio of 0.44 demonstrated the formation of pristine Cu–Mn spinel oxide, with a crystal structure corresponding to pure spinel $Cu_{1.5}Mn_{1.5}O_4$, devoid of any secondary phases of Cu or Mn oxide, which is in good agreement with the previous study.[319] Accordingly, in order to understand the relationships between the oxidation state of the transition element sites and the electrochemical activity with the corresponding OER performance, electrochemical characteristics were studied to assess the electrochemical performance of the $Cu_{1.5}Mn_{1.5}O_4$ electrocatalysts including assessment of further fluorine doping on the electrochemical activity and stability of the spinel oxide.

Thus, employing theoretical as well as experimental investigations, the present study examines the modulated active sites of the transition metal elements in the ordered-disordered spinel structures combined with understanding of their site coordinated oxidation states influences on the activity and stability behaviors of the $Cu_{1.5}Mn_{1.5}O_4$ and corresponding fluorine doped oxide spinel electrocatalysts for acidic OER.

8.3 Theoretical Methodology

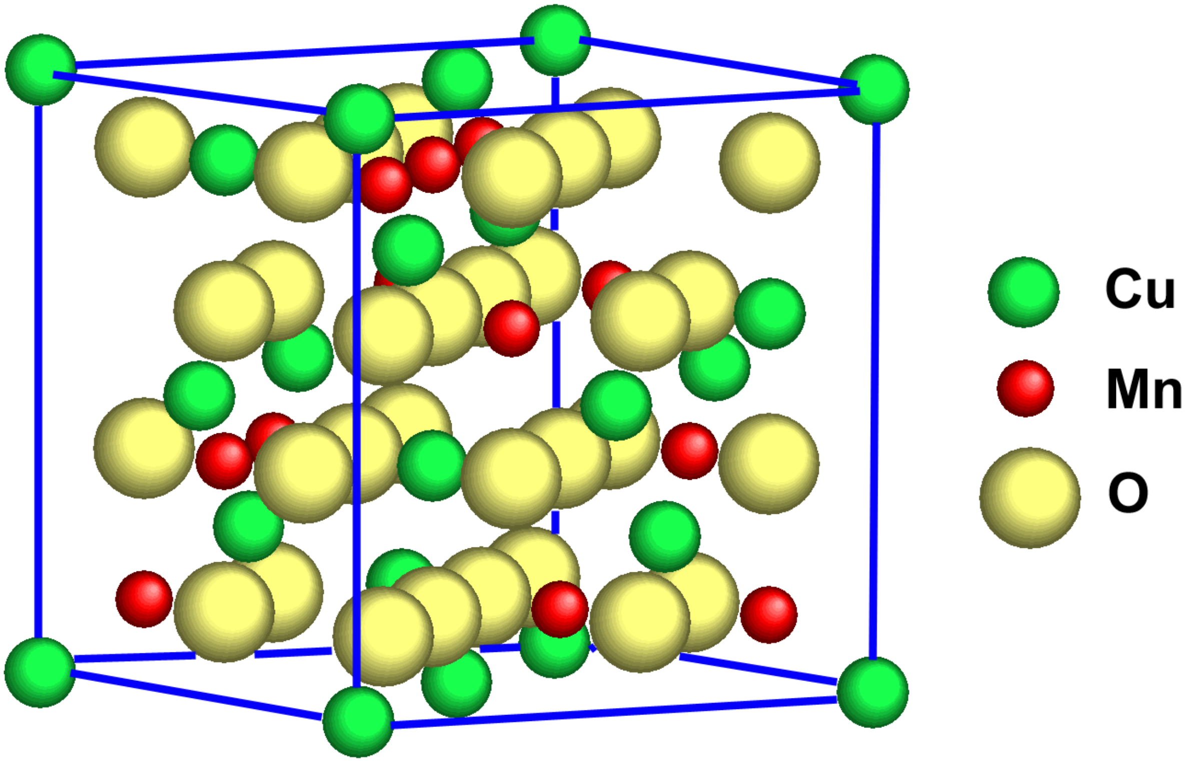

Figure 8-1 The unit cell of fully ordered $Cu_{1.5}Mn_{1.5}O_4$ crystal structure

Regular spinel structure with the compositional formula AB_2O_4 has an elementary unit cell comprising eight formula units i.e. $A_8B_{16}O_{32}$. In this unit cell, A-metals with lower oxidation states occupy 8 tetrahedral sites surrounded by 4 oxygen ions, while B-metals with higher oxidation states occupy 16 octahedral sites with 6 oxygen ions in their vicinity. Figure 8-1**Fig. 1** illustrates the fully ordered $Cu_{1.5}Mn_{1.5}O_4$ structure wherein an entire unit cell comprises 12 Cu, 12 Mn, and 32 O ions ($Cu_{12}Mn_{12}O_{32}$), where all 8 tetrahedral sites are occupied by Cu ions with remaining 4 Cu ions in 4 octahedral sites, while all 12 Mn ions occupy other 12 octahedral sites in the unit cell.[320] Assuming that the ions occupying higher coordinated sites are prone to increase their oxidation states for fulfilling the positive and negative charge balance and vice-versa, one can conclude that the 12 octahedral sites contain 12 Mn^{4+}, with the additional 4 octahedral sites containing 4 Cu^{2+}, and all the 8 tetrahedral sites are occupied with remaining Cu^{1+} ions. Such a charge distribution corresponds to the formula $Cu^{16+}Mn^{48+}O^{64-}$ with the as desired completely charge balanced structure.

In the case of completely disordered structure of $Cu_{1.5}Mn_{1.5}O_4$, on the other hand, the 8 tetrahedral sites are randomly occupied by 4 Mn^{3+} and 4 Cu^{1+} ions, while the 16 octahedral sites are occupied by 8 Mn^{4+} and 8 Cu^{2+} ions. Compared to the fully ordered structure, the disordered structure contains 4 Mn^{3+} and 8 Cu^{2+} ions *vs.* complete absence of Mn^{3+} and 4 Cu^{2+} in the ordered state, resulting in the following formula $Cu^{20+}Mn^{44+}O^{64-}$ which also has a complete and fully charge balanced crystal structure. To support this consideration, the Bader charge analysis of the charge distribution within an elementary unit cell has been conducted for both, the fully ordered and disordered structures using the density functional theory computational approach implemented in the Vienna *Ab-initio* Simulation Package (VASP).[103-105] Bader charges are calculated by integrating the electron densities within zero flux surfaces where the charge density has minima and thus separates two adjacent atoms in the unit cell.[321] Using this technique, the effective electronic charges of the constituent ions in the ordered and disordered $Cu_{1.5}Mn_{1.5}O_4$ crystal structures have been correspondingly calculated and collected in **Table 8-1.** From the data presented in **Table 8-1**, it can be seen as assumed above, in the ordered structure, all the 12 Mn ions occupying the octahedral sites have an effective oxidation state close to 4+, while the Cu ions in the octahedral and tetrahedral sites exhibit charge values close to 2+ and 1+, respectively. Correspondingly, in the fully disordered structure, the Mn ions occupying tetrahedral sites reduce their effective charges approximately from 4+ to 3+, thus increasing the amount of catalytically active Mn^{3+} ions. This happens simply because, during stabilization of the disordered state, some Mn ions move from the octahedral to the tetrahedral sites resulting in reducing their oxidation states from 4+ to 3+, while the Cu ions move from tetrahedral to octahedral sites thus in turn replacing the Mn ions and increasing their oxidation state from 1+ to 2+ and also increasing the overall catalytic activity.

Table 8-1 Ionic charges of Cu, Mn, and O calculated from Bader analysis in fully ordered and disordered $Cu_{1.5}Mn_{1.5}O_4$. The numbers preceding the charge values represent the number of corresponding sites in the unit cell

Ions	**Tetrahedral**	**Octahedral**	**Oxygen**	**Tetrahedral**	**Octahedral**	**Oxygen**
	Ordered			Disordered		
Mn	-	12 +3.79	-	4 +2.93	8 +3.82	-
Cu	8 +0.85	4 +1.91	-	4 +0.88	8 +1.86	-
O	-	-	32 -1.85	-	-	32 -1.88

As for the structural and chemical stability of both the ordered and disordered $Cu_{1.5}Mn_{1.5}O_4$, the same crystallographic approach suggests that why the disordered structure can be less stable than the corresponding ordered counterpart. One can see that an ordered structure consists of 72 Mn-O bonds (12 MnO_6 octahedrons) and 56 Cu-O bonds (4 CuO_6 octahedrons with an additional 8 CuO_4 tetrahedrons). Accordingly, in the fully disordered structure there are an equal amount of Mn-O and Cu-O bonds (64 of each type), thus decreasing the amount of Mn-O bonds at the expense of Cu-O ones. Since Cu-O bonds are weaker than Mn-O bonds (for example, diatomic molecule dissociation energies for Cu-O and Mn-O are 287.4 kJ mol^{-1} and 362 kJ mol^{-1}, respectively[179]), it can be inferred that the disordered structure with less number of Mn-O bonds should be chemically less stable than the fully ordered structure. This argument is also well supported by the density functional theory calculations of the cohesive energies of the ordered and disordered structures, which are -47.5 and -46.6 eV/formula unit, respectively. Consequently, the obtained computational results are competently validated by experimental modulation of the cationic distributions of CMO by synthesizing and heat treating the CMO structures at different temperatures as described in the following sections.

8.4 Experimental Methodology

8.4.1 Synthesis of $Cu_{1.5}Mn_{1.5}O_4$ Electrocatalysts

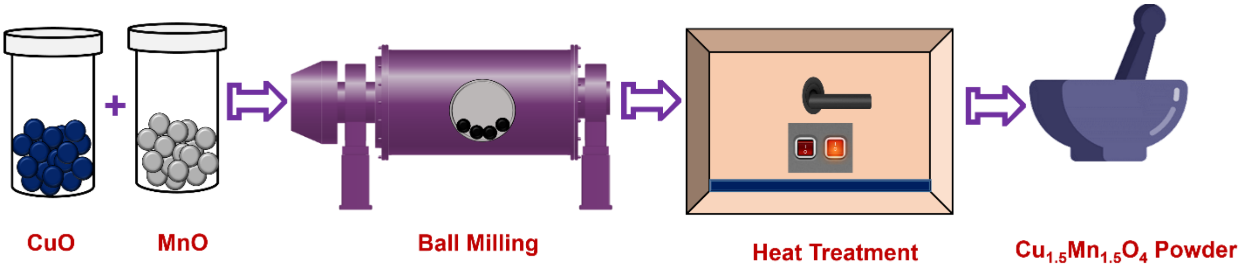

Figure 8-2 Schematic illustration showing the steps in the high energy mechanical milling (HEMM) process used to synthesize the $Cu_{1.5}Mn_{1.5}O_4$ electrocatalysts

Copper oxide, CuO (Alfa Aesar, 99.5%) and manganese oxide, MnO (Alfa Aesar, 99.5%) were used as the precursors for synthesizing the spinel electrocatalyst materials. Nafion 117 (5 wt. % solution in lower aliphatic alcohols, Sigma Aldrich) was used as the binder to generate the electrocatalyst ink. Deionized (DI) water (18 MΩ cm, MilliQ Academic, Millipore) was used throughout the experiments. All the chemical reagents were used as received without any further purification. A schematic illustration of the synthesis process used for generating the spinel $Cu_{1.5}Mn_{1.5}O_4$ particles is depicted in **Figure 8-2**. Mixtures of the precursor powders of CuO and MnO, corresponding to the stoichiometric composition (Cu/Cu+Mn = 0.44 to 0.5) were loaded into stainless steel (SS) vials containing SS balls with a diameter of 2 mm as the milling media. The ratio of 0.44-0.5 was optimally selected to generate the spinel composition. The ball to powder weight ratio (BPR) utilized was maintained at 10:1, and the total weight of the starting mixture was kept at 3 g. The mixtures were then subjected to dry milling in a high energy Shaker Mill (8000, Spex Industries, Edison, NJ) for 5 h. Following dry milling, the milled powders were thermally treated in stagnant air with the temperatures ranging from 200 to 800 ^{o}C for 4 h employing a ramp rate of 10^{o}C min^{-1}. To validate the influence of the cation order and disorder on the electrocatalytic activity of the pure oxide spinel as well as the fluorine doped compositions in light of our previous publication[281], spinel compositions following 200^{o}C and 800^{o}C heat treatment were correspondingly doped with 10 wt.% fluorine as described in the supplemental information .

8.5 Results and Discussions

8.5.1 Physical Characterizations

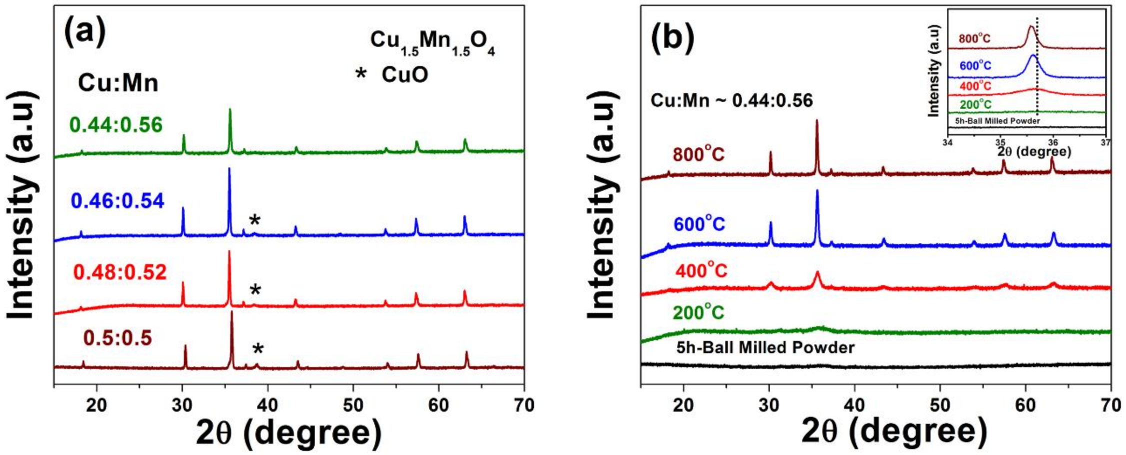

Figure 8-3 Powder XRD patterns of the $Cu_{1.5}Mn_{1.5}O_4$ obtained from (a) using different Cu:Mn ratios synthesized following heat treatment at 800ºC, (b) subjecting the precursors to thermal treatments at different temperatures employing a constant Cu:Mn ratio of 0.44:0.56

The crystal structure and phase purity of the as-synthesized electrocatalysts are characterized by powder X-ray diffraction (XRD, **Figure 8-3**). **Figure 8-3(a)** shows the XRD patterns of the as-synthesized materials with different atomic ratios of Cu and Mn. The XRD patterns of mechanically milled CuO and MnO powder followed by thermal treatment at 800^{o}C, indicate formation of the crystalline spinel cubic structure, corresponding to the composition,

$Cu_{1.5}Mn_{1.5}O_4$ (JCPDS:70–0260) reported by us previously.[281] However, XRD patterns of electrocatalyst compositions corresponding to Cu/Cu+Mn ratios of 0.5, 0.48 and, 0.46 are mainly comprised of spinel $Cu_{1.5}Mn_{1.5}O_4$, coexisting with the impurity phase of unreacted CuO phase (Tenorite, JCPDS 72-0629), suggesting the formation of a mixed oxide materials. These XRD results are also in good agreement with the results reported by Zhao et al. and Behar et al. [312, 315] Nevertheless, as can be seen in **Figure 8-3(a)**, Cu/Cu+Mn ratio of 0.44 reveals complete reaction of the CuO and MnO to form single phase of $Cu_{1.5}Mn_{1.5}O_4$, devoid of any undesired unreacted CuO or MnO phases, suggesting the successful generation of single phase crystalline spinel oxide, $Cu_{1.5}Mn_{1.5}O_4$. This result also agrees well with the previous study conducted by Wei et al.[319] wherein they obtained pure single-phase spinel $Cu_{1.5}Mn_{1.5}O_4$ via solid state and high temperature reaction of CuO and MnO_2 as the starting precursors utilizing the Cu/Cu+Mn ratio of ~ 0.43.

It is well-known that the $Cu_{1.5}Mn_{1.5}O_4$ is an intermediate phase with a range of solid solubility of Cu and Mn rather than a fixed composition line compound typically characteristic of intermetallics. In the intermediate phase of the materials the fluctuations in atomic composition can be realized by atomic sites being either vacant or disordered in the intermediate phase region. The intermediate phase of spinel cubic structured $Cu_{1.5}Mn_{1.5}O_4$ (JCPDS:70–0260)), therefore, could exist in a wide range of compositions (as shown below). The observed order-disorder transformation in the present study also indirectly suggests that the studied system is an intermediate phase rather than a fixed composition or a line compound. Based on these XRD results, in the present study, in order to investigate the thermal treatment induced order-disorder effect on the electrochemical performance of pure $Cu_{1.5}Mn_{1.5}O_4$ phase, we have accordingly synthesized spinel $Cu_{1.5}Mn_{1.5}O_4$ oxide with the Cu/Cu+Mn ratio of 0.44 at different temperatures. As mentioned in the experimental synthesis, in order to synthesize the $Cu_{1.5}Mn_{1.5}O_4$ powder electrocatalyst, CuO and MnO precursor powders were ball milled for 5 h [**Figure 8-3(b)**] and the milled powders were then subjected to thermal treatments at temperatures varying from 200°C to 800°C for 4h at each temperature. **Figure 8-3(b)** shows the XRD patterns of the as-synthesized $Cu_{1.5}Mn_{1.5}O_4$, oxide spinel composition of Cu/Cu+Mn ratio of 0.44 as well as the oxide heat treated at temperatures varying from 200 °C to 800°C for 4h. The $Cu_{1.5}Mn_{1.5}O_4$ -thermally treated at 200°C for 4h (denoted as CMO-200), demonstrates the formation of less crystalline/nanocrystalline (or disordered) $Cu_{1.5}Mn_{1.5}O_4$ phase. Heat treatment of the Cu-Mn-O catalyst at a higher temperature (400°C, 600°C, and 800°C for 4h at each temperature denoted correspondingly as CMO-400, CMO-600, and CMO-800, respectively) reveals the gradual evolution of the crystalline (ordered) spinel phase of $Cu_{1.5}Mn_{1.5}O_4$, devoid of any undesired phases.

With increasing thermal treatment temperature from 200 to 800°C, an increase in the crystallization viewed by the increase in the intensities of the diffraction peaks and atomic rearrangement to more ordered structure of spinel phase is achieved with attainment of highly crystalline CMO phase following heat treatment at the temperature of 800°C for 4h. It is also noteworthy to mention that close inspection of these XRD patterns demonstrated the negative shifts in the peak maximum angle towards lower 2θ angles with the increasing annealing temperature. Such negative shifts in the 2θ positions of the peak intensities indicate expansion of the crystalline lattice[218] of the as-synthesized CMO samples, which can be attributed to the atomic rearrangement of Cu and Mn ions to a more ordered structure with increasing temperatures[322, 323]. As tabulated in **Table 8-2**, the as-synthesized CMO-400 exhibits lattice parameter and unit cell volume of 8.29 Å and 569.72 $Å^3$, respectively, which increased to 8.33 Å and 578 $Å^3$, respectively for the CMO-800 sample and thus, suggests the influence of atomic rearrangement brought about by the thermal treatment.

In addition, the crystallite size of the electrocatalysts was calculated by utilizing the Debye–Scherrer's equation. As shown in **Table 8-2**, the crystallite sizes of the CMO samples are progressively increased with the increasing thermal treatment temperatures. It is to be noted that as no diffraction lines are detected on the nearly amorphous CMO-200 spinel composition, the crystallite size is therefore below detection limits for this sample. As tabulated in **Table 8-2**, at higher temperature of 800°C, the CMO-800 spinel obtained exhibited a larger crystallite size of ~110 nm, which is indeed a consequence of the thermal treatment induced crystallite growth[324]. Furthermore, the annealing effect on the microstrain of the as-synthesized electrocatalyst samples is investigated by plotting the average microstrain *vs.* thermal treatment temperatures**.** As shown in **Appendix D Figure 1**, the average microstrain decreased with increase in the heat treatment temperature, suggesting a reduction in the concentration of lattice imperfections and an increase in the grain size[325, 326]. Furthermore, as tabulated in **Table 8-2**, CMO-200 exhibits BET surface area of ~ 1.86 m^2 g^{-1} which is then marginally decreased with the increasing thermal treatment temperature. Such small decline in the BET surface can be correlated to the particle coalescence processes occurring due to the elevated annealing temperatures[324, 327].

Table 8-2 The lattice parameters, unit cell size, molar volumes, crystallite size and BET surface area of the as-synthesized electrocatalysts

Electrocatalyst	Lattice parameter (Å)	Volume		Crystallite size (nm)	BET surface area (m^{2}g^{-1})
		Unit cell (Å^3)	Molar (cm^{3}mol^{-1})		
CMO-200	--	--	--	--	1.86
CMO-400	8.2952	569.72	42.88	20	0.85
CMO-600	8.3148	573.85	43.19	53	0.32
CMO-800	8.3371	578.0	43.51	110	0.12

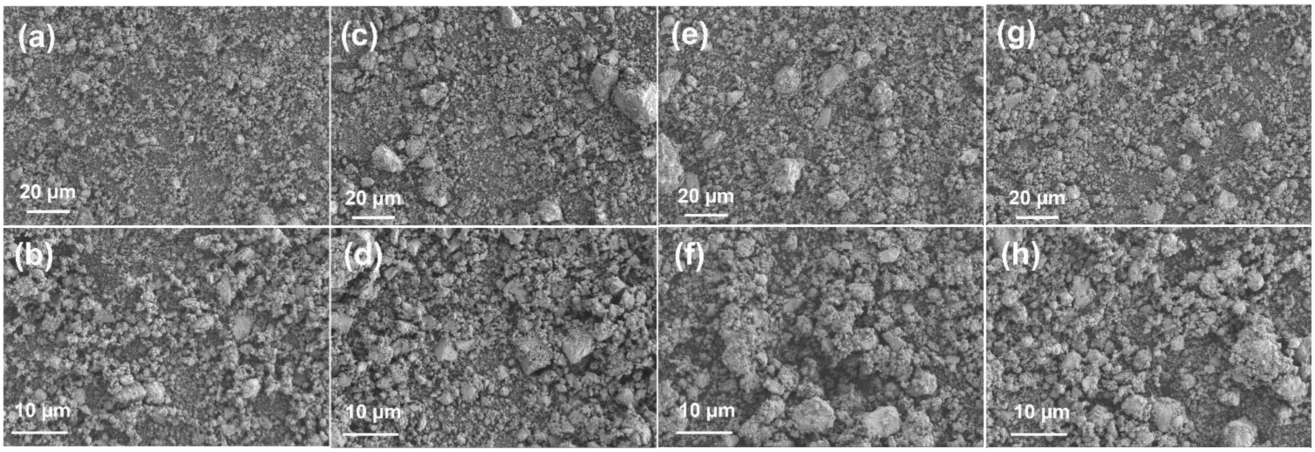

Figure 8-4 SEM micrographs showing the particle size and morphology of the as-synthesized (a-b) CMO-200, (c-d) CMO-400, (e-f) CMO-600, and (g-h) CMO-800 electrocatalysts

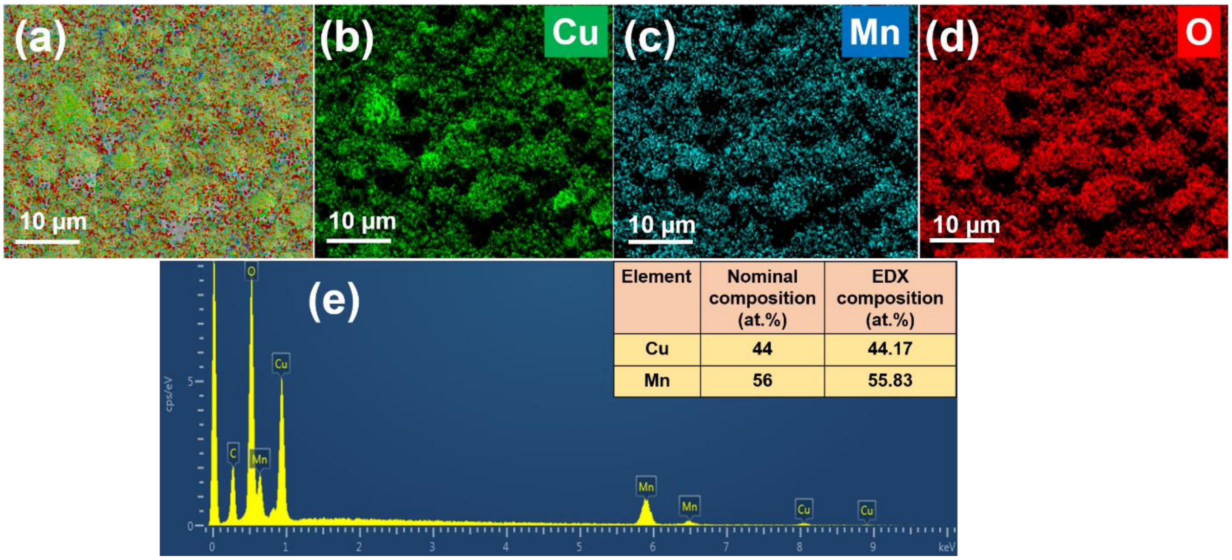

Element	Nominal composition (at.%)	EDX composition (at.%)
Cu	44	44.17
Mn	56	55.83

Figure 8-5 EDX elemental analysis showing (a) layered composite image of all the elements; elemental map of (b) Cu, (c) Mn, (d) O, and (e) EDX spectrum of the as-synthesized CMO-800 showing good match of the elements present to the nominal composition

The SEM images of the as-synthesized $Cu_{1.5}Mn_{1.5}O_4$ powders synthesized at the different temperatures are displayed in **Figure 8-4**. The high resolution induvial representative images for CMO-200 and CMO-800 are shown in **Appendix D Figure 2**. The as-prepared CMO-200 powder consists of spherical particles as well few aggregates in the size ranging from ~20 nm to sub-micron range. Furthermore, at higher thermal treatment temperature, larger particle size as well as higher solitary aggregates are observed. Furthermore, **Figure 8-5 (a)** shows the energy dispersive X-ray spectroscopy (EDX) based elemental mapping images of the layered image combining all three maps of Cu, Mn, and O for the CMO-800 sample. It can be seen from the elemental mapping images that there is a homogeneous distribution of these elements within the as-synthesized electrocatalyst powder. In addition, the quantitative elemental analysis of CMO-800 derived from the EDX spectrum demonstrates the atomic ratio of Cu:Mn as 44.17: 55.83, which is in very good agreement with the selected nominal composition (Cu:Mn ~ 44:56) as well as the composition determined from XPS (Cu:Mn ~ 44.26: 55.74) and ICP-OES (Cu:Mn ~ 44.31: 55.69), suggesting the formation of a pure $Cu_{1.5}Mn_{1.5}O_4$, devoid of any undesired impurities.

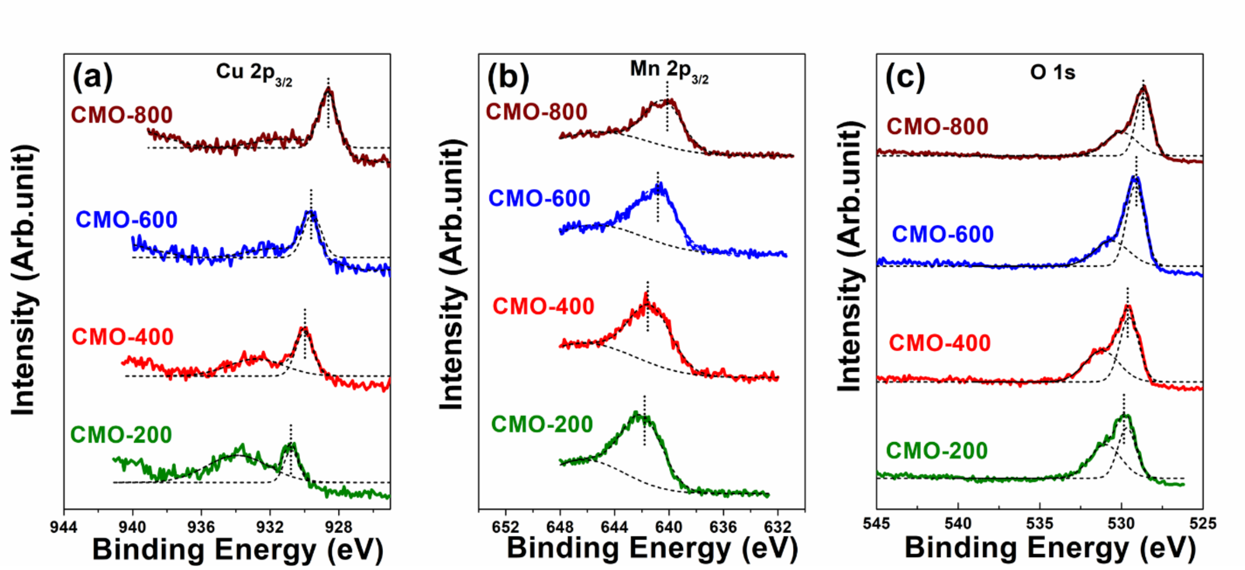

Figure 8-6 (a) XPS spectra of (a) Cu 2p, (b) Mn 2p, and (c) O 1s collected on the CMO-200, CMO-400, CMO-600, and CMO-800 electrocatalyst samples

The electronic properties and the chemical valence states of the elements of Cu, Mn, and O in the as-synthesized $Cu_{1.5}Mn_{1.5}O_4$ electrocatalysts annealed at different temperature were investigated by XPS analysis (**Figure 8-6**). The Cu $2p_{3/2}$ spectra of the as-synthesized CMO samples demonstrate peaks located at ~ 931 eV and ~ 933.5 eV which are accredited to the presence of Cu^+ and Cu^{2+} species, respectively, suggesting the presence of both monovalent (Cu^+) and divalent copper (Cu^{2+}) in the CMO samples, which are in good agreement with the previous XPS results obtained by us and others on $Cu_{1.5}Mn_{1.5}O_4$[281, 328-330]. Herein, it is also important to mention that the gradual negative peak shifts towards lower binding energy in the Cu $2p_{3/2}$ peak positions are witnessed with the increase in annealing temperature from 200 to 800°C. Such negative shifts in the binding energies with respect to increasing annealing temperatures are well-known in the literature and are possibly attributed to the atomic rearrangements at elevated temperatures[164, 182]. Similar results regarding negative shifts in binding energies at higher temperatures are observed in various literature reports[331, 332]. The ordered structure contains more of the lower valence state of Cu^{1+} at higher temperatures of 800°C in the octahedral coordination as also demonstrated by the Bader analysis discussed in the previous section justifying the negative shift of the $Cu2p_{3/2}$ peak to lower energy values. In addition, ordering of the structure (at elevated temperatures) can result in localization of the electron environment around the elemental species causing the characteristic elemental peaks for Cu to be located closer to the theoretical values further validating the observed negative shift in binding energy[331-334]. Justifiably also, calculation of the ratio of Cu^{1+}/ Cu^{2+} via integrated peak areas indicates an increase with corresponding increase in thermal treatment temperature (i.e. Cu^{1+}/ Cu^{2+} obtained as ~ 0.53, 1.38, 2.75, and 3.63 for 200, 400, 600, and 800°C, respectively), suggesting an alternation in the electronic and occupation sites of the ions in octahedral and tetrahedral states as discussed in the Bader analysis earlier. These changes in the occupation of the ions in the octahedral and tetrahedral sites in the spinel structure is also in line with the literature results.[333] Similarly, as demonstrated by the XPS spectra of Mn 2p, the major peak at ~ 642 eV and a satellite peak at ~ 645 eV correspond to the presence of Mn^{3+} and Mn^{4+} species, respectively which is consistent with the earlier reported studies[328-330].

Moreover, similar to the case of the Cu $2p_{3/2}$ peaks, negative shits are observed in the binding energy values of the Mn 2p peak positions with the increasing thermal treatment temperature of the $Cu_{1.5}Mn_{1.5}O_4$ samples, which can be again ascribed to the atomic rearrangements at elevated temperatures as well as further localization of the electron environment causing the characteristic elemental peaks to be positioned closer to the theoretical values justifying the negative shift in the observed binding energy [164, 182, 333, 334]. Furthermore, it can be seen that the ratio of Mn^{3+}/ Mn^{+4} tends to decrease with increasing thermal treatment temperature (Mn^{3+}/ Mn^{+4} obtained as ~ 4.10, 3.70, 2.51, and 1.35 for 200°C, 400°C, 600°C, and 800°C, respectively) which is again in good agreement with the literature result[333]. Additionally, **Figure 8-6(c)** shows the XPS results of the O1 s for samples annealed at different temperatures. A dominant peak for O 1s at the binding energy of ~ 529.8 eV was observed which corresponds to the metal-oxygen bond or the lattice oxygen. A similar negative shift in the binding energies for O1s with respect to increasing annealing temperatures are witnessed, consistent with the XPS results of Cu and Mn.

In the numerous literature studies, it is elucidated that the oxidation state of Mn^{3+} and Mn^{+4} have a remarkable influence on the electrocatalytic activity[278, 280, 335-337]. Motivated by the findings of these various published studies and the present results discussed above, it was concluded that the active sites for the oxygen evolution reaction are likely to be also influenced by the presence of Mn^{3+} and Cu^{2+} species on the oxide surfaces. Accordingly, the experimental as well as theoretical correlations of the obtained cationic distributions discussed herein with the electrochemical performance are further elucidated by the electrochemical and theoretical results in the sections to follow.

8.5.2 Electrochemical Characterizations

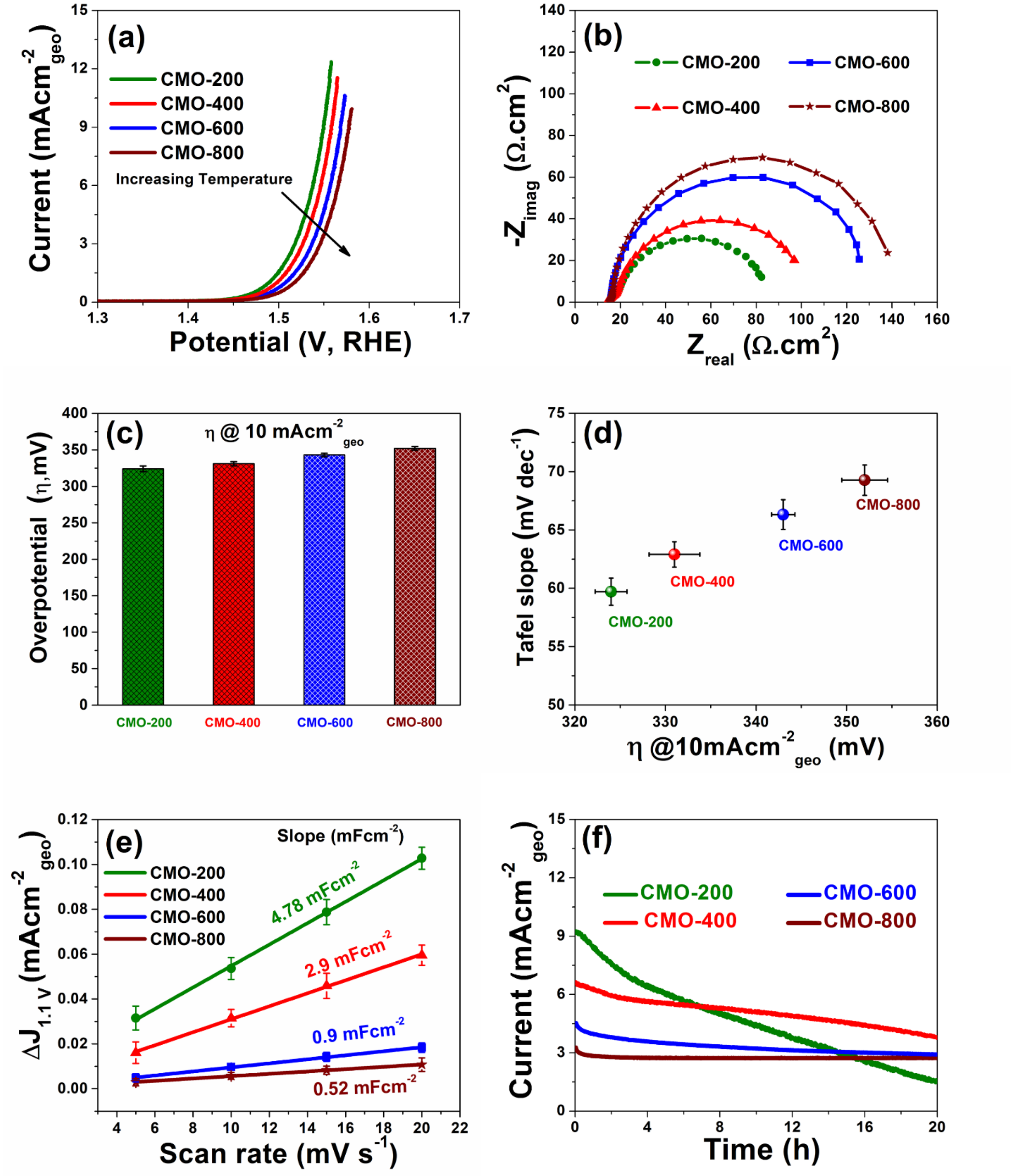

Figure 8-7 Comparison of the electrochemical performances of the as-synthesized electrocatalysts measured in 1 N H_2SO_4 electrolyte at 40°C (a) OER polarization (mA cm$^{-2}_{geo}$ vs. potential) curves with a scan rate of 10

mVs^{-1}, (b) EIS plots performed at 1.55 V (vs. RHE), (c) overpotential required to achieve current density of 10 mAcm$^{-2}{}_{geo}$, (d) Tafel slope vs. overpotential (at 10 mA cm$^{-2}{}_{geo}$, (e) Capacitive current vs. different scan rates of as-prepared electrodes and the corresponding, and (f) chronoamperometric response of as-prepared CMO-200, CMO-400, CMO-600, and CMO-800 electrodes measured at 1.55 V (vs RHE)

The electrocatalytic activity of the CMO samples synthesized at different temperatures was assessed using a three-electrode electrochemical cell. **Figure 8-7(a)** demonstrates the anodic polarization curves collected using 1N sulfuric acid electrolyte solution at 40°C. It can be observed from the OER polarization curves that the CMO-200 electrocatalyst exhibits a higher electrocatalytic activity for OER in comparison to the CMO electrocatalyst synthesized at 400°C, 600°C, and 800°C, respectively. Specifically, at ~1.55 V *vs* RHE (the potential considered for assessing electrochemical activity for OER), the as-prepared CMO-200 electrocatalyst demonstrates a current density of ~ 9.2 mA cm$^{-2}{}_{geo}$ which is ~ 1.4, ~ 2, and ~ 2.7-fold higher than that of CMO-400 (6.7 mA cm$^{-2}{}_{geo}$), CMO-600 (4.68 mA cm$^{-2}{}_{geo}$) and CMO-800 (3.42 mA cm$^{-2}{}_{geo}$) electrocatalyst, respectively. Thus, these results unequivocally suggest the decline in the catalytic activity with respect to increase in thermal temperatures alluding to the ordering of the lattice and variation in the cationic sites of Cu and Mn. Based on various literature studies, mixed valence of Mn^{3+} and Mn^{4+} is considered to be a criterion for determining good catalytic activity[278, 280, 335-337].

Table 8-3 Results of electrochemical characterization of OER for the as-synthesized electrocatalysts conducted in 1N H_2SO_4 electrolyte solution at 40°C

Electrocatalyst Composition	**Charge transfer resistance (R_{ct}, $\Omega.cm^2$)**	**Current density at ~1.55 V (mA $cm^{-2}{}_{geo}$)**	**Overpotential (η in mV) at 10 mA $cm^{-2}{}_{geo}$**	**Tafel slope (mV dec^{-1})**	**ECSA (m^2 g^{-1})**
CMO-200	73	9.2	324	59.71	6.82
CMO-400	92	6.7	331	62.90	4.14
CMO-600	117	4.68	343	66.32	1.28
CMO-800	130	3.42	352	69.27	0.74

Correspondingly, it should be mentioned that higher electrocatalytic activity of CMO-200 electrocatalyst can be ascribed to the higher Mn^{3+}/ Mn^{4+} ratio in comparison to that of the CMO-400, CMO-600, and CMO-800 electrocatalyst samples heat treated to elevated temperatures. According to several literature reports on the water oxidation activity of manganese oxides, it is known that the Mn^{3+} ions represent a critical state contributing to oxygen evolution[278, 280, 335-337]. For example, in the study conducted by C. N. R. Rao and co-workers[337], it was reported that the higher OER activity of Mn^{3+} in the spinel oxides is ascribed to the configuration of Mn^{3+} in the spin state of $t_{2g}^3e_g^1$ which ensures the facile electron transfer from the metal ion. Additionally, this study and another study performed by Robinson et al.[338] elucidate that the active electrocatalyst materials possessing $Mn^{3+}(d^4)$ in edge-sharing octahedra exhibit longer (Jahn−Teller distorted)

Mn−O bonds in comparison to that of Mn^{4+} (d^3) which results in the formation of weaker Mn−O bonds (for Mn^{3+} species) owing to the occupation of the antibonding e_g orbital. The presence of a single electron in the antibonding e_g orbital (e_g^1) of Mn^{3+} can easily form σ-bonds with the anion adsorbates which is expected to yield just the appropriate binding strength between oxygen-related intermediate species and the electrocatalyst, ultimately enhancing electrochemical oxygen evolution (OER). Furthermore, according to Iyer et al.[339], the higher OER activity of less crystalline manganese oxides (akin to the electrocatalyst obtained herein CMO-200) is also likely accredited to the higher mobility of oxygen atoms within the disordered spinel lattice presented by the electrocatalyst heat treated at 200°C (CMO-200).

Accordingly, the obtained electrochemical results presented in the current studies are in excellent agreement with the literature reports which demonstrate that electrocatalysts possessing a higher Mn^{3+} content are primarily responsible for enhancing electrochemical activity and facilitating OER. Additionally, it is worth mentioning that Cu ion exhibiting higher oxidation state (Cu^{2+}) is also well-known for the oxidation of water, phenols, alcohols, etc. For example, various complexes such as Cu(II)–bipyridine, polynuclear Cu(II) complexes, Cu(II)/triglycylglycine macrocyclic complex, etc. are widely employed as an effective water oxidation catalysts[340-342]. Similarly, it is important to mention here that the observed higher electrocatalytic activity of the CMO-200 electrocatalyst is indeed attributed to the synergetic catalytic effect between the higher amount of Cu^{2+} and Mn^{3+} species present in the spinel phase of $Cu_{1.5}Mn_{1.5}O_4$-200. The obtained experimental results discussed here are therefore indeed in good agreement with the density functional theory (DFT) based Bader charge analysis.

Following the electrochemical activity results discussed above, in order to obtain more insights into the electrochemical activity, electrochemical impedance spectroscopy (EIS) was performed on the electrocatalyst samples heat treated at different temperatures (200-800°C). As shown in **Figure 8-7(b)** and **Table 8-3**, the $Cu_{1.5}Mn_{1.5}O_4$ electrocatalyst obtained following heat treatment at a lower temperature of 200°C (CMO-200) exhibits the lowest charge transfer resistance ($R_{ct} \sim 73\ \Omega.cm^2$), whereas the corresponding electrocatalysts obtained with increasing thermal temperature resulted in a significant rise in the R_{ct} i.e. CMO-400 ($92\ \Omega\ cm^2$), CMO-600 ($117\ \Omega\ cm^2$), and CMO-800 ($130\ \Omega\ cm^2$). Therefore, these EIS results indicate a higher charge transfer kinetics and lower activation polarization and consequently yielding a higher OER activity for CMO-200 in comparison to that of CMO-400, CMO-600, and CMO-800 electrocatalyst samples obtained following higher temperature heat treatments.

The obtained current density trends are indeed in good agreement with the EIS results which reveal a higher electrocatalytic activity lower surface charge transfer resistance for the less crystalline $Cu_{1.5}Mn_{1.5}O_4$ (CMO-200). In addition, as shown in **Figure 8-7(c)**, the as-synthesized CMO-200 electrocatalyst attained a current density of $10\ mA\ cm^{-2}_{geo}$ at a lower over-potential (η) of ~324 mV than that of CMO-400 (331 mV), CMO-600 (343 mV), and CMO-800 (352 mV) electrocatalysts. In the temperature-dependent activity study conducted by Vukovic et al.[343, 344], for IrO_2 thin films, the key reasons for observed decline in electrocatalytic activity with increasing annealing temperatures are reported to be the presence of lower amount of accessible active sites due to sintering phenomena. The lower amount of accessible active sites at higher thermal treatment temperatures are evidently observed in the electrochemically active surface (ECSA) characterizations (discussed later). Therefore, the obtained activity trends shown in the present study are indeed in good agreement with the various literature studies. Furthermore, as can be seen from **Figure 8-7(d)**, the lower Tafel slope of the electrocatalyst obtained at lower heat treatment temperature, CMO-200 ($59.71\ mV\ dec^{-1}$) and lower overpotential for attaining a current density of 10mA cm^{-2} in comparison to the electrocatalyst treated at higher temperatures corresponding to CMO-400 (62.90 mV dec^{-1}), CMO-600 (66.32 mV dec^{-1}), and CMO-800 (69.27 mV dec^{-1}) evidently suggests the favorable OER kinetics with faster electron transport as well as enhanced electrocatalytic activity of the lower temperature treated electrocatalyst, CMO-200[187].

To gain deeper insights further into the intrinsic or specific OER electrocatalytic activity, the electrochemically active surface area (ECSA) for the as-synthesized samples was investigated. To determine the ECSA of the electrocatalyst materials, the electrical double-layer capacitance (EDLC) measurements were carried out in an acidic 1 N H_2SO_4 electrolyte at 40°C. The cyclic voltammogram (CV) curves recorded at various scan rates in a non-faradaic voltage range of 1 to 1.2 V *vs* RHE are depicted in **Appendix D Figure 5**. As described in the experimental details, the ECSA was measured from the double-layer capacitance (C_{dl}) and the linear slope of the current density ($\Delta J_{1.1\ V} = j_{anode} - j_{cathode}$) *vs* scan rate (wherein slope = 2 ×C_{dl}) was used to characterize the ECSA [187]. Thus, it can be seen from **Figure 8-7(e)** that the as-prepared electrocatalyst subjected to heat treatment at 200°C, CMO-200 exhibits a higher slope of 4.78 mF cm^{-2} and thereby higher C_{dl} value (2.39 mF cm^{-2}) than that of the corresponding electrocatalyst heat treated to 400°C, 600°C and 800°C, namely, CMO-400 (1.45 mF cm^{-2}), CMO-600 (0.45 mF cm^{-2}), and CMO-800 (0.26 mF cm^{-2}). These results thus evidently suggest that the low temperature heat treated spinel electrocatalyst, CMO-200 possesses a higher electrocatalytically active surface than the corresponding electrocatalyst subjected to higher heat treatment temperatures.[91] The corresponding ECSA ($m^2\ g^{-1}$) values for the specific spinel electrocatalyst, $Cu_{1.5}Mn_{1.5}O_4$ prepared at different temperatures are obtained by dividing the measured double layer capacitance (C_{dl}) by the general specific capacitance (C*) of ~ 0.035 mF cm^{-2} for noble metal based electrocatalyst electrodes active for acidic oxygen evolution (see the Supplemental Material for calculation details)[91, 252]. Accordingly, the higher ECSA of the electrocatalyst heat treated at 200°C, CMO-200 (6.82 m^2 g^{-1}) as compared to that of the spinel electrocatalyst, CMO synthesized at higher temperatures evidently accentuates the superior presence of effective active sites corresponding to the higher Mn^{+3}/Mn^{+4} (4.10) and Cu^{+2}/Cu^{+1} (1.89) ratios corresponding to the less crystalline or higher disordered spinel electrocatalyst which has been also witnessed in the case of earlier electrocatalyst systems studied [345, 346]. For example, in the recent OER study conducted by Faustini et al.[345], at thermal treatment temperature of 400°C, the as-synthesized IrO_2 exhibited a C_{dl} of 5.65 µF cm^{-2}, which progressively decreased to 5.06, 3.57, 1.97 and 1.26 µF cm^{-2} at temperatures of 450, 500, 550 and 600 °C, respectively, suggesting a reduction in the active sites and thus, correspondingly reducing the electrochemically active surface area (ECSA) with increasing annealing temperature[347].

Commensurate with the higher electrocatalytic activity, the electrochemical stability is also an important standard for assessing the high-performance of the OER electrocatalysts. Thus, in order to investigate the electrochemical stability for OER of the as-synthesized spinel electrocatalyst materials, chronoamperometry (CA) tests were conducted at the constant potential of 1.55 V (vs. RHE) considered as the representative standard potential for assessing electrochemical activity and stability as previously mentioned in 1N H_2SO_4 at 40°C. **Figure 8-7(f)** shows the CA curves obtained for the $Cu_{1.5}Mn_{1.5}O_4$ spinel electrocatalyst synthesized and heat treated at 200, 400, 600 and 800°C. As anticipated from theoretical investigations, the as-synthesized spinel electrocatalyst heat treated at 200°C, CMO-200 demonstrates a significant decay (~88%) in the current density during the prolonged OER operation.

The electrochemical stability of the less crystalline or disordered electrocatalysts is well reported in the literature which goes hand in hand with the higher electrochemical activity of the less crystalline (less ordered) or amorphous materials[164]. As can be deciphered from the CA curves of CMO-400, CMO-600, and CMO-800, an increase in the thermal treatment temperature evidently offered progressive enhancement in the electrochemical stability. In particular, at the end of chronoamperometric operation, CMO-400, CMO-600, and CMO-800 retained ~60 %, 73%, and 90% of their initial current density, respectively. Thus, these results indicate the beneficial influence of the annealing temperature, increased crystallinity, and ordering on the electrochemical stability. In the literature, there are reports of assessing the electrochemical stability by defining activity stability factor (ASF) as a measure of the initial current density compared to the dissolution current discussed in the supplemental section. Based on the current work, we have defined an activity stability index (ASI) which compares the over-potential in addition to the decay in current density, which we believe is a more comprehensive assessment of the true electrochemical stability of the electrocatalyst. The ASI equation we believe is more representative of the true electrochemical performance of an electrocatalyst for OER since it provides an indication of both the electrocatalytic activity as well as the electrochemical durability of the electrocatalyst, both of which are extremely relevant for ascertaining true performance of an electrocatalyst. Accordingly, the ASI for the current spinel electrocatalyst system outlining the influence of the cationic disorder and order on the electrocatalytic activity as well as stability is depicted in **Appendix D Table 4**. In line with the above discussion, ASI for CMO-200 is only 4.37 since the system presents good electrochemical activity due to the higher presence of electrocatalytically active species of Mn^{3+} and Cu^{+2} present on the surface which are however, unstable in acidic medium at 1.55 V (vs. RHE) while the ASI for CMO-800 is 32, indicative of the combined optimal electrochemical activity as well as the desired electrochemical stability.

The stability of the electrocatalyst and the specific electrochemical performance displayed in a combined fashion by the ASI as discussed above can be further elucidated based on the theoretical results discussed earlier. Correspondingly, the largely disordered CMO structures obtained at low temperature heat treatment of 200°C (CMO-200) possess higher Mn^{3+}/Mn^{4+} (4.10) and Cu^{2+}/Cu^{1+} (1.89) ratios thus presenting lower amount of Mn-O bonds (64 for completely disordered) in comparison to the larger amount of Mn-O bonds (72) for fully ordered CMO structures. Furthermore, as the Mn-O bonds are stronger than Cu-O bonds (for example, diatomic molecule dissociation energies for Cu-O and Mn-O are 287.4 kJ mol^{-1} and 362 kJ mol^{-1}, respectively[179]), it can therefore explain that the CMO spinel structure with less number of Mn-O bonds exhibit lower stability as in the case of the CMO-200 electrocatalyst than the fully ordered CMO-800 spinel electrocatalyst structure. Thus, the as-performed theoretical investigations are indeed in good agreement with the experimental results.

Additionally, to validate the electrochemical stability ascertained from theoretical DFT studies and experimental chronoamperometric studies, inductively coupled plasma-optical emission spectroscopy (ICP-OES) analysis was executed on the electrolyte solutions collected after the CA tests. As anticipated from the CA tests in line with ASI values, the ICP-OES results suggest a much lower electrocatalytic dissolution for the CMO-800 electrode in comparison to that of CMO-600, CMO-400, and CMO-200 (**Appendix D Table 5**). More specifically, the CMO-200 electrocatalyst exhibits ~230-fold higher dissolution of Cu and Mn species compared to the CMO-800 electrocatalyst, clearly indicative of the effects of cationic ordering. Thus, these results evidently suggest that although the less crystalline oxide materials show higher electrochemical activity than well-crystallized materials, this is however at the expense of the material stability[164, 345]. Finally, it is also imperative to correlate the influence of Cu^{1+}/Cu^{2+} and Mn^{3+}/Mn^{4+} ratios on the electrochemical stability. The inherent instability of Mn^{3+} in acidic conditions is well known in the literature. Particularly, Mn^{3+} is unstable at lower pH values due to the charge disproportionation (CD) reaction which results in the formation of unstable Mn^{2+} species [278, 280, 336]. In this context, in the OER study reported by Morita et al.[336] on the MnO_x electrocatalysts in 1N H_2SO_4, they have demonstrated that the anodic dissolution reaction proceeds at Mn^{3+} sites, suggesting Mn^{3+} sites are more favorable for dissolution than the Mn^{4+} sites. Accordingly, the chronoamperometry results obtained in the present study are in an excellent agreement with the above discussions which demonstrate that the CMO-200 possessing higher Mn^{3+} content reveal more rapid anodic dissolution while the CMO-800 electrocatalyst containing higher Mn^{4+} content exhibits higher electrochemical durability in comparison to that of CMO-600, CMO-400, and CMO-200.

The influence of the order-disorder effects discussed above on the electrochemical activity and stability of the pristine oxide electrocatalysts are also translated to the fluorine doped corresponding structures and are not affected by incorporation of fluorine. To show the influence of the defect states on the fluorine doped structures, the CMO-200 and CMO-800 samples representing the two heat treatment temperature extremes were correspondingly doped with 10 wt. % fluorine discussed in the supplemental section. The **Appendix D Figure 6** demonstrates that fluorine doping to a large extent do not influence the order – disorder effects on the electrochemical activity and stability. The CMO-200:10F and CMO-800:10F electrocatalyst samples exhibit similar XRD patterns as the undoped pristine oxide counterparts depicting solid solution formation. The fluorine doping also did not significantly influence the change in the Mn^{3+}/Mn^{4+} and Cu^{2+}/Cu^{1+} ratios, thus maintaining the same influence of Mn^{3+} on the higher electrochemical activity of the CMO-200:10F (current density of ~9.85 mA $cm^{-2}{}_{geo}$ at 1.55 V) sample in the same range as the CMO-200 (current density of ~9.2 mA cm^{-2}_{geo} at 1.55 V). Similarly, the CMO-800:10F exhibited a lower activity (current density of ~4.40 mA cm^{-2}_{geo} at 1.55 V) very similar to the CMO-800 (current density of ~3.42 mA cm^{-2}_{geo}). The slight improvement in the electrochemical activity is obviously a direct consequence of fluorine doping known to improve the electrocatalytic activity largely due to the improved electronic conductivity and electronic structure of d-band shift towards that of the noble metal system as we have discussed in our earlier publication[281]. The F doping also marginally affected the Mn^{3+}/ Mn^{4+} and Cu^{2+}/ Cu^{1+} ratios from the undoped systems, therefore maintaining the main premise of the manuscript that defect structures and the ordered-disordered states influence the electrochemical activity and stability of the spinel electrocatalyst intact.

In summary, the present study underlines the crucial role of oxidation states of electrocatalytic species on the overall electrochemical activity and stability. Both crystallographic studies conducted experimentally, and the first-principles approaches confirm that the disordered structure, although demonstrating higher electrochemical catalytic activity unfortunately possess lower electrochemical stability, validated by the experimental results presented in this study.

8.6 Conclusions

Utilizing the simple high energy mechanical milling approach followed by thermal treatments at different temperatures, we report the synthesis of the $Cu_{1.5}Mn_{1.5}O_4$ (CMO) spinel structures subjected to systematic heat treatments combined with physical, electrochemical, and theoretical characterizations of the generated $Cu_{1.5}Mn_{1.5}O_4$ (CMO) structures for acid mediated oxygen evolution reaction (OER). In order to unravel the temperature-dependent structure, activity, and electrochemical stability trends, $Cu_{1.5}Mn_{1.5}O_4$ electrocatalyst materials are fabricated with the Cu:Mn ratio as 0.44:0.56 and subjecting them to annealing temperatures ranging from 200 to 800^{o}C. Thermal treatments at different temperatures yielded CMO electrocatalysts with varying degrees of crystallinity and microstrain. Correspondingly, less crystalline, or less ordered $Cu_{1.5}Mn_{1.5}O_4$ (CMO-200) are obtained at the lower thermal treatment of 200^{o}C, while forming highly crystalline or ordered (CMO-800) electrocatalyst at a higher temperature of 800^{o}C. Commensurate with the heat treatment temperature, XPS characterization of the as-synthesized electrocatalysts demonstrated that the Mn^{3+}/ Mn^{4+} and Cu^{2+}/ Cu^{1+} ratios tend to decrease with the increasing temperatures. The ratios of these oxidation states display a significant influence on the electrocatalytic activity, exhibiting lower charge transfer resistance (R_{ct}) and higher current density for the as-synthesized CMO-200 correspondingly possessing a higher Mn^{3+}/ Mn^{4+} (4.10) and Cu^{2+}/ Cu^{1+} (1.89) ratios than that of CMO-400, CMO-600, and CMO-800. The as-synthesized CMO-200 revealed a current density of ~ 9.2 mA cm^{-2}_{geo} at an overpotential of ~320 mV which is ~ 1.4, ~ 2 and ~ 2.7-fold higher than the CMO-400, CMO-600, and CMO-800, respectively. In addition, lower overpotential (324 mV) to deliver a current of 10 mA cm^{-2}_{geo} and lower Tafel slope (59.71 mV dec^{-1}) of CMO-200 suggest the higher activity of CMO-200 which is evidently supported by its higher electrochemically active surface area (ECSA) (6.82 m^2g^{-1}). The electrochemical activity results unveiled that the higher Mn^{3+} and Cu^{2+} contents are crucial for facilitating OER. On the other hand, owing to the high crystalline nature and higher Mn^{4+} and Cu^{1+} content, the as-synthesized CMO-800 display excellent OER electrochemical stability, superior to other counterparts, reflecting the higher robustness of the $Cu_{1.5}Mn_{1.5}O_4$ formed at 800^{o}C. Fluorine doping also does not change or affect these conclusions obtained on the undoped systems. Furthermore, the obtained experimental results are in good agreement with the DFT studies suggesting that the disordered structure, although demonstrating higher electrocatalytic activity exhibits lower electrochemical stability for acidic OER. The present study results therefore coherently and convincingly shed light on the significant influence of synthesis conditions, crystallinity, and variable oxidation states on the electrochemical performance. We believe that the findings of this study reported herein will offer useful pathways for fabricating novel, more active Mn and Cu-oxide based electrocatalytic materials for acid mediated water splitting applications.

9.0 Specific Aim 1B - To Identify and Develop High Performance Electrocatalysts For Oxygen Reduction Reaction (ORR) in Proton Exchange Membrane Fuel Cells (PEMFCs)

9.1 Abstract

The identification and development of platinum group metal (PGM)-free electrocatalysts is important for the commercial development of proton exchange membrane fuel cells (PEMFCs). The spinel oxide, $Cu_{1.5}Mn_{1.5}O_4$ (CMO) is a promising PGM-free electrocatalyst known for oxygen reduction reaction (OER) of PEMFC. Herein, the structurally disordered CMO electrocatalysts were synthesized by thermal treatment to 200°C (CMO-200). The disorder – order transitions of CMO related change in surface atomic arrangement and alteration in the Mn^{3+}/ Mn^{4+} and Cu^{2+}/ Cu^{1+} states are modulated via corresponding heat treatment (200-800°C) of CMO, revealing significant influence on ORR electrocatalytic activity and durability. The disordered CMO-200 revealed higher ORR electrocatalytic activity in comparison to the ordered CMO which is attributed to higher Mn^{3+}/ Mn^{4+} and Cu^{2+}/ Cu^{1+} states, signifying the beneficial role of Mn^{3+} and Cu^{2+} for facilitating ORR. The ordered CMO (CMO-800) containing lower Mn^{3+}/ Mn^{4+} and Cu^{2+}/ Cu^{1+} ratios exhibit higher ORR stability than disordered CMO. The present work, thus, provides fundamental insights into the influence of ordered-disordered structures and rearrangement of oxidation state of active species and their combined synergistic effects on the ORR electrochemical performance for PEMFC.

9.2 Introduction

Rapidly increasing global population along with diminishing fossil fuels and growing environmental concerns have triggered the pursuit for sustainable, non-carbonaceous, and highly efficient energy conversion and storage technologies, such as fuel cells and metal-air batteries [348]. Among various power generation sources, hydrogen fueled proton exchange membrane fuel cell (PEMFC) is one the most efficient and reliable energy sources which has gathered massive attention due to its low temperature operation, zero-pollutant emission, high efficiency, fast start up time, compact system, and fuel flexibility. PEMFC operation involves cathodic oxygen reduction reaction (ORR) and anodic hydrogen oxidation reaction (HOR)[74-76, 111, 281]. In comparison to HOR which is two-electron process, ORR is a complex multistep four-electron process which makes its reaction kinetics sluggish and demanding high overpotentials to operate the PEMFCs. In order to ameliorate ORR and thus, PEMFC kinetics, assistance of efficient electrocatalysts (ECs) is imperative. Owing to its good electrocatalytic activity, facile reaction kinetics, high durability to withstand the PEMFC operating environment, and excellent corrosion resistance, carbon supported platinum (Pt/C) is considered as an ideal state-of-the-art EC for the ORR as well as HOR in the PEMFCs. However, the high cost and environmental scarcity of noble-metal-based Pt are the major bottlenecks for its large-scale application and thus, successful commercialization of PEMFCs [76, 111, 349]. Therefore, current research in the PEMFC area is focused on the exploration of non-platinum (NPM) as well as platinum group metal-free (PGM-free) earth-abundant ECs, exhibiting superior electrochemical activity, stability, electrical conductivity, and good charge transfer kinetics for the ORR [76, 111].

In recent years, owing to their considerable activity and durability, along with low cost, high abundance, and environmental friendliness, manganese oxides and Mn-based composite oxides have gained attention as a potential PGM-free ORR ECs[350, 351]. Among them, spinel-type (AB_2O_4) Mn-oxides consisting of metal cations occupying tetrahedral (four-coordination) and octahedral (six-coordination) sites, flexible valence states, and controllable compositions and structures are an attractive candidate for ORR. For example, Mn based Mn_3O_4, $Mn_xFe_{3-x}O_4$, $Ni_xAl_{1-x}Mn_2O_4$, $Mn_xCu_{1-x}Co_2O_4$, $Co_xMn_{3-x}O_4$, and $Cu_{1.5}Mn_{1.5}O_4$, etc. have evidently shown their promise for ORR in alkaline and acidic media[350, 352].

In our own previous work on the identification of PGM-free spinel ORR electrocatalyst system[281], we have studied the $Cu_{1.5}Mn_{1.5}O_4$ (CMO) and fluorine (F) doped CMO as an active ORR (as well as oxygen evolution reaction, OER) EC system for PEMFC. The significant activity of 10 wt. % F doped $Cu_{1.5}Mn_{1.5}O_4$:10F system was attributed to the optimized surface d-band structure, contributing better electronic conductivity and electrocatalytic activity for acidic ORR and OER. In addition, it has been reported that the electrocatalytic performance is expected to vary depending on the various aspects such as the ionic distribution, thermal treatment temperature, and crystallinity, etc.[315]. Accordingly, in order to show the influence of active sites and ionic distributions (Mn^{3+}/ Mn^{4+} and Cu^{1+}/ Cu^{2+}) of $Cu_{1.5}Mn_{1.5}O_4$ on the OER electrocatalytic activity and stability, we experimentally as well as computationally studied the ordered and disordered states of the transition metals in the $Cu_{1.5}Mn_{1.5}O_4$ crystal structures[351]. This recent work elucidated the effect of temperature modulated order-disorder crystal structure on the distribution of Cu^{1+}/Cu^{2+} and Mn^{3+}/Mn^{4+} and their corresponding influence on the OER activity and stability[351].

In order to unravel the temperature-dependent structure, OER activity, and electrochemical stability trends, $Cu_{1.5}Mn_{1.5}O_4$ ECs were fabricated with the optimized Cu:Mn ratio as 0.44:0.56

and subjected to annealing temperatures ranging from 200 to 800°C. Such thermal treatments at different temperatures formed CMO electrocatalysts with variable degrees of crystallinity and microstrain. Correspondingly, the less crystalline or less ordered $Cu_{1.5}Mn_{1.5}O_4$ (CMO-200) was obtained at the lower thermal treatment of 200°C, whereas highly crystalline or ordered (CMO-800) was generated at higher temperature of 800°C. On the basis of XPS characterization, it was witnessed that the Mn^{3+}/ Mn^{4+} and Cu^{2+}/ Cu^{1+} ratios in the as-synthesized CMO ECs tend to decrease with the increasing temperatures. The ratios of these oxidation states displayed significant impact on the electrocatalytic activity, exhibiting higher OER activity for the CMO-200, possessing a higher Mn^{3+}/ Mn^{4+} (4.10) and Cu^{2+}/ Cu^{1+} (1.89) ratios than that of CMO-400, CMO-600, and CMO-800. These activity results suggested that the higher Mn^{3+} and Cu^{2+} contents are crucial for facilitating OER.

Accordingly, in order to investigate the similar temperature-dependent structure, activity, and electrochemical stability trends, in the present work CMO ECs fabricated at 200, 400, 600, and 800°C are studied for ORR of PEMFC.

9.3 Experimental Methodology

The methodology followed for the electrocatalyst synthesis can be referred at[351] and also described in detail in Chapter 8.

9.3.1 Electrochemical Characterization

A rotating disk electrode (RDE) was used for ORR characterizations. The electrocatalyst ink consisting of 85 wt.% CMO electrocatalyst and 15 wt.% Nafion 117 (5 wt.% solution in lower aliphatic alcohols, Aldrich) was sonicated and applied to a glassy carbon disk (geometric area=0.19 cm^2). The total loading utilized was 50 $\mu g\ cm^{-2}$. A Pt wire (Alfa Aesar, 0.25 mm thick, 99.95%) was used as the counter electrode and Hg/Hg_2SO_4 (XR-200, Hach) with a potential of +0.65 V with respect to reversible hydrogen electrode (RHE) was used as reference electrode. All potential values in this study are reported with respect to reversible hydrogen electrode (RHE), calculated from the formula[74, 75, 281]:

$$E_{RHE} = E_{Hg/Hg2SO4} + E^0_{Hg/Hg2SO4} + 0.059pH$$

E_{RHE} is the potential versus RHE. $E_{Hg/Hg2SO4}$ is the potential measured against the Hg/Hg_2SO_4 reference electrode. $E^0_{Hg/Hg2SO4}$ is the standard electrode potential of Hg/Hg_2SO_4 reference electrode (+0.65 V *vs* NHE).

The ORR electrochemical characterizations were carried out in an electrochemical workstation (VersaSTAT 3, Princeton Applied Research) using a three-electrode cell configuration at 26^0C (maintained using a Fisher Scientific 910 Isotemp refrigerator circulator). The cyclic voltammetry was conducted in N_2-saturated 1N H_2SO_4 electrolyte by scanning the potential between 0 V (*vs* RHE) and 1.23 V (*vs* RHE) at scan rate of 5 mV sec^{-1}. 1N H_2SO_4 solution was initially saturated with N_2 to remove oxygen present in the solution. ORR measurements were carried out by performing polarization studies in O_2-saturated 1N H_2SO_4 solution at 26^0C at rotation speed of 2500 rpm and scan rate of 5 mV sec^{-1} [353]. The Koutechy-Levich equation was used to determine the number of electrons (n) involved in the reaction[76].

$$i^{-1} = i_k^{-1} + i_L^{-1} \qquad (9\text{-}1)$$

$$i_L = 0.620\ n\ F\ A_e\ D_0^{2/3}\ \omega^{1/2}\ \nu^{-1/6}\ C_o^{*} \qquad (9\text{-}2)$$

Here, i_L is the limiting current (A, Ampere) at ~0.6 V (*vs* RHE), i_k is the kinetic current (A, Ampere) observed in the absence of any mass transfer limitation, F is Faraday constant (96489 C mol^{-1}), A_e is the geometric area of electrode (0.19 cm^2), D_0 is diffusivity of O_2 in 1N M H_2SO_4 solution (2.2×10^{-5} cm^2 s^{-1}), ω is rotation speed (rad s^{-1}), ν is the kinematic viscosity of water (0.01 cm^{2}s^{-1}) and C_o^{*} is the saturated concentration of O_2 in 1N M H_2SO_4 solution (0.25×10^{-6} mol cm^{-3})[354, 355].

In addition, rotating ring disk electrode (RRDE) approach was utilized for the calculation of electron transfer number (n) and intermediate product i.e., % peroxide (H_2O_2) formation during ORR process of CMO-200 and CMO-800. The following equations were used for the calculations[356]:

$$n = \frac{4 \times I_d}{I_d + \frac{I_r}{N}} \qquad (9\text{-}3)$$

$$\%H_2O_2 = \frac{100 \times (4 - n)}{2} \qquad (9\text{-}4)$$

where I_d and I_r are the disk and ring currents at 2500 rpm respectively. The RRDE working electrode was glassy carbon disk electrode with platinum ring electrode (collection efficiency N = 37%) from Pine Research Instrumentation[356].

Electrochemical impedance spectroscopy (EIS) was used to determine the charge transfer resistance (or polarization resistance) (R_{ct}) of electrocatalysts[76, 111]. EIS was conducted in the frequency range of 100 mHz-100 kHz (Amplitude = 10 mV) at ~0.9 V (*vs* RHE which is typical potential for assessing electro-catalyst activity for ORR[353]) in O_2-saturated 1N H_2SO_4 solution. The experimentally obtained EIS plot was fitted using the ZView software from Scribner Associates with a circuit model $R_\Omega(R_{ct}Q_1)$, where

R_Ω = Ohmic resistance, .i.e., resistance of various components including, electrolyte and electro-catalyst layer[76, 111, 124, 281]

R_{ct} = Charge transfer resistance (i.e., polarization resistance) [76, 111, 124, 281]

Q_1 = Constant phase element representing capacitance behavior of the electro-catalyst surface [76, 111, 124, 281]

The electrochemical stability was investigated by performing cyclic voltammetry by scanning potential between 0.6 V (*vs* RHE) and 1.23 V (*vs* RHE) in N_2-saturated 1N H_2SO_4 electrolyte solution at 26°C at scan rate of 5 mV sec^{-1} for 6000 cycles, followed by conducting polarization in O_2-saturated 1N H_2SO_4 solution at rotation speed of 2500 rpm and scan rate of 5 mV sec^{-1}.[353] Elemental analysis of the electrolyte solution was performed after 6000 cycles by inductively coupled plasma optical emission spectroscopy (ICP-OES, iCAP 6500 duo Thermo Fisher) to determine the amount of elements leached out in the electrolyte solution [76, 111, 124, 281].

Membrane electrode assembly preparation and single cell test analysis

The anode and cathode EC inks were prepared using 85 wt.% EC powder and 15 wt.% Nafion 117 solution (5 wt.% solution in lower aliphatic alcohols, Aldrich). For the anode, Pt loading of commercial 40% Pt/C (Alfa Aesar) electro-catalyst was 0.2 mg_{Pt} cm^{-2}. For the cathode, the total loading of 0.3 mg cm^{-2} was used for CMO ECs. The electrodes were prepared by spreading the ink on teflonized carbon paper. For the single cell testing [76, 111, 124, 281], a membrane electrode assembly (MEA) was fabricated by using a Nafion 115 membrane which was sandwiched between the anode and cathode. The Nafion 115 membrane was pretreated first with 3 wt.% hydrogen peroxide solution to its boiling point to oxidize any organic impurities. Then it was boiled in D.I. water followed by boiling 1N H_2SO_4 to eliminate any impurities. Finally, it was washed multiple times in D.I water to remove any traces of residue acid. This membrane was then stored in D.I. water to avoid dehydration. Sandwiching of Nafion 115 membrane between anode and cathode was carried out by hot-pressing in a 25T hydraulic lamination hot press at a temperature of 125^{o}C and pressure of 40 atm applied for 30 sec. This MEA was then used in the single cell test analysis, carried out using the fuel cell test set up obtained from Electrochem Incorporation at 80^{o}C and 0.1 MPa with UHP-H_2 (200 ml min^{-1}) and UHP-O_2 (300 ml min^{-1}) as reactant gases[76, 111, 124, 281].

9.4 Results and Discussion

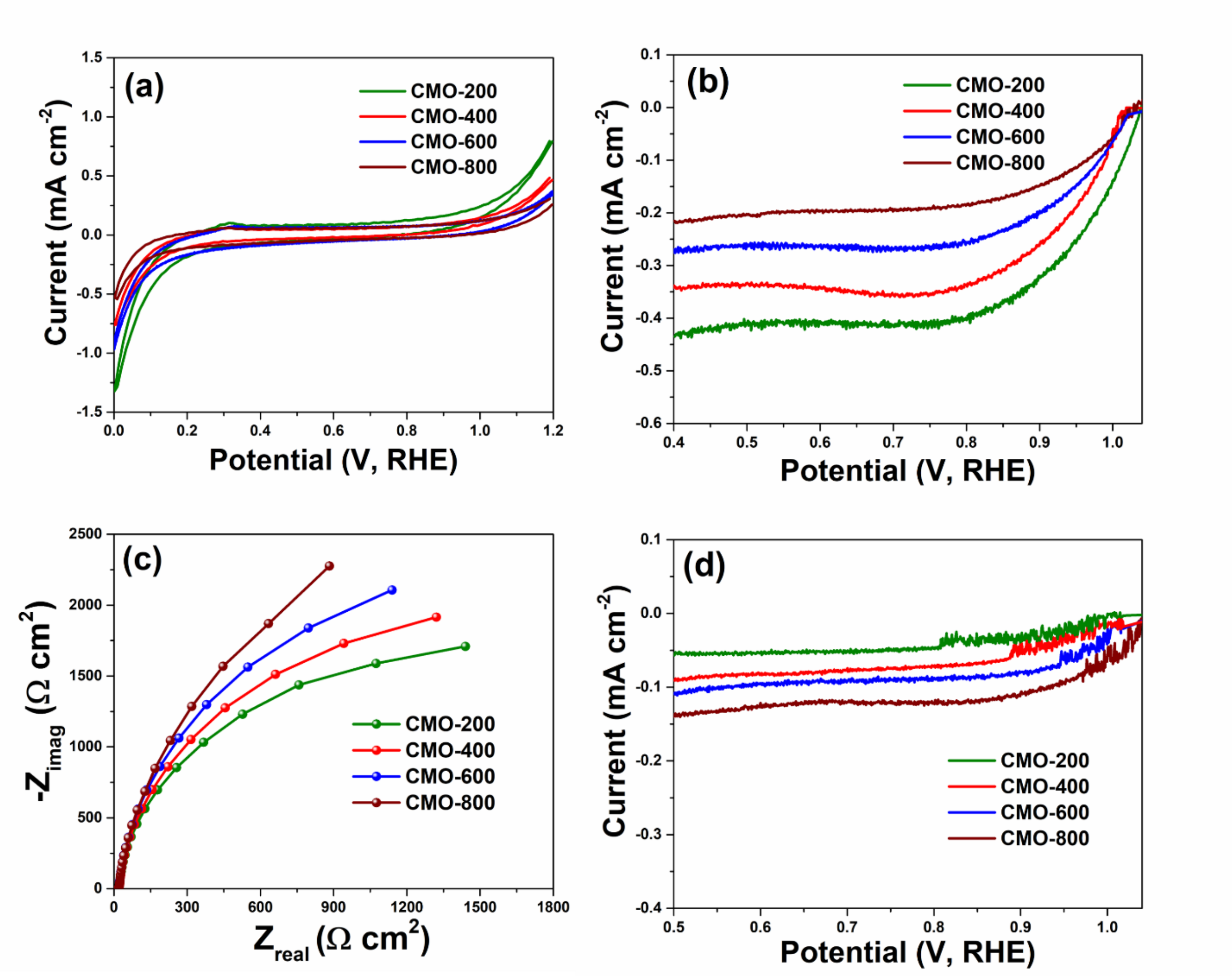

Figure 9-1 (a) The cyclic voltammograms measured in N_2-saturated 1N H_2SO_4, (b) polarization curves obtained in O_2-saturated 1N H_2SO_4 solution at 26^0C with rotation speed of 2500 rpm, (c) electrochemical impedance spectroscopy obtained in O_2-saturated 1N H_2SO_4 solution, (d) polarization curves (after 6000 cycles) obtained in O_2-saturated 1N H_2SO_4

The cyclic voltammograms (CVs) of as-synthesized CMO ECs in N_2-saturated 1N H_2SO_4 electrolyte are shown in **Figure 9-1(a)**. As can be seen from these CV curves, as-synthesized

CMO-200 shows relatively higher current density in comparison to the CMO-400, 600, and 800 compositions. In addition, the LSV studies are carried out to evaluate the ORR activity of the CMO ECs. **Figure 9-1(b)** shows the LSV curves for the CMO ECs in oxygenated 1N H_2SO_4 solution carried out at 2500 rpm. The as-synthesized CMO-200 shows higher ORR activity in comparison to the CMO-400, 600, and 800 compositions. The higher ORR activity and current density of CMO-200 can be attributed to its lower charge transfer resistance (R_{ct}) than CMO-400, CMO-400, and CMO-800. The diameter of the semi-circle in the low frequency region of the EIS plot [**Figure 9-1(c)**] suggests the R_{ct}. This result thus suggests the better reaction kinetics (lower activation polarization) of CMO-200 than that of other CMO ECs. The obtained current density trends are indeed in good agreement with the EIS results which reveal a higher ORR activity and lower surface charge transfer resistance for the less crystalline and disordered CMO-200.

It is noteworthy that the higher ORR activity of CMO-200 can also be ascribed to the higher Mn^{3+}/ Mn^{4+} ratio in comparison to that of the CMO-400, CMO-600, and CMO-800. According to various literature reports, it is known that the presence of higher Mn^{3+} is important for oxygen electrocatalysis[278, 280, 335-337]. For example, in the study conducted by C. N. R. Rao and co-workers[337], it was reported that the higher OER as well ORR activity of Mn^{3+} in the spinel oxides is ascribed to the configuration of Mn^{3+} in the spin state of $t_{2g}^3e_g^1$ which ensures the facile electron transfer from the metal ion. Furthermore, another study performed by Robinson et al.[338] elucidate that the electrocatalyst possessing $Mn^{3+}(d^4)$ in edge-sharing octahedra exhibit longer (Jahn−Teller distorted) Mn−O bonds in comparison to that of Mn^{4+} (d^3) which results in the formation of weaker Mn−O bonds (for Mn^{3+} species) due to the occupation of the antibonding e_g orbital. The existence of a single electron in the antibonding e_g orbital (e_g^1) of Mn^{3+} can easily form σ-bonds with the anion adsorbates which is expected to yield just the appropriate binding strength between oxygen-related intermediate species and the electrocatalyst, ultimately enhancing electrochemical oxygen reduction reaction.

The electrochemical stability of as-synthesized CMO ECs was studied by conducting cyclic voltammetry between voltage window of 0.6 V-1.23 V (*vs* RHE) in N_2-saturated 1N M H_2SO_4 electrolyte solution at 26^{o}C at a scan rate of 5 mV sec^{-1} for 6000 cycles[353]. The polarization curve was then obtained for CMO ECs after 6000 cycles in O_2-saturated 1N M H_2SO_4 solution [**Figure 9-1(d)**]. It is interesting to notice that the polarization curves obtained after 6000 cycles show the higher current density for CMO-800, followed by CMO-600, 400, and 200 ECs, suggesting the minimum current density decay and thus, higher ORR durability for the CMO-800 in comparison to the other CMO ECs. The electrochemical stability of the less crystalline or disordered electrocatalysts is well reported in the literature which goes hand in hand with the higher electrochemical activity of the less crystalline (less ordered) or amorphous materials [164]. Accordingly, the obtained results evidently show the higher ORR durability for ordered CMO than the disordered CMO. Also, it should be noted that the obtained ORR activity-stability trends of CMO are indeed in excellent agreement with the activity-stability trends of OER on PEM water splitting[351].

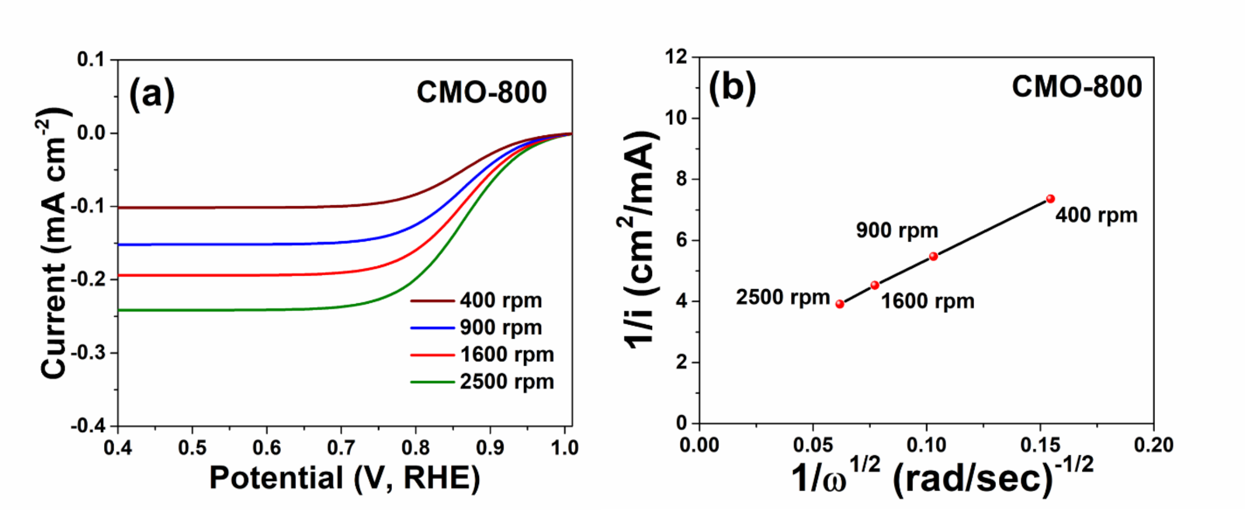

Figure 9-2 (a) The polarization curve for ORR of CMO-800 at different rotation speeds measured in O_2-saturated 1N H_2SO_4 solution, (b) Koutechy-Levich plot for ORR of CMO-800 at 0.6 V (*vs* RHE)

Furthermore, in order to evaluate the number of electrons involved in the ORR for the stable CMO-800, the Koutechy-Levich equation was utilized. As shown in **Figure 9-2**, using Koutechy-Levich equation, the number of electrons for ORR of CMO-800 are obtained as ~ 3.4, suggesting the desired ORR pathway close to ideal four electron pathway of ORR.

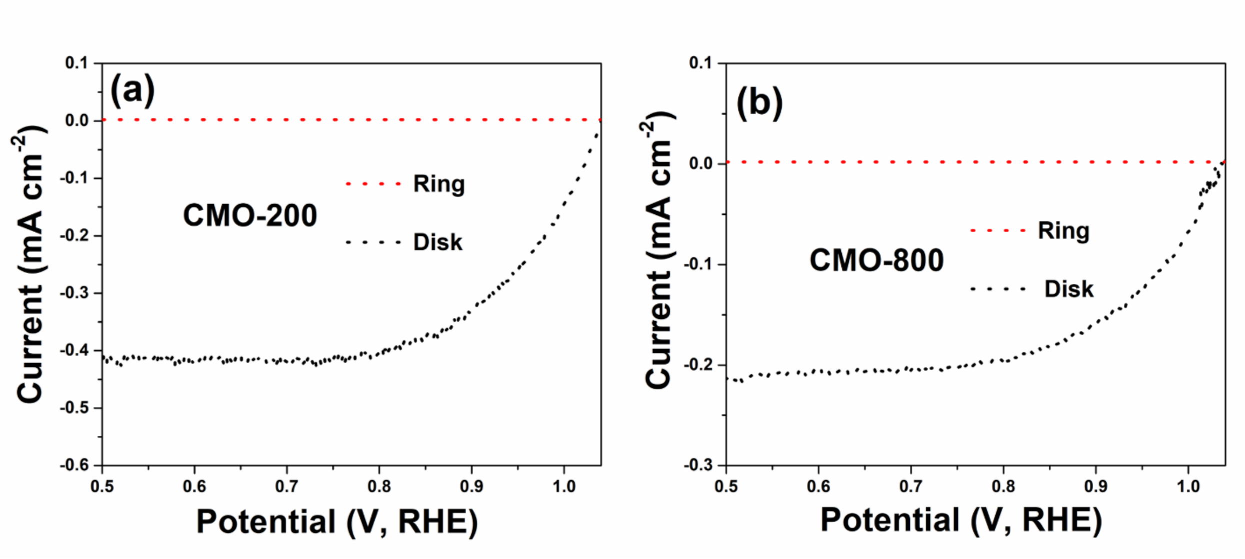

Figure 9-3 RRDE results of CMO-200 and CMO-800

The rotating ring disk electrode (RRDE) method was employed for the calculation of electron transfer number (n) and intermediate product i.e., % peroxide (H_2O_2) formation during ORR process of CMO-200 and 800 (**Figure 9-3)**. Accordingly, for CMO-200 and CMO-800, the number of electrons (n) are obtained as ~3.43 and 3.12, respectively. The % peroxide (H_2O_2) is obtained as ~ 28% and 43% for the CMO-200 and CMO-800, respectively. Herein, the higher number of electrons and lower % H_2O_2 suggests the higher ORR kinetics and activity of CMO-200 in comparison to that of CMO-800.

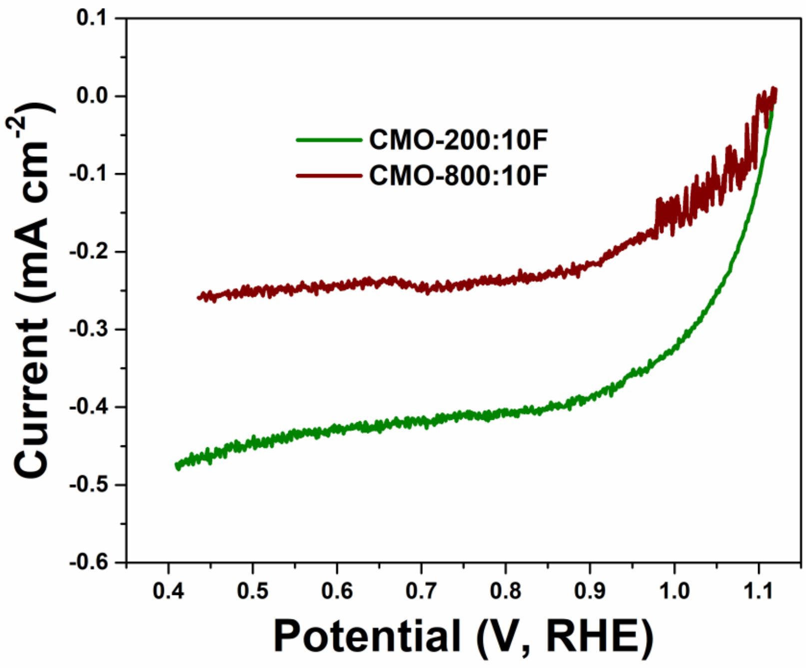

Figure 9-4 The polarization curve for ORR of F doped CMO-200 and 800 obtained in O_2-saturated 1N H_2SO_4 solution at 26°C with rotation speed of 2500 rpm

The influence of the order-disorder effects discussed above on the ORR activity of the pristine CMO ECs are also translated to the fluorine doped corresponding CMO ECs. To show the influence of the defect states on the fluorine doped structures, the CMO-200 and CMO-800 samples representing the two heat treatment temperature extremes were correspondingly doped with 10 wt. % fluorine. The F doped CMO ECs i.e., CMO-200:10F and CMO-800:10F revealed comparable yet slightly higher ORR activity as compared to undoped CMO-200 and CMO-800, suggesting the slight enhancement in the ORR activity **(Figure 9-4)**.

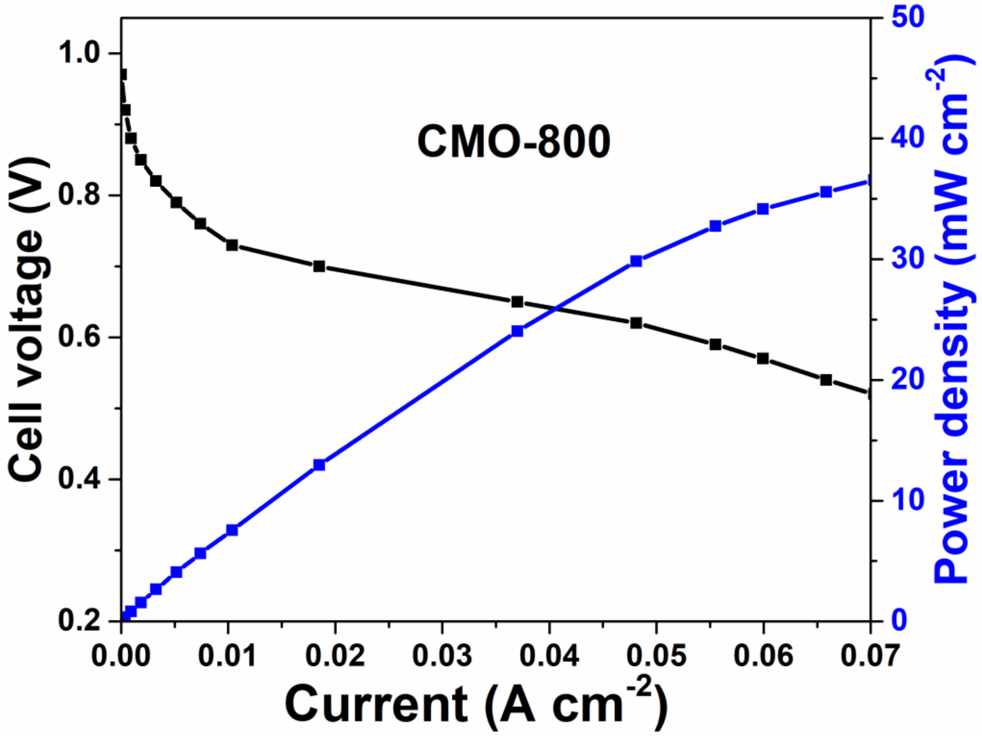

Figure 9-5 Performance of single PEMFC full cell with CMO-800 as cathode electrocatalyst and commercial 40% Pt/C (Alfa Aesar) as anode electrocatalyst, obtained at 80^{0}C and 0.1 MPa with UHP-H_2 (200 ml min^{-1}) and UHP-O_2 (300 ml min^{-1}) as reactant gases

The polarization curve of single PEMFC full cell with CMO-800 (total loading of 0.3 mg cm^{-2}) as cathode electrocatalyst and commercial Pt/C as anode electrocatalyst (Pt loading of 0.2 mg$_{Pt}$ cm^{-2}) is shown in **Figure 9-5**. The maximum power density obtained using single PEMFC with CMO-800 as cathode electrocatalyst is ~ 37 mW cm^{-2}.

The present study thus demonstrates the potential of CMO as ORR electrocatalyst system for PEMFC. The electrochemical activity results for ORR suggest that the higher Mn^{3+}

and Cu^{2+} contents are crucial for facilitating ORR. On the other hand, owing to the high crystalline nature and higher Mn^{4+} and Cu^{1+} content, the as-synthesized CMO-800 displays high ORR electrochemical stability, superior to other counterparts, reflecting the higher robustness of the $Cu_{1.5}Mn_{1.5}O_4$ formed at 800°C.

10.0 Specific Aim 2A - To Develop Multi-Metal Containing Phosphosulphide Based Electrocatalyst Materials for Hydrogen Evolution Reaction (HER) in Proton Exchange Membrane-Based Water Electrolysis (PEMWE)

Excerpts reprinted with permission from Ghadge, Shrinath Dattatray, et al. "Computational and experimental investigation of Co and S-doped Ni_2P as an efficient electrocatalyst for acid mediated proton exchange membrane hydrogen evolution reaction" Catalysis Science & Technology, 2021, 11, 861-873.

10.1 Abstract

Engineering earth-abundant and high performance electrocatalysts to facilitate hydrogen evolution reaction (HER) for generation of sustainable hydrogen fuel has been a major scientific and technological challenge in the electrolytic water splitting area. Herein, employing theoretical first principles calculations of HER thermodynamics and kinetics-based density functional theory (DFT), we report a platinum group metal (PGM)-free Co and S containing Ni_2P [$(Ni_{0.95}Co_{0.05})_2P$:x at. % S (x = 5, 10, 15)] system as highly active and robust electrocatalysts for acidic HER. On the basis of the DFT calculations, $(Ni_{0.95}Co_{0.05})_2P$:15S composition reveals optimal hydrogen adsorption free energies (ΔG_{H*}) and beneficial modification of the surface electronic structure. Accordingly, $(Ni_{0.95}Co_{0.05})_2P$:15S electrocatalyst, synthesized via a simple and facile low temperature solid state approach, demonstrates significantly higher HER performance in

comparison to pristine Ni_2P and comparable HER performance to state-of-the-art Pt/C. Owing to the unique modification of the electronic structure i.e. change in density of state (DOS) and optimized ΔG_{H*}, the $(Ni_{0.95}Co_{0.05})_2P$:15S composition exhibits considerably lower charge transfer resistance (6.82 Ω cm^2), lower over-potential (44 mV at 10 mA cm^{-2}), smaller Tafel slope (31.25 mV dec^{-1}), smaller water contact angle (7^o) and correspondingly, a smaller bubble break-off diameter (0.38 mm) with a higher mass activity (43.75 A g^{-1} at -0.05 V) in comparison to $(Ni_{0.95}Co_{0.05})_2P$:x at.% S (x = 0, 5, 10) and Ni_2P. The highly active composition, $(Ni_{0.95}Co_{0.05})_2P$:15S also displays a long term electrochemical HER stability, similar to Pt/C, with no major degradation in the activity, reflective of its excellent structural robustness for acidic HER. Consequently, the present experimental study fortified by theory provides novel synergistic insights into designing promising and efficient multi-component HER electrocatalysts.

10.2 Introduction

Hydrogen (H_2), a non-carbonaceous fuel with higher energy density (~120 MJ/kg) than the fossil fuels based conventional energy sources (~45 MJ/kg) is considered as one of the most promising and sustainable energy carriers[50, 271, 303]. Among the various hydrogen production technologies such as coal gasification and steam reforming, hydrogen generation via electrocatalytically water splitting involving cathodic hydrogen evolution reaction (HER) and anodic oxygen evolution reaction (OER) constitutes one of the most environmentally friendly, clean, and reliable approaches, devoid of any substantial carbon footprints[357-359]. Owing to their significant electrocatalytic activity with minimum overpotential and adequate electrochemical durability, various state-of-the-art platinum group metal (PGM) based electrocatalysts such as Pt,

IrO_2, RuO_2, etc. are commonly utilized as OER and HER electrocatalysts in electrochemical water splitting. However, the prohibitive cost (~\$210,000/kg_{Pt}) and scarcity of global reserves (~0.001-0.005 ppm in earth's crust) of PGM electrocatalysts represent major bottlenecks thwarting the progress towards their large-scale utilization in operation of water electrolyzers[29, 31].

The identification, synthesis, and improvement of earth-abundant, cost-efficient, and PGM-free electrocatalysts, exhibiting comparable/superior electrochemical performance in comparison to the state-of-the art and expensive electrocatalysts to expedite the HER-OER kinetics is therefore an integral and principal research objective of researchers engaged in the electrocatalysis arena. In relation to HER, numerous transition-metal (e.g. Fe, Cu, Ni, Co) phosphides (TMPs), sulfides, carbides, selenides, nitrides, etc. have been explored for the more advantageous proton exchange membrane (PEM) based acidic hydrogen evolution [46-48]. Amongst these systems, TMPs, owing to their excellent hydrodesulfurization (HDS) characteristics which rely on reversible binding of hydrogen on the catalyst surface, similar to HER, are highly promising and widely studied HER electrocatalyst systems.[49] In recent years, therefore, various TMPs such as copper phosphides, nickel phosphide, iron phosphides, molybdenum phosphides, tungsten phosphides, etc. have been studied as an active HER electrocatalysts[50, 51]. Among these TMP systems, Ni_2P has been reported to be a highly promising HER electrocatalyst owing to the presence of (i) a weak "ligand effect" due to Ni-P bonds, expediting the dissociation of molecular H_2, (ii) the "ensemble effect" of P which decreases the number of active sites on the surface preventing the poisonous effects due to high coverage, and (iii) presence of P sites providing an adequate bonding strength to the evolved H_2 molecule[49, 52]. Nevertheless, despite demonstrating noticeable HER performance, pristine Ni_2P suffers from a larger overpotential (>150 mV) and thus, lower HER performance in the stringent acidic electrolytes in comparison to the characteristic HER performance of benchmark, state-of-the-art Pt/C electrocatalyst.

In the present study, correspondingly, in order to engineer non-PGM HER electrocatalysts exhibiting excellent electrocatalytic activity, durability, and optimized electronic structure, compatible to that of Pt/C electrocatalyst, we have executed theoretical first-principles electronic structure calculations involving determination of the hydrogen binding energy (ΔG_{H*}) to the surface of electrocatalysts. Correspondingly, we have identified cobalt (Co) and sulphur (S) incorporated Ni_2P, denoted as $(Ni_{0.95}Co_{0.05})_2P$: x at. % S (x = 5, 10, 15) as high performance HER electrocatalyst systems, for very first time to the best of our knowledge. There are various electrocatalyst development strategies and introduction of heteroatom into the parent electrocatalyst (herein Ni_2P) is one of the most utilized approaches to modulate the electronic structure, consequently, altering the electrocatalytic activity.

The as-performed density functional theory (DFT) calculations conducted in the present work reveal that the synergistic effect of incorporating Co and S into Ni_2P can beneficially modify the electronic structure and d-band of bimetallic phosphosulphide [$(Ni_{0.95}Co_{0.05})_2P$: S], resulting in the hydrogen adsorption free energy (ΔG_{H*}) shifting towards the thermoneutral position.[360] In the present study, the rationale for selecting Co and S as dopant atoms is their ability to offer the promotional effect i.e. lowering the charge transfer resistance (R_{ct}), improving the electronic conductivity, and thus, enhancing the HER performance as evidently reported in the various HER, OER as well as HDS based electrocatalyst studies[50]. Based on the theoretical results predicting the optimized surface electronic structure for HER, we have devised a synthetic strategy to fabricate the solid solution of $(Ni_{0.95}Co_{0.05})_2P$: x at. % S (x = 5, 10, 15) compositions via a simple, economical, and facile solid-state synthesis approach. Relying on the beneficial synergistic effect of Co and S incorporation, the as-prepared $(Ni_{0.95}Co_{0.05})_2P$:15S electrocatalyst exhibits a high electrocatalytic performance towards acidic HER with the optimized ΔG_{H^*}, cohesive energy (E_{coh}), significantly lower overpotential, excellent HER activity and durability, comparable to Pt/C. The present work therefore putatively, documents the simultaneous incorporation of Co and S into the Ni_2P lattice, offering a promising opportunity for tailoring the physical, electronic, and electrocatalytic properties of bimetallic phosphosulphide to match the Pt/C based HER system.

10.3 Computational Methodology

The electrocatalytic activity of HER electrocatalyst can be described by a single parameter ΔG_{H^*}, which is the free energy of adsorbed hydrogen atom on the electrocatalytic surface. The low value of ΔG_{H^*} (i.e. close to zero) indicates the more optimal adsorption and desorption of hydrogen species at the electrocatalyst surface and thus, offering higher overall electrocatalytic activity of the electrocatalyst material[113, 114, 361]. In general, ΔG_{H^*} is represented by the following relation: $\Delta G_{H^*} = \Delta E_{H^*} + \Delta ZPE - T\Delta S$, where the reaction energy ΔE_{H^*} is calculated using the DFT based methodology as shown below:

$$\Delta E_{H^*} = E(\text{slab} + nH) – E(\text{slab} + (n\text{-}1)\ H) – 1/2\ E(H_2).$$

Here, E(slab + nH) is the total energy of a catalyst surface slab with n hydrogen atoms adsorbed on the surface, E(slab + (n-1)H) is the total energy of the corresponding catalyst surface slab with (n-1) hydrogen atoms (after removal of one hydrogen atom from the given site), and $E(H_2)$ is the total energy of the hydrogen molecule in the gas phase. Also, for calculations of ΔG_{H^*} for all the electrocatalyst materials, the zero point energy correction ΔZPE minus the entropy term

TΔS (ΔZPE - TΔS) has been taken as 0.24 eV, following the computational study by Nørskov et al.[361]

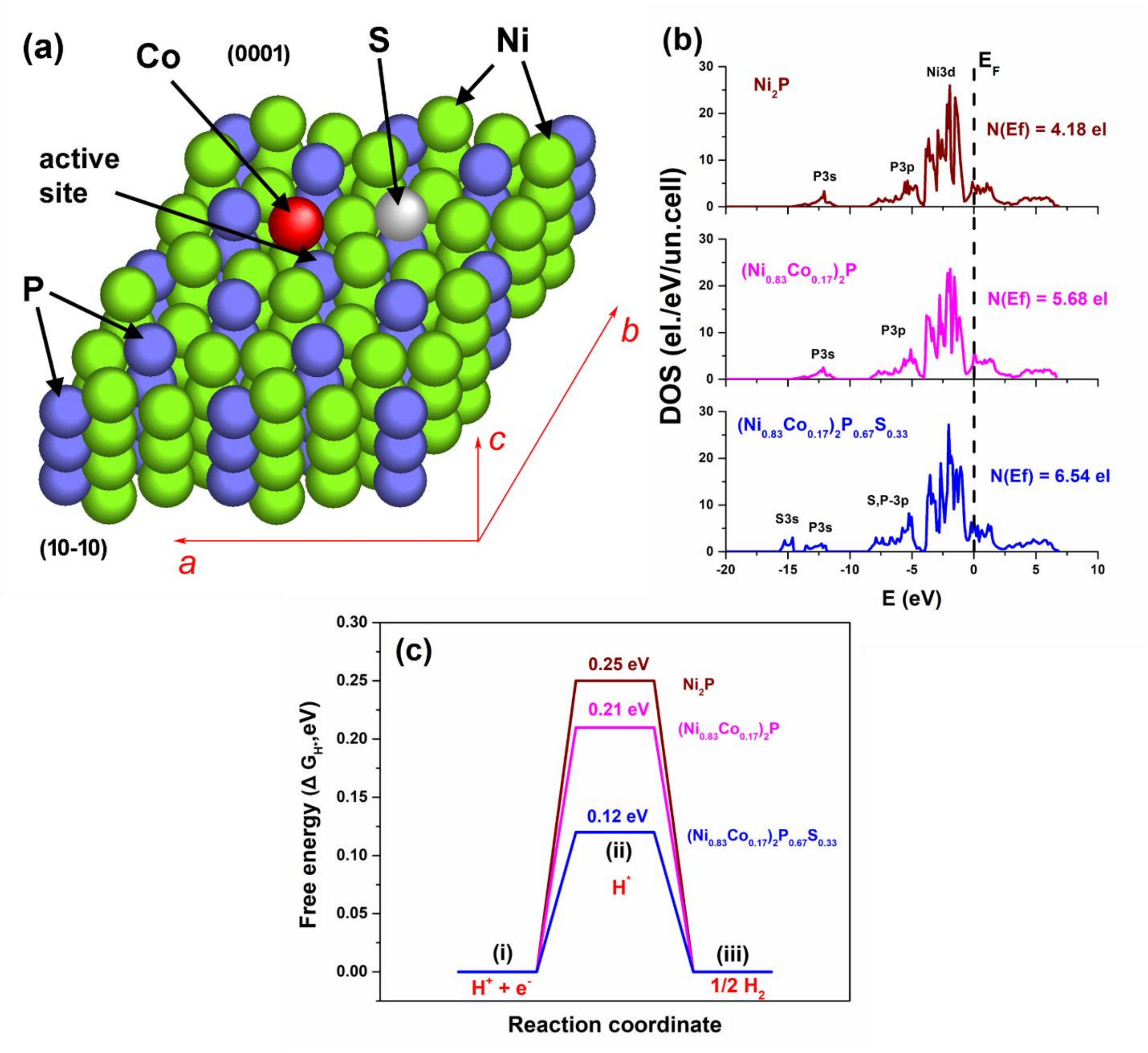

Figure 10-1 (a) Crystal structure of Ni_2P with Ni_3P_2 termination of (0001) surface. Green atoms – Ni, blue - P, gray - S, and red - Co. Arrow denotes triple-Ni active sites. Vectors *a, b,* and *c* correspond to the bulk crystal

structure lattice parameter directions, (b) calculated total density of electronic states for pure Ni_2P, $(Ni_{0.87}Co_{0.17})_2P$, and $(Ni_{0.87}Co_{0.17})_2P_{0.67}S_{0.33}$; Fermi level is set to zero energy. Labels indicate major contributions from corresponding projected electronic states, and (c) free energy with respect to HER reaction pathway

For calculations of the bulk and surface properties of Ni_2P:S, a hexagonal crystal structure P-62m (space group #189) with three formula units in the unit cell and the lattice parameters $a = b = 5.859$Å and $c = 3.382$Å have been considered as shown in **Figure 10-1(a)**[362, 363]. In all the calculations, one monolayer of H-coverage on the (0001) surface has been considered. There are two terminations of (0001) surfaces of Ni_2P structure, namely Ni_3P and Ni_3P_2. Previous DFT study conducted by Q. Li and X. Hu showed that the (0001) surface prefers Ni_3P_2 terminations due to higher stability.[364] Thus, this surface termination has been chosen with triple-Ni sites considered being catalytically active for the present DFT study of hydrogen binding energies as a qualitative descriptor of the HER catalytic activity.

The common surface slab used in the present DFT study consists of five atomic layers corresponding to two lattice parameters in the c direction which is perpendicular to (0001) crystallographic plane and separated by vacuum layer of ~20 Å to prevent the interaction between the slab and its image. The first two layers are fixed with bulk structural parameters, while the remaining three top layers were allowed to relax together with all the adsorbed hydrogen atoms on the surface. Herein, since the purpose of the present theoretical study is to illuminate the effects of introduction of Co and S elements on the overall electrocatalytic activity of Ni_2P, thus, only one composition of each dopant has been selected for the calculation of ΔG_{H*} and other properties of the corresponding compounds. Therefore the ΔG_{H*} values been calculated for pure Ni_2P, $(Co_{0.17}Ni_{0.83})_2P$, and $(Co_{0.17}Ni_{0.83})_2P_{0.67}$:$S_{0.33}$ compositions.

10.4 Experimental Methodology

Figure 10-2 Schematic illustration for the synthesis process of $(Ni_{0.95}Co_{0.05})_2P$:x at. % S electrocatalysts

Schematic illustration of the various steps involved in the synthesis of $(Ni_{0.95}Co_{0.05})_2P$:S electrocatalyst is outlaid in **Figure 10-2**. Specifically, Nickel (II) chloride hexahydrate ($NiCl_2.6H_2O$, 98%, Acros Organics), cobalt chloride hexahydrate ($CoCl_2.6H_2O$, 98%, Aldrich), sodium hypophosphite hydrate ($NaH_2PO_2.xH_2O$, Aldrich), and sodium thiosulfate pentahydrate ($Na_2S_2O_3.5H_2O$, ≥99.5%, Aldrich) were used as the sources for Ni, Co, P, and S, respectively. The optimal mixtures of stoichiometric amounts of these precursors were mechanically ground using a mortar and pestle [($NiCl_2.6H_2O$ + $CoCl_2.6H_2O$) = 10 mol%; ($NaH_2PO_2.xH_2O$ + $Na_2S_2O_3.5H_2O$) = 90 mol%)]. The ratio of $NaH_2PO_2.xH_2O$, and $Na_2S_2O_3.5H_2O$ were then correspondingly altered to obtain $(Ni_{0.95}Co_{0.05})_2P$: x at. % S (x= 0, 5, 10, 15) with the desired nominal percentage of S and P in the final system. The resulting solid mixtures were transferred in alumina crucible and the crucibles containing the solid mixtures were subjected to heat treatment in ultra-high purity argon atmosphere (Matheson; 99.99%, flow rate = 100 cm^3 min^{-1}) at 250°C for 1 h (Ramp rate = 10°C min^{-1}). The thermally treated solid mixtures were naturally cooled to room temperature in continuous Ar gas flow. The obtained products were then crushed using a mortar and pestle and thoroughly washed with ethanol followed by vacuum drying at room temperature.

10.5 Results and Discussion

10.5.1 Theoretical Study illuminating the Effect of Co and S on the Electrochemical Activity and Stability $(Ni,Co)_2P$:S Compounds

The electrocatalytic activity of any electrocatalyst is anticipated to depend on the electronic structure as well as the electronic conductivity, while the long-term stability of the electrocatalyst is assumed to qualitatively depend on the cohesive energy of the system. The effect of compositions on the electronic and catalytic properties as well as on the structural stability of the material can be investigated from the theoretical studies. As mentioned in the ‘Computational Methodology’ section, the key purpose of the computational component of the present study is to investigate the effects of Co and S dopants on the electrocatalytic activity as well as the structural and electrochemical stability of Ni_2P during HER. Accordingly, the electronic structure, hydrogen adsorption free energies (ΔG_{H^*}), and the cohesive energies of the materials as a qualitative measure of the electrochemical activity and stability, have all been evaluated for the different electrocatalyst compositions in the present study.

For a good HER electrocatalyst, it is critical that the ΔG_{H^*} should be close to zero which will enable facile adsorption and desorption of hydrogen atoms from the surface of the electrocatalyst during HER. Therefore, it is imperative to estimate the free binding energy of the hydrogen to the electrocatalytic surface. Accordingly, modification of the electrocatalytic surface electronic structure by altering the chemical composition in such a way that the resulting ΔG_{H^*} is close to zero can significantly improve the electrocatalytic activity of the material. Thus, the hydrogen binding free energies have been obtained from DFT calculations by subtracting the free energy of the pristine electrocatalyst surface and a half of a hydrogen molecule in the gas phase from the corresponding free energy of the electrocatalyst surface with hydrogen atom bonded to the site. Similar methodology has been used in the computational study by Nørskov et al. in the previous report[361].

Table 10-1 Calculated free energy of hydrogen adsorption (ΔG_{H}*), the electronic density of states at the Fermi level [($N(E_F)$)], and cohesive energy ($-E_{coh}$) for all materials considered in the present DFT study

Materials	ΔG_{H^*} (in eV)	$N(E_F)$ el./eV/unit cell	$-E_{coh}$ (eV/f. un.)
Ni_2P	0.25	4.18	15.41
$(Co_{0.17}Ni_{0.83})_2P$	0.21	5.68	15.57
$(Co_{0.17}Ni_{0.83})_2P_{0.67}S_{0.33}$	0.12	6.54	15.35

Table 10-1 tabulates the values of the ΔG_{H*}, density of states at the Fermi level [$N(E_F)$], and cohesive energies (E_{coh}) for all the different materials considered in the present study. It can be seen that the adsorption of hydrogen to the surface of pure Ni_2P is too weak and quite far from the optimal value which results in an inferior electrocatalytic activity for HER. From the electronic structure consideration, it can be inferred that since Ni-3d electrons locate relatively deep below the Fermi level (the Ni-3d band center lies around -2.2 eV vs. Fermi level), the hybridization between these electrons and H-1s states located above the Fermi level becomes very weak and thus, renders the adsorption of hydrogen atoms practically impossible [**Figure 10-1(b)**].

It is noteworthy however, that introduction of Co into the Ni_2P lattice; substituting for Ni reduces the ΔG_{H*} noticeably bringing its value toward the more optimal energy value [**Figure 10-1(c)**]. Herein, new Co-3d electronic states are generated, locating closer to the Fermi level and hybridize with H-1s electrons slightly better resulting in stronger interaction between hydrogen atoms and the surface of the material (in particular, with Co atoms). This result is also ably supported by the fact that the decomposition energy of diatomic molecule Co-H is ~245 kJ mol^{-1}, while the same for Ni-H molecule is ~240 kJ mol^{-1}, which is slightly weaker[179]. Such alteration in the electronic structure is anticipated to advance the electrocatalytic activity of the electrocatalyst. The substitution of phosphorus by sulfur in $(Ni_{0.83}Co_{0.17})_2P$ brings the hydrogen adsorption energy even more closely to the zero value of ~0.1 eV. This result demonstrates improvement in the strength of the hydrogen-surface interaction due to the stronger H-S bonds in comparison to the H-P bonds (bond dissociation energies for diatomic molecules are 353.6 kJ mol^{-1} *vs*. 297.0 kJ mol^{-1}, respectively)[179]. This outcome of the sulfur addition is estimated to further increase the electrocatalytic activity of $(Ni_{0.83}Co_{0.17})_2P$:S. Thus, utilizing the concept of free energy of hydrogen adsorption to the electrocatalytic surface, the present study has demonstrated the beneficial effect of incorporation of Co and S on the expected catalytic activity of Ni_2P electrocatalyst for HER. In addition, both the incorporation of S dopant and the presence of P vacancy can both effectively optimize the ΔG_{H*}, remarkably promoting the desorption of H* and thus, the HER activity[365, 366]. Also, by replacing P with S, more electrons are taken from the metal atoms. Therefore, the desorption of the HER intermediates can be promoted by the substitution of P with S, ultimately increasing the utilization rate of the Co active sites. Accordingly, utilizing the concept of ΔG_{H*} toward the electrocatalytic surface, the beneficial effect of incorporation of Co and S on the expected HER electrocatalytic activity of Ni_2P is anticipated.

Furthermore, the additional goal of the present study as delineated earlier is to inspect the effect of Co and S doping on the electronic conductivity of Ni_2P. It is well-known that the metallic conductivity is directly proportional to the $N(E_F)$. Thus, the study of density of states indeed offers a qualitative evaluation of the influence of these dopants on the overall electronic conductivity of Ni_2P. The electronic structure of pure Ni_2P as well as the phosphide doped with Co and S calculated in the present study demonstrates a metal-type conductivity for all the three compositions of the proposed electrocatalysts with non-zero density of the electronic states at the Fermi level (Figure 1b). However, the values for the density of electronic states at the Fermi level are different indicating slight improvement in the electronic conductivity with the introduction of Co and S into the Ni_2P crystal structure.

The incorporation of Co into the Ni_2P system thus alters the electronic structure to relay the presence of Co-3d electrons in the vicinity of the Fermi level which increases the number of electrons. This therefore results in a slight improvement in the overall electronic conductivity of the material. Introduction of S into the $(Ni_{0.83}Co_{0.17})_2P$ lattice by substituting for P atoms further improves the conductivity, as the sulfur atoms bind to lower number of Ni- and Co- 4s valence electrons than phosphorus atoms (2 electrons for each S instead of 3 electrons for each P atom). This makes some of Ni- and Co- valence electrons free in the system and thus increases the number of total charge carriers at the Fermi level, as depicted in **Table 10-1**. Such improvements in the electronic conductivity are beneficial for the overall electrocatalytic activity of the material while also favoring the hydrogen adsorption energy to the surface of the electrocatalyst.

Furthermore, another goal of the present theoretical study is the investigation of structural and electrochemical stability of the HER system. This has been gathered by evaluating the cohesive energy E_{coh}. A higher E_{coh} (more negative value) consequently, suggests a higher stability of the electrocatalyst material. **Table 10-1** shows the E_{coh} calculated for the various electrocatalyst compositions. It can be seen that an introduction of Co into the Ni_2P lattice noticeably increases the cohesive energy and thus, offers improvement in the overall stability of $(Ni_{0.83}Co_{0.17})_2P$ due to the presence of the stronger Co-P bonds in comparison to Ni-P [calculated E_{coh} for pure Ni_2P is -15.41 eV/formula unit vs. -15.57 eV/formula unit for $(Ni_{0.83}Co_{0.17})_2P$]. Nevertheless, further introduction of S into the $(Ni_{0.83}Co_{0.17})_2P$ compound results in reducing the cohesive energy which occurs mainly due to the lower ionic charge of S^{2-} *vs.* P^{3-} and thus, leads to significantly weakening of the electrostatic component of Ni-S and Co-S bonds than those of Cu-P and Co-P ionic bonds. Despite a relative decrease in the cohesive energy of $(Ni_{0.83}Co_{0.17})_2P_{0.67}S_{0.33}$, the overall chemical and structural stability of the material is preserved and is not significantly compromised by the introduction of S into the system. The substitution and incorporation of S, therefore, makes this material capable of withstanding the harsh electrochemical conditions during HER.

Consequently, on the basis of the present DFT study, $(Ni,Co)_2P$:S is expected to reveal improved electrochemical performance owing to its optimal hydrogen adsorption energy and improved electronic conductivity, along with the good structural and electrochemical stability.

Such beneficial modification of the electronic structure provides favorable electrocatalytic attributes to this material making it an excellent candidate for HER electrocatalysis. Accordingly, pre-empted by the DFT study, in order to validate these theoretical results, in the present study, experimental synthesis and characterization of different compositions of $(Ni_{0.95}Co_{0.05})_2P$: x at. % S (x=5, 10, 15) have been conducted, the results of which are elucidated in the following sections.

10.5.2 Experimental Results

10.5.2.1 Structural Characterizations

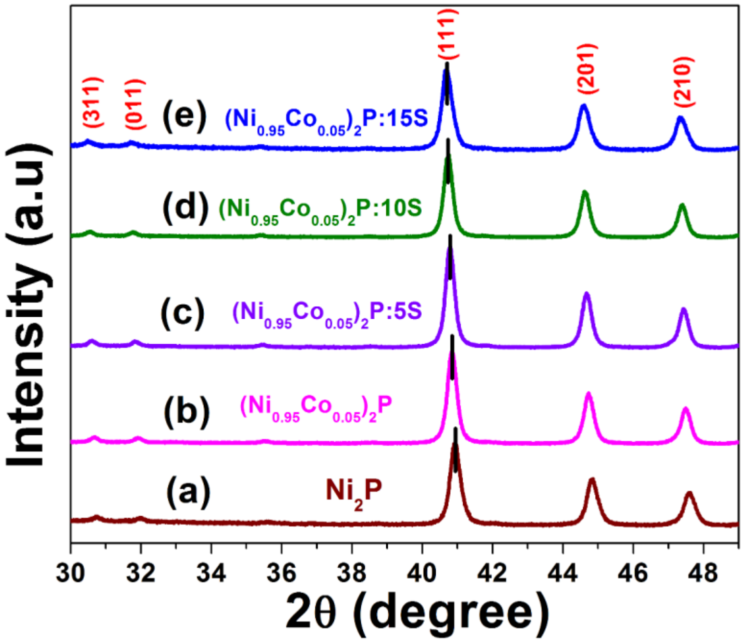

Figure 10-3 Powder XRD patterns of as-synthesized electrocatalysts

The crystalline phase structure and phase purity of as-synthesized electrocatalysts have been characterized by the powder X-ray diffraction (XRD) analysis (**Figure 10-3**). The XRD patterns of as-synthesized Ni_2P show a hexagonal structure (space group P^{-}_{62m}, JCPDS card no: 74-1385) with lattice parameters a = b = 5.859 Å, c =3.382 Å, and unit cell volume of ~116.096 $Å^3$, which is in good agreement with the previously reported literature results[362, 363]. The Co doped Ni_2P i.e. $(Ni_{0.95}Co_{0.05})_2P$ exhibits a hexagonal structure, similar to pure Ni_2P with a slight negative peak shift toward lower diffraction angles, reflective of the expected lattice expansion upon cobalt (5 at. %) incorporation into the Ni_2P lattice. This result has been further substantiated by increase in the lattice parameters and unit cell volume of $(Ni_{0.95}Co_{0.05})_2P$. All the XRD powder diffraction pattern reflections of $(Ni_{0.95}Co_{0.05})_2P$:S with different S concentrations show XRD peaks corresponding to single phase hexagonal structured $(Ni_{0.95}Co_{0.05})_2P$, devoid of any other peaks corresponding to any undesired secondary phases of S-based compounds. In addition, increasing S concentrations in the $(Ni_{0.95}Co_{0.05})_2P$ results in gradual shifts toward lower diffraction angles for the XRD peaks, which further affirms to the successful incorporation of S into the $(Ni_{0.95}Co_{0.05})_2P$ lattice. Similar results depicting slight negative shifts in peak positions are witnessed and documented in earlier published reports of S-doped $CoSe_2$ electrocatalyst[367]. Furthermore, as tabulated in **Table 10-2,** the lattice parameters and unit cell volume of S containing electrocatalysts exhibit slight increase with increasing S concentrations, demonstrating slight lattice expansion upon S incorporation which is also in good agreement with the various S doped electrocatalysts reports in the literature[50]. Therefore, these XRD results suggest the successful S incorporation and formation of single-phase solid solutions of $(Ni_{0.95}Co_{0.05})_2P$: S in the synthesized electrocatalysts. It is also important to mention here that at higher S concentration i.e. $(Ni_{0.95}Co_{0.05})_2P$: 20S, the destruction of advantageous solid solution (**Appendix E Figure 1**) is witnessed, with a consequent phase separation into NiS, NiS_2, CoS_2, and Ni_2P.

Table 10-2 Results of electrochemical characterization for HER of as-synthesized electrocatalysts, performed in 1N H_2SO_4 electrolyte solution at 40°C

Electrocatalyst Composition	Lattice parameters (Å)	Unit Cell Volume (Å^3)	R_Ω (Ω cm^2)	R_{ct} (Ω cm^2)	Overpotential at 10 mA cm$^{-2}{}_{geo}$ (mV)	Overpotential at 100 mA cm$^{-2}{}_{geo}$ (mV)	Tafel slope (mV dec^{-1})	Mass Activity (A g^{-1})
Ni_2P	a = b = 5.859, c =3.382	116.09	17.05	25	112	450	121.3	6.85
$(Ni_{0.95}Co_{0.05})_2P$	a = b = 5.871, c =3.396	117.05	16.6	19	74	385	75.92	12.67
$(Ni_{0.95}Co_{0.05})_2P$:5S	a = b = 5.872, c =3.398	117.16	16.35	14	63	308	73.64	20.55
$(Ni_{0.95}Co_{0.05})_2P$:10S	a = b =5.874, c =3.399	117.27	15.62	9	52	197	52.31	30.45
$(Ni_{0.95}Co_{0.05})_2P$:15S	a = b =5.875, c =3.402	117.42	15	6.82	44	102	31.25	43.75
Pt/C	---	---	14.95	6.25	42	95	30	45

It is moreover, well known that typically mixed phase of electrocatalyst systems demonstrate lower electrochemical performance in comparison to the single phase solid solution systems[97, 298]. In a recent review article detail in the stability challenges for OER-HER electrocatalysts, Strasser and co-workers[298] elucidated that the formation of a solid solution or single-phase electrocatalyst is often a critical prerequisite for achieving good performance of multi-metallic electrocatalysts. On the other hand, the different activity and conductivity of the materials in the mixed (multi-phase) electrocatalysts will preferably corrode the less stable material, consequently, leading to increased deterioration in electrochemical activity and stability, which is indeed observed for the electrochemical performance of higher sulfur containing $(Ni_{0.95}Co_{0.05})_2P$: 20S electrocatalysts.

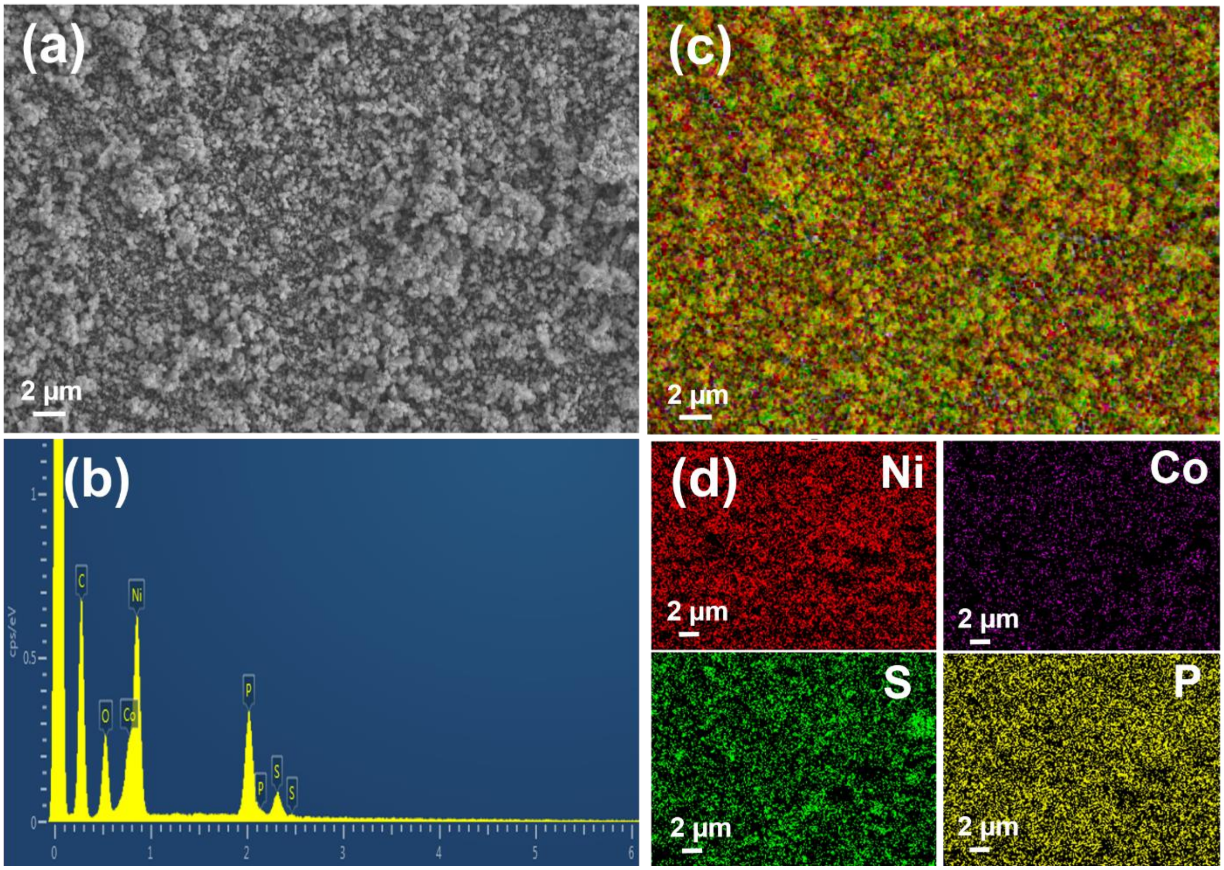

Figure 10-4 (a) SEM micrograph, (b) EDX spectrum, (c, e) elemental x-ray mappings for $(Ni_{0.95}Co_{0.05})_2P$: 15S

The morphology and quantitative elemental compositions of the representative $(Ni_{0.95}Co_{0.05})_2P$: 15S electrocatalyst have been characterized by SEM-EDX measurements. **Figure 10-4(a**) shows the SEM image of as-synthesized $(Ni_{0.95}Co_{0.05})_2P$: 15S electrocatalyst. The EDX pattern of $(Ni_{0.95}Co_{0.05})_2P$: 15S [(**Figure 10-4(b**)] shows the co-existence of Ni, Co, P, and S elements. Quantitative elemental composition analysis of $(Ni_{0.95}Co_{0.05})_2P$: 15S obtained from EDX shows the measured elemental composition (i.e., Ni, Co, P, and S as 63.20, 3.37, 28.16, and 5.27 at. %, respectively) in good agreement with the desired experimental composition, with P:S ratio obtained as ~ 0.8423:0.1577 which is very close to the expected ratio of 85:15. Furthermore, the elemental mapping results of Ni, Co, S, and P of $(Ni_{0.95}Co_{0.05})_2P$: 15S [**Figure 10-4(c-b)**] reveal the uniform distribution of elements within the as-synthesized particles of $(Ni_{0.95}Co_{0.05})_2P$: 15S electrocatalyst powder, devoid of any impurities or segregation at any specific site.

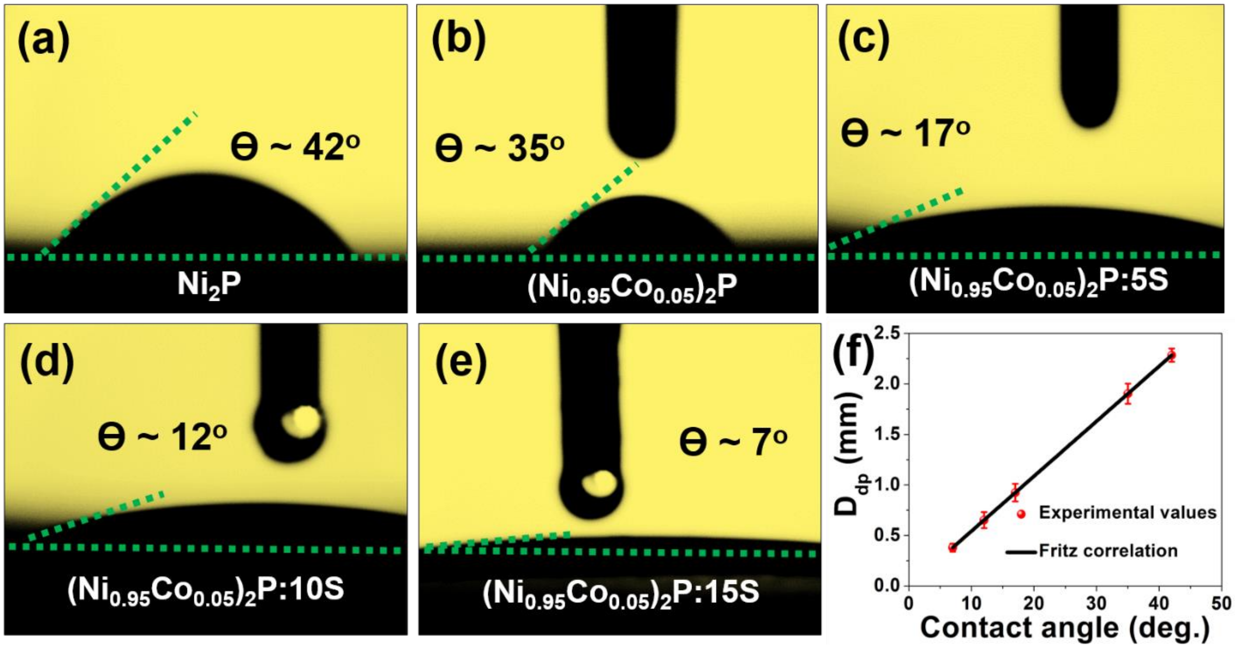

Figure 10-5 (a-e) Contact angles, and (f) bubble break-off diameters for as-synthesized electrocatalysts

The static water contact angle method was employed to investigate the wetting characteristics of the as-synthesized electrocatalysts. As shown in **Figure 10-5**, pure Ni_2P demonstrates a good wettability (hydrophilic nature) with an average water contact angle of ∼42°. Next, $(Ni_{0.95}Co_{0.05})_2P$, $(Ni_{0.95}Co_{0.05})_2P$: 5S, $(Ni_{0.95}Co_{0.05})_2P$: 10S, and $(Ni_{0.95}Co_{0.05})_2P$: 15S electrocatalysts were tested all of which exhibit water contact angles of ∼35°, ∼17°, ∼12°, and ∼7°, respectively, indicating progressive enhancement in wettability of the Co and S doped electrocatalysts in comparison to that of pristine Ni_2P. These results thus suggest the improved affinity of the multi-element containing heterogeneous electrocatalysts for the hydrogen evolution reaction, which in turn can lead to enhancement in their electrocatalytic activities for acid mediated HER[368]. In this regard, various researchers report that the formation of polar bonds by elemental doping as well as by increasing dopant concentrations in the parent electrocatalyst can enhance the wetting characteristic of the doped electrocatalyst[368, 369]. Furthermore, in order to gain deeper insights into the contact angle analysis, employing the Fritz correlation, bubble break-off (or departure) diameters for the as-synthesized electrocatalysts were calculated.

The equation of the Fritz correlation[370] is written as:

$$D_{dp} = 0.20 \times \theta \times \left(\frac{\sigma}{g(\rho_l - \rho_g)}\right)^{0.5} \tag{10-1}$$

where D_{dp} refers to the bubble break-off diameter (m), θ is the contact angle (degree), σ refers to liquid–air surface tension (N m^{-1}), g refers to the acceleration due to gravity (m^2 s^{-1}) and, ρ_l and ρ_g are the density of liquid (water) and gas (air) in units of kg m^{-3}, respectively. According to this equation, a lower contact angle value leads to smaller H_2 bubble diameters. The calculated bubble break-off diameter values for the as-synthesized electrocatalysts are shown in **Figure 10-5**. As can be gleaned from these results, $(Ni_{0.95}Co_{0.05})_2P$: 15S electrocatalyst demonstrates the smallest bubble break-off diameter (~0.38 mm) in comparison to the other synthesized compositions and thus, suggests an expected faster separation of H_2 from the electrode surface. Such characteristics are not only beneficial to free the active sites for subsequent hydrogen evolution reactions, but also to decrease the ohmic resistance (R_Ω) of the electrode, ultimately offering improvement in electrocatalytic activity and HER performance.[371] Accordingly, smaller contact angle and bubble break-off diameter of $(Ni_{0.95}Co_{0.05})_2P$:15S electrocatalyst composition ensures the facile electrolyte penetration as well as rapid H_2 separation from electrode surface, thus leading to expected improved HER kinetics.

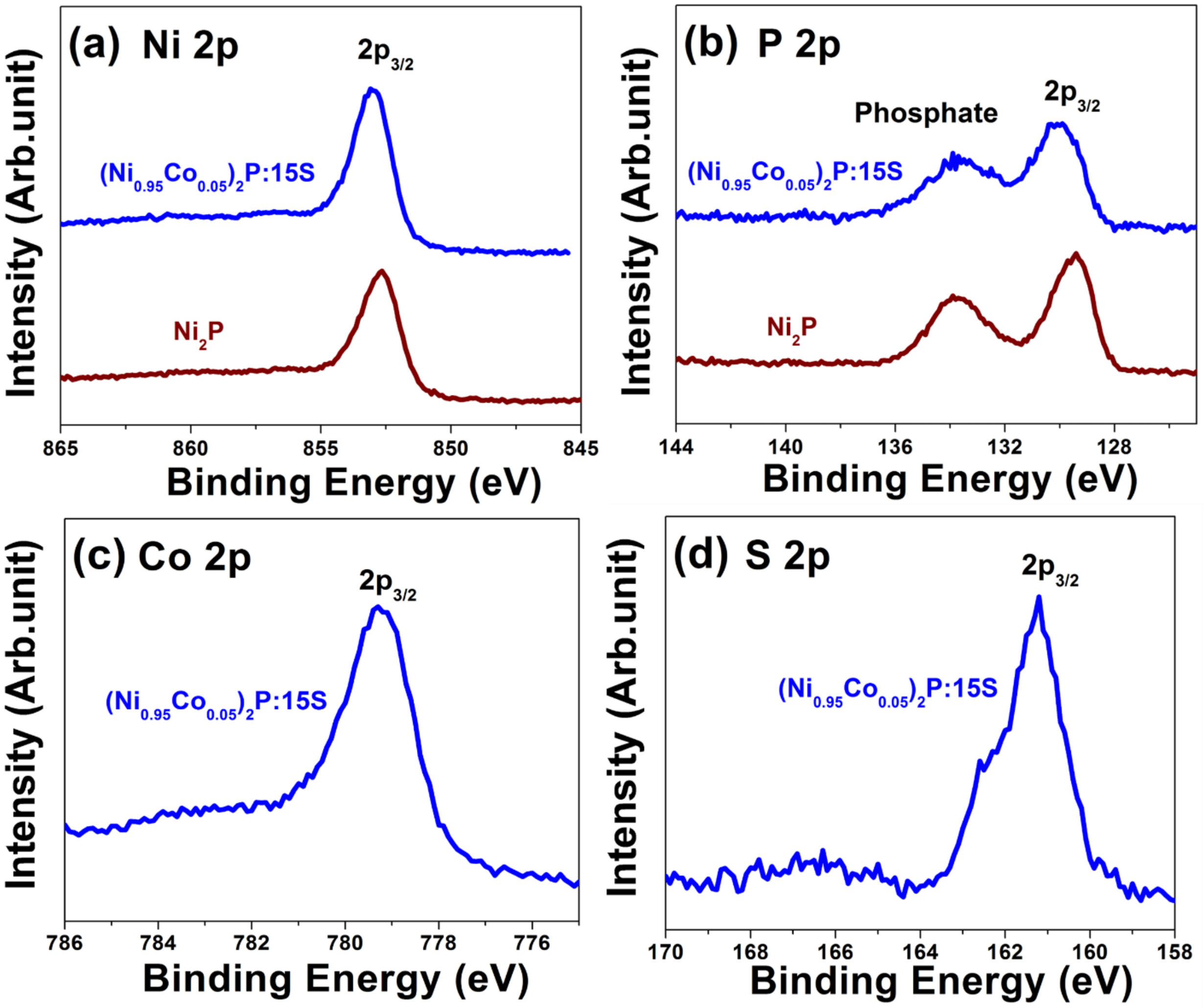

Figure 10-6 (a) XPS spectra for (a) Ni 2p, (b) P 2p, (c) Co 2p, and (d) S 2p of the $(Ni_{0.95}Co_{0.05})_2P$: 15S and Ni_2P

X-ray photoelectron spectroscopy (XPS, **Figure 10-6**) analysis was also performed to investigate the chemical valence states of Ni, P, Co, and S of the as-synthesized pure Ni_2P and the substituted $(Ni_{0.95}Co_{0.05})_2P$: 15S. The XPS spectrum in the Ni $2p_{3/2}$ region for pure Ni_2P shows a peak ~ 852.7 eV which is in good agreement with the earlier published reports[372]. The XPS spectrum of P 2p (for Ni_2P) shows two peaks at ~129.4 and ~133.91 eV which can be ascribed to P $2p_{3/2}$ in Ni_2P and phosphate species (PO_4^{3-}), respectively which can be formed due to the partial oxidation of the surface upon exposure of the Ni_2P particles to air which is commonly observed in all of the various phosphide based electrocatalyst materials reported in the literature.[50] Furthermore, it is important to highlight that the peak at ~ 852.7 eV in the Ni $2p_{3/2}$ region of pure Ni_2P exhibits higher binding energy in comparison to the metallic Ni (~ 852.6 eV)[373] whereas the dominant peak at ~129.4 eV in the P 2p region of pure Ni_2P reflects a lower binding energy in comparison to the elemental P (~130.2 eV)[374]. These results indicate that the Ni metal centers possess a positive partial charge (δ^+) and P pendant bases contain negative partial charge (δ^-), suggesting the transfer of electrons from Ni to P and thus, modification of the charge density of Ni and P in Ni_2P [50, 375]. The obtained results are also indeed in good agreement with various doped (Co, Fe) phosphide electrocatalysts (Co-Cu_3P, Fe-Ni_2P)[50].

In the case of the substituted and doped phosphosulfide, it is important to note that the Ni $2p_{3/2}$ peak for $(Ni_{0.95}Co_{0.05})_2P$:15S demonstrates a higher binding energy value with a positive shift of ~ 0.35 eV in comparison to pristine Ni_2P. This positive shift in the XPS binding energy implies the transfer of electrons from Ni to S and correspondingly, a modification of the charge density due to the formation of the solid solution of phosphosulfide[376]. Similar result of positive shift in the binding energy is observed for the P $2p_{3/2}$ peak of $(Ni_{0.95}Co_{0.05})_2P$:15S which again interprets the modification of electronic structure (as is also substantiated by the DFT results) of the doped and substituted electrocatalyst. Additionally, in the XPS spectrum of Co 2p, the peak at ~779.42 eV can be accredited to Co $2p_{3/2}$ in $(Ni_{0.95}Co_{0.05})_2P$: 15S (which corresponds to Co species in CoP). It is observed that this peak at ~ 779.42 eV contains a shift of ~0.22 eV to higher binding energy in comparison to the typical peak (at ~779.2 eV) in the Co $2p_{3/2}$ region of CoP[377], which can be attributed to electron transfer from Co to S. Moreover, it should be noted that the Co $2p_{3/2}$ peak possesses a higher binding energy than that of metallic Co (~778.4 eV). As elucidated above, this result also suggests the existence of Co (metal centers) with a partial positive charge (δ^+) and P and S (pendant bases) with partial negative charge (δ^-) close to metal center, and consequently, indicating the transfer of electrons from Co to P and S as well as the beneficial improvement in the electronic structure of the $(Ni_{0.95}Co_{0.05})_2P$: 15S electrocatalyst due to the substitution and incorporation of S and Co into the Ni_2P lattice structure[50].

The XPS spectrum of $(Ni_{0.95}Co_{0.05})_2P$:15S in the S 2p region displays a major peak at ~161.16 eV corresponding to the S $2p_{3/2}$ which is in accordance with the S containing phosphide electrocatalysts[50]. Furthermore, to shed more light on the as-obtained XPS results, in the various literature studies it has been reported that the proton relays which are incorporated in a metal complex HER electrocatalyst arise from the pendant acid-base groups. Such groups are adjacent to the metal centers wherein HER is known to occur[375, 378, 379]. The active sites for metal complex hydrogenase enzyme also possess pendant bases which are close to the metal centers[375, 380]. Accordingly, as described above in the XPS results, the as-obtained $(Ni_{0.95}Co_{0.05})_2P$:15S exhibits metal centers Ni, Co (δ^+) and pendant bases P, S (δ^-) that are situated close to the metal centers[50, 375]. It is therefore expected that $(Ni_{0.95}Co_{0.05})_2P$:15S will likely unveil hydrogen evolution mechanism analogous to those of metal complex hydrogenase enzymes reported in the literature[50,

[375]. Based on the above analyses, Ni, Co, P, and S in the active $(Ni_{0.95}Co_{0.05})_2P$:15S electrocatalyst can thus likely exhibit hydride-acceptor and proton-acceptor centers, respectively[50, 375]. Based on the above combination of promising attributes, it can be speculated that the Co and S containing Ni_2P solid solution can offer superior electrochemical response for the hydrogen evolution reaction as documented and described in the sections to follow.

10.5.2.2 Electrochemical characterization of electrocatalysts

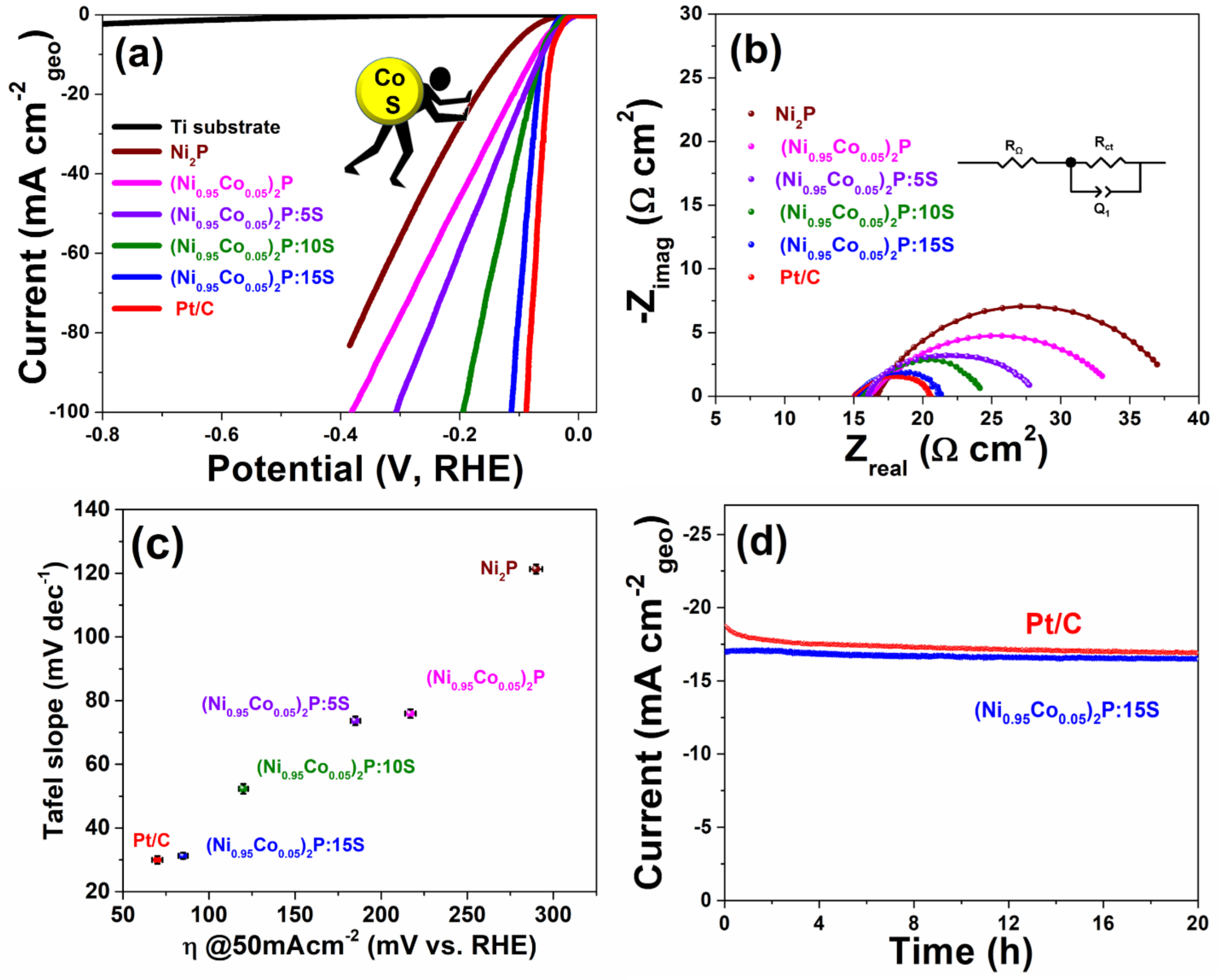

Figure 10-7 Comparison of electrochemical performances of the as-synthesized electrocatalysts measured in a 1 N H_2SO_4 electrolyte at 40 °C (a) HER polarization (mA cm^{-2}$_{geo}$ *vs*. potential) curves with a scan rate of 10 mVs^{-1}, (b) EIS plots performed at -0.05 V (*vs*. RHE), (c) Tafel slope *vs.* overpotential at 50 mA cm^{-2}$_{geo}$, and (d) chronoamperometric response of as-prepared Pt/C and $(Ni_{0.95}Co_{0.05})_2P$: 15S electrodes measured at -0.05 V (*vs* RHE)

The HER activity of as-synthesized electrocatalysts was evaluated in 1N H_2SO_4 solution using a typical three-electrode cell comprising platinum wire as the counter electrode. **Figure**

10-7(a) shows the HER polarization curves of the as-prepared electrodes. The electrochemical performance of the electrodes was compared with state-of-the art commercial Pt/C as a benchmark HER electrocatalyst. As shown in **Figure 10-7(a)**, the current collector - Ti substrate expectedly demonstrates negligible current density in comparison to all of the other active electrocatalysts synthesized and used in the current study and thus, suggests its poor electrochemical activity towards the acid mediated HER. In sharp contrast, the as-synthesized Ni_2P exhibits good HER response by exhibiting an over-potential of 112 mV and 450 mV to deliver current density of 10 and 100 mA $cm^{-2}{}_{geo}$, respectively. Also, in good agreement with the DFT results, the Co doped Ni_2P [$(Ni_{0.95}Co_{0.05})_2P$] demonstrates significantly improved HER activity by attaining a current density of 10 mA $cm^{-2}{}_{geo}$ at an over-potential of 74 mV, 38 mV lower than that of Ni_2P. This activity improvement is attributed to enhanced reaction kinetics (lower activation polarization), reduced hydrogen adsorption free energy, and lower charge transfer resistance (R_{ct}) than Ni_2P as evidently confirmed by the electrochemical impedance spectroscopy (EIS) analysis, discussed later. It is important to highlight that this obtained result is in excellent agreement with the previous literature reports wherein Co incorporation significantly improved the HER kinetics[50].

These studies conclude that the introduction of Co into the parent electrocatalyst material optimizes the overall electronic structure of electrocatalyst, offering reduction of the kinetic energy barrier of H atom adsorption (ΔG_{H^*}) for the doped electrocatalyst and thus, gives rise to improved reaction kinetics and electrocatalytic activity. Furthermore, it is interesting to note that S incorporation into the $(Ni_{0.95}Co_{0.05})_2P$ system noticeably enhances the HER activity. It can be seen from **Figure 10-7(a)** that $(Ni_{0.95}Co_{0.05})_2P$:15S composition demonstrates higher activity by delivering a current density of 10 mA $cm^{-2}{}_{geo}$ at an over-potential of only 44 mV whereas Pt/C, $(Ni_{0.95}Co_{0.05})_2P$:10S, $(Ni_{0.95}Co_{0.05})_2P$:5S, and $(Ni_{0.95}Co_{0.05})_2P$ display overpotentials of ~ 42, 52, 63, and 74 mV, respectively. These results thus clearly suggest that the HER kinetics and activity of $(Ni_{0.95}Co_{0.05})_2P$:15S is comparable to Pt/C and much superior to other PGM-free as-synthesized electrocatalysts. Such enhanced HER activity upon incorporation of optimal amount of S can be ascribed to the further improvement in the electronic structure, charge transfer, and reduction in ΔG_{H*}, as evidently demonstrated by the DFT results. It is also important to mention here that the $(Ni_{0.95}Co_{0.05})_2P$:20S composition exhibits significantly lower HER activity (**Appendix E Figure 2**) in comparison to other studied compositions. As elucidated in the XRD discussions, such reduction in the electrocatalytic activity can be attributed to destruction of the advantageous solid solution state of the electrocatalyst. Similarly, in the literature, various electrocatalysts with different degree of S concentration are reported for HER as well as OER wherein after a certain concentration of S doping, there is decline in the electrocatalytic activity[381, 382]. According to these reports, the excess S concentration hinders the contact between the active sites on the electrocatalyst and reactant (i.e. blocking the active sites), which correspondingly causes a reduction in the electrochemical activity thus displaying a relatively lower HER activity than the sample with appropriate proportion of S. Thus, in the present system, 15 at. % S is observed as an optimal S concentration that exhibits no phase separation, and shows superior HER activity in comparison to 5, 10, and 20 at. % S compositions.

Furthermore, in order to evaluate the interfacial/charge transfer kinetics of hydrogen evolution reaction, electrochemical impedance spectroscopy (EIS) analysis was conducted at -0.05 V *vs* RHE in the frequency range of 100 mHz-100 kHz with an amplitude of 10 mV, using the circuit model of $R_{\Omega}(R_{ct}Q_1)$. As depicted in **Figure 10-7(b),** the EIS plot of the as-prepared electrodes show a well-formed semicircular arc wherein the diameter of semicircular arc represents the surface charge transfer resistance (R_{ct}) while the initial point of semi-circular arc on the X-axis represents the ohmic resistance (R_{Ω}). It can be seen from **Figure 10-7(b)**that the pristine Ni_2P exhibits higher ohmic (R_{Ω} ~ 17.05 Ω cm^2) as well as higher surface charge transfer resistance (R_{ct} ~ 25Ω cm^2). The R_{Ω} as well as R_{ct} values for $(Ni_{0.95}Co_{0.05})_2P$ on the other hand, are obtained as ~ 16.6 Ω cm^2 and ~ 19 Ω cm^2, respectively. The reduction in the resistance values suggest the improved charge transfer kinetics in comparison to that of Ni_2P. In addition, the S-doped electrocatalysts demonstrate further reduction in the impedance values, with a lowest values of R_{Ω} ~ 15 Ω cm^2 and R_{ct} ~ 6.82 Ω cm^2 obtained for $(Ni_{0.95}Co_{0.05})_2P$:15S in comparison to all of the other electrocatalysts containing 10S and 5S compositions. Moreover, the R_{Ω} and R_{ct} values of the $(Ni_{0.95}Co_{0.05})_2P$:15S electrocatalyst are almost similar to commercial Pt/C. Consequently, these results evidently reflect the higher charge transfer rate and faster HER kinetics achieved for the optimum composition of $(Ni_{0.95}Co_{0.05})_2P$:15S. It is also important to mention that, since pure Ni_2P and $(Ni_{0.95}Co_{0.05})_2P$:15S exhibit comparable surface area (~1.55 m^2g^{-1}), the enhanced charge transfer kinetics and HER activity is attributed to the optimized surface electronic structure of Co and S containing $(Ni_{0.95}Co_{0.05})_2P$:15S for HER as well as lower water contact angle ensuring the facile electrolyte penetration and thus, offering lower ohmic as well as charge transfer resistance. The mass activity and turn over frequency for the $(Ni_{0.95}Co_{0.05})_2P$:15S electrocatalyst is also superior compared to the other electrocatalysts studied in this work (**Appendix E Table 1**).

Additionally, in order to obtain more insights into the electrochemical kinetics of as-synthesized electrocatalysts and compare their HER activity, as depicted in **Figure 10-7(c)**, Tafel slopes and over-potential to attain the current density of 50 mA cm^{-2} $_{geo}$ are reported. The $(Ni_{0.95}Co_{0.05})_2P$:15S demonstrated smaller Tafel slope (31.25 mV dec^{-1}) and overpotential (85 mV at 50 mA cm^{-2} $_{geo}$) which is comparable to that of Pt/C, and is also consistent with the previous literature of Pt/C while also being remarkably lower than all of the other as-synthesized electrocatalyst[50]. Typically, three possible reaction steps are known for the HER in acidic electrolytes namely, the discharge step (Volmer reaction, $H_3O^+ + e^- \rightarrow H_{ads} + H_2O$), the catalytic recombination step (Tafel reaction, $H_{ads} + H_{ads} \rightarrow H_2$), and finally, the electrochemical desorption step (Heyrovsky reaction, $H_{ads} + H_3O^+ + e^- \rightarrow H_2 + H_2O$). In this context, the comparable Tafel slope values achieved for $(Ni_{0.95}Co_{0.05})_2P$:15S and Pt/C suggest that the HER process is dominated by a Volmer-Tafel reaction mechanism, in which the recombination of the two adsorbed species (H_{ads}) is the rate-limiting step[367]. It is important to also note that the Tafel slopes values for the other electrocatalyst compositions are obtained in the range of 40-120 mV dec^{-1}, which implies that the HER would likely occur via a Volmer-Heyrovsky reaction process , wherein electrochemical desorption of H_2 is considered as the rate-limiting step[367]. The HER performance of $(Ni_{0.95}Co_{0.05})_2P$:15S is also superior compared to other reported non-noble metals based electrocatalysts in acid medium (**Appendix E Table 2)**.

The electrochemical stability of $(Ni_{0.95}Co_{0.05})_2P$:15S was investigated by performing the chronoamperometry (CA) test at constant potential of -0.05 V *vs* RHE. As displayed in **Figure 10-7(d)**, the as-synthesized $(Ni_{0.95}Co_{0.05})_2P$:15S demonstrates good HER durability, comparable to that of the state-of-the-art Pt/C, with a negligible change in current density. In addition, as illustrated in **Appendix E Figure 5**, the response of the $(Ni_{0.95}Co_{0.05})_2P$:15S electrocatalyst following the stability tests, demonstrated no significant change in the activity and charge transfer resistance after the durability test, suggesting robust HER electrocatalysis of the $(Ni_{0.95}Co_{0.05})_2P$:15S in acidic electrolyte. For example, the LSV and EIS of $(Ni_{0.95}Co_{0.05})_2P$:15S following the stability tests reveal negligible change in the electrocatalytic activity i.e. attaining current density of 10 and 100 mA cm^{-2}_{geo} at an overpotential of only ~ 46 mV and ~108 mV, respectively, and exhibiting R_{ct} and R_{Ω} of ~ 7.35 and ~ 15.20 Ω cm^2 (at -0.05V), respectively, which are very close to the values exhibited by the $(Ni_{0.95}Co_{0.05})_2P$:15S electrocatalyst electrode prior to the stability test with negligible change. Furthermore, as shown by the post-stability XRD (**Appendix E Figure 6**), SEM, elemental map, and EDX results collected on the electrode following the chronoamperometry stability tests (**Appendix E Figure 7**), the crystal structure, morphology, microstructure, and chemical composition of the electrocatalyst, $(Ni_{0.95}Co_{0.05})_2P$:15S are well-preserved after the stability test operation, indicating the structural robustness and mechanical integrity of the electrocatalyst composition for acidic HER. Furthermore, the post-stability XPS (**Appendix E Figure 8**) collected on the electrocatalyst following the stability test results clearly reveal no major changes in the oxidation states or peak positions, suggesting the good structural and electrochemical durability of the $(Ni_{0.95}Co_{0.05})_2P$:15S electrocatalyst composition toward acidic HER. Finally, inductively coupled plasma optical emission spectroscopy (ICP-OES) analysis was conducted on the electrolyte solution collected after the CA test for $(Ni_{0.95}Co_{0.05})_2P$:15S of three samples from three independent tests which indicates minimal elemental dissolution in the electrolyte solution (**Appendix E Table 3**). Consequently, these results suggest the excellent electrochemical stability of $(Ni_{0.95}Co_{0.05})_2P$:15S electrode under the operating conditions of acidic HER.

As described above, the present theoretical and experimental study demonstrate the promising electrochemical performance of $(Ni_{0.95}Co_{0.05})_2P$:15S, comparable to that of commercial Pt/C for acid mediated HER. The as-performed DFT and experimental results elucidate the novel and unique modification of the electronic structure due to the introduction of Co and S in the Ni_2P lattice. Thus, in sum total based on the results discussed above, PGM-free $(Ni_{0.95}Co_{0.05})_2P$:15S electrocatalyst, owing to its facile synthesis, low cost, high wettability, and high electrocatalytic performance is indeed a promising HER electrocatalyst.

10.6 Conclusions

In summary, utilizing earth abundant materials and implementing a simple solid-state synthesis approach, we have synthesized $(Ni_{0.95}Co_{0.05})_2P$:x at. % S (x =0, 5, 10, 15) and demonstrated the highly active and robust nature of these electrocatalysts for acid mediated HER. The as-synthesized $(Ni_{0.95}Co_{0.05})_2P$:15S possessing optimized hydrogen adsorption free energy (ΔG_{H*}) and beneficial surface electronic modification from DFT analysis experimentally demonstrated excellent electrocatalytic activity in comparison to that of pure Ni_2P and $(Ni_{0.95}Co_{0.05})_2P$: x at. % S (x = 0, 5, and 10). The $(Ni_{0.95}Co_{0.05})_2P$:15S electrocatalyst exhibited a lower charge transfer resistance (6.82 Ω cm^2), a lower over-potential (44 mV) at 10 $mAcm^{-2}$, a much smaller Tafel slope (31.25 mV dec^{-1}), and a higher mass activity (43.75 A g^{-1}) in comparison to the other electrocatalyst compositions. Additionally, the highly active $(Ni_{0.95}Co_{0.05})_2P$:15S electrocatalyst displayed good long term electrochemical HER stability in the acidic media, with no major degradation in the current density thus, suggesting its excellent structural robustness and mechanical integrity for prolonged HER. The superior electrochemical performance of $(Ni_{0.95}Co_{0.05})_2P$:15S is also adequately supported by our DFT calculations which revealed that the $(Ni_{0.95}Co_{0.05})_2P$:15S composition exhibits the highest electronic density of states at the Fermi level $N(E_F)$ and reduced reaction barrier (0.12 eV) thus, offering improved electrocatalytic activity for HER. Therefore, on the basis of the theoretical calculations and electrochemical studies, the present work demonstrates the excellent promise of simultaneous incorporation of Co and S into Ni_2P to enhance the electrochemical performance of these Co and S containing phosphide systems validating their potential use as electrocatalysts for the highly efficient acid mediated hydrogen evolution reaction.

11.0 Specific Aim 2B - To Identify and Develop High Performance Electrocatalysts for Hydrogen Oxidation Reaction (HOR) in Proton Exchange Membrane Fuel Cells (PEMFCs)

Ultra-Low Platinum Containing Titanium Silicide Alloys – New High Performance Hydrogen Oxidation Reaction Electrocatalysts for Acid Mediated Proton Exchange Membrane Fuel Cell

11.1 Abstract

Proton exchange membrane fuel cell (PEMFC) research has garnered much attention over the years as a promising and sustainable approach to power generation with reduced greenhouse gas emissions at much higher efficiencies in comparison to conventional combustion-based technologies. The technology still is very much dictated by expensive platinum group metal (PGM) containing electrocatalysts. It is thus vital to identify reduced PGM containing electrocatalysts exhibiting electrochemical performance matching or superior to state-of-the-art electrocatalysts thus signifying significant cost reduction of PEMFC. Accordingly, in the present work, Pt containing titanium silicide [$(Ti_{1-x}Pt_x)_5Si_3$] alloy based solid solution electrocatalysts are identified and engineered for the first time for hydrogen oxidation reaction (HOR) ably supported by density functional theory (DFT) calculations and further validated by experiments. The results demonstrate high electrocatalytic activity as well as good electrochemical and structural stability for the novel $(Ti_{1-x}Pt_x)_5Si_3$ electrocatalysts. These alloy electrocatalysts are synthesized via a simple, scalable, and economical mechanical milling process. Results reveal lower HOR electrocatalytic activity as expected for pure Ti_5Si_3, while silicide alloys containing much reduced Pt content demonstrated significant improvement in HOR electrocatalytic activity and kinetics. Accordingly, pure Ti_5Si_3 exhibited a charge transfer resistance (R_{ct}) of ~ 43 Ω cm^2. On the other hand, ~ 3.75 at. % Pt alloyed silicide $(Ti_{0.94}Pt_{0.06})_5Si_3$ revealed R_{ct} of ~16 Ω cm^2, ~3X lower than pure Ti_5Si_3 and comparable to commercial Pt/C (~14 Ω cm^2), suggesting beneficial improvement in transport and kinetics with introduction of reduced amount of Pt in Ti_5Si_3. In addition, the HOR peak current density (at ~ 0.05 V vs. RHE) for Pt/C, 2.5, and 3.75 % Pt doped Ti_5Si_3 is ~ 0.9, 0.54 and 0.75 mA cm^{-2}, respectively, significantly higher than for pure Ti_5Si_3 (~0.22 $mAcm^{-2}$) while not much lower than Pt/C. The improved charge transfer kinetics and HOR performance are also successfully validated by DFT calculations, revealing optimal hydrogen adsorption free energies (ΔG_{H*}) and cohesive energy ($-E_{coh}$) for the reduced Pt containing Ti_5Si_3. Durability tests conducted for $(Ti_{0.94}Pt_{0.06})_5Si_3$ in H_2 saturated 1N H_2SO_4 also display minimal current density loss, indicating good electrochemical stability towards HOR. The theoretical aided experimental results outlined here clearly demonstrate the promise of ultra-low PGM containing $(Ti_{0.94}Pt_{0.06})_5Si_3$ electrocatalyst for HOR, delineating a path towards development of earth abundant and reduced PGM based electrocatalysts for PEMFCs.

11.2 Introduction

In recent years, proton exchange membrane fuel cells (PEMFCs) have garnered significant interest owing to their reliable and sustainable pathway towards unremitting power production with reduced greenhouse gas emissions contrasted with conventional fossil fuels based combustion technologies[45, 50, 70, 189, 358, 383, 384]. However, in spite of the promising attributes of PEMFCs, in order to realize the complete potential of PEMFCs translating into a commercially viable technology, there is a critical need to identify earth abundant and inexpensive electrocatalyst systems which can unveil high electrocatalytic performance for oxygen reduction (ORR) and hydrogen oxidation (HOR) reactions in comparison to the currently employed state-of-the-art and expensive platinum group metal (PGM) based electrocatalysts[76, 111, 385-388]. Although significant advances have been made related to identification and development of ultra-low PGM containing including PGM-free ORR electrocatalysts for PEMFC, there has been comparatively, much less research directed towards development of reduced PGM based HOR electrocatalysts.

In the pursuit of lowering the cost of PGM based electrocatalysts, a widely employed approach followed is alloying reduced amounts of noble metals (e.g. Pt, Ir, Ru) with earth abundant and inexpensive transition metals such as Sn, Ni, Mo, Fe, Ti etc., resulting in improved electronic structure together, offering electrochemical performance that is comparable or superior to the noble metal based electrocatalysts[389-395]. Various literature reports convincingly demonstrate the high performance of Pt supported or reduced Pt containing electrocatalysts ascribing the favorable response to reduction in the Pt-Pt interatomic distance, attainment of uniform dispersion of Pt over the support material, and beneficial modification of the electronic structure due to the solid solution formation in Pt containing electrocatalysts, together offering high electrocatalytic activity primarily because of the optimal adsorption/dissociation energies for hydrogen[396, 397]. Accordingly, in recent years various Pt containing electrocatalyst systems such as Pt–Sn/C, Pt–Sn–Ir/C, Pt–Ru, Pt–Ru–Os–Ir, Pt–Co, Pt–Ti/C, Pt–Ni–Cr/C, Pt–CuO/C, Pt–Ni/C, Pt-WC, Pt–WO_3–TiO_2/C, etc. have been investigated for various reactions such as ethanol oxidation, oxygen reduction reaction, and hydrogen oxidation reactions, demonstrating the promise of alloying or solid solution formation as a pathway to high performance reduced noble metal containing electrocatalysts[398-401].

Therefore, in the present study, employing the first-principles calculations of the electronic structures and cohesive energies, we have investigated low Pt containing transition metal silicides (titanium silicide, Ti_5Si_3) based electrocatalysts for acid mediated HOR. Exploiting their favorable attributes of high electrical and thermal conductivity, high oxidation resistance, temperature strength and creep resistance, and earth abundance, the transition metal (e.g. Ti, Nb, Ni, Fe) silicides have made a mark as outstanding candidates for myriad electrochemical applications such as in water electrolyzer and fuel cells utilizing their electrocatalytic ability for hydrogen/oxygen evolution reaction (HER/OER) and oxygen reduction reaction (ORR) including microelectronics and nano-electronics based integrated circuit industry harnessing their excellent electronic conductivities for use as interconnects, ohmic contacts and as gate materials in microelectronic transistors, etc. [402-405].

In addition, the theoretical calculations reported by Wirth et al[402], have revealed that strong covalent bonds between Ti and Si atoms offer excellent chemical stability to the titanium silicides, suggesting their potential for use in acidic oxidation as well as reduction reactions. Accordingly, in the present work, Ti_5Si_3 synthesized via high energy mechanical milling approach has been studied as the parent electrocatalyst system. The incorporation of reduced amounts of Pt into the Ti_5Si_3 [$(Ti_{1-x}Pt_x)_5Si_3$] has been determined to be sufficient to modify the electronic structure of Pt containing Ti_5Si_3. The as-synthesized alloyed solid solution electrocatalysts corresponding to $(Ti_{1-x}Pt_x)_5Si_3$ system thus, clearly demonstrate significantly improved electrochemical charge transfer kinetics and electrochemical activity towards HOR in comparison to pristine Ti_5Si_3. In doing so, the present report documents the experimental and theoretical studies of the $(Ti_{1-x}Pt_x)_5Si_3$ alloy system revealing its potential as a favorable hydrogen oxidation reaction (HOR) electrocatalysts for acid mediated PEMFC.

11.3 Experimental Methodology

11.3.1 Synthesis of Ti_5Si_3 and $(Ti_{1-x}Pt_x)_5Si_3$

Elemental titanium (99.9%, −325 mesh), silicon (99.9%, −325 mesh), and 40% Pt/C (Alfa Aesar) were used as precursors for the synthesis of the electrocatalysts. A schematic depicted in **Figure 11-1** illustrates the various steps involved in synthesizing the Pt alloyed Ti_5Si_3 system. Thus, to synthesize the parent Ti_5Si_3 and $(Ti_{1-x}Pt_x)_5Si_3$ (x = 0.04 and 0.06) alloys, elemental powder mixtures were first prepared according to the desired elemental stoichiometry. The blended powder mixtures were then subsequently loaded into stainless steel (SS) vials containing SS balls with a diameter of 2 mm used as the milling media. The ball to powder weight ratio (BPR) was utilized as 5:1.The mixtures were then subjected to dry milling in a high energy Shaker Mill (8000, Spex Industries, Edison, NJ) for 195 minutes to generate the Ti_5Si_3 phase reported by Rodrigues et al [406].

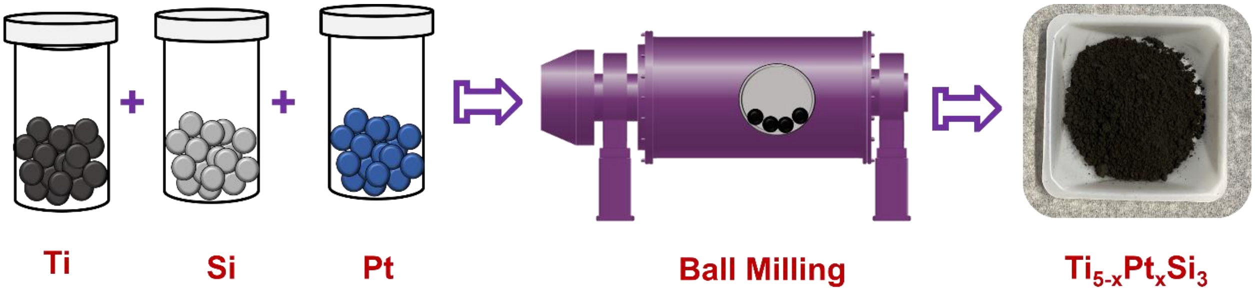

Figure 11-1 Illustration of the synthesis process followed for generating all of the Pt-alloyed Ti_5Si_3

11.3.2 Structural Characterization

X-ray diffraction (XRD) was used for conducting qualitative phase analysis utilizing the Philips XPERT PRO system employing CuK_{α} radiation source (λ = 0.15406 nm) operating at a current and voltage of 40 mA and 45 kV, respectively[303, 351]. Scanning electron microscopy (SEM) was used to investigate the microstructure of the synthesized materials and energy dispersive x-ray spectroscopy (EDX) was employed for conducting the elemental analysis and ascertaining the distribution of individual elements. X-ray photoelectron spectroscopy (XPS, ESCALAB 250 Xi) was performed to investigate the oxidation states of the elements in as-synthesized electrocatalysts, [45, 358].

11.3.3 Electrochemical Characterization

Electrochemical characterizations of the electrocatalysts were conducted using a H_2 saturated 1N sulfuric acid (H_2SO_4) solution at 40°C (using a Fisher Scientific 910 Isotemp refrigerator circulator) employing an electrochemical workstation (VersaSTAT 3, Princeton Applied Research). A three-electrode configuration was used for the test cell setup. The working electrodes were prepared using the electrocatalyst ink consisting of 85 wt.% catalyst and 15 wt.% Nafion 117 (5 wt.% solution in lower aliphatic alcohols, Aldrich) that was spread onto the teflonized carbon paper with a total electrocatalyst loading of ~ 0.4 mg cm^{-2}[116]. A Pt wire and mercury/mercurous sulfate (Hg/Hg_2SO_4) electrode (XR-200, Hach) (+0.65V *vs* RHE) were used as the counter electrode and reference electrode, respectively. The electrochemical performance for HOR of the parent non platinum containing unalloyed Ti_5Si_3 and Pt-doped Ti_5Si_3 was compared with that of the state-of-the-art Pt/C electrocatalyst. The electrochemical characterizations of commercial 40% Pt/C electrocatalyst (Alfa Aesar, 0.4 mg of Pt loading on 1cm^{-2} area) were also conducted under the same operating conditions.

Electrochemical impedance spectroscopy (EIS) was also used to investigate the ohmic resistance (R_Ω) (which includes resistance of all the components including electrolyte and electrode) and the charge transfer resistance (R_{ct}) of all the synthesized electro-catalyst materials. The frequency range of 100 mHz-100 kHz at ~0.05 V and 10mV amplitude was used for the EIS characterization. The ZView software from Scribner Associates with circuit models, $R_\Omega(R_{ct}Q_1W_o)$, where Q_1 is constant phase element, representing capacitance behavior of the catalyst surface and W_o is open circuit terminus Warburg element was used for comparison and correlating the experimentally obtained EIS data with the map generated using the equivalent circuit[76, 111, 407]. The ohmic resistance, R_Ω was used for calculating the ohmic loss correction (iR_Ω) in the LSV curves of electrocatalyst materials and the charge transfer resistance (R_{ct}) for obtaining information on the HOR kinetics[116].

Cyclic voltammetry (CV) curves were also obtained by scanning the potential between -0.1 V (*vs* RHE) and 1 V (*vs* RHE) at a scan rate of 10 mV s^{-1}. Linear sweep voltammetry (LSV) was carried out by scanning the potential between 0 V (*vs* RHE) and 0.35 V (*vs* RHE) at 10 mV s^{-1}. LSV of the electrocatalyst materials were also iR_Ω corrected, where R_Ω is the ohmic resistance determined from the electrochemical impedance spectroscopy (EIS) analysis mentioned above.

A rotating disk electrode (RDE) was employed to study the HOR kinetics. The catalyst ink (85 wt.% catalyst and 15 wt.% Nafion 117) was sonicated and coated to a glassy carbon (GC) disk (geometric area=0.19 cm^2) followed by drying in air at room temperature. A thin layer of the synthesized electrocatalyst (1.15 mg cm^{-2}) applied on the surface of the disk was used as the working electrode[116]. The Pt wire and Hg/Hg_2SO_4 were used as the counter electrode and reference electrode, respectively. The polarization studies were carried out in 1N H_2SO_4 at 40°C in a H_2 stream with a rotation speed of 100, 400, 900, and 1600, respectively. The Koutechy-Levich equation was employed to evaluate the number of electrons involved in the reaction (n)[76, 116, 408]:

$$i^{-1} = i_k^{-1} + i_L^{-1} \tag{11-1}$$

$$i_L = 0.62\, n\, F\, A_e\, D_0^{2/3}\, \omega^{1/2}\, \nu^{-1/6}\, C_o^{*} \tag{11-2}$$

Here, i_L is the limiting current (A), i_k is the kinetic current (A) observed in the absence of mass transfer limitations, F is Faraday constant (96485 C mol^{-1}), A_e is the geometric area of the electrode (0.19 cm^2), D_0 is diffusivity of H_2 in the electrolyte solution (5×10^{-5} cm^2 s^{-1}), ω is rotation speed (rad s^{-1}), ν is the kinematic viscosity of the electrolyte (0.01 cm^2 s^{-1}), C_o^* is the bulk concentration of H_2 in 1N H_2SO_4 (7.8×10^{-7} mol cm^{-3})[116, 409].

The electrochemical stability of the electrocatalysts was studied by conducting chronoamperometry (CA) (current density *vs* time) for 24 h using H_2 saturated 1N H_2SO_4 as the electrolyte at 40°C at a constant voltage of ~0.05V *vs* RHE, the typical potential used for assessing HOR. An inductively coupled plasma optical emission spectroscopy (ICP-OES, iCAP 6500 duo Thermo Fisher) was used to investigate the dissolution of electrocatalyst materials after the stability tests. Three independently prepared electrocatalyst samples were subjected to CA testing and the electrolyte solution collected was then subjected to ICP analysis following the stability tests.

Finally, membrane electrode assemblies (MEAs) were prepared for conducting the single cell studies, following the protocol used by us in our previously published reports on HOR systems [76, 116]. The electrocatalyst ink was generated by mixing 85 wt. % electrocatalyst powder and 15 wt. % Nafion 117 solution (5 wt.% solution in lower aliphatic alcohols, Sigma-Aldrich) for the anodes (working electrode) utilizing a total mass loading of ~0.2 mg cm^{-2}. For comparison, commercially obtained 40% Pt/C (Alfa Aesar) was also studied as the anode electrocatalyst in single cell test studies using an identical loading of 0.2 mg cm^{-2}. Correspondingly, for the cathode, the electrocatalyst ink was prepared using 40% Pt/C electro-catalyst (Alfa Aesar) as the active electrocatalyst utilizing the same amount as mentioned above, i.e., 85 wt.% electrocatalyst and 15 wt.% Nafion 117 solution (5 wt.% solution in lower aliphatic alcohols, Sigma-Aldrich). A mass loading comprising of 0.3 mg of Pt cm^{-2} was used for the cathode, consistent with our previously published reports on HOR studies [76, 116].

The electrodes were prepared by spreading the electrocatalyst ink on teflonized carbon paper. The MEA was fabricated by using a Nafion 115 membrane which was sandwiched between the anode and cathode. Prior to the MEA, the Nafion 115 membrane was pretreated first with a 3 wt. % hydrogen peroxide solution to its boiling point to oxidize any organic impurities present. It was then boiled in D.I. water followed by boiling 1N sulfuric acid solution to eliminate any impurities. Finally, it was treated several times in D.I. water to remove any traces of residual acid. This membrane was then stored in D.I. water to avoid dehydration. The Nafion 115 membrane was then sandwiched between the anode and the cathode by hot-pressing using a 25T hydraulic lamination hot press with dual temperature controller (MTI Corporation). The hot press was operated at a temperature of 125°C and pressure of 40 atmospheres applied for 30 seconds to ensure and maintain good contact between the electrodes and the membrane. This MEA prepared in the above manner was then used for conducting the single cell PEMFC test analysis. The fuel cell tests were carried out using the fuel cell test set up obtained from Electrochem Incorporation at 80°C and 0.1 MPa using ultra-high purity (UHP)-H_2 (200 ml/min) and UHP-O_2 (300 ml/min) as the reactant gases and 1N sulfuric acid electrolyte solution [76].

11.3.4 Computational Methodology

Traditionally the electrocatalytic activity of an HER/HOR electrocatalyst can be described by a single parameter ΔG_{H*} which is the free energy of adsorbed hydrogen atom on the electro-catalytic surface and the overall catalytic reaction attains the optimal rate when ΔG_{H*} becomes close to 0 eV. The closer the value of ΔG_{H*} to zero indicates the attainment of more optimal adsorption and desorption conditions for hydrogen atoms at the electro-catalyst surface and thus, consequently, a higher overall electro-catalytic activity of the material will be observed[113, 114, 361]. In general, ΔG_{H*} is represented by the following relation:

$$\Delta G_{H*} = \Delta E_{H*} + \Delta ZPE - T\Delta S \qquad (11\text{-}3)$$

where the reaction energy ΔE_{H*} is calculated using the density functional theory methodology (DFT) as follows:

$$\Delta E_{H*} = E(\text{slab} + nH) - E(\text{slab} + (n-1)\ H) - 1/2\ E(H_2) \qquad (11\text{-}4)$$

Here, E(slab + nH) is the total energy of a catalyst surface slab with n hydrogen atoms adsorbed on the surface, E(slab + (n-1)H) is the total energy of the corresponding catalyst surface slab with (n-1) hydrogen atoms (after removal of one hydrogen atom from the given site) and $E(H_2)$ is the total energy of the hydrogen molecule in the gaseous phase. Also, the zero point energy correction ΔZPE minus the entropy term TΔS has been taken equal to 0.24 eV, following the publication of Nørskov et al.[361] for calculations of ΔG_{H*} for all the materials considered in their study.

For calculations of the bulk and surface properties of pure and Pt-alloyed Ti_5Si_3, a hexagonal crystal structure $P6_3/mcm$ (space group #193) with two formula units in the unit cell and the lattice parameters a=b=7.465Å and c=5.163Å has been considered as shown in Figure 11-2[410]. The presence of Pt atom is also shown in this figure. In all the calculations, 1 monolayer of H-coverage of the (0001) surface has been used. For the present computational study involving hydrogen binding energies ΔG_{H*} as qualitative descriptors of the HOR catalytic activity, the crystallographic plane (0001) with triple-Ti sites denoted by arrow in **Figure 11-2** were considered to be catalytically active.

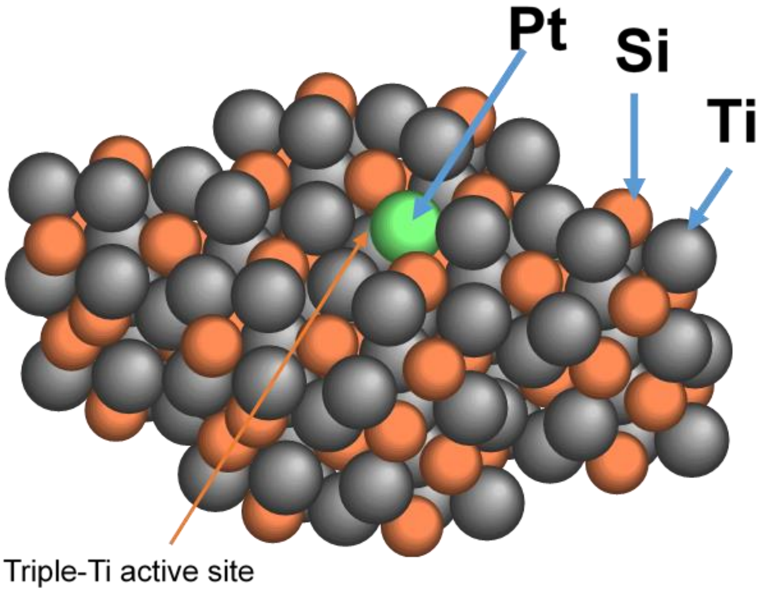

Figure 11-2 Crystal structure of Ti_5Si_3 with Pt atom located around the triple-Ti active site at (0001) crystallographic surface. Gray atoms – Ti, orange - Si, green - Pt. Orange arrow denotes triple-Ti active sites

The common surface slab used in the present DFT study consists of five atomic layers (three pure Ti layers and two Ti-Si mixed once) corresponding to one lattice parameter in the *c* direction which is perpendicular to (0001) crystallographic plane and separated by vacuum layer of ~20 Å to prevent any interaction between the slab and its images. The first two layers are fixed with bulk structural parameters, while the remaining three top layers were allowed to relax together with all the adsorbed hydrogen atoms on the surface. Since, the purpose of the present theoretical study is to elucidate the effect of introduction of Pt on the overall catalytic activity of Ti_5Si_3, only one minimal amount of Pt has been chosen for calculating ΔG_{H*} and other bulk and surface properties of the corresponding alloys. Thus, the bulk properties, such as the electronic structure and the cohesive energy have been calculated for Ti_5Si_3 and $Ti_{4.5}Pt_{0.5}Si_3$ (with one Pt atom placed on the Ti-site within the 16 atom unit cell), while the free energies of hydrogen adsorption on the pure and Pt-containing (0001) Ti_5Si_3 surfaces have been calculated at the triple-Ti active site for pure Ti_5Si_3 surface and at the corresponding active site comprised of two Ti and one Pt site for the Pt-alloyed compound as shown in **Figure 11-2**. Note, that $Ti_{4.5}Pt_{0.5}Si_3$ corresponds to 24.5wt. % or 6.25 at. %.

In the present study for all the DFT calculations, the Vienna Ab-initio Simulation Package (VASP) has been used within the projector-augmented wave method[103, 104, 214] and the generalized gradient approximation for the exchange-correlation energy functional in a form established by Perdew and Wang.[411] The standard projector augmented-wave (PAW) potentials were employed for the Ti, Si and Pt potentials containing four, four, and ten valence electrons, respectively. For all the materials considered in this study, the plane wave cutoff energy of 520 eV has been chosen to maintain a high accuracy of the total energy calculations. The lattice parameters and internal positions of atoms were fully optimized employing the double relaxation procedure. The total electronic energies were converged to within 10^{-5} eV/un.cell resulting in the residual force components on each atom to be lower than 0.01 eV/Å/atom. The Monkhorst-Pack scheme was used to sample the Brillouin Zone and generate the ***k***-point grid for all materials considered in the present study.

11.4 Results and Discussion

11.4.1 Experimental Results

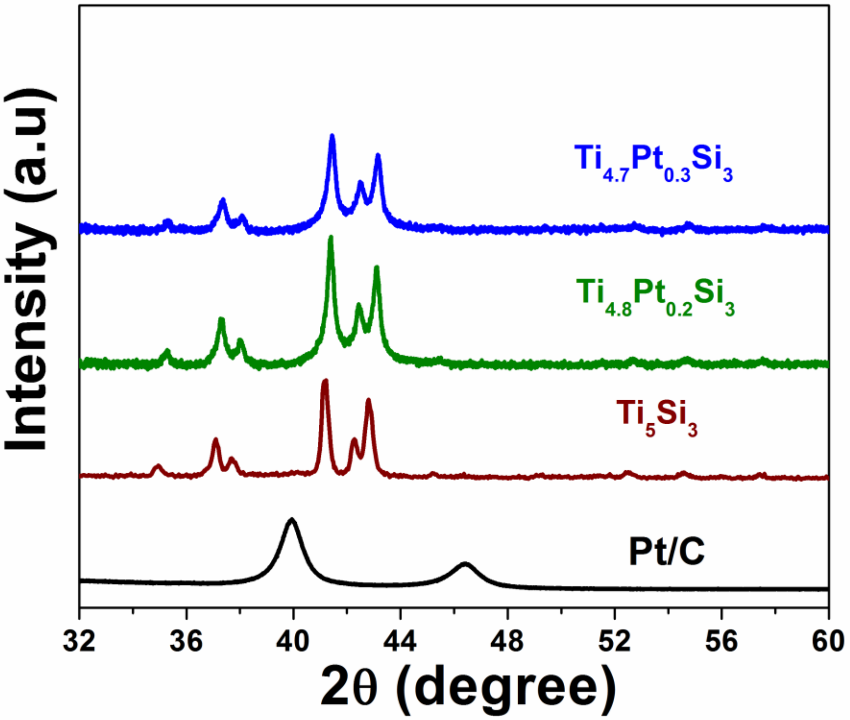

Figure 11-3 Powder XRD patterns of the as-synthesized pure and Pt-alloyed silicide electrocatalysts

Figure 11-3 illustrates the XRD spectrum of commercial Pt/C with observable peaks which are all in good agreement with the previous reports[412]. The XRD patterns of the as-synthesized Ti_5Si_3 reveals the hexagonal structure (P6$_3$/mcm) without the presence of any secondary phases of Ti and Si containing compounds as well as any impurities arising from high-energy milling process. The as-synthesized Ti_5Si_3 reveals lattice parameters of a = 7.45 Å and c = 5.14 Å and unit cell volume (V) of ~ 285.28 Å^3 which are almost identical to the values of the lattice parameters of pure and bulk Ti_5Si_3[410]. This result indicates the formation of pure and crystalline Ti_5Si_3 powder, devoid of any undesired impurities. Also, as can be seen from **Figure 11-3**, the Pt-alloyed samples, $(Ti_{1-x}Pt_x)_5Si_3$ (x= 0.04 and 0.06), also denoted as $Ti_{4.8}Pt_{0.2}Si_3$ and $Ti_{4.7}Pt_{0.3}Si_3$ exhibit the XRD patterns similar to the hexagonal structured pristine Ti_5Si_3. This indicates that there is successful incorporation of Pt as a solute into the Ti_5Si_3 lattice, without creating any secondary phases of Ti/Si or Pt containing alloys or compounds, suggesting the formation of single-phase solid solution electrocatalysts. Also, it should be noted that all the peaks in the XRD patterns of $(Ti_{1-x}Pt_x)_5Si_3$ (x= 0.04 and 0.06) in **Figure 11-3** exhibit a slight positive shift (towards a higher angle) in the peak positions, indicting a slight lattice contraction as indicated by the unit cell volume in **Table 11-1**, which is also in good agreement with the earlier studied on Pt containing compounds[413].

Table 11-1 Results of the physical and electrochemical characterizations of HOR electrocatalysts

Electrocatalyst	Lattice parameters (Å)	Unit cell volume (Å^3)	R_{ct} (Ω cm^2)	Current density at 0.05 V vs. RHE (mA cm^{-2})	Tafel slope (mV dec^{-1})
Ti_5Si_3	a = 7.4520, *c* = 5.1452	285.28	43	0.22	175.6
$Ti_{4.8}Pt_{0.2}Si_3$	a = 7.4436, *c* = 5.1275	283.41	22	0.54	146.9
$Ti_{4.7}Pt_{0.3}Si_3$	a = 7.4315, *c* = 5.1160	282.09	16	0.75	136.2
Pt/C	a = b = c = 3.9110	63.56	14	0.9	112.1

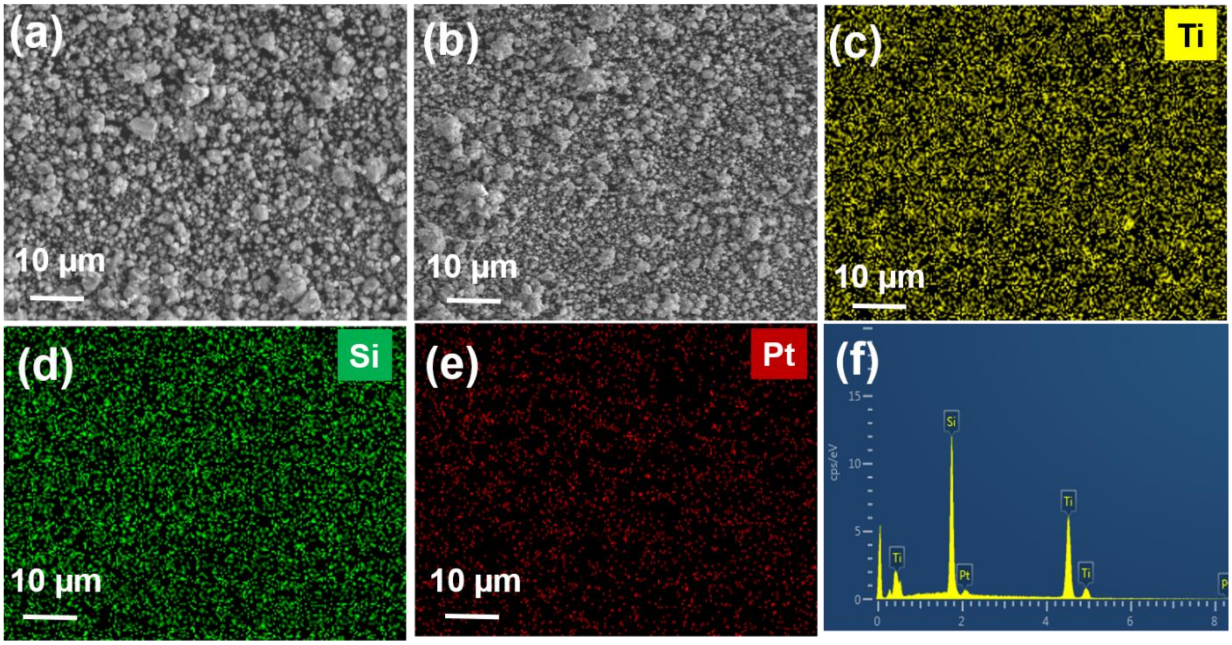

Figure 11-4 SEM micrographs of (a) pure Ti_5Si_3, (b) $Ti_{4.7}Pt_{0.3}Si_3$, Elemental x-ray mapping images of (c) Ti, (d) Si, (e) Pt, and (f) EDX spectrum for $Ti_{4.7}Pt_{0.3}Si_3$

Scanning electron microscopy (SEM) micrographs of the as-synthesized Ti_5Si_3 and $Ti_{4.7}Pt_{0.3}Si_3$ are shown in **Figure 11-4 (a) and (b)**, respectively. These SEM images reveal the fragmented powder particles in the range of 1–10 µm. The energy dispersive X-ray (EDX) spectroscopy based elemental mapping images of $Ti_{4.7}Pt_{0.3}Si_3$ **(Figure 11-4 c, d, and e)** demonstrate the uniform and homogeneous distribution of the Ti, Si, and Pt within the as-synthesized electrocatalyst powder devoid of the presence of any undesired secondary impurity elements. In addition, based on the quantitative elemental analysis (EDX, **Figure 11-4f**), the percentage atomic content of Ti, Si and, Pt is obtained as ~59.80, 36.58, and 3.62, in good agreement with the selected nominal as well as XPS determined composition (~59.43:37.24:3.33).

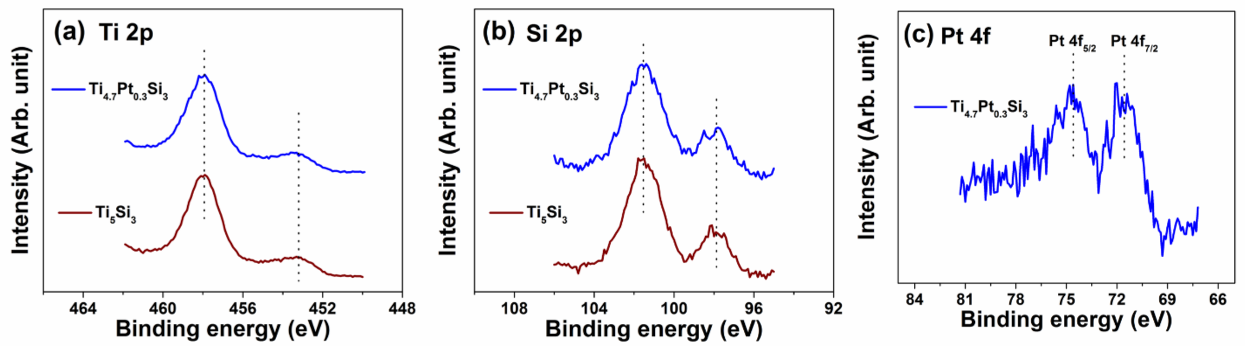

Figure 11-5 XPS spectra of (a) Ti 2p, (b) Si 2p, and (c) Pt 2p of Ti_5Si_3 and $Ti_{4.7}Pt_{0.3}Si_3$ electrocatalysts

The surface chemical states the as-synthesized electrocatalysts were investigated from the XPS analysis. As depicted in **Figure 11-5(a)**, the XPS peaks at binding energy of ~453.2 eV and ~458 eV correspond to the titanium in silicide, Ti_5Si_3 and surface oxidized titanium (TiO_x) implying that the surface of the silicide electrocatalyst is primarily composed of titanium oxide layer which is in good agreement with the earlier literature studies[414, 415]. The as-synthesized Ti_5Si_3 and $Ti_{4.7}Pt_{0.3}Si_3$ also exhibit similar XPS binding energies suggesting that there is no change in the chemical states of pure and Pt-alloyed Ti_5Si_3 samples. In other words, the alloying of Pt into the Ti_5Si_3 silicide does not change the chemical state of Ti in the alloyed silicide. Similarly, as can be seen from **Figure 11-5(b)**, the Si 2p peaks at ~98 eV and ~101.9 eV can also be ascribed to the binding energy of silicon in the silicide, Ti_5Si_3 and surface oxidized silicon (SiO_x) suggesting that the surface of the silicide consists of silicon oxides[414, 415]. Furthermore, as depicted in **Figure 11-5(c)**, the peak binding energies at ~ 71.3 eV and ~ 74.4 eV are ascribed to the Pt4f $_{7/2}$ and Pt4f $_{5/2}$, respectively, corresponding to the elemental state of platinum, Pt(0) in agreement with the published literature[416, 417].

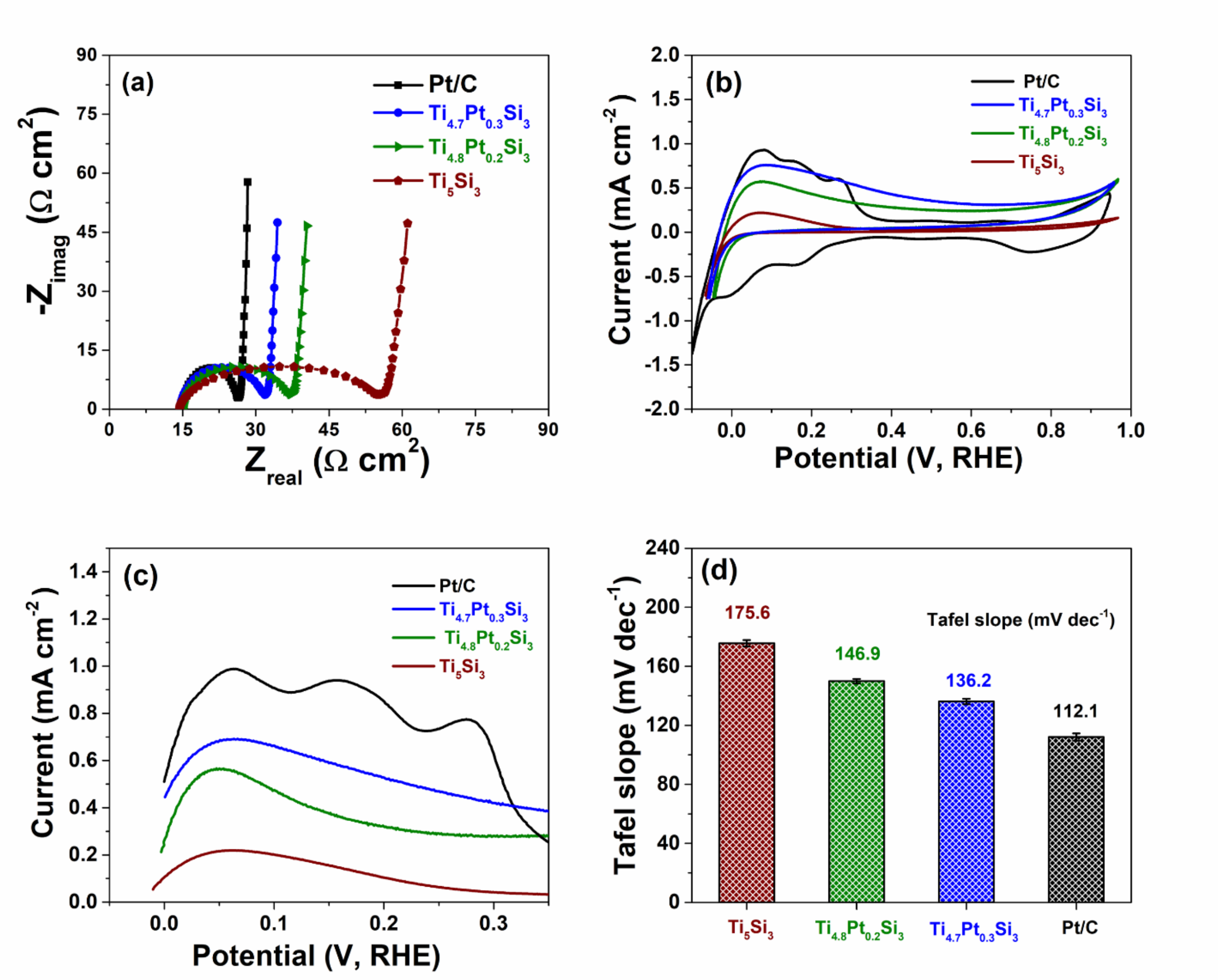

Figure 11-6 Comparison of the electrochemical performances of the as-synthesized silicide electrocatalysts measured in a H_2 saturated 1 N H_2SO_4 electrolyte at 40°C (a) The obtained EIS plots for the EIS tests performed at 0.05 V (*vs*. RHE) in the frequency range of 100 mHz to 100 kHz, (b) cyclic voltammetry (CV) curves for HOR, (c) linear scan voltammogram (LSV) curves for HOR, and (d) Tafel slope values obtained for all of the synthesized silicide and Pt/C electrocatalysts

Electrochemical characterization was conducted to ascertain the electrochemical response for HOR for the novel Pt alloyed electrocatalyst. In order to study the hydrogen oxidation reaction kinetics of the as-synthesized electrocatalysts, electrochemical impedance spectroscopy (EIS) is performed at a potential of 0.05 V (vs. RHE), the typical potential considered as mentioned earlier for HOR in the frequency range of 100 mHz to 100 kHz at an amplitude of 10 mV. As shown in **Figure 11-6(a)**, the as-synthesized pure and non-Pt alloyed Ti_5Si_3 exhibits a charge transfer resistance (R_{ct}) of ~ 43 Ω cm^2 which is significantly higher than the benchmark Pt/C (14 Ω cm^2). Furthermore, as shown in **Figure 11-6(a),** the R_{ct} of Ti_5Si_3 decreases following the incorporation of Pt. For example, $(Ti_{1-x}Pt_x)_5Si_{3,}$ x= 0.04 and 0.06) i.e., $Ti_{4.8}Pt_{0.2}Si_3$ and $Ti_{4.7}Pt_{0.3}Si_3$ reveal R_{ct} of ~ 22 Ω cm^2 and 16 Ω cm^2, respectively. The substantial reduction in the R_{ct} observed clearly suggests an improvement in the electronic conductivity as well as favoring the HOR kinetics of Pt alloyed silicide electrocatalysts.

Additionally, **Figure 11-6(b)** shows the cyclic voltammetry (CV) curves collected for the as-synthesized electrocatalysts along with that obtained for commercial Pt/C, conducted in the H_2-saturated 1N H_2SO_4 electrolyte solution at 40°C. The hydrogen oxidation peak at ~0.05 V (vs. RHE) for Pt/C and for the silicide electrocatalysts suggest their electrochemical activity towards HOR. As seen in **Figure 11-6(b),** pure Ti_5Si_3 exhibits minimal current density indicating its poor electrochemical activity for HOR whereas Pt incorporation in the Ti_5Si_3 i.e., $Ti_{4.8}Pt_{0.2}Si_3$ and $Ti_{4.7}Pt_{0.3}Si_3$ reveals improved HOR activity in comparison to the pristine non-Pt alloyed $Ti_5Si_{3.}$ This result suggests the modification of the electronic structure with the alloying of Pt and a consequence of the reduced charge transfer resistance of Pt containing silicide electrocatalysts measured as indicated above, supported by the DFT (discussed later) and EIS results discussed earlier.

Furthermore, as can be seen from the HOR polarization curves [**Figure 11-6(c)**], the HOR peak current density (at ~ 0.05 V vs. RHE) for Ti_5Si_3 is obtained as ~ 0.22 $mAcm^{-2}$. Upon Pt incorporation of 2.5 at. %, i.e., for $Ti_{4.8}Pt_{0.2}Si_3$ a sharp increase in the current density to a value of ~ 0.54 $mAcm^{-2}$ is obtained. In the case of $Ti_{4.7}Pt_{0.3}Si_3$ corresponding to only 3.75 at. % incorporation of Pt, there is further increase in current density to a measured value of ~ 0.75 mA cm^{-2}, almost 3.4X improvement in the current density observed, rendering the system closer to the value measured for Pt/C, (0.9 mA cm^{-2}). This improvement in current density measured is again attributed to the optimal hydrogen adsorption free energies (ΔG_{H^*}) discussed later, and the reduction in charge transfer resistance for the Pt alloyed silicide electrocatalysts. In addition, as can be seen from Tafel slope values [**Figure 11-6(d)**], there is a steady decrease in the Tafel sloped measured for the Pt alloyed silicide electrocatalysts from the measured value for the as-synthesized non-Pt alloyed Ti_5Si_3. Correspondingly, pure Ti_5Si_3 exhibits a Tafel slope of ~175.6 mV dec^{-1} while the Pt alloyed Ti_5Si_3 displayed reduced Tafel slope values of ~ 146.9 mV dec^{-1} for $Ti_{4.8}Pt_{0.2}Si_3$ and ~136.2 mV dec^{-1} for $Ti_{4.7}Pt_{0.3}Si_3$. These Tafel slope values (an average of three independently synthesized electrocatalysts) are clearly a reflection of the enhanced electrocatalytic activity of the Pt alloyed silicides compared to the non-Pt alloyed silicide electrocatalysts. Following the above measurements, the electrocatalytic stability of the synthesized Pt alloyed silicide, $Ti_{4.7}Pt_{0.3}Si_3$ showing the best electrochemical performance was determined and compared with the state-of-the-art Pt/C electrocatalyst. Hence, both Pt/C and the synthesized Pt alloyed silicide, $Ti_{4.7}Pt_{0.3}Si_3$ were subjected to chronoamperometry analysis for 24 h at a constant potential of 0.05 V (vs. RHE), which is closer to 0 V (the standard redox potential of HOR). As shown in **Figure 11-7(a)**, the as-synthesized $Ti_{4.7}Pt_{0.3}Si_3$ displaying the best electrochemical performance exhibited excellent electrochemical stability, with a minimum dissolution of the elements (Ti, Si, and Pt dissolution

~ 1.73± 0.02, ~ 0.81 ± 0.03, and ~ 0.05 ± 0.01 ppm, respectively) and current density decay with ~ 98-99% retention of initial current density, comparable to that of Pt/C.

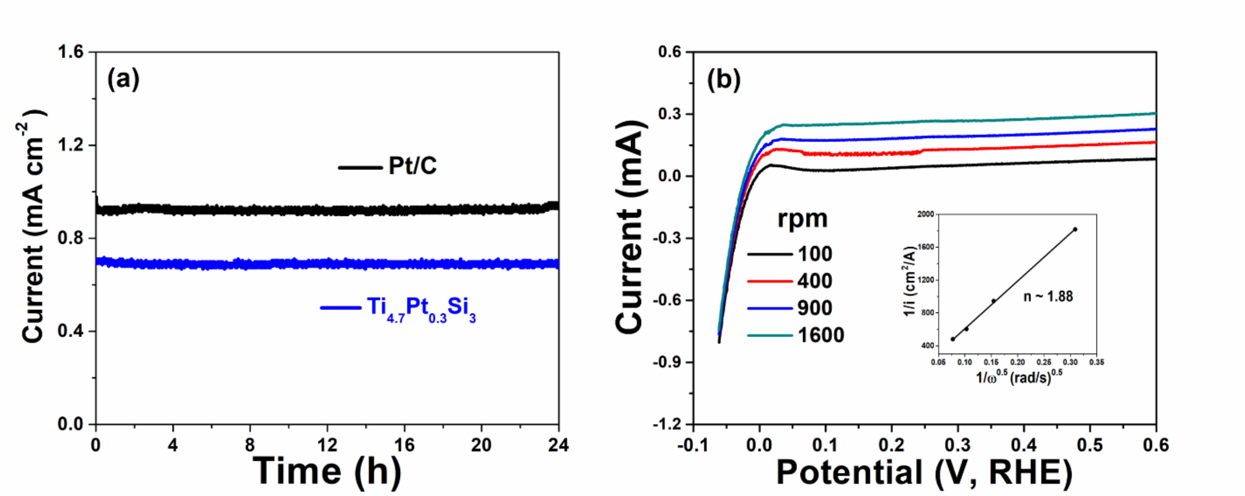

Figure 11-7 (a) chronoamperometric response of the as-prepared Pt/C and the as-synthesized $Ti_{4.7}Pt_{0.3}Si_3$ electrodes measured at 0.05 V (vs RHE), (b) polarization curves for the HOR of $Ti_{4.7}Pt_{0.3}Si_3$ obtained on a rotating disk electrode (RDE), measured in H_2 saturated 1N H_2SO_4 solution at 40°C with a scan rate of 10 mVs^{-1}. Inset shows the Koutechy–Levich plot for the as-synthesized $Ti_{4.7}Pt_{0.3}Si_3$ containing only 3.75 at. % Pt

Subsequent to the electrochemical characterizations discussed above, in order to gain more insights into the electrochemical kinetics, a rotating disk electrode (RDE) analysis was also performed and the results of which are shown in **Figure 11-7(b)**. The figure shows the polarization curves for the RDE tests carried out in 1N H_2SO_4 solution at 40°C in H_2 stream with the rotation speeds of 100, 400, 900, and 1600 rpm. As describe in Electrochemical characterization section, using the Koutechy-Levich equation with a F ~ 96485 C mol^{-1}, A_e ~0.19 cm^2, D_0 ~ 5×10^{-5} cm^2 s^{-1}, ν ~ 0.01 cm^2s^{-1}, and C_o^* ~7.8×10^{-7} mol cm^{-3}, the number of electrons produced in the reaction (n) are obtained as 1.88 which is ~ 94% of the theoretical value, i.e. 2, suggesting that the reaction prefers a two-electron pathway ($H_2 \rightarrow 2H^+ + 2e^-$) for HOR.

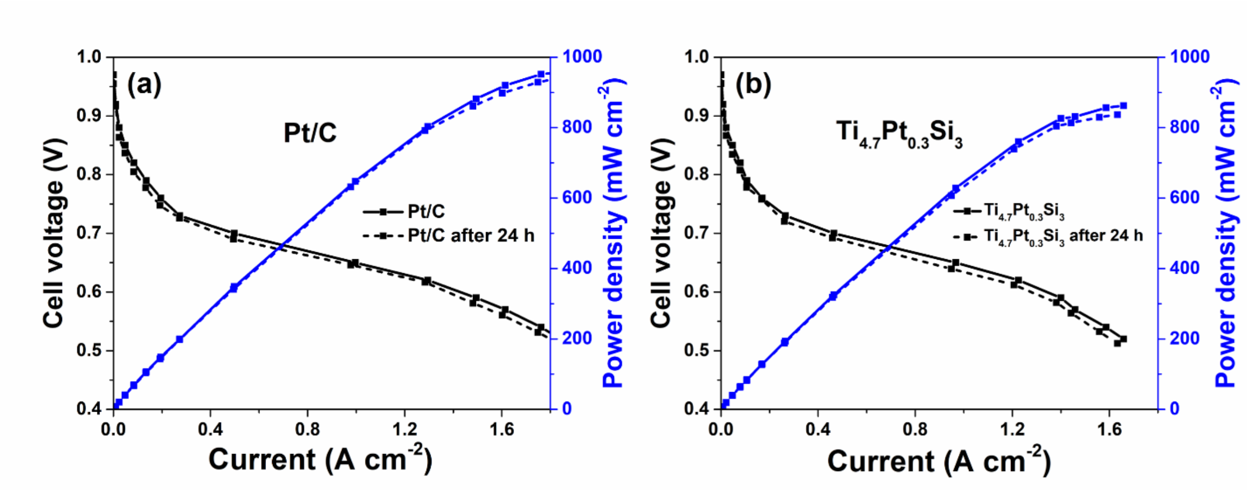

Figure 11-8 Performance of a single PEMFC (initial and after 24 h of operation) with (a) Pt/C as anode and cathode electrocatalyst, and (b) 3.75 at. % Pt containing $Ti_{4.7}Pt_{0.3}Si_3$ as anode and Pt/C cathode electrocatalyst at 80°C and 0.1 MPa with UHP-H_2 (200 ml min^{-1}) and UHP-O_2 (300 ml min^{-1}) as reactant gases

Finally, the performance of the optimal electrocatalyst, $Ti_{4.7}Pt_{0.3}Si_3$ was further evaluated in a single full cell to ascertain the true electrochemical response of the synthesized electrocatalyst. **Figure 11-8** shows the current–voltage and power density curves obtained for a single PEMFC using state of the art Pt/C electrocatalysts serving as the anode and cathode as well as for synthesized $Ti_{4.7}Pt_{0.3}Si_3$ serving as the anode and Pt/C as the cathode electrocatalyst. An electrocatalyst loading of ~ 0.2 mg of cm^{-2} was used for the Pt/C and $Ti_{4.7}Pt_{0.3}Si_3$ anode electrocatalysts while Pt/C as the cathode electrocatalyst was loaded at an electrocatalyst loading of 0.3 mg cm^{-2} under H_2/O_2 flow conditions described in the experimental section. As shown in **Figure 11-8,** the open circuit potential for the Pt/C, PEMFC is obtained as ~ 0.97 which is comparable to the as-synthesized $Ti_{4.7}Pt_{0.3}Si_3$. In addition, the maximum power density obtained using the single PEMFC with Pt/C as anode electrocatalyst is ~960 mW cm^{-2}, which is in good agreement with the previous PEMFC literature studies, investigated under similar operating conditions.[76, 116, 418] As depicted in **Figure 11-8(b)**, the as-synthesized $Ti_{4.7}Pt_{0.3}Si_3$ exhibited the maximum power density of ~ 855 mW cm^{-2}, suggesting the good electrocatalytic performance towards HOR. In addition, the current–voltage and power density curves plotted after 24 h of HOR operation exhibit negligible change in the power density values, indicating the excellent electrocatalytic activity of the synthesized Pt alloyed$Ti_{4.7}Pt_{0.3}Si_3$ containing only 3.75 at. % Pt for acid mediated PEM based HOR.

11.4.2 Computational Results

Table 11-2 Calculated free energy of hydrogen adsorption ΔG_{H*} and cohesive energy -E_{coh} for pure and Pt-alloyed Ti_5Si_3

Electrocatalyst	**ΔG_{H*} (in eV)**	**-E_{coh} (eV/f. un.)**
Ti_5Si_3	+0.26	47.38
$Ti_{4.5}Pt_{0.5}Si_3$	+0.18	47.41

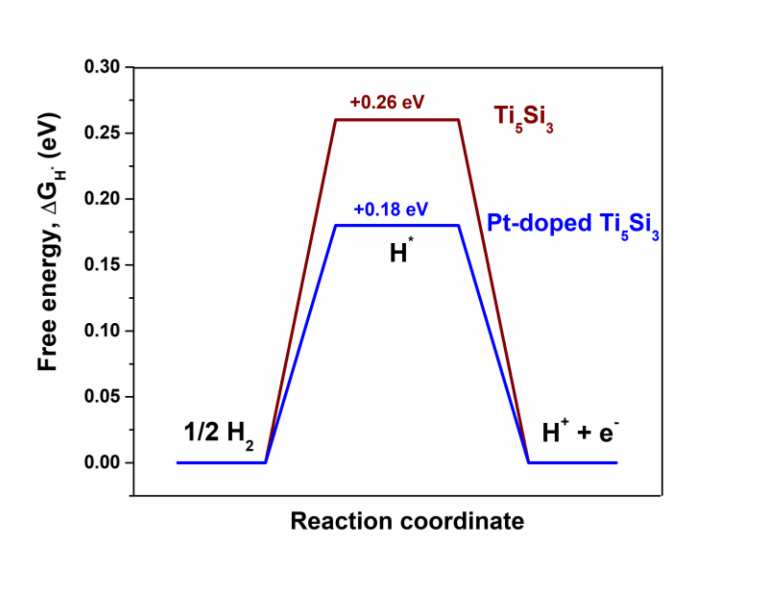

Figure 11-9 The hydrogen adsorption free energy (ΔG$_{H^*}$) calculated for the pure, non-Pt alloyed and Pt-alloyed Ti_5Si_3 at the (0001) crystallographic plane. Reaction coordinate axis denotes the the hydrogen oxidation reaction process

As mentioned in the earlier section of the manuscript, the main purpose of the computational study presented here is to elucidate the effect of Pt alloying and solid solution formation on the electrocatalytic activity of the parent unalloyed Ti_5Si_3 during HOR. In order to shed light on this reaction, the electronic structure, hydrogen adsorption free energies ΔG$_{H^*}$ as well as the cohesive energies of the materials have been calculated for the pure and Pt-alloyed Ti_5Si_3, serving as a qualitative measure of the structural and chemical stability. As mentioned earlier, for a good HOR electrocatalyst, it is vital that the free energy of the adsorbed H (ΔG$_{H^*}$) be close to zero such that the hydrogen atoms would be able to easily adsorb and desorb from the surface during the HOR process. Thus, the strategy involving modifying the electrocatalytic surface electronic structure juxtaposed with changing the chemical composition together, in such a way that the resulting ΔG$_{H^*}$ becomes close to zero, may also substantially improve the electro-catalytic activity of the material. To achieve this and ascertain the nature of the alloyed electrocatalyst, DFT calculated ΔG_{H*} have been determined using methodology very similar to that presented by Nørskov *et al.* in their earlier report.[361]

Accordingly, **Figure 11-9** shows the calculated hydrogen adsorption free energies, ΔG_{H*} determined for pure and Pt-alloyed Ti_5Si_3 at the (0001) crystallographic plane, which are also tabulated in **Table 11-2**. It can be seen that the value of ΔG_{H*} for the pure non-Pt alloyed Ti_5Si_3 is relatively large (+0.26 eV) and appears quite far from the optimal (zero) value resulting in too weak interaction between hydrogen atom and the electrocatalyst surface, implying that the adsorption of the hydrogen atoms on the electrocatalyst surface is practically impossible, thus providing suboptimal electrocatalytic activity, as also witnessed experimentally in the present study. However, upon introduction of Pt into the Ti_5Si_3 lattice and substituting for Ti decreases ΔG_{H*} noticeably, bringing the value towards the more optimal energy value (+0.18 eV). This indicates an increase in the strength of the hydrogen-surface interaction due to the significantly stronger Pt5d-H1s bonds compared to the Ti3d-H1s bonds (bond dissociation energies for diatomic Pt-H and Ti-H molecules are 330 kJ mol^{-1} *vs*. 204.6 kJ mol^{-1}, respectively[179]). This effect of Pt introduction is expected to noticeably improve the electrocatalytic activity of Pt-alloyed Ti_5Si_3 in comparison to the pristine Ti_5Si_3, which is competently supported by the experimental results discussed in the previous sections of the manuscript. Another aspect to be highlighted in the present theoretical study is the structural and electrochemical stability of the system for which the cohesive energy, E_{coh} can be considered as the qualitative indicator. A higher E_{coh} (the more negative value) value would imply a more chemically robust and durable electro-catalyst material which can be thus expected to display long term stability and durability when considered over the entire duration of the long term HOR electro-catalytic process. The calculated E_{coh} value for all the synthesized electrocatalyst silicide materials are also tabulated in **Table 11-2**. As shown in **Table 11-2**, an introduction of Pt into the Ti_5Si_3 lattice slightly increases the cohesive energy and thus, makes the overall stability of $Ti_{4.5}Pt_{0.5}Si_3$ even better than that of pure Ti_5Si_3 which can be ascribed to the presence of stronger Pt-Si bonds in comparison to the corresponding Ti-Si binds (calculated E_{coh} for pure Ti_5Si_3 is -47.38 eV/formula unit *vs.* -47.41 eV/formula unit for $Ti_{4.5}Pt_{0.5}Si_3$). Thus, Pt introduction does not compromise the structural and electrochemical stability and indeed makes this material capable of withstanding the harsh electrochemical conditions during the acid mediated HOR process.

Thus, based on results of the DFT study, Pt-alloyed Ti_5Si_3 is expected to demonstrate improved electrocatalytic activity due to the more optimal hydrogen adsorption onto the silicide electrocatalyst surface in comparison to that of pure non-Pt alloyed Ti_5Si_3 material combined with marginally improved structural and chemical stability with no adverse influence thus rendering the material a good candidate HOR electrocatalyst exhibiting promising high performance response as clearly demonstrated by the systematic experimental results discussed in this manuscript.

11.5 Conclusions

In summary, the present study demonstrates an experimental and complementary theoretical investigation of Pt-alloyed Ti_5Si_3 as a potential anode electrocatalysts for acid mediated PEMFCs. XRD analyses indicated the formation of a single-phase solid solution for all of the Pt-alloyed Ti_5Si_3 alloys synthesized via a simple and scalable high-energy mechanical milling approach. The as-synthesized $Ti_{4.7}Pt_{0.3}Si_3$ powders demonstrated superior electrochemical activity in comparison to the $Ti_{4.7}Pt_{0.3}Si_3$ and Ti_5Si_3 making it an optimal Pt containing solid solution composition. The experimental results demonstrate a significantly lower charge transfer resistance (R_{ct}) for ~ 3.75 at. % Pt doped silicide ($Ti_{4.7}Pt_{0.3}Si_3$ ~ 16 Ω cm^2) in comparison to pure Ti_5Si_3 (R_{ct} ~43 Ω cm^2) almost matching that of state-of-the-art Pt/C (~14 Ω cm^2) indicating the beneficial improvement in the electronic conductivity and reaction kinetics upon Pt incorporation. In addition, $Ti_{4.7}Pt_{0.3}Si_3$ electrocatalyst revealed a higher electrocatalytic activity for HOR, comparable to state-of-the-art Pt/C in comparison to 2.5 at. % Pt containing $Ti_{4.8}Pt_{0.2}Si_3$ and pure non-Pt containing Ti_5Si_3. Such improved electrocatalytic activity upon Pt incorporation is successfully validated by the DFT calculations which unveiled that the Pt contacting Ti_5Si_3 exhibits optimal hydrogen adsorption free energies (ΔG_{H^*} ~ 0.18 eV), lower than pure Ti_5Si_3 (~0.26 eV), suggesting the reduced reaction barrier and enhanced HOR kinetics. In addition, the optimal composition of $Ti_{4.7}Pt_{0.3}Si_3$ electrocatalyst containing only 3.75 at. % Pt demonstrated good electrochemical durability under HOR operation conditions in both half-cell as well as single cell PEMFC tests, comparable to Pt/C, devoid of any major structural and activity degradation, which is also evidently supported by the theoretical calculations of cohesive energy ($-E_{coh}$). Furthermore, the maximum power density of the reduced PGM containing anode $Ti_{4.7}Pt_{0.3}Si_3$ is obtained as 855 mW cm^{-2}, which is as good as that of the conventional Pt/C of 960 mW cm^{-2}. The results obtained herein thus strongly indicate that the as-synthesized Pt alloyed $Ti_{4.7}Pt_{0.3}Si_3$ electrocatalyst containing only 3.75 at. % Pt is a promising candidate for HOR in a PEMFC with much lower cost and comparable performance to that of the benchmark Pt/C.

12.0 Specific Aim 3- To Synthesize of Bilayer Structured 1-D Multi-Metal Oxide Semiconductor Nanostructures to Enhance the Fundamental Optoelectronic Properties (By Modification of Electronic Structure) for Photo-Anode Applications in Photo-Electrochemical (PEC) Water Splitting via Systematic Bandgap Engineering

Molybdenum doped Bilayer Photoanode for Enhanced Photoelectrochemical Water Splitting

12.1 Abstract

In order to address the alarming global energy crisis and environmental problems, converting solar energy into hydrogen energy via photoelectrochemical (PEC) water splitting is one of the most promising approaches for generation of clean and sustainable hydrogen energy. To achieve superior PEC performance and solar to hydrogen efficiency (STH), identification, synthesis, and development of efficient photoelectrocatalysts with suitable band gap and optoelectronic properties along with high PEC activity and durability is highly imperative. With the aim of improving the performance of our previously reported bilayer photoanode of WO_3 and Nb and N co-doped SnO_2 nanotubes i.e. WO_3-$(Sn_{0.95}Nb_{0.05})O_2$:N NTs, herein, we report a simple and efficient strategy of molybdenum (Mo) doping into WO_3 lattice to tailor the optoelectronic properties such as band gap, charge transfer resistance, and carrier density, etc. The Mo doped bilayer i.e. $(W_{0.98}Mo_{0.02})O_3$-$(Sn_{0.95}Nb_{0.05})O_2$:N revealed higher light absorption ability with reduced band gap (1.88 eV) in comparison to that of the undoped bilayer (1.94 eV). In addition,

Mo incorporation offered improvements in the charge carrier density, photocurrent density, with reduction in charge transfer resistance, contributing to a STH (~3.12 %), an applied bias photon-to-current efficiency (ABPE ~ 8% at 0.4V), including a carrier density (N_d ~ 7.26 × 10^{22} cm^{-3}) superior to that of undoped bilayer photoanode (STH ~2%, ABPE ~ 5.76%, and N_d ~5.11× 10^{22} cm^{-3}, respectively). The substitution of Mo^{6+} for W^{6+} in the monoclinic lattice, forming the W–O–Mo bonds altered the band structure, which enabled further enchantment in the PEC reaction kinetics and charge transfer. Additionally, doped bilayer photoanode revealed excellent long term PEC stability under illumination, suggesting its robustness for PEC water splitting. The present work herein provides a simple and effective Mo doping approach for high performance photoanodes for PEC water splitting.

12.2 Introduction

The continually increasing global population and rapidly decreasing fossil fuel reserves along with alarming air pollution-induced health and environmental issues have steered intense research direction towards the exploration of alternative, renewable, and environmentally benign (low carbon footprint) energy resources to achieve the sustainable energy supply. In this context, owing to its non-carbonaceous nature and higher energy density (120 MJ kg^{-1}) than gasoline-based energy (44.4 MJ kg^{-1}), hydrogen has been hailed as one of the most promising energy carriers to replace conventional fossil fuels[351, 359, 419]. Currently, the large-scale (~ 96%) hydrogen is produced from the steam reforming of natural gas, partial oxidation of hydrocarbons, and coal gasification[116]. However, these conventional hydrogen production approaches suffer from severe disadvantages. For example, in the last two decades, ~75% of the global CO_2 emissions are attributed to the burning of coal, oil, and natural gas[420, 421]. In addition, these approaches require high operating temperatures (700°C-1000°C) which increases the overall operating cost of hydrogen production. Also, the hydrogen produced from these approaches is not of high purity and is often contaminated with pollutants such as SO_x, NO_x, CO_2, CO, etc. On the other hand, currently only ~ 4% hydrogen is produced from the water electrolysis - a highly reliable approach for clean and non-carbonaceous hydrogen production[303, 419, 422].

Utilizing solar energy-based photoelectrochemical (PEC) water splitting for hydrogen production is one of the most reliable alternatives to resolve the growing energy and global warming crisis, since the sun delivers a massive amount of energy (~ 173,000 TW per year) to the earth’s surface, out of which ~ 30 % is reflected by the clouds and earth's surface, and thus, retains ~ 120,000 TW power on the surface of the earth[423]. As water splitting is an endothermic reaction, it demands external energy [$\Delta G^o = 237.13$ kJ mol^{-1} or 1.23 eV/(electron in H_2O)] to split the water into hydrogen and oxygen [54, 55]. Since the discovery of PEC water splitting via low-cost semiconductor material i.e. titania (TiO_2) by Fujishima and Honda in 1972, significant attention has been given to engineering novel high-performance semiconductor photoelectrocatalysts to expediate the overall performance of PEC cells[54, 56].

Henceforth, a various semiconductor system such as single metallic oxides (ZnO, Fe_2O_3, SnO_2, WO_3), bimetallic oxides ($BiVO_4$, $SrTiO_3$ $CuWO_4$), chalcogenides (CdS, ZnS), nitrides (TaN, Ta_3N_5), two-dimensional materials (graphene, MoS_2), transition metals like (Co, Pt, Ni, Fe, Zn, Bi) composites), and carbon based nanomaterial catalysts (CNTs, CQDs) have been investigated for PEC water splitting [424, 425]. Amongst these various photoactive systems, transition metal oxides (TMOs) have garnered special attraction towards PEC water splitting owing to their high chemical stability, good electron mobility, natural abundance and thus, low cost, tunable band gap, and suitable redox potentials [424, 425]. However, TMO based systems often encounter some drawbacks which include wide bandgap, inferior light absorption, and high rate of charge carrier recombination, which ultimately limits the high performance of the PEC cells. Therefore, various approaches for the architectural engineering of TMO photoelectrodes such as systematic band gap engineering via doping, cocatalyst loading, hybridization, surface passivation, alternation in crystallinity, dimensionality (1D/2D/3D), and morphology (nanorods, nanotubes, core-shell, etc.) are typically utilized to improve the optoelectronic properties of photoelectrodes, which can offer enhanced PEC activity and stability [425].

Accordingly, in order to improve the photoelectrocatalytic performance of SnO_2 based photoanodes, we have investigated niobium (Nb) and nitrogen (N) doped SnO_2 as an efficient photoanode system for acid-mediated PEC water splitting in our previous report [74]. The $(Sn_{0.95}Nb_{0.05})O_2$:N photoanode synthesized in an advantageous one-dimensional (1D) nanotubular (NTs) architecture demonstrated significantly improved PEC performance in comparison to the pristine SnO_2 photoanode. In this study, Nb and N co-doping strategy for SnO_2 effectively resulted in better light absorption properties, improved carrier density, and facile electrochemical charge transfer. In various literature studies, Nb incorporation into SnO_2 has also offered improved charge transfer and thus, electronic conductivity [426-429]. Owing to its abundant electronic states and minor influence on SnO_2 lattice structure [as ionic radii of Nb^{4+} (69 pm) is lower as compared to Sn^{4+} (71 pm)], the solid solution of Nb incorporated SnO_2 evidently introduces additional electronic states of Nb in the band gap of SnO_2, reducing the band gap of SnO_2 and thus, improving light absorption properties [430, 431]. In addition, nitrogen was also used as a dopant for $(Sn,Nb)O_2$ system in order to achieve the hybridization of the substitutional N 2p states with O 2p states, offering further reduction in the band gap [74, 432-436]. Accordingly, our previous experimental as well as computational studies have evidently demonstrated that the introduction of Nb and N in the SnO_2 [$(Sn_{0.95}Nb_{0.05})O_2$:N NTs] reduces band gap of SnO_2 from ~3.5 eV to ~1.99 eV, offering superior light absorption and PEC activity [74]. Furthermore, in our another previous study, in order to further enhance the PEC activity of $(Sn_{0.95}Nb_{0.05})O_2$:N NTs, we explored WO_3 coupled $(Sn_{0.95}Nb_{0.05})O_2$:N NTs as a promising bilayer photoanode system, achieving efficiency superior to $(Sn_{0.95}Nb_{0.05})O_2$:N NTs with minimum or zero applied potential in addition to solar energy[423].

Among the various TMOs, n-type semiconductor WO_3 is a multifunctional material that has good thermal stability, photosensitivity, stability against photo-corrosion, and good electron transport properties [437, 438]. Due to such beneficial properties, WO_3 has been extensively investigated for photoanodes in PEC cells, dye-sensitized solar cells, smart windows, rechargeable batteries, supercapacitors, for CO_2 reduction, sensors, pollutants degradation, air purification, and as an antimicrobial agent [437, 438]. In addition, as the conduction band of WO_3 is lower than that of $(Sn_{0.95}Nb_{0.05})O_2$:N NTs, the photo-generated electrons easily flow from the conduction band of $(Sn_{0.95}Nb_{0.05})O_2$:N NTs to the WO_3 conduction band, retaining the holes in the $(Sn_{0.95}Nb_{0.05})O_2$:N NTs, which ultimately improves carrier separation and reduces the charge recombination [64, 65, 439, 440]. Accordingly, our previous study evidently demonstrated the promise of bilayer or coupling strategy to improve the activity of bilayer WO_3-$(Sn_{0.95}Nb_{0.05})O_2$:N NTs, which was significantly higher in comparison to other well studied semiconductor materials, such as TiO_2, ZnO, and Fe_2O_3. Further enhancement in the charge transfer kinetics, electronic conductivity, and correspondingly, the PEC activity of WO_3-$(Sn_{0.95}Nb_{0.05})O_2$:N NTs could be achieved via numerous strategies such as morphological control, transition metal-doping, noble-metal-loading, and surface sensitization, etc. Amongst such various approaches, several studies conducted on the WO_3 have evidently demonstrated doping as an effective strategy for tailoring the optical, structural, and electronic properties of WO_3. In the literature, doping of several metals such as Ti, Ta, Mo, Zn, Dy, Te, V, Cu, Ag, Ce, Mg, and Ni into WO_3 has been reported to enhance the PEC activity and charge transfer kinetics of WO_3. Among such various dopants, Mo is a well-studied highly promising dopant candidate for WO_3 which has demonstrated significant improvement in the optoelectronic properties of pristine WO_3 [441, 442]. In order to obtain a solid solution of a doped oxide instead of phase separation or dopant oxide clusters in the host oxide material, Mo is a suitable dopant for WO_3 as Mo^{6+} and W^{6+} ions possess comparable ionic radii and electron structure, allowing for direct incorporation of Mo into the WO_3 lattice [441, 442]. Furthermore, it has been reported that the doping WO_3 with an iso-valent element like Mo does not create charge mismatch issues which limit the formation of other defects such as anion or cation vacancies[442]. Various literature studies on structural, optical, and electronic properties of Mo doped WO_3 evidently showed that the Mo doping into WO_3 reduced the bandgap of WO_3 and increased its light absorption[441-443]. Also, these studies revealed that Mo doping resulted in a significant reduction in charge transfer resistance (R_{ct}), suggesting enhanced charge kinetics for the PEC water splitting. Therefore, inspired by these literature studies, in the present work, in order to further increase the optoelectronic properties of our previously reported bilayer WO_3-$(Sn_{0.95}Nb_{0.05})O_2$:N NTs, 2 at. % Mo incorporated WO_3 based $(W_{0.98}Mo_{0.02})O_3$-$(Sn_{0.95}Nb_{0.05})O_2$:N NTs was selected as an efficient bilayer photoanode system for further investigation.

It is noteworthy that, apart from doping, the morphological dimension contributes significant benefits to the physical and optoelectronic properties of the electrocatalyst materials. For example, owing to their promising attributes such as large aspect ratio (L/D), lower charge transfer resistance (R_{ct}), and thus better electronic conductivity, one dimensional (1D) nanostructured architecture (nanotubes, nanorods, nanowires) is widely reported and utilized in the water splitting research area[45, 144]. Besides, 1D motifs are well-known for exhibiting better electrocatalytic stability in comparison to nano- particular or film based catalyst materials which often experience physical ripening processes and higher catalytic dissolution[207]. Accordingly, in the present study, $(W,Mo)O_3$-$(Sn_{0.95}Nb_{0.05})O_2$:N photoelectrode is fabricated in the 1D vertically aligned nanotube fashion [444-446].

12.3 Experimental Methodology

12.3.1 Synthesis of Bilayer Photoanodes

The undoped and Mo doped bilayer photoanodes [WO_3-$(Sn_{0.95}Nb_{0.05})O_2$:N NTs and $(W_{0.98}Mo_{0.02})O_3$-$(Sn_{0.95}Nb_{0.05})O_2$:N NTs] were synthesized using ZnO nanowires (NWs) as a sacrificial template. A schematic illustration of the entire synthesis procedure is depicted in the **Figure 12-1.** The stepwise synthesis method is described below:

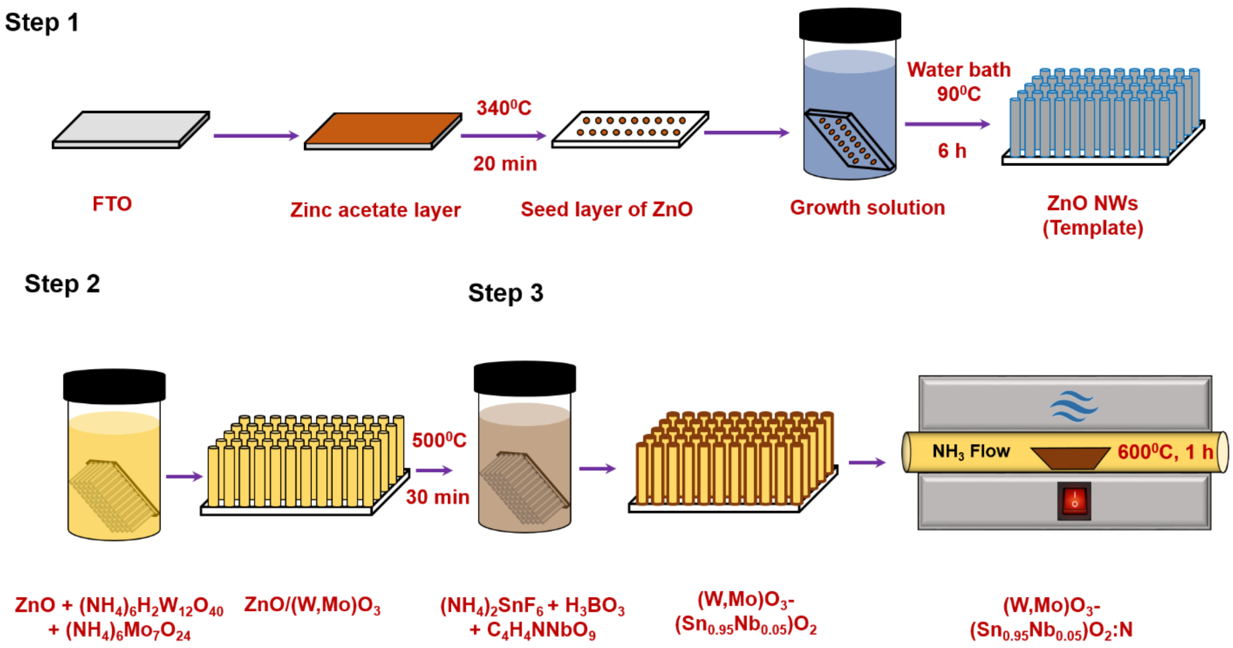

Figure 12-1 Schematic of the synthesis of Mo-doped WO_3-$(Sn_{0.95}Nb_{0.05})O_2$:N NTs

Step 1. Synthesis of sacrificial ZnO NWs template

ZnO NWs as a sacrificial template was synthesized on fluorine doped tin oxide (FTO) coated glass substrate using the hydrothermal method following our earlier published reports [75, 423]. In brief, initially the FTO substrate was thoroughly cleaned by ultrasonication in acetone, ethanol, and D.I. water. 5.5 mM zinc acetate solution in ethanol (anhydrous, 200 proof, 99.5+%, Aldrich) was then spin-coated on cleaned FTO substrate using the Specialty Coating Systems Inc., at 500 rpm for 40 sec and then heated (in air) at 125°C. After that, in order to form the ZnO seed layer, zinc acetate coated FTO substrate was thermally treated in air at 340°C for 20 min. The ZnO seed layer coated FTO substrate was then placed with the conductive surface facing down in a sealed container containing the growth solution of zinc nitrate hexahydrate (0.05 M, Alfa Aesar), hexamethylenetetramine (HMTA, 0.025 M, Alfa Aesar), polyethyleneimine (5.0 mM, end-capped, molecular weight 800 g mol^{-1} LS, Aldrich), and ammonium hydroxide (0.35 M). Next, the sealed container was kept in a water bath, preheated to 90^oC for 6 h. After this step, the formed ZnO NWs were then thoroughly rinsed with ethanol and D.I. water followed by drying at 50^oC for 6 h [75].

Step 2. Synthesis of ZnO/WO_3 and ZnO/($W_{0.98}Mo_{0.02}$)O_3 NWs

ZnO/WO_3 NWs were fabricated employing the protocol reported in our earlier report[423]. The ZnO NWs prepared using the hydrothermal method as outlined above, were placed in the 50 mM solution of ammonium metatungstate (AMT) [$(NH_4)_6H_2W_{12}O_{40}$] for ~1 h. The NWs were then washed with D.I. water and dried at 60^oC for 2 h, followed by heat treatment in air at 500^oC for 30 min for obtaining WO_3. To synthesize 2 at. % Mo doped WO_3, stoichiometric ammonium molybdate tetrahydrate [$(NH_4)_6Mo_7O_{24}$. $4H_2O$] was added in the AMT solution, followed by heat treatments similar to the process for undoped ZnO/WO_3 NWs mentioned above [423, 447].

Step 3. Synthesis of bilayer nanotubes

The as-synthesized ZnO/WO_3 and ZnO/($W_{0.98}Mo_{0.02}$)O_3 NWs were placed in an aqueous solution of 3 ml of 0.3 M ammonium hexafluorostannate (AHFS, Aldrich), stoichiometric amount of ammonium niobate oxalate hydrate (ANOH, Aldrich), 1 mL of 1 M boric acid (H_3BO_3, Aldrich), and 1 mL of D.I. water at 26^oC for 30 min. This hydrolysis process resulted in the deposition of ($Sn_{0.95}Nb_{0.05}$)O_2 on ZnO/WO_3 or ZnO/($W_{0.98}Mo_{0.02}$)O_3 NWs. The acid formed during the hydrolysis process dissolves the sacrificial template (ZnO) resulting in the formation of hollow vertically aligned nanotubes denoted as WO_3-($Sn_{0.95}Nb_{0.05}$)O_2 and ($W_{0.98}Mo_{0.02}$)O_3-($Sn_{0.95}Nb_{0.05}$)O_2, respectively [74, 448-450]. The bilayer photoanodes were finally washed with D.I. water and dried at 60^oC for 2 h. Nitrogen (N) incorporation was then achieved via heat treatment of NTs for 1 h at 600°C in the NH_3 atmosphere (Matheson: 99.99%, flow rate=100 cm^3 min^{-1}) with ramp rate of 10°C min^{-1} similar to our previous report[74, 75].

12.3.2 Materials Characterization

Phase analysis of the as-synthesized materials was carried out by X-ray diffraction (XRD) using the Philips XPERT PRO system employing CuK_α (λ = 0.15406 nm) radiation at an operating voltage and current of 45 kV and 40 mA, respectively. Scanning electron microscopy (SEM) was utilized to study the microstructure of the as-synthesized photoanodes. Quantitative elemental analysis was carried out via energy dispersive x-ray spectroscopy (EDX) analyzer. UV-vis absorption spectra of as-synthesized materials were obtained using the UV-vis spectrophotometer (DU-600, Beckman). X-ray photoelectron spectroscopy (XPS) was used to investigate the oxidation states of the various elements in the undoped and Mo doped composite photoanodes. XPS analysis was carried out using the ESCALAB 250 Xi system (Thermo Scientific) equipped with a monochromated Al Kα X-ray source. The system is operated at a room temperature in an ultra-high vacuum chamber with a base pressure less than 5×10^{-10} mBar.

12.3.3 Photoelectrochemical Characterization

PEC characterizations were conducted in 1N H_2SO_4 electrolyte solution at 26°C in an electrochemical workstation (VersaSTAT 3, Princeton Applied Research) using a H-type cell, divided into the photoanode and cathode compartments separated by Nafion 115 membrane (Dupont) [74, 75]. The photoelectrodes were fabricated by attaching a Cu wire (using a conductive silver glue) on the exposed electrically conductive parts of the photoanode material coated FTO substrates [74, 75]. In the present study, the PEC measurements were carried out using the photoelectrode acting as the working electrode (photoanode), Pt wire as the counter electrode (cathode) (Alfa Aesar, 0.25 mm thick, 99.95%), and mercury/mercurous sulfate (Hg/Hg_2SO_4) electrode (XR-200, Hach) with a potential of +0.65 V with respect to reversible hydrogen electrode (RHE) serving as the reference electrode. Prior to the PEC testing, the test cell was purged with ultra-high purity Ar gas for ~15 min to expel oxygen present in the electrolyte solution. The photoelectrodes were illuminated (100 mW cm^{-2}) using a 300 W xenon lamp (Model 6258, Newport) equipped with an AM 1.5G filter (Model 81094, Newport)[423].

The PEC activity of the as-synthesized photoanodes was evaluated from the linear sweep voltammetry (LSV) using a scan rate of 1 mV sec^{-1} under an illumination of 100 mW cm^{-2}. All the reported values of potential in this study are converted to reversible hydrogen electrode using the Nernst equation[74, 75]:

$$E_{RHE} = E_{Hg/Hg2SO4} + E^{o}_{Hg/Hg2SO4} + 0.059pH$$

E_{RHE} is the potential versus RHE. $E_{Hg/Hg2SO4}$ is the potential measured against the Hg/Hg_2SO_4 reference electrode. $E^{o}_{Hg/Hg2SO4}$ is the standard electrode potential of Hg/Hg_2SO_4 reference electrode. Electrochemical impedance spectroscopy (EIS) was utilized to evaluate the charge transfer resistance (R_{ct}) and ohmic resistance (R_{Ω}) [74-76, 111, 124]. EIS was carried out in the frequency range of 100 mHz-100 kHz (AC Amplitude =10 mV) at ~0.1 V (*vs* RHE) under illumination (100 mW cm^{-2}) in 1N H_2SO_4 solution. The ZView software was utilized to analyze the EIS data employing the circuit model $R_{\Omega}(R_{ct}Q_{dl})$, where R_{Ω} is ohmic resistance, R_{ct} is charge transfer resistance, Q_{dl} is double layer capacitance [74-76, 111, 124]. The obtained R_{Ω} was then used for iR_{Ω} correction in the LSV plots. Also, the EIS measurements for the Mott-Schottky plots were performed at frequency of 7.5 kHz with an AC amplitude of 10 mV between the voltage window of -0.8 V to 1.2 V (*vs* RHE) similar to our reports [74, 75, 440].

In addition, in order to determine the charge carrier density, the Hall effect measurements were performed on 1 cm × 1 cm photoanode sample, employing a magnetic field strength of 1.02 T at room temperature (by Van der Pauw method) and using the Ecopia 3000 system. To evaluate charge transport properties of the bilayer photoanodes, the recombination kinetics of photogenerated carriers is studied by measuring the open circuit potential (V_{oc}) as a function of time under light off conditions. The decay in the V_{oc} as a function of time (dV_{oc}/dt) was used to study the recombination of the photogenerated carriers in photoanodes. The carrier lifetime (τ), a time for which photogenerated carriers exist before recombining was determined using the following equation[423]:

$$\tau = -(k_BT/e)\,(dV_{oc}/dt)^{-1} \qquad (12\text{-}1)$$

where, k_B is Boltzmann constant, T is the absolute temperature (299 K), *e* is electron charge.

In order to study the PEC stability of photoanodes, chronoamperometry (CA) (current density *vs* time) tests were performed for 24 h in 1N H_2SO_4 electrolyte at 26°C and a constant potential of ~0.4 V (*vs* RHE) under illumination (100 mW cm^{-2}). Inductively coupled plasma optical emission spectroscopy (ICP-OES, iCAP 6500 duo Thermo Fisher) was then utilized on the electrolyte solution collected after 24 h of CA testing of bilayers (an average of three independently synthesized bilayers) to determine the amount leached out into the solution during stability tests.

12.4 Results and Discussions

12.4.1 Structural Characterizations

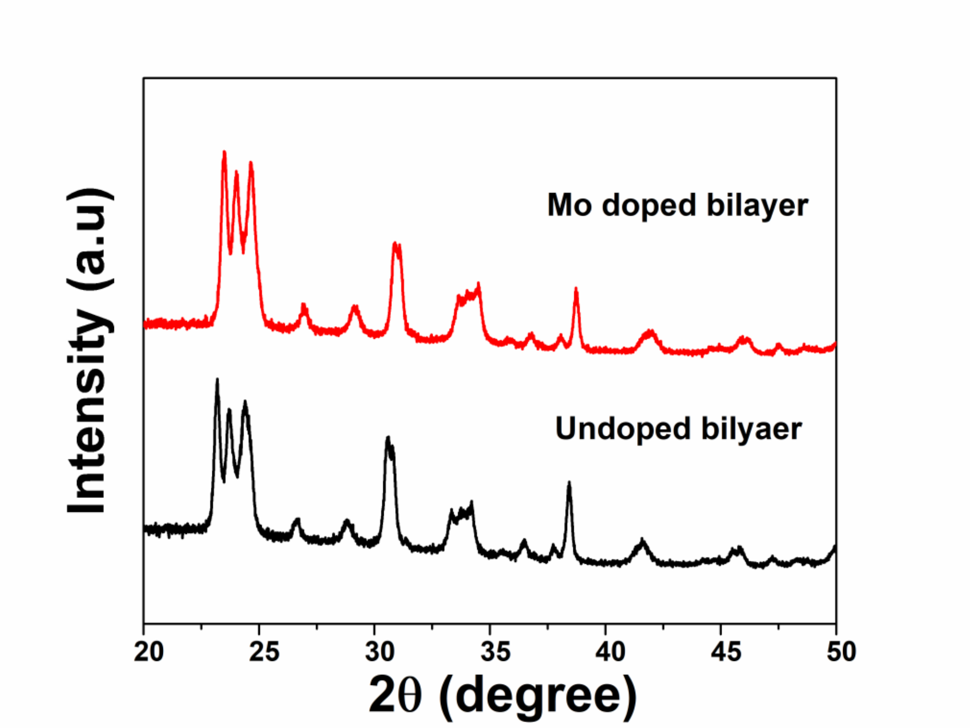

Figure 12-2 **XRD patterns collected on undoped and Mo doped bilayer photoanodes**

The XRD patterns of the as-synthesized photoelectrocatalysts are shown in **Figure 12-2**. The XRD pattern of the undoped bilayer WO_3-$(Sn_{0.95}Nb_{0.05})O_2$:N exhibits presence of both

WO_3 and $(Sn_{0.95}Nb_{0.05})O_2$:N NTs which is in good agreement with our earlier report[423]. The WO_3 peaks at 2θ degree values of 23.18, 23.63, and 24.41 correspond to the [002], [020], and [200] crystal planes of monoclinic phase of WO_3 with lattice parameters of a = 7.296, b = 7.540, and c = 7.688 Å (JCPDS no. 43-1035)[451]. Furthermore, Mo doped WO_3 bilayer material i.e. $(W_{0.98}Mo_{0.02})O_3$-$(Sn_{0.95}Nb_{0.05})O_2$:N reveals XRD pattern similar to undoped bilayer photoanode, without any secondary phases of MoO_3 based materials, suggesting complete incorporation of Mo into the W lattice. Since Mo^{6+} possesses slightly lower ionic radius (59 pm) than W^{6+} (60 pm), Mo can easily be incorporated into the WO_3 lattice. Furthermore, a careful observation of the XRD data of Mo doped bilayer revealed a slight positive shift in the 2θ angles. For example, after Mo doping the peak positions of [002], [020], and [200] planes were found to be shifted to 2θ angles of 23.42, 23.87, and 24.66 respectively. Such positive shifts in 2θ positions evidently suggests occurrence of lattice contraction implying the successful incorporation of Mo in the WO_3 lattice which can be ascribed to the slightly lower ionic radius of Mo^{6+} (59 pm) in comparison the W^{6+} (60 pm). In addition, it is well-known that the peak height associated with the different crystal planes in the XRD pattern indicates the crystal growth direction[451, 452]. Herein, it is noteworthy to also highlight that previous literature studies reveal that the PEC water splitting performance of WO_3 depends on its crystal plane orientation[451, 452]. On the basis of these studies, a [002] plane-oriented WO_3 is observed to be beneficial for efficient PEC water splitting and ultimately shows higher PEC performance in comparison to the [020] and [200] plane-oriented WO_3[451, 452]. Accordingly, herein, the XRD pattern of as-synthesized undoped as well Mo doped WO_3 reveal the dominant peak attributed to the favorable [002] plane which could beneficially influence the PEC water splitting performance for the bilayer systems.

The morphology of the as-synthesized Mo doped and undoped bilayer photoelectrodes has been investigated using SEM. **Figure 12-3(a-c)** depict the view of WO_3-$(Sn_{0.95}Nb_{0.05})O_2$:N at different magnifications, showing a well-spaced nanotube (NT) morphology with a length of ~12-14 µm and diameter of ~ 260-280 nm, similar to our previous report[423]. As shown in **Figure 12-3(d-f)**, the Mo doped bilayer also exhibits similar NT morphology, suggesting the retention of morphology after Mo-incorporation. In addition, the EDX spectrum of Mo-doped bilayer sample (**Figure 12-3g**) shows the presence of desired elements without any undesired impurities (**Appendix F Table 1**).

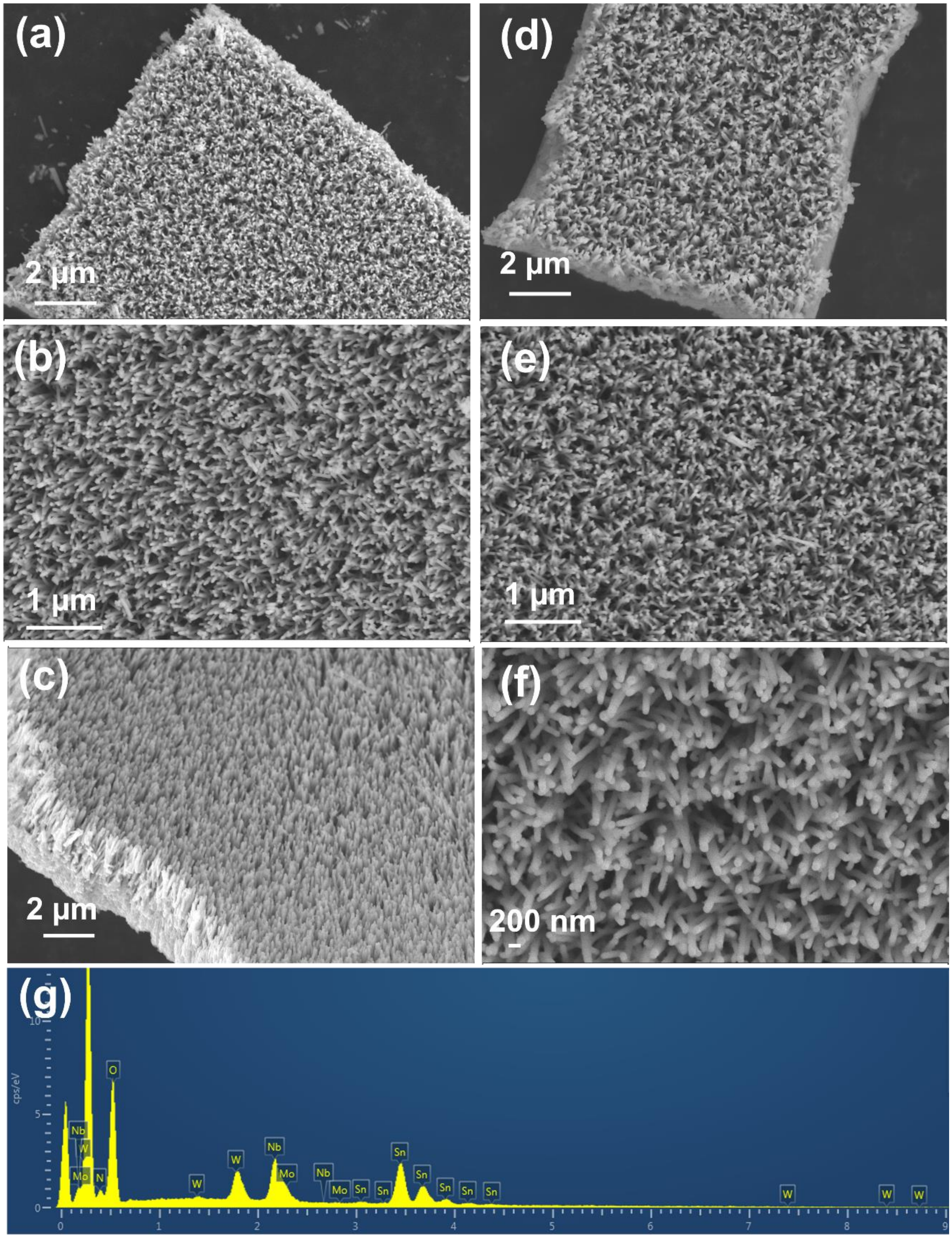

Figure 12-3 SEM micrographs of (a-c) undoped and (d-f) Mo doped bilayer photoanode, (g) EDX spectrum of Mo doped bilayer

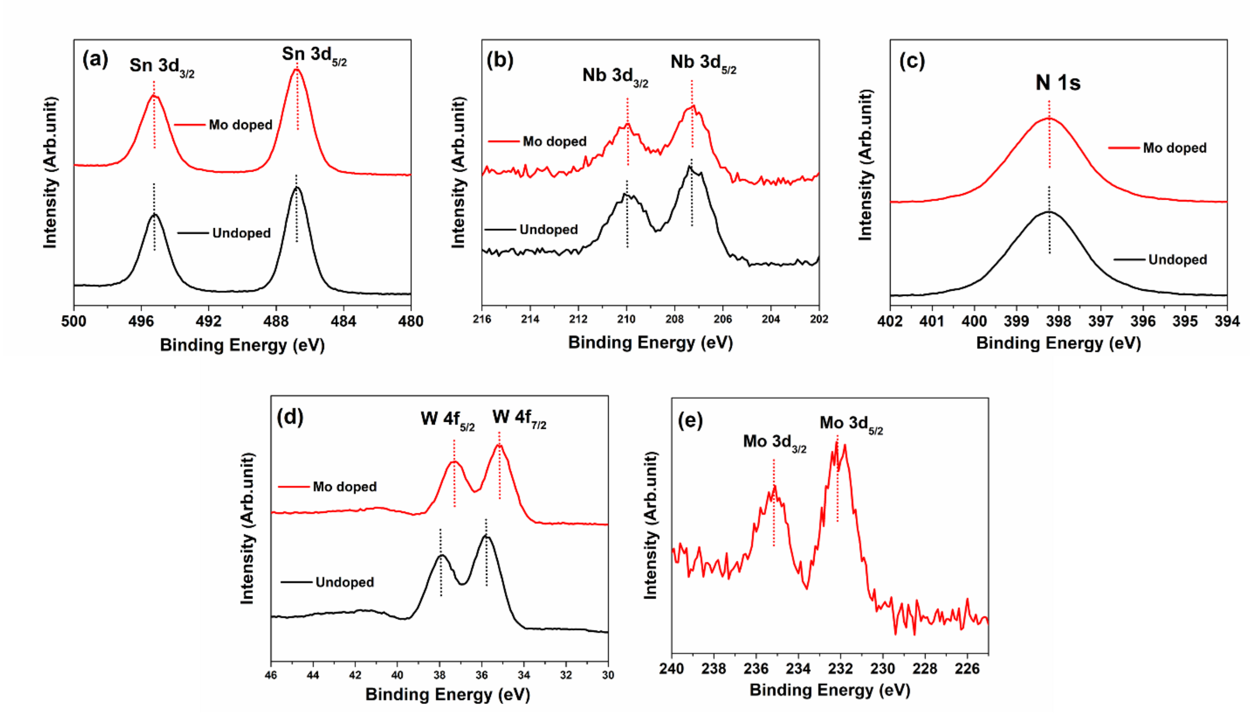

Figure 12-4 The XPS spectra of bilayer materials for (a) Sn, (b) Nb, (c) N, (d) W, and (e) Mo

X-ray photoelectron spectroscopy (XPS) was performed to analyze the chemical states of the elements Sn, Nb, W, Mo, and N in bilayer photoanodes. The XPS spectra of Sn for WO_3-$(Sn_{0.95}Nb_{0.05})O_2$:N and $(W_{0.98}Mo_{0.02})O_3$-$(Sn_{0.95}Nb_{0.05})O_2$:N NTs show [**Figure 12-4(a)**] the presence of Sn $3d_{3/2}$ and $3d_{5/2}$ doublet centered at ~495.27 eV and ~486.8 eV which correspond to Sn^{4+}[74, 135]. **Figure 12-4(b)** shows the XPS spectra of Nb with a Nb $3d_{3/2}$ and $3d_{5/2}$ doublet centered at ~210.3 and ~207.5 eV, respectively for both the bilayer compositions which corresponds to Nb^{4+}[74, 453, 454]. As depicted in the XPS spectra of N [**Figure 12-4(c)],** the N 1s peaks centered at ~398.3 eV for bilayer materials indicate the presence of the oxynitride (O-Sn-N, O-Nb-N). This presence of oxynitride can be ascribed to the substitutional doping of N at O sites in the lattice of $(Sn_{0.95}Nb_{0.05})O_2$:N NTs as reported earlier[74, 75, 455-457]. **Figure 12-4(d)** depicts the W 4f XPS spectra of the undoped and Mo-doped WO_3 bilayer samples. As can be seen from the **Figure 12-4(d)**, the 4f XPS spectra of W in undoped WO_3 exhibits the characteristic peaks at ~ 35.10 and ~37.25 eV, corresponding to the $4f_{7/2}$ and $4f_{5/2}$ states, respectively. It is noteworthy to highlight that the binding energies of W 4f in the Mo doped sample showed negative shifts of ~ 0.2 eV in comparison to that of undoped WO_3. This negative shift in the binding energy for Mo doped WO_3 can be attributed to the substitution of Mo^{6+} for W^{6+} in the monoclinic lattice and thereby suggesting formation of W–O–Mo bonds[442]. Furthermore, as depicted in **Figure 12-4(e)**, the XPS spectrum of Mo 3d exhibits peak binding energies at ~235.3 and ~ 232.4 eV which could be assigned to Mo $3d_{3/2}$ and $3d_{5/2}$, respectively, suggesting the presence of Mo^{6+} state in the Mo doped WO_3 sample.

12.4.2 Study of Pptoelectronic Properties

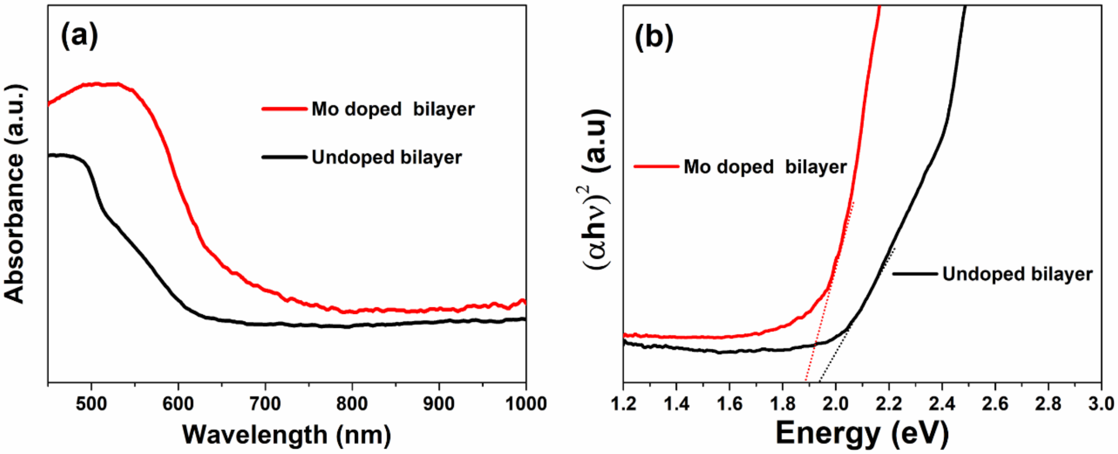

Figure 12-5 (a) UV-vis absorption spectra, (b) Tauc analysis of undoped and Mo doped bilayer

The light absorption properties of bilayer photoanodes were studied from the UV-VIS analysis. As can be seen from **Figure 12-5(a)**, the light absorption in the visible region increases for the Mo doped bilayer, suggesting a reduction in the band gap. Tauc analysis was also carried out to evaluate the bandgap of bilayers. The values of the band gap determined from the Tauc analysis [**Figure 12-5(b)**] are tabulated in **Table 12-1**. As can be seen from these Tauc plots, undoped bilayer photoanode exhibits bandgap of ~1.94 eV whereas Mo doped bilayer reveals bandgap of ~ 1.88 eV which is slightly lower than that of the undoped material. According to various literature reports, the strong hybridization between the orbitals of W, Mo, and O orbitals can result into narrowing of the band gap of Mo-doped NTs [442]. Such reduction in the band gap is indeed critical for the enhanced light absorption which can provide a higher number of photo-generated carriers to induce the desired reactions at both the cathode and the photoanode, respectively[64, 440].

Table 12-1 Results of photoelectrochemical characterization

Bilayer Photoanode	Bandgap (eV)	Charge transfer resistance R_{ct} (Ω cm^2)	Ohmic resistance R_Ω (Ω cm^2)	Photocurrent density (mA cm^{-2}) at ~0.1 V	Carrier density (cm^{-3})		STH (%)	ABPE at 0.4V (%)
					Mott-Schottky	Hall Analysis		
Undoped	1.94	9.65	15.5	2.95	4.94×10^{22}	5.11×10^{22}	2.0	5.76
Mo doped	1.88	7.30	15.2	4.13	7.12×10^{22}	7.26×10^{22}	3.12	8.05

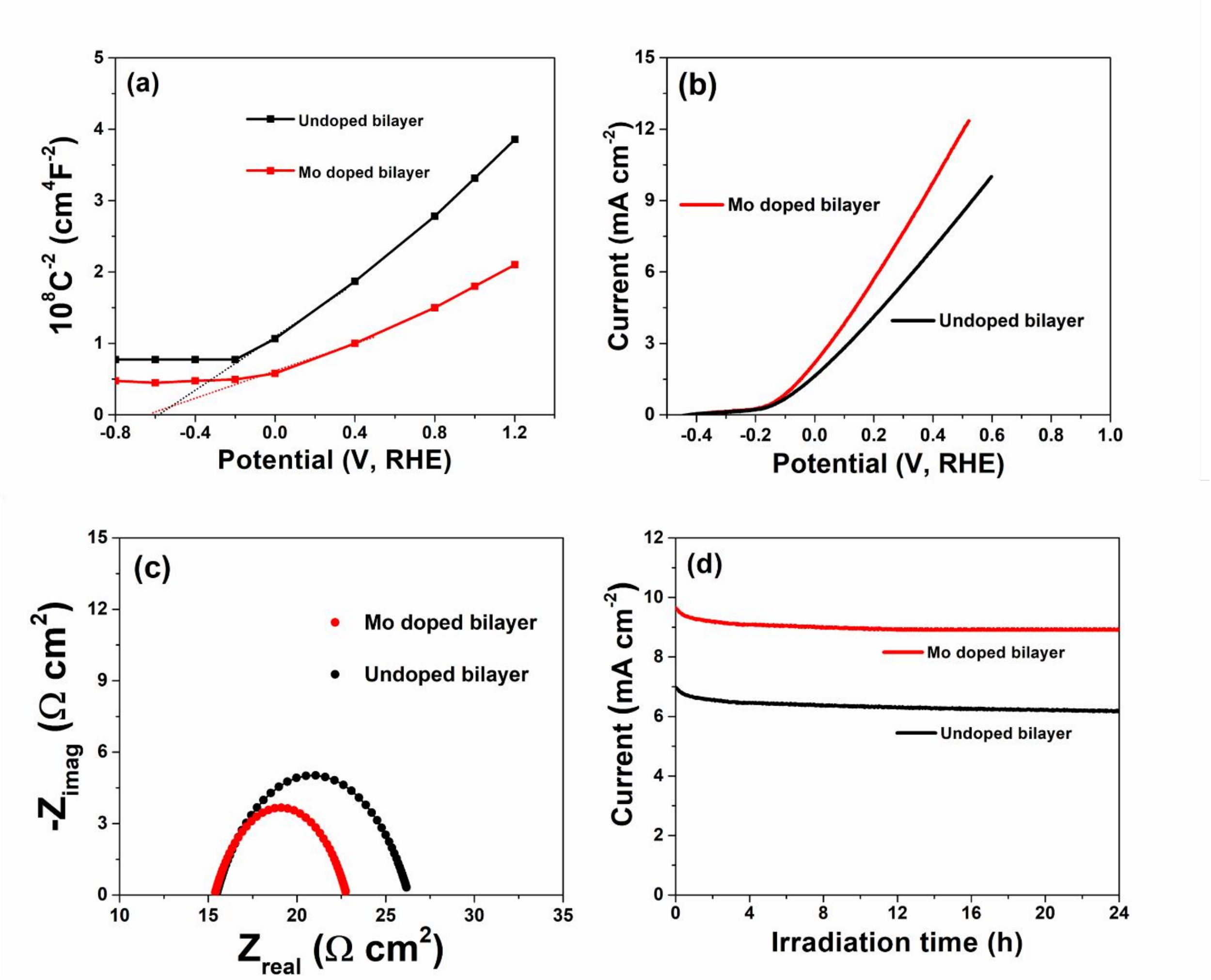

Figure 12-6 Photoelectrochemical performance undoped and Mo doped bilayer photoanodes (a) Mott-Schottky analysis, (b) linear scan voltammogram (LSV) curves of under illumination of 100 mW cm^{-2} measured in 1N H_2SO_4 at 26ºC, (c) EIS spectra obtained at ~0.1 V (*vs* RHE) under illumination of 100 mW cm^{-2}, (d) variation of photocurrent density *vs* irradiation time in the chronoamperometry

The Mott-Schottky analysis was conducted to study the electronic properties of as-prepared photoanodes. The carrier density (N_d) for the photoanode materials is evaluated using the Mott-Schottky equation[75, 458]:

$$1/C^2 = (2/e_0\varepsilon\varepsilon_0N_d)[(V-V_{FB})-kT/e_0] \qquad (12\text{-}2)$$

where, e_0 is the electron charge, ε is the dielectric constant, ε_0 is the permittivity of vacuum, N_d is the carrier density, V is the applied potential, V_{FB} is the flat band potential, k is the Boltzmann constant, T is the absolute temperature (299 K). The Mott-Schottky plots ($1/C^2$ *vs* V) are shown in the **Figure 12-6(a)**. The flat band potential (V_{fb}) can be evaluated from the X-intercept of the linear region of the Mott-Schottky plot. The V_{FB} of undoped and Mo doped samples is obtained as ~-0.59V and ~ -0.62V vs RHE, respectively. This result suggests that the V_{FB} of these materials are more negative than the standard redox potential for water reduction reaction (i.e. hydrogen evolution reaction, HER, 0 V *vs* NHE), suggestive of the more negative position of the conduction band than the standard redox potential for HER[74, 75, 440, 458]. Herein, the Mo doped material shows slightly negative V_{FB} to that of undoped bilayer material. This result suggests that for Mo doped photoanode, there is indeed a downward shift of the conduction band minimum towards the Fermi level. This result is in good agreement with the previous reports of Mo-doped WO_3 based photoanode systems[442]. Furthermore, on the basis of the Mott-Schottky analysis, the carrier density (N_d) was evaluated from the slopes of Mott-Schottky curve using the following equation [74, 75, 457].

$$N_d = (2/e_o\varepsilon\varepsilon_o)[d(1/C^2)/dV]^{-1} \qquad (12\text{-}3)$$

The carrier density for the undoped and Mo doped bilayer materials is obtained as ~4.94 × 10^{22} cm^{-3} and ~7.12 × 10^{22} cm^{-3}, respectively. It is noteworthy to mention that carrier density was also measured using the Hall effect analysis wherein Mo doped and undoped bilayer exhibited N_d values of ~5.11 × 10^{22} cm^{-3} and ~7.26 × 10^{22} cm^{-3}, respectively, which are in excellent agreement with the Mott-Schottky analysis. Therefore, based on the Mott-Schottky and Hall effect measurements, it can be inferred that Mo incorporation evidently offers improvement in the carrier density of in comparison to the undoped bilayer photoanode. Such enhancement in the carrier density is expected to offer superior PEC performance.

12.4.3 Photoelectrochemical Characterization

The photoelectrochemical activity of Mo doped and undoped photoanode materials is investigated in 1N H_2SO_4 electrolyte solution. **Figure 12-6(b)** shows the linear scan voltammogram (LSV) curves of photoanodes under illumination of 100 mW cm^{-2}, obtained using scan rate of 1 mV sec^{-1}. As can be seen from **Figure 12-6(b)**, the Mo doped photoanode reveals higher current density in comparison to that of undoped material. Specifically, undoped and Mo doped photoanodes exhibit a current density of ~ 2.95 and ~4.13 mA cm^{-2}, respectively at potential of 0.1 V vs RHE (~zero bias). This result suggests the higher PEC activity of Mo doped material. Such improvement in the activity can be attributed to the more negative V_{FB} and higher N_d of Mo doped photoanode, leading to more negative position of the Fermi level and also offering more driving force for generating photogenerated electrons [440, 458].

Furthermore, electrochemical impedance spectroscopy (EIS) was conducted to evaluate the charge transfer resistance (R_{ct}) and to study the PEC reaction kinetics for the as-synthesized photoanodes. As depicted in **Figure 12-6(c)** and **Table 12-1**, Mo doped photoanode exhibits a lower R_{ct} (~7.30 Ω cm^2) than the undoped material (~9.65 Ω cm^2). This lower R_{ct} value of Mo doped photoanode suggests its faster interfacial charge transfer and better reaction kinetics [75, 458-460]. Such reduction in R_{ct} value upon Mo incorporation has also been evidently witnessed and reported in the literature[442].

Additionally, following the literature studies, in accordance with IUPAC nomenclature, the solar-to-hydrogen efficiency (STH) of photoanode materials is defined as a term to be used in the absence of bias (for zero applied potential, V = 0) whereas in the presence of bias, the efficiency is considered as applied bias photon-to-current efficiency (ABPE) (also known as photoconversion efficiency with applied bias [461, 462]). ABPE is accordingly calculated using the following equation[463]

$$ABPE = I(1.23-V)\times 100/J_{light} \qquad (12\text{-}4)$$

herein, I is the photocurrent density at the measured potential, V is the applied potential, and J_{light} is the illumination intensity. Herein, under the applied bias (~ 0.4 V), the ABPE for undoped and Mo doped WO_3 is obtained as ~5.76 % and ~ 8.05 %, respectively using the values of current, I = 6.95 mA/cm^2 and 9.70 mA/cm^2, respectively. Similarly, STH (for zero applied potential, V = 0), for undoped and Mo doped WO_3 is obtained as ~ 2 % and ~ 3.12%, respectively using the values of current, I = 1.63 mA/cm^2 and 2.54 mA/cm^2, respectively. These efficiency results elucidate the superior PEC performance and charge transfer (improved reaction kinetics) characteristics displayed by the Mo doped bilayer material.

In addition to the good PEC activity, it is important that the photoanode should possess good photoelectrocatalytic stability for achieving efficient PEC water splitting. Thus, in order to evaluate the PEC stability of bilayer photoanodes, the chronoamperometry (CA) tests were carried out under constant illumination (100 mW cm^{-2}) for 24 h in the 1N H_2SO_4 electrolyte solution. As depicted in **Figure 12-6(d)**, the CA curves of both bilayer photoanodes show excellent PEC stability with minimum loss in current density (~1%) and minimum material dissolution (**Appendix F Table 2**). This result evidently demonstrates the robustness of the bilayer systems under illumination and thus validating their promising operation in a PEC water splitting cell.

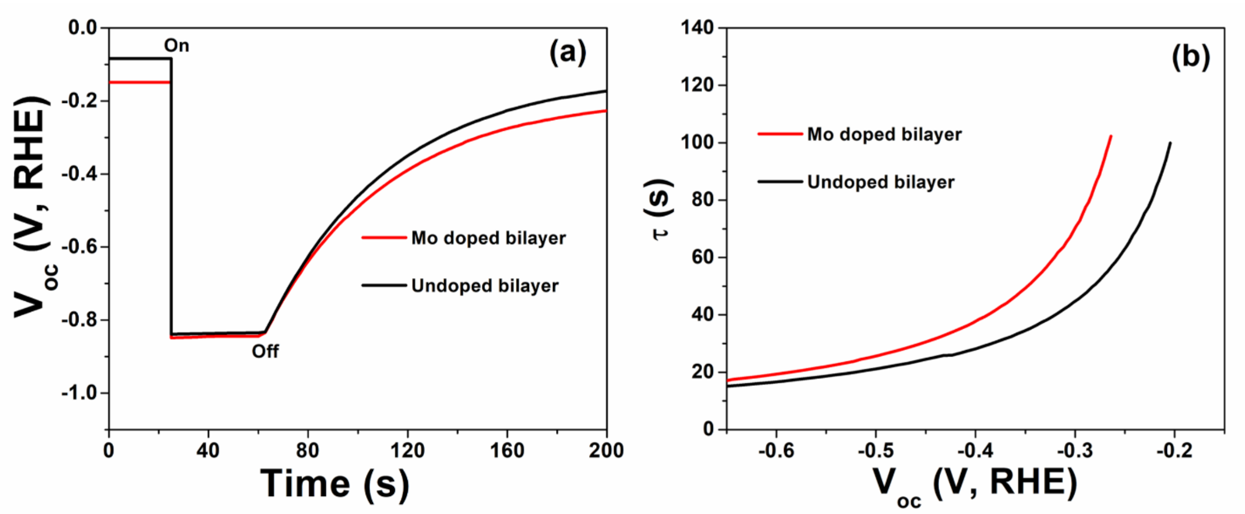

Figure 12-7 (a) Variation of open circuit potential (V_{oc}) under light On/Off conditions with time, (b) Carrier lifetime (τ) as function of open circuit potential (V_{oc})

Furthermore, as mentioned in the experimental section, the carrier lifetime study was conducted to understand the charge transport properties and recombination kinetics of the photogenerated carriers. **Figure 12-7(a)** shows the decay in open circuit voltage (V_{oc}) as function of time. The decay in the V_{oc} as a function of time (dV_{oc}/dt) was used to study the recombination of the photogenerated carriers and carrier lifetime in bilayer photoanodes. Mo doped bilayer exhibits lower V_{oc} decay rate (~6.8 mV s^{-1}) than undoped bilayer (~7.5 mV s^{-1}) which suggest the lower recombination and higher carrier lifetime [**Figure 12-7(b)**] of photogenerated carriers for the Mo doped bilayer. Such reduction in recombination upon Mo doping has been evidently witnessed in various literatures studies in $BiVO_4$ and TiO_2[464, 465]. According to these studies, increased charge carrier density upon Mo doping (as observed from Mott-Schottky and Hall measurements) can reduce the back electron–hole recombination and also, the removal of surface trapping states upon Mo doping reduces the number of surface accumulated holes which are prone to back electron–hole recombination. Similar processes could be occurring in the Mo doped bilayers in our studies here.

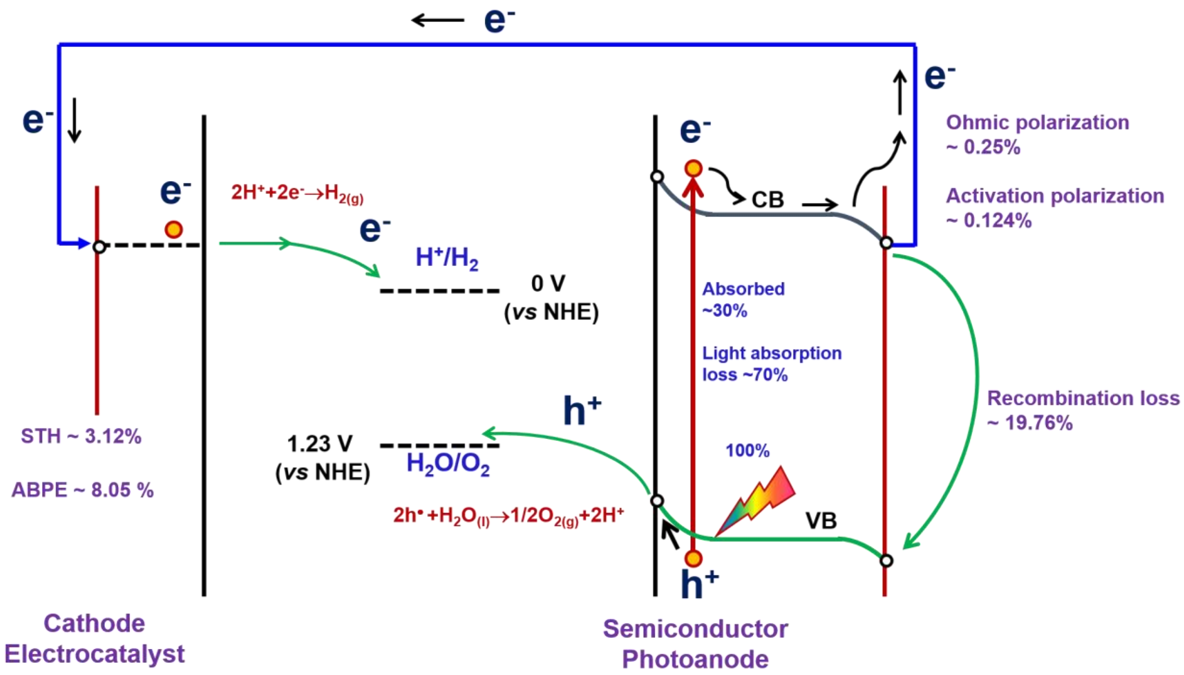

Figure 12-8 Representation of the PEC processes showing loss mechanisms for Mo doped bilayer

Furthermore, it is also imperative to identify the critical losses that limit the attainment of higher photoelectrochemical performance and thus, achieving a high STH efficiency. Accordingly, in order to understand these losses, the energy lost in the recombination process has been evaluated **(Figure 12-8**). The recombination energy loss for undoped bilayer is obtained as ~ 21.5 mW cm^{-2} whereas for Mo doped bilayer photoanode, the slight reduction (~8%) in recombination energy loss (~19.76 mW cm^{-2}) is observed which can be attributed to the higher light absorption, photocurrent density, and reduced charge transfer resistance and bandgap of Mo doped bilayer. In addition, the available energy for PEC water splitting is evaluated as 3.16 and 7.87 mW cm^{-2} for undoped and Mo doped bilayer, respectively. These results thus suggest the beneficial electronic structural modification in the bilayer configuration, minimizing the losses and offering higher PEC response. Moreover, from literature studies it has been identified that the presence of Mo^{6+} into the WO_3 lattice could trap electrons, resulting in suppression of recombination between electrons and holes and thus, offering efficient enhanced PEC reaction kinetic and activity[437, 466].

12.5 Conclusions

In summary, the present study demonstrates the beneficial effect of Mo doping into the-WO_3 coupled $(Sn_{0.95}Nb_{0.05})O_2$:N bilayer photoanode system for acid mediated PEC water splitting. As revealed from the experimental results, Mo incorporation into the WO_3 lattice offers excellent optoelectronic properties, enhanced absorption properties, reduced bandgap, charge transfer resistance with improved PEC water splitting kinetics. In particular, Mo doped bilayer shows a noticeably lower bandgap and R_{ct} of $\sim 7.3\ \Omega\ cm^2$ in comparison to the undoped bilayer ($\sim 9.65\ \Omega\ cm^2$). In addition, the higher ABPE (8.05%) and STH (3.12%) efficiencies obtained for Mo doped bilayer photoanode evidently suggest the improved PEC performance in comparison to the undoped photoanode. On the basis of Mott-Schottky and Hall effect analyses, it is further observed that Mo doping resulted in the enhanced charge carrier density, favoring water oxidation reaction kinetics, which results in the higher photocurrent and STH efficiency. In addition, Mo doped bilayer photoanode exhibited excellent long term photoelectrochemical stability with a very minimal decay in photocurrent density. The present work thus demonstrates that Mo doping into the WO_3 nanowires is indeed a promising strategy to alter the optoelectronic properties of photoelectrocatalyst materials, promoting the PEC activity, and thus, offering efficient and economic hydrogen generation via PEC water splitting.

13.0 Conclusion and Future Work

The overall aim of this dissertation was to identify, synthesize, and develop high-performing, reduced PGM containing as well as PGM-free earth-abundant electrocatalytic systems for acid mediated oxygen and hydrogen evolution reactions (OER-HER) for PEM based water electrolyzers, oxygen reduction and hydrogen oxidation reactions (ORR-HOR) for acid mediated PEM based fuel cell, and photoelectrochemical oxygen evolution reaction (PEC-OER) for PEC water electrolysis. Accordingly, in the present work, ably supported by density functional theory (DFT) based calculations; rationalizing the thermodynamics and kinetics of oxygen and hydrogen electrocatalysis, various experimental solution and solid-state based approaches and systematic characterization methods were exploited to synthesize and engineer several ultra-low PGM as well as PGM-free electrocatalysts and photoelectrocatalysts validating the theoretical findings. The as-synthesized OER, HER, ORR, and HOR electrocatalytic systems revealed excellent electrochemical activity and durability, comparable or superior to state-of-the-art PGM based IrO_2, RuO_2, and Pt electrocatalysts.

One of the innovative strategies identified for lowering the Ir and Pt content was the generation of solid solution electrocatalysts relying on mimicking the structural, electronic, chemical, and electrochemical characteristics of the parent PGM based oxide and PGM electrocatalyst that was determined to be crucial for reducing the investment costs, and subsequently potentially minimizing the steps needed for the commercializing the PEM electrolyzer and PEMFC technology. In addition, in order to enhancing the electrochemical performance of reduced PGM and PGM-free systems, experimental strategies implemented involved generation of 2D and 3D morphologies capitalizing on the inherent advantages of rapid kinetics favored by the preservation and attainment of 1D nanostructures. Accordingly, such tailoring of morphologies in the 1D architecture form putatively offered remarkable enhancement in the charge transfer and reaction kinetics for the 1D electrocatalyst materials. Another important aspect that was studied while preserving solid solution phase stability related to the crystallographic structure and the role of anti-site and site specific cation disorder on the electrochemical activity and electrochemical stability. Thus, to gain fundamental insights into the influence of ordered-disordered structures and rearrangement of oxidation state of electrochemically active species and their combined synergistic effects on the electrochemical performance (OER-ORR), the disorder – order transitions of PGM-free electrocatalysts were modulated by precisely varying the heat treatments in a systematic fashion. These studies unveiled the crucial role of Mn^{3+}/ Mn^{4+} and Cu^{+1}/Cu^{+2} states in dictating the OER and ORR activities of Mn-based Cu-Mn-O spinel ($Cu_{1.5}Mn_{1.5}O_4$ and $Cu_{1.5}Mn_{1.5}O_4$:F) electrocatalysts.

Finally, to enhance the solar energy-based PEC water splitting performance, a simple and effective strategy of Mo doping was executed to alter the band energy structure of the parent PEC anode system of WO_{3}-$(Sn_{0.95}Nb_{0.05})$ O_2:N. The incorporation of Mo into the WO_3 bilayer structured 1-D multi-metal oxide-based semiconductor photoanode beneficially altered the electronic structure and correspondingly, the optoelectronic properties. The as-engineered Mo doped bilayer i.e. $(W_{0.98}Mo_{0.02})O_{3}$-$(Sn_{0.95}Nb_{0.05})O_2$:N photoanode demonstrated excellent PEC performance with promising solar-to-hydrogen efficiency. The results described in this dissertation clearly demonstrated the influence of morphology, structure, composition and synthesis methods on the electrochemical response and electrochemical stability. In doing so, the dissertation provides a detailed account of various strategies to develop novel electrocatalyst materials, displaying an excellent electrochemical and photoelectrochemical response to acid mediated PEM-based water splitting and acid mediated PEM-based fuel cell systems. The strategies identified and implemented in the present work provide a rational framework to synthesize and engineer high-performance electrocatalysts for clean energy applications.

As with any conclusions offered by any structured work conducted to culminate a series of extensive studies such as in this dissertation, there is a need to elucidate a path forward. Thus, with the anticipation of continuing this research theme forward, it is envisaged that in order to make the electrocatalyst materials identified and developed in this dissertation to be applicable not only at the laboratory scale but also at the industrial scale, there is a need to generate these earth-abundant materials at scaled up levels demonstrating similar higher activity and long-term durability for hydrogen and oxygen electrocatalysis in practical electrolyzers and fuel cell stack levels. Demonstration of the activity and durability in field level environments are highly important for advancing the research in the field of clean energy technology. Fundamentally, extension of the synthesis method and the various ensuing parameters (i.e., precursors, temperature, pressure, pH, etc.) when generating the material at the industrial scale are crucial for reproducing and maintaining the electrochemically active surface area, the desired 1D, 2D and 3D morphology, shape, size, crystal structure, and electronic properties of the electrocatalyst. Thus, it is critical to pay special attention to mimicking and reproducing the synthesis methods offering beneficial control over these synthesis factors to generate large quantity (hundreds of grams or kgs) of high quality, pure, defect free, robust, durable, and high performance electrocatalyst products for large-scale industrial applications in PEM based water electrolysis and fuel cell technologies.

In addition, it would be noteworthy to explore the behavior of metal and non-metals as well as the influence of earth-abundant dopants on the electrocatalytic properties utilizing operando characterization methods. Operando characterization techniques such as near-ambient pressure X-ray diffraction, X-ray photoelectron spectroscopy (NAP-XPS), scanning electrochemical microscopy (SECM), and X-ray absorption near edge structure (XANES), also known as near edge X-ray absorption fine structure (NEXAFS) are very powerful tools to evaluate *in-situ* dynamic changes in the local electrochemical behavior of liquid/solid, liquid/gas and liquid/liquid interfaces as well as the structure, composition, and stability of the electrocatalyst while providing insight into the degradation mechanisms under operating conditions. Such studies will indeed provide at an atomic, electronic and molecular level, first-hand knowledge of the changes occurring in the electrocatalyst system enhancing the fundamental understanding of the electrocatalytic processes. These studies will in turn pave the way into further providing pathways for engineering and designing the novel electrocatalysts with improved electrochemical performance.

Finally, while a large portion of the results described in this dissertation was ably supplemented and complemented by theoretical studies, to further understand and comprehend the multi-faceted influence of morphological, structural, and compositional changes occurring during electrochemical testing, not only is there a fundamental need for advanced experimental studies exploring novel and innovative cost-effective synthesis strategies but also an equally pressing need for conducting intense theoretical efforts. Typically, transition metal oxide electrocatalysts are significantly complicated to study due to the added complexity of modeling various facets and surface coverages of various 1D, 2D and 3D morphologies under specific reaction conditions not-withstanding additional complexities introduced by the generation of structural and electronic defects. Although, the role of anti-site defects has been elucidated in this dissertation for the spinel system ($Cu_{1.5}Mn_{1.5}O_4$ and $Cu_{1.5}Mn_{1.5}O_4$:F), the entire gamut of 0-D, 1-D, 2-D and 3-D defects and their role on electrochemical response and stability needs to be explored and studied in detail. Therefore, while theoretical studies can play a crucial role in unraveling the electrochemical mechanisms and their roles in understanding the electrochemical response, an equally important aspect of theory and computation would be in rapid identification and screening of novel high performance electrocatalysts. In this regard, in addition to the ubiquitous DFT and molecular dynamics (MD) approaches that have been exploited to a large extent, a rapidly evolving area with the advent of artificial intelligence and big data mining (BDM) is the holistic machine learning (ML) design framework for accelerating the discovery of high-performance heterogeneous electrocatalysts. The ML approach combined with BDM and DFT approaches can be suitably exploited to rapidly explore a broad chemical space, the ensuing multi-arrays of descriptors for various species, morphologies, and process specific parameters along with the enormous compositional and configurational degrees of freedom for effectively narrowing down the potential electrocatalyst candidates for specific reactions. While execution of such a wide range of computational and theoretical studies will likely present its own challenges, the rapid advances made in the field of computation and the wide access to supercomputing resources and data mining software packages aided by the rapidly growing computational field will likely provide a path of alleviating much of these challenges. These studies will serve to offer tremendous advantages rapidly cutting the time and eliminating tedious processing and characterization steps prior to experimental validation of the theoretical findings. Thus, the integrated computational framework of DFT and ML will facilitate the discovery of promising electrocatalyst systems and will also reduce the efforts and costs involved in the experimental synthesis and testings.

In conclusion, based on the above, substantial advances, both in fundamental research as well as in the technological applications of the electrocatalysts identified and studied in this dissertation for anodic and cathodic reactions of PEM electrolyzer, PEMFC, and PEC based water electrolysis can be expected in the near future. Such advancements in multitude of scientific and technological areas will consequently lead to higher fundamental and applied research investments in the rapidly growing areas of PEM electrolyzers, PEMFCs, and also PEC water electrolyzer systems. It is anticipated that the present dissertation will serve as a foundation for conducting these much awaited critical studies further advancing the respective fields.

Appendix A Supplementary Information: First Report of Vertically Aligned (Sn,Ir)O_2:F Solid Solution Nanotubes : Highly Efficient and Robust Oxygen Evolution Electrocatalyst for PEM Based Water Electrolysis

Specific surface area (SSA) calculation based on the SEM images and the geometrical data of the ($Sn_{0.8}Ir_{0.2}$)O_2:10F nanotubes:

$$SSA\ (m^2g^{-1}) = \frac{Area\ (m^2)}{Volume(m^3) \times Density(gm^{-3})}$$

$$Area\ (m^2) = 2\pi \times h \times (r_1 + r_2)$$

$$Volume\ (m^3) = \pi \times h \times ({r_2}^2 - {r_1}^2)$$

Where, h = average height of nanotubes ~ 10×10^{-6} m

r_1 = inner radius of nanotubes = 70×10^{-9} m

r_2 = outer radius of nanotubes = 110×10^{-9} m

Thus, Area = 1.1304×10^{-11} m^2 and volume = 2.2608×10^{-19} m^3

Density (ρ) of ($Sn_{0.8}Ir_{0.2}$)O_2:10F :

$$\rho\ (gm^{-3}) = \frac{100}{\frac{wt.\%\ Ir}{\rho(IrO_2)}+\frac{wt.\%\ Sn}{\rho(SnO_2)}} = 7.86\times10^6\ gm^{-3}$$

Where $\rho(SnO_2)$ is 6.95 gcm^{-3} and $\rho(IrO_2)$ is 11.66 g cm^{-3}

Thus, approximate SSA of $(Sn_{0.8}Ir_{0.2})O_2$:10F nanotubes = **7.33 m^2g^{-1}**

Electrochemical Active Surface Area (ECSA):

The electrochemically active surface area (ECSA) was obtained by dividing areal double layer capacitance (C_{dl}) by the specific areal capacitance (C^*) of electrocatalyst, similar to the previous reports of ECSA determination[177, 250]. For IrO_2 a specific capacitance (C^*) value was estimated to be 650 μF/cm^2 based on the single-crystal IrO_2(100) CVs recorded by Hepel et al. in 1N H_2SO_4 electrolyte[171]. In the present study, the IrO_2 (100) surface was chosen to estimate the ECSA of as-synthesized electrocatalysts because, to the best of our knowledge, it was the only IrO_2 single-crystal surface reported for electrochemical testing in acidic electrolyte, similar to the earlier report[177].

The electrochemical active surface area (ECSA in $m^2\,g^{-1}$) of the as-prepared electrodes has been calculated using the following equation:

$$ECSA\ (m^2g^{-1}) = \frac{C_{dl}}{C^* \times L}$$

Where, C_{dl} = double-layer capacitance ($mFcm^{-2}$)

Herein, C_{dl} = ½ × linear slope of the current density ($j_{anode} - j_{cathode}$) *vs.* scan rate [162, 169]

C^* = specific capacitance of single crystal IrO_2 ($mFcm^{-2}$) [171, 177]

L = Mass loading of the electrocatalyst ($g\ m^{-2}$)

Sample ECSA calculation for $(Sn_{0.8}Ir_{0.2})O_2$:10F –NTs:

$$ECSA\ (m^2g^{-1}) = \frac{C_{dl}}{C^* \times L}$$

- Linear slope of the current density ($j_{anode} - j_{cathode}$) *vs* scan rate for $(Sn_{0.8}Ir_{0.2})O_2$:10F -NTs (**Fig. 6b**) = 150 mF cm^{-2}

  Accordingly, C_{dl} = ½ × 150 = 75 mF cm^{-2}

- C* = 650 μF/cm^2= 0.65 mF cm^{-2}

- L = 0.3 mg cm^{-2} = 3 g m^{-2}

Note: We have carried out first-principles theoretical calculations of the total energies and electronic structures for the F substituted $(Sn,Ir)O_2$ electrocatalyst system[97]. From this study, it has been identified that the system with 9–10 wt% of F-concentration in the $(Sn,Ir)O_2$ solid solution exhibits d-band center position identical to that of pure IrO_2 (110), mimicking the electronic, crystallographic and electro-catalytic properties of pure IrO_2. Therefore, due to such modification in the electronic structure of $(Sn_{0.8}Ir_{0.2})O_2$:10F, the entire oxide (not only Ir cations) can be assumed to be electro-catalytically active. Thus, herein, the specific capacitance of single crystal (100) IrO_2 (650 μF cm^{-2}) of IrO_2 is used to evaluate ECSA of pure IrO_2 thin film as well as ECSA of $(Sn_{0.8}Ir_{0.2})O_2$:10F NTs and $(Sn_{0.8}Ir_{0.2})O_2$:10F thin film, on the basis of the isoelectronic characteristic of pure IrO_2 and $(Sn_{0.8}Ir_{0.2})O_2$:10F. However, it should be noted that in our previous theoretical studies, calculation have been done for the electronic structures of the stable (110) surfaces for all the above mentioned Ir-based oxides. Thus, IrO_2(110) may likely possess different specific capacitance value than IrO_2(100) as reported earlier.

Thus, for $(Sn_{0.8}Ir_{0.2})O_2$:10F - NTs:

$$\boldsymbol{ECSA\ (m^2 g^{-1})} = \frac{75\ (\mathrm{mF}\ cm^{-2})}{0.65\ (\mathrm{mF}\ cm^{-2}) \times 3(\mathrm{g}\ m^{-2})} = \boldsymbol{38.46\ m^2 g^{-1}}$$

Similar calculations have been carried out to evaluate ECSA for $(Sn_{0.8}Ir_{0.2})O_2$:10F and IrO_2 thin film electrocatalysts. It is possible that if actual specific capacitance (C*) values of single crystal/ monolayer are determined and selected for $(Sn_{0.8}Ir_{0.2})O_2$:10F NTs and $(Sn_{0.8}Ir_{0.2})O_2$:10F thin film, the actual ECSA values will be even more representative. Nevertheless, normalization of the values accounts for the use of the single crystal values for IrO_2.

ECSA normalized current density ($mAcm^{-2}$):

$$= \frac{\text{Curent density obtained from linear scan polarisation (mA cm}^{-2}\text{)}}{\text{Electrocatalyst mass loading (g m}^{-2}\text{)} \times \text{ECSA(m}^{2}\text{g}^{-1}\text{)}}$$

Appendix A Table 1 Results of the electrochemical active surface area (ECSA) calculations of the as-prepared electrocatalysts

Electrocatalyst Composition	**Linear slope of current density ($j_{anode} - j_{cathode}$) *vs.* scan rate (mF cm^{-2})**	**Double layer capacitance (C_{dl}) (mF cm^{-2})**	**ECSA ($m^2 g^{-1}$)**
IrO_2 –Thin film	113.8	56.9	29.17
$(Sn_{0.8}Ir_{0.2})O_2$:10F –Thin film	120.5	60.25	30.89
$(Sn_{0.8}Ir_{0.2})O_2$:10F -NTs	150	75	38.46

Mass activity (A/g)

$$\text{Mass activity, A g}^{-1\ 467} = \frac{j}{\text{m}}$$

Where j = the current density (mA cm^{-2}) measured at particular potential (1.5 V *vs.* RHE) and

m = mass loading of the electrocatalyst

Thus, for $(Sn_{0.8}Ir_{0.2})O_2$:10F –NTs:

$$\text{Mass activity (A g}^{-1}\text{)} = \frac{6.5\ (\text{mA}\ cm^{-2})}{0.3\ (\text{mg}\ cm^{-2})} = \mathbf{21.67\ A\ g^{-1}}$$

Specific activity (mA cm^{-2})

$$\text{Specific activity, mA cm}^{-2}\,{}^{468,\,469} = \frac{j}{10\times \text{m} \times \text{ECSA}}$$

Where j = the current density (mA cm^{-2}) measured at 1.5 V *vs.* RHE,

m = mass loading of the electrocatalyst and

ECSA = electrochemical active surface area (m^2 g^{-1})

Thus, for $(Sn_{0.8}Ir_{0.2})O_2$:10F –NTs:

$$\text{Specific activity (mA cm}^{-2}) = \frac{6.5\ (\text{mA}\ cm^{-2})}{10\times 0.3\ (\text{mg}\ cm^{-2})\times 38.46\ (m^2 g^{-1})} = \mathbf{0.005633\ mAcm^{-2}}$$

Turn over frequency (TOF, s^{-1})

$$\text{TOF, s}^{-1\,467,\,468} = \frac{J\times A}{4\times \text{F}\times \text{n}}$$

Where, j = the current density (A cm^{-2}) measured at 1.5 V *vs.* RHE

A = geometric area of the working electrode (cm^2)

F = Faraday constant (96,485 C mol^{-1}) and

n = number of moles of the electrocatalyst

For $(Sn_{0.8}Ir_{0.2})O_2$:10F the molecular weight has been calculated as:

= 0.9 (0.8× Atomic wt. of Sn + 0.2× Atomic wt. of Ir + 2× Atomic wt. of O) + 0.1× Atomic wt. of F

= 284.75 gmol^{-1}

Thus, for $(Sn_{0.8}Ir_{0.2})O_2$:10F –NTs:

$$\textbf{TOF} = \frac{6.5\times 10^{-3}\ (\text{A}\ cm^{-2})\times 1(cm^2)}{4\times 96485(\text{C}\ mol^{-1})\ \times 1.05356\times 10^{-6}\ (\text{moles})} = \mathbf{0.016\ s^{-1}}$$

Appendix A Table 2 ICP-OES analysis results on 1N H_2SO_4 electrolyte solution collected after 24 h chronoamperometry test

Electrocatalyst Composition	Sn (ppm)	Ir (ppm)
IrO_2 –Thin film	---	$3.1\times10^{-3} \pm 0.002$
$(Sn_{0.8}Ir_{0.2})O_2$:10F –Thin film	$5.7\times10^{-3} \pm 0.001$	$2.4\times10^{-3} \pm 0.001$
$(Sn_{0.8}Ir_{0.2})O_2$:10F -NTs	$2.9\times10^{-3} \pm 0.001$	$1.8\times10^{-3} \pm 0.001$

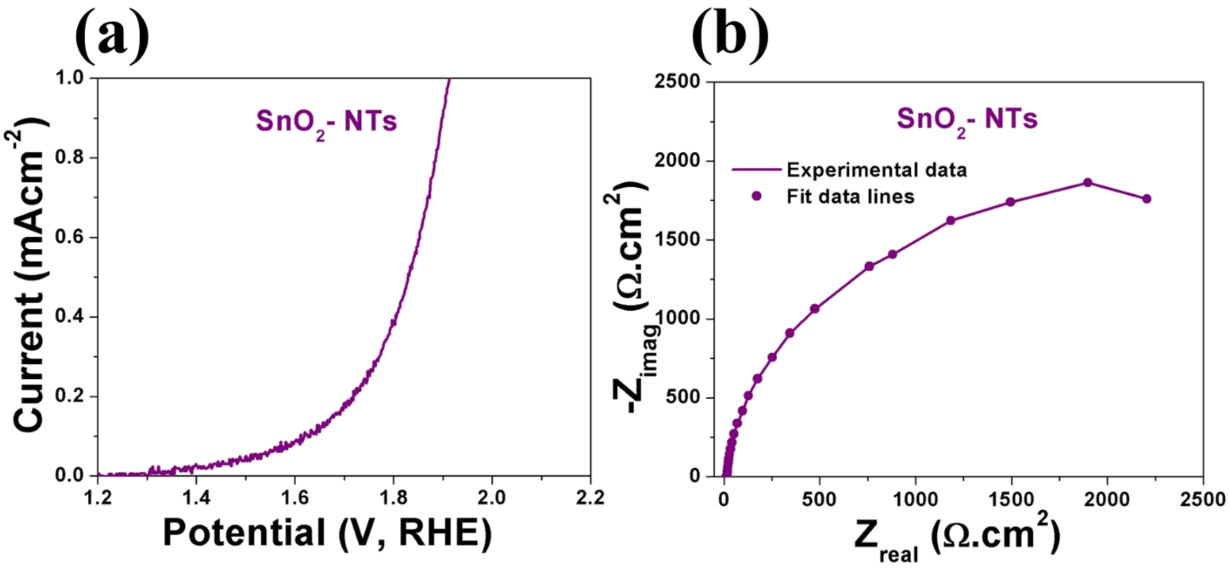

Appendix A Figure 1 The polarization curve of SnO_2 NTs and (b) EIS plot of SnO_2 NTs performed at 1.5 V (vs RHE) in 1N H_2SO_4 at 40°C

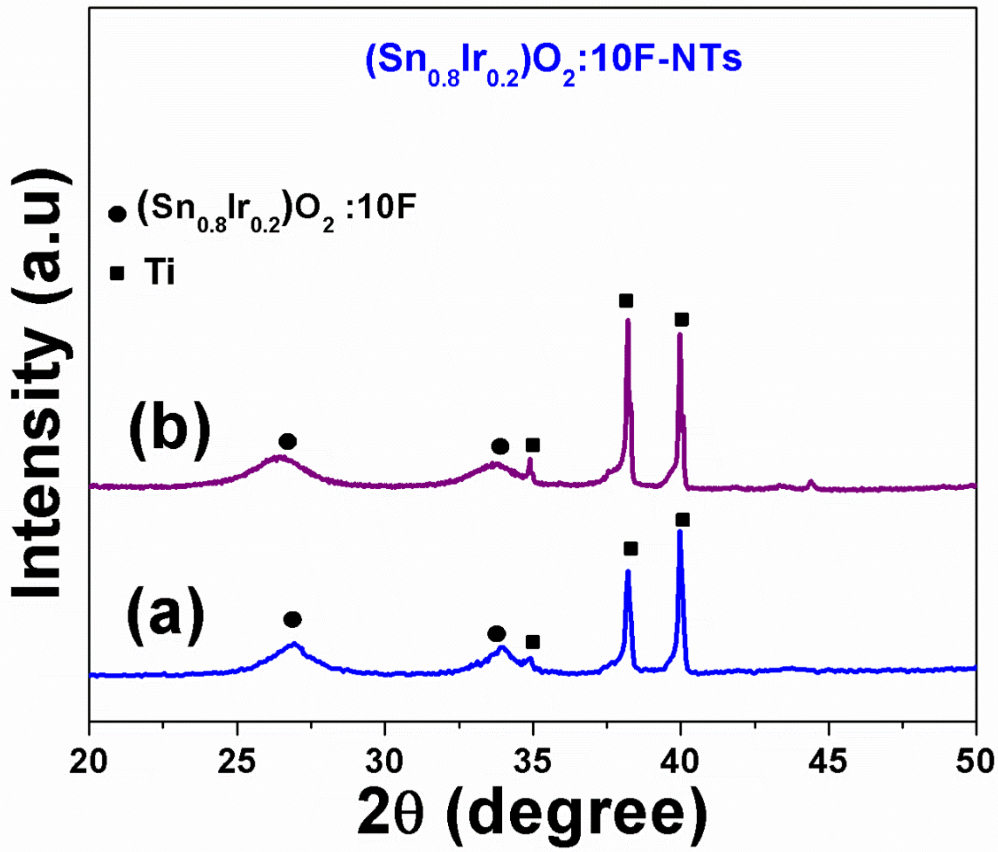

Appendix A Figure 2 The XRD patterns ($(Sn_{0.8}Ir_{0.2})O_2$:10F NTs (a) before and (b) after 24 h chronoamperometry (CA) test

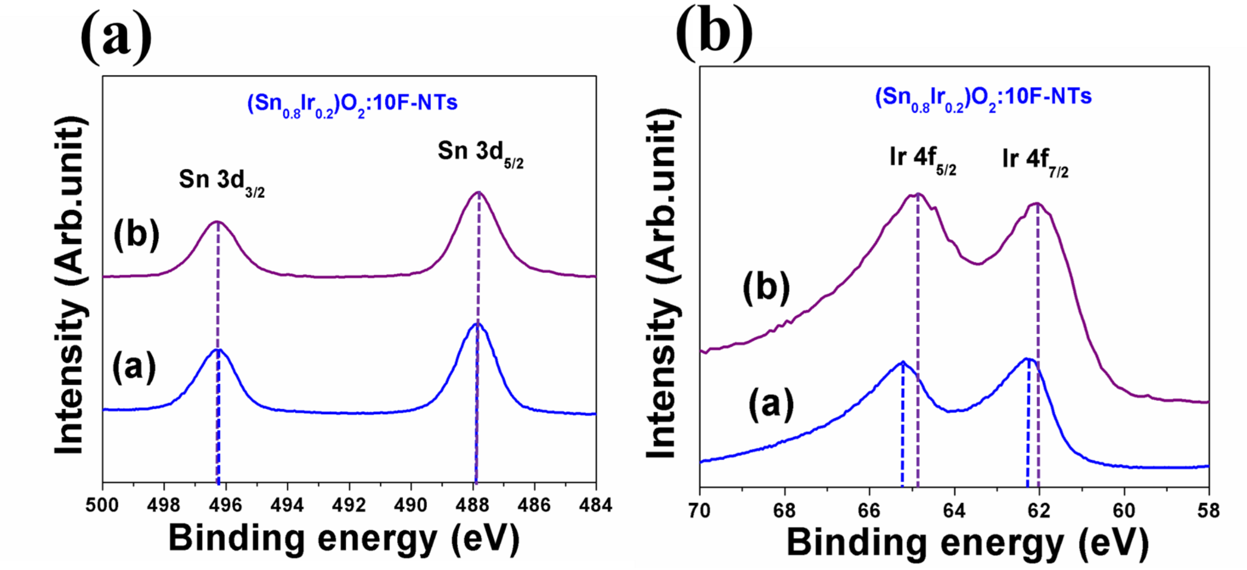

Appendix A Figure 3 The XPS spectra of (a) Sn and(b) Ir of $(Sn_{0.8}Ir_{0.2})O_2$:10F NTs before and after 24 h chronoamperometry (CA) test

Appendix B Supplementary Information: Experimental and Theoretical Validation of High Efficiency and Robust Electrocatalytic Response of One Dimensional (1D) (Mn, Ir)O_2:10F Nanorods for Oxygen Evolution Reaction in PEM Based Water Electrolysis

Calculation of lattice parameters and volume

- d-spacing (for tetragonal crystal structure):

$$\frac{1}{d^2} = \frac{h^2 + k^2}{a^2} + \frac{l^2}{c^2}$$

- Unit cell volume (Å^3) = $a^2 \times c$
- Molar volume (cm^{3}mol^{-1}) = $\frac{\text{Unit cell volume} \times \text{Avogadro's number}}{\text{Coordination number (Z)}}$

Appendix B Table 1 The lattice parameters and unit cell volumes of the computationally studied electrocatalyst compositions

Electrocatalyst composition	Lattice parameters (Å)		Unit cell volume (Å^3)
	a = b	c	
α-MnO_2	9.784	2.867	274.44
$Mn_{0.75}Ir_{0.25}O_2$	9.826	2.906	280.57
$Mn_{0.75}Ir_{0.25}O_{1.37}F_{0.625}$	9.849	2.963	287.41

Appendix B Table 2 The BET surface area, pore volume and average pore width of as-synthesized electrocatalysts

Electrocatalyst composition	BET Surface area (m^2g^{-1})	Pore volume (cm^3g^{-1})	Avg. Pore width (nm)
MnO_2	~3.72	~0.069	~48.31
$(Mn_{0.8}Ir_{0.2})O_2$	~3.70	~0.058	~48.27
$(Mn_{0.8}Ir_{0.2})O_2$:10F	~3.55	~0.052	~48.11
IrO_2	~189	~0.29	4.6

Appendix B Table 3 The binding energies (eV), full width at half maximum (FWHM) and spin-energy separation (ΔS) parameters for as-synthesized electrocatalyst

Compound	**Mn $2p_{3/2}$ (eV)**	**FWHM (Mn $2p_{3/2}$)**	**Mn $2p_{1/2}$ (eV)**	**FWHM (Mn $2p_{1/2}$)**	**ΔS (eV)**
MnO_2	642	3.15	~653.8	3.17	11.8
$(Mn_{0.8}Ir_{0.2})O_2$	642	3.15	~653.8	3.17	11.8
$(Mn_{0.8}Ir_{0.2})O_2$:10F	642.9	3.17	~654.5	3.19	11.6

Compound	**Ir $4f_{7/2}$ (eV)**	**FWHM (Ir $4f_{7/2}$)**	**Ir $4f_{5/2}$ (eV)**	**FWHM (Ir $4f_{5/2}$))**	**ΔS (eV)**
IrO_2	~61.8	1.76	~64.9	3.37	~3.1
$(Mn_{0.8}Ir_{0.2})O_2$	~61.8	1.76	~64.9	3.38	~3.1
$(Mn_{0.8}Ir_{0.2})O_2$:10F	~62.7	1.79	~65.8	3.41	~3.1

Compound	**O1s (eV)**	**FWHM (O1s)**
MnO_2	~ 530.1	2.16
IrO_2	~ 530.1	1.71
$(Mn_{0.8}Ir_{0.2})O_2$	~ 530.1	2.16
$(Mn_{0.8}Ir_{0.2})O_2$:10F	~ 530.8	2.18

Electrochemical Active Surface Area (ECSA):

The electrochemically active surface area (ECSA) was obtained by dividing double capacitance (C_{dl}) by the specific capacitance (C^*) of electrocatalyst, similar to the previous reports of ECSA determination[249-251]. A general specific capacitance (C^*) value of metal electrodes in acidic solutions is taken as 35 μFcm^{-2}[91, 249, 252]. Based on this specific capacitance (C^*) value, ECSA of as-synthesized electrocatalyst has been evaluated.

The electrochemical active surface area (ECSA in m^2 g^{-1}) of the as-prepared electrodes has been calculated using the following equation:

$$ECSA\ (m^2g^{-1}) = \frac{C_{dl}}{C^* \times L}$$

Where, C_{dl} = double-layer capacitance (mFcm^{-2})

Herein, C_{dl} = ½ × linear slope of the current density ($j_{anode} - j_{cathode}$) *vs.* scan rate [162, 169]

C^* = specific capacitance in acidic electrolyte (0.035mFcm^{-2}) [91, 249, 252]

L = Mass loading of the electrocatalyst (g m^{-2})

Sample ECSA calculation for ($Mn_{0.8}Ir_{0.2}$)O_2:10F NRs:

$$ECSA\ (m^2g^{-1}) = \frac{C_{dl}}{C^* \times L}$$

- Linear slope of the current density ($j_{anode} - j_{cathode}$) *vs* scan rate for ($Mn_{0.8}Ir_{0.2}$)O_2:10F NRs (**Fig. 9b**) = 148 mF cm^{-2}

  Accordingly, C_{dl} = ½ × 148 = 74 mF cm^{-2}
- C* = 0.035 mF cm^{-2}
- L = 0.3 mg cm^{-2} = 3 g m^{-2}

Thus, for ($Mn_{0.8}Ir_{0.2}$)O_2:10F - NRs:

$$\boldsymbol{ECSA\ (m^2g^{-1})} = \frac{74\ (\text{mF}\ cm^{-2})}{0.035\ (\text{mF}\ cm^{-2}) \times 3(\text{g}\ m^{-2})} = \boldsymbol{704.76\ m^2g^{-1}}$$

Similar calculations have been carried out to evaluate ECSA for $(Mn_{0.8}Ir_{0.2})O_2$ NRs and IrO_2 electrocatalysts. It should be noted that if the actual monolayer values are determined and selected for $(Mn_{0.8}Ir_{0.2})O_2$:10F NRs and $(Mn_{0.8}Ir_{0.2})O_2$NRs, the actual ECSA values will be more precise and representative.

Surface Roughness Factor (RF)

$$\mathrm{RF}^{470} = \frac{ECSA \times L}{GSA}$$

Where, GSA = geometric area of the electrode (0.5 × 2= 1 cm^2) and

L = mass loading of electrocatalyst = 0.3 mg/cm^2

Thus, for $(Mn_{0.8}Ir_{0.2})O_2$:10F –NRs:

$$\boldsymbol{RF} = \frac{704.76\ (m^2 g^{-1}) \times 0.0003(g)}{0.0001\ (m^2)} = \mathbf{2114.28}$$

<u>Note:</u> In the present study, the ‘typical’ specific capacitance (C*) value to evaluate the ECSA in acidic electrolytes is taken as ~0.035 $mFcm^{-2}$, based on the earlier study conducted by McCrory et al.[91] as well as various other reported studies for acidic OER. [91, 249, 252] However, herein, the authors would like to elucidate that the specific capacitance (C*) values for electrocatalyst materials can be different from ~0.035 $mFcm^{-2}$[91]. For example, for single-crystal IrO_2, the specific capacitance (C^*) value was used as ~0.65 $mFcm^{-2}$ in the 1N H_2SO_4 electrolyte media[171, 251].

Appendix B Table 4 Results of the electrochemical active surface area (ECSA) and Surface roughness factor (RF) of the as-prepared electrocatalysts (For: C* =0.035 mFcm^{-2})

Electrocatalyst Composition	**Linear slope of current density ($j_{anode} - j_{cathode}$) *vs.* scan rate (mF cm^{-2})**	**Double layer capacitance (C_{dl}) (mF cm^{-2})**	**ECSA (m^2 g^{-1})**	**Roughness Factor (RF)**
$(Mn_{0.8}Ir_{0.2})O_2$:10F	148	74	704.76	2114.28
$(Mn_{0.8}Ir_{0.2})O_2$	88	44	419.04	1257.14
IrO_2	45	22.5	214.28	642.85

In the extensive study conducted by Jung et al.[176] , it has been reported that several factors such as pseudo-capacitance due to surface coordination of ions and ion intercalation, chemical capacitance due to the population of trap states, and capacitance from any residual charge-transfer processes in the putative non-faradaic region may contribute to the inaccuracy in the capacitance determinations and therefore the estimated ECSA. Thus, in the present study, to better probe the general discrepancy between the BET and ECSA values, in addition to the ‘typical’ specific capacitance (C^*) of ~0.035 mFcm^{-2}, we have also evaluated the ECSA by considering the specific capacitance (C^*) of IrO_2 as ~0.65 mF cm^{-2}. It is noteworthy to mention that we have also carried out the first-principles theoretical calculations of the total energies and electronic structures for the F substituted $(Mn_{0.8}Ir_{0.2})O_2$:10F electrocatalyst system[70]. From this study, it has been identified that the system with 10 wt.% of F-concentration in the $(Mn,Ir)O_2$ solid solution exhibits d-band center position identical to that of pure IrO_2, mimicking the electronic and electro-catalytic properties of pure IrO_2. Therefore, due to such modification in the electronic structure of

$(Mn_{0.8}Ir_{0.2})O_2$:10F, the entire oxide can be assumed to be electro-catalytically active. As a result, herein, in addition to the specific capacitance of 0.035 mF cm^{-2}, specific capacitance of single crystal (100) of IrO_2 (0.65 mFcm^{-2}) is also utilized to evaluate the ECSA of as-synthesized electrocatalysts. Based on these calculations, ECSA of 1D $(Mn_{0.8}Ir_{0.2})O_2$:10F NRs is obtained as ~ 38 m^2 g^{-1}.

Appendix B Table 5 Results of the electrochemical active surface area (ECSA) and surface roughness factor (RF) of the as-prepared electrocatalysts (For: C* = 0.65 mFcm^{-2})

Electrocatalyst Composition	**Linear slope of current density ($j_{anode} - j_{cathode}$) *vs.* scan rate (mF cm^{-2})**	**Double layer capacitance (C_{dl}) (mF cm^{-2})**	**ECSA (m^2 g^{-1})**	**Roughness Factor (RF)**
$(Mn_{0.8}Ir_{0.2})O_2$:10F	148	74	38	113.84
$(Mn_{0.8}Ir_{0.2})O_2$	88	44	22.56	67.69
IrO_2	45	22.5	11.53	34.61

Normalized current densities:

- *ECSA normalized current density (mA cm^{-2}$_{ECSA}$)*

$$= \frac{\text{Curent density obtained from linear scan polarisation (mA cm}^{-2}\text{)}}{\text{Electrocatalyst mass loading (g m}^{-2}\text{)} \times \text{ECSA(m}^2\text{g}^{-1}\text{)}}$$

- *BET normalized current density (mA cm^{-2} $_{BET}$)*

$$= \frac{\text{Curent density obtained from linear scan polarisation (mA cm}^{-2}\text{)}}{\text{Electrocatalyst mass loading (g m}^{-2}\text{)} \times \text{BET surface area (m}^2\text{g}^{-1}\text{)}}$$

Mass activity (Ag^{-1})

Mass activity, ($A\ g^{-1}$)[471] $= \frac{j}{\mathrm{m}}$

Where j = the current density ($mA\ cm^{-2}$) measured at particular potential (1.45 V *vs.* RHE) and

m = mass loading of the electrocatalyst

Thus, for $(Mn_{0.8}Ir_{0.2})O_2$:10F –NRs:

Mass activity ($A\ g^{-1}$) $= \frac{12(\mathrm{mA}\ cm^{-2})}{0.3\ (\mathrm{mg}\ cm^{-2})}$ **= 40 A g^{-1}**

ECSA Specific activity ($mAcm^{-2}_{ECSA}$)

ECSA specific activity, (**$mAcm^{-2}_{ECSA}$**)[469] $= \frac{j}{10 \times \mathrm{m} \times \mathrm{ECSA}}$

Where j = the current density ($mA\ cm^{-2}$) measured at 1.45 V *vs.* RHE,

m = mass loading of the electrocatalyst and

ECSA = Electrochemical active surface area (ECSA) ($m^2\ g^{-1}$)

Thus, for $(Mn_{0.8}Ir_{0.2})O_2$:10F –NRs:

ECSA specific activity $= \frac{12\ (\mathrm{mA}\ cm^{-2})}{10 \times 0.3\ (\mathrm{mg}\ cm^{-2}) \times 704.76\ (m^2 g^{-1})}$ **= 0.56 μA cm^{-2}_{ECSA}**

BET Specific activity ($mAcm^{-2}{}_{BET}$)

BET specific activity, $mAcm^{-2}{}_{BET}$[469, 472] $= \frac{j}{10 \times \mathrm{m} \times S_{BET}}$

Where j = the current density ($mA\ cm^{-2}$) measured at 1.45 V *vs.* RHE,

m = mass loading of the electrocatalyst and

S_{BET} = BET surface area ($m^2\ g^{-1}$)

Thus, for $(Mn_{0.8}Ir_{0.2})O_2$:10F –NRs:

$$\text{BET specific activity} = \frac{12\ (\text{mA}\ cm^{-2})}{10 \times 0.3\ (\text{mg}\ cm^{-2}) \times 3.55 (m^2 g^{-1})} = \mathbf{0.11\ mAcm^{-2}}_{\mathbf{BET}}$$

Turn over frequency (TOF, s^{-1})

$$\text{TOF}, (s^{-1})^{472} = \frac{J \times A}{4 \times \text{F} \times \text{n}}$$

Where, *j* = the current density (A cm^{-2}) measured at 1.45 V *vs.* RHE

A = geometric area of the working electrode (cm^2)

F = Faraday constant (96,485 C mol^{-1}) and

n = number of moles of the electrocatalyst

For $(Mn_{0.8}Ir_{0.2})O_2$:10F the molecular weight has been calculated as:

= 0.9 (0.8× Atomic wt. of Mn + 0.2× Atomic wt. of Ir + 2× Atomic wt. of O) + 0.1× Atomic wt. of F

= 104.84 $gmol^{-1}$

Thus, for $(Mn_{0.8}Ir_{0.2})O_2$:10F –NRs:

$$\textbf{TOF} = \frac{12 \times 10^{-3}\ (\text{A}\ cm^{-2}) \times 1 (cm^2)}{4 \times 96485 (\text{C}\ mol^{-1})\ \times 2.86 \times 10^{-6}\ (\text{moles})} = \mathbf{0.01\ s^{-1}}$$

Appendix B Table 6 Results of the mass activity, specific activity and normalized current densities at the voltage of 1.45 V

Electrocatalyst Composition	Mass activity at 1.45 V (Ag^{-1})	ECSA normalized current density at 1.45 V ($\mu A\ cm^{-2}_{ECSA}$)	ECSA based specific activity at 1.45 V ($\mu A\ cm^{-2}_{ECSA}$)	BET normalized current density at 1.45 V ($mA\ cm^{-2}_{BET}$)	BET based specific activity at 1.45 V ($mA\ cm^{-2}_{BET}$)
$(Mn_{0.8}Ir_{0.2})O_2$:10F	~40	~5.6	~0.56	~1.1	~0.11
$(Mn_{0.8}Ir_{0.2})O_2$	~18.34	~4.3	~0.43	~0.5	~0.05
IrO_2	~6.67	~3.1	~0.31	~0.0035	~0.00035

Appendix B Table 7 ICP-OES analysis results

Electrocatalyst Composition	Mn (ppm)	Ir (ppm)
IrO_2	---	$2.4\times10^{-3} \pm 0.0002$
$(Mn_{0.8}Ir_{0.2})O_2$	$1.6\times10^{-3} \pm 0.0001$	$2.1\times10^{-3} \pm 0.0002$
$(Mn_{0.8}Ir_{0.2})O_2$:10F	$1\times10^{-3} \pm 0.0002$	$1.1\times10^{-3} \pm 0.0002$

Electrical resistivity and conductivity measurements

The room temperature resistivity (ρ_{300K}) and conductivity (σ_{300K}) values of the as synthesized electrocatalyst samples were investigated by utilizing Jandel Micro position Probe apparatus. The samples for electrical conductivity measurements were prepared by pressing ~500 mg of the powders into the round pellets of average thickness (t) ~1-1.1 mm and a diameter of 13 mm. The pressure of 4 metric tons was used to prepare the pellets. The electrical resistance of the pellet was calculated by utilizing the following equations (provided by the manufacturer-Jandel Engineering Ltd.)

Resistance of the pellet, $R_s = 4.532 \times V/I$, where V and I voltage and current, respectively.

Bulk resistivity of the pellet, $\rho = R_s \times t$

Electrical conductivity, $\sigma = 1/\rho$

Appendix B Table 8 The electronic resistivity and conductivity values of the as-synthesized electrocatalysts

Electrocatalyst Composition	Resistivity (ρ_{300K}) Ω cm	Conductivity (σ_{300K}) S cm^{-1}
MnO_2	312.5	~0.0032
$(Mn_{0.8}Ir_{0.2})O_2$	9.09	~0.11
$(Mn_{0.8}Ir_{0.2})O_2$:10F	0.17	~5.88
IrO_2	0.12	~8.33

The obtained conductivity values of MnO_2 and IrO_2 are in a good agreement with the literature results[37, 264, 265, 473].

Appendix B Table 9 Comparison of OER electrocatalytic activity of as-synthesized $(Mn_{0.8}Ir_{0.2})O_2$:10F NRs with other noble metal containing electrocatalysts in acidic electrolytes

Electrocatalyst	**Acidic Electrolyte**	**Electrocatalyst loading**	**Tafel slope ($mVdec^{-1}$)**	**η (mV *vs.* RHE) @ 10 (mA cm^{-2})**	**Reference**
$(Mn_{0.8}Ir_{0.2})O_2$:10F NRs	1 N H_2SO_4	0.3 $mgcm^{-2}$	38	200	**Present work**
$(Mn_{0.8}Ir_{0.2})O_2$ NRs	1 N H_2SO_4	0.3 $mgcm^{-2}$	46	240	**Present work**
IrO_2 NPs	1 N H_2SO_4	0.3 $mgcm^{-2}$	63	280	**Present work**
$(Mn_{0.8}Ir_{0.2})O_2$:10F film	1 N H_2SO_4	0.3 $mgcm^{-2}$	68	245	[70]
$(Sn_{0.8}Ir_{0.2})O_2$:10F film	1 N H_2SO_4	0.3 $mgcm^{-2}$	62	320	[97]
$(Sn_{0.35}Nb_{0.35}Ir_{0.30})O_2$:10F	1 N H_2SO_4	0.3 $mgcm^{-2}$	77	330	[98]
$Ir_{0.4}Ru_{0.6}Mo_xO_y$	1 N H_2SO_4	1.5 $mgcm^{-2}$	N/A	240	[474]
$(Sn_{0.8}Ru_{0.2})O_2$:10F film	1 N H_2SO_4	0.3 $mgcm^{-2}$	65	280	[136]
$(Nb_{0.75}Ir_{0.25})O_2$:10F NPs	1 N H_2SO_4	0.3 $mgcm^{-2}$	78	270	[282]
$K_{1.65}(Mn_{0.78}Ir_{0.22})_8O_{16}$	0.1 N $HClO_4$	0.2 $mgcm^{-2}$	76	340	[209]
$0.5IrO_2{-}0.5SiO_2$	1 N H_2SO_4	2 $mgcm^{-2}$	80	322	[475]
$IrO_2{-}Ta_2O_5$	1 N H_2SO_4	1 $mgcm^{-2}$	59	362	[476]
$Bi_2Ir_2O_7$	2 N H_2SO_4	0.402 $mgcm^{-2}$	45	365	[477]
IrO_x-Ir	1 N H_2SO_4	130 $\mu g_{(Ir)}cm^{-2}$	44.7	290	[478]
IrO_2/Ni_4N	1 N H_2SO_4	76.5 $\mu g_{(Ir)}cm^{-2}$	64	346	[251]
IrO_2/CoN	1 N H_2SO_4	76.5 $\mu g_{(Ir)}cm^{-2}$	66.9	319	[251]
$Ir_{0.7}Ni_{0.3}O_{2-y}$	1 N H_2SO_4	0.102 $mgcm^{-2}$	57	335	[479]
Ir	1 N H_2SO_4	N/A	N/A	360	[480]

Appendix B Table 9 (continued)

IrO_2 Nano-needles	2 N H_2SO_4	0.25 $mgcm^{-2}$	57	313	481
Ru	1 N H_2SO_4	N/A	N/A	340	480
Ir/Au	0.2 N H_2SO_4	N/A	N/A	410	482
IrNiCu	0.1 N $HClO_4$	20 $\mu g_{(Ir)}cm^{-2}$	48	300	483
IrCoNi- Nanocrystals	0.1 N $HClO_4$	10 $\mu g_{(Ir)}cm^{-2}$	53.8	303	484
Co-IrCu Nanocrystals	0.1 N $HClO_4$	20 $\mu g_{(Ir)}cm^{-2}$	53.8	290	484
$RuIrCoO_x$	1 N H_2SO_4	1 $mgcm^{-2}$	108	390	485
$SrIrO_3$ film	1 N H_2SO_4	N/A	N/A	340	486
Iridium nanodendrites/ITO	0.1 N H_2SO_4	10.2 $mgcm^{-2}$	56.4	390	175
IrO_2/Sb–SnO_2 NWs	1 N H_2SO_4	0.75 $mg_{(Ir)}$ cm^{-2}	54	250	44
$Ir_{0.7}Co_{0.3}O_x$	1 N H_2SO_4	0.102 $mgcm^{-2}$	40	330	276
IrTe nanotubes	0.1 N $HClO_4$	25.5 $mg_{(Ir)}$ cm^{-2}	60.3	290	487
$W_{0.57}Ir_{0.43}O_{3-\sigma}$	2 N H_2SO_4	N/A	125	370	275
$IrNiO_x$	0.1 N H_2SO_4	10.2 μg cm^{-2}	N/A	350	174
IrNi nanocluster	1 N H_2SO_4	12.5 $\mu g_{(Ir)}cm^{-2}$	N/A	350	488

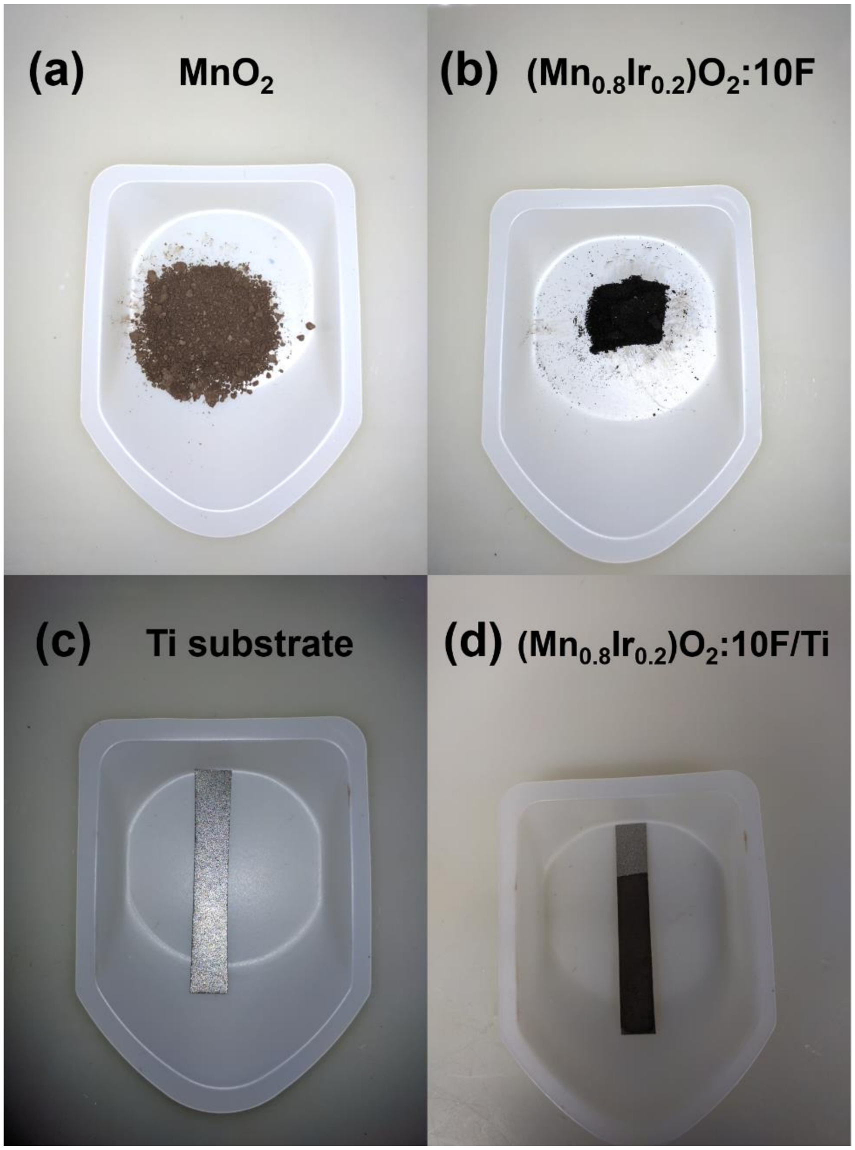

Appendix B Figure 1 Digital images of (a) hydrothermally synthesized MnO_2, (b) $(Mn_{0.8}Ir_{0.2})O_2$:10F NRs, (c) bare Ti substrate, and (d) $(Mn_{0.8}Ir_{0.2})O_2$:10F NRs/Ti

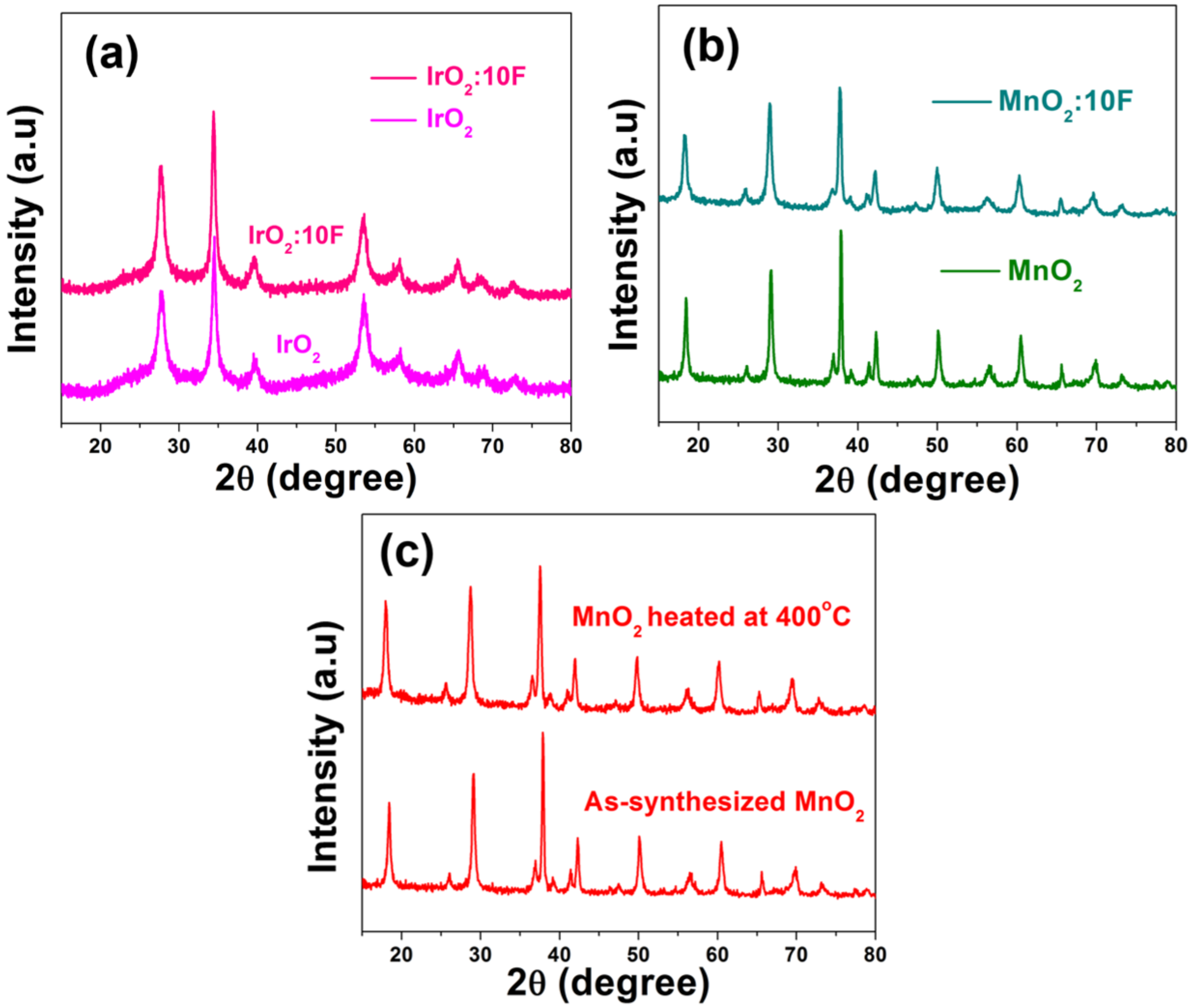

Appendix B Figure 2 Powder XRD patterns of the as-synthesized (a) IrO_2 and IrO_2:10F, (b) MnO_2 and MnO_2:10F NRs, and (c) MnO_2 and MnO_2 -calcined at 400^{o}C, 4h

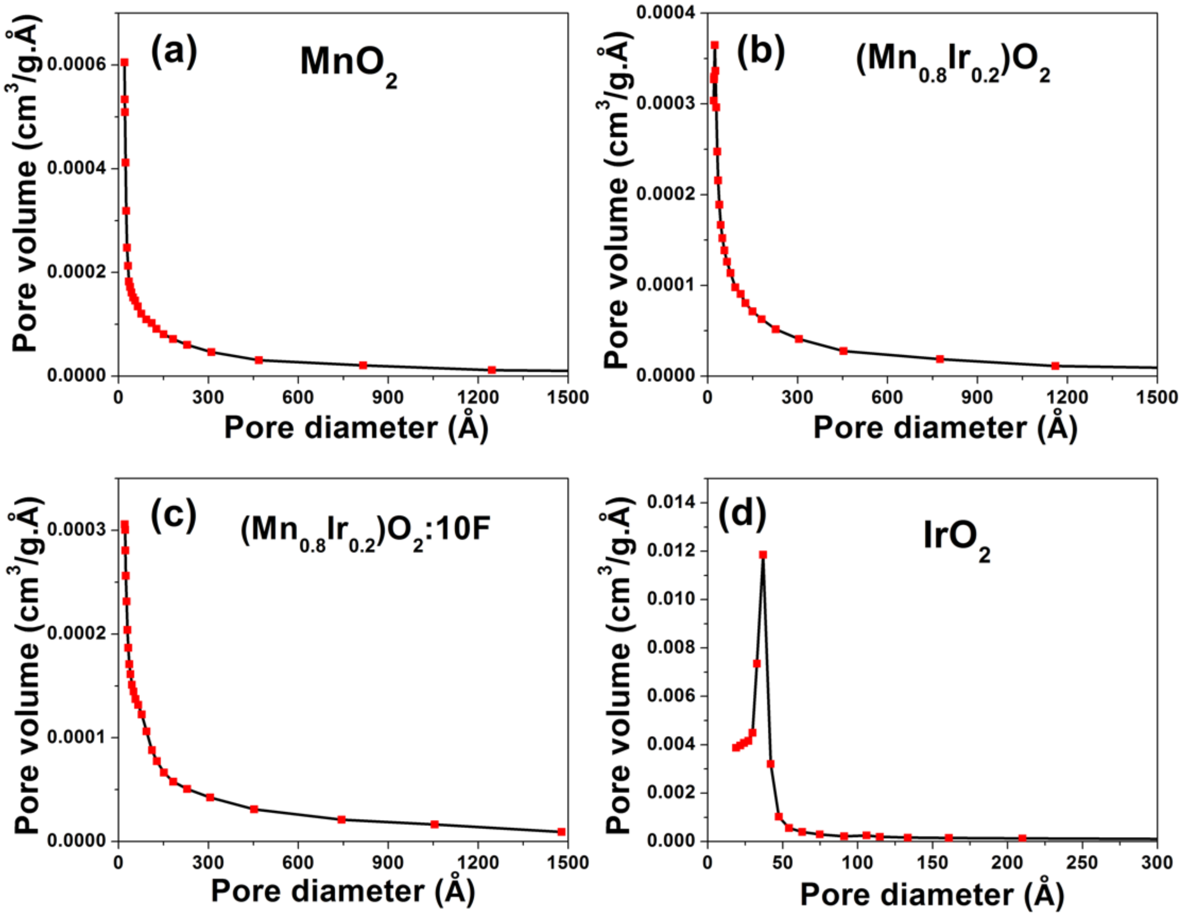

Appendix B Figure 3 Pore size distribution curves of as-synthesized (a) MnO$_2$ NRs, (b) (Mn$_{0.8}$Ir$_{0.2}$)O$_2$ NRs (c) (Mn$_{0.8}$Ir$_{0.2}$)O$_2$:10F NRs and (d) IrO$_2$ NPs. (Tabulated values are shown below)

Electrocatalyst composition	**BET Surface area (m^{2}g^{-1})**	**Pore volume (cm^{3}g^{-1})**	**Avg. Pore width (nm)**
MnO$_2$	~3.72	~0.069	~48.31
(Mn$_{0.8}$Ir$_{0.2}$)O$_2$	~3.70	~0.058	~48.27
(Mn$_{0.8}$Ir$_{0.2}$)O$_2$:10F	~3.55	~0.052	~48.11
IrO$_2$	~189	~0.29	4.6

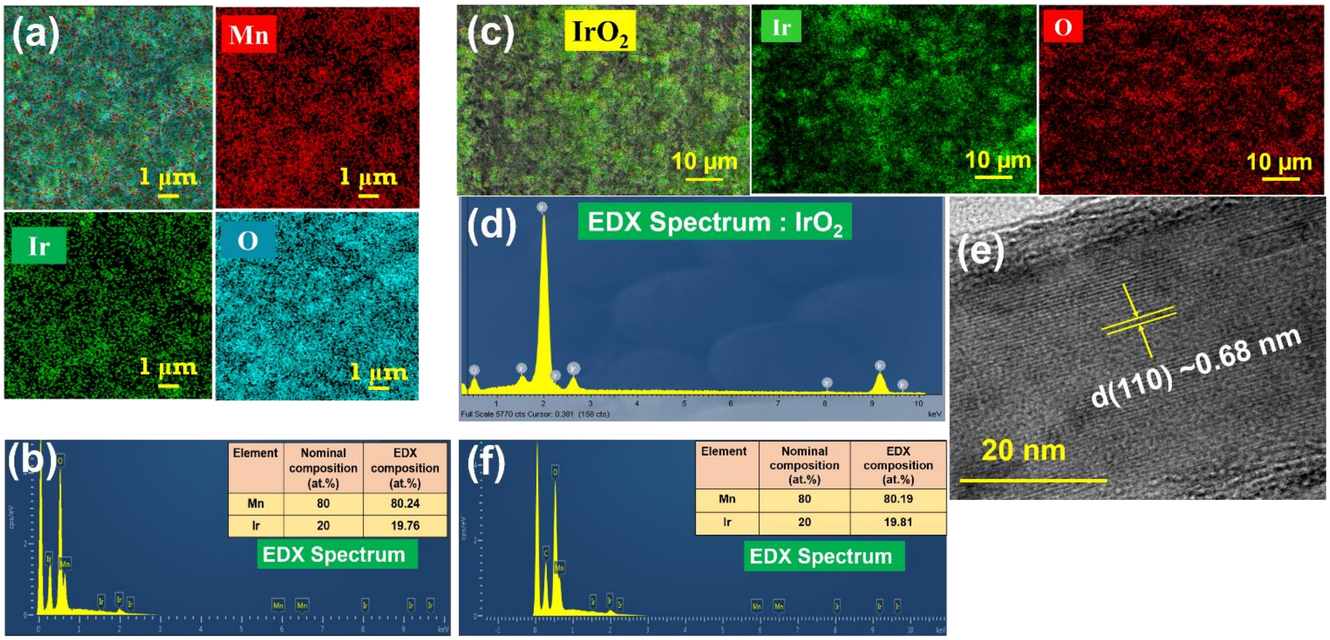

(b)

Element	Nominal composition (at.%)	EDX composition (at.%)
Mn	80	80.24
Ir	20	19.76

(f)

Element	Nominal composition (at.%)	EDX composition (at.%)
Mn	80	80.19
Ir	20	19.81

Appendix B Figure 4 (a) The elemental X-ray mapping of as-synthesized ($(Mn_{0.8}Ir_{0.2})O_2$:10F NRs, (b) energy dispersive X-ray spectroscopy (EDX) of $(Mn_{0.8}Ir_{0.2})O_2$:10F NRs (from SEM), (c) elemental X-ray mapping of IrO_2, (d) EDX of IrO_2, (e) HRTEM image of as-synthesized MnO_2 NR, highlighting lattice fringe of ~ 0.68 nm that corresponds to the (110) plane and (f) EDX of $(Mn_{0.8}Ir_{0.2})O_2$:10F NR (from TEM)

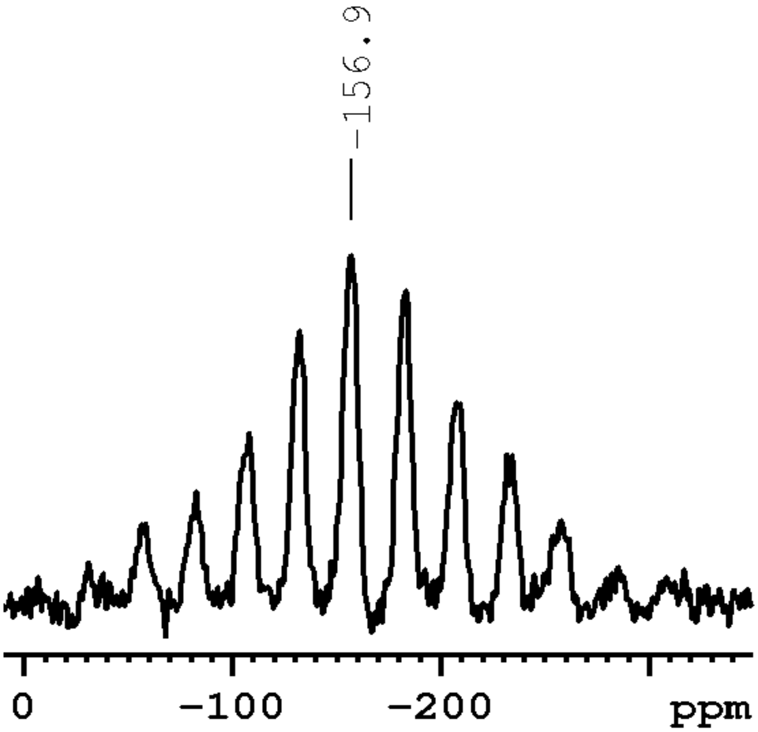

Appendix B Figure 5 19F NMR spectrum of the as-synthesized $(Mn_{0.8}Ir_{0.2})O_2$:10F, collected at 12 kHz MAS. The actual chemical shift is labelled at -156.9 ppm. The other peaks are the spinning side bands

The ^{19}F Magic Angle Spinning (MAS) NMR spectrum was collected on a Bruker Avance 500 Wide Bore NMR spectrometer, using a 3.2 mm CP-MAS probe. Due to the presence of strong ^{19}F background signals from the probe, a background suppression pulse sequence (zgbs) was used to collect the data. The ^{19}F data was collected at a couple of spinning speeds to identify the actual chemical shifts from the spinning side bands.

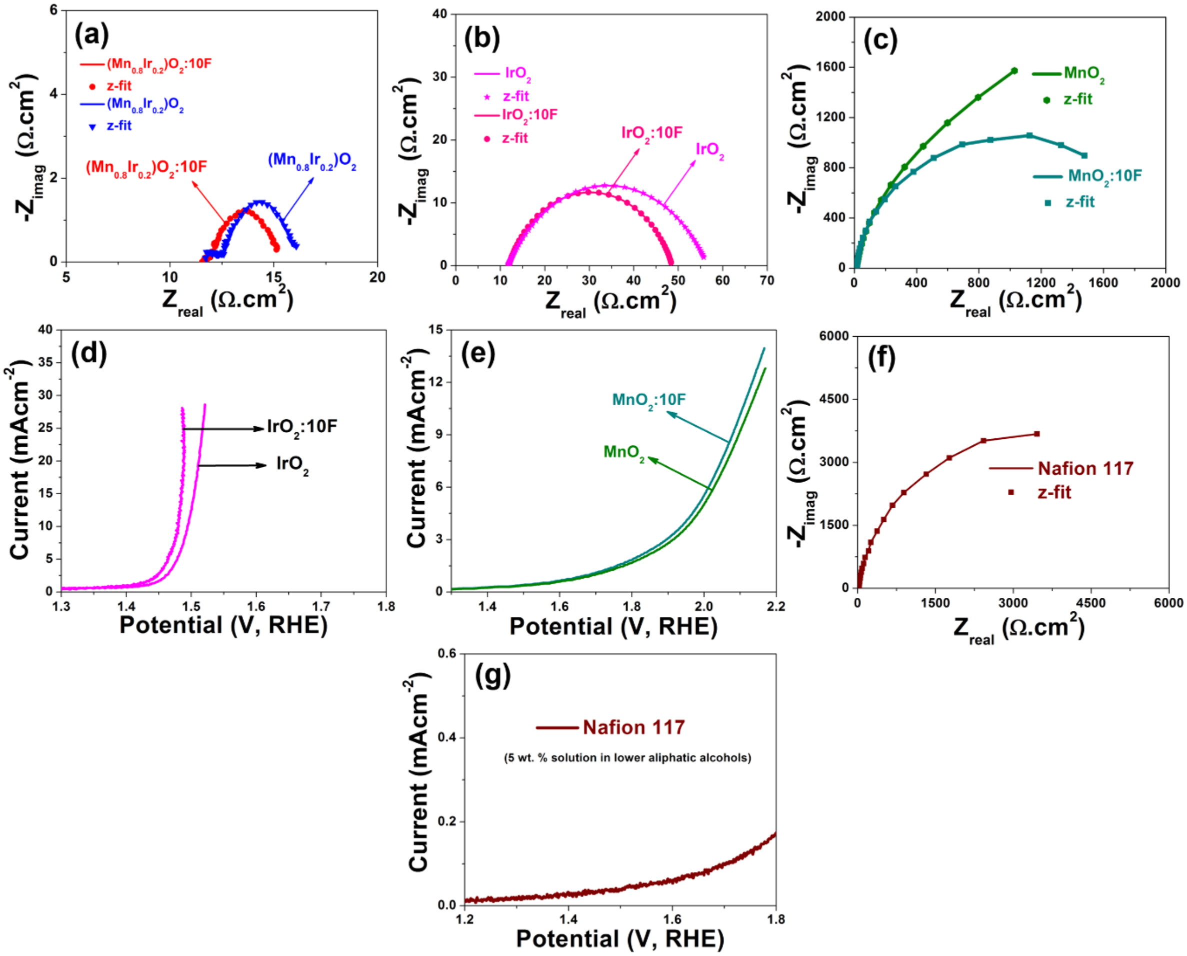

Appendix B Figure 6 (a) Magnified view of EIS curves for $(Mn_{0.8}Ir_{0.2})O_2$ and $(Mn_{0.8}Ir_{0.2})O_2$:10F NRs, performed at 1.45 V (*vs* RHE), EIS plots for as-synthesized (b) IrO_2 and IrO_2:10F and (c) as-synthesized MnO_2 and MnO_2:10F NRs, performed at 1.45 V (*vs* RHE), OER polarization ($mAcm^{-2}{}_{geo}$ *vs.* potential) curves for as-synthesized (d) IrO_2 and IrO_2:10F and (e) MnO_2 and MnO_2:10F NRs with a scan rate of 10 mV s^{-1}, (f) EIS plot for Nafion 117 coated electrode, performed at 1.45 V (*vs* RHE) and (g) OER polarization ($mAcm^{-2}{}_{geo}$ *vs.* potential) curves for Nafion 117 coated electrode with a scan rate of 10 mV s^{-1}

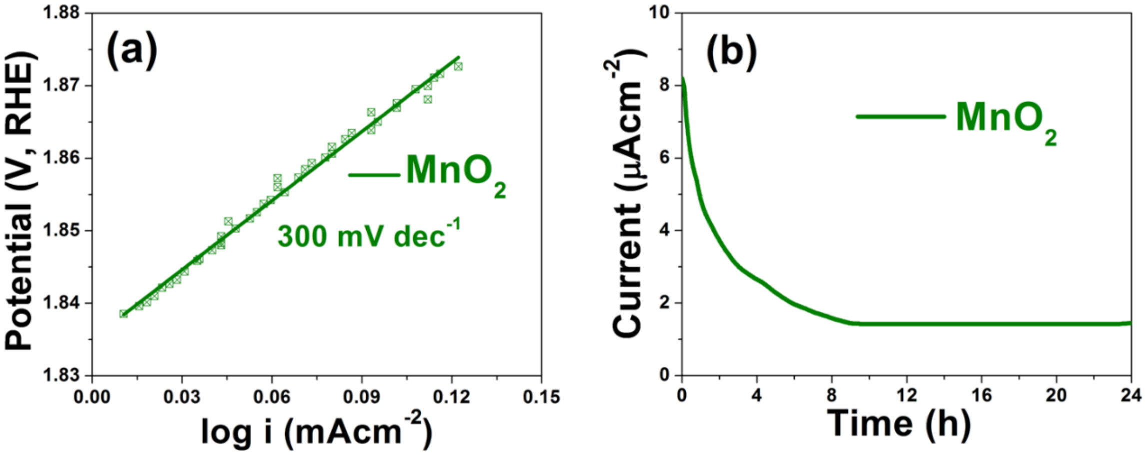

Appendix B Figure 7 (a) Tafel plot of as-synthesized MnO_2 NRs and (b) chronoamperometry (CA) test of as-synthesized MnO_2 conducted in 1N H_2SO_4 solution under a constant potential of 1.45 V (*vs* RHE) at 40ºC for 24 h

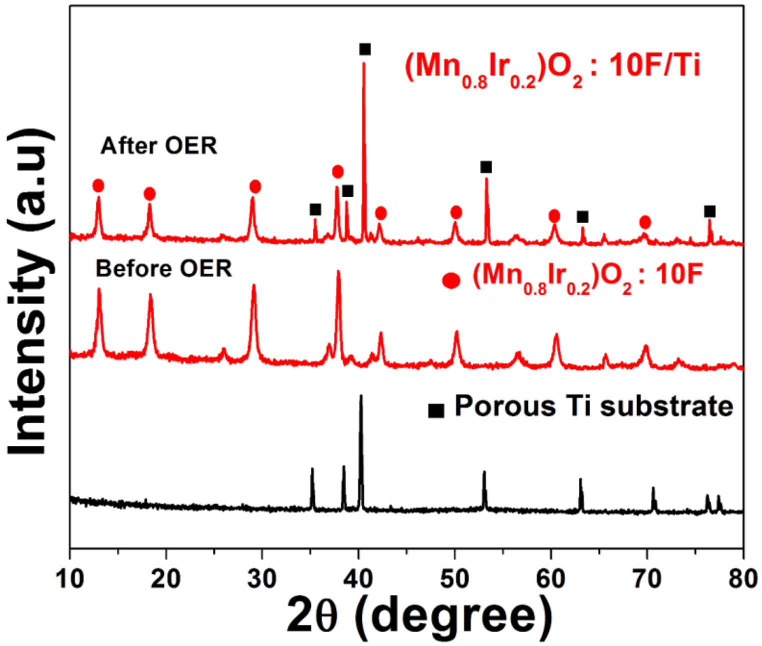

Appendix B Figure 8 XRD spectra of ($Mn_{0.8}Ir_{0.2}$)O_2:10F NRs before (powder) and after(coated on Ti) 24 h OER durability test in 1 N H_2SO_4 at 40ºC

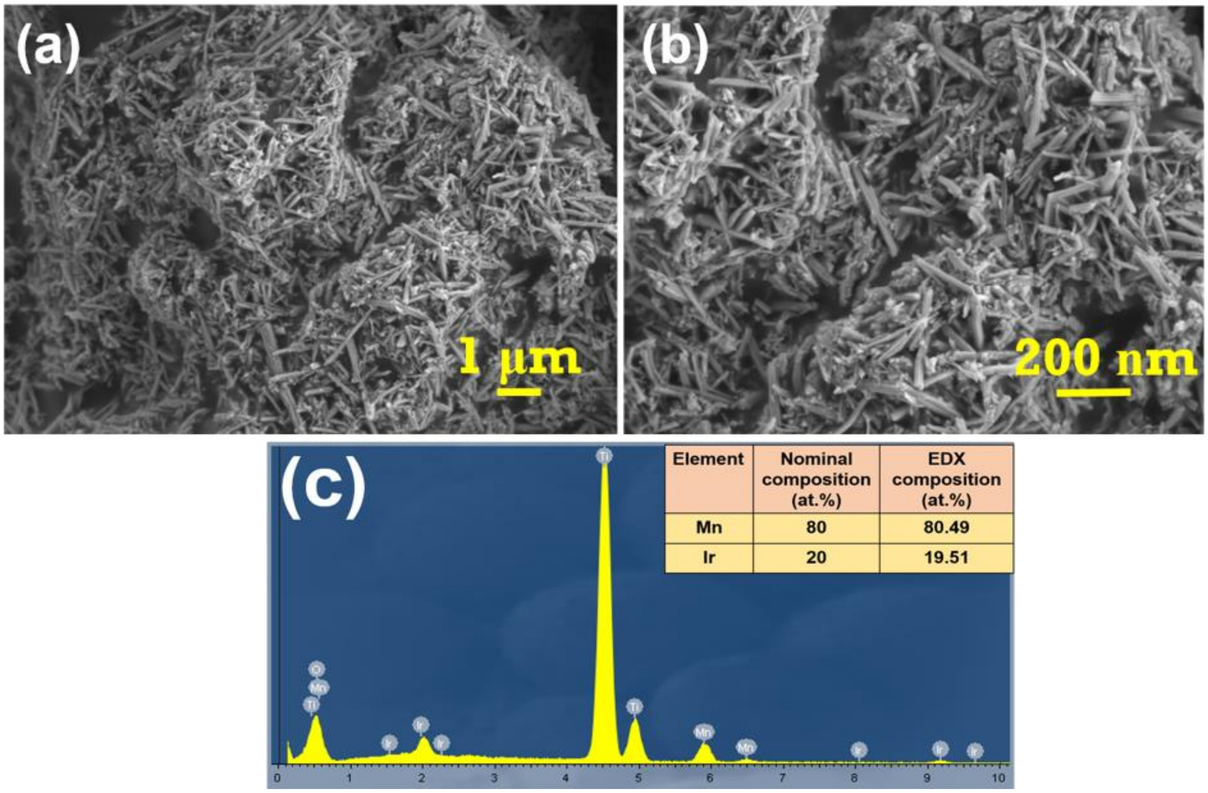

Element	Nominal composition (at.%)	EDX composition (at.%)
Mn	80	80.49
Ir	20	19.51

Appendix B Figure 9 (a-b) SEM images (at different magnifications) of $(Mn_{0.8}Ir_{0.2})O_2$:10F NRs /Ti after the 24 h OER durability test in 1 N H_2SO_4 at 40ºC and (c) energy dispersive X-ray spectroscopy (EDX) of $(Mn_{0.8}Ir_{0.2})O_2$:10F NRs /Ti after its 24 h OER durability test in 1 N H_2SO_4 at 40ºC

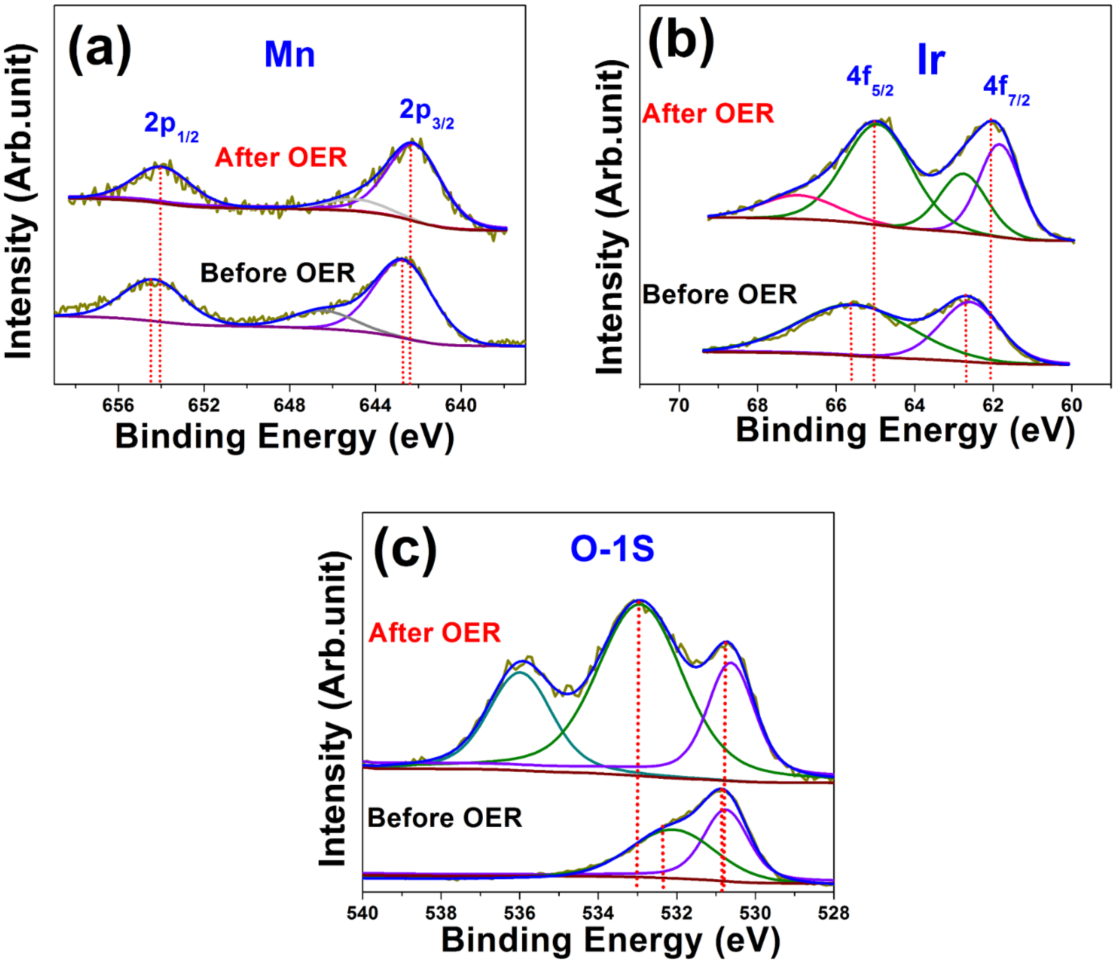

Appendix B Figure 10 XPS spectra of (a) Mn 2p, (b) Ir 4f and (c) O 1s of as-synthesized $(Mn_{0.8}Ir_{0.2})O_2$:10F NRs before and after 24 h OER durability test in 1 N H_2SO_4 at 40ºC

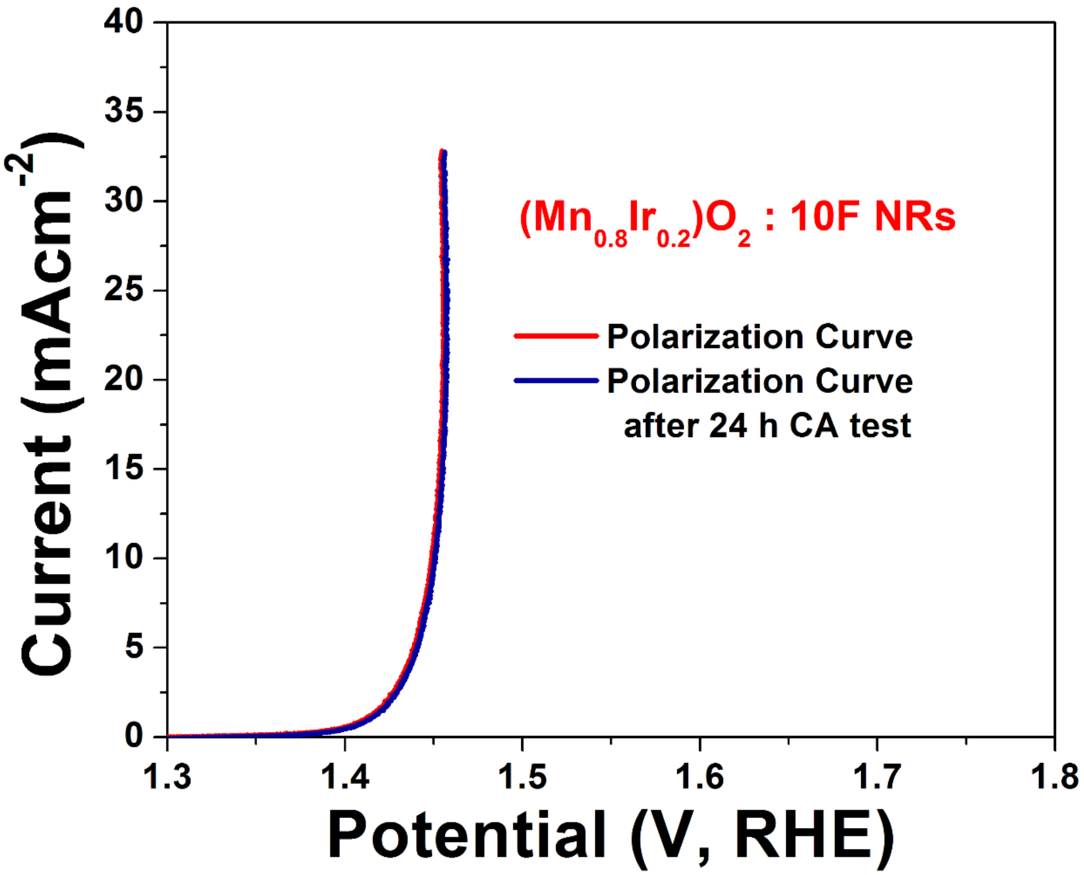

Appendix B Figure 11 The polarization curve of $(Mn_{0.8}Ir_{0.2})O_2$:10F NRs obtained after 24 h of chronoamperometry (CA) test in 1N H_2SO_4 solution at 40ºC

Appendix C Supplementary Information: A Computational and Experimental Study of F Doped $(Mn_{1-X}Nb_X)O_2$ Nanorod Electrocatalysts for Acid Mediated Oxygen Evolution Reaction

Computational Methodology

The density functional theory (DFT) implemented in the Vienna Ab-initio Simulation Package (VASP) with the projector-augmented wave (PAW) method was employed to calculate the electronic structure, total energies, and density of electronic states (DOS) of the electrocatalysts [103, 104, 214]. The spin-polarized generalized gradient approximation (GGA) was used for the exchange-correlation energy function in a form described by PBE (Perdew-Burke-Ernzerhof Perdew).[213, 214] The standard PAW potentials were used for each of the elemental components. Niobium, manganese, oxygen, and fluorine potentials thus contained eleven, seven, six and seven valence electrons, respectively. Additionally, in order to maintain the high precision for total energy calculations for the electrocatalyst compositions, the plane-wave energy cut-off is designated to a value of 520 eV. Moreover, the double relaxation procedure was employed to optimize the internal positions as well as the lattice parameters of atoms.[70] It should also be mentioned herein that the minima of the total energies with respect to the lattice parameters and internal ionic positions are correspondingly evaluated. By minimizing the Hellman–Feynman forces via a conjugate gradient method, the geometry optimization was achieved which will cause the net forces applied on every ion in the lattice to be close to zero. The total electronic energies were converged within 10^{-5} eV/un.cell, resulting into the residual force components on each atom to be lower than 0.01 eV/Å/atom, affording the precise evaluation of the internal structural parameters. The Monkhorst-Pack scheme is used to sample the Brillouin Zone (BZ) and create the k-point grid for the solids and the different isolated atoms considered in the present study. The choice of an appropriate number of k-points in the irreducible part of the BZ was selected to achieve a convergence of the total energy to 0.1 meV/atom. It is noteworthy to mention that for all the Mn-Nb-O-F compositions, the corresponding atomic distributions are uncertain and therefore, different spatial configurations could represent all the compositions considered. This uncertainty, nevertheless, has been omitted by collecting the various atomic configurations for each selected composition and the configuration with the lowest total energies is selected for further computational analysis of these specific binary oxide compositions.

Electrocatalyst Materials Characterization and Electrode Preparation Method

Physicochemical Characterizations

The crystalline structures of the as-synthesized nanorod (NR) materials was studied from the X-ray diffraction (XRD) analysis a Philips XPERT PRO system, with CuK_α ($\lambda = 0.15406$ nm) radiation, at an operating voltage and current of 45 kV and 40 mA, respectively. XRD peak profiles were analyzed using the pseudo-Voigt function to determine Lorentzian and Gaussian contribution of the peaks.[97] The molar volume and lattice parameters of the as-synthesized materials were evaluated by utilizing the least square refinement techniques. The nitrogen adsorption-desorption following the Brunauer-Emmett-Teller (BET) technique was employed to determine the BET specific surface area ($m^2\ g^{-1}$) of the as-synthesized powders. The electrocatalyst powder materials were first vacuum degassed before subjecting to analysis using a Micromeritics ASAP 2020 instrument. Multipoint BET technique was used to obtain the BET surface area values.

ZEISS Sigma 500 VP Scanning electron microscope (SEM) and JEOL JEM-2100F transmission electron microscope (TEM) was utilized to study the morphology of the electrocatalyst powders. In order to perform quantitative elemental compositional analysis and to study the elemental distribution, Energy dispersive x-ray spectroscopy (EDX) was performed using the Philips XL-30FEG system. The atomic ratio of the as-synthesized electrocatalyst materials was also investigated by the ICP-OES (iCAP 6500 duo Thermo Fisher) technique. In order to study the element binding and valence states of the electrocatalysts, X-ray photoelectron spectroscopy (XPS) was conducted using ESCALAB 250 Xi system (Thermo Scientific) equipped with a monochromated Al Kα X-ray source. The XPS system was used in an ultra-high vacuum chamber with the base pressure $< 5 \times 10^{-10}$ mBar. The fitting of the elemental spectra was based on calibrated analyzer transmission functions and Scofield sensitivity factors. The fitting parameters such as Gaussian-Lorentzian mix (tail mix, tail height and tail exponent) were fixed at 30%, 100%, 0% and 0%, respectively, during the fitting of the XPS spectra.[45] In order to determine the element composition of as-synthesized electrocatalysts, an inductively coupled plasma optical emission spectroscopy (ICP-OES, iCAP 6500 duo Thermo Fisher) method was employed. The as-prepared electrocatalyst samples were dispersed in a 4ml supra-pure nitric acid. During this process, the entire black electrocatalyst material gets dissolved in the acid. The analytes (electrocatalyst digested in supra-pure nitric acid) were diluted with the 3% nitric acid and then, subjected to ICP-OES analysis [489].

Electrochemical Characterizations

Electrochemical characterizations of the electrodes made from the as-synthesized NRs were carried out in a three-electrode electrochemical cell comprising the working (as-synthesized electrodes), counter (Pt wire, Alfa Aesar, 0.25 mm thick, 99.95%), and reference electrode (mercury/mercurous sulfate, Hg/Hg_2SO_4, XR-200, Hach) with a potential of +0.65 V with respect to reversible hydrogen electrode (RHE). The tests were conducted utilizing the VersaSTAT 3 (Princeton Applied Research) electrochemical workstation. A 1 N sulfuric acid (H_2SO_4) was used as the electrolyte solution which also served as the proton source for the oxygen evolution reaction (OER). The electrochemical characterizations of the as-synthesized NRs were carried out at a constant temperature of 40^{o}C using a Fisher Scientific 910 Isotemp refrigerator circulator. In order to prepare the anodes i.e., working electrodes (WE), the electrocatalyst inks of different compositions were formed by using 85 wt.% electrocatalyst powder and 15 wt.% Nafion 117 (5 wt.% solution in lower aliphatic alcohols, Aldrich). The produced electrocatalyst inks were then sonicated for ~1 h. The resulting electrocatalyst inks were uniformly coated (electrocatalyst loading ~ 0.3 mg cm^{-2}) on the titanium (Ti) foils (Alfa Aesar) followed by drying at room temperature. The potential values reported in this study were determined with respect to reversible hydrogen electrode (RHE) and calculated using the formula: $E_{RHE} = E_{Hg/Hg2SO4} + E^{o}_{Hg/Hg2SO4} + 0.059pH$, where E_{RHE} is the potential versus RHE and $E_{Hg/Hg2SO4}$ is the potential measured against the Hg/Hg_2SO_4 reference electrode. $E^{o}_{Hg/Hg2SO4}$ is the standard electrode potential of Hg/Hg_2SO_4 reference electrode (+0.65 V *vs* RHE).

Electrochemical Impedance Spectroscopy (EIS)

EIS analysis was executed to determine the charge transfer resistance (R_{ct}) and ohmic resistance for conducting the iR correction of the as-prepared electrodes. The EIS was performed using the electrochemical workstation (Versa STAT 3, Princeton Applied Research) in 1N H_2SO_4 electrolyte solution (maintained at 40^{o}C) at ~1.9 V *vs* RHE and using a frequency range of 100 mHz-100 kHz (amplitude = 10 mV). The ZView software from Scribner Associates using the equivalent circuit model given as $R_s(R_{ct}Q_{dl})$ in which R_s (solution/ohmic resistance)[137, 490] is in series with the parallel combination of the R_{ct} (surface charge transfer resistance) and Q_{dl} (contribution from double layer capacitance and pseudo capacitance). In the present study, the ohmic resistance values obtained from the EIS were used for the iR correction and to plot the iR corrected polarization curves.

Linear Sweep Voltammetry (LSV) and Stability Test

The OER catalytic activity of the as-synthesized electrocatalysts was investigated by performing the LSV measurements in 1 N H_2SO_4 electrolyte solution employing a scan rate of 10 mV sec^{-1} at 40°C. The polarization curves with different electrocatalyst compositions were iR_Ω corrected. The electrocatalytic activity of the as-prepared electrodes was measured and compared at a particular potential (~1.9 V *vs* RHE) which is relatively higher than the onset potentials. Tafel plots are reported using the equation (5-1). The intrinsic catalytic activity of the electrocatalyst was evaluated by normalizing the obtained current density values to the BET as well as the electrochemically active surface area (ECSA) values. In the current study, the current density values referred to geometric surface area (1 cm^2), BET surface area and ECSA are denoted as mA $cm^{-2}{}_{geo,}$ mA $cm^{-2}{}_{BET}$, and mA $cm^{-2}{}_{ECSA,}$ respectively. Further, the electrochemically active surface area (ECSA) values of the electrodes were determined by recording the cyclic voltammetry (CV) curves with various scan rates (5, 10, 15 and 20 mVs^{-1}) in the non-faradic potential range from 1 to 1.2 V (*vs* RHE). The slope of the plot of the differences in current density ($\Delta J_{1.1V} = j_{anode} - j_{cathode}$) at 1.1 V (*vs* RHE) *vs.* scan rate is used to evaluate the double layer capacitance (C_{dl}).[45, 250, 251] Utilizing the obtained C_{dl} ($mFcm^{-2}$) values, the ECSA (m^2 g^{-1}) was calculated. Furthermore, the intrinsic OER activity of the as-prepared materials was measured by calculating the specific activity, mass activity, turnover frequency (TOF), and normalization of current densities by ECSA and BET surface area (m^2 g^{-1}). The electrocatalytic stability of the as-prepared electrodes was then examined by conducting chronoamperometry (CA) test (current *vs* time), wherein the electrodes were operated for OER in the electrolyte solution of 1N H_2SO_4 at 40°C. Additionally, the activity of the electrocatalyst after the stability test was investigated by conducting post-stability LSV and EIS. In order to investigate any electrocatalyst dissolution during the prolong OER, inductively coupled plasma optical emission spectroscopy (ICP-OES, iCAP 6500 duo Thermo Fisher) analyses were conducted on the electrolytes collected after CA test. Furthermore, in order to gain deep insights into structural, phase, electronic environment and electrocatalytic activity changes occurring during the OER, post stability characterizations (XRD, SEM, XPS, LSV, EIS) were carried out on the post stability electrode.

Equations and Calculations

Specific surface area (SSA) calculation

SSA calculation based on the SEM images and the geometrical data[187] of the $(Mn_{0.8}Nb_{0.2})O_2$ nanorods:

$$SSA\ (m^2g^{-1}) = \frac{Area\ (m^2)}{Volume(m^3) \times Density(gm^{-3})}$$

$$Area\ (m^2) = 2\pi rh + 2\pi r^2$$

$$Volume\ (m^3) = \pi r^2 h$$

Where, h = average height of nanorods ~ 2.5×10^{-6} m

r = radius of nanorods ~ 20×10^{-9} m

Density (ρ) of $(Mn_{0.8}Nb_{0.2})O_2$:

$$\rho\ (gm^{-3}) = \frac{100}{\frac{wt.\%\,Mn}{\rho(MnO_2)}+\frac{wt.\%\,Nb}{\rho(NbO_2)}} = 4.89 \times10^6\ gm^{-3}$$

Where $\rho(MnO_2)$ is 5.03 g cm^{-3} and $\rho(NbO_2)$ is 4.6 g cm^{-3}

Thus, approximate SSA of $(Mn_{0.8}Nb_{0.2})O_2$ nanorods ~ 20.65 m^2g^{-1}

Mass activity (A g^{-1})

Mass activity, (A g^{-1})[471] = $\frac{j}{m}$

Where j = the current density (mA cm^{-2}) measured at particular potential (1.9 V *vs.* RHE) and

m = mass loading of the electrocatalyst

Thus, for $(Mn_{0.8}Nb_{0.2})O_2$:10F –NRs:

$$\text{Mass activity (A g}^{-1}\text{)} = \frac{8.7\ (\text{mA}\ cm^{-2})}{0.3\ (\text{mg}\ cm^{-2})} = 29\ \text{A g}^{-1}$$

BET Specific activity (mA cm^{-2}_{BET})

$$\text{BET specific activity (mA cm}^{-2}{}_{\text{BET}}\text{)}^{469} = \frac{j}{10 \times \text{m} \times S_{BET}}$$

Where j = the current density (mA cm^{-2}) measured at 1.9 V *vs.* RHE,

m = mass loading of the electrocatalyst and

S_{BET} = BET surface area (m^2 g^{-1})

Thus, for $(Mn_{0.8}Nb_{0.2})O_2$:10F –NRs:

$$\text{BET specific activity} = \frac{8.7\ (\text{mA}\ cm^{-2})}{10 \times 0.3\ (\text{mg}\ cm^{-2}) \times 5.66\ (m^2 g^{-1})} = 0.051\ \text{mA cm}^{-2}{}_{\text{BET}}$$

Turn over frequency (TOF, s^{-1})

$$\text{TOF, } (s^{-1})^{45} = \frac{J \times A}{4 \times \text{F} \times \text{n}}$$

Where, j = the current density (A cm^{-2}) measured at 1.9V *vs.* RHE

A = geometric area of the working electrode (cm^2)

F = Faraday constant (96,485 C mol^{-1}) and

n = number of moles of the electrocatalyst

For $(Mn_{0.8}Nb_{0.2})O_2$:10F the molecular weight has been calculated as:

= 0.9 (0.8× Atomic wt. of Mn + 0.2× Atomic wt. of Nb + 2× Atomic wt. of O) + 0.1× Atomic wt. of F

= 86.97 g mol^{-1}

Thus, for $(Mn_{0.8}Nb_{0.2})O_2$:10F –NRs:

$$\textbf{TOF} = \frac{8.7 \times 10^{-3}\ (\mathrm{A}\ cm^{-2}) \times 1(cm^{2})}{4 \times 96485(\mathrm{C}\ mol^{-1})\ \times 3.44 \times 10^{-6}\ (\mathrm{moles})} = 0.0065\ \mathrm{s}^{-1}$$

Electrochemically Active Surface Area (ECSA):

The electrochemically active surface area (ECSA) was obtained by dividing the double capacitance (C_{dl}) by the specific capacitance (C^*) of the electrocatalyst, similar to the previous reports of ECSA determination[249-251]. A general specific capacitance (C^*) value of metal electrodes in acidic solutions is taken as 35 μF cm^{-2}.[91, 249, 252] Based on this specific capacitance (C^*) value, ECSA of the as-synthesized electrocatalyst has been calculated.

The electrochemically active surface area (ECSA in $m^2\ g^{-1}$) of the as-prepared electrodes has been calculated using the following equation:

$$ECSA\ (m^2 g^{-1}) = \frac{C_{dl}}{C^* \times L}$$

Where, C_{dl} = double-layer capacitance ($mFcm^{-2}$)

Herein, C_{dl} = ½ × linear slope of the current density ($j_{anode} - j_{cathode}$) *vs.* scan rate [162, 169]

C^* = specific capacitance in acidic electrolyte (0.035 mF cm^{-2})[91, 249, 252]

L = Mass loading of the electrocatalyst (g m^{-2})

Sample ECSA calculation for $(Mn_{0.8}Nb_{0.2})O_2$:10F NRs:

$$ECSA\ (m^2 g^{-1}) = \frac{C_{dl}}{C^* \times L}$$

- Linear slope of the current density ($j_{anode} - j_{cathode}$) *vs* scan rate for $(Mn_{0.8}Nb_{0.2})O_2$:10F NRs = 5.52

  Accordingly, C_{dl} = ½ × 5.52 = 2.76 mF cm^{-2}
- C^* = 0.035 mF cm^{-2}
- L = 0.3 mg cm^{-2} = 3 g m^{-2}

Thus, for $(Mn_{0.8}Nb_{0.2})O_2$:10F - NRs:

$$\boldsymbol{ECSA}\ (\boldsymbol{m^2 g^{-1}}) = \frac{2.76(\mathrm{mF}\ cm^{-2})}{0.035\ (\mathrm{mF}\ cm^{-2}) \times 3(\mathrm{g}\ m^{-2})} = 26.28\ m^2 g^{-1}$$

Similar calculations have been carried out to evaluate the ECSA for the other as-synthesized electrocatalysts.

Surface Roughness Factor (RF):

$$\mathrm{RF}^{470} = \frac{ECSA \times L}{GSA}$$

Where, GSA = geometric area of the electrode (0.5 × 2= 1 cm^2) and

L = mass loading of electrocatalyst = 0.3 mg cm^{-2}

Thus, for $(Mn_{0.8}Nb_{0.2})O_2$:10F –NRs:

$$RF = \frac{26.28\ (m^2 g^{-1}) \times 0.0003(g)}{0.0001\ (m^2)} = 78.86$$

Normalized current densities:

- *ECSA normalized current density (mA cm^{-2}_{ECSA})*

$$= \frac{\text{Curent density obtained from the linear scan polarization (mA cm}^{-2}\text{) at 1.9V}}{\text{Electrocatalyst mass loading (g m}^{-2}\text{)} \times \text{ECSA(m}^2\text{g}^{-1}\text{)}}$$

- *BET normalized current density (mA $cm^{-2}{}_{BET}$)*

$$= \frac{\text{Curent density obtained from the linear scan polarization (mA cm}^{-2}\text{) at 1.9V}}{\text{Electrocatalyst mass loading (g m}^{-2}\text{)} \times \text{BET surface area (m}^2\text{g}^{-1}\text{)}}$$

Appendix C Table 1 The Lattice Parameters, Unit Cell, Molar Volume, and BET Surface Area of the as-synthesized Electrocatalysts

Electrocatalyst composition	Lattice parameter (Å)		Volume		BET Surface area ($m^2\ g^{-1}$)
	a = b	c	Unit cell ($Å^3$)	Molar ($cm^3\ mol^{-1}$)	
MnO_2	~9.79	~2.85	273.15	20.56	3.70
$(Mn_{0.9}Nb_{0.1})O_2$	~9.82	~2.87	276.76	20.83	4.32
$(Mn_{0.9}Nb_{0.1})O_2$:10F	~9.82	~2.87	276.76	20.83	4.1
$(Mn_{0.8}Nb_{0.2})O_2$	~9.86	~2.91	282.90	21.29	6.0
$(Mn_{0.8}Nb_{0.2})O_2$:10F	~9.86	~2.91	282.90	21.29	5.66
$(Mn_{0.7}Nb_{0.3})O_2$	~9.89	~2.93	286.58	21.57	9.47

Appendix C Table 2 The Binding Energies (eV), Full Width at Half-Maximum (FWHM), and Spin-Energy Separation (ΔS) Parameters for Mn, Nb, and O of the as-synthesized Electrocatalysts

Material	Mn $2p_{3/2}$ (eV)	FWHM Mn $2p_{3/2}$	Mn $2p_{1/2}$ (eV)	FWHM Mn $2p_{1/2}$	Mn ΔS (eV)	Nb $3d_{5/2}$ (eV)	FWHM Nb $3d_{5/2}$	Nb $3d_{3/2}$ (eV)	FWHM Nb $3d_{3/2}$	Nb ΔS (eV)	O1s (eV)	FWHM (O1s)
MnO_2	642	3.20	653.8	3.44	11.8	--	--	--	--	--	529.8	2.12
$(Mn_{0.8}Nb_{0.2})O_2$	642	3.20	653.8	3.44	11.8	207.0	1.47	210	1.40	3	529.8	2.12
$(Mn_{0.8}Nb_{0.2})O_2$:10F	643.1	3.29	654.9	3.5	11.8	207.98	1.61	210.81	1.60	2.83	530.3	2.13

Appendix C Table 3 Results of the Mass Activity, Specific Activity, and Normalized Current Densities Calculated at the Voltage of 1.9 V

Electrocatalyst Composition	Ohmic resistance (Ω cm^2)	Mass activity at 1.9 V (A g^{-1})	BET normalized current density at 1.9 V (mA cm^{-2}_{BET})	ECSA normalized current density at 1.9 V (μA cm^{-2}_{ECSA})	BET based specific activity at 1.9 V (μA cm^{-2}_{ECSA})	ECSA based specific activity at 1.9 V (μA cm^{-2}_{ECSA})
MnO_2	14.06	7.33	0.19	79.3	0.019	7.93
$(Mn_{0.9}Nb_{0.1})O_2$	13.92	10.66	0.24	84.8	0.024	8.48
$(Mn_{0.9}Nb_{0.1})O_2$:10F	13.40	13.33	0.32	86.2	0.032	8.62
$(Mn_{0.8}Nb_{0.2})O_2$	13.27	19.83	0.33	95.5	0.033	9.55
$(Mn_{0.8}Nb_{0.2})O_2$:10F	12.25	29	0.51	110.3	0.051	11.03
$(Mn_{0.7}Nb_{0.3})O_2$	14.19	6	0.06	79.7	0.006	7.97

Appendix C Table 4 Results of the Electrochemically Active Surface Area (ECSA) and Surface Roughness Factor (RF) Calculated for the as-prepared Electrocatalysts (For: C* =0.035 mF cm^{-2})

Electrocatalyst Composition	Linear slope of current density ($j_{anode} - j_{cathode}$) *vs.* scan rate (mF cm^{-2})	Double layer capacitance (C_{dl}) (mF cm^{-2})	ECSA (m^2 g^{-1})	Roughness Factor (RF)
MnO_2	1.94	0.97	9.23	27.71
$(Mn_{0.9}Nb_{0.1})O_2$	2.64	1.32	12.57	37.71
$(Mn_{0.9}Nb_{0.1})O_2$:10F	3.248	1.62	15.46	46.4
$(Mn_{0.8}Nb_{0.2})O_2$	4.36	2.18	20.76	62.29
$(Mn_{0.8}Nb_{0.2})O_2$:10F	5.52	2.76	26.28	78.86
$(Mn_{0.7}Nb_{0.3})O_2$	1.58	0.79	7.52	22.57

Appendix C Table 5 ICP-OES Analysis Results on 1N H_2SO_4 Electrolyte Solution Collected after the 24h Chronoamperometry Test (Average of Three Independently Prepared Electrocatalyst Samples)

Electrocatalyst Composition	Mn (ppm)	Nb (ppm)
$(Mn_{0.8}Nb_{0.2})O_2$	0.081 ± 0.0004	0.016 ± 0.0002
$(Mn_{0.8}Nb_{0.2})O_2$:10F	0.078 ± 0.0003	0.015 ± 0.0002

<u>Note:</u> Herein, based on the dissolution results and total electrocatalyst loading (0.3 mg cm^{-2}), the duration for complete dissolution of $(Mn_{0.8}Nb_{0.2})O_2$ and $(Mn_{0.8}Nb_{0.2})O_2$:10F can be projected as ~ 30-33 days. It should be noted that although some electrocatalytic dissolution is observed during the stability test, similar behaviors regarding the electrocatalytic dissolution and activity degradation are observed for various noble or precious group metal (PGM) free electrocatalysts (for example Ti-Mn-O[266], Sb-Mn-O[280], Ag doped Co_3O_4[307], Fe-TiO_x[491], TiB_2 [492]etc.) for acidic OER. In addition, regarding reduced noble metal containing electrocatalyst materials (for example Ir-Ni-O[33], Ir-Co-O[493], Ir-Mn-O[45], Ir-Ni-Co-O[494] etc.), similar trends for non-noble elemental dissolution and activity degradations are detected during the stability tests. It should be underlined that in the literature different electrocatalyst systems employ different mass loadings, concentration of electrolytes, and durations for stability tests which makes it difficult to compare the results generated from different studies in a proper, accurate and meaningful manner.[266] However, based on the ICP results and activity of the electrocatalyst system after the OER stability tests (post stability tests), the system indeed demonstrates comparable or better electrochemical durability than the above mentioned systems.

In addition, as elucidated in the results and discussion section, based on the experimental approaches and DFT-based calculations, various strategies for the mitigation of catalyst dissolution can be utilized which include introduction of 10-20 atomic % iridium as has been evidently demonstrated by our previous works on Ir containing electrocatalyst systems.[45, 69, 70]

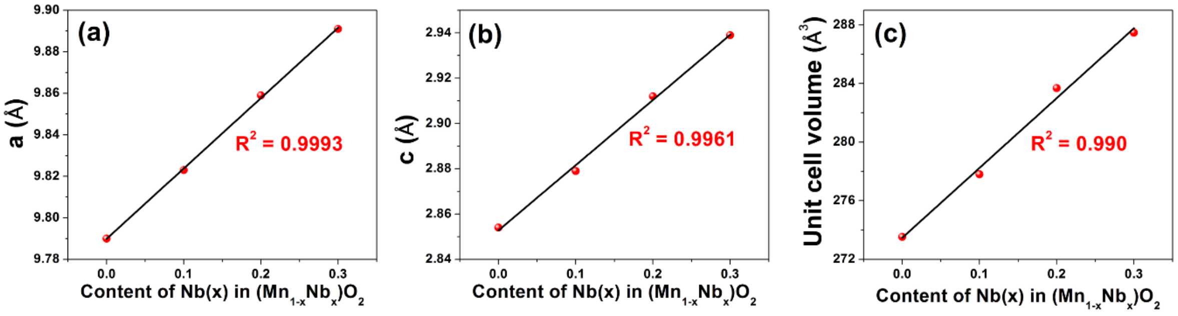

Appendix C Figure 1 Relationships of the (a, b) lattice parameters and (c) unit cell volume with Nb content for $(Mn_{1-x}Nb_x)O_2$ NRs

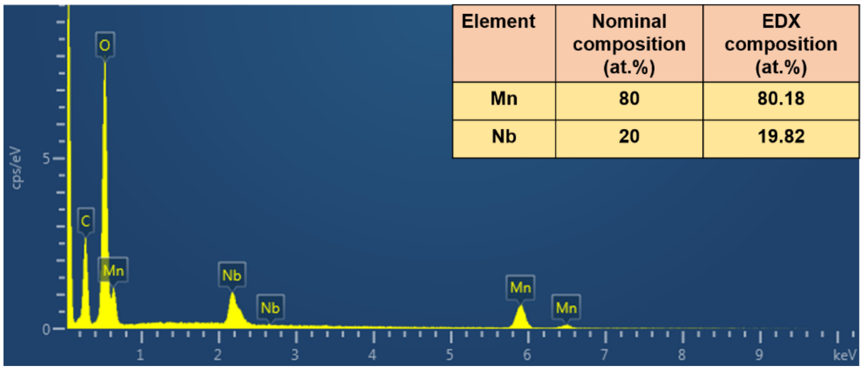

Element	Nominal composition (at.%)	EDX composition (at.%)
Mn	80	80.18
Nb	20	19.82

Appendix C Figure 2 The energy dispersive X-ray spectroscopy (EDX) of the as-synthesized $(Mn_{0.8}Nb_{0.2})O_2$:10F NRs

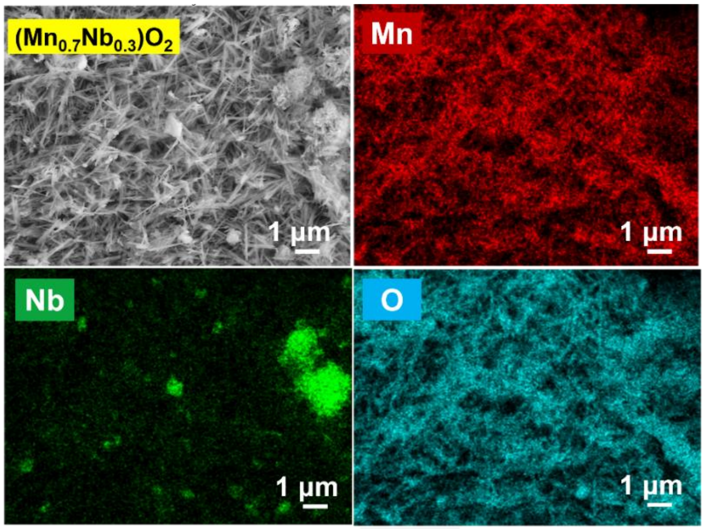

Appendix C Figure 3 The elemental X-ray mapping of the as-synthesized $(Mn_{0.7}Nb_{0.3})O_2$ electrocatalyst

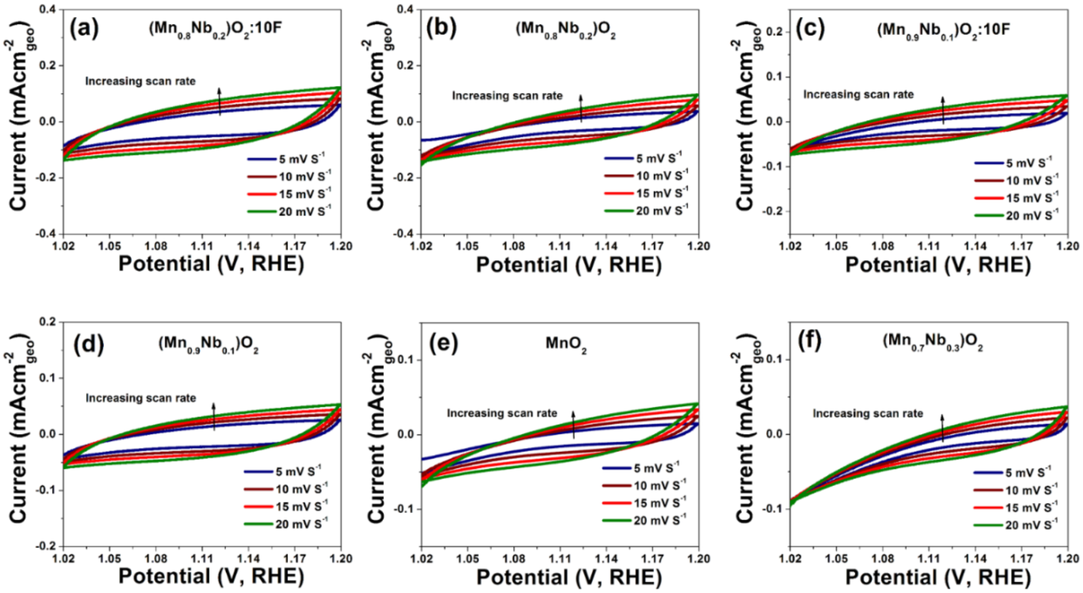

Appendix C Figure 4 Cyclic voltammograms with different scan rates collected in 1N H_2SO_4 solution for the as-synthesized electrocatalysts

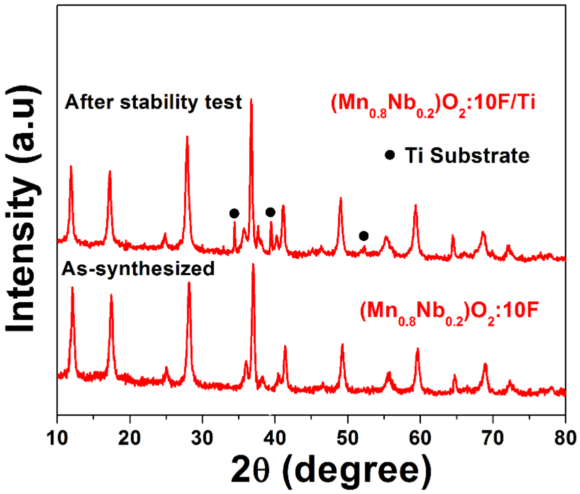

Appendix C Figure 5 XRD spectra of the as-synthesized $(Mn_{0.8}Nb_{0.2})O_2$:10F NRs (powder) and after (coated on Ti) the 24h stability test conducted for in 1 N H_2SO_4 at 40°C

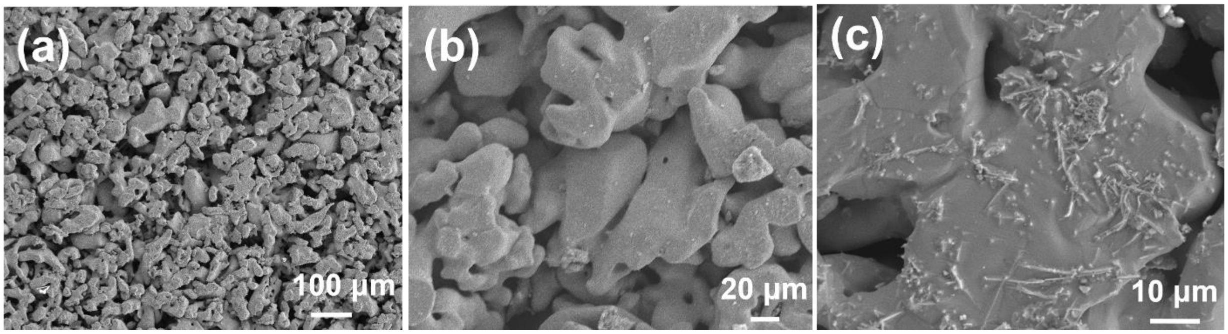

Appendix C Figure 6 SEM images (at different magnifications) of MnO_2 NRs /Ti substrate after the 24 h OER durability test in 1 N H_2SO_4

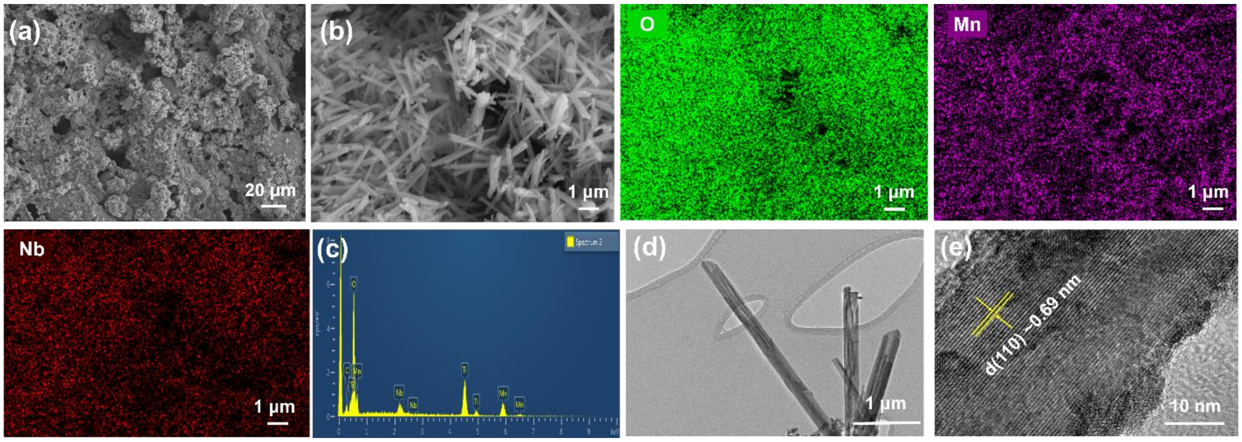

Appendix C Figure 7 (a, b) SEM images and corresponding elemental X-ray mapping, (c) energy dispersive X-ray spectroscopy (EDX), (d) TEM, and (e) HRTEM of $(Mn_{0.8}Nb_{0.2})O_2$:10F NRs NRs /Ti substrate after the 24 h OER durability test in 1 N H_2SO_4

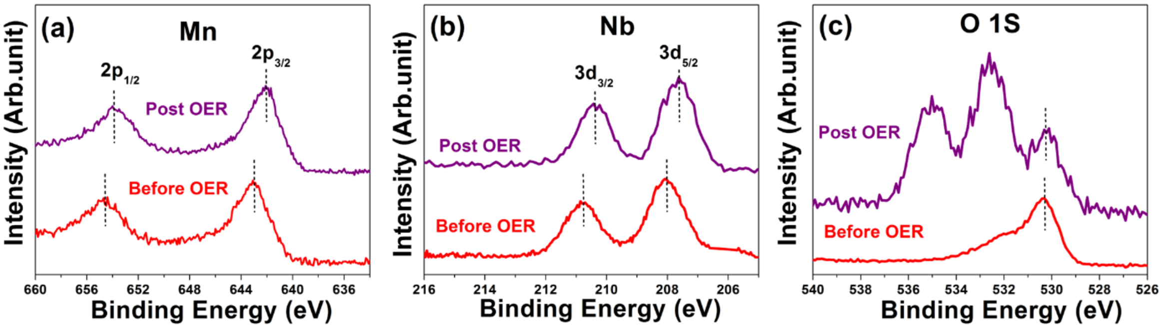

Appendix C Figure 8 XPS spectra of (a) Mn 2P, (b) Nb 3d, and (c) O 1s of $(Mn_{0.8}Nb_{0.2})O_2$:10F electrocatalyst before and after the 24h stability test

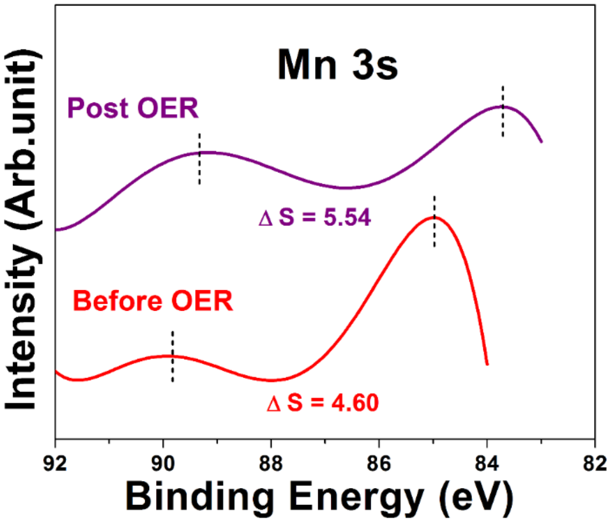

Appendix C Figure 9 XPS spectra of Mn 3s of $(Mn_{0.8}Nb_{0.2})O_2$:10F electrocatalyst before and after the 24h stability test (ΔS = Spin-Energy Separation)

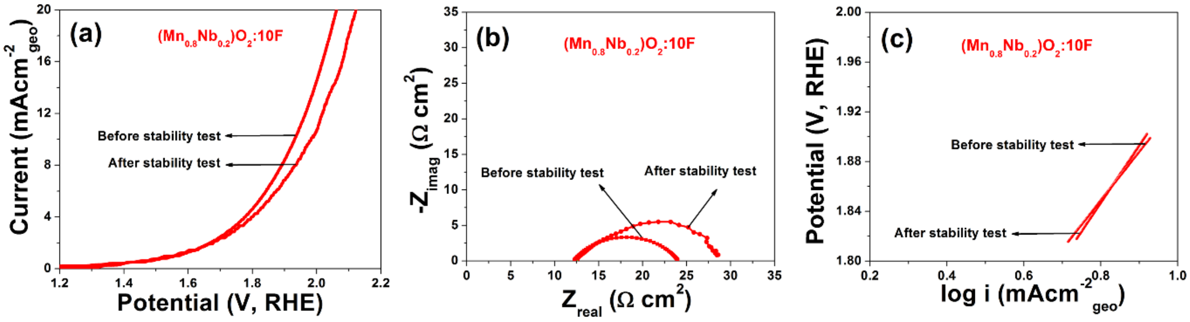

Appendix C Figure 10 (a) The polarization curve and (b) impedance, and (c) Tafel plot of $(Mn_{0.8}Nb_{0.2})O_2$:10F NRs before and after stability test

Appendix C Table 6 Overpotential, charge transfer resistance and Tafel slope values of the $(Mn_{0.8}Nb_{0.2})O_2$:10F electrode following OER stability tests (post-stability)

$(Mn_{0.8}Nb_{0.2})O_2$:10F NRs	**η (mV) at 10 mA cm^{-2}_{geo}**	**R_{ct} (Ω cm^2)**	**Tafel slope (mV dec^{-1})**
Before stability test	680	11.8	371.17
After stability test	755	15.52	452.82

<u>Note:</u> The $(Mn_{0.8}Nb_{0.2})O_2$:10F NRs following OER stability test (post stability) demonstrated increase in the overpotential, charge transfer resistance, and Tafel slope by ~ 75 mV, 3.72 Ω cm^2, and 81.65 mV dec^{-1}, respectively. However, based on ICP results and the 24h stability tests, the present electrocatalyst system indeed demonstrates promising performance for prolonged OER studies. Also, as the present electrocatalyst system comprises earth abundant elements, the electrocatalytic stability can be further improved by employing various strategies as outlined by Strasser and co-workers [298] which includes introduction of 10-20 atomic % iridium, increasing and optimizing the mass loading, utilizing alternative acid stable support/backing electrodes such as precious metal based gold and diamond as well as precious metal free supports such as $SnTa_2O_6$ and $Sn_2Ta_2O_7$[300], including altering the synthesis parameters such as temperature, atmosphere, precursors, as well as identifying other novel PGM-free dopants that are more stable under acidic conditions etc.

Appendix D Supplementary Information: Influence of Defects on Activity-Stability of $Cu_{1.5}Mn_{1.5}O_4$ for Acid-Mediated Oxygen Evolution Reaction

Electrocatalyst Materials Characterization

Physicochemical Characterizations

Qualitative phase information of the electrocatalyst powder synthesized using different Cu:Mn ratios and various heat treatment temperatures was investigated by using X-ray diffraction (XRD) analysis. XRD analysis was executed by using Philips XPERT PRO system, with CuK_α (λ = 0.15406 nm) radiation at an operating voltage and current of 45 kV and 40 mA, respectively. In addition, least square refinement techniques were applied to assess the molar volume and lattice parameters of the synthesized electrocatalysts. The microstrain values are estimated using an in-built pseudo-Voigt function in the X'Pert highscore, which fits both the Gaussian and Lorentzian components and utilizes a Williamson-Hall (W-H) analysis to compute the microstrain.[97, 495-497]. W-H analysis is a simplified integral breadth method wherein both size-induced and strain-induced broadening are de-convoluted by considering the peak width as a function of 2θ. [495, 498, 499] In the current study, W-H method is employed for estimation of crystallite size and lattice strain, according to which, the physical line broadening of the X-ray diffraction peak occurs due to the size and microstrain of the nanocrystals and the total broadening (β_{total}) can be written as[495],

$$\beta_{total} = \beta_{size} + \beta_{strain}$$

Herein, for size broadening (i.e., Debye-Scherrer's equation):

$$\beta(2\theta) = K\,\lambda / (L\cos\theta), \text{ and}$$

for microstrain broadening:

$$\beta(2\theta) = 4\varepsilon\tan\theta$$

where, λ= wavelength of CuK_{α} radiation, K= shape factor (0.9), L= crystalline size, and ε = microstrain.

Accordingly, $\beta_{total} = [K\,\lambda / (L\cos\theta)] + [4\varepsilon\tan\theta]$.

By rearranging the above equation, we get-

$\beta_{total}\cos\theta = K\,\lambda / L + 4\varepsilon\tan\theta$, wherein slope = ε and y-intercept = $K\,\lambda / L$.

The above equations are W-H equations which are utilized in the in X'Pert highscore to evaluate the required parameters.[495] In the present study, the microstrain has been reported for three hkl values i.e. 111, 131, and 151.

The specific surface area (SSA) of the as-synthesized electrocatalyst powders obtained by heat treatment at different temperatures was evaluated from the nitrogen adsorption-desorption analysis utilizing the Brunauer-Emmett-Teller (BET) technique. The as-prepared powder materials were first vacuum degassed and then analyzed using a Micromeritics ASAP 2020 instrument employing the Multipoint BET technique. Scanning electron microscopy (SEM) was used to investigate the morphology and microstructure of the synthesized electrocatalyst powders. Quantitative elemental analysis and distribution of elements within the as-synthesized powders was studied by employing elemental X-ray mapping technique using Energy dispersive X-ray spectroscopy (EDX). A Philips XL-30FEG system (operated at a voltage of 20 kV) was utilized to study the elemental and X-ray mapping analysis. The chemical environments of the elemental binding energies, valence states, and the surface compositions of the synthesized electrocatalysts were evaluated by performing X-ray photoelectron spectroscopy (XPS). The XPS analysis was conducted using the ESCALAB 250 Xi system (Thermo Scientific) equipped with a monochromated Al Kα X-ray source. The micro focused X-ray source was utilized for the analysis spot of $400\times400\ \mu m^2$. The ultra-high vacuum (UHV) chamber with the base pressure less than 5

$\times 10^{-10}$ mBar was used to conduct the XPS analysis. The binding energy (BE) scale of the analyzer was calibrated to produce < 50 meV deviations of the three standard peaks from their standard values (83.98 eV for Au $4f_{7/2}$, 368.26 eV for Ag $3d_{5/2}$, and 932.67 eV for Cu $2p_{3/2}$).[500] The aliphatic C1s peak was observed at 284.6 eV. The elemental XPS data in Cu2p, Mn2p, and O1s regions were obtained with the analyzer pass energy set to 20 eV with an energy resolution of 0.36 eV and the step size set to 0.1 eV [187]. The oxidation state ratios (Cu^{1+} /Cu^{2+} and Mn^{3+} /Mn^{4+}) were obtained from the ratios of integrated areas of respective intensities and tabulated in **Appendix D Table 2**.

Appendix D Table 1 EDX and XPS elemental compositions for CMO samples

Electrocatalyst Material	**EDX Composition Cu: Mn**	**XPS Composition Cu: Mn**
CMO-200	44.20: 55.80	44.27: 55.73
CMO-400	44.63: 55.37	44.50: 55.50
CMO-600	44.48: 55.52	44.33: 55.67
CMO-800	44.17: 55.83	44.26: 55.74

Appendix D Table 2 Binding energy values for CMO samples

Electrocatalyst Material	Cu Binding Energy (eV)		Mn Binding Energy (eV)		Integral peak area ratios	
	Cu^{1+}	Cu^{2+}	Mn^{3+}	Mn^{4+}	Cu^{1+} /Cu^{2+}	Mn^{3+} /Mn^{4+}
CMO-200	930.80	933.42	641.90	644.82	0.53	4.10
CMO-400	930.30	933.13	641.59	644.60	1.38	3.70
CMO-600	930.02	932.71	641.16	644.54	2.75	2.51
CMO-800	929.85	932.40	640.80	643.33	3.63	1.35

Electrochemical Characterizations

The OER electrochemical characterizations of the as-prepared electrocatalyst electrodes were performed in a three-electrode configuration using a VersaSTAT 3 (Princeton Applied Research) electrochemical workstation. 1 N sulfuric acid (H_2SO_4) was used as the electrolyte solution for the OER analysis. The electrolyte solution was maintained at a constant temperature of 40^oC using a Fisher Scientific 910 Isotemp refrigerator circulator during the entire electrochemical characterizations. The electrocatalyst inks of the electrocatalyst powder sample formed at different temperatures were generated using 85 wt.% electrocatalyst powder and 15 wt.% Nafion 117 (5 wt.% solution in lower aliphatic alcohols, Aldrich). The produced electrocatalyst inks were then sonicated for ~1 h. The sonicated catalyst inks were subsequently homogenized using Tissuemiser (Fisher Scientific) for ~ 3 min and then uniformly coated on the titanium (Ti) foils (Alfa Aesar) followed by drying under ambient conditions. A Pt wire (Alfa Aesar, 0.25 mm thick, 99.95%) and mercury/mercurous sulfate (Hg/Hg_2SO_4) electrode (XR-200, Hach) having a potential of +0.65 V with respect to reversible hydrogen electrode (RHE) were used as the counter electrode (CE) and reference electrode (RE), respectively. A total electrocatalyst loading of ~ 1 mg cm^{-2} was used in the present study. The potential values reported in this study have been determined and reported with respect to reversible hydrogen electrode (RHE) and calculated from the formula as below:

$$E_{RHE} = E_{Hg/Hg2SO4} + E^{o}_{Hg/Hg2SO4} + 0.059 \times pH$$

wherein E_{RHE} is the potential versus RHE and $E_{Hg/Hg2SO4}$ is the potential measured against the Hg/Hg_2SO_4 reference electrode. $E^{0}_{Hg/Hg2SO4}$ is the standard electrode potential of Hg/Hg_2SO_4 reference electrode (+0.65 V *vs* RHE).

Electrochemical impedance spectroscopy (EIS) was performed to investigate the ohmic resistance (R_{Ω}) and the charge transfer resistance (R_{ct}) of the as-prepared electrodes. The EIS was performed using the electrochemical workstation (Versa STAT 3, Princeton Applied Research) in 1 N H_2SO_4 electrolyte solution maintained at 40^{o}C and at ~1.55 V (which is the typical potential used for assessing the electrochemical activity of the electrocatalysts for OER). The frequency range of 100 mHz-100 kHz (amplitude = 10 mV) was used to obtain the EIS data. The ZView software (Scribner Associates) employing the equivalent circuit model of $R_s(R_eQ_1)(R_{ct}Q_{dl})$ wherein R_s (solution resistance) is in series with the parallel combination of the R_e (electrode resistance) and Q_1 (constant phase element) and further in series with the parallel combination of the R_{ct} (surface charge transfer resistance) and Q_{dl} (contribution from double layer capacitance and pseudo capacitance). The ohmic resistance ($R_{\Omega} = R_{s} + R_e$) obtained from the EIS data was further used for estimating iR_{Ω} correction in the polarization curves of the as-prepared electrocatalysts. The OER electrocatalytic activity was investigated by performing linear scanning voltammetry (LSV) measurements in 1 N H_2SO_4 electrolyte solution with a scan rate of 10 mV sec^{-1} at 40^{o}C. In order to compare the electrochemical performance of the as-prepared electrocatalyst materials, the current density at ~1.55 V in the iR_Ω corrected polarization curves was measured and reported in the present study. Tafel plots are reported for an average of three independently prepared electrocatalyst samples using the equation as $\eta = a + b \log i$ [i.e., plot of overpotential (η) *vs* log current (log i)] wherein 'a' and 'b' represent the exchange current density and Tafel slope, respectively.

Furthermore, in order to investigate the electrochemically active surface area (ECSA) of the as-prepared electrodes, cyclic voltammetry (CV) curves were recorded with a scan rates of 5, 10, 15, and 20 mVs^{-1} in the potential range of 1 to 1.2 V (*vs* RHE). The double-layer capacitance (C_{dl}, $mF\ cm^{-2}$) values were obtained from the slope i.e., from plot of differences in current density ($\Delta J_{1.1\ V} = j_{anode} - j_{cathode}$) at 1.1 V (*vs* RHE) *vs.* scan rates (average of three independently prepared electrocatalyst samples). The detailed calculations of ECSA ($m^2\ g^{-1}$) are described in the sections to follow. The electrochemical stability of the as-prepared electrocatalyst materials was evaluated from the chronoamperometry (CA) test (current *vs* time) wherein, the working electrodes were maintained at a constant voltage of ~1.55 V *vs* RHE in the electrolyte solution of 1 N H_2SO_4 at 40°C. To estimate any dissolved species in the electrolyte from the electrocatalyst following the chronoamperometry (CA) tests, inductively coupled plasma optical emission spectroscopy (ICP-OES, iCAP 6500 duo Thermo Fisher) was conducted to examine the electrochemical stability of the electrocatalyst materials following the stability tests (average of three independently prepared electrocatalyst samples collected after the stability tests in 1N H_2SO_4).

Equations and Calculations

Electrochemical Active Surface Area (ECSA)

The electrochemically active surface area (ECSA) was evaluated by dividing the double capacitance (C_{dl}) by the specific capacitance (C^*) of electrocatalyst, similar to the previous reports describing the ECSA analysis. [249-251] A general specific capacitance (C^*) value of metal electrodes in acidic solutions is assumed to be 35 µF cm^{-2}. [91, 249, 252] Based on this specific capacitance (C^*) value, the ECSA values of the as-synthesized electrocatalyst materials were calculated.

The electrochemical active surface area (ECSA in $m^2\ g^{-1}$) of the as-prepared electrodes is calculated using the following equation:

$$ECSA\ (m^2 g^{-1}) = \frac{C_{dl}}{C^* \times L}$$

Where, C_{dl} = double-layer capacitance ($mFcm^{-2}$)

The double layer capacitance, C_{dl} = ½ × linear slope of the current density ($j_{anode} - j_{cathode}$) *vs.* scan rate [162, 169]

C^* = specific capacitance in acidic electrolyte (0.035 mF cm^{-2}) [91, 249, 252]

L = Mass loading of the electrocatalyst (g m^{-2})

Appendix D Table 3 Results of the electrochemical active surface area (ECSA) of the as-prepared electrocatalysts (For: C* =0.035 mFcm^{-2})

Electrocatalyst Material	**Linear slope of current density ($\Delta J_{1.1\ V} = j_{anode} - j_{cathode}$) *vs.* scan rate (mF cm^{-2})**	**Double layer capacitance (C_{dl}) (mF cm^{-2})**	**ECSA ($m^2\ g^{-1}$)**
CMO-200	4.78	2.39	6.82
CMO-400	2.9	1.45	4.14
CMO-600	0.9	0.45	1.28
CMO-800	0.52	0.26	0.74

Note: In order to ascertain the electrochemical stability and correlate the stability to the electrochemical performance, the activity stability factor (ASF = $\frac{j-S}{S}$, where j is the geometric current density and S is an equivalent dissolution current) has been recently reported in the literature. [273, 501, 502] Complementing this approach, we have investigated and introduced another term putatively defined as the 'activity stability index' (ASI) represented by the equation below:

$$\text{ASI} = \frac{j_i}{(j_i - j_f)} \times \frac{1.23}{(V - 1.23)}$$

Where j_i is the geometric current density at the beginning of the chronoamperometry stability test, j_f is the geometric current density at the end of the stability test, 1.23 is standard thermodynamic water splitting OER value, and V is the potential at which the stability test is conducted. The ASI equation presented in the current study gives an indication of the true electrocatalytic activity as well the durability (i.e., current retention after stability test), which can be utilized together in the single formula above and accordingly, is more appropriately indicative of the overall electrocatalytic activity of the electrocatalyst materials. It can be viewed from these results that the spinel electrocatalyst obtained following heat treatments at 800^{o}C, CMO-800 exhibits higher ASI demonstrating a superior electrochemical performance in contrast to the spinel electrocatalysts heat treated at temperatures of 200^{o}C, 400^{o}C, and 600^{o}C, CMO-200, 400, and 600, respectively.

Appendix D Table 4 Activity Stability Index (ASI) for the as-synthesized materials

Electrocatalyst	Activity Stability Index (ASI)
CMO-200	4.37
CMO-400	9.61
CMO-600	17.5
CMO-800	32
CMO-200:10F	4.61
CMO-800:10F	41.25

Appendix D Table 5 ICP-OES results after the chronoamperometry tests

Electrocatalyst Sample	Cu (ppm)	Mn (ppm)
CMO-200	18.28 ± 0.003	15.72 ± 0.004
CMO-400	5.61 ± 0.002	4.39 ± 0.002
CMO-600	0.12 ± 0.001	0.10 ± 0.002
CMO-800	0.078 ± 0.002	0.069 ± 0.003

Appendix D Table 6 Comparison of OER performance with literature studies.

Electrocatalyst Sample (Electrolyte)	**Temperature (ºC)**	**Electrocatalyst performance mA cm^2 @ V (vs. RHE)**	**Reference**
$Cu_{1.5}Mn_{1.5}O_4$ ($1N\ H_2SO_4$)	200	9.2 @ 1.55	**Present work**
	400	6.7 @ 1.55	
	600	4.6 @ 1.55	
	800	3.4 @1.55	
Ag-doped Co_3O_4 ($1N\ H_2SO_4$)	400	4.1 @ 1.7	Journal of Materials Chemistry A, 6(14), pp.5678-5686.
	500	1.0 @ 1.7	
	600	0.5 @ 1.7	
CO_2TiO_4 ($1N\ H_2SO_4$)	900	17 @1.55	Inorganic chemistry, 58(13), pp.8570-8576.
IrO_x ($1N\ H_2SO_4$)	100	36 @1.55	Applied Catalysis B: Environmental, 218, pp.287-297
	200	25 @1.55	
	300	18 @1.55	
	400	14 @1.55	
	500	10 @1.55	
IrO_2-RuO_2-SiO_2 ($1N\ H_2SO_4$)	350	32 @ 1.25	International Journal of Hydrogen Energy, 44(2), pp.511-522
	450	27 @ 1.25	
	550	8 @ 1.25	
$CoMoO_4$ (0.1N HCl)	400	1@1.55	Journal of Materials Chemistry A, 7(40), pp.23130-23139
MnMoCoO ($4\ N\ H_2SO_4$)	100	0.1	Scientific reports 5 (2015): 15208.

Appendix D Table 6 (continued)

ϒ-MnO$_2$ (2 N H_2SO_4)	220	~0.1 @ 1.55	Angewandte Chemie, 131(15), pp.5108-5112.
Fe_2O_3 (1 N H_2SO_4)	450	~0 @1.55	Journal of Catalysis, 365, pp.29-35.
Co3O4-derived Xerogel (1 N H_2SO_4)	500	~5 @1.7	ACS Sustainable Chemistry & Engineering, 7(19), pp.16094-16102

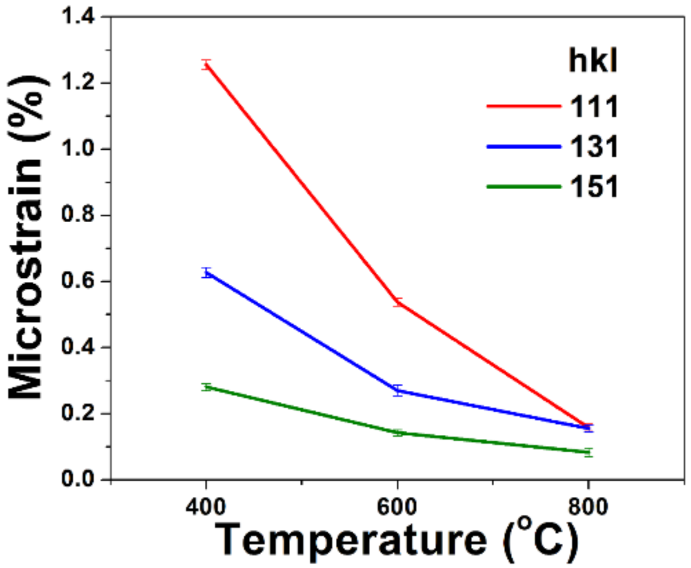

Appendix D Figure 1 Microstrain *vs.* temperatures of the electrocatalyst samples.

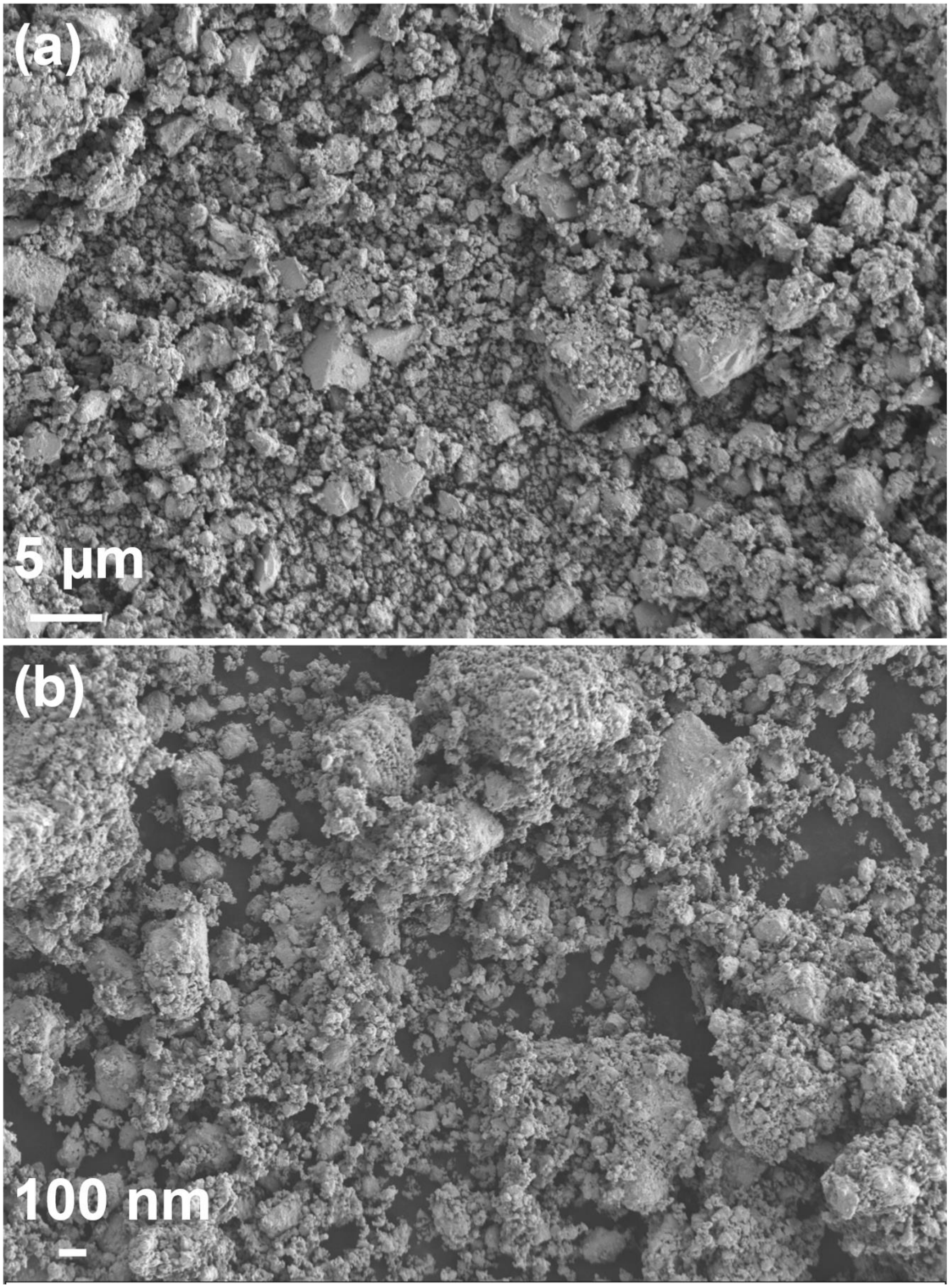

Appendix D Figure 2 High resolution SEM images of CMO-200.

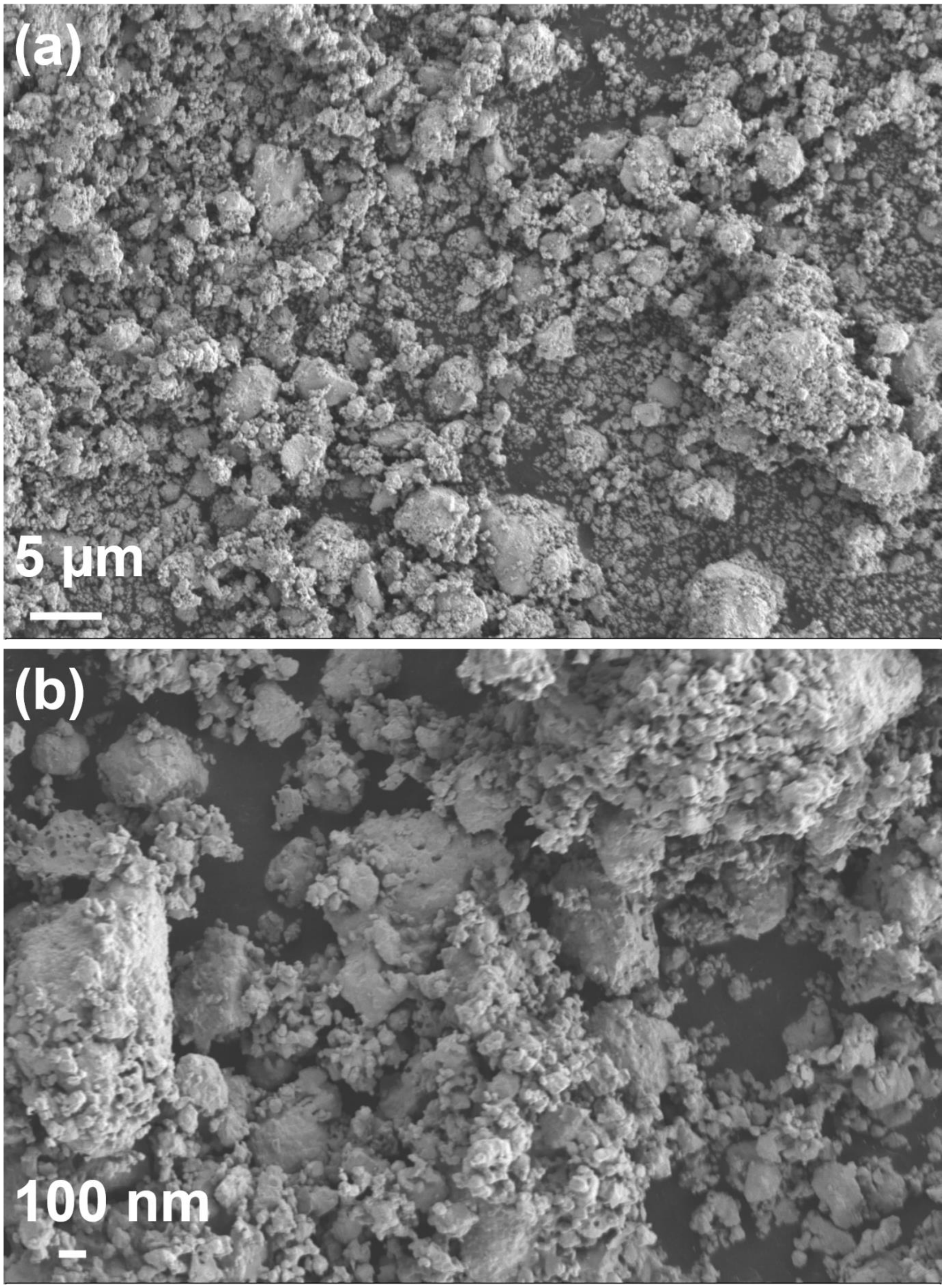

Appendix D Figure 3 High resolution SEM images of CMO-800.

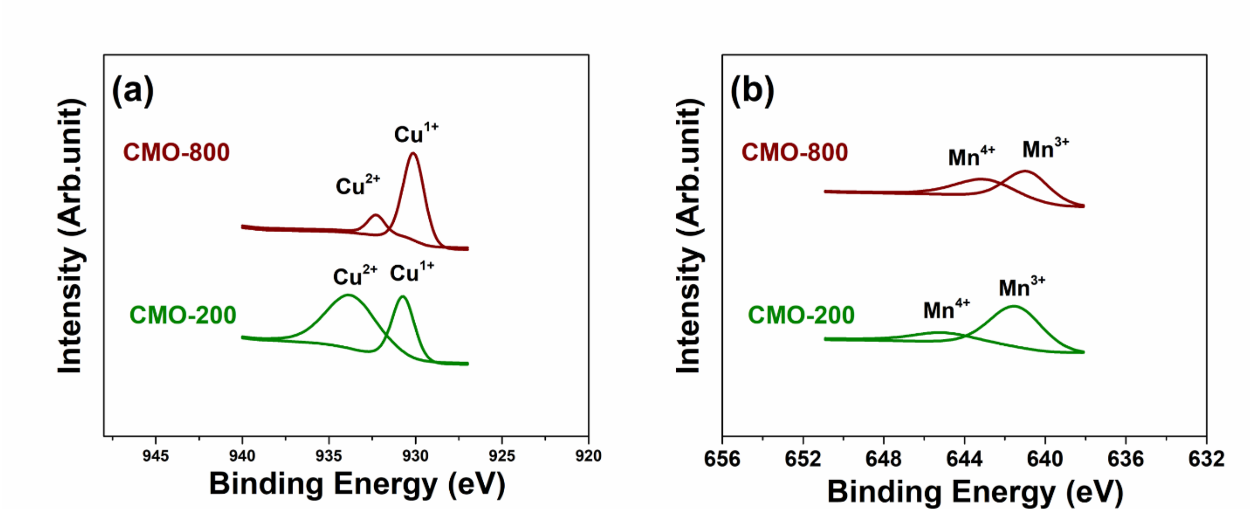

Appendix D Figure 4 XPS spectra of (a) Cu and (b) Mn for CMO-200 and CMO-800.

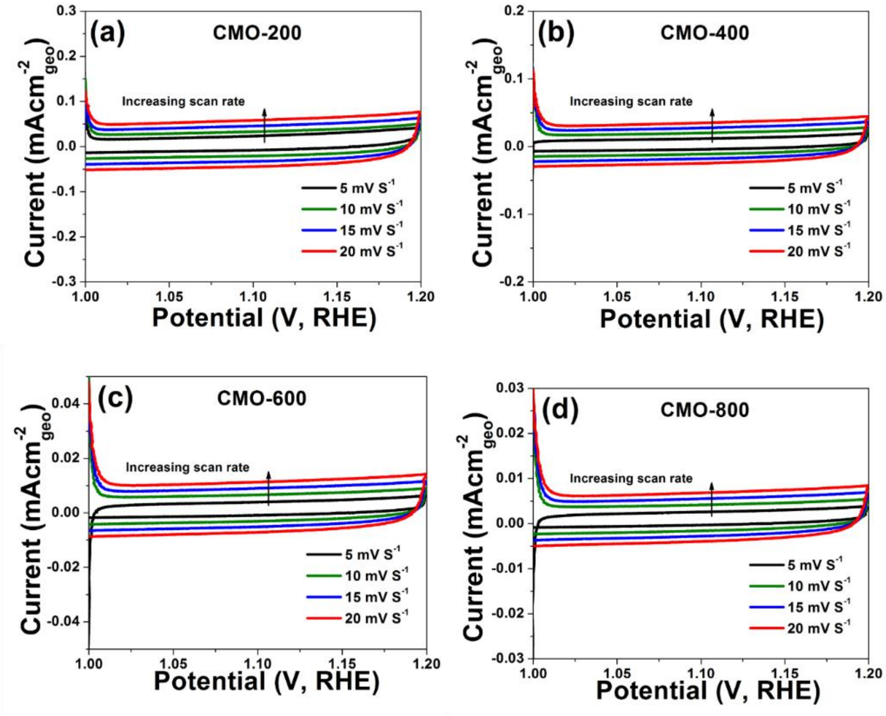

Appendix D Figure 5 Cyclic voltammograms with a scan rate of 5, 10, 15 and 20 mV s $^{-1}$ recorded in 1N H_2SO_4 solution for as-synthesized (a) CMO-200, (b) CMO-400, (c) CMO-600, and (d) CMO-800.

Note: It should also be mentioned that based on our previous experimental as well as computational study, 10 wt. % fluorine doped $Cu_{1.5}Mn_{1.5}O_4$ (CMO:10F) is identified as an optimum F concentration in the $Cu_{1.5}Mn_{1.5}O_4$ system.[281] The beneficial role of F in modifying the surface electronic structure for OER and thus, improving the electrocatalytic activity is extensively reported in several of our previously published studies[70, 97, 98, 102, 187, 282]. Accordingly, herein, based on our previously executed first-principles theoretical calculations of the total energies and electronic structures[281], 10 wt. % F incorporated CMO samples (CMO-200:10F and CMO-800:10F) are synthesized and investigated for OER. These two temperatures were selected to represent the two extremes of disordered and ordered spinel structures. Accordingly, the F-doped

CMO samples are synthesized by mixing stoichiometric powders of the synthesized CMO-200, CMO-800 and commercially obtained ammonium fluoride (NH_4F, 98%, Alfa Aesar) in D.I water, followed by drying 40°C and subsequently subjecting to thermal treatment at 100°C, 1 h.

The as-synthesized CMO-200:10F and CMO-800:10F exhibit XRD patterns similar to that of non-fluorinated samples, suggesting the formation of solid solutions, devoid of any secondary phase formation of F based compounds. The CMO-200:10F and CMO-800:10F samples exhibit charge transfer resistance values of ~67 Ω cm^2 and ~123 Ω cm^2, respectively, which are noticeably lower than that of pure CMO-200 (~73 Ω cm^2) and CMO-800 (~130 Ω cm^2). These results suggest the beneficial role of F in reducing the charge transfer resistance, which is in good agreement with our various previous studies on F-doped OER electrocatalysts for acidic OER.[281, 357, 358] Additionally, the higher current density of ~9.85 and 4.40 mA $cm^{-2}{}_{geo}$ at 1.55 V *vs* RHE, respectively, in comparison to pure CMO-200 (~ 9.2 mA $cm^{-2}{}_{geo}$) and CMO-800 (~ 3.42 mA $cm^{-2}{}_{geo}$) clearly indicates the slight improvement in the electrocatalytic activity as a result of F incorporation.

Finally, it should be noted that F incorporation did not show any significant change in the Mn^{3+}/ Mn^{4+} and Cu^{2+}/ Cu^{1+} ratios of CMO-200:10F (Cu^{1+}/ Cu^{2} ~ 0.52 and Mn^{3+}/ Mn^{4+}~ 4.17) and CMO-800:10F (Cu^{1+}/ Cu^{2} ~ 3.65 and Mn^{3+}/ Mn^{4+}~ 1.33) samples from the values obtained for the non-fluorinated structures. Thus, the higher electrochemical activity and inferior electrochemical stability characteristics attributed to the presence of the disordered state of the lower heat treatment temperature of 200°C depicted by the non-doped pure oxide structures is retained even with the fluorine doping. Consequently, the slight enhancement in the charge transfer kinetics, reduction in activation polarization, and improvement in the electrocatalytic activity can be solely attributed to the improved electronic structure and formation of CUS (coordinatively unsaturated sites) owing to the F incorporation, as evidently reported in our prior as well as present DFT results on the CMO system.[281] Correspondingly, the chronoamperometry stability test conducted on CMO-200:10F and CMO-800:10F demonstrate the electrochemical durability comparable to that of the pristine non-fluorinated spinel oxide compositions. As a result, no noticeable significant improvement in the electrochemical stability is observed. Thus, as anticipated, the as-performed electrochemical results reveal the charge transfer resistance reduction and activity enhancement upon F incorporation into CMO samples.

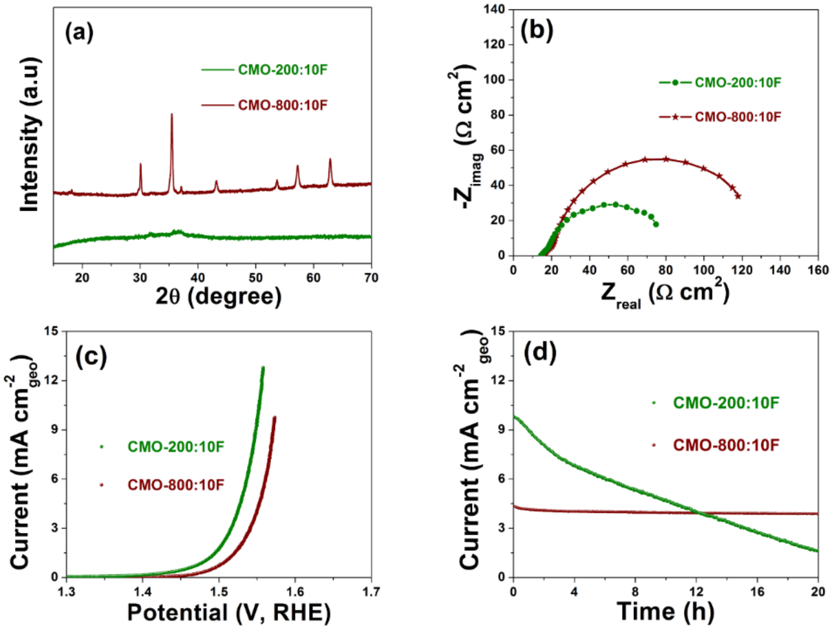

Appendix D Figure 6 (a) XRD patterns of CMO-200:10F and CMO-800:10F, (b) EIS plots performed at 1.55 V (*vs*. RHE), (c) OER polarization curves with a scan rate of 10 mVs^{-1}, and (d) chronoamperometric response of as-prepared CMO-200:10F and CMO-800:10F electrodes measured at ~1.55 V (*vs* RHE).

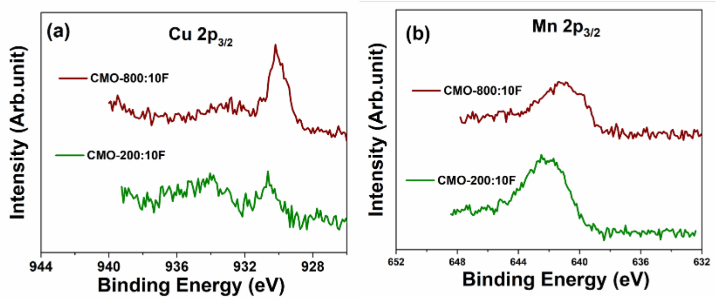

Appendix D Figure 7 XPS spectra for (a) Cu 2p and (b) Mn 2p for the fluorinated CMO-200 and CMO-800.

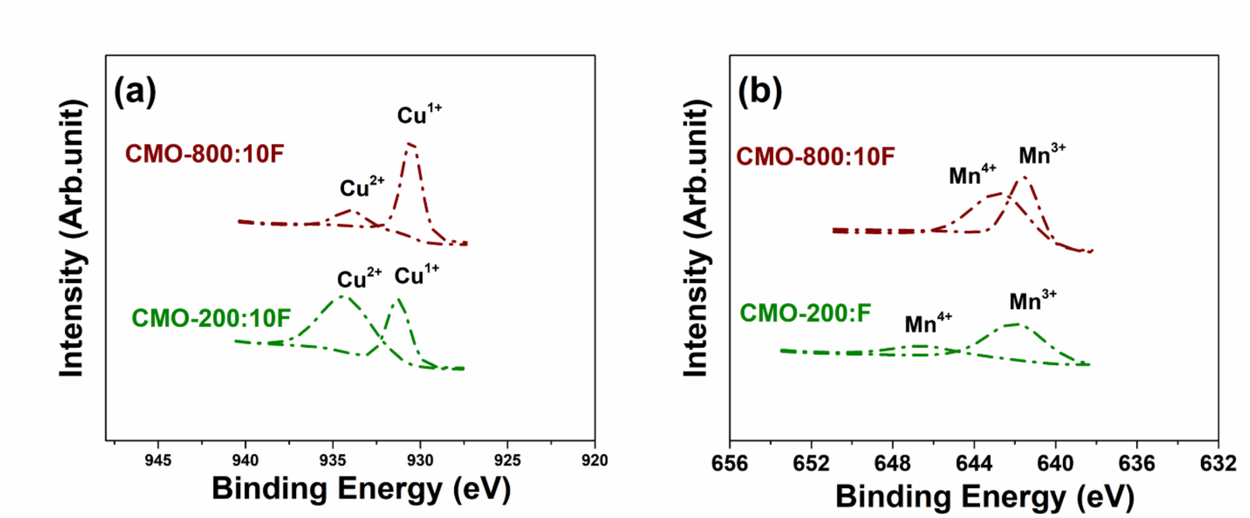

Appendix D Figure 8 XPS spectra of (a) Cu and (b) Mn for CMO-200:10F and CMO-800:10F.

Appendix D Table 7 Binding energy values for CMO samples

Electrocatalyst Material	**Cu Binding Energy (eV)**		**Mn Binding Energy (eV)**		**Integral peak area ratios**	
	Cu^{1+}	Cu^{2+}	Mn^{3+}	Mn^{4+}	Cu^{1+}/Cu^{2+}	Mn^{3+}/Mn^{4+}
CMO-200:10F	931.06	934.71	642	646.20	0.52	4.17
CMO-800:10F	930.35	934	641.50	643.53	3.65	1.33

Appendix E Supplementary Information: Computational and Experimental Investigation of Co and S-Doped Ni_2P as Efficient Electrocatalyst for Acid Mediated Proton Exchange Membrane Hydrogen Evolution Reaction

Computational methodology

For all the DFT calculations, the Vienna Ab-initio Simulation Package (VASP) was used within the projector-augmented wave method [103, 104, 214] and the generalized gradient approximation for the exchange-correlation energy functional in a form established by Perdew and Wang.[411] This program calculates the electronic structure and the inter-atomic forces from first-principles. The standard projector augmented-wave (PAW) potentials were employed for the Ni, Co, P, and S potentials containing ten, nine, five, and six valence electrons, respectively. The plane wave cutoff energy of 520 eV was used to maintain a high accuracy of the total energy calculations. The lattice parameters and internal positions of atoms were all fully optimized using the double relaxation procedure. The minima of the total energies with respect to the lattice parameters and internal ionic positions were also calculated. Optimization of the geometry was obtained by minimizing the Hellman–Feynman forces via a conjugate gradient method, such that the net forces applied on every ion in the lattice are close to zero. The total electronic energies were also converged to within 10^{-5} eV/unit cell resulting in the residual force components on each atom to be lower than 0.01 eV/Å/atom thus, allowing for an accurate determination of the internal structural parameters for the material. The Monkhorst-Pack scheme was employed to sample the Brillouin Zone (BZ) and generate the *k*-point grid for all the electrocatalyst materials studied.

Experimental methodology

Structural characterization

Philips XPERT PRO system with CuK_α radiation source (λ = 0.15406 nm, and operating current and voltage of 40 mA and 45 kV, respectively) was used for all of the XRD analysis of the synthesized electrocatalysts. Scanning electron microscopy (SEM) was conducted to investigate the morphology and microstructure of the $(Ni_{0.95}Co_{0.05})_2P$: x at. %S (x = 0. 5, 5, 10) electrocatalyst systems. Energy dispersive x-ray spectroscopy (EDX) was used for conducting quantitative elemental analysis and determining the distribution of various elements. X-ray photoelectron spectroscopy (XPS) was performed to study the binding energy and chemical states of elements. The XPS analysis was conducted using an ESCALAB 250 Xi system (Thermo Scientific) equipped with a monochromated Al Kα X-ray source. The standard analysis spot of $400 \times 400\ \mu m^2$ was defined by the micro-focused X-ray source. The system is operated in an ultra-high vacuum chamber with the base pressure less than 5×10^{-10} mBar and at a room temperature. The binding energy (BE) scale of the analyzer was calibrated to produce <50 meV deviations of the three standard peaks from their standard values. The aliphatic C1s peak was observed at 284.6 eV. High-resolution elemental XPS data in Ni 2p, Co 2p, S 2p, and P2p regions were acquired with the analyzer pass energy set to 20 eV (corresponding to energy resolution of 0.36 eV) and the step size set to 0.1 eV. The fitting of the elemental spectra based on calibrated analyzer transmission functions, Scofield sensitivity factors, and effective attenuation lengths for photoelectrons from the standard TPP-2M formalism was achieved using the Avantage software package (Thermo Fisher Scientific). The wettability characteristics of as-synthesized electrocatalysts were investigated by using an AST Products VCA 2000 video contact angle goniometer, wherein a water droplet (10 μL) was vertically dropped onto the electrode surface and the contact angle was detected by the sensitive drop method by drawing a tangent to the edge of the droplet and intersecting it with the measurement baseline.[503] The nitrogen adsorption-desorption using the Brunauer-Emmett-Teller (BET) technique was utilized to determine the BET specific surface area (SSA) of the as-synthesized catalyst powders. Multipoint BET technique was used for SSA evaluation using the Micromeritics ASAP 2020 Instrument.[303]

Electrochemical characterization

The electrochemical characterization of as-synthesized electrocatalysts was carried out in a three-electrode configuration using a VersaSTAT 3 (Princeton Applied Research) electrochemical workstation. 1 N H_2SO_4 was used as the electrolyte solution for hydrogen evolution reaction (HER) and maintained at a constant temperature of 40^oC using a Fisher Scientific 910 Isotemp refrigerator circulator. For the preparation of the working electrodes (WE), the electrocatalyst inks of different compositions were made by adding 85 wt. % electrocatalyst to 15 wt. % Nafion (5 wt. % solution in lower aliphatic alcohols, Aldrich). The resulting electrocatalyst inks were then subjected to sonication for 1 h. After sonication, the catalyst inks were discretely homogenized using a Tissuemiser (Fisher Scientific) for ~ 3 min and then uniformly spread on the porous titanium (Ti) foils (Alfa Aesar) with the total electrocatalyst loading of 0.3 mg cm^{-2}. Commercially obtained Pt wire (Alfa Aesar, 0.25 mm thick, 99.95%) was used as the counter electrode (CE) and mercury/mercurous sulfate (Hg/Hg_2SO_4) electrode (XR-200, Hach) having a potential of +0.65 V with respect to reversible hydrogen electrode (RHE) was used as the reference electrode (RE). The potential values reported in this study were determined with respect to reversible hydrogen electrode (RHE) and calculated from the formula as below:[78]

$$E_{RHE} = E_{Hg/Hg2SO4} + E^{o}_{Hg/Hg2SO4} + 0.059pH$$

where E_{RHE} is the potential versus RHE and $E_{Hg/Hg2SO4}$ is the potential measured against the Hg/Hg_2SO_4 reference electrode. $E^o_{Hg/Hg2SO4}$ is the standard electrode potential of Hg/Hg_2SO_4 reference electrode (+0.65 V *vs* RHE).

To determine the ohmic resistance (R_Ω) and charge transfer resistance (R_{ct}) for the synthesized electrocatalysts, electrochemical impedance spectroscopy (EIS) was conducted using the electrochemical workstation (Versa STAT 3, Princeton Applied Research) in 1 N H_2SO_4 solution maintained at 40°C and at -0.05 V (*vs* RHE). Impedance (EIS) tests were performed in the frequency range of 100 mHz-100 kHz (Amplitude = 10 mV). The ZView software from Scribner Associates employing the equivalent circuit model given as $R_\Omega (R_{ct}Q_{dl})$ was used to correlate the impedance data for HER in the present study.[97] The ohmic resistance (R_Ω) obtained from the EIS was further used for iR_Ω correction in the polarization curves of electrocatalysts having different compositions. The Tafel slopes (b) were calculated by using the equation $\eta = a + b \log i$ (plot of potential, η vs. log current, log i). The electrochemical stability of the electrodes was analyzed from the chronoamperometry (CA) test (current *vs* time). The working electrodes were maintained at a constant voltage of -0.05 V *vs* RHE in the electrolyte solution of 1 N H_2SO_4 at 40°C. An inductively coupled plasma optical emission spectroscopy (ICP-OES, iCAP 6500 duo Thermo Fisher) was used to investigate (average of three independently prepared electrocatalyst samples collected after the stability tests in 1N H_2SO_4) the dissolution of electrocatalyst materials after the stability tests.

Mass activity (A g^{-1})

Mass activity, (A g^{-1})[471] = $\frac{j}{\mathrm{m}}$

Wherein j = the current density (mA cm^{-2}) measured at particular potential (-0.05 V *vs.* RHE) and m = mass loading of the electrocatalyst

Turn over frequency (TOF, s^{-1})

TOF, (s^{-1})[467, 468] = $\frac{j \times A}{2 \times \mathrm{F} \times \mathrm{n}}$

Wherein, *j* = the current density (A cm^{-2}) measured at -0.05 V *vs.* RHE

A = geometric area of the working electrode (cm^2)

F = Faraday constant (96,485 C mol^{-1}) and

n = number of moles of the electrocatalyst

Appendix E Table 1 Mass activity and turnover frequency of as-synthesized electrocatalysts

Electrocatalyst	**Mass Activity (Ag^{-1})**	**TOF (s^{-1})**
Ni_2P	6.85	0.0070
$(Ni_{0.95}Co_{0.05})_2P$	12.67	0.012
$(Ni_{0.95}Co_{0.05})_2P$:5S	20.55	0.021
$(Ni_{0.95}Co_{0.05})_2P$:10S	30.45	0.031
$(Ni_{0.95}Co_{0.05})_2P$:15S	43.75	0.044

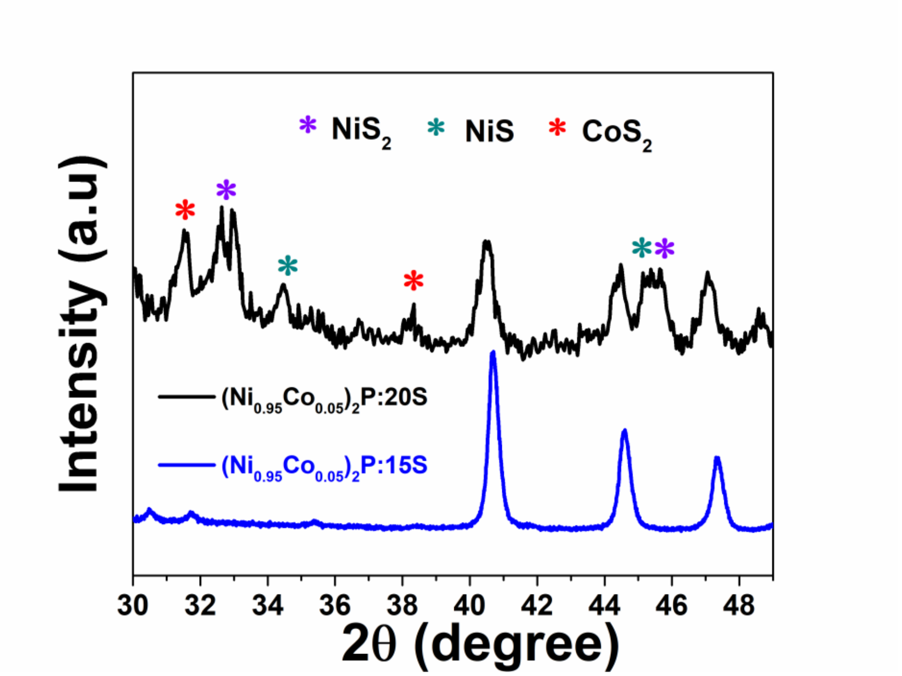

Appendix E Figure 1 Powder XRD patterns of (Ni$_{0.95}$Co$_{0.05}$)$_2$P:15S and (Ni$_{0.95}$Co$_{0.05}$)$_2$P:20S electrocatalysts showing the phase separation and presence of other phases with increase in S content

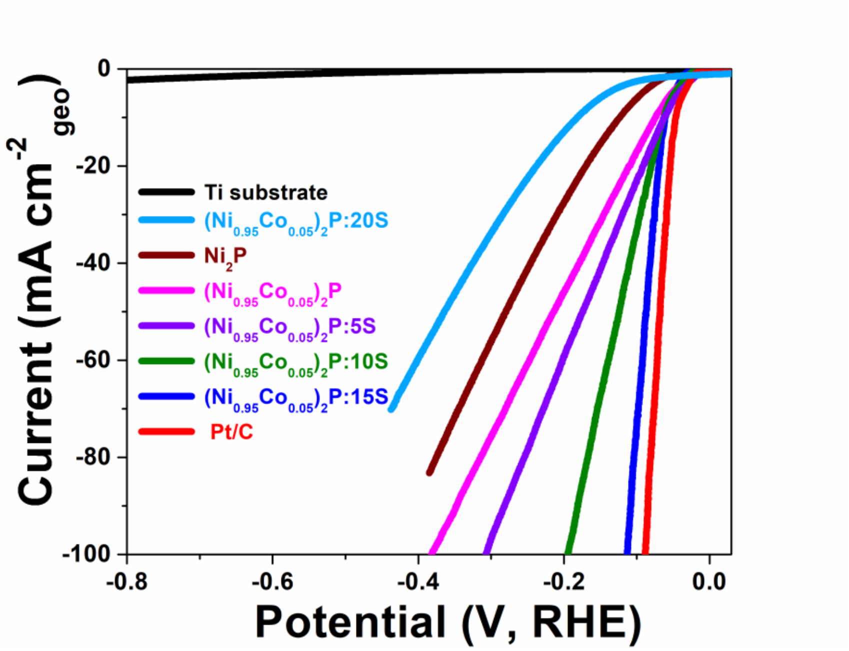

Appendix E Figure 2 HER polarization (mA cm$^{-2}_{geo}$ *vs*. potential) curves collected on the electrocatalysts with a scan rate of 10 mV s^{-1}

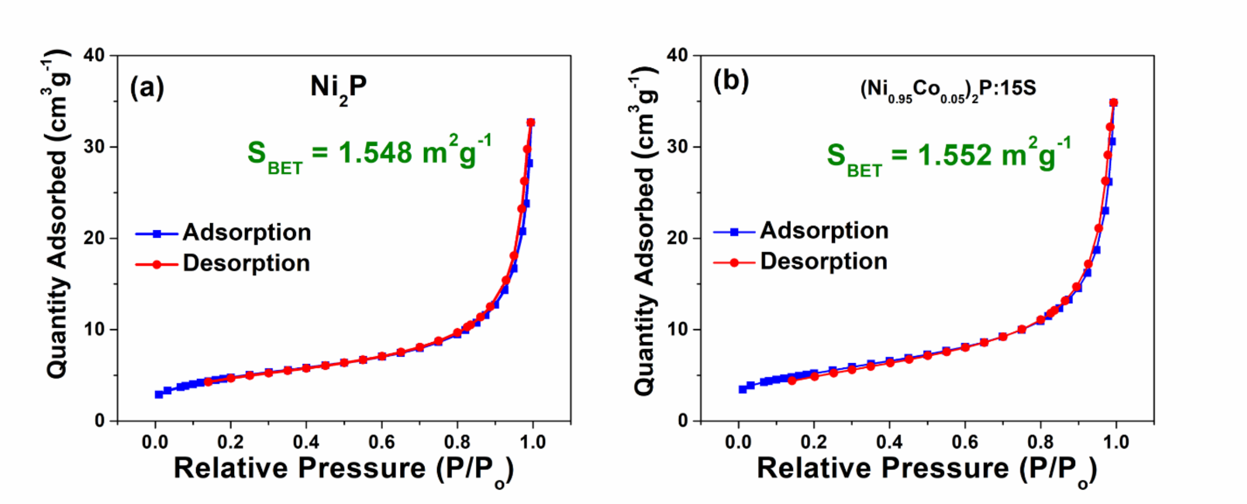

Appendix E Figure 3 N_2 adsorption−desorption isotherms collected on Ni_2P and $(Ni_{0.95}Co_{0.05})_2P$:15S electrocatalysts

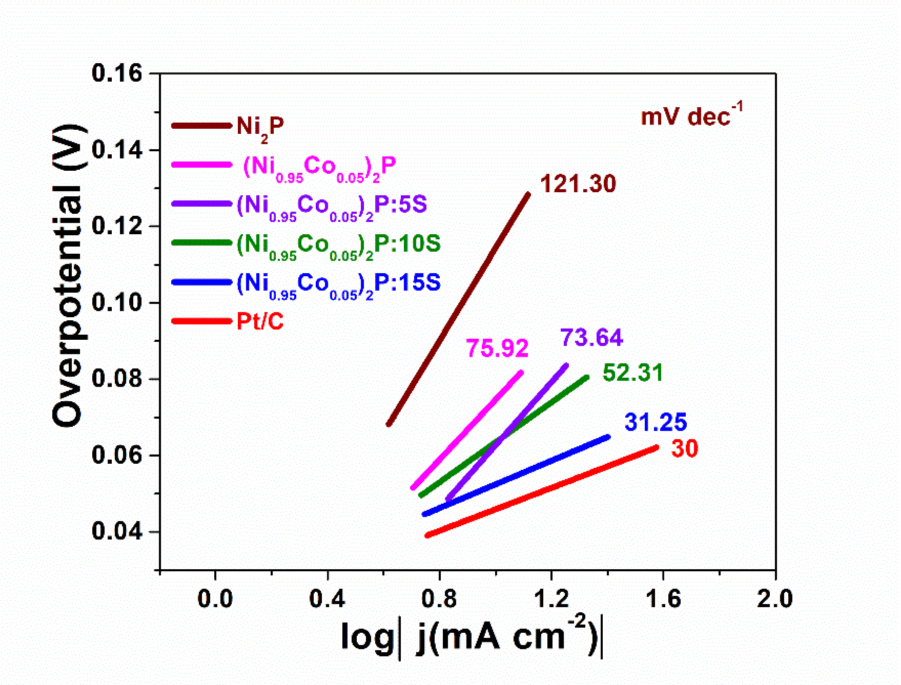

Appendix E Figure 4 Tafel plot for as-synthesized electrocatalysts

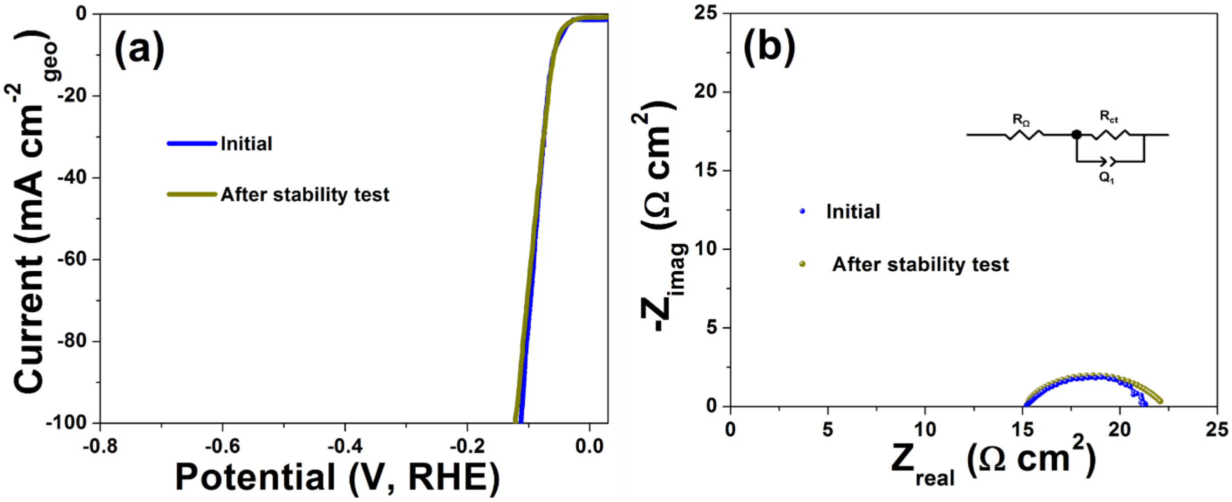

Appendix E Figure 5 Post stability (a) HER polarization and (b) impedance results of $(Ni_{0.95}Co_{0.05})_2P$:15S electrocatalysts

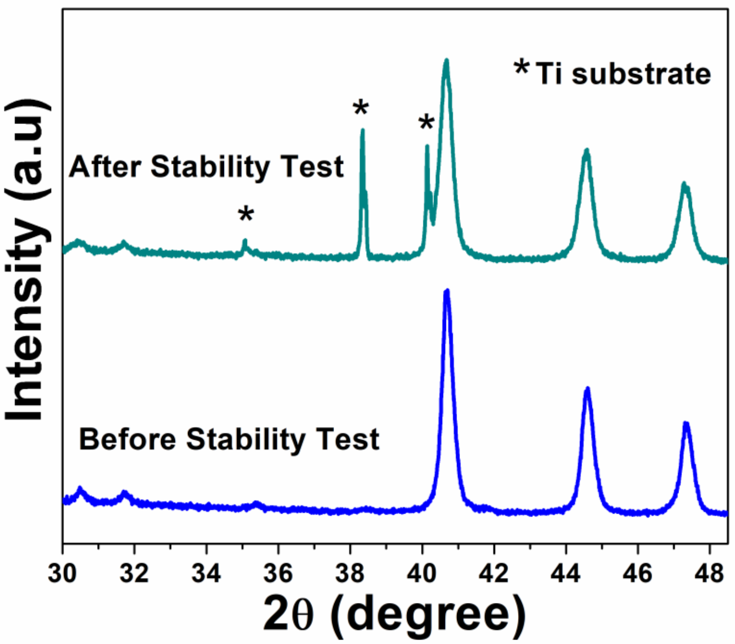

Appendix E Figure 6 Post stability XRD results collected on $(Ni_{0.95}Co_{0.05})_2P$:15S/Ti following the chronoamperometry electrochemical stability test

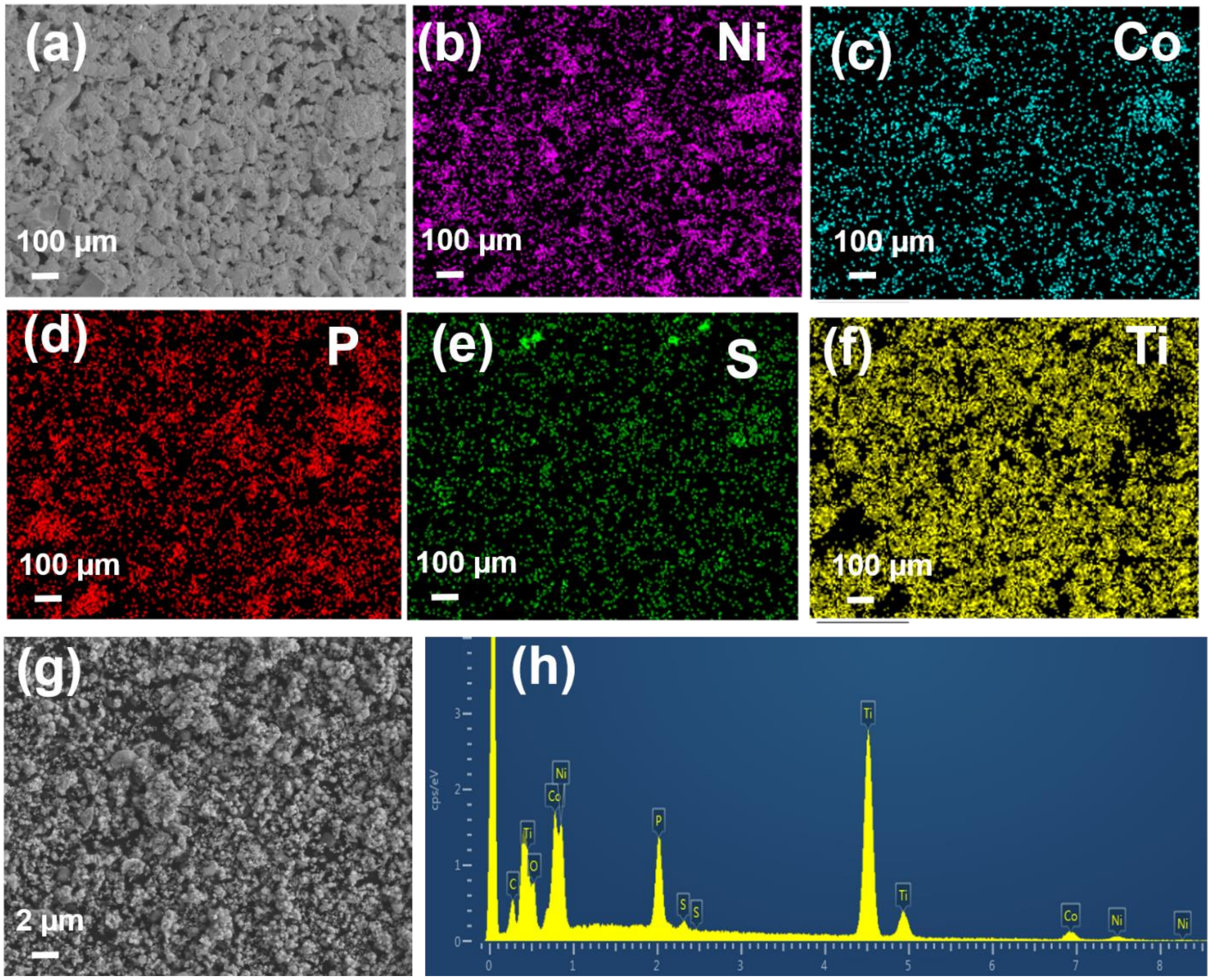

Appendix E Figure 7 **(a) SEM micrograph, (b-f) elemental x-ray mappings collected on the $(Ni_{0.95}Co_{0.05})_2P$:15S/Ti following chronoamperometry stability analysis, (g) SEM micrograph, and (h) EDX spectrum collected on post-stability $(Ni_{0.95}Co_{0.05})_2P$:15S/Ti electrocatalysts after the chronoamperometry tests**

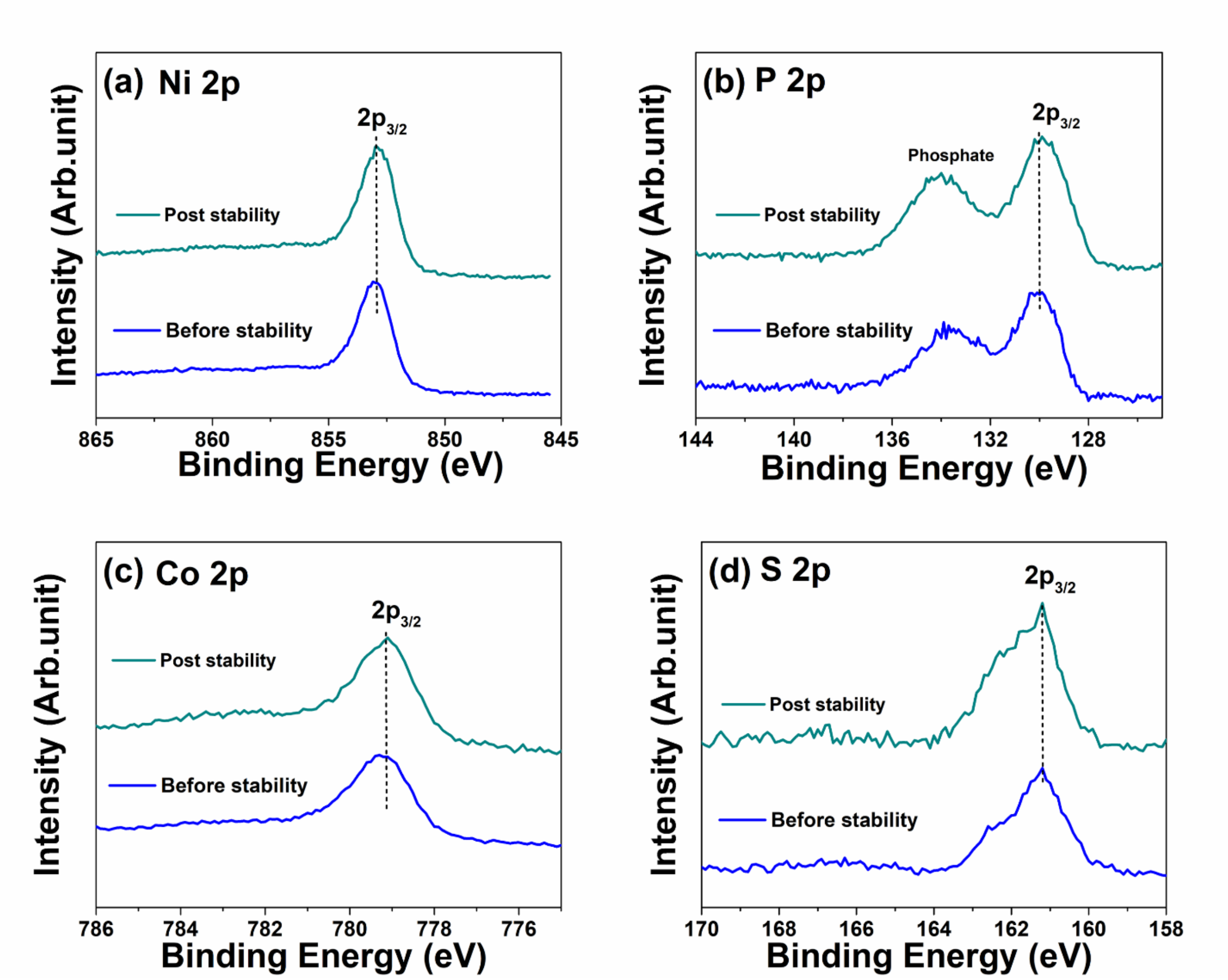

Appendix E Figure 8 (a) XPS spectra for (a) Ni 2p, (b) P 2p, (c) Co 2p, and (d) S 2p collected on the post-stability $(Ni_{0.95}Co_{0.05})_2P$:15S/Ti electrocatalysts following the chronoamperometry stability tests

Appendix E Table 2 Comparison of HER performance of $(Ni_{0.95}Co_{0.05})_2P$:15S with other reported non-precious HER electrocatalysts in acidic media

Electrocatalyst	Electrolyte	Tafel slope (mV dec^{-1})	Current density (j, mA cm^{-2})	η at the corresponding j (mV)	Reference
$(Ni_{0.95}Co_{0.05})_2P$:15S	1N H_2SO_4	31.25	100	102	Present work
Ni_2P	1N H_2SO_4	46	10	116	[504]
			100	180	
FeP	1N H_2SO_4	67	10	~240	[505]
Bulk Mo_2C	0.1N $HClO_4$	87.6	1	204	[506]
Mo_2C/CNT	0.1N $HClO_4$	55.2	10	152	[506]
Oxygen-incorporated MoS_2	1N H_2SO_4	55	126.5	300	[507]
$CoSe_2$ NP/CP	1N H_2SO_4	42.1	10	139	[508]
			100	184	
MoS_3 particles	1N H_2SO_4	54	2	190	[509]
MoS_3/FTO	2N H_2SO_4	40	2	170	[510]
Defect rich MoS_2	1N H_2SO_4	50	13	200	[511]
MoO_3-MoS_2/FTO	1N H_2SO_4	50-60	10	310	[512]
MoS_2 nanosheets	1N H_2SO_4	54	10	195	[513]
Mo_2C nanowires	1N H_2SO_4	53	60	200	[514]
MoN/C	0.1N $HClO_4$	54.5	2	290	[515]
$NiMoN_x$/C	0.1N $HClO_4$	35.9	2	170	[515]
$CoSe_2$ nanobelts	1N H_2SO_4	48	-	-	[516]

Appendix E Table 2 (continued)

WS_2 nanosheets	0.2 N H_2SO_4	60	-	-	517
WS_2/RGO	1N H_2SO_4	58	23	300	518
Co-NRCNTs	1N H_2SO_4	69	1	140	519
			10	260	
CoP/CC (carbon cloth)	1N H_2SO_4	51	10	67	375
			20	100	
			100	204	
MoB	1M H_2SO_4	55	20	210-240	520
Mo_2C	2N H_2SO_4	56	20	210-240	520
Ni_2P nanoparticles	2N H_2SO_4	87	20	140	521
MoS_2/RGO	1N H_2SO_4	41	20	170	522
Amorphous WP	1N H_2SO_4	-	10	120	523
			20	140	
Crystalline WP	1N H_2SO_4	-	10	200	523
			20	223	
MoP	1N H_2SO_4	54	30	180	51
CoP	1N H_2SO_4	50	20	85	524
P-WN/rGO	1N H_2SO_4	54	10	85	525
Cu_3P NWs/CF	1N H_2SO_4	67	10	143	526
Ni-Mo nanopowder	1N H_2SO_4	-	20	80	527
$Co_{0.6}Mo_{1.4}N_2$	0.1N $HClO_4$	-	10	190	528

Appendix E Table 2 (continued)

MoP-graphite nanosheets	1N H_2SO_4	63	10	460	529
Cu_3P NWs	1N H_2SO_4	67	1	79	530
			10	143	
			100	276	
CoP NWs	1N H_2SO_4	54			377
			2	70	
			10	122	
CoP film	1N H_2SO_4	50	10	85	531
MoP|S	1N H_2SO_4	50	10	64	532
			20	78	
			100	120	
WP_2 SMPs	1N H_2SO_4	57	2	115	533
			10	161	
			10	148	
CoP branched nanostructure	1N H_2SO_4	48	20	117	534
CoP nanoparticles	1N H_2SO_4	-	20	100	534

Appendix E Table 3 Results of ICP-OES analysis on 1N H_2SO_4 solution after chronoamperometry test of $(Ni_{0.95}Co_{0.05})_2P$:15S electrocatalysts

Elements	**Concentration (ppm)**
Ni	~$7.2\times10^{-3} \pm 0.002$
Co	~$5.8\times10^{-3} \pm 0.0001$
S	~$3.0\times10^{-3} \pm 0.003$
P	~$4.7\times10^{-3} \pm 0.002$

Appendix F Supplementary Information: Molybdenum Doped Bilayer Photoanode for Enhanced Photoelectrochemical Water Splitting

Incident photon to current efficiency (IPCE)

In order to study the effect of light absorption properties on the photoelectrochemical properties, incident photon to current efficiency (IPCE) was determined for bilayer photoanodes. IPCE was calculated using different bandpass optical filters with wavelength centered at 450, 500, 550, and 600 nm. % IPCE is calculated by the following equation, similar to our previous reports [423, 535]:

$$\text{IPCE (\%)} = \frac{1240 \times J \times 100}{\lambda \times P}$$

where, J is the measured photocurrent density (mA cm^{-2}) at zero bias (0 V), λ is the wavelength (nm), and P is the light intensity (mW cm^{-2})

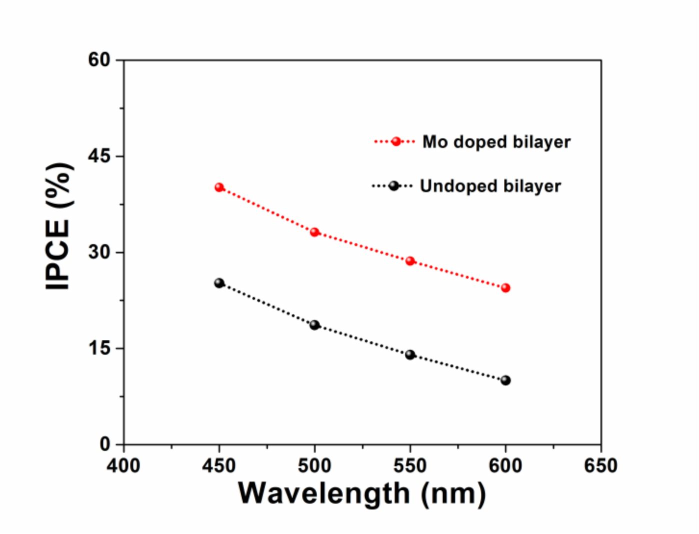

Appendix F Figure 1 IPCE plots for bilayer NTs under zero bias

Appendix F Table 1 The quantitative elemental composition analysis by EDX

Composition	EDX composition (at. %)				
	Sn	Nb	N	W	Mo
Undoped bilayer	78.41	4.64	13.50	3.15	-
Mo doped bilayer	78.45	4.62	13.46	3.08	0.063

Appendix F Table 2 Results of ICP analysis on 1N H_2SO_4 solution after chronoamperometry test of Mo-doped bilayer

Elements	Concentration (ppm)
Sn	$3.6\times10^{-3} \pm 0.002$
Nb	$2.1\times10^{-3} \pm 0.003$
W	$5.7\times10^{-3} \pm 0.001$
Mo	$2.0\times10^{-3} \pm 0.002$

Calculated losses limiting PEC performance of bilayer photoanodes

1. WO_3-$(Sn_{0.95}Nb_{0.05})O_2$:N

- Incident light energy=100 mW cm^{-2}
- Absorbed light (at ~500 nm which is close to the wavelength at which maximum solar irradiance is obtained[536]) = Light absorption×Incident light energy

$$= 26.42\% \times 100 \text{ mW cm}^{-2} = 26.42 \text{ mW cm}^{-2}$$

- IPCE at ~500 nm = 18.65 % (From **Appendix F Figure 1**)
- Energy contribution from excited carriers = IPCE × Absorbed light energy = 18.65% × 26 mW cm^{-2} = 4.92 mW cm^{-2}
- Energy lost in recombination process = Absorbed light energy - energy of excited carriers

  = 26.42 mW cm^{-2} – 4.92mW cm^{-2}

  = 21.5 mW cm^{-2}
- **Photoanode/electrolyte interface:**

The photocurrent density (2.95 mA cm^{-2}) at a finite potential (to overcome overpotential losses) close to zero bias i.e., ~0.1 V (*vs* RHE) in LSV plot is used for the following calculations.

Energy used for ohmic transfer $=I^2R_\Omega=(2.95 \text{ mA cm}^{-2})^2\times 15.5\ \Omega.\text{cm}^2$

$= 0.134 \text{ mW cm}^{-2}$

Energy used for charge transfer (activation polarization loss) $=I^2R_{ct}=(2.95 \text{ mA cm}^{-2})^2\times 9.65\ \Omega.\text{cm}^2= 0.084 \text{ mW cm}^{-2}$

- **Cathode/electrolyte interface:**

The current density (7.7 mA cm^{-2}) at a finite potential of ~30 mV (*vs* RHE, to overcome the overpotential losses) close to 0V (standard potential for HER) in HER polarization plot is used for following calculations (see [537] for electrochemical data of Pt).

Energy used for ohmic transfer$=I^2R_\Omega = (7.7 \text{ mA cm}^{-2})^2\times 15.25\ \Omega.\text{cm}^2$ (see [537] for electrochemical data of Pt)

$= 0.9 \text{ mW cm}^{-2}$

Energy used for charge transfer (activation polarization loss) $=I^2R_{ct}=(7.7\text{mA cm}^{-2})^2\times 10.8\ \Omega.\text{cm}^2= 0.64\text{ mW cm}^{-2}$ (see [537])

- **Energy contributed from free carriers – Total energy used**

  $= 4.92\text{ mW cm}^{-2} – (0.134+0.084+0.9+0.64)\text{ mW cm}^{-2}$

  $= 3.16\text{ mW cm}^{-2}$

2. $(W_{0.98}Mo_{0.02})O_3$-$(Sn_{0.95}Nb_{0.05})O_2$:N

- Incident light energy=100 mW cm^{-2}
- Absorbed light (at ~500 nm which is close to the wavelength at which maximum solar irradiance is obtained[536]) = Light absorption×Incident light energy

  $= 29.56\% \times 100\text{ mW cm}^{-2} = 29.56\text{ mW cm}^{-2}$
- IPCE at ~500 nm = 33.15% (From **Appendix F Figure 1**)
- Energy contribution from excited carriers = IPCE × Absorbed light energy = 33.15% × 29.56 mW cm^{-2} = 9.80 mW cm^{-2}
- Energy lost in recombination process = Absorbed light energy - energy of excited carriers

  $= 29.56\text{ mW cm}^{-2} – 9.80\text{ mW cm}^{-2}$

  $= 19.76\text{ mW cm}^{-2}$
- **Photoanode/electrolyte interface:**

The photocurrent density (4.13 mA cm^{-2}) at a finite potential (to overcome overpotential losses) close to zero bias i.e., ~0.1 V (*vs* RHE) in LSV plot is used for the following calculations.

Energy used for ohmic transfer $=I^2R_\Omega=(\ 4.13\ \text{mA cm}^{-2})^2\times 15.2\ \Omega.\text{cm}^2$

$= 0.25\ \text{mW cm}^{-2}$

Energy used for charge transfer (activation polarization loss) $=I^2R_{ct}=(4.13\ \text{mA cm}^{-2})^2\times 7.30\ \Omega.\text{cm}^2= 0.124\ \text{mW cm}^{-2}$

- **Cathode/electrolyte interface:**

  The current density (7.7 mA cm^{-2}) at a finite potential of ~30 mV (*vs* RHE, to overcome the overpotential losses) close to 0V (standard potential for HER) in HER polarization plot is used for following calculations (see [537] for electrochemical data of Pt).

  Energy used for ohmic transfer$=I^2R_\Omega=(7.7\ \text{mA cm}^{-2})^2\times 15.25\ \Omega.\text{cm}^2$

  $= 0.9\ \text{mW cm}^{-2}$

  Energy used for charge transfer (activation polarization loss)$=I^2R_{ct}=(7.7\text{mA cm}^{-2})^2\times 10.8\ \Omega.\text{cm}^2= 0.64\ \text{mW cm}^{-2}$

Energy contributed from free carriers – Total energy used

$= 9.80\ \text{mW cm}^{-2} – (0.25+0.125+0.9+0.64)\ \text{mW cm}^{-2}$

$= 7.87\ \text{mW cm}^{-2}$

Appendix G Supplementary Information: Electronic Tuning of Ni_2P via Fluorine Doping for Highly Efficient Oxygen Evolution Reaction

Abstract

Engineering high-performance electrocatalysts to expedite oxygen evolution reaction (OER) for the generation of sustainable hydrogen has been major scientific challenge. Utilizing density functional theory (DFT) calculations, we report F-anion doped Ni_2P (Ni_2P:x wt. % F) with enhanced OER performance in alkaline media. Owing to its unique electronic structural modification, Ni_2P:5F reveals lower charge transfer resistance (10.65 Ω cm^2), overpotential (230 mV @ 10mA cm^{-2}), Tafel slope (28.06 mV dec^{-1}), and high durability towards OER. The superior performance of Ni_2P:5F is ably supported by DFT studies, demonstrating an optimized electronic structure with reduced OER barrier and thus, offering improved OER kinetics.

Introduction

Commercial development of water electrolyzers has been bottlenecked by the lack of high performance earth-abundant electrocatalysts (ECs) to facilitate the energy intensive oxygen evolution reaction (OER).[357, 359] Unfortunately, platinum group metal (PGM) based ECs such as IrO_2 and RuO_2 which exhibit high OER performance, suffer from prohibitive cost and environmental scarcity, and thus, engineering of highly active, durable, and PGM-free ECs, demonstrating identical or superior electrochemical performance to that of state-of-the-art PGM based ECS is an integral research in the electrocatalyst field.[98, 189, 302, 358] As majority of the PGM-free ECs (e.g. transition-metal phosphides (TMPs), carbides, selenides, and sulfides) are vulnerable to corrosion and encounter stability issues in the harsh acidic media for OER, it is highly technically as well as economically plausible to conduct water splitting reaction for such materials in the alkaline electrolytes.[46, 47]

Accordingly, in the present study, utilizing the first-principles theoretical calculations of the total energies and electronic structures, we have identified and synthesized novel fluorine (F) doped Ni_2P as a solid solution ECs for alkaline OER. Based on our density function theory (DFT) calculations, F doped Ni_2P denoted as Ni_2P:x wt.%F (x= 2.5, 5, and 7.5) has been explored as a PGM-free high-performance system for OER for the very first time to the best of our knowledge. Among various electrocatalyst development strategies, utilization of various metal/non-metal dopants to optimize the electronic structure and thus, to expedite the OER kinetics as well as electrocatalytic activity of parent metal oxides, sulfides, phosphides etc. is one the most widely applied and promising approaches in the electrocatalyst development research.[357] Thus, herein, employing DFT based calculations for rationalizing the thermodynamics and OER kinetics, earth abundant and promising anionic dopant (F) has been selected for parent Ni_2P. Owing to its pivotal role in modifying the electronic structure as well as enhancing the electronic conductivity of the parent electrocatalyst systems, F is well-known intriguing dopant to accelerate the OER performance.[102, 357] Herein, as investigated from our DFT studies, incorporation of F into Ni_2P evidently modified the electronic structure of Ni_2P in such a way to offer improved OER performance. Accordingly, as-obtained Ni_2P:5F as an optimum composition reveals the superior OER performance in comparison to pure Ni_2P, demonstrating promise of F-doping to improve the electrocatalytic performance.

Computational Methodology

For calculations of the bulk and surface properties of Ni_2P:F, a hexagonal crystal structure P-62m, space group # 189 with three formula units in the unit cell has been considered as shown in **Appendix G Figure 1(a)**.[538] Since, in the present study water splitting has been considered in the alkaline condition, the corresponding anodic OER mechanism could be sequentially written as described in[539]:

$$4OH^- + * \xrightarrow{\text{I}} HO^* + 3OH^- + e^- \xrightarrow{\text{II}} O^* + H_2O(l) + 2OH^- + 2e^- \xrightarrow{\text{III}} HOO^* + H_2O(l) + OH^- + 3e^- \xrightarrow{\text{IV}} * + O_2(g) + 2H_2O(l) + 4e^- \tag{1}$$

where * represents an active site on the metal phosphide surface. There are two terminations of (0001) surface of Ni_2P - Ni_3P and Ni_3P_2. Previous DFT study showed that (0001) surface prefers Ni_3P_2 terminations due to higher stability.[364] Thus, this surface termination has been chosen with triple-Ni sites considered being catalytically active for the present DFT study of OER elementary steps .

For calculations of the total energy, electronic structure and free energy of the OER elementary reactions of pure and F-doped Ni_2P the spin-polarized DFT approach implemented in the Vienna *Ab-initio* Simulation Package (VASP)[103, 104] have been used with the generalized gradient approximation GGA-PBE for exchange-correlation functional and projector augmented wave (PAW) method.[213, 540] The surface slab for the present DFT studies consists of five atomic layers corresponding to two lattice parameters in *c* direction which is perpendicular to (0001) crystallographic plane and separated by vacuum layer of ~20 A to prevent an interaction between the slab and its image. The first two layers are fixed with bulk structural parameters, while the remaining top three layers along with O^*, HO^*, and HOO^* intermediates are fully relaxed.

Experimental methodology

Synthesis of Ni_2P: x wt. % F (x = 0, 2.5, 5, 7.5)

Nickel (II) chloride hexahydrate ($NiCl_2.6H_2O$), sodium hypophosphite hydrate ($NaH_2PO_2.xH_2O$), and ammonium fluoride (NH_4F) were used as the sources for Ni, P, and F respectively. The mixtures of stoichiometric amounts of these precursors were mechanically ground using a mortar and pestle [($NiCl_2.6H_2O$ = 10 mol%, $NaH_2PO_2.xH_2O$= 90 mol%)]. The resulting solid mixtures were transferred in alumina crucible and the crucibles containing the solid mixtures were subjected to heat treatment in ultra-high purity argon atmosphere (Matheson; 99.99%, flow rate = $100cm^3/min$) at 250°C for 1 h (Ramp rate = 10°C/min). The thermally treated solid mixtures were naturally cooled to room temperature in continuous Ar gas flow. The obtained products were crushed using a mortar and pestle and thoroughly washed with D.I. water (18 MΩ.cm, MilliQ Academic, Millipore) followed by drying at room temperature. The synthesis of IrO_2 has been achieved according to the protocol given in the previous report.[137]

The qualitative phase analysis was conducted using X-ray diffraction (XRD), Philips XPERT PRO system employing CuK_α radiation source ($\lambda = 0.15406$ nm) at an operating current and voltage of 40 mA and 45 kV respectively. Scanning electron microscopy (SEM) was carried out to investigate the microstructure of materials. The energy dispersive x-ray spectroscopy (EDX) was conducted for the elemental analysis and distribution of elements. To investigate the oxidation states of Ni and P in Ni_2P:F ECs, X-ray photoelectron spectroscopy (XPS, ESCALAB 250 Xi) was performed. All the NMR experiments were carried out on an Avance 500MHz Wide Bore NMR spectrometer. ^{31}P Magic Angle Spinning (MAS) spectra for Ni_2P and Ni_2P:5 wt.%F were collected using a 4 mm CP-MAS probe at a spinning speed of 8 kHz. ^{19}F MAS NMR for Ni_2P:7.5 wt.%F was collected using a 3.2 mm CP-MAS probe at 20 kHz spinning speed.

The electrochemical characterization of as-synthesized ECs was carried out in a three-electrode configuration using a VersaSTAT 3 electrochemical workstation. 1 M KOH was used as electrolyte solution and maintained at a constant temperature of 40°C. The electrocatalyst inks of different compositions were prepared by adding 85 wt. % electrocatalyst to 15 wt. % Nafion (5 wt. % solution in lower aliphatic alcohols). The catalyst inks were homogenized using Tissuemiser for ~ 3 min and then uniformly spread on the porous titanium (Ti) foils with the total mass loading of 0.3 mg on 1 cm^2 area. Pt wire (0.25 mm thick, 99.95%) was used as the counter electrode (CE) and mercury/mercurous sulfate (Hg/Hg_2SO_4) electrode (XR-200, Hach) having a potential of +0.65 V with respect to reversible hydrogen electrode (RHE) was used as the reference electrode (RE). The charge transfer resistance (R_{ct}) of the materials was evaluated using the electrochemical impedance spectroscopy (EIS) at ~1.55 V in the frequency range of 100 mHz-100 kHz (Amplitude = 10 mV). The ZView software from Scribner Associates employing the equivalent circuit model given as R_Ω ($R_{ct}Q_{dl}$)) was used to correlate the impedance data for OER in the present study. The ohmic resistance (R_Ω) obtained from the EIS was further used for iR_Ω correction in the polarization curves of ECs.

The OER activities were analyzed from the polarization measurements in 1M KOH electrolyte solution with a scan rate of 10 mV sec^{-1} at 40^0C. The experimentally obtained polarization curves of ECs having different compositions were iR_Ω corrected. The chronoamperometry (CA) tests were carried out wherein, the electrode was maintained for 24 h in the electrolyte solution of 1M KOH at 40^0C under a constant voltage of ~1.55 V (*vs* RHE). ICP-OES analysis was conducted on 1M KOH electrolyte solution, collected after 24 h of chronoamperometry test Ni_2P:5F. The turnover frequency was calculated using following equation. TOF (s^{-1})[45] = $\frac{J \times A}{4 \times F \times n}$, where, *j* = the current density (A cm^{-2}) measured at 1.55V *vs*. RHE, A = geometric area of the working electrode (cm^2), F = Faraday constant (96,485 C mol^{-1}) and, n = number of moles of the electrocatalyst.

Results and Discussion

DFT Results

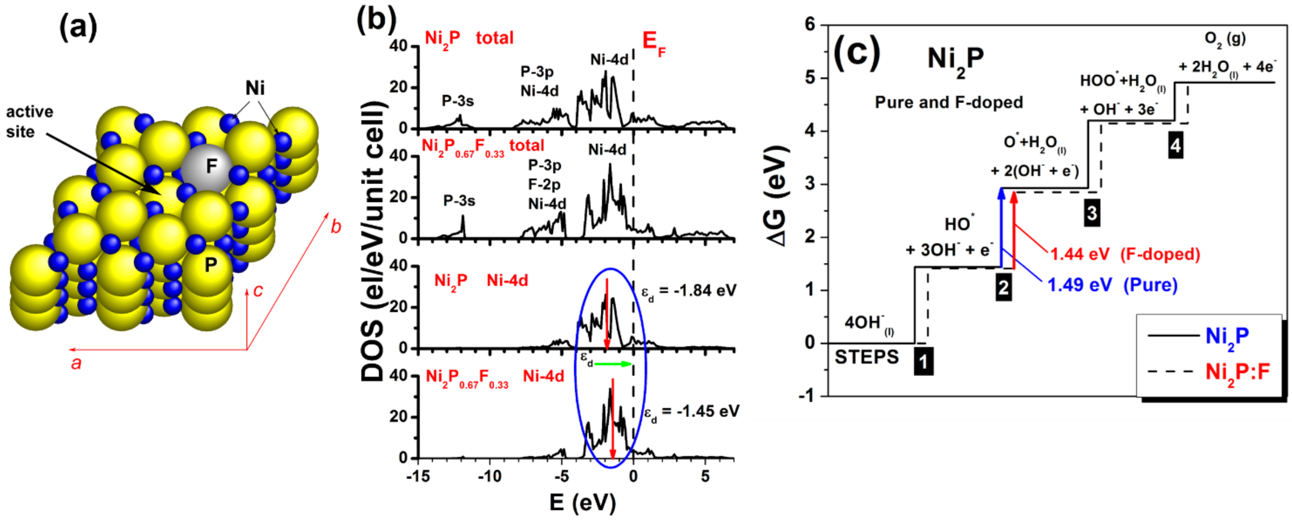

Appendix G Figure 1 (a) Crystal structure of Ni_2P with Ni_3P_2 termination of (0001) surface, (b) Total and projected density of electronic states. Fermi level is set to zero, red arrows denote d-band center positions, (c) Free energies of the intermediate reactions for pure and F-doped Ni_2P with the same triple-Ni active site at (0001) surface

The calculated density of electronic states (DOS) for pure Ni_2P and F-doped one with formula unit $Ni_2P_{0.67}O_{0.33}$ are shown in **Appendix G Figure 1(b)**. It can be seen that both the compounds demonstrate metallic conductivity without any bandgap at the Fermi level, suggesting their good electronic conductivity for facile charge transfer between the surface and intermediates during OER. In the pure Ni_2P, the electronic structure consists of three main zones below the Fermi level: (i) almost non-hybridized Ni4d just below E_F, (ii) hybridized Ni4d-P3p between -8.5 eV and -4.0 eV, and (iii) P3s between -14.5 eV and -11 eV. Note, that zone 1 and zone 2 do not create any band gap between them, thus providing the d-band center position for pure Ni_2P at around -1.84

eV below Fermi level, which is quite far from the optimal position of ~1.33 eV for excellent electrocatalysts such as Pt and IrO_2.[281] However, a substitutional introduction of F in place of P changes the electronic structure such a way that zone 2 which includes also new F2p electronic states and zone 1 become split by energy gap of ~0.8 eV, so that the zone 1 (Ni4d electronic states) moves upward towards the Fermi level shifting the d-band center from -1.84 eV to -1.45 eV, which is more optimal position indicating an improvement in the expected catalytic activity .

For estimation of the overpotential and the rate determining steps (RDS) of the OER for pure and F-doped Ni_2P, the Gibbs free energies (ΔG) of the four elementary steps have been calculated and shown in **Appendix G Figure 1(c)**. One can see that for both cases (without and with F atom at the surface) the RDS is Step 2 (i.e., splitting adsorbed HO^* and forming O^* with the first water molecule) which is the largest among all other elementary steps involved in the OER mechanism. However, presence of F helps to decrease RDS to some extent, namely from 1.49 eV to 1.44 eV, thus reducing the overpotential and improving the electrocatalytic activity. Such reduction of the RDS and the overpotential is due to stronger interaction between adsorbed O^* and the surface in case of F-doped Ni_2P in comparison to undoped one, which is also indirectly confirmed by shifting the d-band center towards the Fermi level as discussed above. Also, strengthening of the O^* binding to the surface in presence of F could be explained by decreasing of the repulsive component of the total energy due to lower negative charge of F^- in comparison to substituted P^{4-} ion at the surface. Since the electrostatic repulsion offers destabilization of the interatomic interactions, the F-doping reduces this repulsion, and thus, making the system more stable with stronger binding between F-doped surface and the intermediate species.[102]

Experimental Results

Appendix G Table 1 Results of electrochemical characterizations for OER

Electrocatalyst Composition	**R_{ct} (Ωcm^2)**	**Current density at ~1.55 V (mA cm^{-2})**	**Overpotential (η) at 10 mA cm^{-2} (mV)**	**Tafel slope (mV dec^{-1})**	**Mass activity at 1.55 V (A g^{-1})**	**TOF at ~ 1.55 V (S^{-1})**
Ni_2P	31.4	8.4	370	37.43	8.4	0.0032
Ni_2P :2.5F	23.2	11	330	35.59	11	0.0041
Ni_2P :5F	10.65	28.3	230	28.06	28.3	0.0104
Ni_2P :7.5F	18.9	15	290	30.46	15	0.0054
IrO_2	34.6	7.6	380	38.72	25.33	0.0147

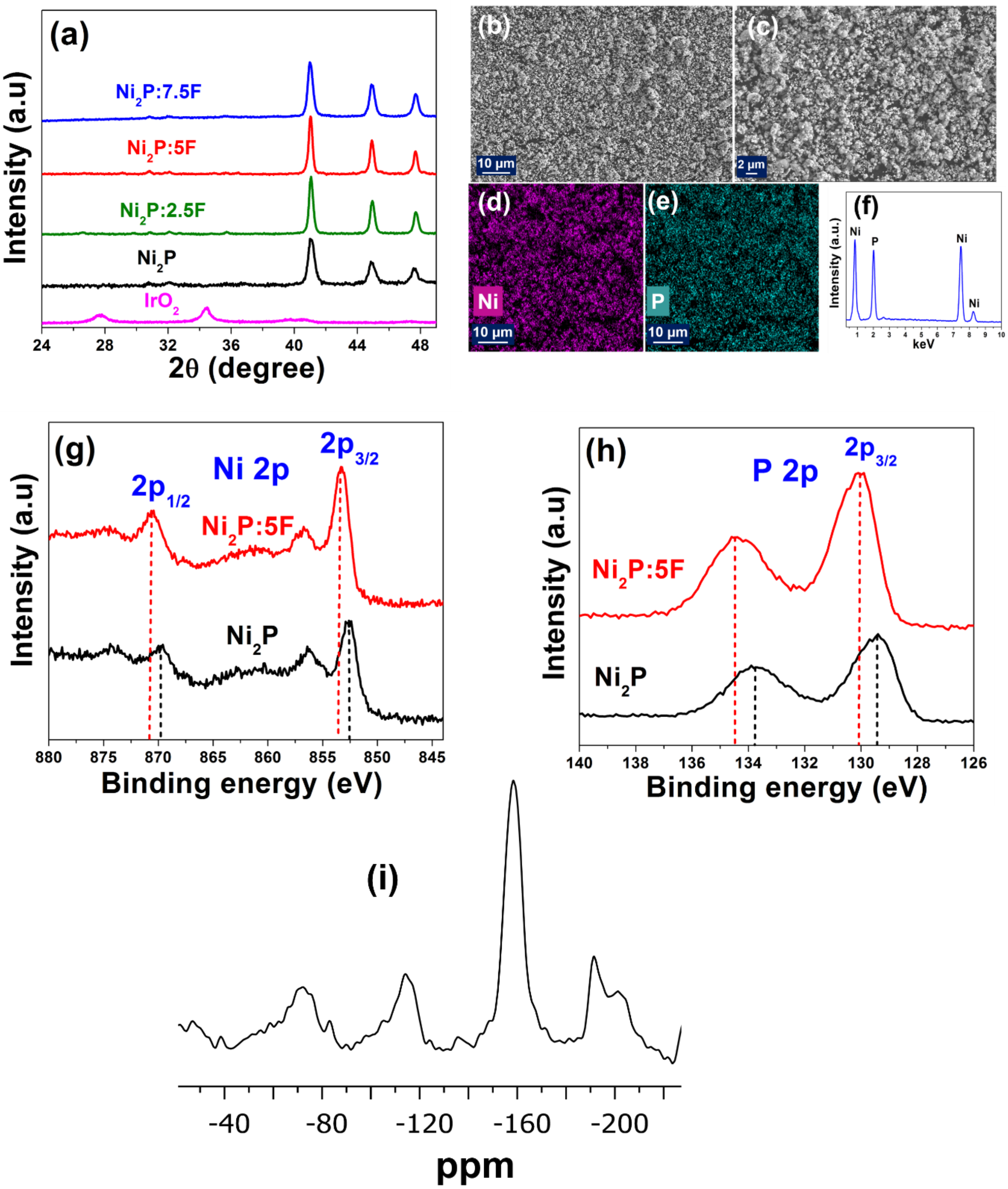

Appendix G Figure 2 (a) XRD patterns, (b, c) SEM micrographs, (d, e) Elemental x-ray mappings, and (f) EDX spectrum of Ni$_2$P :5F, (g) XPS spectra of Ni, (h) XPS spectra of P, and (i) ^{19}F MAS spectra of Ni$_2$P:7.5F at 20 kHz spinning speed

Appendix G Figure 2(a) shows the XRD pattern of as-synthesized IrO_2, which exhibits the rutile type tetragonal structure, similar to earlier studies.[137, 215, 541, 542] The Ni_2P:2.5F, Ni_2P:5F, and Ni_2P:7.5F exhibit hexagonal structure similar to pure Ni_2P without any other peaks of Ni, P or F based compounds; suggesting the formation of homogeneous single phase solid solution of as-synthesized Ni_2P: xF (x= 2.5, 5, 7.5).[362, 363] The SEM micrograph [**Appendix G Figure 2b-c**)] combined with the elemental x-ray maps of representative composition i.e. Ni_2P:5F [**Appendix G Figure 2d-e**)] shows the co-existence of Ni and P elements. The elemental x-ray maps of Ni and P of Ni_2P: 5F reveal that the Ni and P elements are homogeneously present within the as-synthesized particles of Ni_2P: 5F electrocatalyst powder without segregation at any specific site. The quantitative elemental composition analysis of Ni_2P:5F obtained from EDX [**Appendix G Figure 2(f**)] showed the measured elemental composition of Ni and P is close to the nominal composition. The XPS spectrum of Ni in Ni_2P [**Appendix G Figure 2(g**)] shows the presence of Ni $2p_{3/2}$ and $2p_{1/2}$ doublet centered at ~ 852.5 eV and ~ 869.70 eV respectively, while XPS spectrum of P 2p (for Ni_2P) [**Appendix G Figure 2(h**)] displayed a dominant peak at ~ 129.4 eV which is assigned to the P $2p_{3/2}$.[50] The other peak at ~133.7 eV in P 2p region can be ascribed to the oxidized P species.[50] The presence of F in Ni_2P:5F could not be unequivocally determined by the XPS, EDX as well as NMR, which is in agreement with previous studies.[357, 358] However, the positive shifts of ~ 0.4-0.5 eV in binding energy values of Ni 2p and P 2p doublet positions w.r.t. pure Ni_2P, suggests modification of electronic structure after incorporation of highly electronegative F in the solid solution lattice of Ni_2P.[357] The unusually large ^{31}P resonances are due to the metallic nature of the material causing a Knight shift. The 5 wt. % doping of F in Ni_2P does not produce any significant changes to the crystal structure of Ni_2P resulting in a very similar ^{31}P NMR spectrum whereas higher F content (Ni_2P:7.5F) reveals the presence of F in Ni_2P:7.5F

[**Appendix G Figure 2(i)**]. **Appendix G Figure 3** shows the ^{31}P MAS spectra of Ni_2P with 5wt. % F and without F doping. Two very different sets of resonances around 1500 and 4060 ppm are seen for both the materials. This is due to the two crystallographically inequivalent phosphorous atoms in the unit cell of Ni_2P.[543]

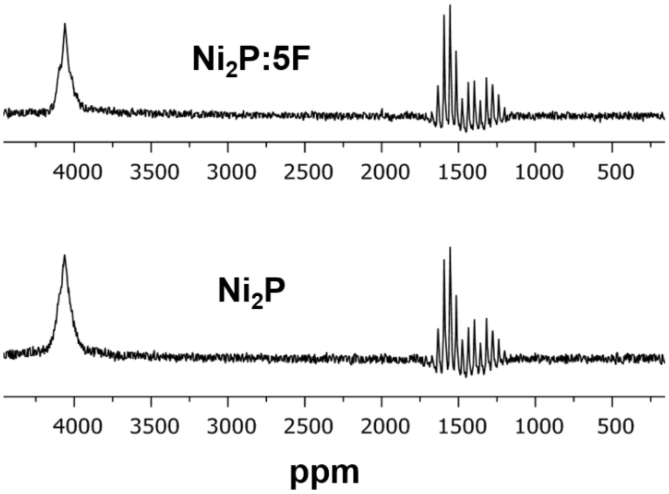

Appendix G Figure 3 ^{31}P MAS spectra of Ni_2P and Ni_2P:5 wt.%F at 8 kHz spinning speed

In order to assess the electrocatalytic activity, the electrochemical impedance spectroscopy (EIS) for Ni_2P: xF (x=0, 2.5, 5 and 7.5) and IrO_2 is performed at 1.55V (*vs* RHE) in the 1 M KOH at 40°C [**Appendix G Figure 4(a)**]. The charge transfer resistance (R_{ct}) determined from the diameter of the semi-circle in the high frequency region of the EIS plot of Ni_2P: 5F (~ 10.65 Ω cm^2) is significantly lower than Ni_2P (~ 31.4 $\Omega.cm^2$), Ni_2P: 2.5F (~ 23.2 Ω. cm^2), Ni_2P: 7.5F (~ 18.9 $\Omega.cm^2$), and IrO_2 (~ 34.6 $\Omega.cm^2$) [**Appendix G Figure 4(a)**] which clearly suggests that the lower activation polarization and higher charge transfer kinetics of Ni_2P: 5F in comparison to other ECs. This result is indeed in good agreement with the DFT results, suggesting the improved electronic structure of Ni_2P: 5F. **Appendix G Figure 4(b)** shows the OER polarization curves of as-synthesized ECs.

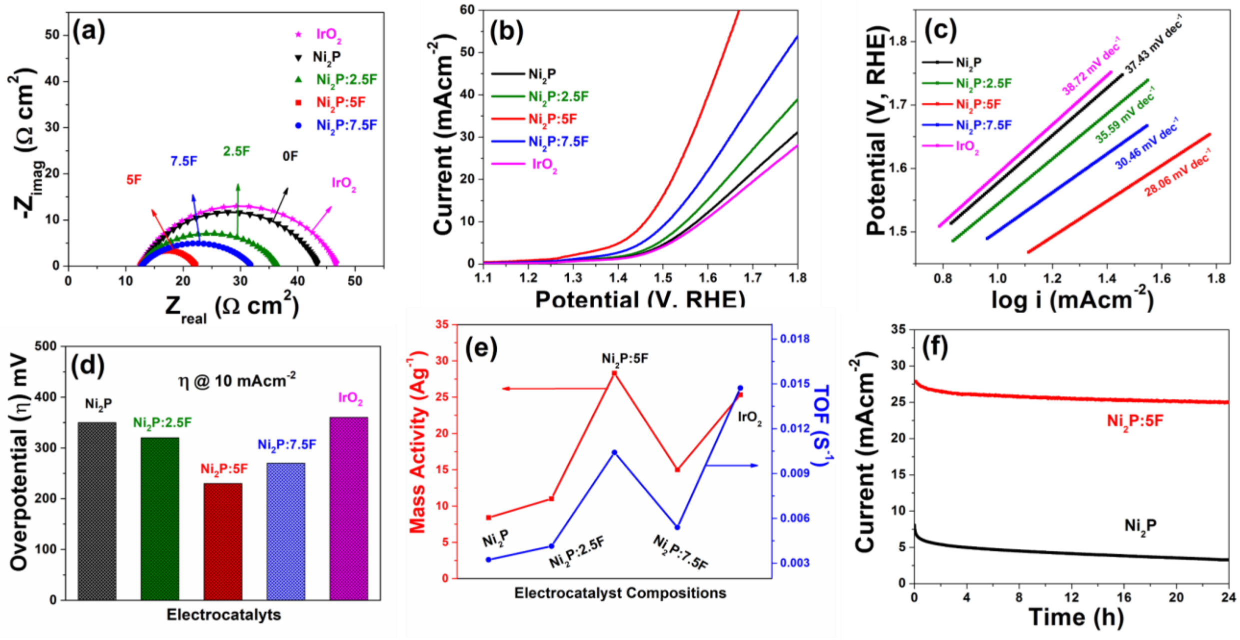

Appendix G Figure 4 (a) EIS spectra, (b) OER polarization curves, (c) Tafel plots, (d) Overpotential at 10 mAcm^{-2}, (e) Mass activity and turnover frequency, and (f) Chronoamperometry tests

It can be viewed that Ni_2P:5F clearly outperforms Ni_2P: xF (x=0, 2.5, and 7.5) and IrO_2 ECs in terms of current density. The superior electrocatalytic activity of Ni_2P: 5F is indeed attributed to the beneficial optimized surface electronic structure and lower R_{ct} as evidenced from theoretical and EIS study, respectively. Furthermore, as can be seen from **Appendix G Figure 4(c)** the lowest Tafel slope of 28.06 mV dec^{-1} and overpotential (η) of only 230 mV to attain 10 mA cm^{-2} for Ni_2P:5F [**Appendix G Figure 4(d)**] in comparison to other counterparts suggests its favorable OER kinetics i.e., likely faster electron transport and enhanced electrocatalytic activity which is ascribed to the reduced OER barrier for fluorinated Ni_2P. Another important parameter to evaluate the activity of ECs is the turnover frequency (TOF). As anticipated from the impedance as well as polarization curves, the Ni_2P:5F electrocatalyst possesses TOF of 0.0104 S^{-1} and mass activity of 28.3 A g^{-1} [**Appendix G Figure 4(e)**] significantly higher than that of other as-synthesized ECs (**Appendix G Table 1**), evidently elucidating the higher OER activity of Ni_2P:5F. Thus, the lower overpotential, smaller Tafel slope, and higher mass activity in comparison to other counterparts are an excellent indicator of the promising OER performance of Ni_2P:5F in alkaline water splitting.

Appendix G Table 2 ICP-OES analysis on 1N KOH electrolyte solution collected after 24 h of chronoamperometry test

Electrocatalyst	**Elements**	**Concentration (ppm)**
Ni_2P	Ni	$11.3\times10^{-3} \pm 0.003$
	P	$8.0\times10^{-3} \pm 0.0002$
Ni_2P:5F	Ni	$7.2\times10^{-3} \pm 0.002$
	P	$6.5\times10^{-3} \pm 0.0001$

Furthermore, the electrocatalytic stability of highly active Ni_2P:5F has been studied by conducting the chronoamperometry (CA) test at constant potential of ~1.55 V (*vs* RHE) in 1M KOH at 40^{o}C. As shown in **Appendix G Figure 4(f)** Ni_2P:5F reveals an excellent electrochemical stability, retaining ~95 % of its initial current density in comparison to pure Ni_2P (~50% current retention) with minimum elemental dissolution (**Appendix G Table 2**). Recently, copious research efforts have been devoted to investigate the stabilizing effect of F on various electrocatalyst materials.[33, 178, 181] In the study conducted by Binninger et al.[181], oxygen anion-free salts containing anion species such as fluorides, chlorides, or sulfates with a very high oxidation potential are favorable candidates for truly thermodynamically stable OER catalysts. Thus, herein, the F doping not only offers enhancement in the activity, but it is also advantageous for the stability of electrocatalyst for prolonged OER. Accordingly, this study thus offers a promising foundation for designing and improving the electrocatalyic activity via F incorporation in the PGM-free ECs.

Conclusions

In conclusion, employing DFT based calculations for rationalizing the thermodynamics and OER kinetics, we report Ni_2P: x wt. %F as a high performance electrocatalyst for OER in alkaline media. The as-synthesized Ni_2P:5F possessing optimized electronic structure and reduced OER barrier demonstrates excellent electrochemical activity with lower charge transfer resistance (10.65 Ω cm^2), lower overpotential (230 mV @ 10 mA cm^{-2}), smaller Tafel slope (28.06 mV dec^{-1}), and higher mass activity (28.3 A g^{-1}), suggesting its promise for efficient water oxidation in comparison to as-synthesized Ni_2P:x wt.%F (x= 0, 2.5, and 7.5). The highly active optimum composition of Ni_2P:5F also displays a superior long term electrochemical stability in the alkaline OER, with no major degradation in the current density. Thus, the present work provides a promising F doping approach for improving electronic structure, and thus, electrocatalytic performance of PGM-free electrocatalysts.

.

Bibliography

1. R. Newell, D. Raimi and G. Aldana, *Resources for the Future*, **8** (2019).

2. T. Shinagawa and K. Takanabe, *ChemSusChem*, **10**, 1318 (2017).

3. G. Resch, A. Held, T. Faber, C. Panzer, F. Toro and R. Haas, *Energy Policy*, **36**, 4048 (2008).

4. X. Peng, C. He, X. Fan, Q. Liu, J. Zhang and H. Wang, *International Journal of Hydrogen Energy*, **39**, 14166 (2014).

5. A. Ursua, L. M. Gandia and P. Sanchis, *Proceedings of the IEEE*, **100**, 410 (2012).

6. X. Kong and Z. Peng, *Materials today chemistry*, **11**, 119 (2019).

7. E. Fabbri and T. J. Schmidt, *ACS Catalysis*, **8**, 9765 (2018).

8. J. Suntivich, K. J. May, H. A. Gasteiger, J. B. Goodenough and Y. Shao-Horn, *Science*, **334**, 1383 (2011).

9. F. Barbir, *Sol. Energy*, **78**, 661 (2005).

10. C. Schroeder, in *The Hydrogen Energy Transition*, S. Daniel and S. C. James Editors, p. 121, Academic Press, Burlington (2004).

11. P. Millet, N. Mbemba, S. A. Grigoriev, V. N. Fateev, A. Aukauloo and C. Etievant, *International Journal of Hydrogen Energy*, **36**, 4134 (2011).

12. M. W. Kanan and D. G. Nocera, *Science*, **321**, 1072 (2008).

13. M. F. Hordeski, *Hydrogen & Fuel Cells: Advances in Transportation and Power*, Fairmont Press (2009).

14. C. J. Winter, *International Journal of Hydrogen Energy*, **34**, S1 (2009).

15. K. Zeng and D. K. Zhang, *Prog. Energy Combust. Sci.*, **36**, 307 (2010).

16. R. E. Clarke, S. Giddey and S. P. S. Badwal, *International Journal of Hydrogen Energy*, **35**, 928 (2010).

17. G. W. Crabtree, M. S. Dresselhaus and M. V. Buchanan, *Phys. Today*, **57**, 39 (2004).

18. Q. He, T. Mugadza, X. Kang, X. Zhu, S. Chen, J. Kerr and T. Nyokong, *Journal of Power Sources*, **216**, 67 (2012).

19. J. I. Levene, M. K. Mann, R. M. Margolis and A. Milbrandt, *Sol. Energy*, **81**, 773 (2007).

20. Y. H. P. Zhang and W.-D. Huang, *Trends in Biotechnology*, **30**, 301 (2012).

21. F. M. Sapountzi, J. M. Gracia, H. O. A. Fredriksson and J. W. H. Niemantsverdriet, *Prog. Energy Combust. Sci.*, **58**, 1 (2017).

22. M. Carmo, D. L. Fritz, J. Mergel and D. Stolten, *International Journal of Hydrogen Energy*, **38**, 4901 (2013).

23. P. Millet and S. Grigoriev, in *Renewable Hydrogen Technologies*, L. M. Gandía, G. Arzamendi and P. M. Diéguez Editors, p. 19, Elsevier, Amsterdam (2013).

24. O. Schmidt, A. Gambhir, I. Staffell, A. Hawkes, J. Nelson and S. Few, *International Journal of Hydrogen Energy*, **42**, 30470 (2017).

25. P. P. Edwards, V. L. Kuznetsov, W. I. F. David and N. P. Brandon, *Energy Policy*, **36**, 4356 (2008).

26. A. Marshall, (2005).

27. Y. Yan, B. Y. Xia, B. Zhao and X. Wang, *Journal of Materials Chemistry A*, **4**, 17587 (2016).

28. S. S. Kumar and V. Himabindu, *Materials Science for Energy Technologies* (2019).

29. L. B. Railsback, *Geology*, **31**, 737 (2003).

30. H. Renner and G. Schmuckler, *Handbook of extractive metallurgy. Wiley-VCH, Weinheim*, 1269 (1997).

31. M. Mahdi Najafpour, D. Jafarian Sedigh, S. Maedeh Hosseini and I. Zaharieva, *Inorganic chemistry*, **55**, 8827 (2016).

32. S. Ardizzone, C. L. Bianchi, G. Cappelletti, M. Ionita, A. Minguzzi, S. Rondinini and A. Vertova, *Journal of Electroanalytical Chemistry*, **589**, 160 (2006).

33. T. Reier, Z. Pawolek, S. Cherevko, M. Bruns, T. Jones, D. Teschner, S. r. Selve, A. Bergmann, H. N. Nong and R. Schlögl, *Journal of the American Chemical Society*, **137**, 13031 (2015).

34. C. K. Dyer, *Journal of the Electrochemical Society*, **132**, 64 (1985).

35. K. Kadakia, M. K. Datta, O. I. Velikokhatnyi, P. Jampani, S. K. Park, P. Saha, J. A. Poston, A. Manivannan and P. N. Kumta, *international journal of hydrogen energy*, **37**, 3001 (2012).

36. M. H. P. Santana and L. A. De Faria, *Electrochimica acta*, **51**, 3578 (2006).

37. A. Marshall, B. Børresen, G. Hagen, M. Tsypkin and R. Tunold, *Materials Chemistry and Physics*, **94**, 226 (2005).

38. R. S. Yeo, J. Orehotsky, W. Visscher and S. Srinivasan, *Journal of The Electrochemical Society*, **128**, 1900 (1981).

39. X.-M. Wang, J.-M. Hu and J.-Q. Zhang, *Electrochimica Acta*, **55**, 4587 (2010).

40. J.-J. Zhang, J.-M. Hu, J.-Q. Zhang and C.-N. Cao, *international journal of hydrogen energy*, **36**, 5218 (2011).

41. M. V. Makarova, J. Jirkovský, M. Klementová, I. Jirka, K. Macounová and P. Krtil, *Electrochimica Acta*, **53**, 2656 (2008).

42. J. Cheng, H. Zhang, H. Ma, H. Zhong and Y. Zou, *international journal of hydrogen energy*, **34**, 6609 (2009).

43. M. H. P. Santana, L. M. Da Silva and L. A. De Faria, *Electrochimica acta*, **48**, 1885 (2003).

44. G. Liu, J. Xu, Y. Wang and X. Wang, *Journal of Materials Chemistry A*, **3**, 20791 (2015).

45. S. D. Ghadge, O. I. Velikokhatnyi, M. K. Datta, P. M. Shanthi, S. Tan, K. Damodaran and P. N. Kumta, *ACS Catalysis*, 2134 (2019).

46. J. Luo, J.-H. Im, M. T. Mayer, M. Schreier, M. K. Nazeeruddin, N.-G. Park, S. D. Tilley, H. J. Fan and M. Grätzel, *Science*, **345**, 1593 (2014).

47. Y. Jiao, Y. Zheng, M. Jaroniec and S. Z. Qiao, *Chemical Society Reviews*, **44**, 2060 (2015).

48. P. Xu, J. Zhang, Z. Ye, Y. Liu, T. Cen and D. Yuan, *Applied Surface Science*, **494**, 749 (2019).

49. M. A. Khan, H. Zhao, W. Zou, Z. Chen, W. Cao, J. Fang, J. Xu, L. Zhang and J. Zhang, *Electrochemical Energy Reviews*, **1**, 483 (2018).

50. P. P. Patel, O. I. Velikokhatnyi, S. D. Ghadge, P. J. Hanumantha, M. K. Datta, R. Kuruba, B. Gattu, P. M. Shanthi and P. N. Kumta, *International Journal of Hydrogen Energy*, **43**, 7855 (2018).

51. P. Xiao, M. A. Sk, L. Thia, X. Ge, R. J. Lim, J.-Y. Wang, K. H. Lim and X. Wang, *Energy & Environmental Science*, **7**, 2624 (2014).

52. P. Liu, J. A. Rodriguez, T. Asakura, J. Gomes and K. Nakamura, *The Journal of Physical Chemistry B*, **109**, 4575 (2005).

53. S. Zhao.

54. X. Chen, S. Shen, L. Guo and S. S. Mao, *Chemical Reviews*, **110**, 6503 (2010).

55. M. G. Walter, E. L. Warren, J. R. McKone, S. W. Boettcher, Q. Mi, E. A. Santori and N. S. Lewis, *Chemical reviews*, **110**, 6446 (2010).

56. A. Fujishima, *nature*, **238**, 37 (1972).

57. U. DOE, *US Department of Energy, Office of Energy Efficiency and Renewable Energy, Hydrogen, Fuel Cells and Infrastructure Technologies Program (HFCIT)*, 1 (2010).

58. E. Miller, N. Gaillard, J. Kaneshiro, A. DeAngelis and R. Garland, *International Journal of Energy Research*, **34**, 1215 (2010).

59. Z. Zhang and J. T. Yates, *Chemical Reviews*, **112**, 5520 (2012).

60. S. Larsson, *Chemical Physics: Electrons and Excitations*, CRC Press (2012).

61. S. J. Pearton, C. R. Abernathy and F. Ren, *Gallium nitride processing for electronics, sensors and spintronics*, Springer Science & Business Media (2006).

62. K. D. Sattler, *Handbook of nanophysics: principles and methods*, CRC Press (2010).

63. G. Wang, H. Wang, Y. Ling, Y. Tang, X. Yang, R. C. Fitzmorris, C. Wang, J. Z. Zhang and Y. Li, *Nano Letters*, **11**, 3026 (2011).

64. A. Kushwaha and M. Aslam, *Electrochimica Acta*, **130**, 222 (2014).

65. R. Sasikala, A. Shirole, V. Sudarsan, T. Sakuntala, C. Sudakar, R. Naik and S. R. Bharadwaj, *International Journal of Hydrogen Energy*, **34**, 3621 (2009).

66. C. W. Lai and S. Sreekantan, *Electrochimica Acta*, **87**, 294 (2013).

67. H. Han, S. Shin, J. Noh, I. Cho and K. Hong, *JOM*, **66**, 664 (2014).

68. C. W. Cheng, W. N. Ren and H. F. Zhang, *Nano Energy*, **5**, 132 (2014).

69. S. D. Ghadge, P. P. Patel, M. K. Datta, O. I. Velikokhatnyi, P. M. Shanthi and P. N. Kumta, *Journal of Power Sources*, **392**, 139 (2018).

70. S. D. Ghadge, P. P. Patel, M. K. Datta, O. I. Velikokhatnyi, R. Kuruba, P. M. Shanthi and P. N. Kumta, *RSC Advances*, **7**, 17311 (2017).

71. M. Ball and M. Wietschel, *International Journal of Hydrogen Energy*, **34**, 615 (2009).

72. I. Katsounaros, S. Cherevko, A. R. Zeradjanin and K. J. J. Mayrhofer, *Angewandte Chemie International Edition*, **53**, 102 (2014).

73. K. Zeng and D. Zhang, *Prog. Energy Combust. Sci.*, **36**, 307 (2010).

74. P. P. Patel, P. J. Hanumantha, O. I. Velikokhatnyi, M. K. Datta, B. Gattu, J. A. Poston, A. Manivannan and P. N. Kumta, *Materials Science and Engineering: B*, **208**, 1 (2016).

75. P. P. Patel, P. J. Hanumantha, O. I. Velikokhatnyi, M. K. Datta, D. Hong, B. Gattu, J. A. Poston, A. Manivannan and P. N. Kumta, *Journal of Power Sources*, **299**, 11 (2015).

76. P. P. Patel, M. K. Datta, O. I. Velikokhatnyi, P. Jampani, D. Hong, J. A. Poston, A. Manivannan and P. N. Kumta, *Journal of Materials Chemistry A*, **3**, 14015 (2015).

77. M. Fischer, M. Werber and P. V. Schwartz, *Energy Policy*, **37**, 2639 (2009).

78. P. P. Patel, M. K. Datta, O. I. Velikokhatnyi, R. Kuruba, K. Damodaran, P. Jampani, B. Gattu, P. M. Shanthi, S. S. Damle and P. N. Kumta, *Scientific Reports*, **6** (2016).

79. K. Shimura and H. Yoshida, *Energy & Environmental Science*, **4**, 2467 (2011).

80. N. Himeshima and Y. Amao, *Green Chemistry*, **7**, 742 (2005).

81. A. T. Marshall, S. Sunde, M. Tsypkin and R. Tunold, *International Journal of Hydrogen Energy*, **32**, 2320 (2007).

82. A. H. A. Rahim, A. S. Tijani, S. K. Kamarudin and S. Hanapi, *Journal of Power Sources*, **309**, 56 (2016).

83. P. Millet, N. Mbemba, S. A. Grigoriev, V. N. Fateev, A. Aukauloo and C. Etiévant, *International Journal of Hydrogen Energy*, **36**, 4134 (2011).

84. S. A. Grigoriev, V. I. Porembsky and V. N. Fateev, *International Journal of Hydrogen Energy*, **31**, 171 (2006).

85. A. S. Aricò, V. Baglio, N. Briguglio, G. Maggio and S. Siracusano, *Fuel Cells: Data, Facts and Figures* (2016).

86. X. Lu and C. Zhao, *Nat Commun*, **6** (2015).

87. J. Xu, M. Wang, G. Liu, J. Li and X. Wang, *Electrochimica Acta*, **56**, 10223 (2011).

88. A. Skulimowska, M. Dupont, M. Zaton, S. Sunde, L. Merlo, D. J. Jones and J. Rozière, *International Journal of Hydrogen Energy*, **39**, 6307 (2014).

89. S. A. Grigoriev, P. Millet and V. N. Fateev, *Journal of Power Sources*, **177**, 281 (2008).

90. Y. Matsumoto and E. Sato, *Materials chemistry and physics*, **14**, 397 (1986).

91. C. C. L. McCrory, S. Jung, J. C. Peters and T. F. Jaramillo, *Journal of the American Chemical Society*, **135**, 16977 (2013).

92. E. Mayousse, F. Maillard, F. Fouda-Onana, O. Sicardy and N. Guillet, *international journal of hydrogen energy*, **36**, 10474 (2011).

93. K. Kadakia, M. K. Datta, P. H. Jampani, S. K. Park and P. N. Kumta, *Journal of Power Sources*, **222**, 313 (2013).

94. K. S. Kadakia, P. Jampani, O. I. Velikokhatnyi, M. K. Datta, S. J. Chung, J. A. Poston, A. Manivannan and P. N. Kumta, *Journal of The Electrochemical Society*, **161**, F868 (2014).

95. J. M. Hu, H. M. Meng, J. Q. Zhang and C. N. Cao, *Corrosion Science*, **44**, 1655 (2002).

96. C. P. De Pauli and S. Trasatti, *Journal of Electroanalytical Chemistry*, **396**, 161 (1995).

97. M. K. Datta, K. Kadakia, O. I. Velikokhatnyi, P. H. Jampani, S. J. Chung, J. A. Poston, A. Manivannan and P. N. Kumta, *Journal of Materials Chemistry A*, **1**, 4026 (2013).

98. K. Kadakia, M. K. Datta, O. I. Velikokhatnyi, P. H. Jampani and P. N. Kumta, *international journal of hydrogen energy*, **39**, 664 (2014).

99. R. G. Gonzalez-Huerta, G. Ramos-Sanchez and P. B. Balbuena, *Journal of Power Sources*, **268**, 69 (2014).

100. W. Sun, L. Cao and J. Yang, *Journal of Materials Chemistry A* (2016).

101. J. Rossmeisl, Z. W. Qu, H. Zhu, G. J. Kroes and J. K. Nørskov, *Journal of Electroanalytical Chemistry*, **607**, 83 (2007).

102. O. I. Velikokhatnyi, K. Kadakia, M. K. Datta and P. N. Kumta, *The Journal of Physical Chemistry C*, **117**, 20542 (2013).

103. G. Kresse and J. Furthmüller, *Physical review B*, **54**, 11169 (1996).

104. G. Kresse and J. Furthmüller, *Computational materials science*, **6**, 15 (1996).

105. G. Kresse and D. Joubert, *Physical Review B*, **59**, 1758 (1999).

106. J. P. Perdew and W. Yue, *Physical review B*, **33**, 8800 (1986).

107. G. N. Murshudov, A. A. Vagin and E. J. Dodson, *Acta Crystallographica Section D: Biological Crystallography*, **53**, 240 (1997).

108. P. R. Zafred, J. T. Dederer, J. E. Gillett, R. A. Basel and A. B. Antenucci, Purge gas protected transportable pressurized fuel cell modules and their operation in a power plant, in, Google Patents (1996).

109. H. Hu, Y. Fan and H. Liu, *International Journal of Hydrogen Energy*, **34**, 8535 (2009).

110. J. A. V. Butler, *Proceedings of the Royal Society of London. Series A, Mathematical and Physical Sciences*, **157**, 423 (1936).

111. P. P. Patel, M. K. Datta, P. H. Jampani, D. Hong, J. A. Poston, A. Manivannan and P. N. Kumta, *Journal of Power Sources*, **293**, 437 (2015).

112. K. S. Kadakia, P. H. Jampani, O. I. Velikokhatnyi, M. K. Datta, S. K. Park, D. H. Hong, S. J. Chung and P. N. Kumta, *Journal of Power Sources*, **269**, 855 (2014).

113. B. Hammer and J. K. Nørskov, *Advances in catalysis*, **45**, 71 (2000).

114. T. Bligaard and J. K. Nørskov, *Electrochimica Acta*, **52**, 5512 (2007).

115. V. Subramanian, H. Zhu, R. Vajtai, P. M. Ajayan and B. Wei, *The Journal of Physical Chemistry B*, **109**, 20207 (2005).

116. P. P. Patel, P. H. Jampani, M. K. Datta, O. I. Velikokhatnyi, D. Hong, J. A. Poston, A. Manivannan and P. N. Kumta, *Journal of Materials Chemistry A*, **3**, 18296 (2015).

117. J. Xu, G. Liu, J. Li and X. Wang, *Electrochimica acta*, **59**, 105 (2012).

118. D. J. Davis, T. N. Lambert, J. A. Vigil, M. A. Rodriguez, M. T. Brumbach, E. N. Coker and S. J. Limmer, *The Journal of Physical Chemistry C*, **118**, 17342 (2014).

119. M. Sugantha, P. A. Ramakrishnan, A. M. Hermann, C. P. Warmsingh and D. S. Ginley, *International Journal of Hydrogen Energy*, **28**, 597 (2003).

120. C. S. Johnson, D. W. Dees, M. F. Mansuetto, M. M. Thackeray, D. R. Vissers, D. Argyriou, C. K. Loong and L. Christensen, *Journal of power sources*, **68**, 570 (1997).

121. K. Kadakia, M. K. Datta, O. I. Velikokhatnyi, P. H. Jampani and P. N. Kumta, *International Journal of Hydrogen Energy*, **39**, 664 (2014).

122. N. Krstajic and S. Trasatti, *Journal of Applied Electrochemistry*, **28**, 1291 (1998).

123. A. Minguzzi, F.-R. F. Fan, A. Vertova, S. Rondinini and A. J. Bard, *Chemical Science*, **3**, 217 (2012).

124. P. P. Patel, P. H. Jampani, M. K. Datta, O. I. Velikokhatnyi, D. Hong, J. A. Poston, A. Manivannan and P. N. Kumta, *Journal of Materials Chemistry A*, **3**, 18296 (2015).

125. A. M. Mohammad, M. I. Awad, M. S. El-Deab, T. Okajima and T. Ohsaka, *Electrochimica Acta*, **53**, 4351 (2008).

126. F. Cheng, Y. Su, J. Liang, Z. Tao and J. Chen, *Chemistry of Materials*, **22**, 898 (2009).

127. M. Morita, C. Iwakura and H. Tamura, *Electrochimica Acta*, **22**, 325 (1977).

128. K. Kadakia, M. K. Datta, P. H. Jampani, S. K. Park and P. N. Kumta, *Journal of Power Sources*, **222**, 313 (2013).

129. R. H. Blessing, *Crystallography Reviews*, **1**, 3 (1987).

130. C. Zhao, H. Yu, Y. Li, X. Li, L. Ding and L. Fan, *Journal of Electroanalytical Chemistry*, **688**, 269 (2013).

131. H. W. Nesbitt and D. Banerjee, *American Mineralogist*, **83**, 305 (1998).

132. X. Liang, C. Hart, Q. Pang, A. Garsuch, T. Weiss and L. F. Nazar, *Nature communications*, **6** (2015).

133. Z. Li, Y. Mi, X. Liu, S. Liu, S. Yang and J. Wang, *Journal of Materials Chemistry*, **21**, 14706 (2011).

134. M. A. Stranick, *Surface Science Spectra*, **6**, 31 (1999).

135. M. Sathish, B. Viswanathan, R. P. Viswanath and C. S. Gopinath, *Chemistry of Materials*, **17**, 6349 (2005).

136. K. Kadakia, M. K. Datta, O. I. Velikokhatnyi, P. Jampani, S. K. Park, S. J. Chung and P. N. Kumta, *Journal of Power Sources*, **245**, 362 (2014).

137. K. S. Kadakia, P. H. Jampani, O. I. Velikokhatnyi, M. K. Datta, S. K. Park, D. H. Hong, S. J. Chung and P. N. Kumta, *Journal of Power Sources*, **269**, 855 (2014).

138. L. Trotochaud, J. K. Ranney, K. N. Williams and S. W. Boettcher, *Journal of the American Chemical Society*, **134**, 17253 (2012).

139. Y. Lu, S. Du and R. Steinberger-Wilckens, *Applied Catalysis B: Environmental*, **199**, 292 (2016).

140. P. Chen, K. Xu, Z. Fang, Y. Tong, J. Wu, X. Lu, X. Peng, H. Ding, C. Wu and Y. Xie, *Angewandte Chemie*, **127**, 14923 (2015).

141. C.-L. Zhang and S.-H. Yu, *Chemical Society Reviews*, **43**, 4423 (2014).

142. S. M. Bergin, Y.-H. Chen, A. R. Rathmell, P. Charbonneau, Z.-Y. Li and B. J. Wiley, *Nanoscale*, **4**, 1996 (2012).

143. K. Gong, F. Du, Z. Xia, M. Durstock and L. Dai, *Science*, **323**, 760 (2009).

144. C. Koenigsmann and S. S. Wong, *Energy & Environmental Science*, **4**, 1161 (2011).

145. Q.-Z. Jiang, X. Wu, M. Shen, Z.-F. Ma and X.-Y. Zhu, *Catalysis Letters*, **124**, 434 (2008).

146. Y. Kim, J. G. Kim, Y. Noh and W. B. Kim, *Catalysis Surveys from Asia*, **19**, 88 (2015).

147. G. Zhang, S. Sun, M. Cai, Y. Zhang, R. Li and X. Sun, *Scientific reports*, **3** (2013).

148. P. P. Patel, P. J. Hanumantha, O. I. Velikokhatnyi, M. K. Datta, D. Hong, B. Gattu, J. A. Poston, A. Manivannan and P. N. Kumta, *Journal of Power Sources*, **299**, 11 (2015).

149. Y. G. Guo, J. S. Hu, H. M. Zhang, H. P. Liang, L. J. Wan and C. L. Bai, *Advanced Materials*, **17**, 746 (2005).

150. H.-M. Zhang, Y.-G. Guo, L.-J. Wan and C.-L. Bai, *Chemical Communications*, 3022 (2003).

151. B. Xiang, P. Wang, X. Zhang, S. A. Dayeh, D. P. R. Aplin, C. Soci, D. Yu and D. Wang, *Nano Letters*, **7**, 323 (2007).

152. V. F. Puntes, K. M. Krishnan and A. P. Alivisatos, *Science*, **291**, 2115 (2001).

153. Y. Wu and P. Yang, *Journal of the American Chemical Society*, **123**, 3165 (2001).

154. S. Y. Li, P. Lin, C. Y. Lee and T. Y. Tseng, *Journal of applied physics*, **95**, 3711 (2004).

155. H. Wang and L. Gao, *Current Opinion in Electrochemistry*, **7**, 7 (2018).

156. F. Aziz, A. A. Bakar, Z. Ahmad, T. M. Bawazeer, N. Alsenany, M. S. Alsoufi and A. Supangat, *Materials Letters*, **211**, 195 (2018).

157. J. R. Ota and S. K. Srivastava, *Nanotechnology*, **16**, 2415 (2005).

158. X. Zhang, Y. Liu and Z. Kang, *ACS applied materials & interfaces*, **6**, 4480 (2014).

159. J. Chung, J. Myoung, J. Oh and S. Lim, *The Journal of Physical Chemistry C*, **114**, 21360 (2010).

160. L. E. Greene, B. D. Yuhas, M. Law, D. Zitoun and P. Yang, *Inorganic chemistry*, **45**, 7535 (2006).

161. H. Liang, F. Meng, M. Cabán-Acevedo, L. Li, A. Forticaux, L. Xiu, Z. Wang and S. Jin, *Nano letters*, **15**, 1421 (2015).

162. Y. Tong, J. Xu, H. Jiang, F. Gao and Q. Lu, *Chemical Engineering Journal*, **316**, 225 (2017).

163. M. Bernicke, E. Ortel, T. Reier, A. Bergmann, J. Ferreira de Araujo, P. Strasser and R. Kraehnert, *ChemSusChem*, **8**, 1908 (2015).

164. S. Geiger, O. Kasian, B. R. Shrestha, A. M. Mingers, K. J. J. Mayrhofer and S. Cherevko, *Journal of The Electrochemical Society*, **163**, F3132 (2016).

165. D. F. Abbott, D. Lebedev, K. Waltar, M. Povia, M. Nachtegaal, E. Fabbri, C. Copéret and T. J. Schmidt, *Chemistry of Materials*, **28**, 6591 (2016).

166. P. P. Patel, P. J. Hanumantha, O. I. Velikokhatnyi, M. K. Datta, B. Gattu, J. A. Poston, A. Manivannan and P. N. Kumta, *Materials Science and Engineering: B*, **208**, 1 (2016).

167. W. K. Choi, H. J. Jung and S. K. Koh, *Journal of Vacuum Science & Technology A: Vacuum, Surfaces, and Films*, **14**, 359 (1996).

168. R. Kötz, S. Stucki and B. Carcer, *Journal of Applied Electrochemistry*, **21**, 14 (1991).

169. X. Sun, L. Gao, C. Guo, Y. Zhang, X. Kuang, T. Yan, L. Ji and Q. Wei, *Electrochimica Acta*, **247**, 843 (2017).

170. J. Yu, F.-X. Ma, Y. Du, P.-P. Wang, C.-Y. Xu and L. Zhen, *ChemElectroChem*, **4**, 594 (2017).

171. T. Hepel, F. H. Pollak and W. E. O'Grady, *Journal of The Electrochemical Society*, **132**, 2385 (1985).

172. H. Wang, C. Xu, F. Cheng, M. Zhang, S. Wang and S. P. Jiang, *Electrochemistry Communications*, **10**, 1575 (2008).

173. H. S. Oh, H. N. Nong and P. Strasser, *Advanced Functional Materials*, **25**, 1074 (2015).

174. H. N. Nong, H. S. Oh, T. Reier, E. Willinger, M. G. Willinger, V. Petkov, D. Teschner and P. Strasser, *Angewandte Chemie International Edition*, **54**, 2975 (2015).

175. H.-S. Oh, H. N. Nong, T. Reier, M. Gliech and P. Strasser, *Chemical Science*, **6**, 3321 (2015).

176. S. Jung, C. C. L. McCrory, I. M. Ferrer, J. C. Peters and T. F. Jaramillo, *Journal of Materials Chemistry A*, **4**, 3068 (2016).

177. B. M. Tackett, W. Sheng, S. Kattel, S. Yao, B. Yan, K. A. Kuttiyiel, Q. Wu and J. G. Chen, (2018).

178. S. Geiger, O. Kasian, A. M. Mingers, K. J. J. Mayrhofer and S. Cherevko, *Scientific Reports*, **7**, 4595 (2017).

179. Y.-R. Luo, *Comprehensive handbook of chemical bond energies*, CRC press (2007).

180. T. Binninger, R. Mohamed, K. Waltar, E. Fabbri, P. Levecque, R. Kötz and T. J. Schmidt, *Scientific reports*, **5** (2015).

181. T. Binninger, R. Mohamed, K. Waltar, E. Fabbri, P. Levecque, R. Kötz and T. J. Schmidt, *Scientific reports*, **5**, 12167 (2015).

182. S. Siracusano, V. Baglio, S. A. Grigoriev, L. Merlo, V. N. Fateev and A. S. Aricò, *Journal of Power Sources*, **366**, 105 (2017).

183. J. F. Moulder, W. F. Stickle, P. E. Sobol and K. D. Bomben, *Eden Prairie, MN*, 119 (1995).

184. V. Pfeifer, T. E. Jones, J. J. V. Vélez, C. Massué, M. T. Greiner, R. Arrigo, D. Teschner, F. Girgsdies, M. Scherzer and J. Allan, *Physical Chemistry Chemical Physics*, **18**, 2292 (2016).

185. S. Cherevko, S. Geiger, O. Kasian, N. Kulyk, J.-P. Grote, A. Savan, B. R. Shrestha, S. Merzlikin, B. Breitbach and A. Ludwig, *Catalysis Today*, **262**, 170 (2016).

186. B. Obama, *Science*, **355**, 126 (2017).

187. S. D. Ghadge, P. P. Patel, M. K. Datta, O. I. Velikokhatnyi, P. M. Shanthi and P. N. Kumta, *J. Power Sources*, **392**, 139 (2018).

188. S. Dunn, *International journal of hydrogen energy*, **27**, 235 (2002).

189. P. P. Patel, O. I. Velikokhatnyi, S. D. Ghadge, P. H. Jampani, M. K. Datta, D. Hong, J. A. Poston, A. Manivannan and P. N. Kumta, *International Journal of Hydrogen Energy*, **42**, 24079 (2017).

190. G. Azadi, R. Bagheri, R. Bikas, Y. Mousazade, J. Cui, Z. Song, V. Kinzhybalo, J.-R. Shen, S. I. Allakhverdiev and M. M. Najafpour, *International Journal of Hydrogen Energy*, **43**, 22896 (2018).

191. D. M. F. Santos, C. A. C. Sequeira and J. L. Figueiredo, *Química Nova*, **36**, 1176 (2013).

192. R. Badam, M. Hara, H.-H. Huang and M. Yoshimura, *International Journal of Hydrogen Energy*, **43**, 18095 (2018).

193. M. Tariq, W. Q. Zaman, W. Sun, Z. Zhou, Y. Wu, L.-m. Cao and J. Yang, *ACS Sustainable Chemistry & Engineering*, **6**, 4854 (2018).

194. H. B. Wu, G. Zhang, L. Yu and X. W. D. Lou, *Nanoscale Horizons*, **1**, 27 (2016).

195. R. S. Devan, R. A. Patil, J. H. Lin and Y. R. Ma, *Advanced Functional Materials*, **22**, 3326 (2012).

196. J. Li and G. Zheng, *Advanced Science*, **4**, 1600380 (2017).

197. Y. P. Zhu, Y. P. Liu, T. Z. Ren and Z. Y. Yuan, *Advanced Functional Materials*, **25**, 7337 (2015).

198. L.-L. Feng, G. Yu, Y. Wu, G.-D. Li, H. Li, Y. Sun, T. Asefa, W. Chen and X. Zou, *Journal of the American Chemical Society*, **137**, 14023 (2015).

199. S. Kundu, T. C. Nagaiah, W. Xia, Y. Wang, S. V. Dommele, J. H. Bitter, M. Santa, G. Grundmeier, M. Bron and W. Schuhmann, *The Journal of Physical Chemistry C*, **113**, 14302 (2009).

200. I. S. Cho, Z. Chen, A. J. Forman, D. R. Kim, P. M. Rao, T. F. Jaramillo and X. Zheng, *Nano letters*, **11**, 4978 (2011).

201. J. Liu, H. Bai, Y. Wang, Z. Liu, X. Zhang and D. D. Sun, *Advanced Functional Materials*, **20**, 4175 (2010).

202. A. Wolcott, W. A. Smith, T. R. Kuykendall, Y. Zhao and J. Z. Zhang, *Small*, **5**, 104 (2009).

203. H. He, P. Xiao, M. Zhou, F. Liu, S. Yu, L. Qiao and Y. Zhang, *Electrochimica Acta*, **88**, 782 (2013).

204. S. M. Alia, S. Shulda, C. Ngo, S. Pylypenko and B. S. Pivovar, *ACS Catalysis*, **8**, 2111 (2018).

205. H. Wang, Z. Lu, D. Qian, Y. Li and W. Zhang, *Nanotechnology*, **18**, 115616 (2007).

206. H. Liu, C. Song, L. Zhang, J. Zhang, H. Wang and D. P. Wilkinson, *Journal of Power Sources*, **155**, 95 (2006).

207. Z. Chen, M. Waje, W. Li and Y. Yan, *Angewandte Chemie International Edition*, **46**, 4060 (2007).

208. S. Garbarino, A. Ponrouch, S. Pronovost, J. Gaudet and D. Guay, *Electrochemistry Communications*, **11**, 1924 (2009).

209. W. Sun, L.-m. Cao and J. Yang, *Journal of Materials Chemistry A*, **4**, 12561 (2016).

210. F. Cheng, J. Zhao, W. Song, C. Li, H. Ma, J. Chen and P. Shen, *Inorganic chemistry*, **45**, 2038 (2006).

211. Z.-Y. Yuan, T.-Z. Ren, G. Du and B.-L. Su, *Chemical physics letters*, **389**, 83 (2004).

212. Z.-G. Ye, H.-M. Meng, D. Chen, H.-Y. Yu, Z.-S. Huan, X.-D. Wang and D.-B. Sun, *Solid state sciences*, **10**, 346 (2008).

213. J. P. Perdew, K. Burke and M. Ernzerhof, *Physical review letters*, **77**, 3865 (1996).

214. G. Kresse and D. Joubert, *Physical Review B*, **59**, 1758 (1999).

215. R.-S. Chen, Y.-S. Huang, Y.-M. Liang, D.-S. Tsai, Y. Chi and J.-J. Kai, *Journal of Materials Chemistry*, **13**, 2525 (2003).

216. R. K. Kawar, P. S. Chigare and P. S. Patil, *Applied Surface Science*, **206**, 90 (2003).

217. N. Shilpa, J. Manna, P. Rajput and R. K. Rana, *ACS Catalysis*, **6**, 5699 (2016).

218. A. V. Deshmukh, S. I. Patil, S. M. Yusuf, A. K. Rajarajan and N. P. Lalla, *Journal of Magnetism and Magnetic Materials*, **322**, 536 (2010).

219. H.-T. Chung, J.-G. Kim and H.-G. Kim, *Solid State Ionics*, **107**, 153 (1998).

220. J.-H. Choy, D.-K. Kim, S.-H. Hwang, G. Demazeau and D.-Y. Jung, *Journal of the American Chemical Society*, **117**, 8557 (1995).

221. Y. Wu, S. Li, Y. Cao, S. Xing, Z. Ma and Y. Gao, *Materials Letters*, **97**, 1 (2013).

222. W. Yuan, B. Wang, H. Wu, M. Xiang, Q. Wang, H. Liu, Y. Zhang, H. Liu and S. Dou, *Journal of Power Sources*, **379**, 10 (2018).

223. L. Li, C. Nan, J. Lu, Q. Peng and Y. Li, *Chemical Communications*, **48**, 6945 (2012).

224. X. Liang, C. Hart, Q. Pang, A. Garsuch, T. Weiss and L. F. Nazar, *Nature communications*, **6**, 5682 (2015).

225. V. Pfeifer, T. E. Jones, J. J. Velasco Vélez, C. Massué, R. Arrigo, D. Teschner, F. Girgsdies, M. Scherzer, M. T. Greiner and J. Allan, *Surface and Interface Analysis*, **48**, 261 (2016).

226. S. J. Freakley, J. Ruiz-Esquius and D. J. Morgan, *Surface and Interface Analysis*, **49**, 794 (2017).

227. Z.-X. Lu, Y. Shi, C.-F. Yan, C.-Q. Guo and Z.-D. Wang, *International Journal of Hydrogen Energy*, **42**, 3572 (2017).

228. G. K. Wertheim and H. J. Guggenheim, *Physical Review B*, **22**, 4680 (1980).

229. H.-S. Oh, H. N. Nong, T. Reier, A. Bergmann, M. Gliech, J. Ferreira de Araújo, E. Willinger, R. Schlögl, D. Teschner and P. Strasser, *Journal of the American Chemical Society*, **138**, 12552 (2016).

230. H. N. Nong, L. Gan, E. Willinger, D. Teschner and P. Strasser, *Chemical Science*, **5**, 2955 (2014).

231. G. Zhang, X. Han, W. Bian, J. Zhan and X. Ma, *RSC Advances*, **6**, 3919 (2016).

232. M. Ishfaq, M. Rizwan Khan, M. F. Bhopal, F. Nasim, A. Ali, A. S. Bhatti, I. Ahmed, S. Bhardwaj and C. Cepek, *Journal of Applied Physics*, **115**, 174506 (2014).

233. Y. Sheng, M. L. Botero, M. Y. Manuputty, M. Kraft and R. Xu, *ACS Applied Energy Materials*, **1**, 655 (2018).

234. A. A. Shaltout, H. H. Afify and S. A. Ali, *Journal of Electron Spectroscopy and Related Phenomena*, **185**, 140 (2012).

235. F. M. Amanullah, K. J. Pratap and V. H. Babu, *Materials Science and Engineering: B*, **52**, 93 (1998).

236. M. Fantini and I. Torriani, *Thin Solid Films*, **138**, 255 (1986).

237. X. Sun, Y. Zhang, P. Song, J. Pan, L. Zhuang, W. Xu and W. Xing, *ACS catalysis*, **3**, 1726 (2013).

238. A. Borras, C. Lopez, V. Rico, F. Gracia, A. R. Gonzalez-Elipe, E. Richter, G. Battiston, R. Gerbasi, N. McSporran and G. Sauthier, *The Journal of Physical Chemistry C*, **111**, 1801 (2007).

239. D. P. Dubal, W. B. Kim and C. D. Lokhande, *Journal of Physics and Chemistry of Solids*, **73**, 18 (2012).

240. Y. Hu, H. Zhu, J. Wang and Z. Chen, *Journal of Alloys and Compounds*, **509**, 10234 (2011).

241. R. Li, L. Liu, Y. Zhang and F. Yang, *RSC Advances*, **6**, 20542 (2016).

242. D. E. Moilanen, I. R. Piletic and M. D. Fayer, *The Journal of Physical Chemistry C*, **111**, 8884 (2007).

243. C. Korzeniewski, E. Adams and D. Liu, *Applied spectroscopy*, **62**, 634 (2008).

244. Y. M. Vol'fkovich, V. E. Sosenkin and N. F. Nikol'skaya, *Russian Journal of Electrochemistry*, **46**, 438 (2010).

245. A. Sivanantham, P. Ganesan and S. Shanmugam, *Advanced Functional Materials*, **26**, 4661 (2016).

246. F. Cheng, Y. Su, J. Liang, Z. Tao and J. Chen, *Chemistry of Materials*, **22**, 898 (2009).

247. T. Reier, M. Oezaslan and P. Strasser, *Acs Catalysis*, **2**, 1765 (2012).

248. R. Kötz and S. Stucki, *Electrochimica acta*, **31**, 1311 (1986).

249. K.-L. Yan, J.-Q. Chi, J.-Y. Xie, B. Dong, Z.-Z. Liu, W.-K. Gao, J.-H. Lin, Y.-M. Chai and C.-G. Liu, *Renewable Energy*, **119**, 54 (2018).

250. M. Abreu-Sepulveda, P. Trinh, S. Malkhandi, S. R. Narayanan, J. Jorné, D. J. Quesnel, J. A. Postonr and A. Manivannan, *Electrochimica Acta*, **180**, 401 (2015).

251. B. M. Tackett, W. Sheng, S. Kattel, S. Yao, B. Yan, K. A. Kuttiyiel, Q. Wu and J. G. Chen, *ACS Catal.*, **8**, 2615 (2018).

252. J. S. Mondschein, K. Kumar, C. F. Holder, K. Seth, H. Kim and R. E. Schaak, *Inorganic chemistry*, **57**, 6010 (2018).

253. J. N. Tiwari, R. N. Tiwari and K. S. Kim, *Progress in Materials Science*, **57**, 724 (2012).

254. T. Takashima, K. Hashimoto and R. Nakamura, *Journal of the American Chemical Society*, **134**, 1519 (2012).

255. M. Wang, J. Jiang and L. Ai, *ACS Sustainable Chemistry & Engineering*, **6**, 6117 (2018).

256. T. Takashima, K. Hashimoto and R. Nakamura, *Journal of the American Chemical Society*, **134**, 18153 (2012).

257. F. Huang, Z. Wan, Y. Jin and L. Wen, *Journal of The Electrochemical Society*, **164**, B632 (2017).

258. X. Dong, Y. Xu, S. Yan, S. Mao, L. Xiong and X. Sun, *Journal of Materials Chemistry A*, **3**, 670 (2015).

259. T. Kwon, H. Hwang, Y. J. Sa, J. Park, H. Baik, S. H. Joo and K. Lee, *Advanced Functional Materials*, **27**, 1604688 (2017).

260. J. Lim, S. Yang, C. Kim, C.-W. Roh, Y. Kwon, Y.-T. Kim and H. Lee, *Chemical Communications*, **52**, 5641 (2016).

261. P. Lettenmeier, L. Wang, U. Golla-Schindler, P. Gazdzicki, N. A. Cañas, M. Handl, R. Hiesgen, S. S. Hosseiny, A. S. Gago and K. A. Friedrich, *Angewandte Chemie*, **128**, 752 (2016).

262. Y. Fu, H. Y. Yu, C. Jiang, T. H. Zhang, R. Zhan, X. Li, J. F. Li, J. H. Tian and R. Yang, *Advanced Functional Materials*, **28**, 1705094 (2018).

263. V. Tripkovic, H. A. Hansen and T. Vegge, *ChemSusChem*, **11**, 629 (2018).

264. T. Li, J. Wu, X. Xiao, B. Zhang, Z. Hu, J. Zhou, P. Yang, X. Chen, B. Wang and L. Huang, *RSC Advances*, **6**, 13914 (2016).

265. C. Xu, F. Kang, B. Li and H. Du, *Journal of materials research*, **25**, 1421 (2010).

266. R. Frydendal, E. A. Paoli, I. Chorkendorff, J. Rossmeisl and I. E. L. Stephens, *Advanced Energy Materials*, **5**, 1500991 (2015).

267. A. Shinde, R. J. R. Jones, D. Guevarra, S. Mitrovic, N. Becerra-Stasiewicz, J. A. Haber, J. Jin and J. M. Gregoire, *Electrocatalysis*, **6**, 229 (2015).

268. I. A. Moreno-Hernandez, C. A. MacFarland, C. G. Read, K. M. Papadantonakis, B. S. Brunschwig and N. S. Lewis, *Energy & Environmental Science*, **10**, 2103 (2017).

269. M. Huynh, T. Ozel, C. Liu, E. C. Lau and D. G. Nocera, *Chemical science*, **8**, 4779 (2017).

270. M. Huynh, D. K. Bediako and D. G. Nocera, *Journal of the American Chemical Society*, **136**, 6002 (2014).

271. P. Di Sia, *J Nanosci Adv Tech*, **2**, 6 (2018).

272. R. O'Hayre, S.-W. Cha, F. B. Prinz and W. Colella, *Fuel cell fundamentals*, John Wiley & Sons (2016).

273. W. L. Kwong, C. C. Lee, A. Shchukarev, E. Björn and J. Messinger, *Journal of Catalysis*, **365**, 29 (2018).

274. W. Sun, Y. Song, X.-Q. Gong, L.-m. Cao and J. Yang, *Chemical Science*, **6**, 4993 (2015).

275. S. Kumari, B. P. Ajayi, B. Kumar, J. B. Jasinski, M. K. Sunkara and J. M. Spurgeon, *Energy & Environmental Science*, **10**, 2432 (2017).

276. W. Hu, H. Zhong, W. Liang and S. Chen, *ACS applied materials & interfaces*, **6**, 12729 (2014).

277. V. K. Puthiyapura, S. Pasupathi, S. Basu, X. Wu, H. Su, N. Varagunapandiyan, B. Pollet and K. Scott, *international journal of hydrogen energy*, **38**, 8605 (2013).

278. R. Pokhrel, M. K. Goetz, S. E. Shaner, X. Wu and S. S. Stahl, *Journal of the American Chemical Society*, **137**, 8384 (2015).

279. B. Rodríguez-García, Á. Reyes-Carmona, I. Jiménez-Morales, M. Blasco-Ahicart, S. Cavaliere, M. Dupont, D. Jones, J. Rozière, J. R. Galán-Mascarós and F. Jaouen, *Sustainable Energy & Fuels*, **2**, 589 (2018).

280. L. Zhou, A. Shinde, J. H. Montoya, A. Singh, S. Gul, J. Yano, Y. Ye, E. J. Crumlin, M. H. Richter, J. K. Cooper, H. S. Stein, J. A. Haber, K. A. Persson and J. M. Gregoire, *ACS Catalysis*, 10938 (2018).

281. P. P. Patel, M. K. Datta, O. I. Velikokhatnyi, R. Kuruba, K. Damodaran, P. Jampani, B. Gattu, P. M. Shanthi, S. S. Damle and P. N. Kumta, *Scientific reports*, **6**, 28367 (2016).

282. K. S. Kadakia, P. H. Jampani, O. I. Velikokhatnyi, M. K. Datta, P. Patel, S. J. Chung, S. K. Park, J. A. Poston, A. Manivannan and P. N. Kumta, *Materials Science and Engineering: B*, **212**, 101 (2016).

283. M. H. P. Santana and L. A. De Faria, *Electrochimica acta*, **51**, 3578 (2006).

284. W. Hu, S. Chen and Q. Xia, *international journal of hydrogen energy*, **39**, 6967 (2014).

285. X. Wang, M. Yin, H. Xue, Y. Su and S. Tian, *Ionics*, **24**, 2583 (2018).

286. J. Rossmeisl, Z. W. Qu, H. Zhu, G. J. Kroes and J. K. Nørskov, *Journal of Electroanalytical Chemistry*, **607**, 83 (2007).

287. D. Qu, D. Diehl, B. E. Conway, W. G. Pell and S. Y. Qian, *Journal of Applied Electrochemistry*, **35**, 1111 (2005).

288. H. An and H.-J. Ahn, *Materials Letters*, **93**, 88 (2013).

289. A. J. Gardecka, *Thesis for the Degree of Doctor of Philosophy, University College London, 2016*

290. L. Xiong, Y. Xu, C. Zhang, Z. Zhang and J. Li, *Journal of Solid State Electrochemistry*, **15**, 1263 (2011).

291. Y. Sato, H. Akizuki, T. Kamiyama and Y. Shigesato, *Thin Solid Films*, **516**, 5758 (2008).

292. W. Zhou, M. Zhao, F. Liang, S. C. Smith and Z. Zhu, *Materials Horizons*, **2**, 495 (2015).

293. H. A. Tahini, X. Tan, U. Schwingenschlögl and S. C. Smith, *ACS Catalysis*, **6**, 5565 (2016).

294. J. Yue, C. Suchomski, P. Voepel, R. Ellinghaus, M. Rohnke, T. Leichtweiss, M. T. Elm and B. M. Smarsly, *Journal of Materials Chemistry A*, **5**, 1978 (2017).

295. N. Maximova, *Chemical Engineering Master's Theses. Paper 1* (2008).

296. B. Tazi and O. Savadogo, *Electrochimica Acta*, **45**, 4329 (2000).

297. E. S. Ilton, J. E. Post, P. J. Heaney, F. T. Ling and S. N. Kerisit, *Applied Surface Science*, **366**, 475 (2016).

298. C. Spoeri, J. T. H. Kwan, A. Bonakdarpour, D. P. Wilkinson and P. Strasser, *Angewandte Chemie International Edition*, **56**, 5994 (2017).

299. S. Geiger, O. Kasian, A. M. Mingers, S. S. Nicley, K. Haenen, K. J. J. Mayrhofer and S. Cherevko, *ChemSusChem*, **10**, 4140 (2017).

300. O. I. Velikokhatnyi and P. N. Kumta, *Physica B: Condensed Matter*, **404**, 1737 (2009).

301. A. Marshall, B. Børresen, G. Hagen, M. Tsypkin and R. Tunold, *Energy*, **32**, 431 (2007).

302. A. T. Marshall and R. G. Haverkamp, *Electrochimica Acta*, **55**, 1978 (2010).

303. S. D. Ghadge, O. I. Velikokhatnyi, M. K. Datta, P. M. Shanthi, S. Tan and P. N. Kumta, *ACS Applied Energy Materials*, **3**, 541 (2020).

304. Z. Zhang, J. Zhang, T. Wang, Z. Li, G. Yang, H. Bian, J. Li and D. Gao, *Rsc Advances*, **8**, 5338 (2018).

305. V. D. Silva, L. S. Ferreira, T. A. Simões, E. S. Medeiros and D. A. Macedo, *Journal of colloid and interface science*, **540**, 59 (2019).

306. J. S. Mondschein, J. F. Callejas, C. G. Read, J. Y. C. Chen, C. F. Holder, C. K. Badding and R. E. Schaak, *Chemistry of Materials*, **29**, 950 (2017).

307. K.-L. Yan, J.-F. Qin, J.-H. Lin, B. Dong, J.-Q. Chi, Z.-Z. Liu, F.-N. Dai, Y.-M. Chai and C.-G. Liu, *Journal of Materials Chemistry A*, **6**, 5678 (2018).

308. S. Anantharaj, K. Karthick and S. Kundu, *Inorganic Chemistry*, **58**, 8570 (2019).

309. N. M. Deraz and O. H. Abd-Elkader, *Int J Electrochem Sci*, **8**, 10112 (2013).

310. E. Ríos, S. Abarca, P. Daccarett, H. N. Cong, D. Martel, J. F. Marco, J. R. Gancedo and J. L. Gautier, *International Journal of Hydrogen Energy*, **33**, 4945 (2008).

311. A. Espejo, J. Ortiz, E. Rios, F. Herrera, D. Alburquenque and J. Gautier, *Journal of the Chilean Chemical Society*, **59**, 2502 (2014).

312. S. Behar, P. Gonzalez, P. Agulhon, F. Quignard and D. Świerczyński, *Catalysis today*, **189**, 35 (2012).

313. M. Krämer, T. Schmidt, K. Stöwe and W. F. Maier, *Applied Catalysis A: General*, **302**, 257 (2006).

314. A. Wöllner, F. Lange, H. Schmelz and H. Knözinger, *Applied Catalysis A: General*, **94**, 181 (1993).

315. H. Zhao, K. Fang, J. Zhou, M. Lin and Y. Sun, *International Journal of Hydrogen Energy*, **41**, 8819 (2016).

316. B. Zhu, G. Yang, D. Gao, Y. Wu, J. Zhao, Y. Fu and S. Ma, *Journal of Alloys and Compounds*, **806**, 163 (2019).

317. H.-Y. Wang, S.-F. Hung, H.-Y. Chen, T.-S. Chan, H. M. Chen and B. Liu, *Journal of the American Chemical Society*, **138**, 36 (2015).

318. A. Eftekhari, *Materials Today Energy*, **5**, 37 (2017).

319. P. Wei, M. Bieringer, L. M. D. Cranswick and A. Petric, *Journal of materials science*, **45**, 1056 (2010).

320. R. E. Vandenberghe, E. Legrand, D. Scheerlinck and V. A. M. Brabers, *Acta Crystallographica Section B: Structural Crystallography and Crystal Chemistry*, **32**, 2796 (1976).

321. G. Henkelman, A. Arnaldsson and H. Jónsson, *Computational Materials Science*, **36**, 354 (2006).

322. A. J. Saldivar-Garcia and H. F. Lopez, *Metallurgical and Materials Transactions A*, **35**, 2517 (2004).

323. L.-G. Liu, T. Takahashi and W. A. Bassett, *Journal of Physics and Chemistry of Solids*, **31**, 1345 (1970).

324. Y.-F. Chen, C.-Y. Lee, M.-Y. Yeng and H.-T. Chiu, *Journal of crystal growth*, **247**, 363 (2003).

325. V. Balasubramanian, P. N. Kumar and D. Sengottaiyan, *Materials Science-Poland*, **35**, 329 (2017).

326. M. Dongol, A. El-Denglawey, M. S. A. El Sadek and I. S. Yahia, *Optik*, **126**, 1352 (2015).

327. G. C. da Silva, N. Perini and E. A. Ticianelli, *Applied Catalysis B: Environmental*, **218**, 287 (2017).

328. P. Ma, Q. Geng, X. Gao, S. Yang and G. Liu, *Materials Letters*, **179**, 170 (2016).

329. X. X. Zhou, H. Zhao, W. M. Huang, H. R. Chen and J. L. Shi, *Dalton Transactions*, **46**, 6111 (2017).

330. J. Wang, P. Tian, K. Li, B. Ge, D. Liu, Y. Liu, T. Yang and R. Ren, *Bioresource technology*, **222**, 107 (2016).

331. J. Wang, H. Zhao, J. Song, T. Zhu and W. Xu, *Catalysts*, **9**, 726 (2019).

332. K. Nakatsuka, T. Yoshii, Y. Kuwahara, K. Mori and H. Yamashita, *Chemistry–A European Journal*, **24**, 898 (2018).

333. R. Bayón, G. San Vicente, C. Maffiotte and Á. Morales, *Solar Energy Materials and Solar Cells*, **92**, 1211 (2008).

334. C. Wang, F. Li, Z. Sun and Q. Song, *Indoor and Built Environment*, **28**, 7 (2019).

335. Z. M. Chan, D. A. Kitchaev, J. N. Weker, C. Schnedermann, K. Lim, G. Ceder, W. Tumas, M. F. Toney and D. G. Nocera, *Proceedings of the National Academy of Sciences*, 201722235 (2018).

336. M. Morita, C. Iwakura and H. Tamura, *Electrochimica Acta*, **24**, 357 (1979).

337. U. Maitra, B. S. Naidu, A. Govindaraj and C. N. R. Rao, *Proceedings of the National Academy of Sciences*, **110**, 11704 (2013).

338. D. M. Robinson, Y. B. Go, M. Mui, G. Gardner, Z. Zhang, D. Mastrogiovanni, E. Garfunkel, J. Li, M. Greenblatt and G. C. Dismukes, *Journal of the American chemical Society*, **135**, 3494 (2013).

339. A. Iyer, J. Del-Pilar, C. K. King'ondu, E. Kissel, H. F. Garces, H. Huang, A. M. El-Sawy, P. K. Dutta and S. L. Suib, *The Journal of Physical Chemistry C*, **116**, 6474 (2012).

340. M. M. Najafpour, S. Mehrabani, Y. Mousazade and M. Hołyńska, *Dalton Transactions*, **47**, 9021 (2018).

341. Z. Chen and T. J. Meyer, *Angewandte Chemie International Edition*, **52**, 700 (2013).

342. H.-H. Huang, J.-W. Wang, P. Sahoo, D.-C. Zhong and T.-B. Lu, *Chemical Communications*, **53**, 9324 (2017).

343. M. Vuković, *Journal of applied electrochemistry*, **17**, 737 (1987).

344. M. Vuković, *Journal of applied electrochemistry*, **20**, 969 (1990).

345. M. Faustini, M. Giraud, D. Jones, J. Rozière, M. Dupont, T. R. Porter, S. Nowak, M. Bahri, O. Ersen, C. Sanchez, C. Boissière, C. Tard and J. Peron, *Advanced Energy Materials*, **0**, 1802136 (2018).

346. D. Inohara, H. Maruyama, Y. Kakihara, H. Kurokawa and M. Nakayama, *ACS Omega*, **3**, 7840 (2018).

347. H. Qin, S. Lao, Z. Liu, J. Zhu and Z. Li, *international journal of hydrogen energy*, **35**, 1872 (2010).

348. J. Nowotny, T. Bak, D. Chu, S. Fiechter, G. E. Murch and T. N. Veziroglu, *International Journal of Hydrogen Energy*, **39**, 4151 (2014).

349. X. Yang and C. Wang, *Applied Physics Letters*, **86**, 224104 (2005).

350. R. Pal and S. Basu, *Ferroelectrics*, **519**, 90 (2017).

351. S. D. Ghadge, M. K. Datta, O. I. Velikokhatnyi, R. Kuruba, P. M. Shanthi and P. N. Kumta, *Journal of The Electrochemical Society*, **167**, 144511 (2020).

352. K. Li, R. Zhang, R. Gao, G.-Q. Shen, L. Pan, Y. Yao, K. Yu, X. Zhang and J.-J. Zou, *Applied Catalysis B: Environmental*, **244**, 536 (2019).

353. X. Zhao, S. Chen, Z. Fang, J. Ding, W. Sang, Y. Wang, J. Zhao, Z. Peng and J. Zeng, *Journal of the American Chemical Society*, **137**, 2804 (2015).

354. Y. Jin, M. Shi, Y. Chu, Y. Xu, W. Jia, Q. Yuan, J. Chen, D. Chen and S. Chen, *Journal of The Electrochemical Society*, **161**, F246 (2014).

355. M. Ammam and E. B. Easton, *Journal of Power Sources*, **236**, 311 (2013).

356. M. S. Garapati and R. Sundara, *International Journal of Hydrogen Energy*, **44**, 10951 (2019).

357. S. D. Ghadge, O. I. Velikokhatnyi, M. K. Datta, P. M. Shanthi, S. Tan, K. Damodaran and P. N. Kumta, *ACS Catalysis*, **9**, 2134 (2019).

358. S. D. Ghadge, P. P. Patel, M. K. Datta, O. I. Velikokhatnyi, P. M. Shanthi and P. N. Kumta, *Journal of Power Sources*, **392**, 139 (2018).

359. S. D. Ghadge, P. P. Patel, M. K. Datta, O. I. Velikokhatnyi, R. Kuruba, P. M. Shanthi and P. N. Kumta, *RSC advances*, **7**, 17311 (2017).

360. J. Xiong, J. Li, J. Shi, X. Zhang, N.-T. Suen, Z. Liu, Y. Huang, G. Xu, W. Cai and X. Lei, *ACS Energy Letters*, **3**, 341 (2018).

361. J. K. Nørskov, T. Bligaard, A. Logadottir, J. Kitchin, J. Chen, S. Pandelov and U. Stimming, *Journal of The Electrochemical Society*, **152**, J23 (2005).

362. R.-K. Chiang and R.-T. Chiang, *Inorganic chemistry*, **46**, 369 (2007).

363. R. Fruchart, A. Roger and J. P. Senateur, *Journal of Applied Physics*, **40**, 1250 (1969).

364. Q. Li and X. Hu, *Physical Review B*, **74**, 035414 (2006).

365. Y. Qi, L. Zhang, L. Sun, G. Chen, Q. Luo, H. Xin, J. Peng, Y. Li and F. Ma, *Nanoscale*, **12**, 1985 (2020).

366. J. Lin, Y. Yan, T. Liu, J. Cao, X. Zhou, J. Feng and J. Qi, *International Journal of Hydrogen Energy* (2020).

367. X. Fang, Z. Wang, Z. Jiang, J. Wang and M. Dong, *Electrochimica Acta*, **322**, 134739 (2019).

368. H. Zhao, Y. Wang, L. Fang, W. Fu, X. Yang, S. You, P. Luo, H. Zhang and Y. Wang, *Journal of Materials Chemistry A*, **7**, 20357 (2019).

369. H. Ang, H. T. Tan, Z. M. Luo, Y. Zhang, Y. Y. Guo, G. Guo, H. Zhang and Q. Yan, *Small*, **11**, 6278 (2015).

370. H. T. Phan, N. Caney, P. Marty, S. Colasson and J. Gavillet, *International Journal of Heat and Mass Transfer*, **52**, 5459 (2009).

371. Q. Zhang, T. Li, J. Liang, N. Wang, X. Kong, J. Wang, H. Qian, Y. Zhou, F. Liu and C. Wei, *Journal of Materials Chemistry A*, **6**, 7509 (2018).

372. I. I. Abu and K. J. Smith, *Journal of Catalysis*, **241**, 356 (2006).

373. H. W. Nesbitt, D. Legrand and G. M. Bancroft, *Physics and Chemistry of Minerals*, **27**, 357 (2000).

374. H. Pfeiffer, F. Tancret and T. Brousse, *Electrochimica Acta*, **50**, 4763 (2005).

375. J. Tian, Q. Liu, A. M. Asiri and X. Sun, *Journal of the American Chemical Society*, **136**, 7587 (2014).

376. Y. Teng, A. Wang, X. Li, J. Xie, Y. Wang and Y. Hu, *Journal of Catalysis*, **266**, 369 (2009).

377. P. Jiang, Q. Liu, C. Ge, W. Cui, Z. Pu, A. M. Asiri and X. Sun, *Journal of Materials Chemistry A*, **2**, 14634 (2014).

378. A. D. Wilson, R. H. Newell, M. J. McNevin, J. T. Muckerman, M. Rakowski DuBois and D. L. DuBois, *Journal of the American Chemical Society*, **128**, 358 (2006).

379. A. D. Wilson, R. K. Shoemaker, A. Miedaner, J. T. Muckerman, D. L. DuBois and M. R. DuBois, *Proceedings of the National Academy of Sciences*, **104**, 6951 (2007).

380. Y. Nicolet, A. L. de Lacey, X. Vernède, V. M. Fernandez, E. C. Hatchikian and J. C. Fontecilla-Camps, *Journal of the American Chemical Society*, **123**, 1596 (2001).

381. J. Chang, K. Li, Z. Wu, J. Ge, C. Liu and W. Xing, *ACS applied materials & interfaces*, **10**, 26303 (2018).

382. X. Cui, Z. Chen, Z. Wang, M. Chen, X. Guo and Z. Zhao, *ACS Applied Energy Materials*, **1**, 5822 (2018).

383. S. Lu and Z. Zhuang, *Science China Materials*, **59**, 217 (2016).

384. W. Sheng, H. A. Gasteiger and Y. Shao-Horn, *Journal of The Electrochemical Society*, **157**, B1529 (2010).

385. F. Tzorbatzoglou, A. Brouzgou, S. Jing, Y. Wang, S. Song and P. Tsiakaras, *International Journal of Hydrogen Energy*, **43**, 11766 (2018).

386. L. Lu, L. Peng, L. Li, J. Li, X. Huang and Z. Wei, *Journal of Energy Chemistry*, **40**, 52 (2020).

387. M. Oezaslan, F. Hasché and P. Strasser, *The Journal of Physical Chemistry Letters*, **4**, 3273 (2013).

388. J. Chen, Y. Li, Z. Gao, G. Wang, J. Tian, C. Jiang, S. Zhu and R. Wang, *Electrochemistry Communications*.

389. F. Silva, V. Dalmazzo, M. Becker, M. Souza, R. Souza and E. A. Martini, *Ionics*, 1 (2013).

390. L. G. S. Pereira, V. A. Paganin and E. A. Ticianelli, *Electrochimica Acta*, **54**, 1992 (2009).

391. Y. Dai, Y. Liu and S. Chen, *Electrochimica Acta*, **89**, 744 (2013).

392. M. Götz and H. Wendt, *Electrochimica Acta*, **43**, 3637 (1998).

393. J. E. Hu, Z. Liu, B. W. Eichhorn and G. S. Jackson, *International Journal of Hydrogen Energy*, **37**, 11268 (2012).

394. M. Nagarajan, G. Paruthimal kalaignan and G. A. Pathanjali, *International Journal of Hydrogen Energy,* **36**, 14829 (2011).

395. D. Ham, S. Han, C. Pak, S. Ji, S.-A. Jin, H. Chang and J. Lee, *Top Catal*, **55**, 922 (2012).

396. D. Geng, S. Jayabal, G. Saranya, X. Meng and L.-Y. Lin, *Journal of Materials Chemistry A* (2020).

397. M. Kato, K. Ogura, S. Nakagawa, S. Tokuda, K. Takahashi, T. Nakamura and I. Yagi, *ACS omega*, **3**, 9052 (2018).

398. J. Tayal, B. Rawat and S. Basu, *International Journal of Hydrogen Energy*, **36**, 14884 (2011).

399. J. Xu, X. Liu, Y. Chen, Y. Zhou, T. Lu and Y. Tang, *Journal of Materials Chemistry*, **22**, 23659 (2012).

400. M. K. Jeon and P. J. McGinn, *Journal of Power Sources*, **188**, 427 (2009).

401. R. S. Amin, R. M. Abdel Hameed, K. M. El-Khatib, H. El-Abd and E. R. Souaya, *International Journal of Hydrogen Energy*, **37**, 18870 (2012).

402. S. Wirth, F. Harnisch, M. Weinmann and U. Schröder, *Applied Catalysis B: Environmental*, **126**, 225 (2012).

403. C. R. Kachelmyer, I. O. Khomenko, A. S. Rogachev and A. Varma, *Journal of materials research*, **12**, 3230 (1997).

404. Y. Pan and Y. Lin, *Journal of Electronic Materials*, **47**, 1786 (2018).

405. G. Rodrigues, C. A. Nunes, P. A. Suzuki and G. C. Coelho, *Intermetallics*, **14**, 236 (2006).

406. B. K. Yen, T. Aizawa and J. Kihara, *Journal of the American Ceramic Society*, **81**, 1953 (1998).

407. A. Ehsani, M. G. Mahjani and M. Jafarian, *Turkish Journal of Chemistry*, **35**, 735 (2011).

408. R. Jiang and D. Chu, *Electrochimica acta*, **45**, 4025 (2000).

409. D. L. Wise and G. Houghton, *Chemical Engineering Science*, **21**, 999 (1966).

410. P. Pietrokowsky and P. Duwez, *JOM*, **3**, 772 (1951).

411. J. P. Perdew and W. Yue, *Physical Review B*, **33**, 8800 (1986).

412. P. Sharma and R. K. Sharma, *RSC Advances*, **5**, 102481 (2015).

413. B. Narayanamoorthy, K. K. R. Datta, M. Eswaramoorthy and S. Balaji, *RSC Advances*, **4**, 55571 (2014).

414. W. H. Lee, Y. W. Cheon, Y. H. Jo, J. G. Seong, Y. J. Jo, Y. H. Kim, M. S. Noh, H. G. Jeong, C. J. Van Tyne and S. Y. Chang, *The Scientific World Journal*, **2015** (2015).

415. L. Liu, J. Xu, Z.-H. Xie and P. Munroe, *Journal of Materials Chemistry A*, **1**, 2064 (2013).

416. T. Ito, S. Kaneko, M. Kunimatsu, Y. Hirabayashi, M. Soga and K. Suzuki, *International Journal of Electrochemistry*, **2011** (2011).

417. K. Benaissi, L. Johnson, D. A. Walsh and W. Thielemans, *Green Chemistry*, **12**, 220 (2010).

418. W. Zhang, L. Li, W. Ding, S. Chen, H. Wang and Z. Wei, *Journal of Materials Chemistry A*, **2**, 10098 (2014).

419. S. D. Ghadge, O. I. Velikokhatnyi, M. K. Datta, P. M. Shanthi, S. Tan, K. Damodaran and P. N. Kumta, *ACS Catalysis*, **9**, 2134 (2019).

420. K. Dong, X. Dong and Q. Jiang, *The World Economy*, **43**, 1665 (2020).

421. P. Nejat, F. Jomehzadeh, M. M. Taheri, M. Gohari and M. Z. A. Majid, *Renewable and sustainable energy reviews*, **43**, 843 (2015).

422. V. E. Balderas-Hernandez, K. P. L. Maldonado, A. Sánchez, A. Smoliński and A. D. L. Rodriguez, *International Journal of Hydrogen Energy*, **45**, 5687 (2020).

423. P. P. Patel, S. D. Ghadge, P. J. Hanumantha, M. K. Datta, B. Gattu, P. M. Shanthi and P. N. Kumta, *International Journal of Hydrogen Energy*, **43**, 13158 (2018).

424. M. Z. Iqbal and S. Siddique, *International Journal of Hydrogen Energy*, **43**, 21502 (2018).

425. Z. Haider, H. W. Yim, H. W. Lee and H.-i. Kim, *International Journal of Hydrogen Energy*, **45**, 5793 (2020).

426. Y. Wang, T. Brezesinski, M. Antonietti and B. Smarsly, *ACS nano*, **3**, 1373 (2009).

427. V. Gokulakrishnan, S. Parthiban, K. Jeganathan and K. Ramamurthi, *Journal of materials science*, **46**, 5553 (2011).

428. M. Stefik, M. Cornuz, N. Mathews, T. Hisatomi, S. Mhaisalkar and M. Grätzel, *Nano letters*, **12**, 5431 (2012).

429. G. Turgut, E. Keskenler, S. Aydın, M. Yılmaz, S. Doğan and B. Düzgün, *Physica Scripta*, **87**, 035602 (2013).

430. S.-i. Shamoto, T. Nakano, Y. Nozue and T. Kajitani, *Journal of Physics and Chemistry of Solids*, **63**, 1047 (2002).

431. R. Katiyar, P. Dawson, M. Hargreave and G. Wilkinson, *Journal of Physics C: Solid State Physics*, **4**, 2421 (1971).

432. K. Maeda, *Physical Chemistry Chemical Physics*, **15**, 10537 (2013).

433. R. Asahi, T. Morikawa, T. Ohwaki, K. Aoki and Y. Taga, *Science*, **293**, 269 (2001).

434. C. Burda, Y. Lou, X. Chen, A. C. S. Samia, J. Stout and J. L. Gole, *Nano Letters*, **3**, 1049 (2003).

435. R. Beranek, B. Neumann, S. Sakthivel, M. Janczarek, T. Dittrich, H. Tributsch and H. Kisch, *Chemical Physics*, **339**, 11 (2007).

436. S. Hoang, S. Guo, N. T. Hahn, A. J. Bard and C. B. Mullins, *Nano Letters*, **12**, 26 (2011).

437. N. Li, H. Teng, L. Zhang, J. Zhou and M. Liu, *RSC Advances*, **5**, 95394 (2015).

438. C. C. Mardare and A. W. Hassel, *physica status solidi (a)*, **216**, 1900047 (2019).

439. Y. Wang, Q. Wang, X. Zhan, F. Wang, M. Safdar and J. He, *Nanoscale*, **5**, 8326 (2013).

440. S. Hernández, V. Cauda, A. Chiodoni, S. Dallorto, A. Sacco, D. Hidalgo, E. Celasco and C. F. Pirri, *ACS Applied Materials & Interfaces*, **6**, 12153 (2014).

441. J. V. Silveira, E. C. Moraes, J. V. B. Moura, A. Ghosh, C. A. Senna, B. S. Archanjo, T. L. Vasconcelos, A. G. Souza Filho, P. T. C. Freire and C. Luz-Lima, *Journal of Materials Science*, **55**, 6429 (2020).

442. S. S. Kalanur and H. Seo, *Journal of Colloid and Interface Science*, **509**, 440 (2018).

443. F. Wang, C. Di Valentin and G. Pacchioni, *The Journal of Physical Chemistry C*, **116**, 8901 (2012).

444. M. Law, L. E. Greene, J. C. Johnson, R. Saykally and P. Yang, *Nature materials*, **4**, 455 (2005).

445. A. Kushwaha and M. Aslam, *Journal of Applied Physics*, **112**, 054316 (2012).

446. L. Mai, X. Tian, X. Xu, L. Chang and L. Xu, *Chemical reviews* (2014).

447. M. Sadakane, K. Sasaki, H. Kunioku, B. Ohtani, R. Abe and W. Ueda, *Journal of Materials Chemistry*, **20**, 1811 (2010).

448. S. Deki, S. Iizuka, A. Horie, M. Mizuhata and A. Kajinami, *Chemistry of Materials*, **16**, 1747 (2004).

449. J.-H. Lee, I.-C. Leu, M.-C. Hsu, Y.-W. Chung and M.-H. Hon, *The Journal of Physical Chemistry B*, **109**, 13056 (2005).

450. U. V. Desai, C. Xu, J. Wu and D. Gao, *The Journal of Physical Chemistry C*, **117**, 3232 (2013).

451. S. S. Kalanur, *Catalysts*, **9**, 456 (2019).

452. S. Wang, H. Chen, G. Gao, T. Butburee, M. Lyu, S. Thaweesak, J.-H. Yun, A. Du, G. Liu and L. Wang, *Nano Energy*, **24**, 94 (2016).

453. D. D. Sarma and C. N. R. Rao, *Journal of Electron Spectroscopy and Related Phenomena*, **20**, 25 (1980).

454. J. Jouve, Y. Belkacem and C. Severac, *Thin Solid Films*, **139**, 67 (1986).

455. R. Ohnishi, M. Katayama, K. Takanabe, J. Kubota and K. Domen, *Electrochimica Acta*, **55**, 5393 (2010).

456. M. Himmerlich, M. Koufaki, G. Ecke, C. Mauder, V. Cimalla, J. A. Schaefer, A. Kondilis, N. T. Pelekanos, M. Modreanu and S. Krischok, *ACS applied materials & interfaces*, **1**, 1451 (2009).

457. X. Yang, A. Wolcott, G. Wang, A. Sobo, R. C. Fitzmorris, F. Qian, J. Z. Zhang and Y. Li, *Nano Letters*, **9**, 2331 (2009).

458. Q. Liu, H. Lu, Z. Shi, F. Wu, J. Guo, K. Deng and L. Li, *ACS applied materials & interfaces*, **6**, 17200 (2014).

459. F. Su, T. Wang, R. Lv, J. Zhang, P. Zhang, J. Lu and J. Gong, *Nanoscale*, **5**, 9001 (2013).

460. Y. Yang, X.-j. Li, J.-t. Chen and L.-y. Wang, *Journal of Photochemistry and Photobiology A: Chemistry*, **163**, 517 (2004).

461. J. Luo, J. Chen, H. Wang and H. Liu, *Journal of Power Sources*, **303**, 287 (2016).

462. Y. Mi, L. Wen, R. Xu, Z. Wang, D. Cao, Y. Fang and Y. Lei, *Advanced Energy Materials* (2015).

463. R. H. Coridan, A. C. Nielander, S. A. Francis, M. T. McDowell, V. Dix, S. M. Chatman and N. S. Lewis, *Energy & Environmental Science*, **8**, 2886 (2015).

464. M. Rohloff, B. Anke, S. Zhang, U. Gernert, C. Scheu, M. Lerch and A. Fischer, *Sustainable Energy & Fuels*, **1**, 1830 (2017).

465. V. Kumaravel, S. Rhatigan, S. Mathew, M. C. Michel, J. Bartlett, M. Nolan, S. J. Hinder, A. Gascó, C. Ruiz-Palomar and D. Hermosilla, *Journal of Physics: Materials*, **3**, 025008 (2020).

466. W. Choi, A. Termin and M. R. Hoffmann, *The Journal of Physical Chemistry*, **98**, 13669 (2002).

467. M. Tahir, L. Pan, F. Idrees, X. Zhang, L. Wang, J.-J. Zou and Z. L. Wang, *Nano Energy* (2017).

468. J. Yang, J. Zheng, M. Xu, Z. Zhuo, W. Yang, L.-W. Wang, L. Dai, J. Lu, K. Amine and F. Pan, *ACS Catalysis* (2017).

469. M. Chauhan, K. P. Reddy, C. S. Gopinath and S. Deka, *ACS Catalysis*, **7**, 5871 (2017).

470. G. Liu, K. Wang, X. Gao, D. He and J. Li, *Electrochimica Acta*, **211**, 871 (2016).

471. M. Tahir, L. Pan, F. Idrees, X. Zhang, L. Wang, J.-J. Zou and Z. L. Wang, *Nano Energy*, **37**, 136 (2017).

472. J. Yang, J. Zheng, M. Xu, Z. Zhuo, W. Yang, L.-W. Wang, L. Dai, J. Lu, K. Amine and F. Pan, *ACS Catal.*, **8**, 466 (2017).

473. V. K. Puthiyapura, M. Mamlouk, S. Pasupathi, B. G. Pollet and K. Scott, *Journal of Power Sources*, **269**, 451 (2014).

474. J. Cheng, H. Zhang, H. Ma, H. Zhong and Y. Zou, *international journal of hydrogen energy*, **34**, 6609 (2009).

475. J.-J. Zhang, J.-M. Hu, J.-Q. Zhang and C.-N. Cao, *Int. J. Hydrogen Energy*, **36**, 5218 (2011).

476. J.-M. Hu, J.-Q. Zhang and C.-N. Cao, *International Journal of Hydrogen Energy*, **29**, 791 (2004).

477. K. Sardar, S. C. Ball, J. D. B. Sharman, D. Thompsett, J. M. Fisher, R. A. P. Smith, P. K. Biswas, M. R. Lees, R. J. Kashtiban and J. Sloan, *Chemistry of Materials*, **24**, 4192 (2012).

478. P. Lettenmeier, L. Wang, U. Golla-Schindler, P. Gazdzicki, N. A. Cañas, M. Handl, R. Hiesgen, S. S. Hosseiny, A. S. Gago and K. A. Friedrich, *Angew. Chem. Int. Ed.*, **55**, 742 (2016).

479. S. Xu, Y. Liu, J. Tong, W. Hu and Q. Xia, *Russian Journal of Electrochemistry*, **52**, 1021 (2016).

480. C. C. L. McCrory, S. Jung, I. M. Ferrer, S. M. Chatman, J. C. Peters and T. F. Jaramillo, *Journal of the American Chemical Society*, **137**, 4347 (2015).

481. J. Lim, D. Park, S. S. Jeon, C. W. Roh, J. Choi, D. Yoon, M. Park, H. Jung and H. Lee, *Advanced Functional Materials*, **28**, 1704796 (2018).

482. S. H. Ahn, H. Tan, M. Haensch, Y. Liu, L. A. Bendersky and T. P. Moffat, *Energy & Environmental Science*, **8**, 3557 (2015).

483. J. Park, Y. J. Sa, H. Baik, T. Kwon, S. H. Joo and K. Lee, *ACS nano*, **11**, 5500 (2017).

484. J. Feng, F. Lv, W. Zhang, P. Li, K. Wang, C. Yang, B. Wang, Y. Yang, J. Zhou and F. Lin, *Advanced Materials*, **29**, 1703798 (2017).

485. J. L. Corona-Guinto, L. Cardeño-García, D. C. Martínez-Casillas, J. M. Sandoval-Pineda, P. Tamayo-Meza, R. Silva-Casarin and R. G. González-Huerta, *International Journal of Hydrogen Energy*, **38**, 12667 (2013).

486. L. C. Seitz, C. F. Dickens, K. Nishio, Y. Hikita, J. Montoya, A. Doyle, C. Kirk, A. Vojvodic, H. Y. Hwang and J. K. Norskov, *Science*, **353**, 1011 (2016).

487. Q. Shi, C. Zhu, D. Du, J. Wang, H. Xia, M. H. Engelhard, S. Feng and Y. Lin, *Journal of Materials Chemistry A*, **6**, 8855 (2018).

488. Y. Pi, Q. Shao, P. Wang, J. Guo and X. Huang, *Advanced Functional Materials*, **27**, 1700886 (2017).

489. S. Ganguli, S. Das, S. Kumari, H. R. Inta, A. K. Tiwari and V. Mahalingam, *ACS Omega*, **3**, 9066 (2018).

490. Z. Zhang, D. Zhou, X. Bao, G. Huang and B. Huang, *International Journal of Hydrogen Energy*, **44**, 2877 (2019).

491. L. Zhao, Q. Cao, A. Wang, J. Duan, W. Zhou, Y. Sang and H. Liu, *Nano Energy*, **45**, 118 (2018).

492. M. J. Kirshenbaum, M. H. Richter and M. Dasog, *ChemCatChem*, **11**, 1 (2018).

493. W. Q. Zaman, W. Sun, Z.-h. Zhou, Y. Wu, L. Cao and J. Yang, *ACS Applied Energy Materials*, **1**, 6374 (2018).

494. W. Q. Zaman, Z. Wang, W. Sun, Z. Zhou, M. Tariq, L. Cao, X.-Q. Gong and J. Yang, *ACS Energy Letters*, **2**, 2786 (2017).

495. V. D. Mote, Y. Purushotham and B. N. Dole, *Journal of Theoretical and Applied Physics*, **6**, 6 (2012).

496. T. H. De Keijser, J. I. Langford, E. J. Mittemeijer and A. B. P. Vogels, *Journal of Applied Crystallography*, **15**, 308 (1982).

497. Y. Nakamura, K. Oguro, I. Uehara and E. Akiba, *Journal of alloys and compounds*, **298**, 138 (2000).

498. G. K. Williamson and W. H. Hall, *Acta metallurgica*, **1**, 22 (1953).

499. O. B. Bembalge and S. K. Panigrahi, *Metallurgical and Materials Transactions A*, **50**, 4288 (2019).

500. P. M. Shanthi, P. J. Hanumantha, B. Gattu, M. Sweeney, M. K. Datta and P. N. Kumta, *Electrochimica Acta*, **229**, 208 (2017).

501. Y.-T. Kim, P. P. Lopes, S.-A. Park, A. Y. Lee, J. Lim, H. Lee, S. Back, Y. Jung, N. Danilovic and V. Stamenkovic, *Nature communications*, **8**, 1449 (2017).

502. Y. Yang, H. Yao, Z. Yu, S. M. Islam, H. He, M. Yuan, Y. Yue, K. Xu, W. Hao and G. Sun, *Journal of the American Chemical Society*, **141**, 10417 (2019).

503. S. F. Chini and A. Amirfazli, *Colloids and Surfaces A: Physicochemical and Engineering Aspects*, **388**, 29 (2011).

504. E. J. Popczun, J. R. McKone, C. G. Read, A. J. Biacchi, A. M. Wiltrout, N. S. Lewis and R. E. Schaak, *Journal of the American Chemical Society*, **135**, 9267 (2013).

505. Y. Xu, R. Wu, J. Zhang, Y. Shi and B. Zhang, *Chemical Communications*, **49**, 6656 (2013).

506. W. F. Chen, C. H. Wang, K. Sasaki, N. Marinkovic, W. Xu, J. T. Muckerman, Y. Zhu and R. R. Adzic, *Energy & Environmental Science*, **6**, 943 (2013).

507. J. Xie, J. Zhang, S. Li, F. Grote, X. Zhang, H. Zhang, R. Wang, Y. Lei, B. Pan and Y. Xie, *Journal of the American Chemical Society*, **135**, 17881 (2013).

508. D. Kong, H. Wang, Z. Lu and Y. Cui, *Journal of the American Chemical Society*, **136**, 4897 (2014).

509. H. Vrubel, D. Merki and X. Hu, *Energy & Environmental Science*, **5**, 6136 (2012).

510. D. Merki, S. Fierro, H. Vrubel and X. Hu, *Chemical Science*, **2**, 1262 (2011).

511. J. Xie, H. Zhang, S. Li, R. Wang, X. Sun, M. Zhou, J. Zhou, X. W. Lou and Y. Xie, *Advanced Materials*, **25**, 5807 (2013).

512. Z. Chen, D. Cummins, B. N. Reinecke, E. Clark, M. K. Sunkara and T. F. Jaramillo, *Nano Letters*, **11**, 4168 (2011).

513. M. A. Lukowski, A. S. Daniel, F. Meng, A. Forticaux, L. Li and S. Jin, *Journal of the American Chemical Society*, **135**, 10274 (2013).

514. L. Liao, S. Wang, J. Xiao, X. Bian, Y. Zhang, M. D. Scanlon, X. Hu, Y. Tang, B. Liu and H. H. Girault, *Energy & Environmental Science*, **7**, 387 (2014).

515. W.-F. Chen, K. Sasaki, C. Ma, A. I. Frenkel, N. Marinkovic, J. T. Muckerman, Y. Zhu and R. R. Adzic, *Angewandte Chemie International Edition*, **51**, 6131 (2012).

516. Y.-F. Xu, M.-R. Gao, Y.-R. Zheng, J. Jiang and S.-H. Yu, *Angewandte Chemie International Edition*, **52**, 8546 (2013).

517. D. Voiry, H. Yamaguchi, J. Li, R. Silva, D. C. B. Alves, T. Fujita, M. Chen, T. Asefa, V. B. Shenoy, G. Eda and M. Chhowalla, *Nat Mater*, **12**, 850 (2013).

518. J. Yang, D. Voiry, S. J. Ahn, D. Kang, A. Y. Kim, M. Chhowalla and H. S. Shin, *Angewandte Chemie International Edition*, **52**, 13751 (2013).

519. X. Zou, X. Huang, A. Goswami, R. Silva, B. R. Sathe, E. Mikmeková and T. Asefa, *Angewandte Chemie International Edition*, **53**, 4372 (2014).

520. H. Vrubel and X. Hu, *Angewandte Chemie International Edition*, **51**, 12703 (2012).

521. L. Feng, H. Vrubel, M. Bensimon and X. Hu, *Physical Chemistry Chemical Physics*, **16**, 5917 (2014).

522. Y. Li, H. Wang, L. Xie, Y. Liang, G. Hong and H. Dai, *Journal of the American Chemical Society*, **133**, 7296 (2011).

523. J. M. McEnaney, J. Chance Crompton, J. F. Callejas, E. J. Popczun, C. G. Read, N. S. Lewis and R. E. Schaak, *Chemical Communications*, **50**, 11026 (2014).

524. E. J. Popczun, C. G. Read, C. W. Roske, N. S. Lewis and R. E. Schaak, *Angewandte Chemie International Edition*, **53**, 5427 (2014).

525. H. Yan, C. Tian, L. Wang, A. Wu, M. Meng, L. Zhao and H. Fu, *Angewandte Chemie*, **127**, 6423 (2015).

526. J. Tian, Q. Liu, N. Cheng, A. M. Asiri and X. Sun, *Angewandte Chemie International Edition*, **53**, 9577 (2014).

527. J. R. McKone, B. F. Sadtler, C. A. Werlang, N. S. Lewis and H. B. Gray, *ACS Catalysis*, **3**, 166 (2012).

528. B. Cao, G. M. Veith, J. C. Neuefeind, R. R. Adzic and P. G. Khalifah, *Journal of the American Chemical Society*, **135**, 19186 (2013).

529. S. J. Aravind, K. Ramanujachary, A. Mugweru and T. D. Vaden, *Applied Catalysis A: General*, **490**, 101 (2015).

530. J. Tian, Q. Liu, N. Cheng, A. M. Asiri and X. Sun, *Angewandte Chemie International Edition*, **53**, 9577 (2014).

531. F. H. Saadi, A. I. Carim, E. Verlage, J. C. Hemminger, N. S. Lewis and M. P. Soriaga, *The Journal of Physical Chemistry C*, **118**, 29294 (2014).

532. J. Kibsgaard and T. F. Jaramillo, *Angewandte Chemie International Edition*, **53**, 14433 (2014).

533. Z. Xing, Q. Liu, A. M. Asiri and X. Sun, *ACS Catalysis*, **5**, 145 (2014).

534. E. J. Popczun, C. W. Roske, C. G. Read, J. C. Crompton, J. M. McEnaney, J. F. Callejas, N. S. Lewis and R. E. Schaak, *Journal of Materials Chemistry A*, **3**, 5420 (2015).

535. B. AlOtaibi, H. P. T. Nguyen, S. Zhao, M. G. Kibria, S. Fan and Z. Mi, *Nano Letters*, **13**, 4356 (2013).

536. M. Chen and R. E. Blankenship, *Trends in Plant Science*, **16**, 427 (2011).

537. P. P. Patel, P. J. Hanumantha, M. K. Datta, O. I. Velikokhatnyi, D. Hong, J. A. Poston, A. Manivannan and P. N. Kumta, *International Journal of Hydrogen Energy*, **42**, 17049 (2017).

538. E. LarssoN, *Ark. Kemi*, **23**, 335 (1965).

539. J. Zhang, Z. Zhao, Z. Xia and L. Dai, *Nature nanotechnology*, **10**, 444 (2015).

540. P. E. Blöchl, *Physical review B*, **50**, 17953 (1994).

541. W. Hu, Y. Wang, X. Hu, Y. Zhou and S. Chen, *Journal of Materials Chemistry*, **22**, 6010 (2012).

542. A. Korotcov, R.-S. Chen, H.-P. Hsu, Y.-S. Huang, D.-S. Tsai and K.-K. Tiong, *Journal of Nanomaterials*, **2007** (2007).

543. E. Bekaert, J. Bernardi, S. Boyanov, L. Monconduit, M. L. Doublet and M. Ménétrier, *The Journal of Physical Chemistry C*, **112**, 20481 (2008).